

J.-M. Lourtioz · H. Benisty · V. Berger
J.-M. Gérard · D. Maystre · A. Tchelnokov

Photonic Crystals

Towards Nanoscale Photonic Devices

Translated by Pierre-Noel Favennec

With 128 Figures



Authors

Jean-Michel Lourtioz
Université Paris-Sud
Institut d'Electronique Fondamentale
91405 Orsay Cedex, France

Henri Benisty
Institut d'Optique
Laboratoire Charles Fabry
Centre Scientifique d'Orsay
91403 Orsay Cedex, France

Vincent Berger
Université Paris VII – Denis Diderot
Matériaux et Phénomènes Quantiques
2 place Jussieu
75251 Paris Cedex 05, France

Jean-Michel Gérard
CNRS-CEA
Laboratoire de Nanophysique et Semiconducteurs
17 rue des Martyrs
38054 Grenoble Cedex 9, France

Daniel Maystre
Institut Fresnel
Faculté des Sciences et Techniques de Saint Jérôme
Ave. Escadrille Normandie-Niemen
13397 Marseille Cedex 20, France

Alexis Tchelnokov
CEA-LETI
17 rue des Martyrs
38054 Grenoble Cedex 9, France

ISBN-10 3-540-24431-X Springer Berlin Heidelberg New York
ISBN-13 978-3-540-24431-8 Springer Berlin Heidelberg New York

Library of Congress Control Number: 2005922825

This work is subject to copyright. All rights are reserved, whether the whole or part of the material is concerned, specifically the rights of translation, reprinting, reuse of illustrations, recitation, broadcasting, reproduction on microfilm or in other ways, and storage in data banks. Duplication of this publication or parts thereof is permitted only under the provisions of the German Copyright Law of September 9, 1965, in its current version, and permission for use must always be obtained from Springer-Verlag. Violations are liable to prosecution under German Copyright Law.

Springer is a part of Springer Science+Business Media

springeronline.com

© Springer-Verlag Berlin Heidelberg 2005
Originally published in French by Hermès Science, France, 2003.
Printed in Germany

The use of general descriptive names, registered names, trademarks, etc. in this publication does not imply, even in the absence of a specific statement, that such names are exempt from the relevant protective laws and regulations and therefore free for general use.

Typesetting: Data conversion by the author.
Final processing by PTP-Berlin Protago-TeX-Production GmbH, Germany
Cover-Design: deblik, Berlin
Printed on acid-free paper 62/3141/Yu - 5 4 3 2 1 0

Foreword

The Analogy between electronic Waves and electromagnetic Waves

Since the advent of quantum mechanics and the clear demonstration of the existence of 'matter waves', physicists have never failed to take advantage of concepts and theoretical methods developed in the fields of optics and electromagnetism. Thus, a number of phenomena in solid state physics are commonly interpreted by analysing electronic excitations in terms of electronic waves. By contrast, the opposite situation has rarely occurred, and only on a few occasions have optics and electromagnetism borrowed concepts and theoretical methods from solid state physics. From this point of view, the emergence of photonic bandgap materials and photonic crystals at the end of the 1980s can be seen as a revenge to the benefit this time of optics and electromagnetism. In the same way as the periodicity of solid state crystals determines the energy bands and the conduction properties of electrons, the periodical structuring of optical materials at wavelength scales has turned out to be main viable approach towards the control of the energies and of the fluxes of photons occurring in these materials.

The analogy between electronic waves and electromagnetic waves is a mere consequence of the formal relation between the Schrödinger's equation for electronic wavefunctions and Maxwell equations for electromagnetic waves. Indeed, leaving aside the spins of the particles, an harmonic electromagnetic wave in a dielectric lossless medium satisfies Eq. 1.a, which formally is analogous to the equation ruling the wave function for an electron with mass m in a potential V (Eq. 1.b) :

$$\nabla \times [\nabla \times \mathbf{E}(\mathbf{r})] = \frac{\omega^2}{c^2} \epsilon_r(\mathbf{r}) \mathbf{E}(\mathbf{r}) \quad (1.a)$$

$$\nabla^2 \Psi(\mathbf{r}) = -\frac{2m}{\hbar^2} (E - V(\mathbf{r})) \Psi(\mathbf{r}) \quad (1.b)$$

The spin difference between the photons, which are bosons, and the electrons, which are fermions, results in different statistics for the energy state populations, as well as in the different nature of these two equations: indeed, the equation for

photons is vectorial whereas the equation for electrons is scalar. We shall return later to the resolution of Eq. 1.a, which applies here to the electric field \mathbf{E} . A brief comparison between this equation and Eq. 1.b shows that the relative dielectric permittivity $\epsilon_r(\mathbf{r})$ (the square of the refractive index n) is for photons the analogue of the potential V for electrons. In analogy with the electronic band gaps of semiconductors, it then becomes intuitive that a periodic variation of $\epsilon_r(\mathbf{r})$ may result in the formation of photonic band gaps. In other terms, for a certain range of frequencies, or equivalently of wavelengths, light cannot propagate in the dielectric, whatever its polarisation and direction of propagation are. Remaining within the assumption of a lossless dielectric, a light beam incident on this material will be totally reflected.

Of course, the analogy between electronic waves and electromagnetic waves is not restricted to the concept of energy gap. This can be shown by considering the simple system formed by a planar waveguide consisting of a high-permittivity (ϵ_1) layer sandwiched between two semi-infinite cladding layers with lower permittivity ($\epsilon_2 < \epsilon_1$). Such a system is but the analogue of a potential well V_1 sandwiched between two potential barriers ($V_2 > V_1$). Assuming the propagation constant of light to be larger than $\epsilon_2 \omega/c$ in the plane of the waveguide, guided propagation modes occur at discrete frequencies, in much the same way as electronic levels may exist at discrete energies in the potential well. A transverse distribution of the light intensity ($\alpha|\mathbf{E}|^2$) is associated with each guided mode, owing to the fact that the presence of an electron along the transverse axis is characterised by a probability ($\alpha|\psi|^2$).

Photonic Bandgap Materials or Photonic Crystals?

In view of the preceding introduction, the reader might gather the impression that photonic bandgap material and photonic crystal are two terms which can be indifferently used for the same structures. This is not the case however, since the term photonic crystal actually applies to any periodic dielectric or metallic structure irrespective of the presence of a photonic band gap in this structure. Further, the very concept of a photonic band gap originally emerged with the desire of achieving a complete control of the spontaneous emission and, ultimately, of designing single-mode microcavities. However, since the pioneering works which had been carried out during the 1990s, the interest in photonic band gaps is no longer restricted to omnidirectional photonic bandgap structures, and the very concept of a photonic crystal has ‘exploded’.

It is quite clear that the search for a complete three-dimensional photonic band gap still remains an actual problem. The problem consists in finding the most appropriate cavity structure for solid state microsources with a number of individual emitters as small as possible, possibly a single emitter. The three-dimensional photonic crystal microcavity is a promising candidate which could address this challenge. However, technological difficulties cannot be overlooked, and it is now recognised within the scientific community that there is a long way before the

original three-dimensional microwave experiments conducted by E. Yablonovitch *et al* can be reproduced at near-infrared and visible wavelengths¹. For this reason, efforts have shifted for the most part from the consideration of three-dimensional photonic crystals to that of two-dimensional photonic crystals, with the underlying idea that two-dimensional photonic band gaps and photonic crystals could develop into a direct continuation of planar integrated optics, with the tremendous advantage however of allowing the realisation of optical devices much more compact (wavelength-scaled) than currently existing devices. Fortunately enough, this idea has coincided with the tremendous growth of 1.3-1.5 μm telecommunication systems which requires the development of an 'optical circuitry' capable of simultaneously analysing an ever increasing number of optical signals, both in fibre and in planar substrate configurations. Indeed, the recent developments of photonic band gaps and photonic crystals in the years extending between the end of the 20th century and the beginning of the 21st century have benefited from the strong demand for innovative devices and systems in optical communications.

In the last decade, considerable advances have been achieved concerning the theoretical understanding, the technical fabrication and the experimental characterisation of photonic crystals. Not only has the concept of a photonic crystal been extended from three-dimensional structures to one and two-dimensional structures, but the guiding, dispersion and refraction properties of periodic structures have also been considered anew in the light of these developments, with the same attention as the properties of photonic band gaps themselves. Giant dispersion effects, including superprism as well as negative refraction effects have thus been demonstrated. Periodic metallic structures have also been revisited in the continuity of the pioneering works on artificial dielectrics conducted during the 1950s, revealing new potentialities for microwave antennas, for terahertz circuits and for the control of plasmon waves at optical wavelengths. Photonic crystals have also made their way into the world of nonlinear optics, where they are likely to open new perspectives for frequency conversion or for the generation of harmonic waves. In this context, we shall see that periodic ensembles of materials for nonlinear optics do not necessarily involve photonic band gap effects.

The study of the physical and optical properties of photonic crystals has generated a burst of new ideas for optical devices and systems. Special mention needs to be made here of photonic crystal silica fibres, which are likely to become in the near future the first application of photonic crystals to the real world of optical communications.

In the field of semiconductors and metals, the fabrication of photonic crystals has represented an important challenge for micro- and nanotechnology. In turn, these technologies have benefited from the validation of processes which have thus been completed. In this respect, the evolution of photonics has paralleled the revolution which has been taking place in the field of electronics with the devel-

¹ Yablonovitch E., Gmitter T.J., Leung K.M. *Photonic band structures: the face-centered-cubic case employing non-spherical atoms*, *Phys. Rev. Lett.* 67, p. 2295, 1991

opment of nanotransistors and quantum dot memories. Nanophotonics are now being recognised as a special branch of optics, in much the same way as nanoelectronics form a special branch of electronics. As will be seen in this book, some of the technological problems which had appeared at the time of the first studies on photonic crystals, are currently in the process of being solved. However, it should be stressed that the future development of photonic crystals is definitively dependent on the degree of accuracy which can be achieved in the fabrication of micro- and nanostructures.

Basic One, Two and Three-Dimensional Structures

In the following chapters, the reader will explore the large variety of photonic structures which have been either imagined or fabricated in the world of photonic crystals. However, some among these structures are quite emblematic, and as such they will be systematically used as references throughout this book. It seems therefore useful to acquire a familiarity with these structures. They are represented here in Fig. 1, where they are ordered from the simplest to the most complex.

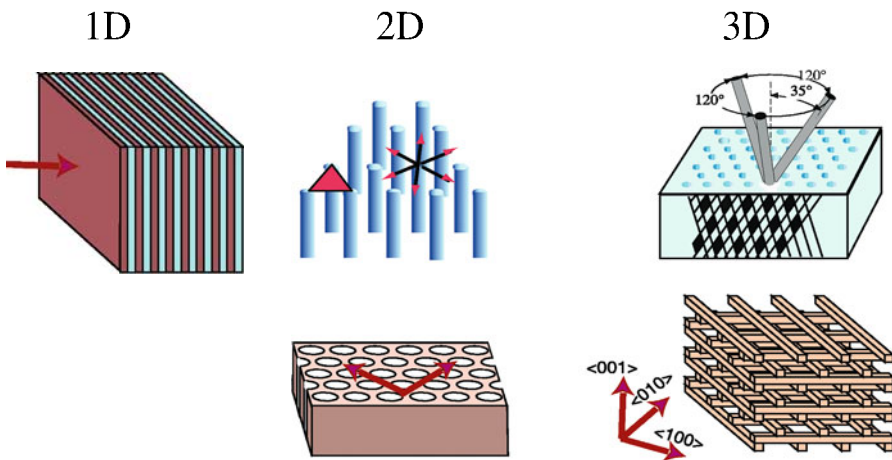


Fig. 1. Emblematic photonic crystals. *From left to right:* One-dimensional structure: Bragg mirror. Two-dimensional structures: hexagonal lattices formed by rods or pores. Three-dimensional structures: 'yablonovite' and 'wodpile' structures

As is the case in reference textbooks on solid state physics², one-dimensional structures are commonly used as reference models, more particularly for understanding the formation of energy band diagrams. In the field of optics, one-dimensional photonic crystals consisting of periodic stacks of thin dielectric layers with a $\lambda/4$ optical thickness are actually nothing else than Bragg mirrors (Fig. 1, left). Contrary to one-dimensional solid state crystals, these structures are not artificial and they are actually used in a variety of optical devices. The fabrication of monolithic Bragg mirrors from III-V semiconductors has reached maturity at the end of the 1980s. The first experiments on optoelectronic devices based on the use of planar microcavities were reported at near-infrared wavelengths during the same period. However, the efficiency of Bragg mirrors is strongly dependent on the angle of incidence with respect to the normal to the dielectric layers. When the incidence angle is progressively increased, the reflectivity decreases and the mirror tends to become transparent in the end. Under these conditions, it turns out impossible to achieve an omnidirectional photonic band gap.

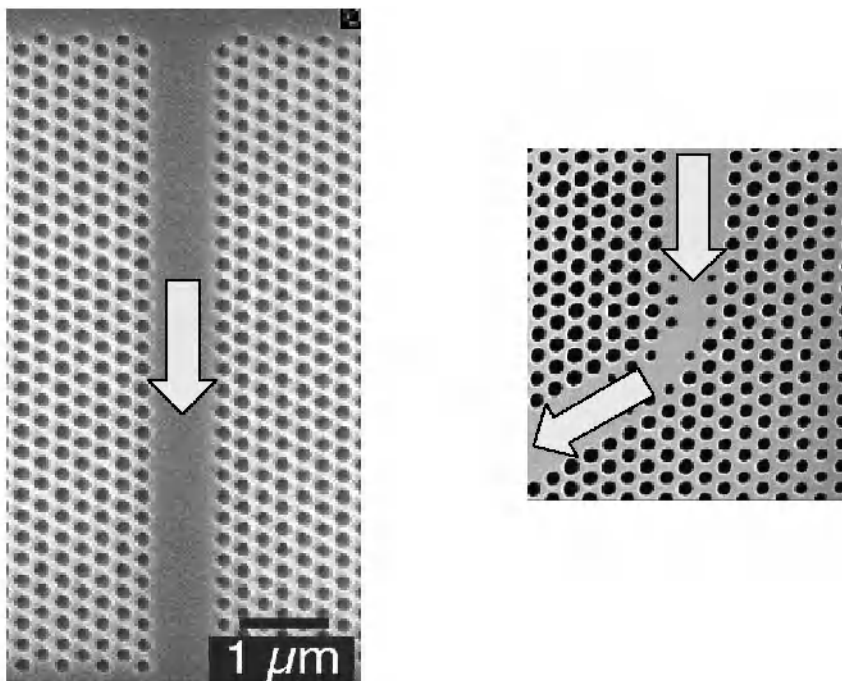


Fig. 2. Channel optical waveguide (*left*) and light bend (*right*) fabricated in a two-dimensional photonic crystal

² Kittel C. *Introduction to Solid State Physics*, J. Wiley & Sons, 1971

While two-dimensional photonic crystals are more difficult to fabricate than one-dimensional crystals, they nevertheless remain of a moderate complexity (Fig. 1, *middle*). The interest in these structures originates in their potential applications to planar integrated optics and to 'photonic circuitry'. Basically, two different types of such structures exist: the first one consists of disconnected dielectric cylinders (Fig. 1, *middle top*) while the other is formed by air pores drilled in a dielectric matrix (Fig. 1, *middle bottom*). If the in-plane confinement of light could be achieved in a thin slab of such a photonic crystal, the propagation of light could then be totally controlled along two directions. This is illustrated in Fig. 2, which shows how to obtain either a channel waveguide or a light bend by removing a series of patterns from a two-dimensional photonic crystal. This leads to the possibility of envisioning planar photonic circuits that would be analogous to electronic circuits fabricated on silicon wafers. We shall later see that the main problem in this context is actually to prevent the light from escaping out of the plane, i.e. out of the dielectric slab. This issue has been addressed in a number of studies. Theoretical investigations often remain complex due to both the finite thickness of the crystal slab and to the local disruptions of the periodicity of the crystal.

Actually, only three-dimensional photonic crystals really allow for omnidirectional photonic band gaps. The last decade has been marked by two main types of structures, represented in the right-hand part of Fig. 1. The so-called yablonovite (Fig. 1, *top right*) was promoted by the famous experiments conducted by Eli Yablonovitch and his group in 1991 (Yablonovitch 1991). Indeed, the fabrication of the first prototype at centimetre scales and the subsequent demonstration of a complete photonic band gap around 12 GHz aroused tremendous interest in photonic crystals within the scientific community. The second emblematic three-dimensional photonic crystal (Fig. 1, *bottom right*), which is referred to either as a 'woodpile' or 'layer-by-layer' structure, consists of a multilayer stack where each layer is formed by a one-dimensional array of dielectric rods. Existing methods of fabrication, i.e. those used in semiconductor technology, can be applied successfully for the realisation of such structures. Actually, both the yablonovite and the woodpile photonic crystals present the same crystalline structure as diamond or silicon. Indeed, in the first case, the periodic array of pores drilled in the dielectric matrix with an angle of 120° between one another reproduces the empty <110> galleries of the face centred cubic (fcc) lattice with two atoms per cell. In the second case, the intersections between the dielectric rods are organised into two fcc lattices in the same way as carbon atoms are in the diamond crystal. In practice, the similarity with solid state crystals can be neglected, and photonic structures can be considered as specific instances of two or three-dimensional diffraction gratings. This more traditional optical approach can be quite useful and it will therefore be adopted at various points of this book.

Objectives of this Book

The growing interest for photonic crystals has generated an extensive literature on this subject. The interested reader is invited to consult websites which, like for instance <http://home.earthlink.net/~jpdowling/pbgbib.html>, still try to maintain an exhaustive bibliography. Contrary to the valuable books which have already been published on this subject, this book does not intend only at describing ideal photonic structures with infinite dimensions in all directions of space, but rather aims at going from photonic crystals to the realisation of actual optical devices, and beyond to the development of a photonic circuitry. In this respect, the confinement of light in a ‘photonic cage’ can be viewed as a first step towards the design of optical devices at the wavelength scale with ultimate properties for storing, filtering, guiding and emitting light. It is also part of a tendency towards the extreme miniaturisation of devices and systems, which is made necessary by the manipulation of an ever increasing number of data.

From a more academic point of view, the study of photonic crystals has been, (and it still remains) a unique opportunity of bringing together a large diversity of skills from such different fields as solid state physics, optics, microwaves and microelectronics. During the last years, the ‘Groupe de Recherche’ (GDR) organised by the CNRS on ‘Microcavities and Photonic Crystals’ has been the French example of such a cooperation between researchers from these different fields. The present book can also be seen as the result of this cooperation.

The six authors, coming from different scientific fields, have joined efforts to provide students and researchers with the necessary theoretical background on photonic crystals and their optical properties, while at the same time presenting a large variety of optical and microwave devices to which photonic crystals can be applied.

The book is divided into three parts which can be independently approached. In the first part, the reader will become familiar with photonic band diagrams and theoretical models for both infinite and finite photonic crystals. We address the problem of analysing the presence of local disruptions in the periodicity of photonic crystals, which are also referred to as crystal defects in analogy with solid state physics. We shall finally consider different issues related to quasi-crystals as well as the main specificities of periodic metallic structures.

The second part of this book is devoted to the specific properties of photonic structures in terms of optical confinement, guiding, ultra-refraction and frequency conversion. Novel concepts of mirrors, waveguides and optical resonators based on photonic crystals will then be discussed. A particular attention shall be devoted to the problem of a solid state emitter in a microcavity and to the control of its spontaneous emission, which still remains one of the major problems in nanophotonics. A detailed bibliography, covering all topics addressed in this book, will allow the reader to delve deeper in the subject, and should provide him with a precise idea of the most recent advances in research.

The last part of the book will be devoted to a review of the potential applications of photonic crystals and of the different methods which have been developed

for their fabrication and their characterisation. We shall successively consider semiconductor devices in planar integrated optics, light microsources and photonic crystal fibres. The potential applications of photonic crystals to microwave and THz devices and antennas will also be presented in order to complete this review and to show the many common aspects shared by optics and microwaves. In most cases, photonic crystals will be compared to other technical solutions implemented in existing devices. Finally, a specific chapter will be devoted to three-dimensional photonic crystals in optics. While these crystals are more futuristic due to the difficulty of fabricating them, they nonetheless are a possible prefiguration of what could be three-dimensional optoelectronics.

Jean-Michel Lourtioz

Table of Contents

Foreword	V
Part I Theoretical Models for Photonic Crystals	1
Introduction to Part I.....	3
1 Models for Infinite Crystals.....	5
1.1 Plane Wave Expansion.....	5
1.1.1 Maxwell's Equations	5
1.1.2 The Floquet-Bloch Theorem	6
1.1.3 Hermiticity of the Field Operator.....	10
1.1.4 Simple Examples of Bloch Functions.....	11
1.1.5 General Plane Wave Method	13
1.2 Other Methods for the Calculation of the Photonic Band Gaps of an Infinite Crystal: the KKR Method	21
1.3 Photonic Band Diagram	21
1.3.1 The Irreducible Brillouin Zone	22
1.3.2 Band Diagrams of One-Dimensional Crystals	25
1.3.3 Band Diagrams of Two-Dimensional Photonic Crystals.....	33
1.3.4 Off-Axis Propagation in One and Two-Dimensional Photonic Crystals.....	40
1.3.5 Band Diagrams of Three-Dimensional Photonic Crystals.....	41
1.4 Infinite Crystals with Defects	43
1.4.1 Point Defects.....	44
1.4.2 Coupling of Point Defects	50
1.4.3 Supercell Method.....	52
1.4.4 Methods derived from Tight-Binding Methods in Solid-State Physics.....	53
1.4.5 Extended Defects	54
1.4.6 Semi-Infinite Crystals and Surface Defects.....	56
1.4.7 Density of States in Photonic Crystals with or without Defects.....	59
2.2 Models for Finite Crystals.....	63
2.1 Transfer, Reflection and Transmission Matrix Formulations.....	63
2.1.1 Reflection and Transmission Matrices	64
2.1.2 Pendry Method.....	70

2.2 Finite Difference in Time Domain (FDTD) Method	78
2.2.1 Numerical Formulation of Maxwell's Equations.....	78
2.2.2 Case of an Incident Pulse	82
2.2.3 Absorption Region and Boundary Conditions	84
2.2.4 Practical Implementation and Convergence of the FDTD Method	85
2.2.5 Examples of Results obtained with the FDTD for a Point Source Method	87
2.3 Scattering Matrix Method	89
2.4 Other Methods: Integral and Differential Methods, Finite Element Method, Effective Medium Theory	98
2.5 Numerical Codes available for the Modelling of Photonic Crystals.....	102
3 Quasi-Crystals and Archimedean Tilings.....	105
3.1 Photonic Quasi-Crystals.....	106
3.2 Archimedean Tilings.....	110
3.3 From Photonic Quasi-Crystals to the Localisation of Light.....	113
4 Specific Features of Metallic Structures	119
4.1 Bulk Metals: Drude Model, Skin Effect and Metallic Losses.....	119
4.1.1 Drude Model.....	121
4.1.2 Low-Frequency Region: Skin Effect and Metallic Losses	122
4.1.2 From the Infrared to the Visible and UV Regions	123
4.2 Periodic Metallic Structures at Low Frequencies	124
4.2.1 Plasmon-Like Photonic Band Gaps	124
4.2.2 Transmission Spectra of Metallic and Dielectric Photonic Crystals	127
4.2.3. Complete Band Gaps in Metallic Photonic Crystals.....	129
4.2.4. Structures with Continuous Metallic Elements and Structures with Discontinuous Metallic Elements	130
4.3 Periodic Metallic Structures at Optical Frequencies. Idealised Case of a Dispersive Lossless Dielectric	132
4.4 Surface Waves.....	135
4.4.1 Surface Plasmons at a Metal/Dielectric Plane Interface	135
4.4.2 Propagation of Surface Plasmons along a Periodically Modulated Metal/Dielectric Interface and Local Enhancement of the Field	138
4.4.3 Wood's Anomalies: Phenomenological Theory	142
4.4.4 Photonic Band Gaps for the Propagation of Surface Plasmons at Periodically Modulated Metal/Dielectric Interfaces	146
4.4.5 The Photon Sieve.....	148
4.4.6 Surface Waves in Metals at Radiofrequencies	149
Part II Optical Properties of Photonic Crystals.....	155
Introduction to Part II. The Many 'Facets' of Photonic Crystals	157

5 Control of Electromagnetic Waves	161
5.1 The Photonic Crystal Mirror	161
5.1.1 The Semi-Infinite Photonic Crystal: Mirror or Diffraction Grating? ..	161
5.1.2 Specular Reflection at a Semi-Infinite Crystal	164
5.1.3 Finite Photonic Crystals as Semi-Transparent Mirrors	165
5.2 Photonic Crystal Waveguides	166
5.2.1 Index Guiding and Photonic-Bandgap Guiding	166
5.2.2 Three-Dimensional Photonic Crystal Waveguides	168
5.2.3 Two-Dimensional Photonic Crystal Waveguides	170
5.2.4 Density of States and Multiplicity of Guided Modes	173
5.2.5 Coexistence of Index Guiding and Photonic Bandgap Guiding	175
5.3 Resonators	182
5.3.1 Localised Modes. Origin of Losses	182
5.3.2 Density of States	183
5.3.3 Waveguide formed by Coupled Cavities	184
5.4 Hybrid Structures with Index Guiding. The Light Line	186
5.4.1 Light Cone of a Uniform Waveguide	187
5.4.2 Fictitious Periodicity	187
5.4.3 True One-Dimensional Periodicity	189
5.4.4 Channel Waveguides in Two-Dimensional Photonic Crystals	191
6 Refractive Properties	193
6.1 Phase Refractive index, Group Refractive Index and Energy Propagation	193
6.1.1 Phase Velocity and Group Velocity	193
6.1.2 Refractive Indexes and Dispersion Diagrams	196
6.1.3 Effective Phase Index and Group Refractive Index	197
6.2 Refraction of Waves at the Interface between a Periodic Medium and a Homogeneous Medium	199
6.2.1 Summary of Refraction Laws in Homogeneous Media	199
6.2.2 Some Well-Known Anisotropic Media: Birefringent Solid State Crystals	199
6.2.3 Construction of Transmitted Waves in a Photonic Crystal	201
6.3 Superprism and Ultra-Refraction Effects	202
6.3.1 The Superprism Effect	202
6.3.2 Ultra-Refraction	203
6.4 Metamaterials	204
6.4.1 Simultaneous Control of the Dielectric Permittivity and of the Magnetic Permeability	205
6.4.2 Fabrication of Negative Refractive Index Metamaterials at Centimeter Wavelengths	206
7 Confinement of Light in Zero-Dimensional Microcavities	211
7.1 Microcavity Sources. Principles and Effects	212
7.1.1 A Classical Effect: the Angular Redistribution of the Spontaneous Emission and the Example of Planar Microcavities	212

7.1.2. Spontaneous Emission Dynamics in Microcavities	216
7.2 Three-Dimensional Optical Confinement in Zero-Dimensional Microcavities	230
7.2.1. Different Types of Zero-Dimensional Microcavities.....	230
7.2.2 Control of the Spontaneous Emission in Weak Coupling Regime. Some Experimental Results	234
7.2.3 Single-Mode Coupling of the Spontaneous Emission	238
7.2.4 Towards Strong Coupling Regime for Solid State ‘Artificial Atoms’.....	240
8 Frequency Conversion.....	243
8.1 The Problem of Phase-Matching	244
8.2 $\chi^{(1)}$ Photonic Crystals	246
8.2.1 One-Dimensional $\chi^{(1)}$ Photonic Crystals	246
8.2.2 Two-Dimensional $\chi^{(1)}$ Photonic Crystals.....	254
8.3 $\chi^{(2)}$ Photonic Crystals	254
8.3.1 One-Dimensional $\chi^{(2)}$ Photonic Crystals	254
8.3.2 Two-Dimensional $\chi^{(2)}$ Photonic Crystals.....	257
Part III Fabrication, Characterisation and Applications of Photonic Band Gap Structure	261
Introduction to Part III	263
9 Planar Integrated Optics.....	265
9.1 Objectives, New Devices and Challenges.....	265
9.2 Fundamentals of Integrated Optics and Introduction of Photonic Crystals	268
9.2.1 Conventional Waveguides	268
9.2.2 Photonic Crystals in Integrated Optics	272
9.3 Buried Waveguides	278
9.3.1 DFB and DBR Laser Diode Structures	278
9.3.2 Photonic Crystals, a Strong Perturbation for Guided Modes	279
9.3.3 Choice of the Diameter of the Holes and of the Period of the Crystal	280
9.3.4 Specific Parameters for InP- and GaAs-Based Systems.....	281
9.3.5 Deep Etching	282
9.4 Membrane Waveguide Photonic Crystals.....	283
9.4.1 Free-Standing Membranes	283
9.4.2 Reported Membranes	285
9.5 Macroporous Silicon Photonic Substrates.....	286
9.6 Characterisation Methods for Photonic Crystals in Integrated Optics.....	289
9.6.1 Internal Light Source Method.....	289

9.6.2 End-Fire Method.....	292
9.6.3 Wideband Transmission-Reflection Spectroscopy	294
9.7 Losses of Photonic Crystal Integrated Optical Devices.....	295
9.7.1 Analysis of the Losses.....	295
9.7.2 Measurement of Propagation Losses in Straight Photonic Crystal Waveguides	296
9.7.3 Waveguide Bends in Photonic Crystals and Bend Losses.....	297
9.7.4 Photonic Crystal Resonators and Quality Factors.....	298
9.8 Some Noteworthy Devices and Functions	301
9.8.1 Coupled Resonators and Waveguides.....	301
9.8.2 Other Devices and Optical Functions	303
10 Microsources.....	305
10.1 High-Efficiency Light-Emitting Diodes.....	305
10.1.1 Solutions for the Extraction of Light without Confinement	305
10.1.2. Enhanced Extraction Efficiency through Planar Confinement.....	307
10.1.3 Increase of the Extraction Efficiency Using Two-Dimensional Photonic Crystals	309
10.2 Ridge-Type Waveguide Lasers Confined by Photonics Crystals	311
10.3 Photonic Crystal Band Edge Lasers	313
10.4 Microcavity Lasers.....	316
10.5 Potential Interest for Single Photon Sources.....	320
11 Photonic Crystal Fibres.....	325
11.1 Another Implementation of Periodic Structures	325
11.2 Fabrication of Photonic Crystal Fibres.....	326
11.3 Solid-Core Microstructured Optical Fibres.....	328
11.3.1 Confinement Losses and Second Mode Transition.....	328
11.3.2 Chromatic Dispersion Properties	331
11.3.3 Main Applications of Solid-Core Microstructured Optical Fibres ...	332
11.4 True Photonic Crystal Fibres	333
11.4.1 Photonic Bandgap Cladding.....	333
11.4.2 Losses of Photonic Crystal Fibres with Finite Cladding.....	335
11.4.3 Main Applications of Photonic Crystal Fibres	337
12 Three-Dimensional Structures in Optics.....	339
12.1 Geometrical Configurations proposed for Three-Dimensional Structures	340
12.1.1 Structures with Omnidirectional Photonic Band Gaps	340
12.1.2 Incomplete Band Gap Three-Dimensional Structures	343
12.2 Examples of Fabrication Processes and Realisations of Three-Dimensional Photonic Crystals in the Optical Region.....	345
12.2.1 Complete Band Gap Structures.....	345
12.2.2 Incomplete Band Gap Structures	351
12.3 Metallic Three-Dimensional Photonic Crystals in the Optical Region....	356
12.4 Three-Dimensional Photonic Crystals and Light Emitters	357

13 Microwave and Terahertz Antennas and Circuits.....	359
13.1 Photonic Crystal Antennas	360
13.1.1 Photonic-Crystal Antenna Substrates	361
13.1.2 Photonic-Crystal Antenna Mirrors	364
13.1.3 Photonic-Crystal Antenna Radomes or Superstrates	368
13.2 Controllable Structures and Metamaterials	370
13.2.1 Principles and Characteristics of Electrically Controllable Photonic Crystals.....	370
13.2.2 Electrically Controllable Photonic Crystal Antennas	372
13.2.3 Antennas and Metamaterials.....	375
13.3 Microwave Circuits and Ultra-Compact Photonic Crystals	376
13.3.1 Ultra-Compact Photonic Crystals	376
13.3.2 Microwave Filters and Waveguides realised from Ultra-Compact Photonic Crystals	379
13.4 From Microwaves to Terahertz Waves	381
13.5 From Microwaves to Optics	382
13.5.1 Impedance Matching of Photonic Waveguides.....	383
13.5.2 Photonic Crystal THz Imaging System	385
Conclusion and Perspectives.....	387
Appendix. Scattering Matrix Method: Determination of the Field for a Finite Two-Dimensional Crystal formed by Dielectric Rods.....	391
A.1 Incident Field.....	391
A.2 Field inside the Rods	391
A.3 Field in the Vicinity of a Rod	394
References	401

Part I

Theoretical Models for Photonic Crystals

Introduction to Part I

The necessity of developing numerical tools capable of accurately predicting the properties of photonic crystals was recognised very early after the pioneering works in this field. There is no doubt that heuristic considerations based on solid state physics have sown the seeds of the concept of a photonic crystal, and that they continue to provide physical interpretations for the basic characteristics of photonic crystals. However, considerations of such a nature cannot provide experimenters with reliable guidelines for the design of a photonic crystal with certain given properties. Only by combining the use of the fundamental laws of electromagnetism, of mathematics and of sophisticated methods of numerical analysis can such numerical tools be developed.

It might be recalled here that the numerical modelling of scattering from periodic structures had been investigated much earlier. Since the end of the 1960s, the emergence of powerful computation tools has resulted in spectacular advances in the numerical modelling of scattering and propagation phenomena in the field of electromagnetism. These advances have been particularly rapid and strong for diffraction gratings (Maystre 1993; Moharam 1986; Petit 1980). Yet, the first methods developed for photonic crystals were based on the adaptation to electromagnetism of the modelling of the properties of an electron in a crystal. The chief cause for this state of affairs was the desire of solid state physicists to use simple numerical tools which had already been extensively checked in their field. Unfortunately, the resolution of problems of electromagnetism is in general much more difficult than is the case for similar problems of electron modelling. The first reason is to be found in the vector character of electromagnetic waves. A second reason lies in the concern of physicists working in the field of electromagnetism to avoid as much as possible theoretical approximations.

While simple to implement, the very well-known 'plane wave method' rests on certain strong hypotheses. The prerequisite of this method is indeed the assumption that the crystal is infinite along all directions of space. On the other hand, the theory of this method and its numerical implementation are within the reach of a good postgraduate student, even in the case of three-dimensional crystals. This method has played and still plays a vital role in the calculation of photonic band gaps. However, this method suffers from an inherent deficiency. Indeed, actual photonic crystals are always limited in size: as a consequence, inside the photonic band gap, a part of the light illuminating the crystal will be able to propagate through it. The amount of transmitted light can be more or less important, depending on the width of the photonic crystal. But in any case, it turns out that being capable of accurately determining the amount of transmitted light is a crucial

issue for most practical applications of these optical components. As an example, one may easily imagine the problems faced by an experimenter when wanting to fabricate a laser cavity with a photonic crystal if he cannot retrieve any reliable prediction concerning the crystal width that would reduce the light losses below a given threshold.

The development of numerical tools that would account for the finite size of actual photonic crystals has thus been recognised as a necessity for their investigation. In general, these numerical methods have their origin in the wide set of modern methods of electromagnetic modelling. Depending on the realism and on the sophistication of the model which is adopted, the computation times and memory storage may greatly differ. At the beginning of the 21st century, it should be acknowledged that there still exists serious obstacles on the way to the numerical modelling of certain photonic crystals of a considerable practical importance, for instance three-dimensional photonic crystals with a finite size, and this is likely to remain true well into the next decade.

1 Models for Infinite Crystals

1.1 Plane Wave Expansion

1.1.1 Maxwell's Equations

In this chapter, photonic crystals will be assumed to extend infinitely along all directions of space. A photonic crystal is characterised by a relative dielectric permittivity $\epsilon_r(x,y,z)$ assumed to be real and periodic along N directions (with $N = 1, 2$ or 3) and invariant along the other $3 - N$ orthogonal directions. In what follows, the materials from which the crystals are made will be assumed to be non-magnetic. Let us denote by $\mathbf{a}_i, i \in \{1, \dots, N\}$ the vectors describing the elementary cell of the lattice. The system generated from these vectors is not assumed to be either orthogonal nor normed. An elementary cell of the crystal will be obtained from the extremities of the vectors \mathbf{r} defined by the equation:

$$\mathbf{r} = \sum_{i=1,N} p_i \mathbf{a}_i, \quad p_i \in [0,1] \quad (1.1)$$

The electric and magnetic fields \mathbf{E} and \mathbf{H} satisfy the time-harmonic Maxwell's equations (Born 1965; Kong 2000). Using a time dependence in $\exp(-i\omega t)$ and the standard symbolic notations for the vector operators, these equations can be represented in the following form:

$$\nabla \times \mathbf{E} - i\omega \mu_0 \mathbf{H} = 0 \quad (1.2)$$

$$\nabla \times \mathbf{H} + i\omega \epsilon_0 \epsilon_r(x,y,z) \mathbf{E} = 0 \quad (1.3)$$

$$\nabla \cdot [\epsilon_r(x,y,z) \mathbf{E}] = 0 \quad (1.4)$$

$$\nabla \cdot \mathbf{H} = 0 \quad (1.5)$$

where ϵ_0 and μ_0 denote the electric permittivity and magnetic permeability of vacuum respectively. In what follows, we shall assume that the fields constitute physically acceptable solutions of Maxwell's equations. This means that these fields should contain a locally bounded electromagnetic energy, which in turn entails that they should be square integrable.

Combining Eqs. 1.2 and 1.3 leads to the following equations:

$$\frac{1}{\epsilon_r(x, y, z)} \nabla \times [\nabla \times \mathbf{E}] - \frac{\omega^2}{c^2} \mathbf{E} = 0 \quad (1.6a)$$

$$\nabla \times \left[\frac{1}{\epsilon_r(x, y, z)} \nabla \times \mathbf{H} \right] - \frac{\omega^2}{c^2} \mathbf{H} = 0 \quad (1.7a)$$

with $c = \sqrt{\epsilon_0 \mu_0}$ and $\frac{\omega}{c} = k_0 = \frac{2\pi}{\lambda_0}$, where c and k_0 represent the speed and the wave number of light in vacuum respectively.

The propagation equations (Eqs. 1.6a and 1.7a) are to be considered in the sense of distributions (Schwartz 1961). This is to say that these equations include the boundary conditions at the interfaces of the different materials, and in the case under consideration that they include the continuity of the tangential components of the electric and magnetic fields. More generally, and introducing here a symbolic notation, these equations are of the form:

$$O\mathbf{F} = k_0^2 \mathbf{F} \quad (1.8)$$

where \mathbf{F} stands for one of the fields and O is an operator on the space of the locally square integrable functions \mathbf{F} . It thus turns out that any arbitrary solution of Maxwell's equations is an eigenfunction of the operator O , and that the eigenvalue corresponding to it is the square of the wave number.

In what follows, we shall first demonstrate that the solutions of the equation of propagation assume the form of Bloch modes. These modes satisfy Maxwell's equations for crystals formed from any type of material, and can be regarded as a form of generalisation of the notion of an homogeneous plane wave, which plays an essential role for homogeneous materials, to the more complicated case of a periodically inhomogeneous material.

1.1.2 The Floquet-Bloch Theorem

We shall first define the set of translation operators T in the following way:

$$T[\mathbf{F}(\mathbf{r})] = \mathbf{F}(\mathbf{r} + \sum_{i=1, N} n_i \mathbf{a}_i) \quad (1.9)$$

where the n_i are relative integers.

It can be easily demonstrated that, due to the invariance of the crystal with respect to any translation along an arbitrary vector $\sum_{i=1,N} n_i \mathbf{a}_i$, these operators commute with O (Powell 1965; Cohen-Tannoudji 1973). The possibility therefore exists of finding a common set of eigenvectors for O and T . An eigenvector \mathbf{u} of T satisfies the equation:

$$T[\mathbf{u}] = \rho \mathbf{u} \quad (1.10)$$

In general, the eigenvalues ρ can be expected to be complex. However, we need to exclude here eigenvalues which have a non-unitary modulus, since the corresponding field \mathbf{u} would not in this case remain bounded at infinity and therefore would not contain a locally integrable electromagnetic energy. The demonstration is quite straightforward: it suffices to apply either T or $(T)^{-1}$ with $|\rho| \neq 1$ an infinite number of times, which of course leads to the divergence of the field. Therefore, we may restrict ourselves to the consideration of the eigenvectors of O which satisfy Eq. 1.10 with $|\rho| = 1$, which entails that $\rho = \exp(i\varphi)$, where φ is real. These vectors, referred to as ‘pseudo-periodic’ vectors, would be periodic if ρ were equal to 1.

Further, any translation T may be decomposed onto the N translations T_i which correspond to the vectors \mathbf{a}_i of the direct lattice:

$$T = \sum_{i=1,N} n_i T_i \quad (1.11)$$

where the n_i are relative integers.

It therefore turns out that $\varphi = \sum_{i=1,N} n_i \varphi_i$, where φ_i is the phase shift of \mathbf{u} (i.e. the argument of ρ) for a translation along the vector \mathbf{a}_i of the lattice. Introducing a vector \mathbf{k} defined in such a way that $\forall i \mathbf{k} \cdot \mathbf{a}_i = \varphi_i$ with $-\pi < \mathbf{k} \cdot \mathbf{a}_i < +\pi$, the eigenvalue ρ can then be expressed as follows:

$$\rho = \exp\left(i\mathbf{k} \cdot \sum_{i=1,N} n_i \mathbf{a}_i\right) \quad (1.12)$$

Let us now demonstrate that the function $\mathbf{v} = \mathbf{u} \exp(-i\mathbf{k} \cdot \mathbf{r})$ presents the same periodicity as the crystal. For this purpose, it will be enough to show that \mathbf{v} remains invariant under application of the translation operator T . This is achieved by using Eq. 1.12 for deriving from Eq. 1.9 that:

$$\begin{aligned}
T[\mathbf{v}] &= T[\mathbf{u} \exp(-i\mathbf{k.r})] = T[\mathbf{u}] \exp\left(-i\mathbf{k} \cdot \left(\mathbf{r} + \sum_{i=1,N} n_i \mathbf{a}_i\right)\right) \\
&= \rho \mathbf{u} \exp\left(-i\mathbf{k} \cdot \sum_{i=1,N} n_i \mathbf{a}_i\right) \exp(-i\mathbf{k.r}) \\
&= \mathbf{u} \exp(-i\mathbf{k.r}) = \mathbf{v}
\end{aligned} \tag{1.13}$$

This crucial result will allow us to express \mathbf{u} in the form of a series of pseudo-periodic functions. For this purpose, we shall first introduce the reciprocal lattice, which has the same dimensions as the physical (direct) lattice and whose basis vectors \mathbf{G}_j are defined from the basis vectors \mathbf{a}_i of the direct lattice through the following equation:

$$\mathbf{a}_i \cdot \mathbf{G}_j = 2\pi \delta_{i,j}, \forall i, j \in [1, N] \tag{1.14a}$$

where δ is the Kronecker delta symbol.

An arbitrary spatial vector r can be defined on the basis of Eq. 1.1, under the provision however that the coordinates $\{p_i\}$ should now be allowed to take any value ranging from $-\infty$ to $+\infty$. In this case, Eqs 1.1 and 1.14a lead to the following equation:

$$p_j = \mathbf{r} \cdot \mathbf{G}_j / 2\pi \tag{1.14b}$$

The possibility always exists of considering \mathbf{v} as a periodic function of the variables p_j . As such, it can be developed into a Fourier series of variables p_j with unit period along each axis of the direct lattice. The elements in this series are given by the formula $\mathbf{V} \exp(2\pi i \sum_{j=1,N} n_j p_j)$, where the vector \mathbf{V} depends on the relative integers n_j . From Eq. 1.14b, this term can be re-written in the form $\mathbf{V} \exp(i\mathbf{r} \cdot \sum_{j=1,N} n_j \mathbf{G}_j) = \mathbf{V}(\mathbf{G}) \exp(i\mathbf{r} \cdot \mathbf{G})$, where \mathbf{G} is a linear combination of the vectors of the reciprocal lattice. Denoting by G the entire set of these N vectors, the function \mathbf{v} can finally be written in the form:

$$\mathbf{v} = \sum_{\mathbf{G} \in G} \mathbf{V}(\mathbf{G}) \exp(i\mathbf{G.r}) \tag{1.15}$$

From the relation between \mathbf{u} and \mathbf{v} , it thus follows that:

$$\mathbf{u} = \exp(i\mathbf{k.r}) \sum_{\mathbf{G} \in G} \mathbf{V}(\mathbf{G}) \exp(i\mathbf{G.r}) \tag{1.16a}$$

Eq. 1.16a is fundamentally a mere expression of the Floquet-Bloch theorem, which states that the eigenvectors of O and T are characterised by a wave vector \mathbf{k} and can be expressed in the form of a product of a plane wave $\exp(i\mathbf{k} \cdot \mathbf{r})$ and a Fourier series. The eigenvector is also referred to as the Bloch mode. The interested reader will find more extensive developments concerning this notion in the textbooks on *Solid State Physics* (Kittel 1971; Ashcroft 1976), where Eq. 1.16a is often presented in the more concise, albeit less precise form from a mathematical point of view:

$$\mathbf{u} = \exp(i\mathbf{k} \cdot \mathbf{r}) \sum_{\mathbf{G}} \mathbf{V}(\mathbf{G}) \exp(i\mathbf{G} \cdot \mathbf{r}) \quad (1.16b)$$

The fact that a solution of the fundamental laws of electromagnetics in a photonic crystal can be expressed in the form of a Bloch mode is itself a crucial result. However, it should be pointed out that the converse proposition does not in general hold true, since the function \mathbf{u} given by Eq. 1.16a will not in most cases satisfy the equation of propagation (Eq. 1.6a). One can easily convince oneself of this proposition by simply limiting the sum in the right-hand part of Eq. 1.16a to a single term, for example to the term corresponding to $\mathbf{G} = 0$. The function \mathbf{u} becomes in this case an homogeneous plane wave with wave number $|\mathbf{k}|$ and since the crystal is inhomogeneous, this plane wave obviously cannot satisfy the equation of propagation at every point of the crystal. This result should not come out as a surprise. Let us indeed recall here that Bloch modes are eigenvectors of the translation operators T . As has been seen, it is possible to find a common system of eigenvectors for O and T , and then to search for eigenvectors of O in the form of Bloch modes. This however does not entail that the expression in the right-hand part of Eq. 1.16a, where arbitrary coefficients $\mathbf{V}(\mathbf{G})$ have been introduced, is an eigenvector of O . In such a case, this expression may well be an eigenvector of T , but not an eigenvector of O .

Another remark may be made here on the subject of Bloch modes. Since we were considering here an infinite space, we have been led to select the eigenvalues ρ of the translation operators having an unit modulus so that the field could contain a locally integrable electromagnetic energy. In practice however, photonic crystals are bounded and, since the property of pseudo-periodicity fails in such a case, it is no longer possible to demonstrate that the field can be represented in the form of Bloch modes. While it may seem reasonable at first sight to conjecture that Bloch modes would still represent relatively adequately the field extending beyond the very near vicinity of the boundary of the crystal, this conclusion is not sound. Indeed, since the crystal is bounded, there is no reason to exclude non unit values of ρ . In other terms, new Bloch modes presenting an evanescent behaviour have to be introduced.

1.1.3 Hermiticity of the Field Operator

We shall now proceed to establish an important property of Bloch modes by demonstrating that the operator O is Hermitian in the space \mathcal{H}_k of the pseudo-periodic functions corresponding to a given value of \mathbf{k} . For this purpose, we need to show that:

$$\langle O\mathbf{v}, \mathbf{w} \rangle = \langle \mathbf{v}, O\mathbf{w} \rangle \quad (1.17a)$$

where $\mathbf{v} \in \mathcal{H}_k$ and $\mathbf{w} \in \mathcal{H}_k$. Proceeding from Eq. 1.6a, it turns out that:

$$O\mathbf{v} = \frac{1}{\epsilon_r(x, y, z)} \nabla \times [\nabla \times \mathbf{v}] \quad (1.17b)$$

By definition:

$$\langle \mathbf{u}, \mathbf{v} \rangle = \int_P \epsilon_r \bar{\mathbf{u}} \cdot \mathbf{v} d^3 r \quad (1.18)$$

The domain of integration is the elementary cell P of the crystal, as defined by Eq. 1.1. Hence:

$$\langle O\mathbf{v}, \mathbf{w} \rangle = \int_P [\nabla \times (\nabla \times \bar{\mathbf{v}})] \cdot \mathbf{w} d^3 r \quad (1.19a)$$

By applying twice the following identity:

$$\nabla \cdot (\mathbf{a} \times \mathbf{b}) = \mathbf{b} \cdot (\nabla \times \mathbf{a}) - \mathbf{a} \cdot (\nabla \times \mathbf{b}) \quad (1.20)$$

it can be demonstrated that the integrand in Eq. 1.19a can be written in the following form:

$$[\nabla \times (\nabla \times \bar{\mathbf{v}})] \cdot \mathbf{w} = \bar{\mathbf{v}} \cdot [\nabla \times (\nabla \times \mathbf{w})] - \nabla \cdot [\bar{\mathbf{v}} \times (\nabla \times \mathbf{w}) + (\nabla \times \bar{\mathbf{v}}) \times \mathbf{w}] \quad (1.21)$$

The problem thus comes down to a difference between two integrals. The second integral, which corresponds to the integration of the second term in the right-hand part of Eq. 1.21, reduces to the flux of a vector (function of \mathbf{v} and \mathbf{w}) through the boundary surface of the elementary cell P . However, since we are working in a space of pseudo-periodic functions and since \mathbf{v} is conjugated, it turns out that this

vector is periodic and therefore that the integral of the flux is null. We thus obtain the following equation:

$$\langle O\mathbf{v}, \mathbf{w} \rangle = \int_P \bar{\nabla} \cdot [\nabla \times (\nabla \times \mathbf{w})] d\mathbf{r} = \langle \mathbf{v}, O\mathbf{w} \rangle \quad (1.19b)$$

The operator O is therefore an Hermitian operator in the space \mathcal{H}_k of the locally integrable pseudo-periodic functions. The eigenvalues of this operator are real, while its eigenvectors (Bloch modes) form a complete set.

1.1.4 Simple Examples of Bloch Functions

The first example that will be considered here is the case of a three-dimensional crystal presenting a simple rectangular parallelepiped symmetry with periods a_x , a_y and a_z along the x , y and z axes respectively, as is represented in Fig. 1.1. The reciprocal lattice exhibits a rectangular symmetry as well, and is characterised by vectors parallel to the vectors of the direct lattice and with modulus $2\pi/a_x$, $2\pi/a_y$ and $2\pi/a_z$ respectively.

In this case, Eq. 1.16a will assume the following form:

$$\mathbf{E}(x, y, z) = \exp(i\mathbf{k.r}) \sum_{m=-\infty}^{+\infty} \sum_{n=-\infty}^{+\infty} \sum_{p=-\infty}^{+\infty} \mathbf{E}_{m,n,p} \exp\left\{im \frac{2\pi}{a_x} x + in \frac{2\pi}{a_y} y + ip \frac{2\pi}{a_z} z\right\} \quad (1.22)$$

where m , n and p are integers.

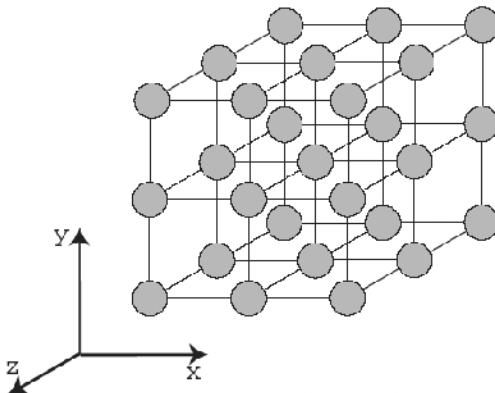


Fig. 1.1. Three-dimensional photonic crystal with a rectangular symmetry

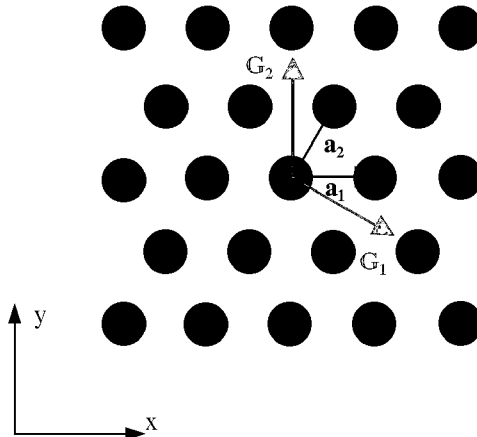


Fig. 1.2. Two-dimensional photonic crystal with an hexagonal symmetry

A more complicated example can be given in the form of a two-dimensional crystal presenting an hexagonal symmetry with a period a along the x axis and with the same period a along an axis rotated from 60° with respect to the x axis (Fig. 1.2).

In this case, the direct lattice is formed by the vectors \mathbf{a}_1 and \mathbf{a}_2 with modulus a , as given by the two following equations respectively:

$$\mathbf{a}_1 = a\hat{x} \quad (1.23)$$

$$\mathbf{a}_2 = a\left(\frac{\hat{x}}{2} + \frac{\hat{y}\sqrt{3}}{2}\right) \quad (1.24)$$

where \hat{x} and \hat{y} are unit vectors along the x -axis and y -axis respectively.

From the consideration of the orthogonality relations between the vectors describing the direct and reciprocal lattices, it can then be demonstrated that the two vectors \mathbf{G}_1 and \mathbf{G}_2 of the reciprocal lattice have the same modulus $4\pi/a\sqrt{3}$ and are given by the following two equations:

$$\mathbf{G}_1 = \frac{4\pi}{a\sqrt{3}}\left(\frac{\hat{x}\sqrt{3}}{2} - \frac{\hat{y}}{2}\right) \quad (1.25)$$

$$\mathbf{G}_2 = \frac{4\pi}{a\sqrt{3}}\hat{y} \quad (1.26)$$

In this case, the directions of the reciprocal lattice and of the direct lattice do not coincide, and the expansion of the field into Bloch modes will thus be given by the equation:

$$\mathbf{E}(x, y, z) = \exp(i\mathbf{k}\cdot\mathbf{r}) \sum_{m=-\infty}^{+\infty} \sum_{n=-\infty}^{+\infty} \mathbf{E}_{m,n} \exp\{i(m\mathbf{G}_1 + n\mathbf{G}_2)\cdot\mathbf{r}\} \quad (1.27)$$

1.1.5 General Plane Wave Method

The plane wave method remains the reference method for the calculation of band gaps in photonic crystals (Joannopoulos 1995b). Indeed, the expression which has previously been given in the form of the right-hand part of Eq. 1.16a for the field \mathbf{u} , where \mathbf{u} may denote either the electric or the magnetic field, is a representation of these fields in terms of plane waves. In fact, two different methods exist, depending on whether the electric or the magnetic field is actually considered: these two methods, respectively referred to as the E and the H methods, will be successively described here. However, the numerical precision of both of these methods is restricted by problems of truncation, and a third intermediate method, known as the Ho method, needs often to be used (Ho 1990).

E method

This method proceeds by first re-writing Eq. 1.6a in the following form:

$$\nabla \times [\nabla \times \mathbf{E}] = \frac{\omega^2}{c^2} \epsilon_r(x, y, z) \mathbf{E} \quad (1.6b)$$

The application of Eq. 1.16a to the vector yields:

$$\epsilon_r(x, y, z) \mathbf{E} = \exp(i\mathbf{k}\cdot\mathbf{r}) \sum_{\mathbf{G} \in G} \mathbf{D}(\mathbf{G}) \exp(i\mathbf{G}\cdot\mathbf{r}) \mathbf{E} \quad (1.16c)$$

Eq. 1.6b can then be re-written in the form:

$$\nabla \times \left[\nabla \times \frac{1}{\epsilon_r(\mathbf{r})} (\epsilon_r(\mathbf{r}) \mathbf{E}) \right] = \frac{\omega^2}{c^2} (\epsilon_r(\mathbf{r}) \mathbf{E}) \quad (1.6c)$$

Therefore, by reinserting the right-hand part of Eq. 1.16c into Eq. 1.6c and then by using the periodicity of $\eta(\mathbf{r}) = \frac{1}{\varepsilon_r(\mathbf{r})}$ which allows us to write down the following equation:

$$\eta(\mathbf{r}) = \sum_{\mathbf{G}'' \in G} \hat{\eta}(\mathbf{G}'') \exp(i\mathbf{G}''.\mathbf{r}) \quad (1.28)$$

we finally arrive to the equation:

$$\nabla \times \left[\nabla \times \sum_{\mathbf{G} \in G} \sum_{\mathbf{G}' \in G} \hat{\eta}(\mathbf{G} - \mathbf{G}') \mathbf{D}(\mathbf{G}') \exp(i(\mathbf{k} + \mathbf{G}).\mathbf{r}) \right] = \frac{\omega^2}{c^2} \sum_{\mathbf{G} \in G} \mathbf{D}(\mathbf{G}) \exp(i(\mathbf{k} + \mathbf{G}).\mathbf{r}) \quad (1.29)$$

where $\mathbf{G} = \mathbf{G}' + \mathbf{G}''$.

By applying twice the generic relation $\nabla \times (\mathbf{V} \exp(i\mathbf{u}.\mathbf{r})) = i\mathbf{u} \times \mathbf{V} \exp(i\mathbf{u}.\mathbf{r})$ where \mathbf{u} and \mathbf{V} are constants, the following equation can be derived:

$$\sum_{\mathbf{G} \in G} \sum_{\mathbf{G}' \in G} \hat{\eta}(\mathbf{G} - \mathbf{G}') (\mathbf{k} + \mathbf{G}) \times [(\mathbf{k} + \mathbf{G}) \times \mathbf{D}(\mathbf{G}')] \exp(i(\mathbf{k} + \mathbf{G}).\mathbf{r}) = -\frac{\omega^2}{c^2} \sum_{\mathbf{G} \in G} \mathbf{D}(\mathbf{G}) \exp(i(\mathbf{k} + \mathbf{G}).\mathbf{r}) \quad (1.30)$$

Finally, the projection of the equation onto the basis functions $\exp[i(\mathbf{k} + \mathbf{G}).\mathbf{r}]$, where $\mathbf{G} \in G$ leads to the equation:

$$\sum_{\mathbf{G}' \in G} \hat{\eta}(\mathbf{G} - \mathbf{G}') (\mathbf{k} + \mathbf{G}) \times [(\mathbf{k} + \mathbf{G}) \times \mathbf{D}(\mathbf{G}')] = -\frac{\omega^2}{c^2} \mathbf{D}(\mathbf{G}) \quad (1.31)$$

Maxwell's equation $\nabla \cdot (\varepsilon_r \mathbf{E}) = 0$ imposes the transversality of $\mathbf{D}(\mathbf{G})$ with respect to the associated direction of propagation, hence $\forall \mathbf{G} \quad \mathbf{D}(\mathbf{G}) \cdot (\mathbf{k} + \mathbf{G}) = 0$. The vector $\mathbf{D}(\mathbf{G})$ present in Eq. 1.31 can therefore be projected onto two unit and orthogonal vectors $\mathbf{e}_{1,G}$ and $\mathbf{e}_{2,G}$ respectively, chosen in such a way as to ensure that $\{\mathbf{e}_{1,G}, \mathbf{e}_{2,G}, \mathbf{k} + \mathbf{G}\}$ form a direct trihedron. The following relation thus holds true: $\mathbf{k} + \mathbf{G} = |\mathbf{k} + \mathbf{G}|(\mathbf{e}_{1,G} \times \mathbf{e}_{2,G})$.

Using the same notations as above, we may write that:

$$\mathbf{D}(\mathbf{G}) = d_{1,G} \mathbf{e}_{1,G} + d_{2,G} \mathbf{e}_{2,G} \quad (1.32)$$

where $d_{1,G}$ and $d_{2,G}$ denote the components of $\varepsilon_r(x,y,z)\mathbf{E}$ in the coordinate system defined by the orthogonal unit vectors $\{\mathbf{e}_{1,G}, \mathbf{e}_{2,G}\}$.

From Eq. 1.32 it follows that Eq. 1.31 can therefore be written in the following form:

$$\sum_{\mathbf{G}' \in G} \hat{\eta}(\mathbf{G} - \mathbf{G}') |\mathbf{k} + \mathbf{G}|^2 \begin{bmatrix} \mathbf{e}_{1,G} \cdot \mathbf{e}_{1,G'} & \mathbf{e}_{1,G} \cdot \mathbf{e}_{2,G'} \\ \mathbf{e}_{2,G} \cdot \mathbf{e}_{1,G'} & \mathbf{e}_{2,G} \cdot \mathbf{e}_{2,G'} \end{bmatrix} \begin{bmatrix} d_{1,G'} \\ d_{2,G'} \end{bmatrix} = \frac{\omega^2}{c^2} \begin{bmatrix} d_{1,G} \\ d_{2,G} \end{bmatrix} \quad (1.33)$$

Thus, for any given value for \mathbf{k} , we are led to an infinite eigenvalue problem. If this equation is truncated by restricting G to a set of M vectors \mathbf{G} , Eq. 1.33 directly shows that the linear system to be inverted is of dimension $2M \times 2M$, the unknowns being the set formed by the $d_{1,G}$ and $d_{2,G}$ components.

The resolution of the eigenvalue problem leads to the possibility of determining the values allowed for ω when a given value for \mathbf{k} is given and therefore of establishing their dispersion relations. The validity of the truncation can be verified by using larger values for M . It might be noted here that it is not necessary to determine these relations over the entire range for \mathbf{k} and that it suffices to consider only the irreducible Brillouin zone. This latter subject will be addressed in more detail in Section 1.3.1.

H Method

This method proceeds from the consideration of Eq. 1.7a which is first re-written in the form:

$$\nabla \times [\eta(x, y, z) \nabla \times \mathbf{H}] = \frac{\omega^2}{c^2} \mathbf{H} \quad (1.7b)$$

On the other hand, the application of Eq. 1.16a to the magnetic field yields:

$$\mathbf{H}(\mathbf{r}) = \exp(i\mathbf{k} \cdot \mathbf{r}) \sum_{\mathbf{G} \in G} \mathbf{H}(\mathbf{G}) \exp(i\mathbf{G} \cdot \mathbf{r}) = \sum_{\mathbf{G} \in G} \mathbf{H}(\mathbf{G}) \exp(i(\mathbf{k} + \mathbf{G}) \cdot \mathbf{r}) \quad (1.16d)$$

By introducing the right-hand part of Eq. 1.16d in Eq. 1.7b, we arrive at the following equation:

$$\sum_{\mathbf{G} \in G} \sum_{\mathbf{G}' \in G} \hat{\eta}(\mathbf{G} - \mathbf{G}') (\mathbf{k} + \mathbf{G}) \times [(\mathbf{k} + \mathbf{G}') \times \mathbf{H}(\mathbf{G}')] \exp(i(\mathbf{k} + \mathbf{G}).\mathbf{r}) = -\frac{\omega^2}{c^2} \sum_{\mathbf{G} \in G} \mathbf{H}(\mathbf{G}) \exp(i(\mathbf{k} + \mathbf{G}).\mathbf{r}) \quad (1.34)$$

Finally, the projection of this equation onto the basis functions $\exp[i(\mathbf{k} + \mathbf{G}).\mathbf{r}]$, where $\mathbf{G} \in G$, leads to the equation:

$$\sum_{\mathbf{G}' \in G} \hat{\eta}(\mathbf{G} - \mathbf{G}') (\mathbf{k} + \mathbf{G}) \times [(\mathbf{k} + \mathbf{G}') \times \mathbf{H}(\mathbf{G}')] = -\frac{\omega^2}{c^2} \mathbf{H}(\mathbf{G}) \quad (1.35)$$

Maxwell's equation $\nabla \cdot \mathbf{H} = 0$ (Eq. 1.5) imposes the transversality of $\mathbf{H}(\mathbf{G})$ with respect to the associated direction of propagation, hence $\nabla \cdot \mathbf{H}(\mathbf{G}) \cdot (\mathbf{k} + \mathbf{G}) = 0$. Each vector $\mathbf{H}(\mathbf{G})$ in Eq. 1.16d can therefore be projected onto the unit and orthogonal vectors $\mathbf{e}_{1,G}$ and $\mathbf{e}_{2,G}$ defined in Section 1.1.5:

$$\mathbf{H}(\mathbf{r}) = \sum_{\mathbf{G} \in G} (h_{1,G} \mathbf{e}_{1,G} + h_{2,G} \mathbf{e}_{2,G}) \exp(i(\mathbf{k} + \mathbf{G}).\mathbf{r}) \quad (1.16e)$$

where $h_{1,G}$ and $h_{2,G}$ denote the components of $\mathbf{H}(\mathbf{G})$ in the coordinate system defined by the orthogonal unit vectors $\{\mathbf{e}_{1,G}, \mathbf{e}_{2,G}\}$.

Proceeding along the same lines as in Section 1.1.5, i.e. using twice the relation $\nabla \times (\mathbf{V} \exp(i\mathbf{u} \cdot \mathbf{r})) = i\mathbf{u} \times \mathbf{V} \exp(i\mathbf{u} \cdot \mathbf{r})$, where \mathbf{u} and \mathbf{V} are constants, and then the classical rule on triple vector product, Eq. 1.35 becomes:

$$\sum_{\mathbf{G}' \in G} \hat{\eta}(\mathbf{G} - \mathbf{G}') |\mathbf{k} + \mathbf{G}'| |\mathbf{k} + \mathbf{G}| \begin{bmatrix} \mathbf{e}_{2,G} \cdot \mathbf{e}_{2,G'} & -\mathbf{e}_{2,G} \cdot \mathbf{e}_{1,G'} \\ -\mathbf{e}_{1,G} \cdot \mathbf{e}_{2,G'} & \mathbf{e}_{1,G} \cdot \mathbf{e}_{1,G'} \end{bmatrix} \begin{bmatrix} h_{1,G'} \\ h_{2,G'} \end{bmatrix} = \frac{\omega^2}{c^2} \begin{bmatrix} h_{1,G} \\ h_{2,G} \end{bmatrix} \quad (1.36a)$$

The truncation of Eq. 1.36a which can be performed by restricting G to a set of M vectors \mathbf{G} directly demonstrates that the eigenvalue problem to be resolved is of dimension $2M \times 2M$, the unknowns being the set formed by the $h_{1,G}$ and $h_{2,G}$ components.

Two-Dimensional Crystals

In the two-dimensional case, all derivatives with respect to the z coordinate vanish as soon as the study is restricted to the propagation along the cross-section plane of the crystal, i.e. along the xy plane. It might be noted that a direct consequence of Maxwell's equations (Eq. 1.2) is that the transverse, i.e. parallel to the xy plane, components of the electric field can be expressed in terms of the longitudinal component H_z of the magnetic field. Likewise, it follows from Eq. 1.3 that the transverse components of the magnetic field can be deduced from the longitudinal component E_z of the electric field. We may therefore limit ourselves to the study of the two longitudinal components E_z and H_z . The projection of the propagation equations (Eqs. 1.6a and 1.7a) onto the three coordinate axes reveals that these two components obey two uncoupled propagation equations:

$$\mathbf{P}_E E_z = \frac{1}{\epsilon_r(x, y, z)} \nabla^2 E_z = -k_0^2 E_z \quad (1.37)$$

$$\mathbf{P}_H H_z = \nabla \cdot \left(\frac{1}{\epsilon_r(x, y, z)} \nabla H_z \right) = -k_0^2 H_z \quad (1.38)$$

The propagation equation satisfied by each longitudinal component of the fields therefore turns out to be a scalar equation. This crucial property opens the possibility of separately studying the problems corresponding to the two so-called fundamental cases of polarisation. These polarisation modes will be referred to as TM and TE polarisations depending on whether $E_z \neq 0$ and $H_z = 0$, or $E_z = 0$ and $H_z \neq 0$ respectively. It might be noted here that these two polarisation modes are in optics classically referred to as s and p polarisations respectively. For an arbitrary polarisation, a general solution to this problem can be readily expressed from the solutions of Eqs. 1.37 and 1.38.

As has been foreshadowed, we shall now successively consider Eq. 1.36a for each fundamental polarisation mode. Since all the vectors $\mathbf{k} + \mathbf{G}$ are parallel to the xy plane, the vectors $\mathbf{e}_{1,G}$ can therefore be chosen in such a way as to coincide with the unit vector of the z axis. The vector $\mathbf{e}_{2,G}$ can then be easily deduced from these two vectors (Fig. 1.3).

TM (or s) Polarisation. In this polarisation mode, $\mathbf{H}(\mathbf{r})$ is parallel to the xy plane and therefore has no component along the z axis. Accordingly, $\forall \mathbf{G} \cdot h_{1,G} = 0$. On the other hand, $\mathbf{e}_{1,G} \cdot \mathbf{e}_{1,G} = 1$, whence it follows that $\mathbf{e}_2 \cdot \mathbf{e}_{1,G} = 0$. Eq. 1.36a thus reduces to the equation:

$$\sum_{\mathbf{G}' \in G} \hat{\eta}(\mathbf{G} - \mathbf{G}') |\mathbf{k} + \mathbf{G}'| |\mathbf{k} + \mathbf{G}| h_{2,G} = \frac{\omega^2}{c^2} h_{2,G} \quad (1.36b)$$

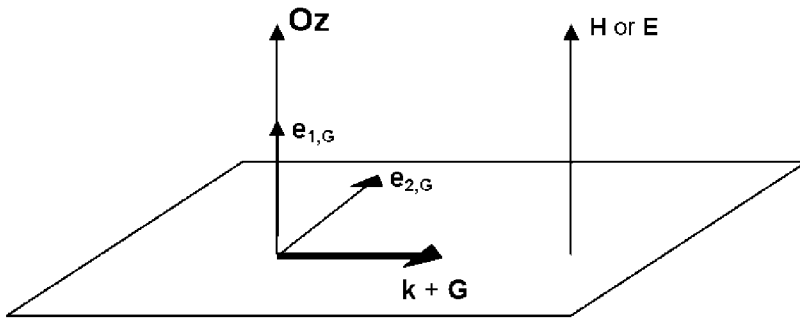


Fig. 1.3. Schematic representation of the vectors in the equations of the H method applied to a two-dimensional crystal

By limiting G to a set of M vectors \mathbf{G} , we thus obtain a linear system of M equations, where the \mathbf{k} -dependent eigenvalue to be determined is represented by ω^2/c^2 .

TE (or p) Polarisation. In this polarisation mode, $\mathbf{H}(\mathbf{r})$ is parallel to the z axis, and therefore $\nabla \cdot \mathbf{H} = 0$. On the other hand, since $\mathbf{e}_{1,G} \cdot \mathbf{e}_{2,G} = 0$, Eq. 1.36a assumes the following form:

$$\sum_{\mathbf{G}' \in G} \hat{\eta}(\mathbf{G} - \mathbf{G}') |\mathbf{k} + \mathbf{G}'| |\mathbf{k} + \mathbf{G}| (\mathbf{e}_{2,G} \cdot \mathbf{e}_{2,G'}) h_{1,G} = \frac{\omega^2}{c^2} h_{1,G} \quad (1.36c)$$

Further, since the angle formed by $\mathbf{e}_{2,G}$ and $\mathbf{e}_{2,G'}$ is equal to the angle formed by $\mathbf{k} + \mathbf{G}$ and $\mathbf{k} + \mathbf{G}'$, it follows that $|\mathbf{k} + \mathbf{G}| |\mathbf{k} + \mathbf{G}'| (\mathbf{e}_{2,G} \cdot \mathbf{e}_{2,G'}) = (\mathbf{k} + \mathbf{G}) \cdot (\mathbf{k} + \mathbf{G}')$, and therefore that Eq. 1.36c can be written in the form:

$$\sum_{\mathbf{G}' \in G} \hat{\eta}(\mathbf{G} - \mathbf{G}') (\mathbf{k} + \mathbf{G}') (\mathbf{k} + \mathbf{G}) h_{1,G'} = \frac{\omega^2}{c^2} h_{1,G} \quad (1.36d)$$

Determination of the Fourier Transform of η

A prerequisite for the resolution of the linear systems of equations corresponding to the E and H methods is the determination of the Fourier transform of $\eta(\mathbf{r})$. While the calculation itself of the Fourier transform does not present any specific problem, it may be useful to briefly expose here the lines along which these calculations should proceed for a typical example, that of a two-dimensional crystal

consisting of dielectric rods with relative permittivity ϵ_a periodically placed inside a dielectric material with relative permittivity ϵ_b . Accordingly, this structure may indifferently be viewed either as a lattice of dielectric rods extending in the air, or as a lattice of air holes inside a dielectric. The rods are cylindrical and, for the sake of simplicity, the assumption will be made that they present a circular cross-section with a radius R_c such that $R_c \leq a$, where a is the period of the crystal. In addition, it will be further assumed that only one rod is present inside the elementary cell. The space dependence of the inverse of the permittivity η in this elementary cell can be expressed as follows:

$$\eta(\mathbf{r}) = \eta_b + \sum_{\mathbf{R}} (\eta_a - \eta_b) \theta(\mathbf{r} - \mathbf{R}) \quad (1.39)$$

where $\theta(\mathbf{r})$ is the Heaviside function which takes the value 1 in the rods and 0 outside the rods, $\eta_a = 1/\epsilon_a$, $\eta_b = 1/\epsilon_b$, while \mathbf{R} is the vector associated to any arbitrary point of the direct lattice: $\mathbf{R} = n_1 \mathbf{a}_1 + n_2 \mathbf{a}_2$, where n_1 and n_2 are relative integers.

The following equation provides an expression of the Fourier component $\hat{\eta}(\mathbf{G})$ as a function of $\eta(\mathbf{r})$:

$$\hat{\eta}(\mathbf{G}) = \frac{1}{S_{cell}} \int_{S_{cell}} \eta(\mathbf{r}) \exp(-i\mathbf{G} \cdot \mathbf{r}) d^2 r \quad (1.40)$$

where S_{cell} is the surface of the elementary cell. We may then proceed to reinser the right-hand part of Eq. 1.39 in the right-hand part of Eq. 1.40 through the introduction of a change of variable $\mathbf{r}-\mathbf{R} \rightarrow \mathbf{r}$ using the relation $\mathbf{R} \cdot \mathbf{G} = 2p\pi$, where p is a relative integer. Since there is only one rod in each elementary cell, we finally obtain the following equation for the Fourier transform:

$$\hat{\eta}(\mathbf{G}) = \eta_b \delta_{\mathbf{G},0} + (\eta_a - \eta_b) \frac{1}{S_{cell}} \int_{S_{cell}} \theta(\mathbf{r}) \exp(-i\mathbf{G} \cdot \mathbf{r}) d^2 r \quad (1.41a)$$

where $\delta_{\mathbf{G},0} = 1$ if $\mathbf{G} = \mathbf{0}$ and $\delta_{\mathbf{G},0} = 0$ if $\mathbf{G} \neq \mathbf{0}$. The scalar product $\mathbf{G} \cdot \mathbf{r}$ in the right-hand part of Eq. 1.41a can be expressed in the form $|\mathbf{G}| r \sin \varphi$, where φ denotes the angle formed by the two vectors \mathbf{G} and \mathbf{r} . By taking into account the circular symmetry of the system, Eq. 1.41a can then be written in the form:

$$\hat{\eta}(\mathbf{G}) = \eta_b \delta_{\mathbf{G},0} + (\eta_a - \eta_b) \frac{1}{S_{cell}} \int_{r=0}^{R_c} \int_{\varphi=0}^{2\pi} \exp(i |\mathbf{G}| r \sin \varphi) dr d\varphi \quad (1.41b)$$

By drawing upon the expansion of $\exp(i\xi \sin \varphi)$ into a series of Bessel functions (Abramovitz 1970; Angot 1982) and by integrating in φ , we finally arrive at the following equation :

$$\hat{\eta}(\mathbf{G}) = \eta_b \delta_{\mathbf{G},0} + (\eta_a - \eta_b) \frac{2\pi R_c^2 J_1(|\mathbf{G}| R_c)}{S_{cell} |\mathbf{G}| R_c} \quad (1.42)$$

where $J_1(\xi)$ is a Bessel function of the first kind of first order.

Ho Method

The Ho method (Ho 1990) can be derived from the master field equation used for the Emethod, Eq. 1.6.b, by developing \mathbf{E} rather than $\varepsilon_r \mathbf{E}$ into a Bloch series, while at the same time writing down $\varepsilon_r(\mathbf{r})$ in the form of a Fourier series:

$$\varepsilon(\mathbf{r}) = \sum_{\mathbf{G}'' \in G} \hat{\varepsilon}(\mathbf{G}'') \exp(i\mathbf{G}'' \cdot \mathbf{r}) \quad (1.43)$$

Proceeding along the same lines as in Section 1.1.5, we obtain an equation formally similar to Eq. 1.29, with the difference that its right-hand part is now the product of a matrix ε with components $\hat{\varepsilon}(\mathbf{G})$ by a column matrix with components $\mathbf{E}(\mathbf{G})$. By multiplying the two sides of this equation by ε^{-1} , inverse of the matrix ε , we obtain the following equation:

$$\sum_{\mathbf{G}} \varepsilon^{-1}(\mathbf{G}'' - \mathbf{G})(\mathbf{k} + \mathbf{G}) \times [(\mathbf{k} + \mathbf{G}) \times \mathbf{E}(\mathbf{G})] + \frac{\omega^2}{c^2} \mathbf{E}(\mathbf{G}'') = 0 \quad (1.44)$$

For the sake of convenience, let us define: $\mathbf{F}(\mathbf{G}) = (\mathbf{k} + \mathbf{G}) \times \mathbf{E}(\mathbf{G})$. The vector product of the two sides of Eq. 1.44 with $\mathbf{k} + \mathbf{G}''$ then yields:

$$(\mathbf{k} + \mathbf{G}'') \times \left[\sum_{\mathbf{G}} \varepsilon^{-1}(\mathbf{G}'' - \mathbf{G})(\mathbf{k} + \mathbf{G}) \times \mathbf{F}(\mathbf{G}) \right] + \frac{\omega^2}{c^2} \mathbf{F}(\mathbf{G}'') = 0 \quad (1.45)$$

The resulting equation for the $\mathbf{F}(\mathbf{G})$ vectors is formally similar to the equation for the $\mathbf{H}(\mathbf{G})$ vectors that can be derived from Eqs. 1.7b and 1.16d, the only difference being that $\eta(\mathbf{G} - \mathbf{G}'')$ is replaced here by $\varepsilon^{-1}(\mathbf{G} - \mathbf{G}'')$. It might be emphasized that, as a consequence of the truncation, these two matrices are not equal. Using the equation $(\mathbf{k} + \mathbf{G}) \cdot \mathbf{F}(\mathbf{G}) = 0$, we may proceed along the same lines as in the H method, which finally leads to the resolution of a matrix system of dimension $2M \times 2M$.

The Ho method generally yields more precise results than the H method for the same number of plane waves taken into consideration. The comparison between the results obtained using these two methods generally allows proceeding to the evaluation of the convergence of the precision of the numerical calculations.

When the results are very similar, it might be admitted that they converge towards the solution, although a rigorous demonstration would require a convergence test conducted by increasing M. It might be noted here that, in the case of a three-dimensional photonic crystal with diamond symmetry, 3000 plane waves are required in order to limit the discrepancy between the results obtained with these two methods to less than 5 percent at the level of the fundamental band gap.

1.2 Other Methods for the Calculation of the Photonic Band Gaps of an Infinite Crystal: the KKR Method

The use of the plane wave method frequently leads to numerical instabilities, which might be explained from the fact that the permittivity of the crystal is discontinuous between two materials, as well as certain components of the electromagnetic field. It is well known that the truncation of the Fourier series of such functions leads to a slow convergence of their development (in $1/n$ where n denotes the number of terms in the series) and results, whatever the order of the truncation is, in the occurrence of the Gibbs phenomenon in the vicinity of the discontinuities. These discontinuous functions therefore fail to be adequately represented in the vicinity of the discontinuities and the numerical instabilities which can be observed are but the consequence of this defect. Other methods, which originate in the analysis of the Schrödinger equation, have been advanced for calculating the band diagrams of infinite photonic crystals. While from a theoretical point of view, these methods are more complicated than plane wave methods, they generally provide a much higher stability from a numerical point of view. Describing these methods would be beyond the scope of this book and the interested reader is referred to (Moroz 1995) where such a detailed description is provided. The most well known of these methods, referred to as the KKR (Korringa-Kohn-Rostocker) method, derives from the method initially described by Korringa (Korringa 1947, 1957). This method relies on the use of the scattering matrix of the elementary cell (for a definition of this matrix, see Chap. 2), while the Green function of the periodic structure is developed on the basis of the spherical harmonics in the three-dimensional case (Moroz 1995). One of the most interesting features of the KKR method is that it directly provides the Green function. As will be seen, the density of states and the local density of states, both of which can be easily deduced from the Green function, are important parameters in the study of the physical phenomena associated with photonic crystals.

1.3 Photonic Band Diagram

The photonic band diagram allows to survey all the dispersion characteristics $\omega(\mathbf{k})$ of the photonic crystal which can be calculated from the plane wave model. In principle, it would be necessary in order to be exhaustive to consider all possible

propagation directions inside the photonic crystal. Actually however, by using the same considerations as in the field of solid state physics (Kitson 1986), the possibility exists of drawing upon the symmetries of the crystal for restricting the calculations to the wave vectors \mathbf{k} contained in a limited region of the reciprocal space referred to as the irreducible Brillouin zone. It is quite obvious that the complexity of the diagram depends on the dimensionality of the crystal, which may range from one to three dimensions. In this section, we shall first recall elementary considerations leading to the definition of the irreducible Brillouin zone in some simple cases, before discussing the band diagrams of the main types of photonic crystals with an increasing complexity.

1.3.1 The Irreducible Brillouin Zone

The first Brillouin zone can be defined as the region of the reciprocal space formed by the points which are closer to the origin than to any other vertex of the periodical lattice. In Fig. 1.4 are represented various examples of photonic crystals with their corresponding Brillouin zones. As can be seen, the first Brillouin zone is constructed by drawing the perpendicular bisectors (in the one and two-dimensional cases) or the bisecting planes (in the three-dimensional case) of every lattice vector joining the origin to the nearest vertexes of the reciprocal lattice. Each bisector or bisecting plane divides therefore the reciprocal space into two half-spaces, the origin being contained in one these half-spaces. The first Brillouin zone is defined as the intersection of all the half-spaces which contain the origin. By definition, all the values for \mathbf{k} which lie outside this zone can be reached from within the zone using the translations of the vectors $\mathbf{G} \in G$, and are therefore redundant. In other terms, it suffices to consider the variation of \mathbf{k} within the Brillouin zone for representing the entire set of the dispersion curves of the photonic crystal. The range over which \mathbf{k} is considered can be further reduced by using the symmetries of the crystal, as is illustrated in the different examples represented in Fig. 1.4.

In the one-dimensional case, the crystal displays an obvious symmetry with respect to the origin. Thus, if a wave of vector \mathbf{k} and frequency ω is found to be a solution to the master equation, the counterpropagating wave with the same frequency and vector $-\mathbf{k}$ will also be a solution to this equation. This allows restricting the study to the interval $[0, +\pi/a]$ instead of the entire $[-\pi/a, +\pi/a]$ interval.

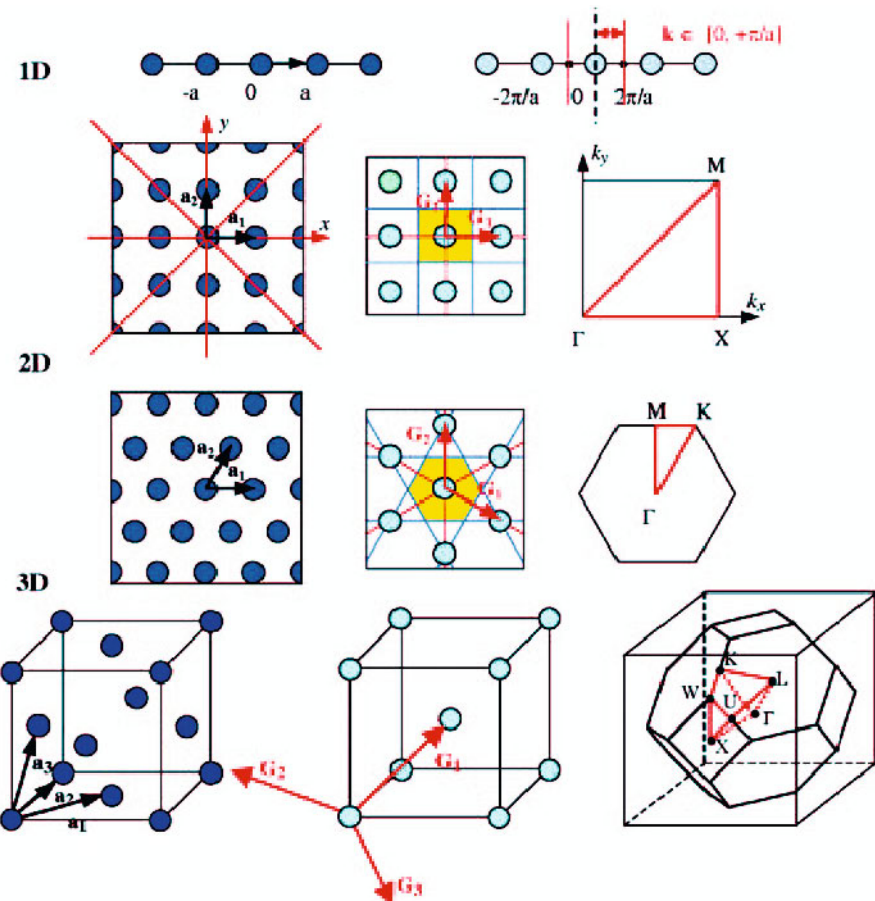


Fig. 1.4. One-, two- and three-dimensional photonic crystals (left) with their corresponding Brillouin zones (middle and right). For the one-dimensional crystal, the first Brillouin zone and the irreducible Brillouin zone are formed by the intervals $[-\pi/a, +\pi/a]$ and $[0, \pi/a]$ respectively. For two-dimensional crystals, the middle figures represent the first Brillouin zones (light grey area) while the right figures show the irreducible Brillouin zones (thick lines). For the fcc crystal, the middle figure represents the centred cubic reciprocal lattice and the right-hand figure represents the two Brillouin zones: the first Brillouin zone is a truncated octahedron, while the irreducible Brillouin zone is the polyhedron with apexes Γ , X , U , L , W and K

Let us now consider a two-dimensional crystal with a square symmetry of the same type as the example represented in Fig. 1.4. The assumption is made here that this structure consists of infinite dielectric rods extending in the air and parallel to the z axis. The structure presents four axes of symmetry, represented here by thin lines, which can be deduced from one another through rotations of $\pi/4$. The reciprocal lattice presents also a square symmetry, and the first Brillouin zone will be defined by the following inequalities:

$$-\frac{\pi}{a} < k_x < \frac{\pi}{a} , \quad -\frac{\pi}{a} < k_y < \frac{\pi}{a} \quad (1.46)$$

We are interested here in two-dimensional solutions of the propagation equations, and these solutions are obviously independent from the z coordinate. For the sake of simplicity, we may restrict ourselves to the consideration of a single polarization of the field, for instance, the s-polarisation. Let us first analyse the consequence of the rotational symmetry of the structure with respect to an axis parallel to Oy . If $E_z(x, y)$ is a solution to the propagation equation (Eq. 1.37) with the wave vector \mathbf{k} of coordinates (k_x, k_y) , then the double x -derivative in the Laplacian implies that $E_z(-x, y)$ will also be a solution to this equation with, from Eq. 1.16c, the wave vector of coordinates $(-k_x, k_y)$. But since these two solutions correspond to the same frequency ω , it is unnecessary to consider both of them for the calculations of the band diagram. It suffices to consider only one of these solutions, and we may therefore restrict ourselves to the half of the Brillouin zone defined by $0 < k_x < \pi/a, -\pi/a < k_y < \pi/a$. This result can also be obtained in a more ‘mathematical’ way. For this purpose, let us define the symmetry operator with respect to Oy in the following way:

$$S_y u(x, y) = u(-x, y) \quad (1.47)$$

It can easily be seen from Eq. 1.37 that S_y commutes with the operator \mathbf{P}_E . Hence, if E_z is a proper vector of \mathbf{P}_E with the proper value k_0^2 , $S_y E_z$ will also be a proper vector of \mathbf{P}_E with the same proper value k_0^2 .

The range over which \mathbf{k} is studied can be further reduced by considering the four other symmetries which are indicated in Fig. 1.4. It might be noted that only three symmetries need to be considered here, since the fourth one is but a combination of the first three ones. Accordingly, the range considered for \mathbf{k} simply reduces to an isosceles right triangle with two edges of equal length π/a : the apexes of the triangle are traditionally denoted by Γ , X and M . This triangle, represented here in thick lines in Fig. 1.4 (right), constitutes the irreducible Brillouin zone of the square lattice. Actually, as far as band diagram calculations are concerned here, it is generally sufficient to let the wave vector \mathbf{k} describe the edge of the irreducible Brillouin zone while the inner region is ignored. Although this simplification does not rely on any rigorous mathematical analysis, it can intuitively be

justified from the symmetry of the structure, which entails that the three edges of the triangle represent symmetry axes for the functions $\omega(\mathbf{k})$, solutions of Eq. 1.31. Indeed, assuming that the derivative of $\omega(\mathbf{k})$ is continuous along all directions, the extrema of the function $\omega(\mathbf{k})$ are located along the edges of the triangle. Restricting the study to the three directions ΓX , ΓM and MX therefore comes down to assuming that no other extremum of interest lies inside the irreducible Brillouin zone.

The second example represented in Fig. 1.4 of a two-dimensional lattice is the triangular lattice, which exhibits an hexagonal symmetry. The reciprocal lattice exhibits the same symmetry, while the first Brillouin zone is an hexagon. In this case, six symmetry axes exist which can be deduced from one another by rotations of $\pi/6$ with an invariance under rotation equal to $\pi/3$. Following a similar line of reasoning than in the case of the square lattice, it can be demonstrated that the irreducible Brillouin zone is the half of an equilateral triangle with apexes Γ , K and M (Fig. 1.4, right). Here again, the assumption is made that it suffices to let the wave vector \mathbf{k} describe the edge of the irreducible Brillouin zone (along the directions ΓK , ΓM and MK) for reaching the extrema of $\omega(\mathbf{k})$ which are of interest.

The three-dimensional structure represented in Fig. 1.4 (bottom left) is a face-centred-cubic (fcc) lattice. It might be recalled here that diamond and the main semiconductors (silicon, germanium, gallium arsenide, etc) crystallise in such a lattice, and that the famous ‘Yablonovite’ itself is but the ‘photonic’ analogue of the diamond. More precisely, the diamond structure consists of two fcc lattices which are shifted from one another by a quarter of the main diagonal of the cube. In other terms, this structure is a fcc lattice with two atoms per unit cell. The reciprocal lattice is a centred cubic (cc) lattice (Fig. 1.4, bottom middle) and, by construction, the first Brillouin zone is a dodecahedron which may also be viewed as a truncated octahedron, as represented in thick lines in Fig. 1.4 (bottom right). From symmetry considerations somewhat more elaborated than those previously used in the case of two-dimensional crystals (Kitson 1986), it can be demonstrated that the irreducible Brillouin zone is a four-face polyhedron whose apexes are traditionally denoted by Γ , L , U , X , W and K (Landolt-Börnstein 1982). The main dispersion curves of the band diagram of the fcc lattice will be analysed by allowing the wave vector \mathbf{k} to describe the edge of the polyhedron.

1.3.2 Band Diagrams of One-Dimensional Crystals

One-dimensional crystals traditionally consist of alternated dielectric layers with different dielectric constants. By analogy with the Bragg reflection in solid state crystals, these structures are often referred to as Bragg mirrors or as Bragg multi-layer stacks. The possibility however exists in the field of ‘photronics’ of imagining different structures where the dielectric permittivity varies in a periodical manner, for instance structures with a sinusoidal modulation of the dielectric permittivity. Although they are much less widely used, these structures lend themselves to a simpler analytical formulation than Bragg mirrors, which allows an

easier insight into their dispersion characteristics. We shall therefore begin with this simpler case as a first approach before recalling the optical properties of classical Bragg mirrors.

Sinusoidal Modulation of the Dielectric Permittivity

Let us assume here that the dielectric permittivity ϵ_r presents a sinusoidal modulation along the z axis. If the modulation occurs around an average value ϵ_m with an amplitude ϵ_d and a period a_z , the equation for ϵ_r will simply be:

$$\epsilon_r(z) = \epsilon_m + \epsilon_d \sin\left(\frac{2\pi}{a_z} z\right) = \epsilon_m + \frac{\epsilon_d}{2i} \left(\exp\left(i \frac{2\pi}{a_z} z\right) - \exp\left(-i \frac{2\pi}{a_z} z\right) \right) \quad (1.48)$$

The basis vector of the reciprocal lattice is $\mathbf{G}_1 = 2\pi/a_z \hat{z}$. The other vectors are expressed in the form $\mathbf{G}_p = p\mathbf{G}_1$ where p is a relative integer. From Eq. 1.48, it can be easily demonstrated that the Fourier transform of ϵ_r possesses only three non-zero components:

$$\epsilon(\mathbf{0}) = \epsilon_m \quad ; \quad \epsilon(\mathbf{G}_1) = \frac{\epsilon_d}{2i} \quad ; \quad \epsilon(-\mathbf{G}_1) = -\frac{\epsilon_d}{2i} \quad (1.49)$$

The transverse electric field of an electromagnetic wave propagating along Oz can be arbitrarily assumed to be parallel to Ox . The plane-wave expansion of this field can therefore be written as follows:

$$E_x = \operatorname{Re} \left\{ \sum_{p=-\infty}^{+\infty} E_p \exp(i(k + \mathbf{G}_p)z) \right\} \quad (1.50)$$

Using Eqs. 1.49 and 1.50 in the master field equation¹ leads to a system of recursive equations, each of which contains three main terms. For instance, the equation of order p is:

¹ In the absence of discontinuities in the dielectric function, the possibility exists of using, in the E method as described in Sect. 1.1.5, the electric field \mathbf{E} in place of the displacement vector \mathbf{D} . After performing straightforward calculations, we then obtain the following equation in place of Eq. 1.31:

$$(\mathbf{k} + \mathbf{G}) \times [(\mathbf{k} + \mathbf{G}) \times \mathbf{E}(\mathbf{G})] + \frac{\omega^2}{c^2} \sum_{\mathbf{G}' \in G} \hat{\epsilon}(\mathbf{G} - \mathbf{G}') \mathbf{E}(\mathbf{G}') = 0$$

$$\left[\left(k + \frac{2\pi}{a_z} p \right)^2 - \varepsilon_m \frac{\omega^2}{c^2} \right] E_p + \frac{\varepsilon_d}{2i} \frac{\omega^2}{c^2} E_{p+1} - \frac{\varepsilon_d}{2i} \frac{\omega^2}{c^2} E_{p-1} = 0 \quad (1.51)$$

Let us first consider a modulation with a zero amplitude ($\varepsilon_d = 0$), and let us restrict ourselves to the consideration of the values of k which are contained within the first Brillouin zone, i.e. such that $|k_z| \leq \pi/a_z$. This amounts to considering an homogeneous material (ε_m) with a fictitious period a_z . Under these conditions, Eq. 1.51 has non-zero solutions ($E_p \neq 0$) only in the case where:

$$k = k_p^\pm = \pm \sqrt{\varepsilon_m} \frac{\omega}{c} - p \frac{2\pi}{a_z} \quad (1.52)$$

where $\omega > 0$.

In the case where $p = 0$, this equation actually reduces to the linear dispersion relation in an homogeneous material $k_0^\pm = \pm \sqrt{\varepsilon_m} \omega/c$. For $p \neq 0$, the solutions result merely from the folding of the band within the first Brillouin zone. In this case, the band diagram consists of an infinite series of lines which intersect at the values $k = 0$, $k = \pi/a_z$ or $k = -\pi/a_z$, as can be seen in the upper part of Fig. 1.5. For instance, the two lines $k_0^+(\omega)$ and $k_{-1}^-(\omega)$ intersect at the edge of the zone $k = \pi/a_z$ for the frequency $\omega_0 = \pi c / (a_z \sqrt{\varepsilon_m})$. This specific band diagram is also referred to as the free-photon diagram in order to point to the fact that it corresponds to the case of an homogeneous material in the absence of any loss, reflection or diffraction.

Let us now assume a proper sinusoidal modulation ($\varepsilon_d \neq 0$), but with only a moderate amplitude ($\varepsilon_d < \varepsilon_m$). The second and third terms in Eq. 1.51 may be regarded as perturbative terms. All the field components E_p are linked to one another. However, within a given range of values for k and ω , the ‘perturbed’ solutions remain close to the ‘unperturbed’ solutions that were obtained for $\varepsilon_d = 0$. For instance, at the edge of the Brillouin zone $k = \pi/a_z$ and at frequencies close to the previously defined frequency ω_0 , the field components E_0 and E_{-1} are predominant. We thus need to solve a system of two equations which for $k = \pi/a_z$ can be written as follows:

$$-\frac{\varepsilon_d}{2i} \frac{\omega^2}{c^2} E_{-1} + \left[\frac{\pi^2}{a_z^2} - \varepsilon_m \frac{\omega^2}{c^2} \right] E_0 = 0 \quad (1.53a)$$

$$\left[\frac{\pi^2}{a_z^2} - \varepsilon_m \frac{\omega^2}{c^2} \right] E_{-1} + \frac{\varepsilon_d}{2i} \frac{\omega^2}{c^2} E_0 = 0 \quad (1.53b)$$

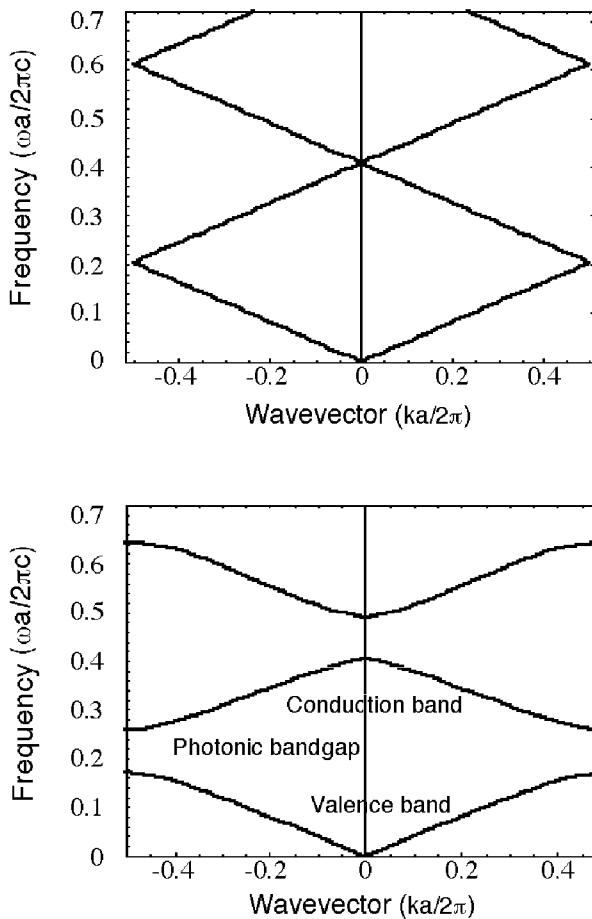


Fig. 1.5. Band diagrams of one-dimensional crystals obtained through a sinusoidal modulation of the dielectric permittivity *Top*. Modulation with a zero amplitude $\epsilon_d = 0$ ('free photon diagram') *Bottom*. Modulation with a moderate amplitude $\epsilon_d = 5$. In either cases, the average value for the permittivity is $\epsilon_m = 6$

Requiring that the solutions be non-zero results now in two frequencies instead of a unique frequency ω_0 :

$$\frac{\omega^2}{c^2} \left(\epsilon_m \pm \frac{\epsilon_d}{2} \right) = \frac{\pi^2}{a_z^2} \quad (1.54)$$

In other terms, there no longer exists any intersection point at ($k = \pi/a_z$, $\omega = \omega_0$) and the dispersion curves separate from one another, leading to the appearance of a photonic band gap. Within the assumption that $\epsilon_d < \epsilon_m$, it is quite straightforward to demonstrate from Eq. 1.54 that an approximate expression for the relative width of the gap is given by the equation:

$$\frac{\Delta\omega}{\omega_0} \approx \frac{\epsilon_d}{2\epsilon_m} \quad (1.55)$$

As might have been expected, the width of the gap increases with the amplitude of the modulation. The lower part of Fig. 1.5 represents the band diagram calculated for $\epsilon_d = 5$ and $\epsilon_m = 6$, which entails that ϵ_r varies between 1 and 11. The calculations are performed for the first three bands by using only six equations similar to Eq. 1.51: a pocket calculator would actually be enough for solving this system of equations. A comparison of the present diagram with the ‘free-photon diagram’ represented in the upper part of Fig. 1.5 clearly evidences the appearance of new band gaps at harmonic frequencies $2\omega_0$, $3\omega_0$, ...and for the wave numbers $k = \pi/a_z$, $-\pi/a_z$ and 0. In the present case where the dielectric permittivity exhibits a sinusoidal modulation, all band gaps are of the same width. The calculated relative width of the gap (~38%) is close to the value determined from the analytical expression given in Eq. 1.55 (~41%).

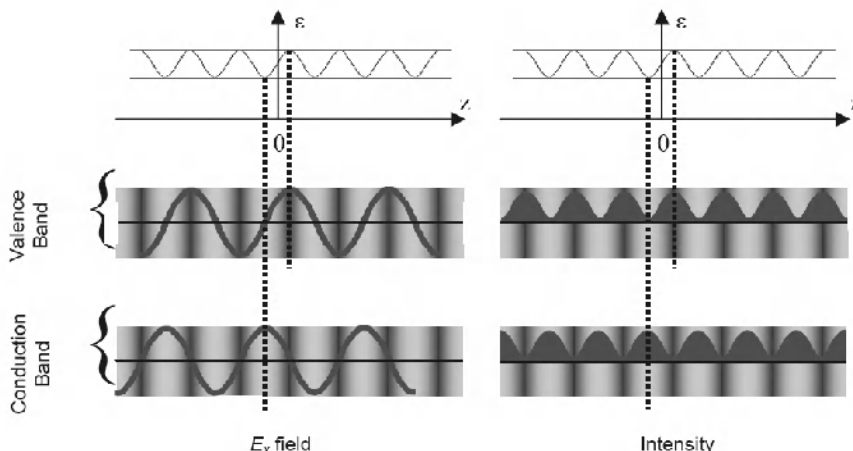


Fig. 1.6. Evolutions of the transverse electric field (left) and of the optical intensity (right) along the one-dimensional photonic crystal for frequencies located at the edges of the valence band (middle) and conduction band (bottom) respectively. The maxima for the field and the intensity are plotted with respect to the minima and maxima of the dielectric permittivity (upper curves)

Let us now consider the relationship between the field components E_0 and E_{-1} , expressed by Eqs. 1.53a and 1.53b respectively, for each of the frequencies given by Eq. 1.54. At the lower frequency (i.e at the edge of the valence band, plus sign in Eq. 1.54), the application of Eqs. 1.53a and 1.53b leads to $E_{-1} = iE_0$. Using a plane wave expansion of E_x to the first order (Eq. 1.50), the transverse electric field can then be expresses in the form:

$$E_x \propto \cos\left(\frac{\pi}{a_z}z - \frac{\pi}{4}\right) \quad (1.56a)$$

At the higher frequency (i.e at the edge of the conduction band, minus sign in Eq. 1.54), it now turns out that $E_{-1} = -iE_0$. Using here again a plane wave expansion of E_x to the first order, the equation for the transverse electric field becomes now:

$$E_x \propto \cos\left(\frac{\pi}{a_z}z + \frac{\pi}{4}\right) \quad (1.56b)$$

The longitudinal evolutions of the electrical field, optical intensity and dielectric permittivity are reported in Fig. 1.6 for the two frequencies of interest here. As can be seen from the observation of this figure, the field and intensity maxima coincide at the edge of the valence band with the permittivity maxima. The opposite situation occurs at the edge of the conduction band, where both the amplitude of the field and the optical intensity become zero when the permittivity reaches its maximum value. In the same way as the fundamental level of an electron can be achieved by localising the wave function of the electron in the region where the potential is the lowest, the electromagnetic mode with lower energy will be obtained by concentrating the electric field, or more precisely the displacement vector, to the region with higher permittivity. A demonstration of the possibility of extending this result to any type of photonic crystal can be found in (Joannopoulos 1995).

Bragg Multilayers

In Fig. 1.7 are displayed the dispersion diagrams of two different Bragg multilayers, represented by thick and dashed curves respectively. In both these two cases, each period consists of a high permittivity layer ($\epsilon_1=13$) and of an air layer ($\epsilon_2=1$). In the diagram represented in thick curves and taken from (Joannopoulos 1995), the widths of the two layers are $d_1 = 0.2a$ and $d_2 = 0.8a$ respectively. These values approximately correspond to the same optical thickness $n_1d_1 \sim n_2d_2$, where $n = \sqrt{\epsilon}$ denotes the refractive index. In the diagram represented in dashed curves, the widths of the layers are equal to $d_1 = 0.3a$ and $d_2 = 0.7a$ respectively, which represents a significant difference in terms of optical thickness. It might be noted that the highest (resp. lowest) value ϵ_1 (resp. ϵ_2) for the permittivity is about the same

than the maximum (resp. minimum) value $\varepsilon_m + \varepsilon_d = 11$ (resp. $\varepsilon_m - \varepsilon_d = 1$) for the permittivity which had previously been chosen in the case of a permittivity with a sinusoidal modulation (Fig. 1.5). In this respect, the diagram presented in the lower part of Fig. 1.5 and the diagrams presented in Fig. 1.7 are strikingly similar. The symmetry with respect to the frequency axis confirms the fact that for one-dimensional crystals the study of the dispersion relations can be restricted to the half of the Brillouin zone $[0, \pi/a]$. At the lower frequencies, the dispersion is linear and the crystals behave as an homogeneous material whose dielectric constant is given respectively by $(d_1\varepsilon_1 + d_2\varepsilon_2)/a$ for Bragg multilayers and by ε_m for the structure with a sinusoidal modulation of the permittivity. Band gaps appear periodically as the frequency increases. The fundamental band gap of Bragg multilayers is centred at $\omega = \pi c/[a(d_1n_1 + d_2n_2)]$. The latter equation merely expresses the fact that the optical thickness of one bilayer is equal to half the wavelength, which is also the condition of a maximum reflectivity for a Bragg reflector.

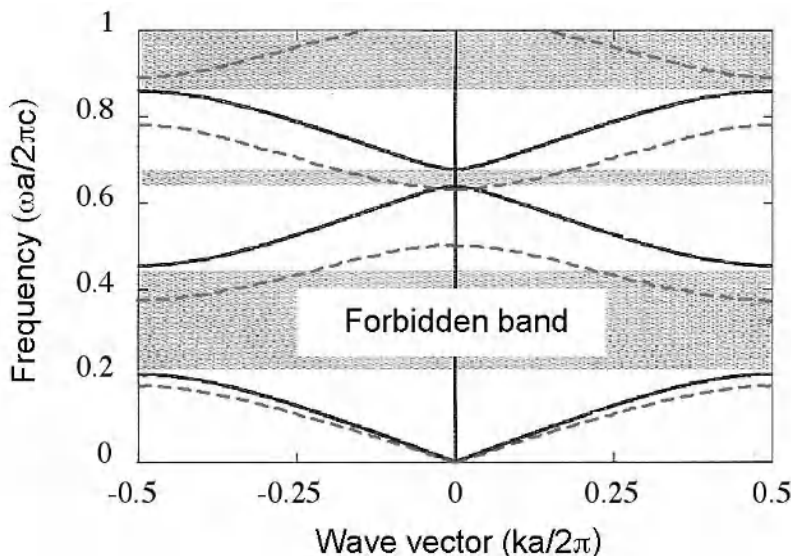


Fig. 1.7. Band diagrams of two one-dimensional photonic crystals in the form of two multilayer films consisting of periodically alternating layers with different widths d_1 and d_2 and different permittivities ε_1 and ε_2 . In both cases, the permittivities of the layers are equal to $\varepsilon_1 = 13$ and $\varepsilon_2 = 1$ respectively. The thick dispersion curves were calculated for $d_1 = 0.2a$ and $d_2 = 0.8a$, where a is the period of the lattice (Joannopoulos 1995), while the dashed curves were calculated for $d_1 = 0.3a$ and $d_2 = 0.7a$.

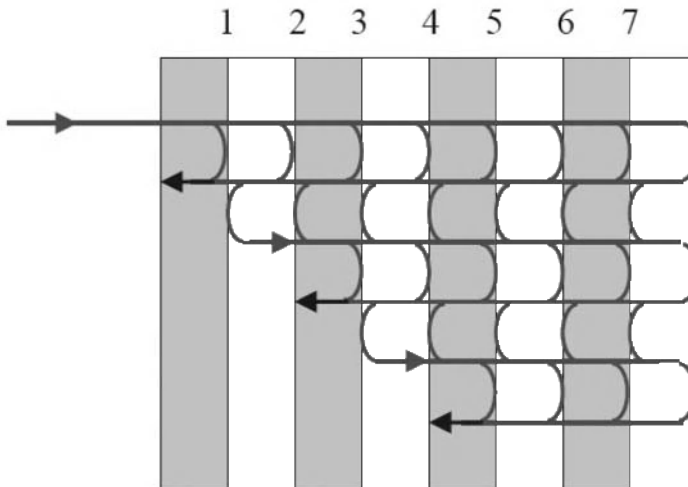


Fig. 1.8. Construction of multiple interferences in the Bragg reflector

Nevertheless, contrary to the structure exhibiting a permittivity with a sinusoidal modulation, Bragg multilayers might present band gaps with different widths at the fundamental and at the different harmonic frequencies $\omega, 2\omega, 3\omega, 4\omega \dots$ It is apparent that the band gaps at the even harmonic frequencies $2\omega, 4\omega \dots$ may be much narrower than band gaps at the fundamental and at the odd harmonic frequencies $3\omega, 5\omega \dots$ Further, when all the layers of the stacks have the same optical thickness, the band gaps even come to disappear at the even harmonic frequencies $2\omega, 4\omega \dots$ This can be explained from the fact that, at the harmonics $2\omega, 4\omega, 6\omega$, each layer constitutes an optical resonator with length $\lambda/2, \lambda, 3\lambda/2, \dots$ where stationary waves might be contained. It is quite obvious in this case that the existence of stationary waves is incompatible with the existence of a photonic band gap.

The behaviour of Bragg reflectors can be explained in a more traditional way in terms of a construction of multiple interferences inside the periodic stack of layers. As is schematically represented in Fig. 1.8, a wave propagating successively throughout the different layers will undergo multiple reflections at the different interfaces. Each reflection is accompanied with a phase change of π if the wave propagates from the medium with lower index towards the medium with higher index, while it occurs without any phase change in the opposite situation. When the overall width of each bilayer is equal to $\lambda/2$, the wave reflected at the interface (1) is in phase with the waves reflected at the interfaces (3), (5), (7)... As a consequence of these constructive interferences, a phenomenon of total internal reflection occurs: the reflectivity tends towards unity as the number of periods, i.e. of bilayers, increases towards infinity. In other terms, the wave cannot penetrate far into the multilayer stack. Only evanescent waves with an exponential decay may

exist in the structure, while the actual propagation of waves is forbidden, which actually amounts to the appearance of a photonic band gap. In the specific case where all individual layers present the same optical thickness $\lambda/4$, all the waves reflected at the different interfaces (1), (2), (3), (4) are in phase and, as might easily be imagined, such a situation correspond to the largest band gap. Conversely, at the even harmonic frequencies $2\omega, 4\omega, 6\omega, \dots$ the band gaps disappear for the same reasons which have already been mentioned.

1.3.3 Band Diagrams of Two-Dimensional Photonic Crystals

The analysis developed for one-dimensional photonic crystals has already revealed some of the most fundamental features of photonic structures, which are independent from the dimension of the crystal. However, the very simplicity of the one-dimensional case, where the propagation of waves is restricted to a single direction, did not permit to address certain points which become crucial at higher dimensions. Thus, the existence of photonic band gaps, as well as their corresponding frequency ranges, might easily have been anticipated by a reader already familiar with Bragg reflectors. By contrast, in the two-dimensional case to be presently considered, not only are there now two main directions of propagation instead of a single one, but the polarisation of the wave itself has a decisive influence which can no longer be ignored. For this reason, the very possibility of achieving a complete photonic band gap both for all in-plane directions of propagation and for the two main polarisations (TE and TM) is far from being self-evident. The existence of a complete two-dimensional band gap may not be, as will be seen in the second and third parts of this book, an absolute requirement as far as applications are concerned. Nonetheless, the search for the structures most likely to allow such a complete photonic band gap has driven numerous of theoretical and experimental researches in the past decade (Cassagne 1996; Gadot 1997; Gérard 1993; Grüning 1996; Joannopoulos 1995a, 1995b, Rowson 1999a). In what follows, we shall discuss the band diagrams of two-dimensional photonic crystals with increasing symmetry (square and hexagonal), and examine how the characteristics of the structure depend on whether the regions with high dielectric permittivity are connected to one another or not.

The Square Lattice

The square lattice has been previously introduced in Section 1.3.1 and can also be seen in Fig. 1.4. The irreducible Brillouin zone of this lattice is an isoscele, right-angled triangle ($\Gamma X M$) whose hypotenuse ΓM is parallel to the diagonal of each elementary square. In the same way as for one-dimensional photonic crystals (Fig. 1.5, top), a first approach to the band diagram consists in arbitrarily assuming that all the components of the square lattice have the same dielectric permittivity ϵ_m ('free photon' diagram, represented in the upper part of Fig. 1.9).

It might be useful here to briefly recall the construction of the 'free photon' diagram which by its very nature is polarisation independent. For instance, let us

follow the ΓX direction in the reciprocal lattice. Proceeding from the origin, the first edge of the Brillouin zone is reached at a point with coordinates $(1/2, 0)$. Proceeding from the vertex $(-1, 0)$ of the lattice, the edge of the Brillouin zone is reached at a point with coordinates $(-1/2, 0)$. The length of the path is the same in both cases, and the two points at the edge of the Brillouin zone are strictly equivalent. The corresponding dispersion curves $\omega(\mathbf{k})$ thus intersect at the frequency $\omega = (1/2) 2\pi c/(a \sqrt{\epsilon_m})$. The ‘free photon’ diagram is then constructed by following the different directions ΓX , $X M$, ΓM , starting from vertices of the reciprocal lattice located at increasing distances from the origin. The curvature which might be observed for certain dispersion lines simply results from the fact that the trajectory followed by the extremity of the wave vector \mathbf{k} does not pass at the origin in the reciprocal lattice. In other terms, the modulus of the wave vector \mathbf{k} does not follow a linear variation².

Fig. 1.9 (bottom) represents the band diagram calculated for a square lattice of cylindrical dielectric rods with permittivity $\epsilon = 9$ extending in the air ($\epsilon = 1$). The TM and TE polarisations are represented in this diagram by thick and dashed curves respectively. Here again, one notices the similitude with the ‘free photon’ diagram represented in the upper part of Fig. 1.9, with the difference however that photonic band gaps now appear in regions where the dispersion curves previously intersected in the ‘free photon’ diagram. The centre frequency of the fundamental TM band gap (X point) is at the normalised frequency $(\omega a / 2\pi c) \approx 0.35$, which is in agreement with the value of the frequency observed at the intersection point X in the diagram represented in the upper part of Fig. 9. Far from being a fortuitous coincidence, this reflects the fact that the value ϵ_m used for the dielectric permittivity in the calculation of the ‘free photon’ diagram is equal to the average permittivity of the square lattice formed by dielectric rods.

One of the most important results presented in Fig. 9 is the different behaviour which can be observed between the TM and TE polarisations. The band gaps are thus found to be much larger in TM polarisation than in TE polarisation. Further, contrary to what is the case for TE band gaps, the fundamental TM band gaps tend to overlap along the three main propagation directions, and therefore along any in-plane direction of propagation. The obvious consequence to be drawn is the absence of a complete photonic band gap for the square lattice. It might also be observed that TM band gaps occur at lower photon energies than the corresponding TE band gaps. All these differences between TM and TE polarisations can actually be explained from the fact that the dielectric rods are not connected to one another.

² The possibility also exists of trajectories of the wave vector \mathbf{k} leading to almost horizontal dispersion curves (see for instance those originating from the vertices of the lattices $(0,1)$ and $(0,-1)$ in Fig. 1.9). This corresponds to the case where the Bloch waves have a very low group velocity v_g (see Chapter 6). Actually, the propagating wave can be viewed as the superposition of two waves whose field distributions are symmetrical with respect to the direction of propagation. Under these conditions, the transverse component $v_{g,\perp}$ becomes zero, while the longitudinal component $v_{g,\parallel}$ remains non zero.

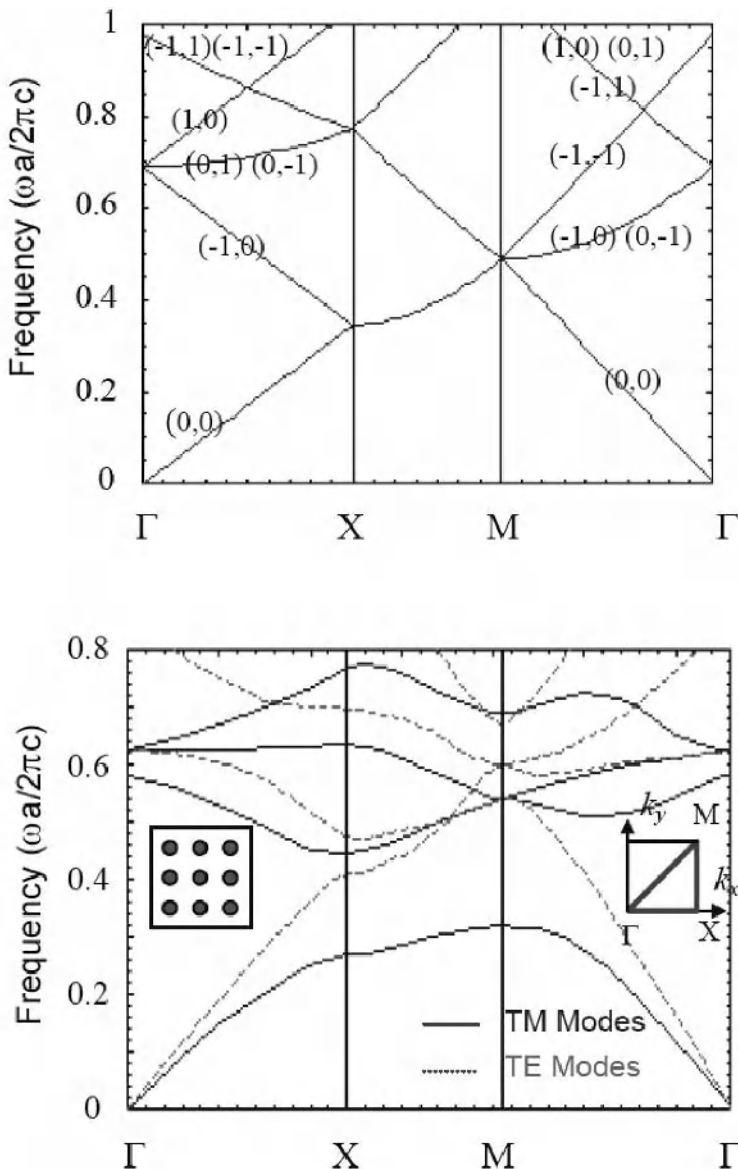


Fig. 1.9. Photonic band diagrams of square lattices. *Top*. ‘Free photon’ diagram calculated for the dielectric permittivity $\epsilon_m = 2.1$. *Bottom*. Band diagram calculated for a square lattice of cylindrical dielectric rods ($\epsilon = 9$) in the air ($\epsilon = 1$). The radius of the rods is $r = 0.2a$, where a is the period of the lattice. The average permittivity of the lattice is equal to ϵ_m

For TM modes, the electric field is parallel to the axes of the cylinders, and remains such when crossing the interface between the dielectric and the air. In this case, the displacement vector $\mathbf{D} = \epsilon\mathbf{E}$ may be strongly localised within the cylinders, thereby minimising the energy of the fundamental mode. In contrast, for the first excited mode, the field is for the most part localised inside the air region: its energy is therefore much higher and a large energy gap separates this mode from the fundamental mode. In TE polarisation, the electric field extends within the propagation plane perpendicular to the cylindrical rods. The continuous field lines of the TE modes are therefore forced to penetrate inside the air region if they are to connect the neighbouring rods. This applies not only to the excited modes, but also to the fundamental mode as well. The energy separation between the first excited TE mode and the fundamental mode is therefore reduced, resulting in smaller TE band gaps. On the other hand, since they are more localised inside the air region, TE modes generally present higher energies than the TM modes of the same order.

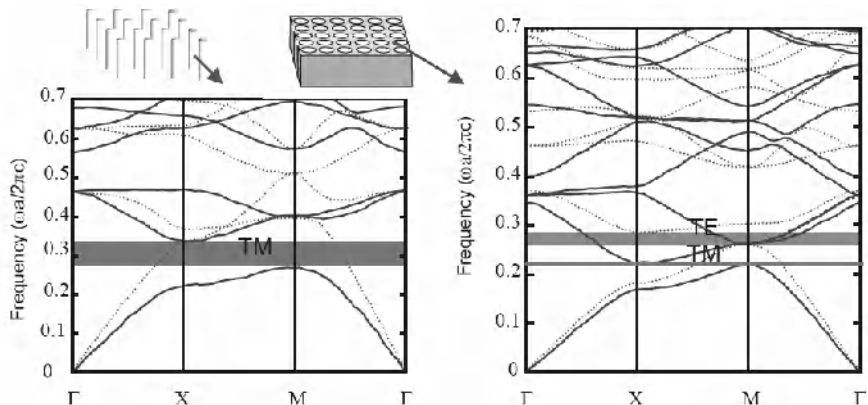


Figure 1.10. Comparison between the band diagrams calculated for a square lattice of dielectric rods in the air (left) and a square lattice of holes drilled inside a dielectric substrate (right). The square lattice formed by the dielectric rods is slightly different from the lattice represented in Fig. 1.9: the rods have a dielectric permittivity $\epsilon = 11.7$ and a radius $r = 0.2a$, where a is the period of the lattice. The lattice of holes is assumed to be fabricated from a dielectric with the same permittivity ($\epsilon = 11.7$) while the radius of the holes is equal to $r = 0.4a$. In either case, the dashed curves correspond to TE modes, while the thick curves correspond to TM modes. The fundamental band gaps are indicated in each figure for both TM and TE modes. Contrary to the lattice formed by dielectric rods in the air, the lattice consisting holes inside a dielectric substrate presents the two types of band gaps (TE and TM band gaps). In this case however, the TM band gap is much narrower and it does not overlap with the TE band gap

The opposite situation occurs when the regions of high dielectric permittivity are connected to one another, as is the case of a lattice formed by air columns drilled inside a dielectric substrate. Fig. 1.10 present a direct comparison between the band diagrams of these two types of structures. As can be seen, contrary to the square lattice of dielectric rods in the air (Fig. 1.10, left), the square lattice formed by air columns in a dielectric substrate (Fig. 1.10, right) exhibits larger photonic band gaps in TE polarisation than in TM polarisation. Here again, the TM and TE band gaps do not overlap, and a complete photonic band gap cannot be achieved for these two polarisations. A possible solution consists in trying to combine the characteristics of the two types of lattices. As will be described in the next section, a triangular lattice formed by holes with a large diameter created inside a dielectric substrate offers in this respect an interesting compromise.

The Triangular Lattice

The triangular lattice has already been introduced in Sections 1.1.4 and 1.3.1, and can also be seen in Fig. 1.4. The triangular lattice is actually the two-dimensional lattice which presents the highest symmetry if we limit ourselves here to the consideration of lattices with a single ‘atom’ per cell. The Brillouin zone is an hexagon, with a nearly circular shape. The crystal therefore exhibits a high degree of isotropy, which is a favourable condition for the appearance of omnidirectional band gaps. In the same way as for the square lattice, the possibility exists of designing either structures formed from disconnected dielectric cylinders or structures where the different dielectric regions are connected to one another. For each of these structures, the same polarisation-dependent behaviour reported in the last section can be observed: TM band gaps tend to occur in lattices formed by isolated high-permittivity regions, and TE band gaps in connected lattices. Nevertheless, as a direct consequence of the geometry of triangular lattices, and of their higher degree of compactness, the connected lattice tends to combine these two advantages in the case where the diameter of the holes approaches the period of the lattice. In this case indeed, the walls of the pores become so thin that the residual dielectric ‘veins’ are almost isolated. The fact that such a structure may actually provide a complete two-dimensional band gap has been vindicated by different experiments, conducted first in the mid-infrared region (Grüning 1996), and more recently at telecommunication wavelengths (Rowson 1999a). In Fig. 1.11 is represented the photonic band diagram of a triangular lattice formed by pores created by photochemical etching in a silicon substrate where $\epsilon \approx 11.7$, while the refractive index is ≈ 3.4 (Rowson 1999a). The period of the lattice is equal to $2 \mu\text{m}$ while the diameter of the pores is equal to $1.98 \mu\text{m}$, corresponding to an air filling factor equal to $\approx 72\%$. As can be seen from the consideration of Fig. 1.11, the complete two-dimensional photonic band gap is centred at a wave number equal to $\approx 2100 \text{ cm}^{-1}$ i.e. at $\lambda \approx 5 \mu\text{m}$. The relative width of the gap is $\approx 9\%$.

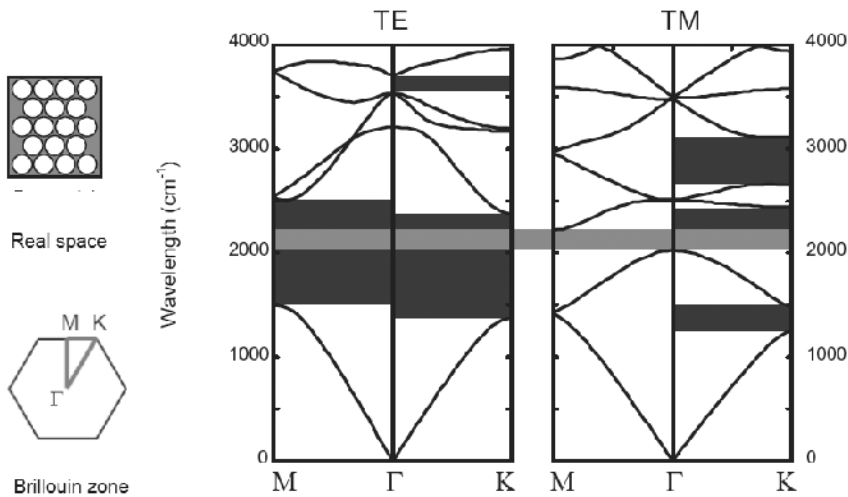


Fig. 1.11. *Left.* Triangular lattice formed by pores created in a dielectric substrate and corresponding Brillouin zone. *Right.* Band diagram calculated for a dielectric substrate with a permittivity $\epsilon = 11.7$ and a period $a = 2\mu\text{m}$, while the radius of the pores is $r/a = 0.45$. The band gaps are indicated by grey bands

The Graphite-Type Hexagonal Lattice

To the best of our knowledge, the triangular lattice formed by pores created in a dielectric substrate is the only ‘simple’ lattice which exhibits a complete two-dimensional photonic band gap between the first transmission bands. Such a situation has never been reproduced for any other two-dimensional lattice, including the dual structure formed by dielectric rods in the air. Only the unrealistic alternative of using dielectric materials with a very high permittivity ($\epsilon \gg 11$) would sufficiently widen the band gaps of any of these other lattices to the point where complete photonic band gaps could appear at lower frequencies. This being said, there do exist certain ‘simple’ two-dimensional lattices fabricated from standard dielectric materials which may present a complete photonic band gap between high-order bands. The graphite-type hexagonal lattice, also referred to as the honeycomb lattice, is an example of such a lattice. More complex examples of such structures can be found in (Dobson 1999). The graphite-type lattice is represented in Fig. 1.12 (left). Contrary to the triangular lattice, this lattice possesses two ‘atoms’ per unit cell. The reciprocal lattice is also an hexagonal lattice and the corresponding irreducible Brillouin zone is the same as for the triangular lattice. The main directions of propagation are denoted in this figure as ΓK and ΓM . A complete band gap was for the first time theoretically predicted in the case of a

structure formed from isolated dielectric cylinders (Cassagne 1996, 1997). These theoretical predictions were vindicated a year later in experiments conducted in the millimeter wave region (Gadot 1997). The structure was composed of alumina rods ($\epsilon = 9$) extending in the air. The diameter of the rods was equal to 1.5 mm, while the distance between two neighbouring rods was equal to 2.9 mm. The corresponding band diagram is reported in Fig. 1.12 (right). In perfect agreement with the calculations, a complete band gap was experimentally found to occur between the seventh and eighth TM transmission bands and between the fifth and sixth TE transmission bands respectively. The measured values for the centre frequency of the gap and its relative width were found to be equal to 59 GHz and 6%, respectively (Gadot 1997). A similar demonstration of a complete photonic band gap in a graphite-type lattice was also reported for a structure formed by pores created in a dielectric substrate (Rowson 1998). In the latter case, the photonic crystal was fabricated from silicon by photochemical etching. Experiments conducted in the mid-infrared region revealed the existence of a complete photonic band gap extending in the 5 μm wavelength region.

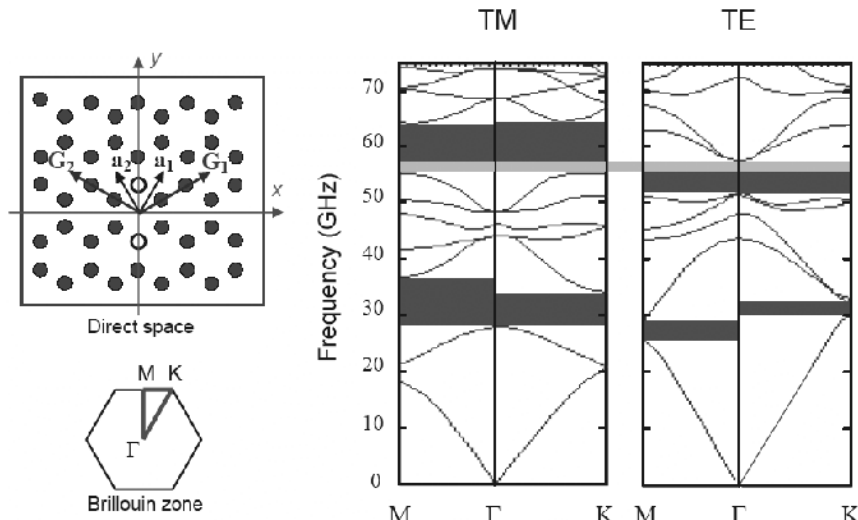


Figure 1.12. Photonic band diagram of a graphite-type hexagonal lattice. **Left.** Schematic representation of the structure, displaying the basis vectors of the direct and reciprocal lattices (top) and its irreducible Brillouin zone (bottom). **Right.** Band diagram of a lattice of dielectric rods ($\epsilon = 9$) extending in the air ($\epsilon = 1$). The radius of the rods is equal to $r \approx 0.26d$, where d is the distance between two neighbouring rods. The photonic band gaps are represented here in the form of grey bands. The vertical scale for the frequencies is the same as was used for the first demonstration of a complete photonic band gap in such a graphite-type lattice (Gadot 1997)

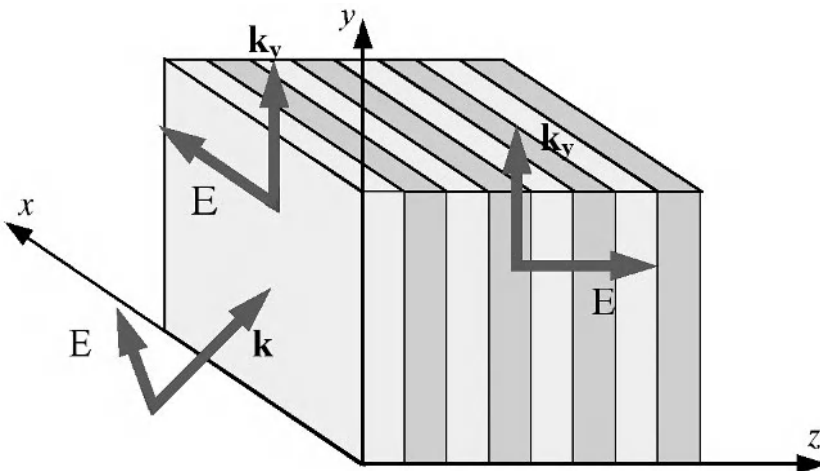


Fig. 1.13. Off-axis propagation in a one dimensional photonic crystal: general case and limit cases ($k_x = k_z = 0, k_y \neq 0$) for two different polarisations of the field

1.3.4 Off-Axis Propagation in One and Two-Dimensional Photonic Crystals

The one and two-dimensional photonic crystals which have been presented in the preceding sections do not allow the total control of light for all directions of propagation. This can be illustrated by considering for instance the case of a Bragg multilayer stack with an off-axis illumination ($k_x = 0, k_y \neq 0, k_z \neq 0$), as represented here in Fig. 1.13. No assumption is made here concerning the nature of the medium surrounding the multilayer stack. First, the off-axis propagation of the wave entails that different behaviours will occur depending on the polarisation of the field, i.e. depending on whether the electric field is parallel or perpendicular to the incidence plane. Secondly, the band gaps that were achieved in the case of an on-axis propagation along the Oz axis tend to become narrower as the incidence angle, i.e. k_y , increases and they may even vanish for a certain value of the incidence angle.

In order to fully understand the influence exerted by the polarisation of the field, it should be borne in mind first that the reflection coefficient at each interface, or Fresnel coefficient, comes to depend on the polarisation as soon as the incidence is not normal (Born 1965). Further, the variation of the distribution of the displacement vector depending on the polarisation of the field should also be considered here. For the sake of simplicity, we shall consider here the case, repre-

sented in Fig. 1.13, where k_y assumes a small value and where $k_z = k_x = 0$. This corresponds to the case of a long wavelength radiation. When the electric field is parallel to the dielectric layers, i.e. along the Ox axis, the continuity of the field at the interfaces tends to cause the displacement vector to be localised in the high-permittivity layers, thereby minimising the electromagnetic energy. When the field is polarised perpendicularly to the dielectric layers, i.e. along the Oz axis, the continuity of the displacement vector at the interfaces imposes the uniform distribution of this vector in the whole structure, with the consequence that a higher electromagnetic energy will be contained in the structure. As a result, the dispersion curves of the two polarisation modes diverge starting from the origin.

In order to understand the effects induced by the reduction of the widths of the band gaps in the case of an off-axis propagation, one may consider the limit case where k_y assumes a very high value and where k_z is negligible. This corresponds to the case of a short wavelength radiation. In this case, and whatever is the polarisation of the field, the electromagnetic energy tends to concentrate within the regions of higher dielectric permittivity, which actually tend to behave as planar waveguides. In other terms, the wave becomes evanescent in the regions of lower permittivity, while the periodic coupling within the multilayer structure tends to disappear. But since the existence of such a coupling was actually at the origin of the photonic band gaps themselves, its disappearance causes all these photonic band gaps to vanish. Assuming a continuous variation of the widths of the band gaps, a progressive reduction of these widths then occurs for the intermediate values of k_y . More precisely, the effect of guiding in the dielectric layers becomes significant as soon as $k_y > \omega/c$, since in this case the wave can no longer escape from these layers.

The effects induced by the reduction of the band gaps in two-dimensional photonic crystals can be explained along the same lines when the light propagates outside the (xy) principal plane. In this case, when k_z assumes large values, the electromagnetic energy tends to concentrate within the high-permittivity cylinders which now behave like linear waveguides. However, the propagation of light along the invariant axis may present certain advantages, for instance in the case of microstructured optical fibers, as will be described in Chapter 11.

1.3.5 Band Diagrams of Three-Dimensional Photonic Crystals

The realisation of a complete photonic band gap for any direction of propagation and for any polarisation of the field can be achieved only with three-dimensional photonic crystals. From the beginnings of the researches on photonic crystals, numerous attempts were directed at this objective using the simplest types of three-dimensional lattices (simple cubic lattice, centred cubic lattice, face centred cubic lattice). However, most of these attempts failed (Yablonovitch 1994). Indeed, the structures investigated at this time were often found to behave like semi-metals, where electronic gaps disappear for certain specific directions within the solid-state crystal. The decisive breakthrough came with face centred cubic lattices with

two ‘atoms’ per unit cell, reproducing the structure of the most usual semiconductors (silicon, germanium, gallium arsenide, etc) and of diamond (Ho 1990; Yablonovitch 1991a): very large omnidirectional photonic band gaps were then predicted before being reported in the microwave region. Since these pioneering works, researches have been conducted along a variety of different technological directions in order to reproduce the original experiments at shorter wavelengths and with other types of materials. Some of the cubic structures which had been abandoned after the discovery of the yablonovite were thus reconsidered. An example is the relatively narrow, albeit quite interesting three-dimensional photonic band gap which was recently demonstrated in the case of a simple cubic structure (Lin 2001b). Different aspects associated with three-dimensional photonic crystals shall be discussed in more detail in Chapter 12.

Fig. 1.14 represents the typical band diagram of a ‘yablonovite’ structure. This type of structure was first proposed by E. Yablonovitch and its characteristic have since then been verified by numerous studies (Yablonovitch 1991a). These structures are formed by drilling holes inside a dielectric substrate along three directions which reproduce the $\langle 110 \rangle$ galleries of the diamond crystal, as can be seen from the consideration of Fig. 1 in the preface to this book. In the example represented in Fig. 1.14, the dielectric substrate is assumed to have a permittivity $\epsilon = 13$, while the ratio between the radius of the holes and the period of the lattice is such that the air filling factor is equal to 57% after the holes have been drilled. The Brillouin zone of a Yablonovite is simply that of the fcc lattice, i.e. a truncated octahedron with a nearly spherical shape. The high degree of isotropy presented by such a structure obviously increases the possibility for omnidirectional band gaps to appear. The band diagram represented in Fig. 1.14 was calculated along the $(X, U_3, W, K_3, L_3, \Gamma, L_1, K_1, W, U_1, X)$ path joining the main apexes of the irreducible Brillouin zone. In the present case, the calculations were limited to the first six bands of lower energy. As can be seen, a complete photonic band gap with a relative width $\Delta\omega/\omega$ equal to 15 percent appears for any direction of propagation and any polarisation of the field between the second and the third transmission bands. Of all the parameters of the structure, the air filling factor and the permittivity (or refractive index) contrast have the main influence on the width of the gap. Thus, high values for the air filling factor and the index contrast tend to result in larger bad gaps. A systematic study undertaken on this influence has shown that, for an air filling factor equal to $\sim 60\%$, a complete band gap appears only if the dielectric permittivity is higher than ~ 6 , or equivalently if the refractive index is higher than ~ 2.5 .

It is quite obvious that calculations of band diagrams three-dimensional photonic crystals are more difficult to perform and more time-consuming for than for one-dimensional and two-dimensional photonic crystals. While a decomposition of the field using a basis consisting of a thousand plane waves is generally sufficient for describing the photonic band structure associated with two-dimensional crystals, the accuracy of the results obtained with this method when applied to three-dimensional crystals is less certain, and convergence tests are required before the results can be validated (see Section 1.5 in this chapter).

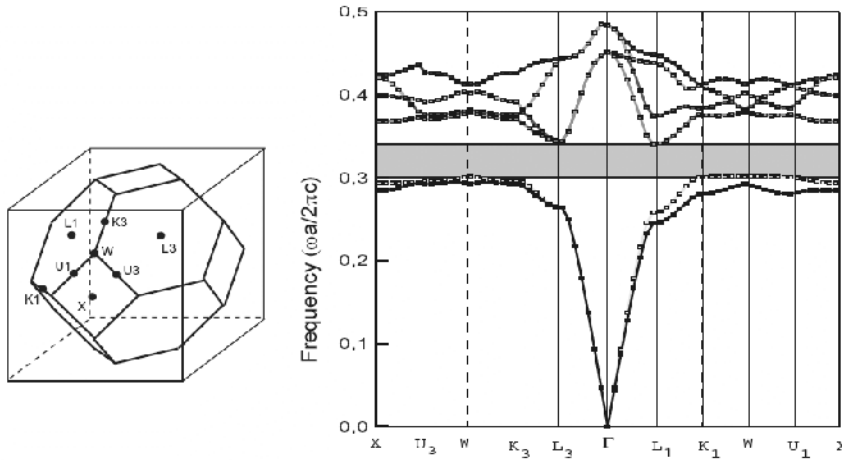


Fig. 1.14. Brillouin zone of the fcc lattice and band diagram of the Yablonovite structure calculated for the first six bands. The permittivity of the dielectric is $\epsilon = 13$, while the ratio between the radius of the holes and the period of the crystal is such that the air filling factor is equal to 57% after the holes have been drilled (David 2003)

1.4 Infinite Crystals with Defects

In the preceding sections, photonic crystals were always assumed to be perfectly periodic systems. Nevertheless, much in the same way as the doping of semiconductor crystals is essential for the realisation of actual electronic devices, the implementation of specific optical functions with photonic crystals generally requires the insertion of defects, either localised or extended, which cause a disruption in the periodicity of the crystal. Certain issues associated with the implementation of optical functions and the realisation of optical devices will be addressed in the second and third parts of this book. In this section, we shall describe the modifications induced by the presence of defects on the band diagram of photonic structures, as well as the appropriate methods of calculation, which are based on expansions of the fields in terms of Bloch modes (see Section 1.1.2 in this chapter). In the strict sense of the term, the translational symmetry of the crystal disappears as soon as the periodicity is disrupted due to the insertion of defects, with the consequence that Bloch modes are no longer solutions of Maxwell's equations. In order to remain within this framework, the introduction of approximations is therefore necessary. However, as is the case for perfectly periodic crystals, the band diagram provides a synthetic view of the spectral properties of doped crystals, even if it is at the price of approximations. In the last resort, a rigorous analysis

of the influence exerted by defects is always necessary, requiring the introduction of electromagnetic models of the same type than those used for photonic crystals of finite size. These models shall be described later in Chapter 2.

In the same way as for solid-state crystals, two main types of defects exist: point defects and extended defects. Point defects are associated to very local disruptions in the periodicity of the crystal, and their presence is revealed through the appearance of electromagnetic modes at discrete frequencies, which may be seen as analogous to isolated electronic states. Likewise, extended defects can be seen as analogous to dislocations of the crystal, and they may result in the appearance of transmission bands in spectral regions where a photonic band gap existed in the case of a perfectly periodic crystal. In what follows, we shall successively illustrate these two types of defects by using different examples with increasing complexity, ranging from one to three dimensions. We shall illustrate the effects of coupling phenomena between point defects, allowing us in turn to introduce the ‘supercell’ method used for the calculations of band diagrams. Other methods of calculations, for instance methods relying on the Wannier functions introduced in solid-state physics (Wannier 1937) will also be discussed in the course of this section. Finally, in order that this presentation be as complete as possible, we shall consider the case of semi-infinite crystals, where electromagnetic modes can be localised at the surface of the crystals. This description will serve as a transition into the finite crystal models that will be addressed in Chapter 2.

1.4.1 Point Defects

Points Defects in One-Dimensional Photonic Crystals

Point defects in a one-dimensional crystal can be obtained by modifying either the refractive index or the thickness of one of the crystal layers. It is quite obvious that such defects are equivalent to Fabry-Perot cavities. Electromagnetic modes may therefore occur at discrete frequencies within the different photonic band gaps, depending on the modifications of the refractive index thus induced or on the length of the optical cavity. The upper part of Fig. 1.15 shows the changes arising in the band diagram of Fig. 1.7 when the thickness of one of the high-index layers is increased by a factor of 2.2, i.e. when $d'_1 = 0.44a$ instead of $d_1 = 0.2a$. In this case, discrete energy levels are indeed found to occur in each of the three first photonic band gaps. The electric field distributions calculated using a multilayer model (Born 1965) and represented in the lower part of Fig. 1.15 show that the electromagnetic modes corresponding to these band gaps exhibit one, two and three oscillations respectively within the central layer forming the cavity. This demonstrates that these modes are actually but the first three modes of a planar cavity bounded on either side by semi-infinite Bragg reflectors. Due to the infinite number of alternations from one Bragg layer to the other, the reflection coefficient of each Bragg reflector has an amplitude equal to the unity, but may exhibit a non-

zero phase $\varphi(\omega)$ which depends on the frequency. For a cavity with a length L , the resonance condition can be expressed for each mode in the simple following form:

$$\frac{2\pi L\omega}{n_l c} + 2\varphi(\omega) = 2p\pi \quad (1.57)$$

where p is an integer and $n_l = \sqrt{\epsilon_1}$ is the refractive index of the dielectric layer formed by the cavity.

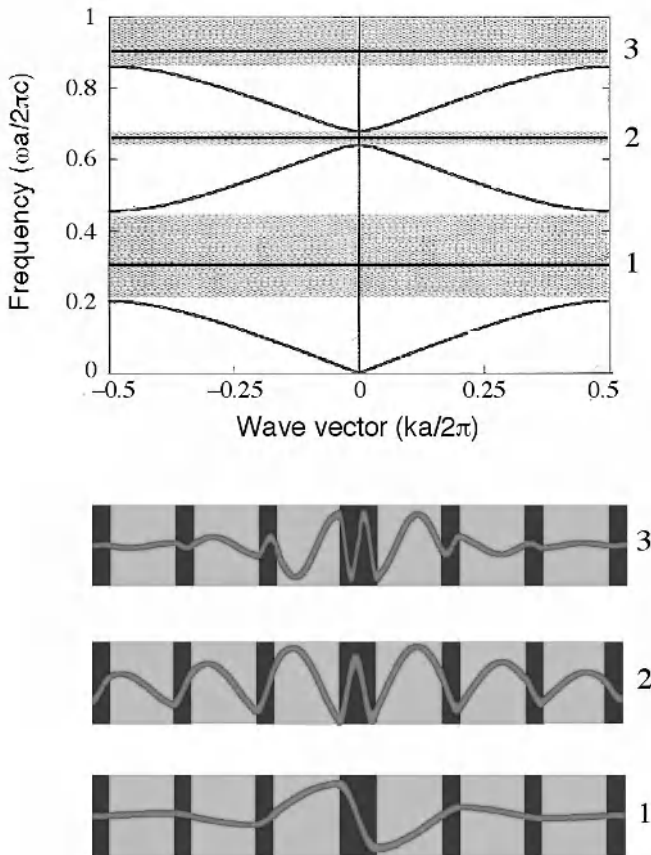


Fig. 1.15. Defect modes created in the one-dimensional crystal of Fig. 7 ($d_1 = 0.2a$, $d_2 = 0.8a$). The thickness of one of the high-index layers is increased here by a factor of 2.2. **Top.** Discrete energy levels occurring within photonic band gaps. **Bottom.** Distributions of the electric field calculated for the first three defect modes. The high-index layers are represented here in black while the low-index layers are represented in grey

In fact, the situation observed in Fig. 1.15 does not represent the general case, and the insertion of point defects does not systematically lead to the existence of discrete energy levels within all photonic gaps. This specific result is due to the choice of both the length of the cavity and the dielectric layers forming the Bragg reflectors. As has already been mentioned in Section 1.3.2, the fact that the optical thickness of the high-index layers ($0.2 a\sqrt{\epsilon_1} \sim 0.72 a$) is slightly different from the optical thickness of the low-index layers ($0.8a\sqrt{\epsilon_2} = 0.8 a$) causes band gaps to appear for all harmonics of the fundamental frequency ω_0 of the gap. The properties of Bragg mirrors depend on the harmonic parity: thus, the band gaps at even harmonics are narrower than band gaps at odd harmonics. The efficiency of the Bragg mirror is therefore lower for even-order band gaps, resulting in this case in a lower confinement of the electric field within the cavity, as can be seen in Fig. 1.15. Further, the phase $\varphi(\omega)$ of the reflection coefficient significantly deviates from zero in this case, while it remains almost zero for resonances in the odd-order band gaps (odd multiples of ω_0). The resonance condition expressed by Eq. 1.57 implies therefore in this case that the frequency difference between the successive resonant modes will not be constant. This phenomenon can be observed in the upper part of Fig. 1.15. When the length of the cavity is modified, resonant modes of odd order sweep across their respective band gaps, while resonant modes of even order may suddenly disappear.

Point Defects in Two and Three-Dimensional Photonic Crystals

Most of the observations which have been made for one-dimensional photonic crystals actually apply to two and three-dimensional photonic crystals as well. In these crystals, point defects can be created by locally modifying the refractive index, by changing the size of the patterns (substitution defect), by displacing one of the periodic patterns (interstitial defect) or by inserting a different pattern (dopant). Here again, the presence of a point defect may lead to discrete energy levels within the photonic gaps. However, contrary to what was the case for one-dimensional photonic crystals, these levels correspond to localised electromagnetic modes only in the case where the band gaps are omnidirectional, be it only for a certain polarisation. If this condition is fulfilled, the electromagnetic field is actually found to be concentrated in the region of the defect and evanescent in the surrounding regions. By contrast, in the case where the band gap is not omnidirectional, a fraction of the electromagnetic energy will constantly leak away from the region of the defect towards directions along which the propagation is allowed. In this case, the presence of a point defect essentially leads to a peak in the density of electromagnetic states (see Section 1.4.7 below). It is quite obvious that the consideration of two or three-dimensional crystals entails a higher degree of complexity in terms of the field distributions than was previously the case. Further, the symmetries of the crystal may result in the degeneracy of the defect modes

Fig. 1.16 represents the field distribution (displacement vector) calculated for a defect created in a two-dimensional square lattice formed by dielectric cylinders

($\epsilon = 9$, $n \approx 3$) in the air. The defect was created here by removing one cylinder, i.e. by introducing a vacancy in the lattice. The incident wave is assumed to be TM polarised, a condition under which an omnidirectional photonic band gap appears between the first two transmission bands (Fig. 1.9). The defect mode represented in Fig. 1.16 appears near the edge of the conduction band. The field distribution presents characteristics similar to those of the Bloch mode associated with the conduction band. As can be seen, two field extrema with opposite signs exist within all dielectric cylinders adjacent to the defect, which means that the field nodes are aligned along the diameter of each such cylinder. Actually, by replacing the lacking cylinder with a dielectric cylinder with variable permittivity, the frequency of the defect can be made to range quasi-continuously from the top of the valence band to the bottom of the conduction band (Mc Call 1991, Meade 1993, Joannopoulos 1995). The frequency of the defect mode increases as the dielectric permittivity of the cylinder forming the defect decreases. This phenomenon simply reflects the reduction in the effective optical diameter $n_{\text{eff}} \Phi$ of the cavity associated with the defect.

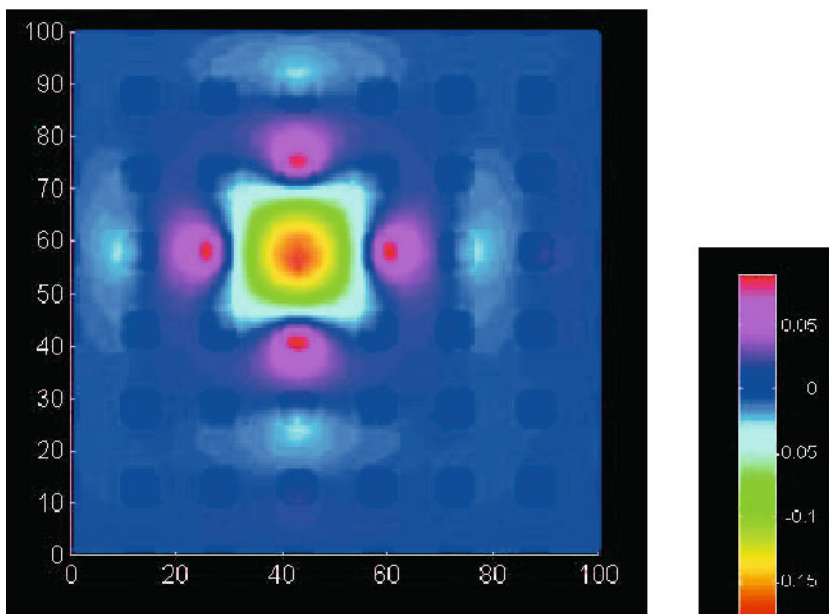


Fig. 1.16. Field distribution (displacement vector) associated with a point defect mode in a two-dimensional square lattice formed of dielectric cylinders ($\epsilon = 9$) extending in the air (Gadot 1998). The radius of the cylinders is equal to $0.25a$, where a is the period of the lattice. The defect, constituted by a single missing cylinder, is equivalent to a vacancy in the lattice. The different shades, ranging from white to black, correspond to different amplitudes of the field

The defects represented in Figs. 1.15 and 1.16 can be said to be point defects only in the sense that the space is voluntarily limited to one and to two dimensions respectively. In the actual space, which by essence is three-dimensional, modifying a whole cylinder is actually equivalent to the insertion of an infinite linear defect, since the field in this case is localised in the whole region extending along the modified cylinder. Likewise, the modification of the thickness of a layer in a one-dimensional photonic crystal is equivalent to the insertion of a planar defect. The concept of a point defect really becomes meaningful when considering three-dimensional photonic crystals. Indeed, in this case, creating such a defect amounts to creating a three-dimensional microcavity, whose dimensions may be sufficiently small as to allow the existence of only a limited number of electromagnetic modes, and even a single mode, within a given frequency region. We shall return later in Chapters 7 and 10 to the possibility of such a total control of electromagnetic waves.

A different example of a point defect in a three-dimensional photonic crystal is represented here in the upper part of Fig. 1.17. In this example, taken from (Chelnokov 1997, 1998), the three-dimensional photonic crystal is of the ‘wood-pile’ type (Ho 1994), and consists of periodic arrays of dielectric (silicon) rods ($\epsilon \sim 13$) vertically stacked on top of one another. The rods of two successive arrays are oriented along two perpendicular directions and form a half-period of the crystal along the vertical direction ($<001>$ direction in figure 1.17). Further, each half-period is shifted from the preceding one by half a square diagonal in the horizontal plane ($<100>$ direction in Fig. 1.17). Four arrays of rods are therefore necessary in order to form one period of the crystal along the vertical direction. The fcc structure thus created is analogous to the diamond structure, and as such it exhibits a complete photonic band gap.

In the experiments corresponding to this example (Chelnokov 1997), the existence of a complete photonic gap was demonstrated at frequencies close to 1 THz (Fig. 1.17, bottom) using a structure with an appropriate sizes. Four point defects, consisting of square parallelepipeds made of silicon, i.e. in the same material than the rods themselves and acting therefore as dopants, were inserted in four different empty regions of the crystal, as can be seen in the upper part of Fig. 1.17. The creation of these defects resulted in the appearance of resonance peaks which can be observed at the low-frequency side of the complete photonic band gap (Fig. 1.17, bottom). According to the conventional terminology used in (Joannopoulos 1995b), these defects can be described as dielectric defects, which present field characteristics similar to those of the Bloch modes associated to the valence band. In the experimental demonstration reported in Fig. 1.17, the low value measured for the transmission at the resonance peak frequency (-27 dB) may seem surprising. Indeed, a transmission close to the unity, as in the case of a lossless Fabry-Perot cavity, might have been expected. This low value was first explained by the residual absorption of silicon in the experiments (Chelnokov 1998), but its chief cause appears to be the weak coupling between the incident plane wave and the localised defect mode. Indeed, a large fraction of the incident energy is not coupled with the defects and is either reflected or diffracted along the allowed directions. While it was thought that the insertion of four defects instead of a single de-

fect would compensate for the weak coupling between the plane wave and the defect mode, the small distance between the defects tends actually to create a coupling between these very defects. As a consequence, the resonance peak broadens but remains of a limited amplitude. The coupling of defects in photonic crystals will be addressed in more detail in the following section.

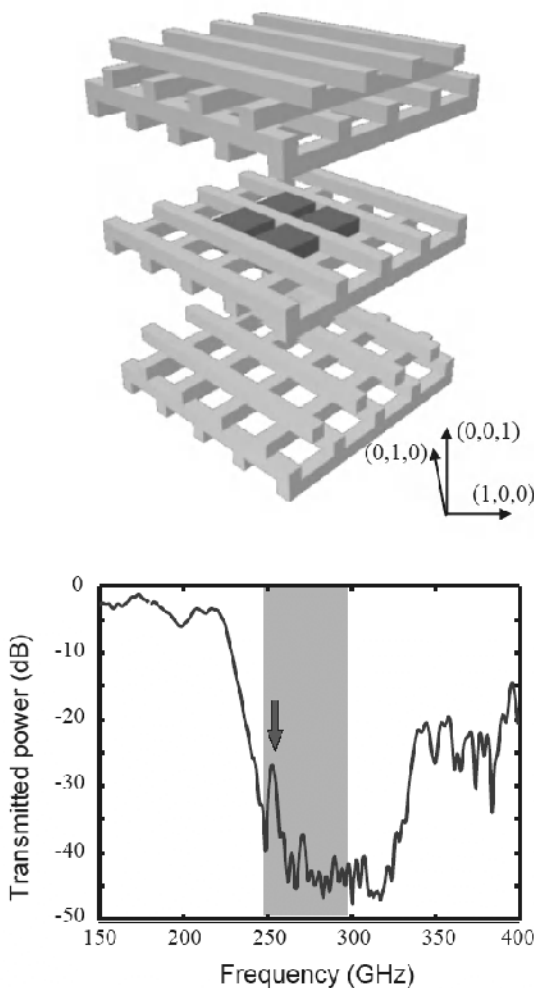


Fig. 1.17. *Top.* Exploded view of a three-dimensional photonic crystal of the ‘woodpile’ type formed from silicon. Four point defects consisting of square silicon parallelepipeds (represented in black) are inserted in the middle of the crystal. *Bottom.* Transmission spectrum of the crystal with defects measured along the (001) direction. The shaded area in this figure corresponds to the complete photonic band gap (Chelnokov 1998)

Experiments similar to those reported in Fig. 1.17 have also been carried out in the infrared region (Lin 1999). The photonic crystal used for these experiments was also of the woodpile type, with the difference however that the defects were obtained by removing parts of certain dielectric rods, i.e. by creating vacancies rather than by inserting dielectric elements. Thus, some of the rods were therefore discontinuous. The dimensions of the defects created in these experiments and the volumes of the corresponding electromagnetic modes ($0.06 \lambda^3$) are not very far from the ultimate values predicted in the case of a three-dimensional crystal ($\sim \lambda^3/4n^3$, i.e. $\sim 0.007 \lambda^3$ for a material with a refractive index $n = 3.3$). A resonance peak, whose relative amplitude comparable to the amplitude reported in Fig. 1.7, was measured around the centre of the photonic band gap.

1.4.2 Coupling of Point Defects

When several point defects of the same nature are present in a photonic crystal, and when the distance between these defects is large enough, their mutual influence can be neglected. In this case, everything happens as if an energy degeneracy of the system occurred several times. Indeed, while the electromagnetic modes associated to the different defects are localised in different regions of the crystal, their field distributions are identical. By contrast, when the distance between the defects decreases, the coupling between these defects leads to the formation of electromagnetic modes with different field distributions: in this case, the energy degeneracy is lifted. Fig. 1.18 illustrates the effects induced by such a coupling through spectral measurements performed for a two-dimensional photonic crystal with a square symmetry (Lourtioz 1997). This photonic crystal, of finite size, is similar to the crystal represented in Fig. 1.16. Two vacancies were introduced by removing dielectric rods. The transmission spectrum of the crystal was then measured for two different distances between the defects. As a consequence of the centimeter size of the crystal, the measured frequencies are in the microwave region.

When the two defects are distant from one another, as is the case in the upper part of Fig. 1.16, a single transmission peak is observed at the high-frequency side of the TM band gap. This corresponds to an air defect, according to the terminology used in (Joannopoulos 1995b). When the defects are at a close distance from one another, the transmission maximum splits into two peaks, thereby revealing the existence of two different electromagnetic modes. Assuming the origin to be at the centre of the structure, the low-frequency mode presents a symmetric field distribution, while the high-frequency mode presents an anti-symmetric field distribution. This phenomenon is quite analogous to the situation occurring when a particle is released in a quantum well (Cohen-Tannoudji 1973): the wave function of the fundamental state is symmetric whereas the wave function of the first excited state is anti-symmetric.

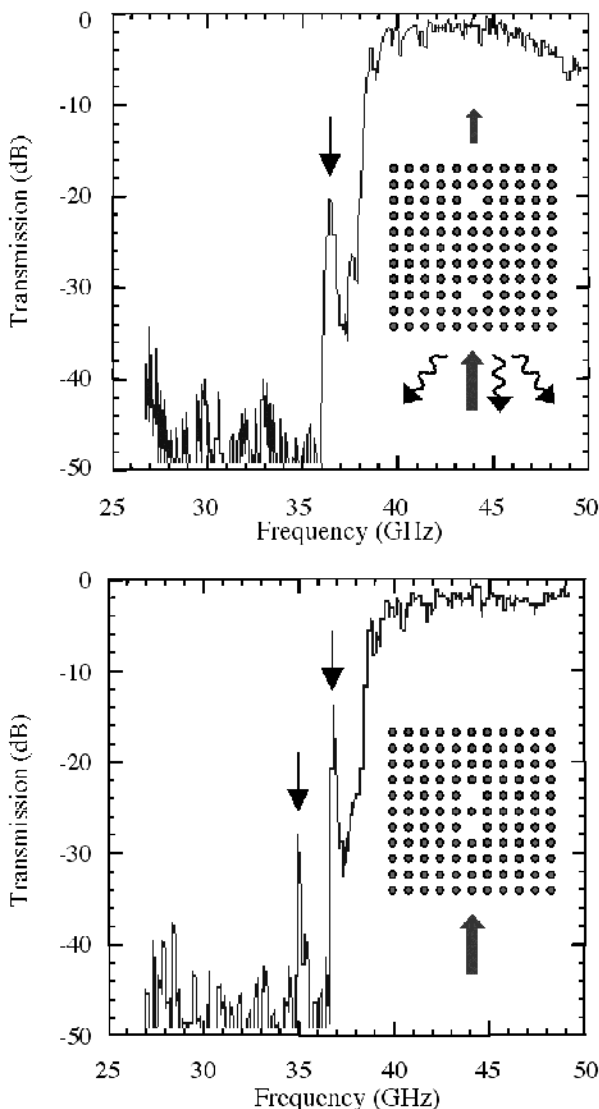


Fig. 1.18. Coupling between two point defects in a two-dimensional photonic crystal with a square symmetry (Gadot 1998). The crystal here is formed by a lattice of alumina rods ($\epsilon = 9$) extending in the air. *Top.* Transmission spectrum measured in weak coupling regime. *Bottom.* Transmission spectrum measured in strong coupling regime

1.4.3 Supercell Method

A necessary requirement for using the plane wave method in the calculation of a defect mode is that the periodicity which has been disrupted by the defect should be artificially reintroduced. To this purpose, the defect is considered as the centre of a new unit cell formed by several successive rows of patterns. The construction of this *supercell* is then repeated along the different spatial directions along which the original photonic crystal is periodically organised. The artificial structure thus defined consists of periodic defects separated by regions of perfect photonic crystal. From what was been previously seen in Section 1.4.2, the spectral properties of this new arrangement can be expected to be quite similar to the properties of the original arrangement, under the condition however that the distance between the periodic defects be large enough, which entails that the dimensions of supercell must be sufficiently large. Two examples of supercells are represented here in Fig. 1.19. The first example corresponds to a square lattice formed by dielectric rods in the air which has already been introduced in Section 1.4.2. Here the defect is associated to a rod with a lower permittivity, or even to a missing rod. The supercell presents itself in the form of a square pattern consisting of 5x5 rods whose centre is the rod with lower permittivity.

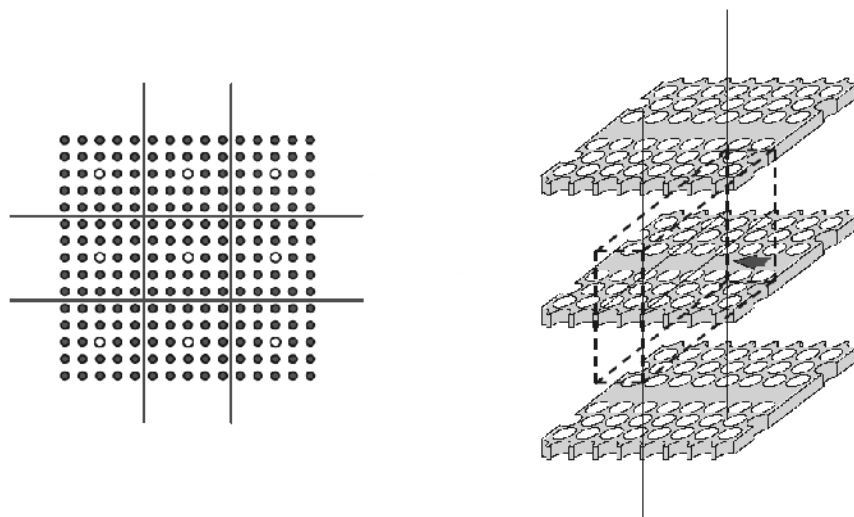


Fig. 1.19. Examples of supercells used for calculating the band diagrams of photonic crystals with defects. *Left*. Two-dimensional lattice of dielectric rods where a zero-dimensional defect was created by modifying the dielectric permittivity of a single rod. *Right*. Two-dimensional lattice of holes in a thin film, where a one-dimensional defect is associated with a row of missing holes. The finite thickness of the film imposes that three-dimensional calculations be performed. The supercell is represented here by the parallelepiped in dashed lines

The second example corresponds to a hexagonal lattice formed by holes created in a semiconductor film with a small thickness. A one-dimensional defect is associated here with a row of missing holes, which amounts to creating a linear waveguide. A first difficulty presents itself due to the finite thickness of the two-dimensional crystal. The solution adopted here consists in replacing the single film with a periodic stack of films at very large distance from one another. An artificial three-dimensional periodic structure is thus obtained where the defect thus ‘periodised’ can now be described using a supercell with a parallelepiped shape. This method allows the correct description of the dispersion curves associated with the guided modes, but it must be handled cautiously when considering leaky modes which may propagate away from the film (Le Vassor d’Yerville 2002). We shall return to the consideration of these issues in Chapter 5 of this book.

1.4.4 Methods derived from Tight-Binding Methods in Solid-State Physics

The method based on the ‘linear combination of atomic orbitals’, or LCAO method, is among the methods which are currently the most used for the calculation of electronic band structures and impurity levels in solid-state crystals. Originally developed by F. Bloch in 1928 (Bloch 1928), this method resorts to a basis of elementary wave functions for electrons, localised around the individual atoms of the crystalline lattice. The atomic interactions are arbitrarily restricted to the interactions arising between neighbouring atoms, while the overlaps between neighbouring orbitals are considered as perturbations. A multiplying factor $\exp(i\mathbf{k} \cdot \mathbf{r})$ is then applied to all basic wave functions in order to account for the periodicity of the crystalline lattice. The calculations of the band diagram proceed then by solving a matrix system of equations, analogous to the system that was obtained with the plane wave method (see Section 1.1.5 in this chapter). However, the use of localised wave functions permits more direct calculations of the impurity levels in the crystal.

The extension of the LCAO method to photonic crystals is far from being obvious, and much effort went into its adaptation. The major difficulty stems from the absence of localised functions for the electromagnetic field in photonic crystals. Among the most recent method developed in order to overcome this difficulty, we shall describe more specifically the method reported in (Albert 2000; Monge 2000) and based on the use of Wannier functions (Wannier 1937). This method proceeds in three successive stages and can be summarized as follows. The first stage consists in predefining localised functions reproducing the main symmetries of the field distributions which are separately calculated using the plane wave method. In general, the analysis can be restricted to *s*- and *p*-type symmetries, in direct analogy with atomic orbitals. After introducing the periodicity of the crystal through the multiplying factor $\exp(i\mathbf{k} \cdot \mathbf{r})$ and after determining the number of ‘atomic’ sites in interaction, the field can be developed in the form of a linear combination of Bloch functions corresponding to different symmetries and differ-

ent atomic sites. The eigenvalue equations of the type $O\mathbf{F} = k_0^2 \mathbf{F}$ (Eq. 1.8) can then be solved. The parameters involved in these equations are simultaneously adjusted in order to reproduce the band diagram of the perfect crystal, calculated using the plane wave method. Actually, obtaining the matrix elements of the operator O does not necessarily require a precise definition of the initial basis functions. The second stage consists in calculating the Wannier functions using a Fourier transformation of the Bloch functions. Contrary to Bloch functions, Wannier functions are not associated with a specific wave vector \mathbf{k} in the Brillouin zone, but with a unit cell of the crystal. These functions are well suited to the description of localised defect states. Finally, in the third stage, the Wannier functions are used for determining the eigenvalues of the matrix equations which correspond to the case of photonic crystal containing defects. The deviation from the ideal case of a periodic crystal is introduced in the equation through an additional perturbation operator V .

1.4.5 Extended Defects

Extended defects of one, two, or three dimensions can be created only in photonic crystals of higher or equal dimension. Of all extended defects, one-dimensional defects are certainly those which have been the most intensively studied, this being due to the fact that these defects can be used as waveguides in photonic crystals. In this respect, the possibility would also exist of imagining two or three-dimensional defects that would be formed by a succession of one-dimensional waveguides connected end-to-end to one another and oriented along different directions, thereby allowing the propagation of light along any path inside the crystal. In this section however, we shall consider exclusively one-dimensional defects, and the issues related to the guiding will be more specifically addressed in Chapters 5 and 9.

The basic example of a one-dimensional defect is that of a linear waveguide inside a two-dimensional crystal. A method for realising such a waveguide consists in aligning identical point defects, regularly spaced along the desired direction. Each point defect constitutes an optical resonator. If the distance between two defects is small enough, as is the case in the example presented in Fig. 1.18, a coupling between these defects arises, resulting in the formation of two defect modes. It is therefore quite apparent that the coupling between an infinite number of identical resonators might lead to the formation of a transmission band consisting of an infinite number of coupled modes. This type of waveguide based on coupled resonators was first suggested in 1999 (Yariv 1999). However, the more generally used method for creating a linear waveguide inside a two-dimensional crystal consists simply in removing or modifying one or several rows of patterns along one of the directions of the crystal. The band diagram is then calculated using the supercell method which has been introduced in Section 1.4.3.

In the left-hand part of Fig. 1.20 are shown the results of calculations conducted along these lines for a triangular lattice of holes where a row of patterns has been

removed along the ΓK direction. The supercell used for the calculations is similar to the supercell represented in Fig. 1.19 (right), but for a film with infinite thickness (pure two-dimensional case). The dielectric permittivity of the substrate is equal to $\epsilon = 13$, while the radius of the holes is $r = 0.4a$, where a is the period of the lattice. For the sake of simplicity, the band diagram is presented here only to the case along the ΓK direction and for TE polarisation. The shaded areas in Fig. 20 correspond to transmission band regions in the case of a perfect crystal without defect: a band gap now appears between the two normalised frequencies $(\omega a/2\pi c) = 0.24$ and $(\omega a/2\pi c) = 0.39$. When the waveguide is taken into account in the calculations, thick dispersion curves are superimposed over the shaded areas representing the transmission bands. These curves actually correspond to guided modes which can be distinguished according to their parity: the field distribution of even modes is symmetric with respect to the axis of the waveguide, while the field distribution of the odd modes is anti-symmetric (see Fig. 1.20, middle). The relatively high number of dispersion curves in the band diagram is due both to the influence of band folding effects and to the existence of high-order guided modes. The band diagram of the structure is further complicated by the presence of anticrossing phenomena. As can be observed in this figure, the waveguide is single-mode only over narrow frequency bands.

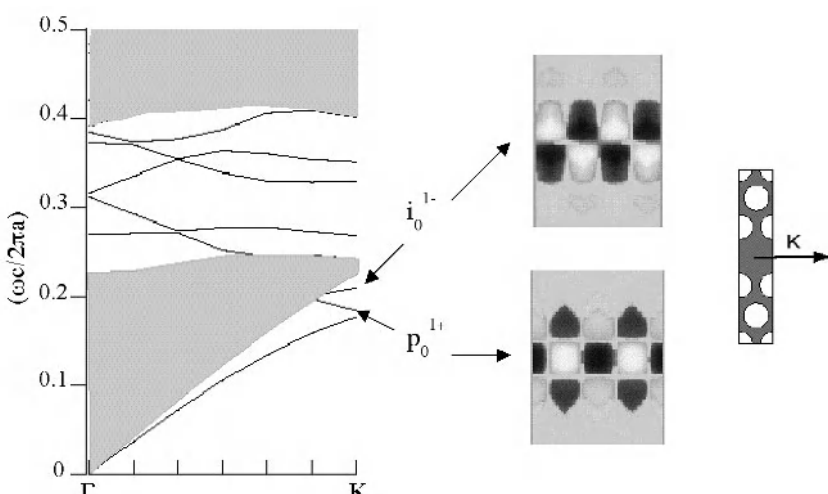


Fig. 1.20. *Left.* Band diagram of a triangular lattice of holes created inside a dielectric substrate ($\epsilon = 13$) where a linear waveguide formed by one row of missing holes along the ΓK direction has been inserted. The diagram is presented here only for the TE polarisation and along the ΓK direction. *Middle.* Field distributions associated with the even mode p_0^{1+} and with the odd mode i_0^{1+} respectively. The index 0 corresponds to the mode order while the exponent 1+ and 1- correspond respectively to the higher and lower branches of the first band folding. *Right.* Supercell used for the calculations

Fig. 20 corresponds to the ideal situation where the photonic crystal is perfectly two-dimensional. In practice, and as will be described in the second part of this book, it is necessary to account for the influence of the finite thickness of actual structures. This is all the more true for photonic crystal waveguides fabricated from thin films, but also for photonic crystal buried waveguides fabricated from bulk substrates. In such cases, three-dimensional calculations need to be performed, for instance by using three-dimensional supercells similar to the example represented in the right-hand part of Fig. 1.19. More elaborate calculations, based on the scattering matrix method, allow the determination of the losses induced by the leaky guided modes which may propagate away from the plane of the waveguide (Le Vassor d'Yerville 2002).

1.4.6 Semi-Infinite Crystals and Surface Defects

To this point, only defects embedded in photonic crystals have been considered. This restriction was quite natural, since thus far photonic crystals have been assumed to be infinite. We did however mention at various places in this chapter the changes that the finite size of actual structures may induce in the properties of photonic crystals (see Sections 1.4.3 and 1.4.5). In this respect, the supercell method has turned out to be a powerful theoretical method for approaching this problem using the band diagram of finite structures. The properties of a photonic crystal with a finite size are strongly dependent on the surface bounding such a crystal: thus, local disruptions in the periodicity of this surface may result in the appearance of specific electromagnetic modes, known as surface modes.

This can be demonstrated by considering the simplest case of a semi-infinite Bragg layer stack where the thickness of the upper layer is either larger or smaller than that of the internal layers with the same dielectric permittivity. Under these conditions, the upper layer forms an asymmetric Fabry-Perot cavity bounded by the air on one side and by the rest of the Bragg mirror on the other side. Stationary waves may be present in this cavity, with the consequence that the electromagnetic field will be evanescent both in the air and in the Bragg mirror. In other terms, one has to deal here with a resonant mode trapped at the surface of a one-dimensional crystal.

In the case of crystals of higher dimension, the situation is obviously more complex. For the sake of simplicity, we shall restrict ourselves here again to the consideration of semi-infinite two or three-dimensional photonic crystals with a plane interface. The properties of such crystals depend not only on the orientation of the plane of the surface with respect to the planes of the crystal, but also on the surface termination, i.e. on the way this plane intersects with the periodic patterns of the crystal. As an example, the upper part of Fig. 1.21 represents a yablonovite crystal whose upper interface corresponds to a (111) fcc crystal plane while the lattice of holes defined by the surface termination is a triangular lattice. It is quite apparent that a different orientation of the surface would have resulted in a lattice of a different nature, and even possibly in an aperiodic lattice. Likewise, if the surface had cut the lattice with the same orientation of the surface, i.e parallel to the

(111) plane, but at a different depth inside the crystal, the resulting patterns may not have been perfectly circular holes.

For a semi-infinite crystal of the same type as the crystal represented in Fig. 1.21, four main types of electromagnetic modes might be distinguished:

1. modes propagating in the air, but evanescent in the crystal (PE),
2. modes propagating in the crystal, but evanescent in the air (EP),
3. modes propagating in the air as well as in the crystal (PP)
4. modes which are evanescent in the air as well as in the crystal, but propagating at the surface of the crystal (EE).

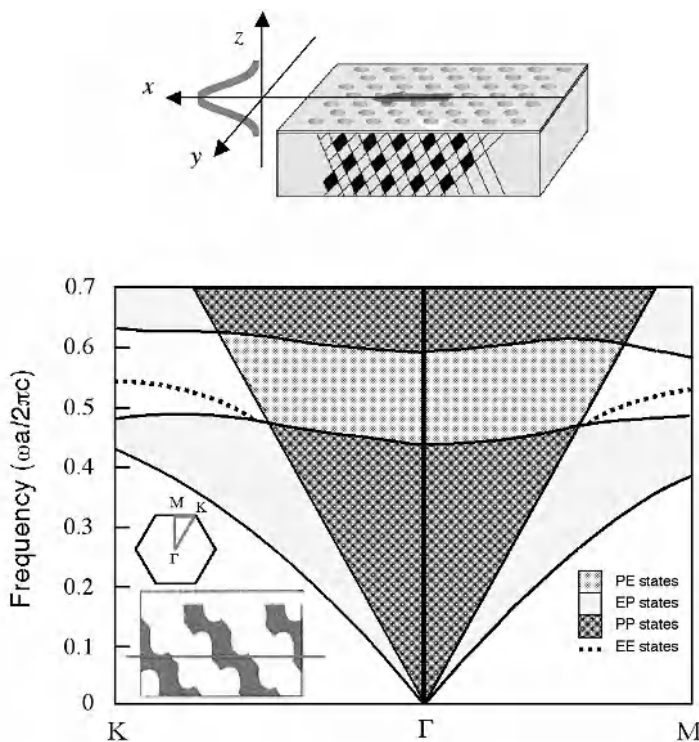


Fig. 1.21. Top. Schematic representation of a surface mode propagating at the surface of semi-infinite Yablonovite crystal. Bottom. Band diagram of the (111) crystal surface, revealing a triangular lattice of holes (Joannopoulos 1995). The different regions correspond to the different electromagnetic modes which may exist in this structure, while the thick dashed lines in the gap correspond to surface modes. The position of the surface plane is indicated by the thin solid line. The insert in the bottom left corner of the figure represents the cross-section of a Yablonovite crystal

In the example represented in Fig. 1.21, the interface plane is parallel to the xy plane, and the wave vectors of the surface modes are therefore parallel to this plane ($\mathbf{k} = \mathbf{k}_{\parallel}$, $k_z = 0$). Since the translational symmetry is disrupted along the z direction, \mathbf{k}_{\parallel} is actually the only vector defined for an eigenmode of the crystal. On the other hand, for a wave propagating from the air towards the crystal or from the crystal towards the air, \mathbf{k}_{\parallel} will be the only vector to be conserved. It is therefore useful to introduce separate band structures for the air and for the three-dimensional crystal projected onto the xy plane, as represented in the lower part of Fig. 1.21. For this purpose, one consider the variation of the vector \mathbf{k}_{\parallel} along the main directions of the surface lattice, which in this case is a triangular lattice of holes, while all solutions allowed for k_z in the three-dimensional crystal are calculated for each couple $(\omega, \mathbf{k}_{\parallel})$. The set of solutions determines the domains of modes which may propagate in the crystal (EP and PP). It then suffices to search for solutions allowed for k_z in the air. For vectors \mathbf{k}_{\parallel} such that $|\mathbf{k}_{\parallel}| \geq \omega/c$, it is apparent that no solution exists. The ‘light line’ $|\mathbf{k}_{\parallel}| = \omega/c$ divides therefore the $(\omega, \mathbf{k}_{\parallel})$ plane into two regions, a region where modes propagate in the air (PE and PP) and a region where they are evanescent in the air (EP and EE). By combining the two separate diagrams, a region EE where surface modes are to be found can now be delimited. This region is represented by the white area in Fig. 1.21. Finally, performing three-dimensional calculations using the supercell method described in Section 1.4.3 in this chapter, allows the exact determination of the dispersion curves $\mathbf{k}_{\parallel}(\omega)$ of these modes. These dispersion curves are represented in thick dashed lines in Fig. 1.21.

The diagram represented in Fig. 1.21 was actually obtained for a specific surface termination of the crystal : the insert in this figure represents a cross-section view of the yablonovite. The position of the surface plane chosen in this example is indicated here by a thin solid line. The question then arises whether, for a given three-dimensional photonic crystal, surface modes may always exist. For this purpose, let us consider here a continuous displacement of the plane of the crystal surface over a period of the crystal along the z direction: one bulk unit cell is thus added per surface unit cell to the semi-infinite crystal. This leads to increasing the total number of allowed states (modes) in the valence band by two (one state per polarisation). As the surface termination changes, the frequencies of the two modes necessarily decrease from the bottom of the conduction band to the top of the valence band, and they sweep across the band gap in much the same way as a point defect mode does when the relative permittivity of a pattern of the crystal increases continuously from the unity to the value corresponding to the dielectric from which the crystal is formed (see Section 1.4.1). Since the electromagnetic modes within the band gap are actually defect modes and, in the present case, surface modes, it thus turns out that for any photonic crystal, surface terminations allowing the existence of localised surface modes can be found.

1.4.7 Density of States in Photonic Crystals with or without Defects

In the same way as the electronic density of states in a semiconductor undergoes significant modifications when the materials are structured at nanometer scales, the periodic modulation of the dielectric permittivity at the scale of optical wavelengths results in a density of photonic states (or of electromagnetic modes) which may be dramatically different from the density of states in free space. Let us recall here that the photonic density of states (DOS) is defined as the number of electromagnetic modes allowed per frequency unit. When the photonic density of states is modified in a certain region of space, the radiative lifetime of any light emitter present in this region is in turn modified. In the upper part of Fig. 1.22 is presented a schematic comparison between the photonic density of states in free space and in a photonic crystal.

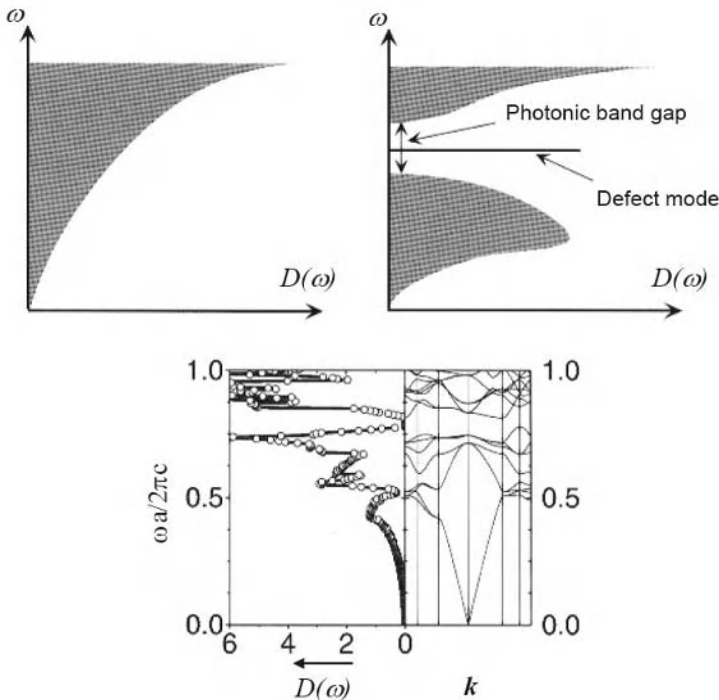


Fig. 1.22. Top. Schematic comparison of the photonic density of states $D(\omega)$ in free space (left) and in a photonic crystal (right). Bottom. Photonic density of states of an fcc inverse opal formed by air in a dielectric substrate ($\epsilon = 11.9$), calculated as a function of the normalised frequency $\omega a/2\pi c$ (Koenderink 2003). The right-hand part of this figure displays the complex dispersion diagram corresponding to wave vectors between the high-symmetry points X, U, L, Γ , X, W, and K, represented here by vertical lines. The photonic density of states in the complete photonic band gap is zero around the frequency $\omega a/2\pi c = 0.8$

In free space, the density of states $D(\omega)$ is proportional to ω^2 , and can be expressed for a volume V by the following equation:

$$D(\omega) = \frac{\omega^2 V}{\pi^2 c^3} \quad (1.58)$$

Eq. 58 still applies to the case of an homogeneous material with a refractive index n assumed to be frequency independent, i.e. to the case of a non-dispersive material, provided however that c be replaced with the speed of light in the material $v = c/n$. By contrast, this equation is no longer valid for photonic crystals, this being a consequence of the dispersion characteristics $\omega(\mathbf{k})$ of the crystal. Assuming these characteristics to be known, the density of states is calculated by counting all allowed states with a given frequency ω , i.e. as an integral of a Dirac δ function over the first Brillouin zone with a summation over all transmission bands:

$$D(\omega) = \sum_i \int_{BZ} d^3k \delta(\omega - \omega_i(\mathbf{k})) \quad (1.59)$$

As can be seen in Fig. 1.22, the typical density of states in a three-dimensional photonic crystal presents a significant deviation from the density of states in free space. It becomes zero at frequencies located in the omnidirectional band gap while presenting maxima near the edges of this gap. In the case of an ideally isotropic crystal (flat bands), the maxima would be located exactly at the band edges, and their values would be infinite. In general, secondary maxima may occur each time the dispersion curves of the crystal present a tangent parallel to the axis of the wave vector ($d\omega/dk = 0$). This phenomenon is also known in solid-state physics, where it is referred to as the van Hove singularity. Such domains of singular dispersion, where the group velocity of light $d\omega/dk$ is close to zero, are of particular significance not only as regards the absorption or the emission of light, but also as regards frequency conversion and other non-linear optical effects. The group velocity is defined as the speed at which the energy of the electromagnetic field propagates in matter: thus when the group velocity decreases, the interaction between the electromagnetic wave and matter tends to be reinforced. The presence of defects in the photonic crystals may also lead to DOS singularities. In particular, for zero-dimensional point defects, Dirac peaks occur in a complete photonic band gap, as can be seen in the upper part of Fig. 1.22 (right).

An example of a DOS calculated in the realistic case of an inverse three-dimensional opal formed by air in a dielectric (fcc lattice) is represented here in the lower part of Fig. 22 (Koenderick 2003). The main characteristics of the photonic density of states which have been discussed above can be observed in this figure. As might be noted here, it has been experimentally demonstrated that changes in the local DOS may significantly affect the power radiated by emitters embedded in such opals. However, for applications to quantum optical experi-

ments in photonic crystals, it is necessary not to consider only the total availability of modes with a frequency ω , but also the local coupling arising between an excited atom emitting a photon at the frequency ω and the electromagnetic environment created by the photonic crystal in the region where the atom is located. In other terms, the overlap which occurs between the matrix element of the dipolar moment of the atom on the one hand, and the electric field of electromagnetic mode(s) on the other hand, is the determining factor of such quantum optical characteristics as the radiative lifetime of the atom. This overlap can be clearly discerned from the local photonic density of states $D(\mathbf{r},\omega)$ defined as follows :

$$D(\mathbf{r},\omega) = \sum_i \int_{ZB} d^3k \left| \mathbf{E}_{ik}(\mathbf{r}) \right|^2 \delta(\omega - \omega_i(k)) \quad (1.60)$$

As far as practical calculations are concerned, the (ω, \mathbf{k}) space needs to be adequately discretised in order to calculate the integrals in Eqs. 1.60 and 1.59 and therefore to use the results obtained by the preliminary calculations of the photonic band structure as optimally as possible.

2 Models for Finite Crystals

The theoretical models which can be applied to photonic crystals with a finite size fall broadly into two categories. The first class of such models includes methods permitting the determination of the reflection and transmission properties of the diffraction grating formed by a layer of a photonic crystal. With the exception of certain theories based on the finite element method, these calculation methods generally rely on formulations in terms of transfer, reflection and transmission matrices.

These models apply for instance to the case where the size of the crystal is assumed to be finite along the vertical direction and infinite along the horizontal directions. This assumption allows taking advantage of the pseudo-periodicity properties of the fields along the horizontal directions, with the consequence of limiting computation times. However, in order to analyse periodicity defects it turns out necessary to use the supercell method which has already been described in Section 1.4.3 of Chapter 1.

The second class of models contains methods which actually apply to crystals with a finite size along any direction of periodicity. In reality, this amounts to considering a scattering problem where the periodicity of the crystal is never actually taken into account, since in the mathematical sense of the term a periodic structure is necessarily infinite. The development of such complex methods generally requires a significant effort in terms of numerical analysis and programming. This effort however is worth the result since numerical codes allow the resolution of most problems which may arise in this field and are therefore unparalleled tools for the study of photonic crystals.

2.1 Transfer, Reflection and Transmission Matrix Formulations

In this section, we shall consider theories based on the notions of transfer, reflection and transmission matrices. These notions are present in various forms in a large variety of methods used in the fields of electromagnetism and acoustics. Therefore, it seemed necessary to first present this notion in a simple case before using it for the description of more complex theoretical methods.

2.1.1 Reflection and Transmission Matrices

For the sake of simplicity, the notions of reflection and transmission matrices will be described here for a two-dimensional crystal presenting a square symmetry. As is represented in Fig. 2.1, the crystal is assumed here to be finite along the y direction but to remain infinite along the x and z directions. The crystal thus defined is but a diffraction grating consisting of a stack of N grids infinite along the x axis which themselves are formed by infinite rods parallel to the z axis. The assumption is made here that the crystal is illuminated by a monochromatic plane wave whose wavelength, polarisation and incidence angle are fixed.

One of the most interesting features of the model based on the diffraction grating model is the possibility of using the numerous studies which were conducted during the last thirty years on diffraction gratings. These theoretical studies have been largely vindicated by experimental results for all wavelength ranges, from X rays to microwaves, and for all types of diffraction gratings. In terms of implementation, not only are these models extremely reliable and versatile, but they have also demonstrated low computation times (Petit 1980; Moharam 1986; Maystre 1993).

A second reason for the interest in the diffraction grating model lies in its capability of predicting phenomena occurring at the interface between the crystal and the air, or the attenuation of the field propagating in the crystal. For instance, in the case of the crystal represented in Fig. 2.1 and for a given band gap, this method can be used for determining the decrease of the transmission as a function of the number N of grids. Multiple examples of such calculations can be found in (Maystre 1994a).

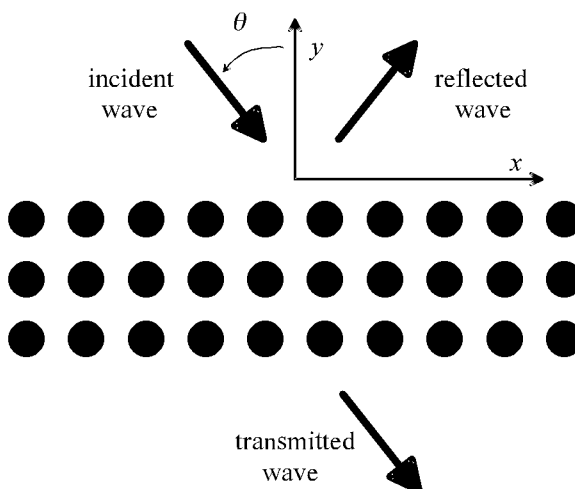


Fig. 2.1. Model of a photonic crystal considered as a diffraction grating

Here again, the mathematical problem to be solved is defined by the two Eqs. 1.2 and 1.3, with the difference however that the permittivity $\epsilon_r(x,y)$ is no longer periodic along y . In addition to these equations, two supplementary conditions, referred to as the radiation conditions at infinity or as the outgoing waves conditions need to be introduced. The physical meaning of these two conditions is quite obvious:

1. the field reflected above the crystal, and defined as the difference between the total and incident fields propagates away from the crystal and therefore towards $y = +\infty$,
2. the total field transmitted under the crystal propagates away from it and therefore towards $y = -\infty$.

The concept of a transfer matrix allows restricting the problem to a single grid. This can be evidenced by considering in Fig. 2.2 the case of one of the grids that were represented in Fig. 2.1, with a period $a_x = a_y = a$ along x and y respectively. When the crystal represented in Fig. 2.1 is illuminated by an incident monochromatic plane wave in s (or TM) polarisation, it can be demonstrated that the field in the two homogeneous regions R^+ and R^- extending above and beneath the grid can be expressed in the form of plane wave expansions, also known as Rayleigh expansions (Maystre 1993). The two regions are said to be homogeneous in the sense that no straight line parallel to the x axis may cross the rods of the grid in these regions. Accordingly, the plane wave expansions that are to be considered here are quite different from the expansions that were previously obtained with the plane wave method.,

Let us now demonstrate the validity of the plane wave expansion for the simple case where the incidence angle θ is equal to zero. As we know, the total field remains of the same polarisation (either s ou p) than the incident field. The total electric field therefore reduces in s polarisation to its component E_z along the z axis. This component, which will be denoted by E in this section, satisfies Eq. 1.37. Further, since the grid is periodic with a period a along the x axis, the total field can be written in the form of a Fourier series, as it would be the case for a Bloch mode not propagating along the x axis, with $k_x = 0$, since $\theta = 0$:

$$E(x, y) = \sum_{n=-\infty}^{+\infty} E_n(y) \exp(i\alpha_n x) \quad (2.1)$$

where:

$$\alpha_n = n \frac{2\pi}{a} \quad (2.2)$$

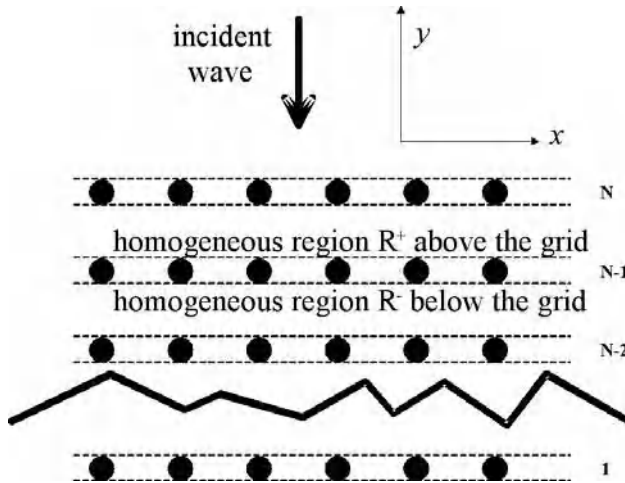


Fig. 2.2. Plane wave expansions in the two homogeneous regions extending along both sides of an arbitrary grid, and numbering scheme for the grids as used in Eqs. 2.11 and 2.12

The relative permittivity $\epsilon_{r,ext}$ is constant in the regions R^\pm . Therefore, it follows from Eq. 1.37 that the field satisfies the Helmholtz equation:

$$\nabla^2 E + k_0^2 \epsilon_{r,ext} E = 0 \quad (2.3)$$

Introducing the Fourier expansion of Eq. 2.1 into Eq. 2.3, we thus obtain, in the regions R^\pm , solutions of the form:

$$E_n(y) = A_n^\pm \exp(-i\beta_n y) + B_n^\pm \exp(+i\beta_n y) \quad (2.4)$$

where:

$$\beta_n = \sqrt{k_0^2 \epsilon_{r,ext} - \alpha_n^2} \quad \text{or} \quad i\sqrt{\alpha_n^2 - k_0^2 \epsilon_{r,ext}} \quad (2.5)$$

The field in the regions R^\pm can therefore be written as follows:

$$E(x, y) = \sum_{n=-\infty}^{+\infty} A_n^\pm \exp(i\alpha_n x - i\beta_n y) + \sum_{n=-\infty}^{+\infty} B_n^\pm \exp(i\alpha_n x + i\beta_n y) \quad (2.6)$$

The expression for the field given by Eq. 2.6 remains valid in the general case where the incidence angle θ is not null, provided however that Eq. 2.2 be replaced with the following equation:

$$\alpha_n = k_0 n_{ext} \sin(\theta) + n \frac{2\pi}{a} \quad (2.7)$$

where n_{ext} denotes the optical index in the regions R^\pm , as given by the equation:

$$n_{ext} = \sqrt{\epsilon_{r,ext}} \quad (2.8)$$

It may be noted, as a consequence of Eq. 2.5, that the number of real-valued β_n is finite, and therefore that only a finite number of homogeneous plane waves can be retained as solutions to Eq. 2.4. All other plane waves present either an increasing or a decreasing exponential behaviour along the y axis. The first summation represents either homogeneous plane waves propagating towards $y = -\infty$ or evanescent waves exponentially decreasing when y tends towards $-\infty$. Conversely, the second summation represents either homogeneous plane waves propagating towards $y = +\infty$ or evanescent waves exponentially decreasing when y tends towards $+\infty$.

The transfer matrix of the grid expresses the linear relation between the set of coefficients A_n^+ and B_n^+ on the one hand, and the set of coefficients A_n^- and B_n^- on the other hand:

$$\begin{pmatrix} A^+ \\ B^+ \end{pmatrix} = \begin{pmatrix} T_1 & T_2 \\ T_3 & T_4 \end{pmatrix} \begin{pmatrix} A^- \\ B^- \end{pmatrix} \quad (2.9)$$

The column matrices A^\pm and B^\pm are of infinite order and contain the different coefficients A_n^\pm and B_n^\pm . The four square matrices T_i are therefore also of an infinite order.

An alternative approach would consist in defining scattering matrices rather than transfer matrices. The scattering matrices thus defined link the amplitudes of the waves B^+ and A^- scattered on both sides of the grid in Fig. 2.2, i.e. waves propagating away from the grid or exponentially decreasing with the distance to the grid on the one hand, to the amplitudes of the incident waves A^+ and B^- , i.e. of the waves propagating towards the grid or exponentially increasing with the distance to the grid on the other hand. In other terms, the scattering matrices express the column matrices B^+ and A^- in terms of the column matrices A^+ and B^- :

$$\begin{pmatrix} B^+ \\ A^- \end{pmatrix} = \begin{pmatrix} S_1 & S_2 \\ S_3 & S_4 \end{pmatrix} \begin{pmatrix} A^+ \\ B^- \end{pmatrix} \quad (2.10)$$

For obvious reasons, the two scattering matrices S_1 and S_4 are referred to as reflection matrices, while the scattering matrices S_2 and S_3 are referred to as transmission matrices.

The equations defining the scattering matrices are direct consequences of the linearity of Maxwell's equations and of the causality relations: the field scattered by a grid, i.e. the field which propagates away from the grid or decreases exponentially with the distance to the grid, can be linearly expressed in terms of the field generating it, i.e. the field which propagates towards the grid or increases with the distance from the grid. By contrast, demonstrating the existence of transfer matrices is more difficult: indeed, while the linearity remains, the causality relation disappears in this case.

In the definition presented here of the notions of transfer and scattering matrices, the presence of waves whose amplitude increases exponentially with the distance to the grid may seem surprising. It is quite apparent that such waves cannot exist in the case where the grid is not surrounded by other grids. The existence of waves with an infinite amplitude at infinity cannot be admitted in this case, as R^\pm would also extend at infinity. However, when R^\pm is limited in space, there is nothing to prevent such 'anti-evanescent waves' to exist. It suffices to note here that an anti-evanescent wave in the region R^+ is actually an evanescent wave in the upper grid. Therefore, not admitting the existence of these anti-evanescent waves would amount to denying the existence of evanescent waves.

The transfer and scattering matrices thus defined are identical for all grids, and this is where their primary significance is. The calculation of these matrices can therefore be realised in a single step, whatever the number of grids in the crystal is. It might be emphasized here that the notion of transfer matrix, and more generally of scattering, reflection or transmission matrices, is of central importance in the fields of electromagnetism and acoustics, and that it essentially comes down to the more general notion of invariant in physics. Assuming the crystal to be illuminated by an incident wave, this can be explained in more precise terms by pointing to the fact that while the amplitudes of the waves propagating in the regions R^\pm are dependent on the number N^\pm of grids extending above R^+ and below R^- , the matrices themselves which have just been defined are not. The problem considered here can therefore be decomposed into two successive stages. First, the scattering matrices are calculated for a single grid. The field reflected and transmitted by the entire stack of grids are then determined through basic operations of addition, multiplication and inversion on the matrices thus calculated. The first step can be achieved by using for instance one of the numerical methods described in this chapter (Sections 2.1.2, 2.1.3 and 2.1.4), or some of the methods elaborated within the framework of the theory of diffraction gratings (Petit 1980; Moharam 1986;

Maystre 1993). Let us describe in more detail the second step in the calculations, and, for this purpose, let us denote by $A_n^{(0)}$ and $B_n^{(0)}$ respectively the coefficients corresponding to the field in the region located below the lower grid of the photonic crystal represented in Fig. 2.1. The radiation condition imposes that $\forall n$, $B_n^{(0)} = 0$. Using the matrix relation given by Eq. 2.9 and thus replacing A^+ , B^+ , A^- and B^- in this equation by $A^{(1)}$, $B^{(1)}$, $A^{(0)}$ and 0 respectively, the column matrices $A^{(1)}$ and $B^{(1)}$ characterising the field above the lower grid can be expressed in terms only of the column matrix $A^{(0)}$. Further, Eq. 2.9 allows to successively pass through all grids by simple matrix multiplications. It thus turns out that the two column matrices $A^{(N)}$ and $B^{(N)}$ characterising the field above the upper grid of the crystal can be expressed in the form of linear combinations of the matrix $A^{(0)}$:

$$A^{(N)} = M_a A^{(0)} \quad (2.11)$$

$$B^{(N)} = M_b A^{(0)} \quad (2.12)$$

$A^{(N)}$ is known from the radiation condition at infinity, due to the fact that the field above the upper grid cannot contain anti-evanescent waves, i.e. waves increasing exponentially when $y \rightarrow \infty$. Moreover, the only homogeneous plane wave that may propagate towards the grid is the incident wave. Accordingly, in the column matrix $A^{(N)}$, only the central coefficient $A_0^{(N)}$ remains nonzero, and its amplitude is equal to the amplitude of the incident wave, which itself is known. Therefore, inverting M_a after having proceeded to its truncation allows the determination, using Eq. 2.11, of the field transmitted by the crystal: this field is defined by the column matrix $A^{(0)}$. Further, Eq. 2.12 yields the field reflected by the crystal and defined by the column matrix $B^{(N)}$. The truncation is realised by restricting all coefficients $A_i^{(n)}$ and $B_i^{(n)}$ in all column matrices $A^{(n)}$ and $B^{(n)}$, where $n \in (0, N)$, to coefficients with index i ranging from $-P$ to $+P$.

The scattering matrices can actually be used instead of the transfer matrices. In this case, it can be easily demonstrated that, proceeding from the lowest to the upper grid, the reflected and transmitted fields can be obtained through matrix multiplications and inversions. From a numerical point of view, it should be pointed out that, due to the larger number of grids present in the stack, scattering matrix formulations present a higher degree of stability than transfer matrix formulations, and therefore that they should be preferred over the latter. Finally, it might be noted that, in contrast with the structure represented in Fig. 2.1, certain photonic crystals may not present any homogeneous region since the upper part of a grid may overhang over the lower part of the grid extending above. An example would be the case of a two-dimensional photonic crystal with an hexagonal symmetry where the ratio of the diameter of the rods over the period is larger than a certain critical value. In such a case, the method described here becomes simply inappli-

cable. However, as will be discussed in the following section, this method can be adapted to apply to such situations.

2.1.2 Pendry Method

As in the preceding section, the Pendry method will be presented here in the specific case of an *s*-polarised plane wave incident onto a two-dimensional crystal with a square symmetry. Accordingly, in such a case all derivatives with respect to *z* will be zero. The Pendry method (Pendry 1994) is almost essentially numerical in character, in the sense that it very directly uses Maxwell's equations, without requiring a complex preliminary mathematical apparatus.

In the case where the incident angle is zero, Eqs. 1.2 and 1.3 become in *s*-polarisation:

$$\frac{1}{i\omega\mu_0} \frac{\partial E_z}{\partial y} = H_x \quad (2.13)$$

$$-\frac{1}{i\omega\mu_0} \frac{\partial E_z}{\partial x} = H_y \quad (2.14)$$

$$-\frac{1}{i\omega\epsilon_0\epsilon_r} \left(\frac{\partial H_y}{\partial x} - \frac{\partial H_x}{\partial y} \right) = E_z \quad (2.15)$$

Eq. 2.13 entails that the *y*-derivative of the field E_z can be expressed in terms of the component H_x of the magnetic field:

$$\frac{\partial E_z}{\partial y} = i\omega\mu_0 H_x \quad (2.16)$$

Likewise, it can be easily demonstrated that the *y*-derivative of H_x can be expressed from the component E_z of the electric field and from the *x*-derivatives. To this purpose, it suffices to introduce the expression for H_y given by Eq. 2.14 in Eq. 2.15. This leads to the following equation:

$$\frac{\partial H_x}{\partial y} = -i\omega\epsilon_0\epsilon_r E_z + \frac{i}{\omega\mu_0} \frac{\partial^2 E_z}{\partial x^2} \quad (2.17)$$

The discretisation of the (*x,y*) space using elementary meshes with widths χ along *x* and τ along *y* respectively allows then us to use the classical formulas for the approximation of derivatives:

$$\frac{\partial H_x}{\partial y} \cong \frac{H_x(x, y + \tau) - H_x(x, y)}{\tau} \quad (2.18)$$

$$\frac{\partial E_z}{\partial y} \cong \frac{E_z(x, y + \tau) - E_z(x, y)}{\tau} \quad (2.19)$$

$$\frac{\partial^2 E_z}{\partial x^2} \cong \frac{E_z(x + \chi, y) + E_z(x - \chi, y) - 2E_z(x, y)}{\chi^2} \quad (2.20)$$

Introducing approximations of the derivatives in Eqs. 2.16 and 2.17, the values of the field at the ordinate $y + \tau$ can then be deduced from its values at the ordinate y :

$$E_z(x, y + \tau) \cong E_z(x, y) + i\omega\mu_0\tau H_x(x, y) \quad (2.21)$$

$$H_x(x, y + \tau) \cong H_x(x, y) + i \frac{\tau}{\omega\mu_0\chi^2} [E_z(x + \chi, y) + E_z(x - \chi, y) + (k_0^2\epsilon_r\chi^2 - 2)E_z(x, y)] \quad (2.22)$$

Determination of the Dispersion Relations in a Periodic Crystal

In this section, we shall first demonstrate that, in the simple case of an infinite crystal with a square symmetry, Eqs. 2.21 and 2.22 allow the determination of the dispersion relations. For this purpose, the values for the widths of the elementary meshes used in the discretisation of space will be set to $\tau = \chi = a/M$, where a is the period of the crystal and M is the number of points at each side of the elementary mesh. Fig. 2.3 provides a schematic representation of the discretisation thus defined.

The origin of the axes is located at the bottom-left corner of the cell. We shall assume here that the values for the fields E_z and H_x at the M points P_m ($m \in (1, M)$) with coordinates $\{y = 0, x = (m-1)\tau\}$ are already known, and we proceed by introducing in the column matrices $\mathbf{E}_z(0)$ and $\mathbf{H}_x(0)$ respectively the M values for $E_z(x, 0)$ and $H_x(x, 0)$ at the points P_m .

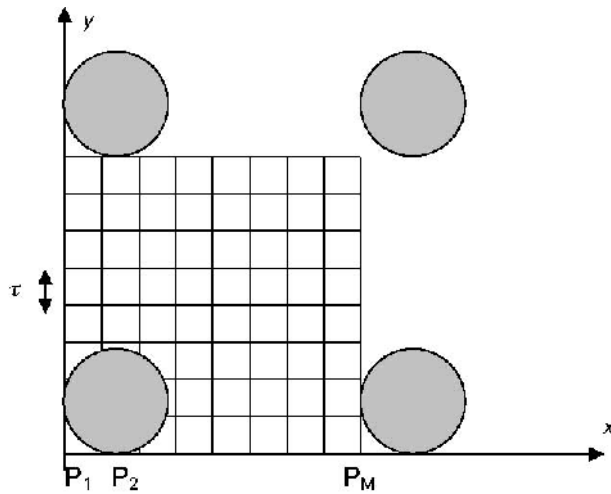


Fig. 2.3. Discretisation of the elementary mesh of a two-dimensional photonic crystal with a square symmetry

The problem then consists in searching for pseudo-periodic solutions satisfying equations analogous to Eq. 1.22. This will in turn allow the determination from the components $\mathbf{E}_z(0)$ and $\mathbf{H}_x(0)$ of the values of the components E_z and H_x at any point of coordinates $\{y = 0, x = (m-1)\tau\}$, where m is now an arbitrary relative number. The values of the field will thus be known at any discretisation point along the y axis. As an example, the following equation yields the value for $E_z(a,0)$:

$$E_z(a,0) = E_z(0,0) \exp(i k_x a) \quad (2.23)$$

Eqs. 2.21 and 2.22 therefore allow us to express the field at any discretisation point along the line $y = \tau$ as a linear combination of the M components of $\mathbf{E}_z(0)$ and $\mathbf{H}_x(0)$, which amounts to saying that $\mathbf{E}_z(\tau)$ and $\mathbf{H}_x(\tau)$ can be expressed in terms of a linear combination of $\mathbf{E}_z(0)$ and $\mathbf{H}_x(0)$. Thus, by proceeding along the y axis step by step, $\mathbf{E}_z(a)$ and $\mathbf{H}_x(a)$ can be expressed in the form of linear combinations of the matrices $\mathbf{E}_z(0)$ and $\mathbf{H}_x(0)$:

$$\mathbf{E}_z(a) = O \mathbf{E}_z(0) + P \mathbf{H}_x(0) \quad (2.24)$$

$$\mathbf{H}_x(a) = Q\mathbf{E}_z(0) + R\mathbf{H}_x(0) \quad (2.25)$$

where O, P, Q and R are square matrices of size $M \times M$.

Further, the relation of pseudo-periodicity given by Eq. 1.22 provides yet another way of expressing $\mathbf{E}_z(a)$ in terms of $\mathbf{E}_z(0)$. Indeed, the following equation holds:

$$\mathbf{E}_z(x, a) = \mathbf{E}_z(x, 0) \exp(i k_y a) \quad (2.26)$$

The same applies to the component H_x . This leads to the following two equations:

$$\mathbf{E}_z(a) = L\mathbf{E}_z(0) \quad (2.27)$$

$$\mathbf{H}_x(a) = L\mathbf{H}_x(0) \quad (2.28)$$

where L is a diagonal square matrix of size $M \times M$, whose diagonal terms are equal to $\exp(i k_y a)$. It is therefore quite straightforward to deduce from Eqs. 2.24, 2.25, 2.27 and 2.28 that:

$$(O - L)\mathbf{E}_z(0) + P\mathbf{H}_x(0) = 0 \quad (2.29)$$

$$Q\mathbf{E}_z(0) + (R - L)\mathbf{H}_x(0) = 0 \quad (2.30)$$

These two equations can be re-written in the form of a linear system of $2M$ equations with $2M$ unknowns:

$$U\mathbf{F}(0) = 0 \quad (2.31)$$

The column matrix $\mathbf{F}(0)$ of size $2M$ in this system contains successively the two column matrices $\mathbf{E}_z(0)$ and $\mathbf{H}_x(0)$, while the square matrix U of size $2M \times 2M$ is given by the equation:

$$U = \begin{pmatrix} O - L & P \\ Q & R - L \end{pmatrix} \quad (2.32)$$

The homogeneous linear system represented by Eq. 2.31 admits a non-null solution only in the case where the determinant of U is zero. Therefore, for a given value ω of the frequency, the characteristics of the Bloch waves associated with the infinite crystal will be obtained by determining the values of k_x and k_y at which the determinant of U becomes zero:

$$\det[U(k_x, k_y)] = 0 \quad (2.33)$$

Application to Finite Crystals

We shall now consider the case of a photonic crystal with a finite width, i.e. a photonic crystal consisting of a finite number of grids assumed to be infinite along the horizontal directions, as represented in Fig. 2.1. The discretisation used here is the same as in Fig. 2.3, with the difference however that the origin is now located at the bottom of the lowest grid, while the discretisation process is continued along the y axis in such a way that the upper part of the mesh at $y = h$ will be located over the upper grid (Fig. 2.4). Applying the same method as in the case of an infinite photonic crystal, the column matrices $\mathbf{E}_z(h)$ and $\mathbf{H}_x(h)$ can be expressed through a linear combination of matrices $\mathbf{E}_z(0)$ and $\mathbf{H}_x(0)$:

$$\mathbf{E}_z(h) = O' \mathbf{E}_z(0) + P' \mathbf{H}_x(0) \quad (2.34)$$

$$\mathbf{H}_x(h) = Q' \mathbf{E}_z(0) + R' \mathbf{H}_x(0) \quad (2.35)$$

For this purpose, the equations like Eq. 1.22 which express the pseudo-periodicity of the Bloch waves, need to be replaced in normal incidence by equations expressing the periodicity of the fields along the x axis. In the case of a non-normal incidence, another pseudo-periodicity equation can be readily derived from Eqs 2.6 and 2.7:

$$E_z(x + a, y) = \exp\left(ik_0 \sqrt{\epsilon_{r,ext}} a \sin(\theta)\right) E_z(x, y) \quad (2.36)$$

Eqs. 2.34 and 2.35 form two matrix equations linking the four column matrices $\mathbf{E}_z(0)$, $\mathbf{H}_x(0)$, $\mathbf{E}_z(h)$ and $\mathbf{H}_x(h)$. The two other equations can be determined using the radiation conditions. A simple way of deducing these equations is by demonstrating that the four column matrices can be expressed as a linear combination of two new column matrices. These two matrices can then be calculated from Eqs. 2.34 and 2.35 alone.

Let us now describe this method in more precise terms. The radiation condition imposes that the field in the region below the crystal must propagate away from the crystal, and therefore towards $y = -\infty$. As a consequence, the coefficients B_n^- in the expression of the field given by Eq. 2.6 become zero. Therefore, if $y < 0$, then the field beneath the crystal can be written in the form:

$$E_z(x, y) = \sum_{n=-\infty}^{+\infty} A_n^- \exp(i\alpha_n x - i\beta_n y) \quad (2.37)$$

Likewise, above the crystal, the amplitudes of the plane waves propagating towards the crystal become zero, with the exception of the amplitude of the incident wave. Therefore, if $y > h$, the field above the crystal can be expressed in the following form:

$$E_z(x, y) = A_0^+ \exp(i\alpha_0 x - i\beta_0 y) + \sum_{n=-\infty}^{+\infty} B_n^+ \exp(i\alpha_n x + i\beta_n y) \quad (2.38)$$

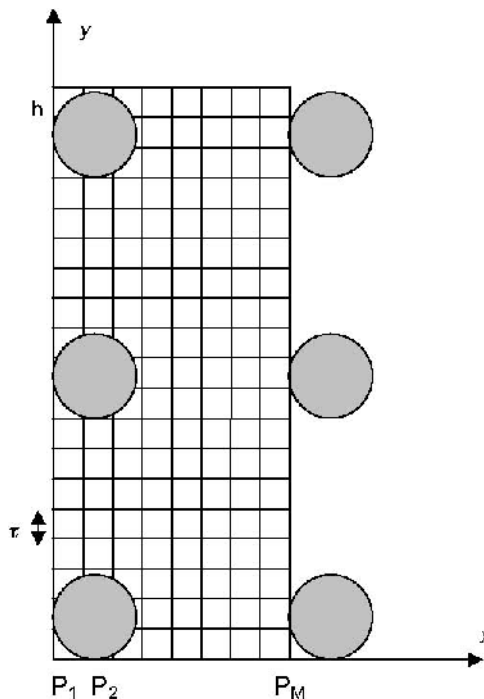


Fig. 2.4. Spatial discretisation for a crystal with a finite width

Eq. 2.13 allows deriving an expression for H_x from Eqs. 2.37 and 2.38:

- if $y < 0$:

$$H_x(x, y) = \frac{-1}{\omega\mu_0} \sum_{n=-\infty}^{+\infty} \beta_n A_n^- \exp(i\alpha_n x - i\beta_n y) \quad (2.39)$$

- if $y > h$:

$$H_x(x, y) = \frac{1}{\omega\mu_0} \left(-\beta_0 A_0^+ \exp(i\alpha_0 x - i\beta_0 y) + \sum_{n=-\infty}^{+\infty} \beta_n B_n^+ \exp(i\alpha_n x + i\beta_n y) \right) \quad (2.40)$$

For the purpose of expressing Eqs. 2.37 to 2.40 in matrix form, let us define two column matrices \mathbf{A}^- and \mathbf{B}^+ of odd order $2P + 1$, where P is a positive integer, containing the amplitudes A_n^- , $n \in [-P, +P]$ and B_n^+ , $n \in [-P, +P]$. The assumption will be made from this point that the number M of discretisation points along x in the elementary mesh is also odd and is equal to $2P + 1$. Assuming for the sake of simplicity that the amplitude A_0^+ of the incident plane wave is equal to unity, elementary calculations allow us to reach the conclusion that Eqs. 2.37 to 2.40 can be written in the form of the following matrix equations:

$$\mathbf{E}_z(0) = \Gamma_E^- \mathbf{A}^- \quad (2.41)$$

$$\mathbf{H}_x(0) = \Gamma_H^- \mathbf{A}^- \quad (2.42)$$

$$\mathbf{E}_z(h) = \mathbf{E}_z^0 + \Gamma_E^+ \mathbf{B}^+ \quad (2.43)$$

$$\mathbf{H}_x(h) = \mathbf{H}_x^0 + \Gamma_H^+ \mathbf{B}^+ \quad (2.44)$$

where \mathbf{E}_z^0 and \mathbf{H}_x^0 are two column matrices defined by the equations:

$$(\mathbf{E}_z^0)_m = \exp(i\alpha_0 x_m - i\beta_0 h) \quad (2.45)$$

$$(\mathbf{H}_x^0)_m = \frac{-\beta_0}{\omega\mu_0} \exp(i\alpha_0 x_m - i\beta_0 h) \quad (2.46)$$

while Γ_E^- , Γ_H^- , Γ_E^+ and Γ_H^+ are square matrices respectively defined as follows :

$$(\Gamma_E^-)_{m,n} = \exp(i\alpha_n x_m) \quad (2.47)$$

$$(\Gamma_H^-)_{m,n} = \frac{-\beta_0}{\omega\mu_0} \exp(i\alpha_n x_m) \quad (2.48)$$

$$(\Gamma_E^+)_{m,n} = \exp(i\alpha_n x_m + i\beta_n h) \quad (2.49)$$

$$(\Gamma_H^+)_{m,n} = \frac{\beta_0}{\omega\mu_0} \exp(i\alpha_n x_m + i\beta_n h) \quad (2.50)$$

The values of x_i are the abscissas of the discretisation points along x in the elementary mesh:

$$x_m = (m-1) \frac{a}{M} \quad (2.51)$$

Introducing in Eqs. 2.34 and 2.35 the expressions given by Eqs. 2.41 to 2.44 respectively of the four column matrices $\mathbf{E}_z(0)$, $\mathbf{H}_x(0)$, $\mathbf{E}_z(h)$ and $\mathbf{H}_x(h)$, it turns out, after proceeding to tedious, albeit elementary calculations that:

$$\nabla \mathbf{F}(0) = \mathbf{S} \quad (2.52)$$

where ∇ is a square matrix of size $2M = 4P + 2$, defined in the following way:

$$\nabla = \begin{pmatrix} (-\Gamma_E^+) \\ O'\Gamma_E^- + P'\Gamma_H^- \\ (-\Gamma_H^+) \\ Q'\Gamma_E^- + R'\Gamma_H^- \end{pmatrix} \quad (2.53)$$

while \mathbf{S} and $\mathbf{F}(0)$ are column matrices of size $2M$, defined by the two following equations respectively:

$$\mathbf{S} = \begin{pmatrix} \mathbf{E}_z^0 \\ \mathbf{H}_x^0 \end{pmatrix} \quad (2.54)$$

$$\mathbf{F}(0) = \begin{pmatrix} \mathbf{E}_z(0) \\ \mathbf{H}_x(0) \end{pmatrix}$$

The inversion of the linear system in Eq. 2.52 permits the direct calculation of the reflected and transmitted amplitudes. The efficiencies ρ_n and τ_n , i.e. the ratios of the reflected or transmitted energies respectively over the incident energy in the different orders of the grating, are given by (Maystre 1993):

$$\rho_n = \frac{\beta_n}{\beta_0} |B_n^+|^2 \quad (2.55)$$

$$\tau_n = \frac{\beta_n}{\beta_0} |A_n^-|^2 \quad (2.56)$$

The Pendry method thus turns out to be particularly simple as regards both its theoretical development and its numerical implementation. The precision of the results could actually be improved by using a slightly more complicated meshing process, according to which the discretisation points along y for H_x will be shifted from half an interval $a/2M$ with respect to the discretisation points for E_z . This applies more specifically to Eqs. 2.16 and 2.17, as will be described in the next section.

2.2 Finite Difference in Time Domain (FDTD) Method

2.2.1 Numerical Formulation of Maxwell's Equations

In contrast with the Pendry method, the FDTD method can be described as one of the general numerical methods in electromagnetism. Its originality lies in the preliminary resolution of a scattering problem in the time domain rather than in the frequency domain. The harmonic solutions are obtained in a second step through a Fourier transformation in time. As will be seen, one of the main advantages of this method lies in the fact that it does not require any matrix inversion. Of course, an exhaustive description of the different existing versions of this method would be largely beyond the scope of this book, and the interested reader is referred for a more extensive presentation, to the original article by K. S. Yee (Yee 1966) or to the book by A. Taflove (Taflove 1995). Descriptions of this method more specifically adapted to the case of photonic crystals can be found in (Joannopoulos 1995b; Reineix 1996).

We shall be led in this section to consider non-harmonic time-dependent fields, and therefore for the time being to abandon the notion of the complex amplitude of the fields. Accordingly, the problem to be addressed is the determination of the total field at any time t and at any point of space when a time-dependent field strikes a photonic crystal with finite size. For the sake of simplicity we shall retain

here the model of a two-dimensional photonic crystal illuminated by an *s*-polarised incident wave and consider the component $E_z(x, y, t)$ of the electric field along the z axis. Like the magnetic field $\mathbf{H}(x, y, t)$, this component must satisfy the time-dependent Maxwell's equations. For non-dispersive materials, these equations assume the following form:

$$\nabla \times E\hat{\mathbf{z}} = -\mu_0 \frac{\partial \mathbf{H}}{\partial t} \quad (2.57)$$

$$\nabla \times \mathbf{H} = \epsilon_0 \epsilon_r \frac{\partial E}{\partial t} \hat{\mathbf{z}} \quad (2.58)$$

As an example, in the case of a Gaussian pulse with a plane wave front, the component E^i along z of the time-dependent incident field is given by:

$$E^i = \exp \left[-\left(t - t_0 - \frac{\mathbf{u} \cdot \mathbf{r}}{v} \right)^2 / \Delta t^2 \right] \quad (2.59)$$

where v denotes the velocity of the pulse, \mathbf{u} is a unit vector oriented along the direction of propagation, t_0 is the reference time and Δt is the width of the pulse. By contrast, in the case of a sinusoidal wave with a plane wave front reaching the origin at time $t = t_0$, the equation for the incident field assumes the following form:

$$E^i = \sin \left[\omega \left(t - \frac{\mathbf{u} \cdot \mathbf{r}}{v} \right) \right] \times \theta \left(t - t_0 - \frac{\mathbf{u} \cdot \mathbf{r}}{v} \right) \quad (2.60)$$

where $\theta(t)$ is the Heaviside function which takes the value 0 for $t < 0$ and is equal to unity for $t > 0$. The assumption is made here that at $t < 0$, the incident field is zero in the region surrounding the crystal. This region shall be defined in more precise terms for $t < 0$ in the course of this section.

In the same way as in the Pendry method, Maxwell's equations are first projected onto the axes, before being discretised along x , y and t . The projection of Eqs. 2.57 and 2.58 onto the axes yields the following equations:

$$\frac{\partial E_z}{\partial y} = -\mu_0 \frac{\partial H_x}{\partial t} \quad (2.61)$$

$$\frac{\partial E_z}{\partial x} = \mu_0 \frac{\partial H_y}{\partial t} \quad (2.62)$$

$$\frac{\partial H_y}{\partial x} - \frac{\partial H_x}{\partial y} = \epsilon_0 \epsilon_r \frac{\partial E_z}{\partial t} \quad (2.63)$$

In order to proceed to the discretisation of these equations, we shall adopt here the two following rules. First, the component E_z of the electric field will be calculated at the times $t = n\Delta t$, where n is a positive or null integer, while the two components of the magnetic field will be calculated at the times $t = (n+1/2)\Delta t$. Secondly, the three components of the field are calculated at precise locations in space, represented in Fig. 2.5 and defined as follows :

- for E_z , $[x = i\Delta x \text{ and } y = j\Delta y]$, where i and j are integers,
- for H_x , $[x = i\Delta x \text{ and } y = (j+1/2)\Delta y]$,
- for H_y , $[x = (i+1/2)\Delta x \text{ and } y = j\Delta y]$.

The theoretical justification, for the discretisation thus performed, which can be traced back to the integral form of Ampere's and Faraday's laws (Taflove 1995), will not be discussed here. It suffices to note that this discretisation permits to re-write Maxwell's equations by replacing the space and time derivatives with centred finite differences. The term centred finite difference is used here to refer to the following approximation of the derivative:

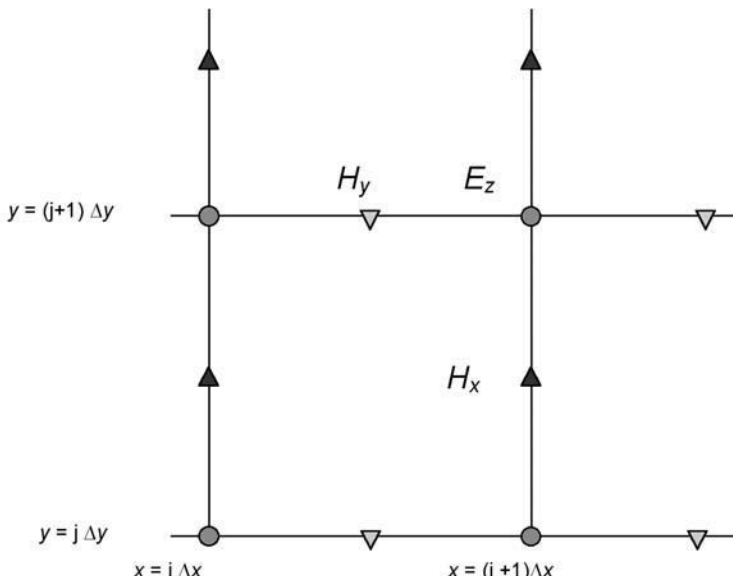


Fig. 2.5. Spatial discretisation used in the FDTD method: the circles, triangles and inverted triangles represent the discretisation points used for E_z , H_x and H_y respectively

$$\frac{df}{du}(u_0) \cong \frac{f(u_0 + \Delta u) - f(u_0 - \Delta u)}{2\Delta u} \quad (2.64)$$

This approximation leads to an error of the second order in Δu . In this respect, let us point out to the fact that non-centred finite differences of the type used in the Pendry method (Eqs. 2.18 and 2.19), lead to an error of the first order.

For the purpose of presenting the finite difference equations in a form as convenient as possible, we shall adopt here the conventions introduced by A. Taflove, which consists in representing the value of any arbitrary component $U(\psi\Delta x, \xi\Delta y, \xi\Delta t)$ of the fields in the form $U|_{\psi, \xi}^{\xi}$. As an example, the value $E_z(i\Delta x, j\Delta y, n\Delta t)$ of the electric field at the point located in the bottom-left corner of Fig. 2.5 ($x = i\Delta x$, $y = j\Delta y$) and at a time $t = n\Delta t$, shall be written in the form $E_z|_{i, j}^n$.

Eqs. 2.61, 2.62 and 2.63 thus become:

$$E_z|_{i, j}^n = E_z|_{i, j}^{n-1} + \frac{\Delta t}{\Delta y \varepsilon_0 \varepsilon_r|_{i, j}} \times \quad (2.65a)$$

$$\left(\frac{H_y|_{i+\frac{1}{2}, j}^{n-\frac{1}{2}} - H_y|_{i-\frac{1}{2}, j}^{n-\frac{1}{2}}}{\Delta x} - \frac{H_x|_{i, j+\frac{1}{2}}^{n-\frac{1}{2}} - H_x|_{i, j-\frac{1}{2}}^{n-\frac{1}{2}}}{\Delta y} \right)$$

$$H_x|_{i, j+\frac{1}{2}}^{n+\frac{1}{2}} = H_x|_{i, j+\frac{1}{2}}^{n-\frac{1}{2}} - \frac{\Delta t}{\Delta y \mu_0} \times \left(E_z|_{i, j+1}^n - E_z|_{i, j}^n \right) \quad (2.66a)$$

$$H_y|_{i+\frac{1}{2}, j}^{n+\frac{1}{2}} = H_y|_{i+\frac{1}{2}, j}^{n-\frac{1}{2}} + \frac{\Delta t}{\Delta x \mu_0} \times \left(E_z|_{i+1, j}^n - E_z|_{i, j}^n \right) \quad (2.67a)$$

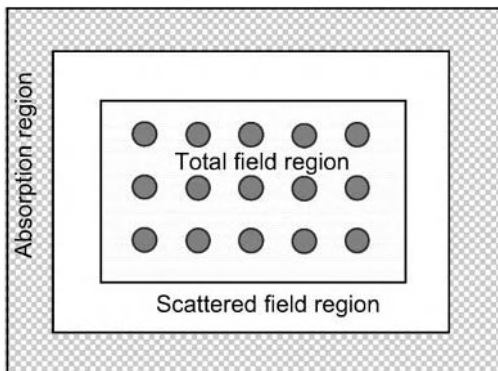


Fig. 2.6. Discretisation realised by decomposing the region of space considered into a total field region and a scattered field region. The latter includes an absorption region

These three equations shall be alternately used for calculating the time variations of the components of the electric and magnetic fields. These equations indeed allow the determination of the components of the field at time t from the values of the same components at the times $(t - \Delta t)$ and $(t - \Delta t/2)$. Since the incident field, and, consequently, the total field for reasons pertaining to causality, are zero in the discretised domain when $t \leq 0$, Eqs. 2.66a and 2.67a can be used for determining the two components of the magnetic field at time $\Delta t/2$. The value of the electric field at time Δt , can then be determined from Eq. 2.65a, and so forth. However, it should be pointed out that since Eqs. 2.66a and 2.67a as they stand now are homogeneous, this process obviously leads to values of the fields which are equal to zero at any time. This actually is not surprising in view of the fact that the existence of an incident field has not been taken into account yet in these equations. As will be described hereafter in Section 2.2.2, the existence of this incident field entails the necessity of introducing complementary terms in the equations which, as a result, will no longer remain homogeneous. The case of an incident pulse will be first discussed here before turning to the consideration of a point source emitting in the vicinity of the crystal.

2.2.2 Case of an Incident Pulse

The approach that will be described in this section is based on the ‘total field - scattered field’ formulation. In this theory, the discretisation proceeds by dividing the region of space considered into two subregions: a total field region extending from the centre and a scattered field region surrounding the first region (Fig. 2.6).

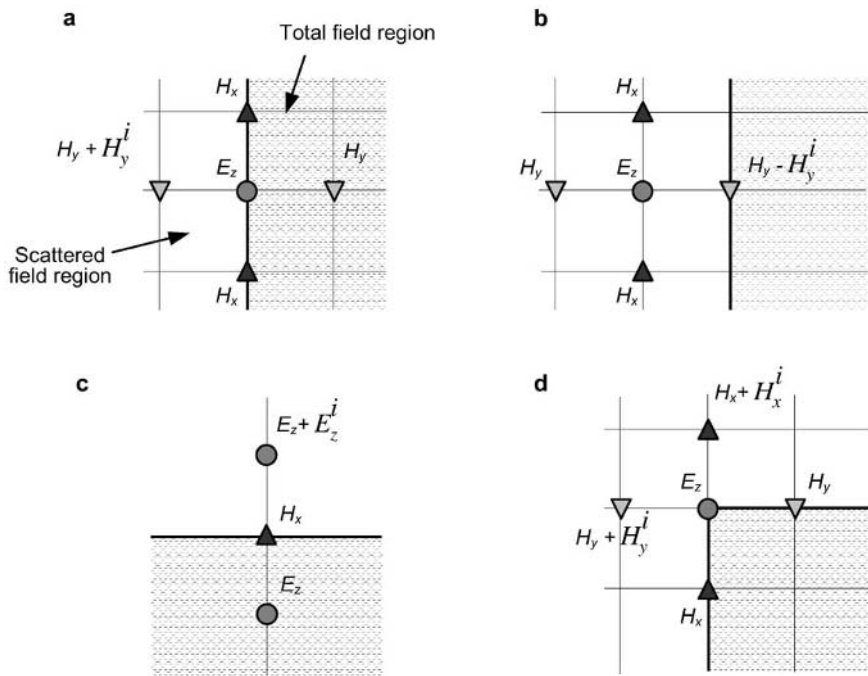


Fig. 2.7. Schematic illustration of the rules used for introducing the incident field at the boundary between the total field region and the scattered field region. In each case, the boundary between these two regions is represented by a thick line while the meshes used in the numerical calculations are represented by thin lines. E_z , H_x and H_y denote the components of the incident field, while the discretisation points for E_z , H_x and H_y are denoted by the same symbols than in Fig. 2.5. The examples represented in the figure are: **a.** Eq. 2.65a, calculation of E_z at the boundary **b.** Eq. 2.65a, calculation of E_z near the boundary in the scattered field region **c.** Eq. 2.66a, calculation of H_x at the boundary **d.** Eq. 2.65a, calculation of E_z at one of the corners of the rectangle delimiting the boundary (Fig. 2.6)

The scattered field region must be homogeneous, which is to say that it must extend outside the region containing the photonic crystal. The scattered field in this region is classically defined as the difference between the total and incident field. The components of the field involved in Eqs. 2.65a, 2.66a and 2.67a will be either identical with the components of the scattered field in the scattered field region, or equal to the total field in the total field region. The boundary between

these two regions forms a rectangle whose sides include the points represented in Fig. 2.5. This boundary is considered as belonging to the total field region.

Of course it would be incorrect to introduce the scattered field at some points of the mesh and the total field at some other points without any change in Eqs. 2.65a, 2.66a and 2.67a. A correct description requires that when the equations simultaneously contain discretisation points in the two separate regions, the incident field should be either added, for points in the scattered field region, or subtracted for points in the total field region. The first or the second rule is used depending on whether the discretisation point corresponding to the left-hand side of the equation is located in the total field region or in the scattered field region, respectively. Fig. 2.7 illustrates the application of these rules in some examples.

2.2.3 Absorption Region and Boundary Conditions

At first sight, it may seem that the scattering problem has now been entirely solved. The use of Eqs. 2.65a, 2.66a and 2.67a allows the determination of the time-dependence of the total field in the total field region, and of the scattered field in the scattered field region, provided that the simple rules previously described for introducing the incident field are followed. However, it should be noted here that the scattered field region cannot be extended at infinity in space. Therefore, for discretisation points associated with the left-hand side of Eqs. 2.65a, 2.66a and 2.67a located at the external boundary of this region, certain discretisation points associated with the right-hand side of this equation will inevitably be located outside this region. A seemingly simple method for overcoming this problem would consist in merely ignoring the corresponding points, i.e. in truncating Eqs. 2.65a, 2.66a and 2.67a in such a way so as to retain only terms associated with points located in the scattered field region. However, it is quite evident that this would lead to dramatic consequences for the calculation of the field. Arbitrarily cancelling the terms corresponding to the points located outside the scattered field region would actually amounts to assuming that the scattered field is zero outside this region. However, the boundary condition thus artificially introduced is incorrect since it does not satisfy the rigorous boundary value problem defined by the elementary laws of electromagnetism. Indeed, according to these laws, the scattered field does not vanish outside the discretised domain. By causality, since this field is continuous at the boundary of this region, it satisfies a radiation condition at infinity, whence it follows that it propagates away from the crystal. It thus turns out that this approach introduces parasitic and artificial reflection phenomena at the boundary and therefore that it should be abandoned.

Since the scattered field region cannot extend at infinity, an alternative approach consists in including an absorption region extending around the external boundary of the scattered field region. This region should be defined in such a way as to progressively absorb the scattered field without generating any artificial reflection phenomena. If such a region can be realised, then the field scattered outside the discretised domain might be assumed to be zero. Indeed, since the scattered field will be almost zero beyond the absorption region, this assumption does

not entail any noticeable consequence for the validity of the calculations. Further, since this absorption region does not generate any artificial reflection of the scattered field, the radiation condition is satisfied. Interestingly enough, this approach reproduces at a theoretical level the experimental arrangement adopted for microwave measurements in anechoic chambers: in order not to perturb the measurement of the field scattered by an object located at the centre of the chamber, an absorbing material is used for covering the walls and thus for preventing any reflection from occurring.

The research of efficient absorbing conditions is probably the issue related to the FDTD method on which the most subtle researches have been conducted. The interested reader will find a more detailed exposition of these researches in (Taflove 1995). Roughly speaking, the absorption region is realised by introducing lossy materials with a conductivity different from zero. This can be attempted for instance by giving ϵ_r a complex value in this region. This solution presents the advantage that Eqs. 2.65a, 2.66a and 2.67a will remain almost the same save for the change in the permittivity of the absorption region. It is plain however that such an approach is too simplistic. Finding materials that would totally absorb a scattered field without generating any reflection is not a trivial task. Indeed, this means that whatever the angle of incidence may be, an incident plane wave on an interface formed by such a material would not generate any reflection. Without going into detail here, the most efficient method to this date seems to be the method developed by JP Bérenger (Bérenger 1994). The perfectly matched layer (PML) formulation suggested by this author does not only consist in the introduction in Maxwell's equations of the complex permittivity and permeability, but also in the separation of E_z into two parts with different electromagnetic constants. This method is remarkably efficient since the width of the absorption region can generally be limited to a number of elementary meshes of the order of five.

2.2.4 Practical Implementation and Convergence of the FDTD Method

The implementation of the FDTD method can be separated into three stages. In the first stage, which might be referred to as the null-field stage, the wave front of the incident field has not reached the discretised domain yet. Eqs. 2.65a, 2.66a and 2.67a are homogeneous and the total field is zero in any point. In the second step, referred to as the illumination stage, the incident field has now reached the discretised domain and it must therefore be introduced in the equations at the boundary between the scattered field region and the total field region, or immediately outside this boundary, as represented in Fig. 2.7. Accordingly, the total field is no longer zero. Finally, in the third stage, referred to as the relaxation stage, the incident field has now passed beyond the discretised domain and therefore tends towards zero in this domain. In this case, no corrections need to be made in Eqs. 2.65a, 2.66a and 2.67a for introducing the incident field, and these equations return to being homogeneous. In contrast with the first situation, the field is not at the beginning of the relaxation stage immediately zero, but it is however expected

to tend towards zero at the end of this stage, since the radiation losses of the scattered field are not compensated by any incident field.

It is obvious that the third stage will assume quite a different form if the incident field is a sinusoidal wave of the form given by Eq. 2.60 rather than an electromagnetic pulse of the type described by Eq. 2.59. In such a case, the incident field remains non-zero and the relaxation step actually becomes a stabilisation step, where the field tends towards a time-harmonic behaviour.

In terms of calculations, the process which has just been described represents an ideal case. However, things may turn out differently in practice, and the calculations may sometimes diverge when time increases, for instance at the third step in the calculations. The possibility that such a divergence may occur can be explained in the following terms. Let us first represent Eqs. 2.65a, 2.66a and 2.67a using an operator notation. At any given time, all the values of the discretised field are ordered in column matrices. Thus, $E_z(n)$ will represent the set of values $E_z|_{i,j}^n$ for all i and j , while $H_x(n-1/2)$ and $H_y(n-1/2)$ will represent the sets of val-

ues of $H_x|_{i,j+\frac{1}{2}}^{n-\frac{1}{2}}$ and $H_y|_{i+\frac{1}{2},j}^{n-\frac{1}{2}}$ respectively. Using this symbolic notation,

Eqs 2.65a to 2.67a now assume the following form:

$$E_z(n+1) = E_z(n) + O_1 H_x(n+1/2) + O_2 H_y(n+1/2) \quad (2.65b)$$

$$H_x(n+1/2) = H_x(n-1/2) + O_3 E_z(n) \quad (2.66b)$$

$$H_y(n+1/2) = H_y(n-1/2) + O_4 E_z(n) \quad (2.67b)$$

where the operators O_i can easily be deduced from Eqs. 2.65a to 2.67a.

Introducing the right-hand sides of Eqs. 2.66b and 2.67b into Eq. 2.65b, we arrive to the following equation:

$$\begin{aligned} E_z(n+1) &= E_z(n) + O_1(H_x(n-1/2) + O_3 E_z(n)) + O_2(H_y(n-1/2) + O_4 E_z(n)) \\ &= O_5 E_z(n) + O_6 H_x(n-1/2) + O_7 H_y(n-1/2) \end{aligned} \quad (2.65c)$$

Further, by converting the three column matrices $E_z(n)$, $H_x(n-1/2)$ and $H_y(n-1/2)$ into a unique column matrix $F(n)$, the equation system formed by Eqs. 2.65b, 2.66b and 2.67b can be written in the following symbolic form:

$$F(n+1) = OF(n) \quad (2.68)$$

This latter equation entails that the values of the electric and magnetic fields at time $(n + 1)\Delta t$ and the values of the magnetic field at time $(n + 1/2)\Delta t$ can be derived from their values at times $n\Delta t$ and $(n - 1/2)\Delta t$ respectively by applying the operator O . This operator is successively applied to each discretisation point in time, from the beginning to the end of the scattering process. It is well known that such a process is numerically stable if no eigenvalue of O has a modulus greater than the unity. However, if this criterion is not satisfied, the numerical calculations may diverge exponentially with time, and this divergence will be all the more noticeable that the calculations are carried out over a longer period. We may for instance consider here the case of a microcavity embedded in a photonic crystal presenting a complete band gap. If the incident pulse causes a resonant oscillation of the field located in the microcavity, the oscillation thus induced may persist a long time due to fact that the radiation losses are small. This behaviour is likely to have dramatic consequences if the calculations have to be continued until the end of the relaxation or of the stabilisation stage are reached. Indeed, it should be borne in mind that the harmonic response of the crystal is calculated either by a Fourier transformation in time of this response in the case of an incident pulse, or by a direct calculation until the stabilisation of the response in the case of a sinusoidal wave front. If precision and stability requirements are to be simultaneously met, the algorithm used in the implementation of the FDTD method needs to be carefully chosen, for instance, by using more accurate values for the centred finite differences than those given in Eq. 2.64.

Let us finally mention that the method which has been described in Sections 2.2.2, 2.2.3 and 2.2.4 of this chapter does not allow the calculations of the scattered field at infinity. This problem can be resolved through the use of methods known as near field/far field transformation techniques. These methods are based on the fact that the value of the field scattered outside a well chosen surface surrounding the photonic crystal can be determined by simple integral calculations from the field at this surface. This result will not come as a surprise for a reader already acquainted with the mathematical form of Huyghens' principle (Born 1965).

2.2.5 Examples of Results obtained with the FDTD Method for a Point Source

The introduction of a point source inside the crystal itself in place of an incident wave arriving from an external region calls for certain changes in the implementation of the FDTD method. These changes, which are made necessary only due to the fact that the field is singular at the point source, will not be described in this section. Fig. 2.8 represents an example where the FDTD method was used for determining the field generated in an angled photonic crystal waveguide by a point source located at the entrance of the waveguide shown in the upper section of the figure. The crystal is a two-dimensional crystal with a finite size and presenting a

square symmetry. Each segment of the waveguide is obtained by removing one line of rods. The field is *s* (or TM) polarised, while the frequency is in the first band gap of the crystal. It can be seen that the wave follows the 90 degree bends without any noticeable loss and that the penetration of the field in the walls of the waveguide is limited. By contrast, and as can be observed in the lower section of the figure, a strong divergence of the field arises at the extremity of the waveguide. This divergence can be explained by the fact that the width of the waveguide is of the same order of magnitude than the wavelength of light.

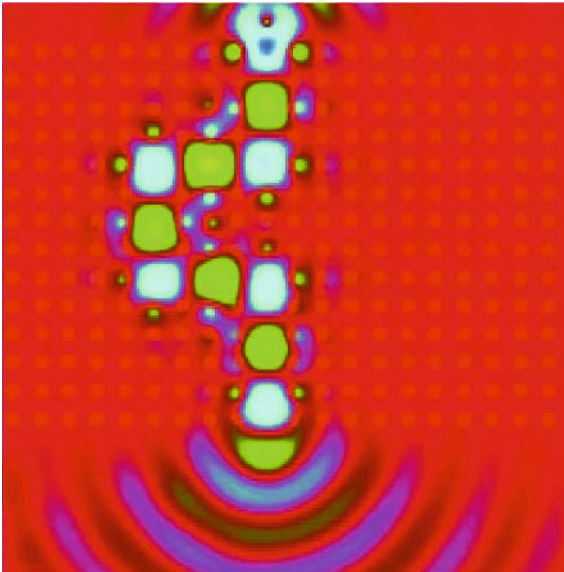


Fig. 2.8. Results of calculations performed using the FDTD method: propagation of the field generated by a point source located inside a photonic crystal angled waveguide. The two-dimensional photonic crystal consists of a square lattice formed by dielectric rods ($\epsilon = 9$) in the air. The ratio of the radius of the rods to the period of the lattice is $r/a = 0.25$, while the wavelength used in the calculations is $\lambda/a = 0.3$ in normalised units. The dark regions in this figure correspond to fields with a very small amplitude, while the light grey and medium grey regions correspond to the highest values of the field modulus. The phase shift in complex amplitude between the latter two regions is equal to π (*a colour version of this figure is also reproduced in the central insert of this book*)

2.3 Scattering Matrix Method

The scattering matrix method, also known as the multipole method, or as the modal method, has proved to particularly efficient for the resolution of scattering problems involving a large, albeit finite number of objects. This method, which can be presented in a rigorous mathematical form, is also based on a physically very intuitive approach to the problem of the scattering by a set of objects. In addition, the mathematical development of this theory is accessible to postgraduate students and its numerical implementation does not present any major difficulty. In marked contrast with the methods previously discussed, the implementation of this method becomes much simpler in the case of two-dimensional photonic crystals with circular rods, or in that of three-dimensional photonic crystals formed by spherical inclusions. This method is of particular interest for the study of crystals with a finite size, irrespective of whether they exhibit periodicity defects or not. It has also demonstrated an remarkable potential for the analysis of the propagation of light in microstructured optical fibers.

The pioneering role in the development of the modal method should be attributed to Lord Rayleigh, who first elaborated it in the electrostatic case (Rayleigh 1892). However, the development of this method in its electromagnetic form dates only from the 1980s, when it was independently developed in various forms by different groups (Chew 1992; Defos du Rau 1997; Elsherbini 1992; Felbacq 1994a, 1994b; Nicorovici 1995; Vlassis 1996; Youssif 1988). As a survey of the studies published on this topic would reveal, the application range of this method is quite large: it may apply to two-dimensional as well as to three-dimensional objects, to dielectric, to metallic or to perfectly conducting objects, and to periodical as well as to random arrangements of objects in space. In all these cases however, the principles of this method remain the same.

While this method can be applied to objects with arbitrary shapes and with different electromagnetic parameters, we shall limit ourselves here, within the framework of the study of photonic crystals, to a set of identical objects. For the sake of simplicity, and in the same way as for the preceding methods, we shall consider here the case of two-dimensional photonic crystals formed by identical circular rods and illuminated under *s*-polarised light. Fig. 2.9 provides a schematic representation of the physical problem to be considered: an incident monochromatic plane wave with a wavelength $\lambda_0 = 2\pi/k_0$ in vacuum, propagating in an homogeneous material with a relative permittivity $\epsilon_{r,ext}$ illuminates in *s* polarisation and with an angle of incidence Θ^{inc} a set of N identical dielectric rods with a radius R and a relative permittivity $\epsilon_{r,int}$. We shall denote by $n_{ext} = \sqrt{\epsilon_{r,ext}}$ and by $n_{int} = \sqrt{\epsilon_{r,int}}$ respectively the optical indices of the materials outside and inside the rods.

The complex amplitude of the incident electric field is given by the following equation:

$$\mathbf{E}^i = E_z^i \hat{z} \quad (2.69)$$

where:

$$E_z^i = \exp(ik_0 n_{ext}(x \sin \Theta^{inc} - y \cos \Theta^{inc})) \quad (2.70)$$

From Eq. 1.37, the total electric field satisfies the Helmholtz equation in the sense of distributions:

$$\nabla^2 E_z + k_0^2 \epsilon_r(x, y) E_z = 0 \quad (2.71)$$

where:

$$\epsilon_r(x, y) = \begin{cases} \epsilon_{r,ext} & \text{outside the rods} \\ \epsilon_{r,int} & \text{inside the rods} \end{cases} \quad (2.72)$$

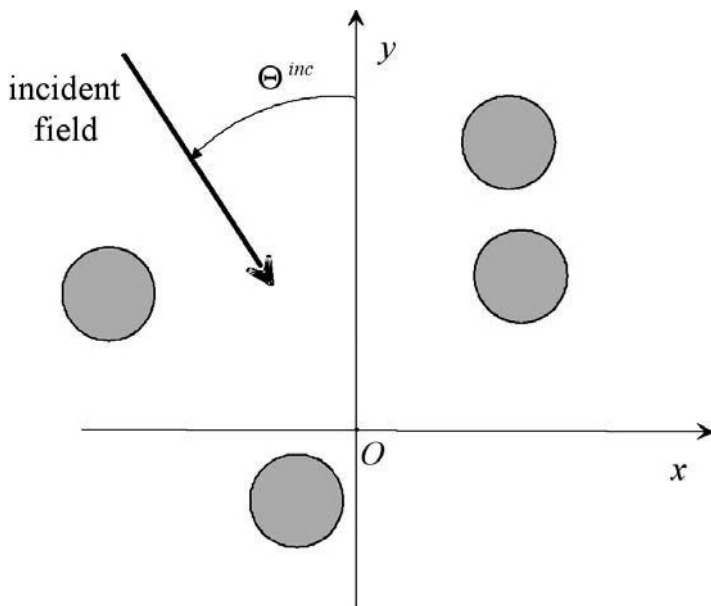


Fig. 2.9. Schematic representation of the scattering problem considered here: N rods are illuminated in s polarisation by an incident plane wave. In this example, $N = 4$

The theoretical development of the method allowing the resolution of Eq. 2.71 will be presented in more detail in the Appendix, and only a brief outline of the formalism shall be presented here. This method proceeds along three steps. The first step consists in showing that in certain regions of space the total field can be expressed in the form of Fourier-Bessel series. This fundamental property can be demonstrated by using for each individual rod a local system of polar coordinates (r_j, θ_j) whose origin is located at the centre of the rod, as is represented in Fig. 2.10. Although we shall limit ourselves here to systems with a circular symmetry, the property to be demonstrated here can be extended to non-circular rods as well. In this case however, the domain of validity of the Fourier-Bessel series does not extend over the entire section of the rod.

For any given value of r_j , it is plain that the electric field is a periodic function of θ_j with a period 2π . Accordingly, this field can be represented in the form of a Fourier series:

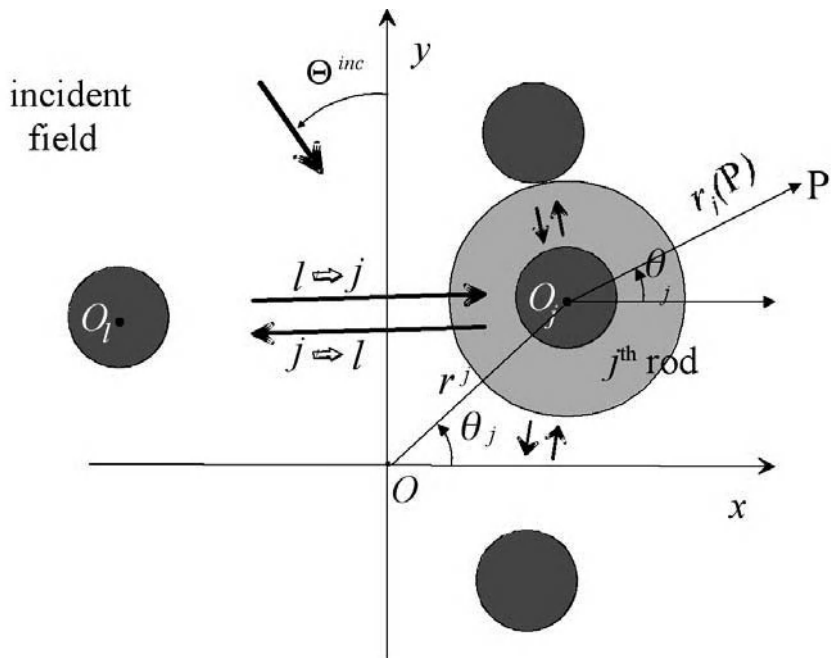


Fig. 2.10. Domains of validity of the Fourier-Bessel series. The dark grey area represents the domains of validity for the expansion of the field into Fourier-Bessel series inside the rods (with Bessel functions of the first kind), while the light grey area represents the domain of validity for this expansion around the j^{th} rod (with Hankel functions). The arrows $l \Rightarrow j$ and $j \Rightarrow l$ point to the fields scattered by the l^{th} and j^{th} rods respectively, which propagate into or out of the latter region

$$E_z(r_j, \theta_j) = \sum_{m=-\infty, +\infty} E_{z,m}(r_j) \exp(im\theta_j) \quad (2.73)$$

More precisely, it can be demonstrated (see the Appendix) that inside each rod the field can be expressed for $r_j < R$ by the following equation:

$$E_z(r_j, \theta_j) = \sum_{m=-\infty, +\infty} c_{j,m} J_m(k_0 n_{int} r_j) \exp(im\theta_j) \quad (2.74)$$

where J_m is the Bessel function of the first kind of order m .

The problem of determining the field in the rods therefore comes down to the calculation of the coefficients $c_{j,m}$ of the Fourier-Bessel series in the right-hand side of Eq. 2.74.

Let us now consider the ring surrounding the j^{th} rod and extending to the nearest point of the immediately neighbouring rod. This region is represented in Fig. 2.10 by a light grey area, and it can be demonstrated that the field in this region assumes the form of a different type of Fourier-Bessel series:

$$\begin{aligned} E_z(r_j, \theta_j) = & \sum_{m=-\infty, +\infty} a_{j,m} J_m(k_0 n_{ext} r_j) \exp(im\theta_j) \\ & + \sum_{m=-\infty, +\infty} b_{j,m} H_m^{(1)}(k_0 n_{ext} r_j) \exp(im\theta_j) \end{aligned} \quad (2.75)$$

where $H_m^{(1)}$ is the Hankel function of the first kind of order m . It is convenient to note that the right-hand side of Eq. 2.75 now contains two Fourier-Bessel series with coefficients $a_{j,m}$ and $b_{j,m}$. On the other hand, the field represented by the summation of these two series can be decomposed into three distinct components having different physical meanings:

1. the incident plane wave, i.e. the source, given by Eq. 2.70,
2. the fields scattered by all other rods in the direction of the j^{th} rod: these fields behave with respect to this rod as any other incident wave,
3. the field scattered by the j^{th} rod which, according to the radiation condition, must propagate away from the rod.

Different physical considerations allow us to reach the conclusion that the first two types of incident fields cannot present any singularity in the light grey region and in the dark gray region corresponding to the j^{th} rod. These fields are therefore represented by the first series in the right-hand side of Eq. 2.75, which will be referred to as the local incident field at the j^{th} rod. The second series corresponds to the third field, i.e. the field scattered by the j^{th} rod and presents a singularity at the

origin (see the Appendix). As a consequence, each coefficient $a_{j,m}$ can be decomposed into two coefficients corresponding respectively to the first two fields:

$$a_{j,m} = a_{j,m}^{\text{source}} + a_{j,m}^{\text{rods}} \quad (2.76)$$

Using the decomposition of a plane wave into Fourier-Bessel series (see the Appendix for more detail), the coefficients $a_{j,m}^{\text{source}}$ turn out to be analytic. These coefficients are given by the equation:

$$a_{j,m}^{\text{source}} = (-1)^m \exp\left(ik_0 n_{r,\text{ext}} r^j \sin(\Theta^{\text{inc}} - \theta^j) - im\Theta^{\text{inc}}\right) \quad (2.77)$$

where r^j and θ^j are the coordinates of O_j in the general coordinate system represented in Fig. 2.10.

The second step of the method can be understood from the following physical interpretation. It has been seen that the local incident field contains two components: the term representing the source, which is known, and the field scattered by the other rods towards the j^{th} rod, which is not. The latter component, represented by the coefficient $a_{j,m}^{\text{rods}}$, is but a sum of terms analogous to the second series in Eq. 2.75, the summation being carried out here over all the rods save the j^{th} one. This means in other words that the coefficients $a_{j,m}^{\text{rods}}$ can be expressed in terms of the set of $(N - 1)$ series of coefficients $b_{l,m}$ with $l \neq j$. The assumption is used here that the expression of the field scattered by one rod, i.e. the right-hand side of Eq. 2.75, will remain valid outside the light grey ring represented in Fig. 2.10 (Maystre 2002). Under this assumption and proceeding once more to coordinate transformations, it turns out after a few calculations that the field scattered along the direction of the j^{th} rod by all other rods can be written in the following form (see the Appendix for more detail):

$$a_{j,m}^{\text{rods}} = \sum_{l \neq j} \sum_{q=-\infty,+\infty} b_{l,q} \exp\left(i(q-m)\theta_j^l\right) H_{m-q}^{(1)}\left(k_0 n_{r,\text{ext}} r_j^l\right) \quad (2.78)$$

where r_j^l and θ_j^l are the coordinates of O_l in the system of polar coordinates system associated with the j^{th} rod (see Fig. A.1 in the Appendix). Adding the coefficient $a_{j,m}^{\text{source}}$ of the incident source field (Eq. 2.77) to the coefficient $a_{j,m}^{\text{rods}}$, it turns out that the coefficient of the total incident field can be expressed in terms of the coefficients of the field scattered by the other rods:

$$a_{j,m} = (-1)^m \exp\left(ik_0 n_{ext} r^j \sin(\Theta^{inc} - \theta^j) - im\Theta^{inc}\right) + \sum_{l \neq j} \sum_{q=-\infty, +\infty} b_{l,q} \exp\left(i(q-m)\theta_j^l\right) H_{m-q}^{(1)}\left(k_0 n_{ext} r_j^l\right) \quad (2.79)$$

The last step in the calculations consists first in rewriting Eq. 2.79 in a matrix form. A second matrix equation is then obtained by applying the boundary conditions of the field on both sides of each rod. For the purpose of representing Eq. 2.79 in a matrix form, we introduce a set of column matrices \mathbf{a}_j and \mathbf{b}_j with components $a_{j,m}$ and $b_{j,m}$, which yields:

$$\mathbf{a}_j = \mathbf{Q}_j + \sum_{l \neq j} \mathbf{T}_{j,l} \mathbf{b}_l \quad (2.80)$$

where \mathbf{Q}_j is a column matrix whose m^{th} component $Q_{j,m}$ is given by the equation:

$$Q_{j,m} = (-1)^m \exp\left(ik_0 n_{ext} r^j \sin(\Theta^{inc} - \theta^j) - im\Theta^{inc}\right) \quad (2.81)$$

while $\mathbf{T}_{j,l}$ is a square matrix whose $(m, q)^{\text{th}}$ component $T_{j,l,m,q}$ is given by the equation:

$$T_{j,l,m,q} = \exp\left(i(q-m)\theta_j^l\right) H_{m-q}^{(1)}\left(k_0 n_{ext} r_j^l\right) \quad (2.82)$$

Eq. 2.80 is a system of N matrix equations formed by the $2N$ column matrices \mathbf{a}_j and \mathbf{b}_j . The notion of a scattering matrix is then used in order to obtain a second system of N equations. It has been seen that the expression in Eq. 2.75 for the field around a given rod contains two sums representing the total incident field and the field scattered by the rod respectively. Further, it has already been demonstrated in Section 2.1 that a causal relation exists between these two fields, and this relation can be expressed in a mathematical form through the use of a scattering matrix defined as follows:

$$\mathbf{b}_j = \mathbf{S}_j \mathbf{a}_j \quad (2.83)$$

where \mathbf{S}_j is a square matrix of infinite order.

In the particular case where the rods are circular, the scattering matrix can be readily derived from the boundary conditions at the surface of a rod. Since Eq. 2.71 is valid in the sense of distributions, the electric field and its normal derivative are continuous across this surface. This property can also be proved from the

continuity of the tangential components of the electric and magnetic fields. By using the expansions of the field given by Eqs. 2.74 and 2.75 inside and outside the rod, and then by identifying the Fourier coefficients on both sides, it can be deduced that:

$$a_{j,m} J_m(k_0 n_{ext} R) + b_{j,m} H_m^{(1)}(k_0 n_{ext} R) = c_{j,m} J_m(k_0 n_{int} R) \quad (2.84)$$

$$a_{j,m} \frac{dJ_m(k_0 n_{r,ext} r_j)}{dr_j} \Big|_{r_j=R} + b_{j,m} \frac{dH_m^{(1)}(k_0 n_{r,ext} r_j)}{dr_j} \Big|_{r_j=R} = \\ c_{j,m} \frac{dJ_m(k_0 n_{r,int} r_j)}{dr_j} \Big|_{r_j=R} \quad (2.85)$$

By eliminating the coefficients $c_{j,m}$ between Eqs. 2.84 and 2.85, the following equation is finally deduced:

$$b_{j,m} = -\frac{J_m(k_0 n_{ext} R) \frac{dJ_m(k_0 n_{int} r_j)}{dr_j} \Big|_{r_j=R} - J_m(k_0 n_{int} R) \frac{dJ_m(k_0 n_{ext} r_j)}{dr_j} \Big|_{r_j=R}}{H_m^{(1)}(k_0 n_{ext} R) \frac{dJ_m(k_0 n_{int} r_j)}{dr_j} \Big|_{r_j=R} - J_m(k_0 n_{int} R) \frac{dH_m^{(1)}(k_0 n_{ext} r_j)}{dr_j} \Big|_{r_j=R}} a_{j,m} \quad (2.86)$$

It might be noted here that the variable r_j in this equation can be replaced by a variable r independent from the rod, which demonstrates that this causal relation does not depend on the rod. All the matrices S_l defined by Eq. 2.83 are therefore diagonal and equal to the matrix S defined by:

$$S_{m,m} = -\frac{J_m(k_0 n_{ext} R) \frac{dJ_m(k_0 n_{int} r_j)}{dr_j} \Big|_{r_j=R} - J_m(k_0 n_{int} R) \frac{dJ_m(k_0 n_{ext} r_j)}{dr_j} \Big|_{r_j=R}}{H_m^{(1)}(k_0 n_{ext} R) \frac{dJ_m(k_0 n_{int} r_j)}{dr_j} \Big|_{r_j=R} - J_m(k_0 n_{int} R) \frac{dH_m^{(1)}(k_0 n_{ext} r_j)}{dr_j} \Big|_{r_j=R}} \quad (2.87)$$

and, if $n \neq m$:

$$S_{n,m} = 0 \quad (2.88)$$

It should be pointed out that the determination of the scattering matrix for non-circular cylinders is much more complex. This requires that the scattering matrix of a single cylinder be first calculated, for instance by using the FDTD method. While these calculations will not be analytic as was previously the case, the FDTD method presents the advantage here of being restricted to a single rod, in contrast with the FDTD calculations which have been presented in Section 2.2, where the problem of the scattering by N rods had to be resolved. Likewise, it might be noted that in the case where the rods are not of the same radius or of the same permittivity, the scattering matrices are no longer identical, but remain diagonal in the case where the rods are circular.

In order to obtain a single matrix equation, we need only to multiply both sides of Eq. 2.80 by $S_l = S$, while Eq. 2.83 is used for simplifying its left-hand side. This leads to the following equation:

$$\mathbf{b}_j - \sum_{l \neq j} ST_{j,l} \mathbf{b}_l = S\mathbf{Q}_j \quad (2.89)$$

which can be written in the more explicit form:

$$\begin{vmatrix} \mathbf{I} & -ST_{1,2} & -ST_{1,3} & \dots & \dots & \mathbf{b}_1 & |S\mathbf{Q}_1| \\ -ST_{2,1} & \mathbf{I} & -ST_{2,3} & \dots & \dots & \mathbf{b}_2 & |S\mathbf{Q}_2| \\ -ST_{3,1} & -ST_{3,2} & \mathbf{I} & \dots & \dots & \mathbf{b}_3 & |S\mathbf{Q}_3| \\ \dots & \dots & \dots & \dots & \dots & \dots & \dots \\ \dots & \dots & \dots & \dots & \dots & \dots & \dots \end{vmatrix} \quad (2.90)$$

We thus arrive at an infinite linear system of equations, with \mathbf{I} as its infinite unit matrix. In order to reduce the size of the system size, the matrices S , $T_{j,l}$, \mathbf{Q}_j and \mathbf{b}_l are truncated by limiting m and q to values ranging from $-M$ to $+M$. The system of equations to be inverted is therefore of size $N(2M+1)$.

Finally, the field at infinity can be easily calculated from the column matrices \mathbf{b}_l . For this purpose, the expression of the field scattered outside each cylinder (right-hand side of Eq. 2.75) is used after having been transformed so as to be adapted to the xy coordinate system. The transition from the local coordinate system associated with a rod to the unique xy coordinate system can be achieved by using Graf's formula (Abramovitz 1970). Thus, if $r \geq r^j$:

$$\begin{aligned} & H_m^{(1)}(k_0 n_{ext} r_j(P)) \cdot \exp(im\theta_j(P)) \\ &= \sum_{q=-\infty, +\infty} \exp(i(m-q)\theta^j) J_{q-m}(k_0 n_{ext} r^j) H_q^{(1)}(k_0 n_{ext} r) \exp(iq\theta) \end{aligned} \quad (2.91)$$

where r and θ are the polar coordinates of a point P of space in the xy coordinates system. At a large distance from the rods, it turns out that:

$$E^d(P) = \sum_{q=-\infty, +\infty} b_q H_q^{(1)}(k_0 n_{ext} r) \exp(iq\theta) \quad (2.92)$$

where:

$$b_q = \sum_{j=1,N} \sum_{m=-\infty}^{+\infty} b_{j,m} \exp(i(m-q)\theta^j) J_{q-m}(k_0 n_{ext} r^j) \quad (2.93)$$

The expression of the field at infinity is obtained by using the asymptotic form at infinity of the Hankel function which is described in the Appendix. Eq. 2.92 thus becomes:

$$E^d(P) = g(\theta) \frac{\exp(ikr)}{\sqrt{r}} \quad (2.94)$$

where:

$$g(\theta) = \sqrt{\frac{2}{\pi k_0 n_{ext}}} \exp\left(-i\frac{\pi}{4}\right) \sum_{q=-\infty, +\infty} b_q \exp\left(-iq\frac{\pi}{2}\right) \exp(iq\theta) \quad (2.95)$$

The intensity of the field at infinity, also referred to as the bistatic differential cross-section in the field of radar detection, is given by the equation:

$$D(\theta) = 2\pi |g(\theta)|^2 \quad (2.96)$$

In the case where all materials, i.e. both the rods and the external medium, are lossless, the energy balance equation assumes the following form:

$$\int_0^{2\pi} |g(\theta)|^2 d\theta + 2\sqrt{\frac{2\pi}{k_0 n_{ext}}} \operatorname{Re} \left[\exp\left(i\frac{\pi}{4}\right) g(\Theta^{inc} + \pi) \right] = 0 \quad (2.97)$$

This equation is of course very useful for testing the validity of a numerical code. However, like the casting out nines test, it does not provide a rigorous demonstration of the validity of the numerical results.

2.4 Other Methods: Integral and Differential Methods, Finite Element Method, Effective Medium Theory

Integral and finite element methods are probably the two most extensively used methods in electromagnetism, in particular for the resolution of the time-harmonic Maxwell's equations. As a general rule, integral methods allow the reduction of a scattering problem to the resolution of an integral equation, or to a system of coupled integral equations.

An integral equation is an equation in which the unknown function appears under an integral sign, with possible occurrences outside this integral sign.

As an example, $\varphi(l) = \varphi_0(l) + \int_D K(l, l')\varphi(l')dl'$ is an integral equation where φ is the unknown function, K is the kernel, i.e. a known function of two variables, and φ_0 is a known function. In electromagnetism, the unknown function is often related to the value of the electric or magnetic field, while l generally is a spatial variable. Boundary integral equations need to be distinguished from volume integral equations. In the latter, the unknown function is defined over the whole space, and the number of spatial variables of integration is therefore equal to the dimension of the scattering problem, for instance to three if the problem at hand is three-dimensional. By contrast, in a boundary integral equation, the unknown function is defined at the boundaries of the scattering objects. The number of spatial variables of integration is therefore reduced by one with respect to the dimension of the scattering problem. Thus, in a three-dimensional problem, the number of variables reduces to only a couple of variables.

Let us consider the case of a two-dimensional photonic crystal with a finite size, illuminated by an incident wave. In such a case, the unknown function in a boundary integral equation shall depend on the value of the fields at the boundaries of the entire set of rods of the crystal, with the variable l ranging over the points at these boundaries. The latter are formed by N circular lines if the number of rods is denoted by N . On the contrary, a volume integral equation shall be defined for each point of the two-dimensional space, with the consequence that the integral will become a double integral.

The classical method for deriving an integral equation relies on the use of the theory of Green's functions and, in more complicated cases, on the theory of dyadic Green's functions. In our opinion however, the most elegant and rigorous way to derive such an equation is the theory of distributions. In this respect, it suffices here to note that the very definition of a Green's function refers to the Dirac function, which itself is but a distribution. The integral equation is an exact repre-

sentation of the scattering problem, and therefore, once this equation has been solved, the field can be very easily determined at any point of space.

From a numerical point of view, a large variety of methods exist for the resolution of integral equations. One of the most used is the finite element method (Bos-savit 1989; Silberstein 2001). This method can be roughly described in the following terms:

- the unknown function is first represented in the form of a sum of finite elements in the variable l . For instance, in the example previously given of an integral equation, this sum will be $\varphi(l) = \sum_{j=1}^Q \varphi_j w_j(l)$. Each finite element $w_j(l)$ is zero everywhere save in an elementary interval of the range of integration. A special form of the finite element method is the so-called Galerkin method, which can be illustrated by considering a boundary integral equation in the very simple case of a two-dimensional crystal reduced to a unique circular rod with a radius R . Let us define a basis of finite elements $w_j(l)$, $j \in \{1, Q\}$, $l \in (0, 2\pi R)$, where Q is a natural integer, l is the curvilinear abscissa of a point at the boundary of the rod and j is the index of the finite element w_j . The latter may assume for instance the form of a rectangle function:

$$\forall j \in \{1, Q\} \quad w_j(l) = \begin{cases} 1 & \text{if } l \in (l_j, l_{j+1}) \\ 0 & \text{if } l \notin (l_j, l_{j+1}) \end{cases}$$

$$\text{where } l_j = (j - 1) \frac{2\pi R}{Q}$$

- the integral equation is then projected onto the same basis, leading therefore to a system of Q linear equations containing Q unknowns φ_j . The validity of the numerical results thus obtained can be tested from the convergence of the function $\varphi(l)$ when Q increases.

Boundary integral equations (Maystre 1994) present the obvious advantage over volume space integral equations that, since the unknown functions and the ranges of integration are limited to the boundaries of the scattering objects, the size Q of the linear system to be solved is much lower than would have been the case for volume space integral equations. In the latter case indeed, the whole space, or at least the interior of all scattering objects, need to be discretised. Further, as soon as the integral equation contains more than one variable of integration, it becomes necessary to use finite elements of several variables, which leads to a meshing of a two-dimensional or three-dimensional space (Guenneau 2001). While very efficient meshing algorithms currently exist, they need most of the time to be adapted to the specific scattering object considered. In addition, when

the integral equation extends to the whole space, and not only to the interior of the scattering objects, the range of integration needs to be truncated with the use of absorbing boundary conditions, as in the FDTD method.

The differential method, as well as the rigorous coupled wave method which belongs to the same class of methods, draw their inspiration from an opposite approach. These methods are characterised by their simplicity as regards both their theoretical development and their numerical implementation. Instead of reducing, like in the integral method, the scattering problem to an integral equation by resorting to non-trivial mathematical notions like Green's functions or distributions, the differential method uses Maxwell's equations in an almost direct way. In its present stage, this method cannot apply to photonic crystals with a finite size along all directions and in principle it is restricted to crystals with an infinite size along the transverse directions, i.e. in the xz plane. Certain ways of overcoming these limitations exist nonetheless (Silberstein 2001).

Let us consider the case of a two-dimensional crystal created by superposing a finite number of infinite dielectric grids, as represented in Fig. 2.1, and let us further assume for the sake of simplicity that this structure is illuminated under normal incidence. Assuming the x axis to be perpendicular to the axis of the rods in the plane of the grids, the differential method is based on the expansion of the fields into Fourier series of the variable x . Since the y axis is therefore perpendicular to the grids, the Fourier series thus obtained are functions of y . These series are then introduced into Maxwell's equations, and it can very easily demonstrated that the Fourier coefficients of these series satisfy a system of coupled differential equations. The resolution of such a system is a most classical problem of numerical analysis, which of course requires that the infinite system be truncated. The differential method and the coupled wave method diverge at this point: while the first method directly proceeds to the resolution of the differential system (Popov 2001a), the latter method replaces the rods by a stair-like structure, after having cut the rods by drawing onto them equidistant lines parallel to the x axis (Moharam 1986). The differential method and the rigorous coupled waves method have proven to be very efficient for the analysis of dielectric structures. The only exception to this concerns metallic structures in the visible, infrared and microwave regions, where the conductivity of the metal becomes very high. In this case indeed, strong numerical instabilities may occur when implementing these methods, although remarkable advances have recently been made in this field. For more information on these recent developments, the reader is referred to (Li 1996; Lalanne 1996; Granet 1996; Popov 2001b) and to (Silberstein 2001) where finite size crystals are more specifically considered.

Although of quite a different nature than the methods described above, the effective medium theory, also known as the homogenisation method (Dautray 1984), cannot be ignored. Indeed, in certain specific cases, this method may allow to simplify the scattering problem to such an extent that its resolution will be considerably simpler than the original problem. The effective medium theory draws its inspiration from a very evident observation: the properties of a periodic material like a photonic crystal tend to approach the properties of an homogeneous material when the wavelength of the light illuminating it tends towards infinity.

This is perhaps best illustrated by the fact that solid state crystals, like for instance diamonds or semiconductors, can be perfectly described by an optical index in the optical region, where the corresponding wavelengths are much larger than the elementary cell of the crystal. This being said, two different problems now arise, concerning on the one hand the calculation of the electromagnetic characteristics of the homogeneous material associated with a given photonic crystal, and on the other hand the limits on the validity of the homogenisation process. Indeed, while the elementary cell of solid state crystals is much smaller than optical wavelengths, this is not true of photonic crystals, since those that we are currently able to realise are of the same order of magnitude than these wavelengths. It should be emphasised that the stakes here are quite high, as the homogenisation process may turn a very difficult problem, where the light illuminates a large number of scattering objects periodically arranged in space, into a very simple problem involving a unique, homogeneous scattering object.

The effective medium theory relies on very sophisticated mathematical methods known by the term limit analysis. Describing these methods would of course be beyond the scope of this section, but it might be noted that they are of two different types. According to the first approach, the photonic crystal is assumed to extend at infinity along all directions, before considering the limits of the characteristics of the material when the wavelength tends to infinity. By contrast, the second method is based on the consideration of a model of a crystal with both a fixed finite size and a fixed wavelength, while the size of the elementary crystal cell tends towards zero, which implies that the number of elementary cells tends towards infinity (Felbacq 1998; Guenneau 2000). The second type of analysis presents a higher degree of complexity than the first one, but it nonetheless offers the advantage of accounting for the phenomena occurring at the boundary of the crystal which sometimes can be very important. This observation can be illustrated by considering a photonic crystal with a finite size, illuminated by a point source placed in the air and in the vicinity of the crystal. This point source generates a field in the direction of the crystal. A part of this field consists of evanescent waves whose amplitude exponentially decreases with the distance to the point source. However, since the point source is located at a very short distance from the crystal, the amplitude of these waves may remain significantly high at the boundary of the crystal. Further, these evanescent waves propagate along a direction parallel to the boundary of the crystal and their transverse wavelength, i.e. the period of the evanescent wave along the direction of propagation, can be much smaller than the actual wavelength of light in vacuum. This transverse wavelength is the decisive element in the validity of the homogenisation process, since it actually represents the true period of the field of the evanescent waves. This is a well known phenomenon in near field optics, where surface features much smaller than the wavelength of light in vacuum can be detected thanks to the small transverse wavelength of the evanescent part of the field generated by an optical antenna located at a very short distance from the surface. This demonstrates that the homogenisation notion which has been initially used, where the finite size of the actual crystal was neglected and where only the ratio between the wavelength and the

size of the elementary cell was considered, is insufficient and that it may lead to erroneous results.

The mathematical study of homogenisation processes is of such a complexity that not all types of photonic crystals can be analysed with this method. However, some very valuable results have been published on this subject, especially for crystals that had been realised from a perfectly conducting metal, which have thus been demonstrated to be equivalent to dielectric materials (Pendry 1996b; Felbacq 1997).

2.5 Numerical Codes available for the Modelling of Photonic Crystals

The electromagnetic modelling of photonic crystals is a time-consuming activity which in addition requires a high level of competence. The efficient and fine modelling of the most complex structures, for instance three-dimensional structures, cannot be achieved save through the combination of expertises in such diverse fields as applied mathematics, electromagnetism, numerical analysis and programming. As a consequence, a research group may be uncertain as to whether it should engage in such a project, especially in view of the availability of both free and commercial electromagnetic simulation software for the modelling of photonic crystals.

Of course, a numerical code internally developed by a research group will necessarily provide greater guarantees in terms of reliability and security, since a personal understanding of its theoretical and numerical foundations generally permits to avoid errors in its utilisation. A numerical code is not a ‘black box’ that would provide an accurate answer to any possible question, and the author of the code will be able to prevent most of the pitfalls in which a not well-informed user might run. Further, only the author of the code generally is in a position of adapting this code to the new cases that might arise. This is a crucial advantage in a field where structures are evolving at an extremely rapid pace.

Nevertheless, it should be acknowledged that these commercial codes may provide valuable services to many users. It is not the purpose of this section to provide an exhaustive review of these numerical programs, and the interested reader is referred to websites such as <http://www.pbglink.com/software.html> for specific resources on photonic crystals or <http://emlib.jpl.nasa.gov> for more general resources on electromagnetic modelling. Most of these codes are based on general methods of electromagnetism, for instance on the finite element method, the FDTD method or the integral methods: thus, the famous ‘High Frequency Sequence Simulator’(HFSS) code is based on the finite element method and uses a meshing automatically refined until the convergence of the result is reached. The introduction of convergence tests leads of course to a reduction of possible errors for not well-informed users. As a general rule, classical physical criteria like the energy balance equation or the reciprocity theorem provide casting out nine tests for ascertaining the validity of the results. For instance, in the case of a photonic

crystal consisting of a finite stack of infinite and lossless dielectric grids, the sum of the transmitted and reflected energies should be equal to the incident energy. By way of conclusion, it should be stressed that beginners need to be extremely cautious before considering numerical results as valid, especially when they do not know the theoretical and numerical foundations of the code used for obtaining these results.

3 Quasi-Crystals and Archimedean Tilings

The consideration of photonic crystals with defects or photonic crystals with finite sizes has already led us to move beyond crystalline periodicity in the strict sense of the term. The photonic quasi-crystals which will be described in this chapter can be regarded as yet another form of deviation from the ideal case of a periodic photonic crystal, and it will be seen that some of the numerical models that were discussed in the previous chapters can be applied to certain of these non-periodic structures.

The *International Union of Crystallography* (IUC) now defines the term ‘crystal’ as applying to ‘any solid having an essentially discrete diffraction diagram’ (IUC 1992). The large family of solid-state crystals thus defined can then be divided into two classes:

1. periodic crystals which exhibit a perfectly periodic structure at the atomic scale:
photonic crystals are the ‘photonic’ analogues of these crystals,
2. aperiodic crystals

The microscopic periodicity thus turns out to be a sufficient, albeit not necessary condition for the existence of a crystalline state. Actually, the definition developed by the IUC rests on the properties of lattices in the reciprocal (or Fourier) space. Diffraction diagrams, like for instance X-ray diffraction diagrams, can indeed be seen as the Fourier transform of the ‘atomic distribution’ of the crystal in the real space. The reciprocal lattice can be defined as the set of all combinations of wave vectors corresponding to peaks in the diffraction diagram. According to this definition, even wave vectors corresponding to the less intense diffraction peaks belong to the reciprocal lattice.

A crystal is said to be periodic if and only if the minimal number of vectors necessary for generating it is equal to the dimensionality of the crystal: for instance, if the crystal is two-dimensional, this minimal number must be equal to 2, and so on. In this case, the diffraction diagram corresponds to the reciprocal lattice of the crystal with which we are familiar.

Nevertheless, other situations may exist where several low intensity peaks appear between the main peaks in the diffraction diagram. The number of these secondary peaks is generally found to increase with the resolution of the Fourier transform. In such a case, the reciprocal lattice is said to be ‘dense’ in the mathematical sense of the term: there is no condition imposing a minimal distance between two wave vectors associated with diffraction peaks. The lattice of the crys-

tal is therefore quasi-periodic. It is precisely the absence of a condition imposing a minimal distance between the vectors of the reciprocal lattice which allows quasi-periodic crystals to exhibit symmetries that could not be achieved in periodic crystals, for instance a rotational invariance of order $N = 5$ or $N > 6$.

3.1 Photonic Quasi-Crystals

A very simple method of constructing quasi-crystals is represented here in Fig. 3.1. This method consists in projecting a structure exhibiting a periodicity in an N -dimensional space onto a space of lower dimensionality. The structure considered here in this figure is a grid G with a square symmetry. A one-dimensional quasi-crystal can be derived from the grid G by considering all the intersections of this grid with a straight line Δ of irrational slope. The intersection points thus generated are indeed distributed according to a quasi-periodic pattern. In practice, a photonic quasi-crystal can be constructed by alternately stacking dielectric layers with permittivities ϵ_1 and ϵ_2 respectively, in such a way that the thickness of the layers will vary with the distance between the successive intersection points represented in Fig. 3.1.

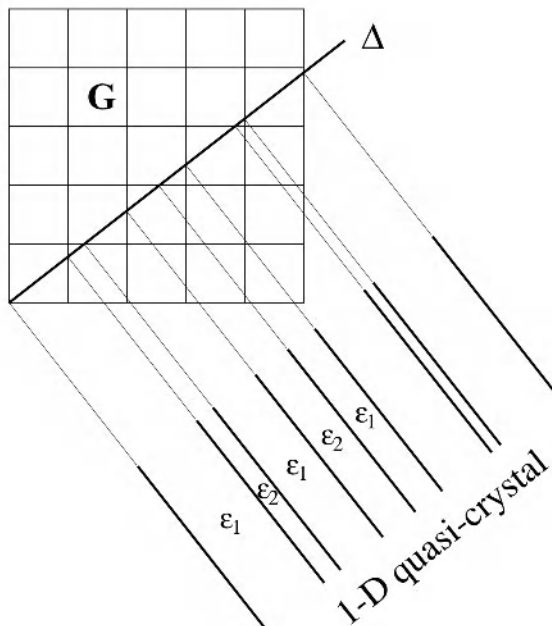


Fig. 3.1. Construction of a one-dimensional photonic quasi-crystal through the projection of a two-dimensional square grid onto a straight line with irrational slope

Quasi-crystals like the example introduced above are deterministic and perfectly ordered structures, which do not present any translational symmetry. As has already been mentioned, two-dimensional quasi-crystals may exhibit a rotational symmetry of unusual order, for instance $N = 5$ or $N > 6$. Solid-state quasi-crystals were discovered in 1984 (Shechtman 1984), and their electrical, thermal and mechanical properties turned out to be very different from the properties of ‘traditional’ crystals (Hippert 1994). More than a decade after the first studies conducted on solid-state quasi-crystals, and at a time when the study of photonic crystals was gaining momentum, a great interest arose in the question whether quasi-periodic electromagnetic (EM) structures might present any unexpected or interesting specific properties. Since quasi-crystals may exhibit a high-order rotational symmetry ($N = 8, 10, 12$, to be compared with the maximal order $N = 6$ for Bravais lattices), these structures were expected to better approach the absolute isotropy than Bravais lattices.

Another interesting feature which originally was envisioned for these structures was the existence of omnidirectional photonic band gaps in two-dimensional photonic quasi-crystals with a low refractive index contrast, in the form ideally of photonic crystals consisting of air and silica (Zoorob 2000). Unfortunately, it was later demonstrated that this claim was unfounded (Zhao 2001).

The theoretical investigation of photonic quasi-crystals really began during the mid-nineties and was presented with the same difficulties than the study of solid quasi-crystals. The lack of periodicity of photonic quasi-crystals implies that calculation methods that were available in the reciprocal space (expansion of the field into a limited number of plane waves) can no longer be directly applied to these crystals. A possible method for overcoming this limitation consists in using a finite truncation of the infinite quasi-crystal and in periodically repeating this truncation. The properties of the periodic structure thus constructed, also referred to as ‘approximants’ can therefore be expected to approximate the properties of the original quasi-crystal. However, in the case of solid-state quasi-crystals, it has been demonstrated that the properties of approximants do not systematically converge, even if the size of the cells of the structure is increased.

An alternative method for approximating the properties of electromagnetic (EM) quasi-crystals relies on the simulation of the propagation of the EM wave in the real space, for instance by using finite difference in time domain (FDTD) methods (see Chapter 2). Here again, one has to deal with a finite structure, i.e., with the truncation of a quasi-crystal. In this respect, it may not be without interest to mention that prior to the proposal of the concept of a photonic crystal, metal patch antennas based on fractal or self-similar shapes had already been investigated independently by different authors. The interested reader is referred to (Baliarda 2000), where further references are also presented. It has thus been demonstrated that the specific EM properties of these antennas, like for instance their operation in several spectral bands or in a single extremely large band, are directly associated with the fractal nature of the patterns.

The two approaches outlined above have both been used by several research groups worldwide for investigating the optical properties of photonic quasi-crystals. An extensive series of simulation results have thus been reported for two-

dimensional photonic quasi-crystals with rotational symmetry of order $N = 8, 10$ and 12 (Chan 1998; Chelnokov 1999; Zoorob 2000). By performing calculations both in the real and in the reciprocal space, it was demonstrated that these structures possess almost perfectly isotropic band gaps. However, the prediction of band gaps at very low frequencies, as well as that of the possibility of achieving complete band gaps in structures with a low index contrast ($\Delta n \leq 1.5$) were invalidated.

The density of states of photonic quasi-crystals is still a much debated question. The first studies investigating this subject were conducted for the simplest type of photonic quasi-crystals, i.e. one-dimensional photonic quasi-crystals consisting of multilayer structures. Certain authors have reached the conclusion that the transmission spectra of a generalised Fibonacci multilayer structure exhibit a fractal behaviour (Dulea 1990; Zoll 1998). In other terms, the transmission bands consist of several transmission peaks densely distributed at the scale of the wavelength and separated by narrow reflection peaks. Under certain specific conditions, Fibonacci multilayer structures may also present stop-bands, whose existence is strongly dependent on the exact sequence of the layers. However, all the one-dimensional structures considered were of finite size and the calculations were performed only in a single dimension. As a consequence, the EM simulations provided precise information concerning only the propagation of light perpendicularly to the multilayers, and not the total density of radiative states in the structure. Indeed, it would have been necessary, in order to determine the total density of states, to consider all directions of the real space.

The situation of two-dimensional and three-dimensional photonic quasi-crystals is even more complex. Certain researches have revealed the existence of proper stop-bands in such structures (Zhang 2001), and these results are actually supported by the exponential dependence of the transmission on the thickness of the crystal. The reported stop-bands were bordered by relatively ‘smooth’ transmission bands. At the same time however, transmission spectra consisting of numerous individual peaks were reported by other studies. The discrepancy between these two series of results can be explained by drawing from similar researches devoted to solid-state quasi-crystals based on Penrose icosahedral lattices (Zijlstra 2000). The electronic density of states in these lattices was calculated with the ‘maximal possible precision’. It turned out that the spectral distribution of the density of states in two-dimensional tilings was not smooth, even if it was not possible to derive any conclusion regarding its fractal character. On the contrary, the spectral distribution of the density of states in three-dimensional quasi-periodic structures was found to be smooth and therefore did not exhibit any fractal feature. The authors also observed that, for three-dimensional structures, sharp peaks appear in the spectral distribution of the density of states when too small an approximant is chosen or when the precision of the calculations is insufficient.

As can be seen, the absence of a translational invariance in quasi-periodic structures results in a greater complexity in the calculations. Further, since each site in such a crystal is different, the properties of the interfaces of the defects or of the guiding structures tend to be dependent on the exact location of the defects or of the waveguides themselves.

The possibility however exists of resorting to the now well-established fact that the properties of quasi-periodic photonic systems with high index contrast, for instance structures consisting of air holes drilled inside a semiconductor matrix, can be reproduced almost exactly using specific strictly periodic structures. The Archimedean tilings that will be discussed in the next section are actually examples of such specific structures.

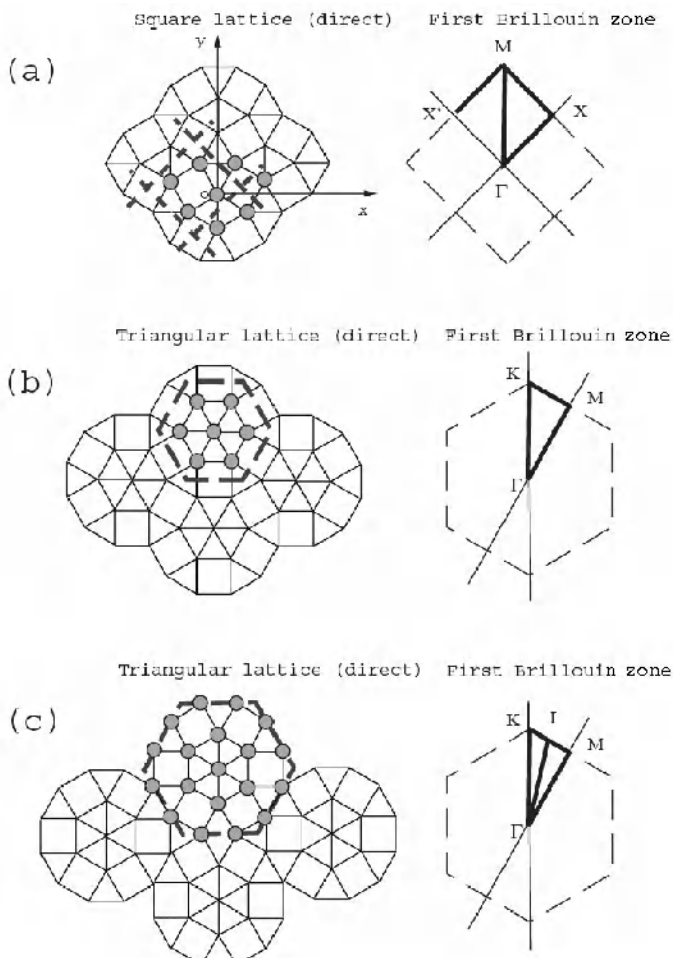


Fig. 3.2. *Left.* Semi-regular photonic crystals constructed from Archimedean tilings. *Right.* Brillouin zones associated with: *a.* a square lattice with a 4-atom unit cell, *b.* a triangular lattice with a 7-atom unit cell, *c.* a triangular lattice with a 13-atom unit cell. For each direct lattice represented on the left-hand part of the figure, the elementary cell is represented in thick dashed lines while the bonds connecting the ‘atoms’ are represented in thin solid lines. The thick lines in the reciprocal lattices (right) correspond to the directions used for the calculation of the band diagrams (Fig. 3.4)

3.2 Archimedean Tilings

Archimedean tilings are periodic two-dimensional structures exhibiting properties which have turned out to be quite similar to those of photonic quasi-crystals. These tilings are constructed from regular convex polygons of one or several types. The plane is tessellated by these polygons without any interval nor overlap between the polygons, so that all the vertices are strictly identical. The ‘atoms’ of the structure are located at these vertices. Eleven different Archimedean tilings exist, including the traditional Bravais lattice (Senechal 1995). The number of possible tilings can be increased by allowing certain specific arrangements of ‘atoms’ around some of the vertices of the lattice. The tilings thus defined are referred to as semi-regular or Archimedean-like tilings. Fig. 3.2 represents the three most elementary Archimedean-like tilings, where the arrangement of the polygons around one vertex differs from the arrangements around the other vertices.

Since these structures are strictly periodic, both an elementary cell and an associated Brillouin zone can be defined, opening the way to the possibility of applying the plane wave method to the study of the properties of these crystals. The structures displayed in Fig. 3.2b and 3.2c present a rotational symmetry of 12th order, while the structure represented in Fig. 3.2a closely ‘approaches’ the same order of symmetry. The symmetry of the structure is clearly revealed in the diffraction diagrams presented in Fig. 3.3.

In all these cases, the distance between an ‘atom’ and its nearest neighbours remains constant, while the number of nearest neighbours is the same either for all ‘atoms’ (Fig. 3.2a) or for all the atoms save one (Figs. 3.2b and 3.2c). As can be seen in Fig. 3.4, the isotropy of the structures is further vindicated by the results of the band diagram calculations. These results were obtained using the plane wave method under the assumption that the lattices consist of air cylinders ($n = 1$) extending in a semiconductor ($n = 3.5$) (David 2000, 2001). The existence of photonic band gaps which were found to be quasi-independent on the direction of propagation has also been confirmed by numerical simulations performed using the finite elements method.

The isotropy of Archimedean-like lattices improves when the number of ‘atoms’ contained in the elementary cells of the lattice increases, whereas the location and the width of the band gaps vary only slightly with the size of the cells. This actually results from the fact that the frequency of the main band gap does not depend on the size of the cells, but is imposed by the distance between two neighbouring ‘atoms’.

A most surprising result is that the structure with the smallest elementary cell, consisting of only four atoms, as represented in Fig. 3.2a, still exhibits properties very close to those of quasi-crystals, not only in terms of isotropy, but also as regards the position and width of the band gaps. In particular, this similitude can be observed in the case of crystals with a high index contrast, where the interaction between an EM wave and the ‘atoms’ of the lattice is therefore strong enough. The properties of the structure are therefore defined by the local order at a small scale, i.e. by the distance between the nearest neighbours and by the number of the near-

est neighbours for each atom. Let us here recall that in photonic crystals with a high refractive index contrast only a few lattice periods are necessary for obtaining stop-band reflectivity approaching 100 percent. The fact that the local order is the main factor determining the properties of these structures opens the way to the possibility of composite structures combining different types of lattices. These structures can be thought of as the photonic analogues of semiconductor heterostructures and superlattices.

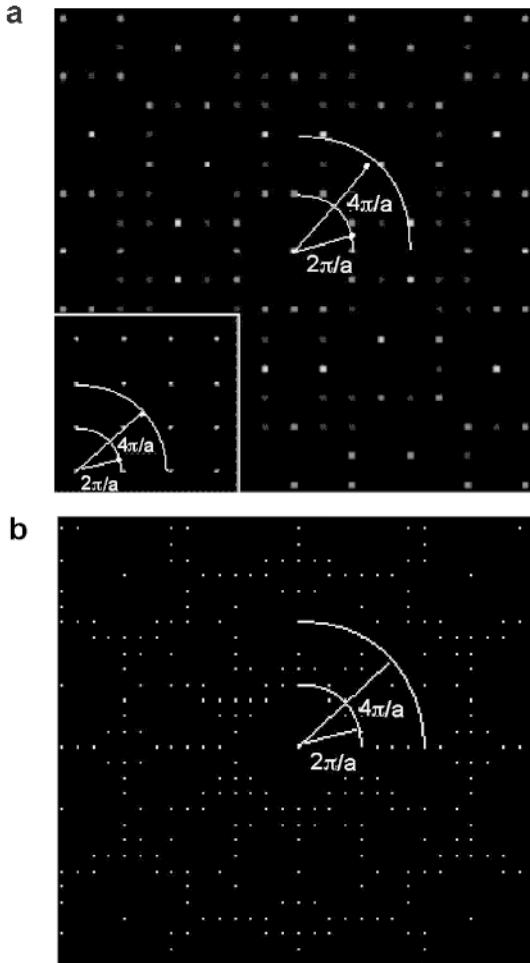


Fig. 3.3. Diffraction patterns calculated for the Archimedean tilings represented in Figs. 3.2a and 3.2b. The circles of radius $n\pi/a$, where n is an integer and a is the distance between a given atom and its nearest neighbours offer an insight in the relative isotropy of the two lattices

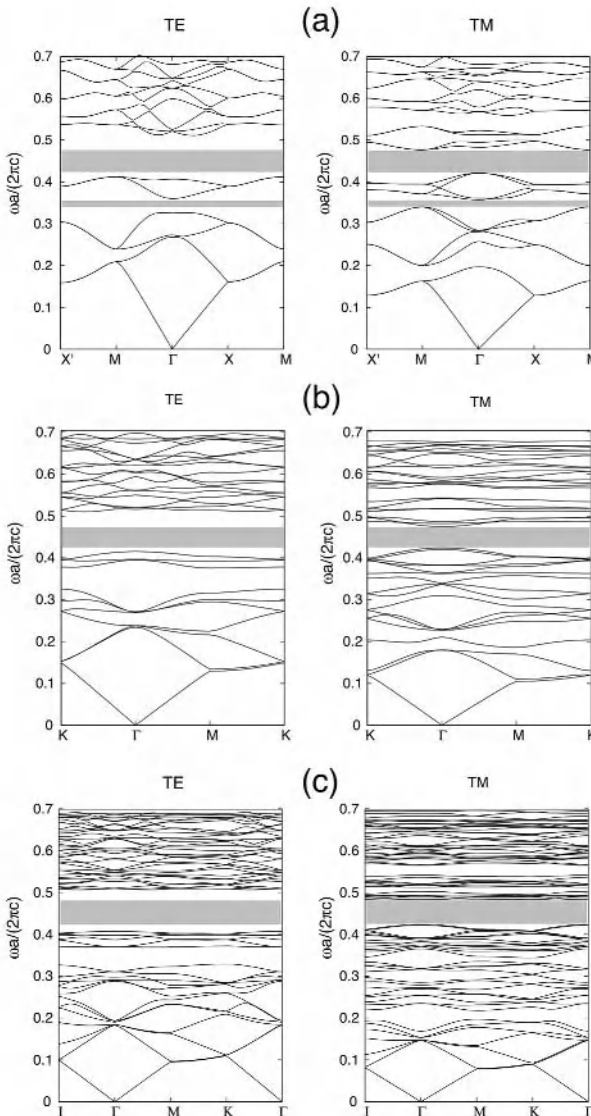


Fig. 3.4. Band diagrams calculated for the Archimedean-like tilings represented in Fig. 3.2. The calculations were performed for both TE and TM polarisations. *a*. Square lattice with a 4-atom unit cell *b*. Triangular lattice with a 7-atom unit cell *c*. Triangular lattice with a 13-atom unit cell. The photonic structures consist of periodic pores ($\epsilon = 1$) in a dielectric material with a high permittivity ($\epsilon = 12$). In all three cases, the air filling factor is equal to 75 %. The grey bands correspond to the complete two-dimensional band gaps

3.3 From Photonic Quasi-Crystals to the Localisation of Light

Extending the line of reasoning developed above on composite photonic crystals, the question may arise whether the spatial symmetry of the lattice is really a necessary requirement for forbidding the propagation of light and for ultimately controlling it.

The localisation of electromagnetic waves in a completely random diffusive medium was first predicted back in the 1980s (Anderson 1985; John 1984), and an experimental demonstration in the infrared wavelength range was first reported in 1997 (Wiersma 1997). A cloud is actually an example of such a random medium. The light emitted by the Sun propagates throughout the cloud by following a randomly ordered path, so that only a fraction of the light reaches the ground. The attenuation of light induced by the cloud can be defined as the ratio of the thickness of the cloud to the mean free path of the light wave, the mean free path being defined itself as the distance that the light wave needs to travel between two successive scatterers in the cloud. The light which is not transmitted across the cloud is reflected, with the consequence that the cloud seems to be white when observed in the direction of the Sun.

The situation changes dramatically when the diffusion of light becomes strong and when the mean free path reaches an order comparable to the wavelength. In this case, two different types of light localisation can be distinguished:

1. weak localisation, which cause the phenomenon of enhanced backscattering,
2. strong localisation, also referred to as Anderson localisation.

These two types of localisation can be produced either by a set of randomly distributed diffusing particles or by randomly rough surfaces, i.e. surfaces with randomly distributed corrugations. The roughness of such a surface can be described by using such statistical parameters as the average height of the corrugations or the average distance between two neighbouring corrugations. A review of the different studies devoted to this subject can be found in (Maystre 1991).

When an ensemble of particles is illuminated by a light beam, as is represented here in Fig. 3.5, the existence of a backscattering effect is revealed by the appearance of a peak in the angular distribution of the scattered field. This peak is directed along the direction opposite to the incident beam, as can be observed in Fig. 3.6. It can be experimentally observed and theoretically demonstrated that the amplitude of the peak can be twice as high as that of the pedestal.

An heuristic explanation of this phenomenon is presented in Fig. 3.5. Let us here consider an incident wave represented by two incident rays, appearing in the figure in the form of a dark grey line and of a light grey line respectively. In the first case (Fig. 3.5a), the dark grey ray is successively scattered by the particles 1, 2, 3 and 4 before emerging out of the randomly diffusing medium with a direction different from the direction of incidence. A second path, represented by the light grey line, is then associated to this first path. The ray corresponding to this path is

successively scattered by the same particles than the first one, but in the inverse order (4, 3, 2, and 1).

In the second case (Fig. 3.5b), the spatial distribution of the particles is the same, but the direction of propagation of the rays emerging from the medium is now directly opposed to the direction of the incident rays. The two incident rays are part of the same beam and are therefore in phase. Since the dark grey and light grey rays follow the same paths but along opposite directions, the principle of reciprocity entails in this case that the emerging backscattered rays will also be in phase. This case thus turns out to be quite different from the situation depicted in Fig. 3.5a, where the phase was not conserved. The rays propagating along the backscattering direction can be grouped into couples consisting of two perfectly coherent rays. This is not the case for any other direction, and the rays propagating along these directions are perfectly incoherent. A peak corresponding to the direction of the backscattered light can therefore be expected to appear in the angular distribution of the scattered light.

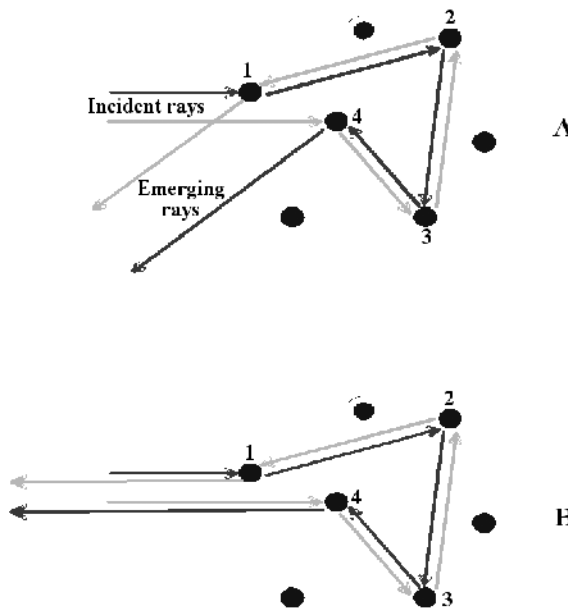


Fig. 3.5. Scattering of light by an ensemble of particles **a.** rays emerging along any arbitrary direction with respect to that of the incident light are not in phase **b.** rays emerging along the direction opposite to that of the incident rays are in phase (backscattering phenomenon)

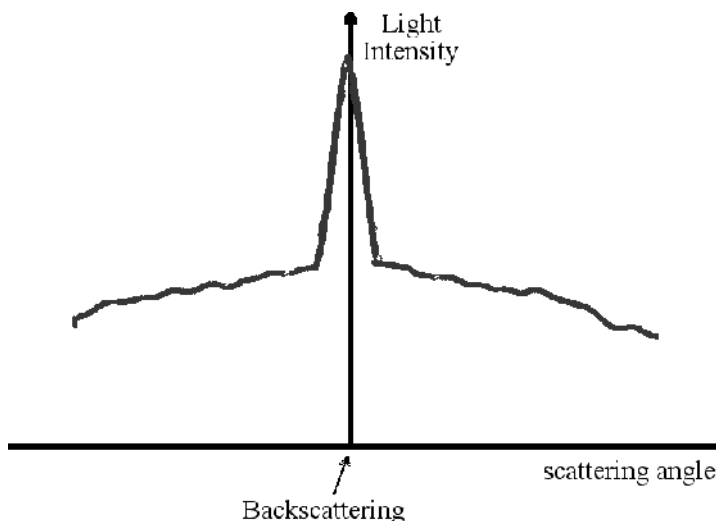


Fig. 3.6. Peak associated with an enhanced backscattering effect

The same type of intuitive explanation can be provided for the situation created when a light beam is incident onto a randomly rough surface. Experimental and numerical illustration of the phenomenon can be found in (Greffet 1991; Kim 1990; Maradudin 1990; Maystre 1994b; O'Donnell 1987; Soto-Crespo 1989). It might be noted that phenomena of enhanced backscattering of light can be observed in everyday life, for instance in when an airplane flies over a cloud layer. In this case, a passenger looking outside the window will not only see the shadow projected by the plane onto the cloud layer, but also a luminous halo extending around this shadow. The appearance of this halo, also known as a 'glory', results from the fact that, in such an optical configuration the eyes of the passenger receive the light which has been backscattered by the cloud.

The phenomenon of strong localisation of light presents itself in the very different form. When particles form a very dense random structure, the effects induced by the interferences become extremely strong and the propagation is made almost impossible. Let d be the thickness of the layer where the diffusive particles are contained. In the strong localisation case, the amplitude of the field decreases exponentially with d (in $e^{-\alpha d}$), which contrasts with the case previously considered of a weakly diffusing medium where the decrease of the field followed a $1/d^2$ dependence.

These mathematical laws are actually of a statistical nature. In other terms, these evolutions are measured only over statistical averages of the fields, by considering multiple successive realisations with the same statistical characteristics of a given set of particles. The term realisation used here denotes any arrangement of a set of N particles randomly distributed inside a given volume. The notion of a realisation can be explained by considering for instance an instantaneous arrangement of micrometer-sized latex spheres agitated inside a liquid. After a time sufficiently long, the spheres will present a completely different arrangement, although the statistical parameters remain the same. This second arrangement is said to represent a different realisation of the same system.

In practice, when considering the instantaneous field for a given realisation, i.e. for a particular observation, a very strong inhomogeneity in the distribution of the field can be observed. The electromagnetic field is granular, with very bright regions separated by dark regions. These localised modes can be interpreted in terms of resonant modes, quite in the same way as if they were inside a resonant cavity. The theory of Anderson localisation for photons is quite complex and resorts to specialised mathematical theorems associated with stochastic processes. We shall not describe this theory here.

However, it might be noted here that a slightly perturbed photonic crystal creates conditions which are particularly favourable to the strong localisation of light at frequencies close to the edge of the band gap (Felbacq 1995). Such a perturbation can be achieved for instance through a random displacement of each ‘atom’ of the crystal. This is not actually surprising in view of the preceding considerations. Let us here consider a photonic crystal illuminated by an electromagnetic wave at a wavelength located in the band gap, but near its edge. If all the ‘atoms’ of the crystal are randomly displaced, for instance by translating the ‘atoms’ over the same distance, but along random arbitrary directions, it is quite plain that the average distance between atoms will be reduced in certain regions of the crystal while increasing in other regions. The band edges of certain regions of the photonic crystal will therefore shift outside the band gap of the original crystal, so that these regions will become transparency regions where the field can propagate. These regions are surrounded with ‘reflecting’ areas where the propagation is forbidden and where the amplitude of the field decreases exponentially. To some extent, the perturbation induced can be seen as creating a series of microcavities embedded in the original photonic crystal. If the resonance wavelength of one of these microcavities lies within the band gap, the electromagnetic field shall resonate in the cavity and form a localised mode with a low amount of loss. The difficulty for the light to propagate between two such ‘light grains’ explains that statistically the field may exponentially decrease in such a random medium with a strong localisation.

A different example of a material allowing the strong localisation of light is that of a more or less monodisperse semiconductor powder, i.e. a perfectly disordered material (Wiersma 1997). However, even if the propagation of light can be totally forbidden in such materials, the corresponding band gaps do not present any clearly defined edge as was the case with photonic crystals.

As previously mentioned, strong localisation phenomena may sometimes occur over randomly rough surfaces. For instance, in the visible wavelengths range, the propagation of a plasmon wave along a rough metallic surface may result in the formation of high-intensity regions separated by dark regions. These bright regions are sometimes referred to as ‘localitons’, from the contraction of the terms ‘localisation’ and ‘plasmons’ (Maystre 1994b).

By way of conclusion, the interaction of light with a medium containing scattering centres may lead to a variety of different situations, ranging from the ‘ideal’ photonic crystals or the photonic quasi-crystals to randomly disordered media where light can be localised and to structures intermediary between periodic and random structures. Drawing a clear boundary between these different configurations is not necessarily simple. For instance, at what point does a photonic crystal turn into a randomly diffusing structure when submitted to increasingly strong perturbations? Likewise, to which extent do electromagnetic quasi-crystals, which are a combination of square and triangular lattices, differ from more ‘traditional’ photonic crystals? These are but two of the questions that these issues raise.

Part II

Optical Properties of Photonic Crystals

4 Specific Features of Metallic Structures

In the preceding chapters, photonic crystals have been essentially considered as (quasi) periodic ensembles of dielectric elements, allowing the control of the propagation of light through the effects of photonic band gaps and transmission bands. It might be pointed out that the first periodic (1, 2 and 3D) ensembles of materials were historically fabricated from metals rather than from dielectrics (Harvey 1963; Marconi 1919). The use of periodic metallic grids for filtering radiofrequency waves with different polarisations can be traced back to the beginnings of the 20th century (Marconi 1919). The idea that any dielectric function could be artificially ‘realised’ from metals, led to the concept of ‘artificial dielectrics’ developed in the 1950s (Harvey 1959, 1963). In either case, these periodic filters and artificial dielectrics were fundamentally photonic crystals, with the provision that realisations at this time were restricted, as regards their applications, to wavelengths much larger than wavelengths in the optical region. This reveals the possibility of extending, in a natural way, the concept of a photonic crystal to metallic as well as to metallocodielectric periodic structures.

This being, standard metals present electromagnetic properties which are fundamentally different from those of dielectrics, and the first part of this chapter will be devoted to reviewing the effects associated with free-charge carriers in metals. We shall then successively consider different types of periodic structures, depending on whether they are adapted to long wavelengths (ranging from microwaves to the far infrared region) or to short wavelengths (extending from the infrared to the visible regions). Finally, we shall discuss the specific effects induced by surface waves for all metallic structures.

4.1 Bulk Metals: Drude Model, Skin Effect and Metallic Losses

In the case of metallic media, Maxwell equations contain an additional term associated to the current density: $\mathbf{j} = \sigma\mathbf{E}$. In the harmonic regime, these equations can be written as follows:

$$\nabla \times \mathbf{E} - i\omega\mu\mathbf{H} = 0 \quad (1.2b)$$

$$\nabla \times \mathbf{H} + i\omega\epsilon\mathbf{E} - \mathbf{j} = \nabla \times \mathbf{H} + i\omega \left(\epsilon + i\frac{\sigma}{\omega} \right) \mathbf{E} = 0 \quad (1.3b)$$

In what follows, we shall confine ourselves to the consideration of non-magnetic metals¹, where $\mu = \mu_0$. Under this condition, Eq. 1.2b turns out to be identical with Eq. 1.2. Further, Eq. 1.3b can be rewritten in the form of Eq. 1.3 if an effective dielectric permittivity $\tilde{\epsilon}$ is introduced in order to account for the free-charge carrier effects associated with the conductivity term σ :

$$\tilde{\epsilon} = \epsilon + i\frac{\sigma}{\omega} \quad (4.1)$$

Let us recall that the ‘true’ dielectric constant ϵ accounts for dipolar interactions involving bound electrons contained inside the metal. These interactions can often be neglected at low frequencies, when $\epsilon \approx \epsilon_0$. Further, the condition of a local electric neutrality of the metal² imposes that:

$$\nabla \cdot (\tilde{\epsilon} \mathbf{E}) = 0 \quad (1.4b)$$

In the case of homogeneous metals, $\tilde{\epsilon}$ is constant and independent of the direction in space, whence it follows that $\nabla \cdot \mathbf{E} = 0$. Using Eq. 1.4b, the combination of Eqs. 1.2 and 1.3b then leads to the familiar Helmholtz equation:

$$\nabla^2 \mathbf{E} + \frac{\omega^2}{c^2} \tilde{\epsilon}_r \mathbf{E} = 0 \quad (4.2)$$

where:

$$\tilde{\epsilon}_r = \tilde{\epsilon}/\epsilon_0$$

In an homogeneous metal, the simplest solution for this equation is here again a plane wave. However, contrary to the case of the dielectric media which were previously considered, a complex wave number is now associated with the wave:

¹ The incorporation of magnetic materials inside photonic crystals of finite size opens the possibility of exploiting certain non-reciprocal effects in the propagation of light. More detailed information on this subject can be found in the different studies which have been devoted to some of these effects (Chul-Sick 2000; Figotin 2001; Inoue 1997; Nishizawa 1997; Sigalas 1997a).

² The electric neutrality can be locally perturbed as a result of local modifications of the charge density. However, the recovery time for metals is typically of the order of 10^{-18} s.

$$\mathbf{E} = \mathbf{E}_0 \exp i(\mathbf{k} \cdot \mathbf{r} - \omega t)$$

where:

$$k^2 = \frac{\omega^2}{c^2} \tilde{\epsilon}_r \quad (4.3)$$

4.1.1 Drude Model

The conductivity of the metal is in general dependent on the frequency. This dependence can be satisfactorily approximated by using the Drude model (Born 1965; Drude 1890). In this model, the motion of a single electron in a metal submitted to an electric field is assumed to be resulting from two opposite forces: the force $e\mathbf{E}$ associated with the electric field itself and a damping force $-v/\tau$ associated with the collisions occurring between the electron and the atoms of the metallic lattice. The damping time τ is typically of the order of 10^{-14} s. The equation for the motion of the electron thus assumes the following form:

$$m \frac{d\mathbf{v}}{dt} + m \frac{\mathbf{v}}{\tau} = -e\mathbf{E} \quad (4.4)$$

where m and e are the mass and the charge of the electron respectively. Denoting by N the electron density in the metal, the instantaneous current density can be expressed in the form: $\mathbf{j} = -Nev$. In the harmonic regime, Eq. 4.4 thus leads to the following relations:

$$\mathbf{j}(\omega) = \sigma(\omega)\mathbf{E}_0 = \frac{Ne^2}{m(1/\tau - i\omega)} \mathbf{E}_0 = \frac{Ne^2(1/\tau + i\omega)}{m(1/\tau + \omega^2)} \mathbf{E}_0 \quad (4.5)$$

Using the expression for the conductivity $\sigma(\omega)$ given in Eq. 4.1 with $\epsilon \approx \epsilon_0$, the following equation yields the effective dielectric permittivity of the metal:

$$\tilde{\epsilon} = \epsilon_0 \left[1 - \frac{\omega_p^2(1 - i/\omega\tau)}{(1/\tau^2 + \omega^2)} \right] \quad (4.6)$$

where ω_p represents the plasma frequency of the electron gas, as given by the equation:

$$\omega_p^2 = \frac{Ne^2}{m\epsilon_0} \quad (4.7)$$

It can be readily verified that the plasma frequency ω_p lies in the ultraviolet region for typical electron densities between 10^{22} and 10^{23} cm^{-3} . As an example, the photon energy corresponding to ω_p is approximately equal to 15 eV for aluminum and to 3.8 eV ($\lambda \sim 328 \text{ nm}$) for silver. A consequence is that the inequality $\omega_p \gg 1/\tau$ is generally satisfied in most cases. By contrast, different situations need to be considered depending on the frequency region under consideration.

4.1.2 Low-Frequency Region: Skin Effect and Metallic Losses

In the low-frequency region, which extends from radiofrequencies to the far infrared region, the following relations hold true: $\omega_p \gg 1/\tau \gg \omega$. In such a case, the conductivity and permittivity of the metal expressed by Eqs. 4.5 and 4.6 respectively can be approximated as follows:

$$\sigma \approx \frac{Ne^2\tau}{m} = \epsilon_0 \omega_p^2 \tau \quad (4.8)$$

$$\tilde{\epsilon} \approx \epsilon_0 \left[1 + i \frac{\omega_p^2 \tau}{\omega} \right] \approx i \frac{\epsilon_0 \omega_p^2 \tau}{\omega} \quad (4.9)$$

The permittivity of the metal is associated with a purely imaginary number, while its conductivity is associated with a real number. In the case of a plane wave with frequency ω propagating within the medium, the corresponding wave number deduced from Eq. 4.3 is thus a complex number k given by the equation:

$$k \approx \frac{1+i}{c} \sqrt{\frac{\sigma\omega}{2\epsilon_0}} = (1+i) \sqrt{\frac{\sigma\omega\mu_0}{2}} \quad (4.10)$$

The imaginary part of k corresponds to the attenuation that the wave undergoes in the metal. More precisely, an electromagnetic wave penetrating inside the metal will be attenuated by a factor equal to $1/e$ over the distance $\delta = \sqrt{2/\sigma\omega\mu_0}$, referred to as the skin depth of the metal. The higher the frequency, the higher is the conductivity, and correlatively the smaller is the skin depth. For instance, at the 10GHz frequency, the skin depth of a copper conductor ($\sigma \sim 5 \times 10^7 \Omega^{-1}\text{m}^{-1}$) is lower than 1 μm . In other words, the electromagnetic energy tends to be expelled out of the metallic conductor and to be reflected by it. In the case of a wave impinging upon a metallic surface, the intensity reflection coefficient is given by the following equation (Born 1965):

$$R = \left| \frac{\tilde{n} - 1}{\tilde{n} + 1} \right|^2 \quad (4.11)$$

where:

$$\tilde{n} = \sqrt{\tilde{\epsilon}/\epsilon_0} \approx (1 + i)\sqrt{\sigma/2\epsilon_0\omega}$$

Since the amplitude of \tilde{n} is much larger than unity, the reflection coefficient is close to 100 percent. The lower the frequency, the closer to unity the reflection coefficient R is. As a consequence, in the low-frequency region ranging from radiofrequency waves to the infrared, the amount of metallic losses is very low, and metals thus tend to behave like perfect reflectors.

4.1.3 From the Infrared to the Visible and UV Regions

In the optical region of high frequencies ranging from the near-infrared to the visible and near UV, the parameters ω_p , $1/\tau$ and ω are ordered in a different manner, so that the following relations typically hold true: $\omega_p \sim \omega > 1/\tau$. By assuming arbitrarily that $\epsilon \approx \epsilon_0$, the effective dielectric permittivity of the metal expressed by Eq. 4.6 can be approximated as follows:

$$\tilde{\epsilon} = \epsilon_0 \left[1 - \frac{\omega_p^2}{\omega^2} + i \frac{\omega_p^2}{\omega^3 \tau} \right] \quad (4.12)$$

The real part in the right-hand side of Eq. 4.12, which is often referred to as the ‘Drude dielectric function’, clearly evidences the role of the plasma resonance in bulk metals. From this point, two different situations need to be separately considered.

In the infrared and visible regions, the optical frequency is usually significantly lower than the plasma frequency. Since the $-(\omega_p / \omega)^2$ term is predominant in the right-hand side of Eq. 4.12, the permittivity of the metal is associated with a negative real number with a large modulus compared to unity. Correspondingly, the refractive index $\tilde{n} = \sqrt{\tilde{\epsilon}/\epsilon_0}$ will be associated with a purely imaginary number of large amplitude. In other terms, metals remain good reflectors in these regions.

In the deep ultraviolet region, the optical frequency reaches at last a larger order than the plasma frequency, and therefore $\omega > \omega_p > 1/\tau$. Accordingly, the permittivity of the metal will be represented by a real positive number smaller than unity. The metal thus tends to behave as a weakly absorbing dielectric and exhibit a permittivity smaller than the permittivity of vacuum. Actually, a metal may also exhibit in this frequency region optical resonances associated with bound electrons, and in general its optical response cannot be described simply as the optical response of a free electron gas.

4.2 Periodic Metallic Structures at Low Frequencies

The radiofrequency and microwave regions remain privileged areas for metals since, as has been described in Section 4.1.2, perfectly conductive materials are also perfect reflectors. It is therefore in this region that the interest for metallic photonic crystals is the highest, and where most studies concerned with their applications are being conducted. The EM properties of periodic metallic structures can be determined with some one of the numerical codes developed for dielectric structures and presented in Chapters 1 and 2, with the provision however that the most adequate formula should be used for the dielectric permittivity (see Section 4.1). To this end, an even more precise solution consists in using the numerical or analytical values which can be found in reference textbooks. It is not entirely surprising that the concept of photonic band gap might still apply to the case of periodic metallic structures. However, as will be described here, the behaviour of periodic metallic structure may be significantly different from that of periodic dielectric structures.

4.2.1 Plasmon-Like Photonic Band Gap

One of the most important features of metallic photonic crystals results from the existence of a photonic band gap which extends from the zero-frequency. In direct analogy with the plasma resonance which can be observed for bulk metals at optical frequencies and which has been described in Sections 4.1.1 and 4.1.2, the latter is generally referred to as a plasmon photonic band gap. This analogy was first suggested by J. Pendry in the specific case of photonic crystals consisting of metallic wires with a very small diameter compared to both the period of the crystal and the wavelength (Pendry 1996, 1998). The argument developed in general terms by J. Pendry will be briefly exposed here. It might be mentioned here that rigorous demonstrations have been developed at the same time by D. Felbacq *et al* on the basis of electromagnetic studies where the wires were assumed to be perfectly conductive (Felbacq 1994a, 1994b, 1997).

Let us here consider briefly a two-dimensional lattice of metallic wires assumed to be parallel to the z -axis and with an infinite length, as is represented in Fig. 4.1. For the sake of simplicity, the lattice of Fig. 4.1 has been chosen with a square symmetry. This choice however is of no consequence on the demonstration. An incident wave may efficiently interact with the crystal and thus induce an elementary current I in each wire, provided that this incident wave is TM polarised, i.e. when the electric field E is parallel to Oz . As a consequence, the magnetic field radiated by a single wire extends within the Oxy plane. At a distance r from the origin much smaller than the wavelength, the magnetic field can be represented by the Henkel function $H_1^{(1)}(k_0 r)$, solution to the Helmholtz equation, which exhibits the same asymptotical behaviour as the function $1/r$ (Abramowitz 1970). The amplitude of the magnetic field can thus be expressed in the form:

$$H(r) = \frac{I}{2\pi r} = \frac{\pi r_c^2 N e v}{2\pi r} \quad (4.13)$$

where I is dependent on the electron charge density N in the wire, on the velocity of the charges v and on the cross-section πr_c^2 of the conducting wire. On the other hand, the vector potential \mathbf{A} can be introduced according to its standard definition:

$$\mathbf{H}(\mathbf{r}) = \mu_0^{-1} \nabla \times \mathbf{A} \quad (4.14)$$

Although the formulation presented above is not in general univocal, the ambiguity can be lifted in the present case owing to the periodicity of the structure. It can readily be verified that \mathbf{A} is parallel to the z -axis. In the case of a square lattice, it can be further demonstrated that its amplitude is satisfactorily approximated by the following formula (Pendry 1998):

$$A(r) = \frac{\mu_0 \pi r_c^2 N e v}{2\pi} \ln(a/r) \quad (4.15)$$

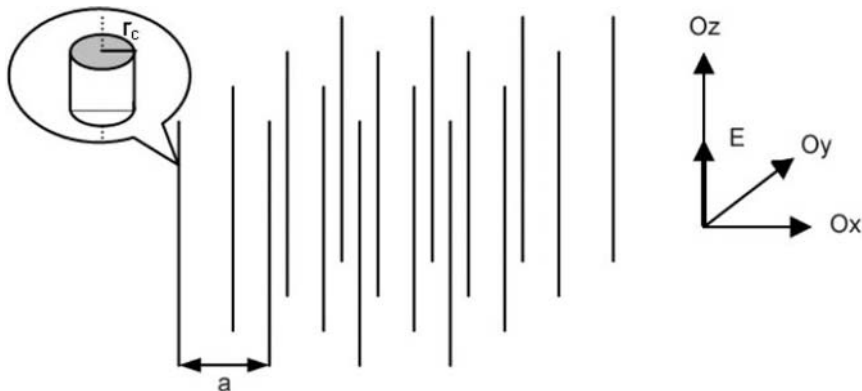


Fig. 1.1 Square array of very thin metallic wires ($r_c \ll a$) parallel to Oz . At low frequencies, the electromagnetic properties of such an array are similar to those of a bulk metal around the plasma resonance

It is known from quantum mechanics that the presence of a magnetic field results in an additional contribution $e\mathbf{A}$ to the velocity of the electron charges. In the present case, this contribution is even predominant when compared to the mv term, which leads to the possibility of introducing an effective electron mass m_{eff} . This effective mass can then be approximated by the equation $m_{\text{eff}}v \approx eA$. In order actually to demonstrate the analogy existing between an array of wires and a bulk metal, one needs now to average the carrier density and the effective mass over the entire space, i.e. to proceed to an homogenisation of the medium. The homogenisation thus performed leads to the following equations for N_{eff} and m_{eff} respectively (Pendry 1996, 1998):

$$N_{\text{eff}} = N \frac{\pi r_c^2}{a^2} \quad (4.16a)$$

$$m_{\text{eff}} = \frac{\mu_0 \pi r_c^2 N e^2}{2\pi} \ln(a/2r_c) \quad (4.16b)$$

Using Eqs. 4.16a and 4.16b into Eq. 4.7 leads to the definition of a plasma frequency below which the homogenised medium totally reflects external waves:

$$\omega_{p,\text{eff}}^2 = \frac{2\pi c^2}{a^2 \ln(a/2r_c)} \quad (4.17)$$

It is apparent from Eq. 4.17 that, contrary to what was the case for bulk metals, the plasma frequency depends on the structural parameters of a lattice and not on some intrinsic parameters of the material. For lattices with a millimeter period and wires with a diameter of a few microns, the plasma frequency typically lies in the domain of gigahertz frequencies. This demonstrates that a ‘pseudo-metal’ where the cutoff plasma frequency can be *a priori* controlled has been actually achieved.

The previously mentioned studies which had been directed at the homogenisation of metallic photonic crystals (Felbacq 1994a, 1994b, 1997; Guida 1998) also permitted to vindicate in a more precise and accurate way the theoretical approach first suggested by J. Pendry. Indeed, at low frequencies, the asymptotic behaviour of a photonic crystal consisting of continuous metallic elements is the same than the behaviour of a lossless (i.e. such that ϵ is a real number) homogeneous dielectric medium exhibiting a plasma resonance. In particular, Eq. 4.17 remains a satisfactory approximation, even in the case where the diameter of the wire is relatively large when compared to the period of the lattice (Guida 1998). Actually, the fact that photonic crystals consisting of continuous metallic elements present in all cases a low-frequency cutoff is far from being surprising. Indeed, it might be enough here to be reminded of the fact that, contrary to a dielectric waveguide, a hollow waveguide with metallic walls does also present such a low-frequency cutoff.

4.2.2 Transmission Spectra of Metallic and Dielectric Photonic Crystals

The differences between the behaviours of metallic and dielectric photonic crystals can be illustrated through the consideration of their calculated and measured transmission spectra. Fig. 4.2 thus displays a comparison between the transmission spectra of two-dimensional lattices with a similar geometry: the upper part of the figure corresponds to the dielectric case while the lower part corresponds to the metallic case. In either case, the lattice presents a square symmetry and is composed of rods extending in the air, while the incident wave is TM polarised. The dielectric lattice consists of eleven rows of 18 alumina rods ($\epsilon \sim 9$) with a diameter $d = 1.5\text{mm}$ and a length $L = 100\text{mm}$. The period a of the lattice is equal to 3 mm. The metallic lattice consists of seven rows of 18 copper rods with the same diameter ($d = 1.5\text{mm}$) but with a length L equal to 50mm. The period a of the lattice is in this case equal to 6 mm. For the sake of calculations, the metal will be assumed to be perfectly conductive. The calculated spectra, represented by black curves, were obtained using a FDTD model (see Chapter 2) where the rods were assumed to be of an infinite length. The measured spectra, represented by grey curves were obtained using a microwave network analyser.

As has been described already in Chapter 1, dielectric photonic crystals always present a transmission band at low frequencies (upper part in Fig. 4.2). The first band gap is associated with the Bragg condition $\lambda/2 \sim a$, where λ represents the wavelength in the crystal. In other words, the centre frequency of the band gap is approximately given by the equation $v \sim c/2n_{\text{eff}} a$, where $n_{\text{eff}} = \sqrt{\epsilon_{\text{eff}}}$ is the effective refractive index at low frequencies, $\epsilon_{\text{eff}} = (1 - f) + f\epsilon$ is the averaged dielectric permittivity and f is the filling factor of the dielectric. In the present case, where $f \approx 0.2$, the value for the centre frequency as determined from the formula above is equal to 31.5 GHz, which is consistent with the experimentally measured value and with the value deduced from the numerical FDTD model. Beyond the first photonic band gap, the transmission spectrum presents a succession of transmission bands and band gaps with a progressive decrease of their respective contrasts.

As can be seen from the observation of the lower figure, the spectrum of the metallic photonic crystal presents the same alternation of transmission bands and band gaps with the same progressive decrease of the transmission contrast. However, the low-frequency region of the spectrum exhibits a fundamentally different aspect: indeed, from the zero-frequency, a strong attenuation of the crystal, associated with the plasmon-like photonic band can be observed in this region. The cut-off frequency numerically calculated from the FDTD model (~ 22 GHz) is close to the value estimated on the basis of the approximate formula given in Eq. 4.17 (~ 16.5 GHz). The plasmon photonic band gap is then followed by a first transmission band whose centre frequency (~ 27 GHz) corresponds to $\lambda/2 \sim a$. The situation thus turns out to be reversed compared to the case of dielectric photonic crystals where the same exact relation corresponded to the first band gap. In the first transmission window, the metallic photonic crystal behaves as an ensemble of Fabry-Perot cavities that would be coupled to one another along the propagation

direction. In the case under consideration, there are six cavities, corresponding to the seven rows of metallic rods, and six resonance peaks can indeed be observed in the transmission spectrum. As an aside, the excellent agreement between experimental measurements and the numerical values calculated the FDTD model can be noted: the shift in amplitude arises simply from the fact that the measurement system is limited in this case to transmission amplitudes higher than -45 dB.

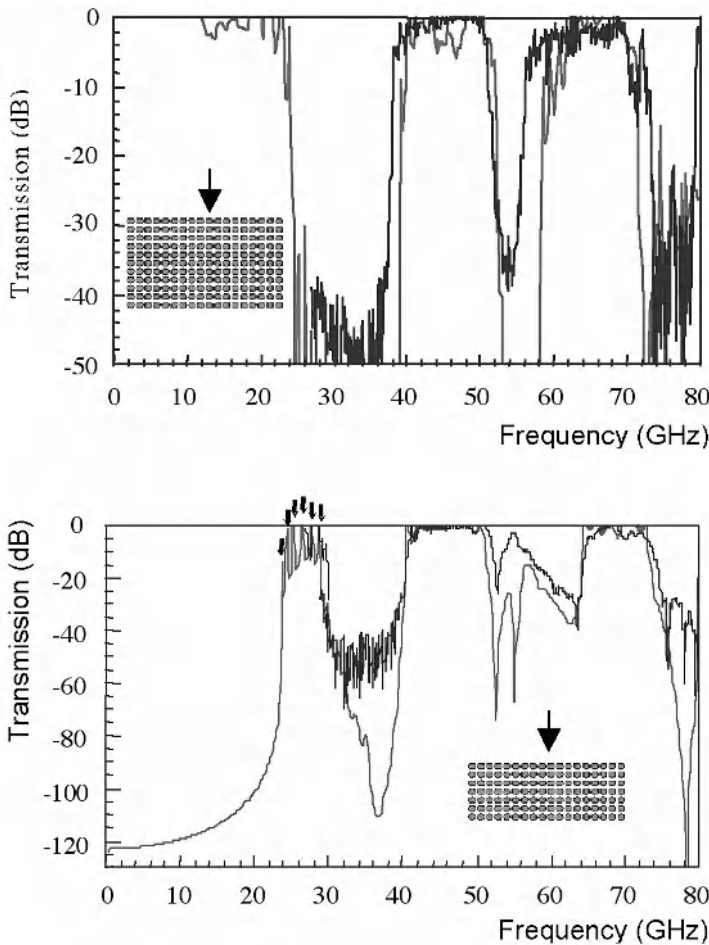


Fig. 4.2. Transmission spectra of square lattices of rods extending in the air for a normal incidence in TM polarisation. The black curves correspond to the calculated spectra, while the grey curves correspond to experimental measurements. *Top.* Dielectric lattice consisting of eleven rows of 18 alumina rods ($\epsilon \sim 9$) with a diameter $d = 1.5$ mm and a length $L = 100$ mm. The period a of the lattice is $a = 3$ mm. *Bottom.* Metallic lattice consisting of seven rows of 18 copper rods with a diameter $d = 1.5$ mm and a length $L = 50$ mm. The period a of the lattice is equal to 6 mm (Gadot 1998)

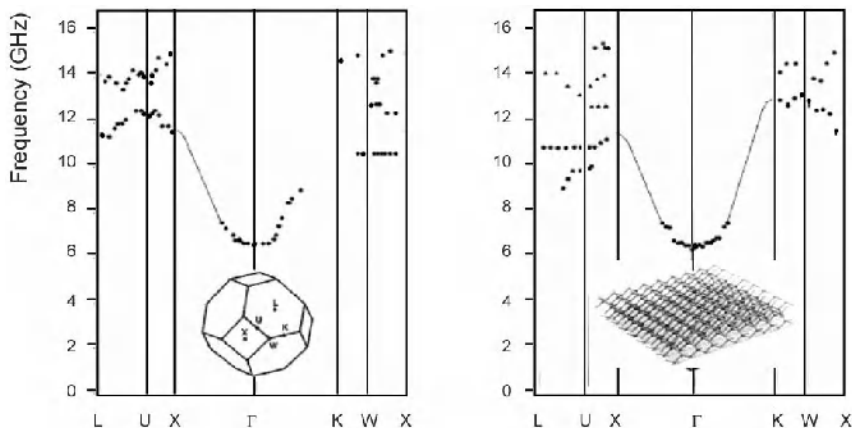


Fig. 4.3. Band diagram of a lattice of connected metallic wires arranged into a diamond structure. Each wire has a one-centimeter length, corresponding to the distance between atoms inside the simulated diamond crystal (Sievenpiper 1996). *Left*. Measured diagram for an *s*-polarised wave incident onto a $<100>$ crystal plane. *Right*. Measured diagram for a *p*-polarised wave incident onto the same crystal plane. The insert in the left-hand figure represents the Brillouin zone of the diamond crystal, while the insert in the right-hand figure represents a partial view of the metallic structure

4.2.3 Complete Band Gaps in Metallic Photonic Crystals

As has been previously emphasized in Section 1.3.3, two-dimensional lattices of disconnected rods exhibit much smaller band gaps in TE polarisation than in TM polarisation. This behaviour can be verified for lattices of dielectric rods as well as for lattices of metallic rods. The difference between the two polarisations is even more marked in the latter case: indeed, while the transmission spectrum in TE polarisation exhibits only limited amplitude variations, a very strong attenuation can be observed in TM polarisation, at least for the first band gaps, as can be seen from the consideration of the lower part of Fig. 4.2. As a result of the strong TM efficiency of two-dimensional lattices formed by metallic rods or wires, a complete photonic band gap can be easily achieved for all propagation directions and all polarisations using a simple cubic lattice formed by metallic rods or wires. A cubic lattice may indeed be viewed as the superposition of three two-dimensional square lattices whose rods (or wires) are aligned with the along the three directions Ox , Oy and Oz respectively. Each of these lattices then presents a plasmon-like band gap for a certain polarisation of the field and for the propagation directions normal to the rows of rods or of wires. When a wave is propagating along a

different direction from the three main directions, several two-dimensional lattices will simultaneously interact with this wave, but a band gap extending from the zero-frequency will nevertheless remain present in all cases. Therefore, the possibility of achieving a complete photonic band gap does not require a metallic structure as elaborate as the ‘yablonovite’. This being, the diamond-like cubic structure with two ‘atoms’ per unit cell have also been reproduced from a lattice of interconnected metallic wires, where the ‘atoms’ were simulated in the diamond structures by the intersections of the wires (Sievenpiper 1996). A complete plasmon-like photonic band gap was thus demonstrated experimentally before being vindicated by a theoretical modelling (Fig. 4.3). The detailed study of this structure also revealed the existence of longitudinal electromagnetic modes.

4.2.4 Structures with Continuous Metallic Elements and Structures with Discontinuous Metallic Elements

Thus far, metallic photonic crystals have always been assumed to consist of continuous metallic rods or wires. However, it is self-evident that the theoretical approach to the plasmon-like band gap presented in Section 4.2.1 is no longer founded as soon as the continuous wires are replaced by discontinuous wires. In the very low frequency region where metallic elements can be considered as localised elements, the introduction of discontinuities between these elements amounts to inducing capacitive effects which combine to the self-inductances induced by the circulating currents. This results in the generation of an impedance of the type $(LC\omega^2 - 1)/C\omega$ instead of the inductive short-circuits $L\omega$ that existed for continuous wires (Bridges 1970; Ulrich 1963, 1967). As a consequence, the metallic photonic crystal will exhibit a transmission band instead of a band gap as is the case at very low frequencies. A general and more detailed explanation will be developed along these lines in Section 4.4.6, where the subject of surface waves will be addressed in more detail. This explanation will allow one to understand why photonic crystals formed by discontinuous metallic wires are actually closer to dielectric photonic crystals than to the purely metallic photonic crystals which were previously considered.

Fig. 4.4 allows a more precise comparison between the transmission spectra of a two-dimensional lattice of continuous metallic rods (upper part of the figure) and of a two-dimensional lattice of discontinuous metallic rods (lower part of the figure) respectively. The parameters are the same as those that were used in the lower part of Fig. 4.2: thus, the lattice has a square symmetry and a period equal to 6 mm, while the diameter d of the rods is equal to 1.5 mm. In the case of seven rows of continuous rods, represented by the dashed curves in the upper part of Fig. 4.4, the same transmission spectrum as in Fig. 4.2 can be observed. For a smaller number of continuous rows ($n = 2$), represented by the solid curves in the upper part of Fig. 4.4, the band gaps are less marked, but the transmission within the ‘plasmon photonic band gap’ falls down to -50 dB while this band extends to frequencies approaching 20 GHz.

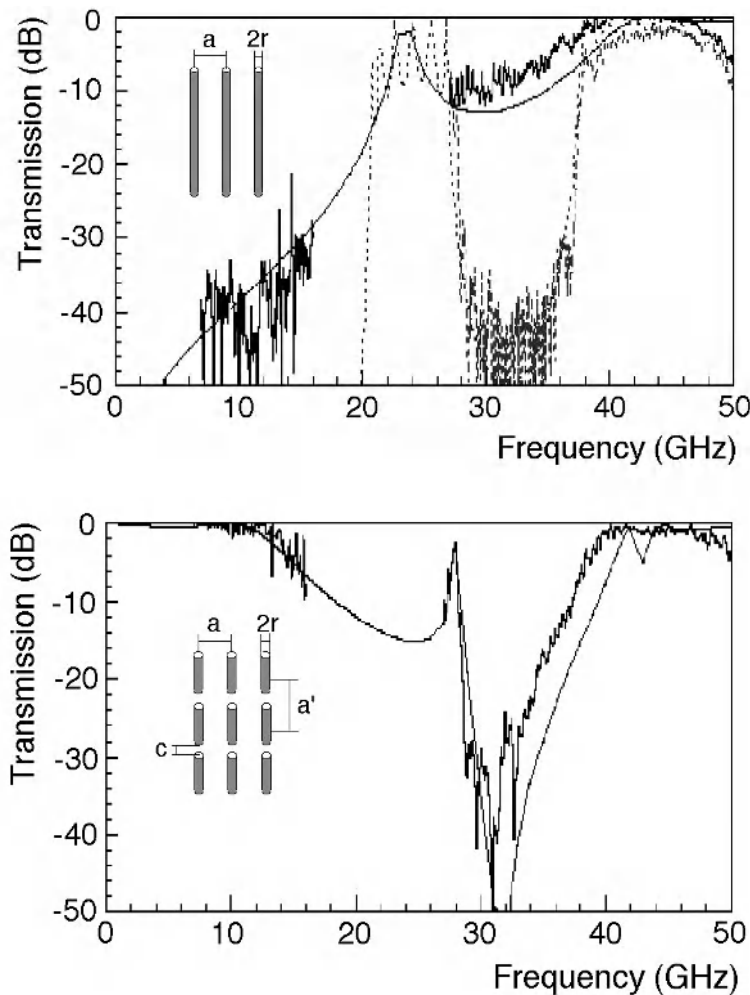


Fig. 4.4. Transmission spectra of square lattices formed of continuous metallic rods (top) and discontinuous metallic rods (bottom). The incident wave here is TM polarised. The thick curves correspond to experimental measurements, while the thin curves correspond to numerical calculations carried out using a finite element model (HFSS software from Hewlett Packard). Lattices with seven rows (*dashed curves*) and with two rows (*solid curves*) of continuous rods are simultaneously considered, while only a lattice with two rows of discontinuous rods is considered. In all three cases, the period of the lattice is equal to 6 mm and the diameter of the rods to 1.5 mm. The discontinuities are formed by air gaps with a 1.5 mm length, periodically distributed along the rods with a period equal to 6.5 mm (Lourtioz 1999)

The comparison with the lattice of discontinuous rods is carried out for this small number of rows. Discontinuities are introduced in the form of air ‘gaps’ with a length equal to 1.5 mm, periodically distributed along each metallic rod with a period of 6.5 mm. As can be seen in the lower part of Fig. 4.4, the transmission spectrum of the lattice of discontinuous rods is fundamentally different from the transmission spectrum of the lattice of continuous rods. Not only does a transmission band appear instead of the ‘plasmon photonic band gap’, but an attenuation of 15 dB, corresponding to the first transmission band in the upper part of Fig. 4.4, also appears within a frequency region extending around 25 GHz. Further, the existence of a narrow, albeit very pronounced attenuation peak corresponding to the second band gap around 32 GHz, can be noted. The attenuation due to two rows of discontinuous rods is as strong (- 50 dB) as the attenuation due to seven rows of continuous rods.

As will be described in Section 13.2, the various behaviours observed in Fig. 4.4 can be exploited for the design of switchable microwave filters. Fig. 4.4 also demonstrates that the numerical results calculated from a finite element model are consistent with the results of experimental measurements. Returning to the consideration of the simple LC model introduced above, the relevant capacitor with respect to the discontinuous rods is simply the capacitor associated with each individual air gap. In the example presented in Fig. 4.4, the capacitor was estimated to be equal to 10 fF. Numerical simulations similar to those reported in Fig. 4.4 were repeated for different gap lengths, i.e. for capacitors with different values (Lourtioz 1999). As predicted by the LC model, the frequency at the edge of the first transmission band was found to be in inverse ratio to the square root of the value of the capacitor.

4.3 Periodic Metallic Structures at Optical Frequencies. Idealised Case of a Dispersive Lossless Dielectric

As has been mentioned already, the reflectivity of a metal is lower at optical wavelengths than at centimeter or millimeter wavelengths, and metallic losses, even when they are low, can never be completely neglected. This phenomenon, combined with the difficulty of realising patterns with a micron or with a submicron size, explains the relative paucity at the present time of studies devoted to metallic photonic crystals in the infrared and visible regions. Thus far, researches in this field have been for the most part directed at the realisation of three-dimensional lattices of small metallic spheres (Moroz 1999; Pendry 1994; Pendry 1994; Zhang 2000), which can be relatively easily fabricated from colloidal solutions containing spheres in suspension (Astratov 1995; Lawendy 1988).

From an historical point of view, the optical properties of (non necessarily periodic) ensembles of metallic spheres with sizes close to the optical wavelength released in a dielectric medium had been first studied at the beginnings of the twentieth century (Maxwell Garnett 1904, 1906; Mie 1908). In particular, Maxwell

Garnett demonstrated the possibility of assimilating such ensembles to a medium with a complex refractive index $n = n'(1+i\kappa')$, and introduced analytical expressions for n' and κ' (Maxwell Garnett 1904, 1906). A few years after, Mie developed a rigorous theory for the diffraction of plane waves by a single sphere, irrespective of its composition, of its size and of the nature of the surrounding medium (Mie 1908). In the context of this book, the possibility always remains of using one of the models developed in Chapters 1 and 2 for the determination of the band diagram of a periodic ensemble of spheres, provided however that the model thus employed accounts for the dispersion of the metal. To a first approximation, the permittivity of a metal around the plasma frequency ω_p can be represented by the real part of the Drude expression (Eq. 4.12). This approximation is well suited to silver in the visible and near UV regions, especially in the wavelength region extending from 310 to 520 nm where silver is only weakly absorbing. In the more general case however, the Drude expression does not take into account the resonant absorption of metals as well as the absorption effects due to surface plasmons (Bohren 1984). The issue of surface plasmons will be briefly discussed in the next section (Section 4.4).

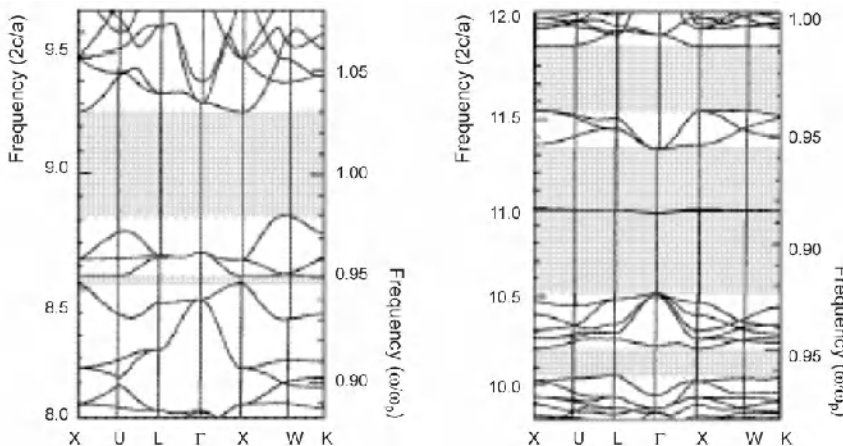


Fig. 4.5 Band diagrams of face-centred cubic lattices consisting of metallic spheres extending in the air (Moroz 1999). The side of the unit cell is referred to as $a = 2r$, where r is the radius of the spheres. The wave frequency ($\omega / 2\pi$, vertical axis) is expressed either in normalised frequency units ($2c/a$) or in plasma frequency units (ω_p). *Left.* Band diagram calculated for $r / \lambda_p = 1.013$, where $\lambda_p = 2\pi c / \omega_p$ is the plasma wavelength. *Right.* Band diagram calculated for $r / \lambda_p = 1.35$

Fig. 4.5 represents the band diagrams of face-centred cubic lattices of metallic spheres extending in the air, calculated by approximating the permittivity of the metal with the real part of the Drude expression in Eq. 4.12 (Moroz 1999). This is obviously an idealisation since the imaginary part of ϵ is being neglected here. The calculations were performed using the KKR model, while the spheres were assumed to be in direct contact to one another. The two diagrams presented in Fig. 4.5 correspond to two arbitrarily chosen values for the frequency (or the wavelength) of the plasma respectively: in the first case, displayed on the left, the ratio of the radius of the sphere to the wavelength of the plasma is equal to 1.013, while in the second case, displayed on the right, this ratio is equal to 1.35. As can be seen, these diagrams are to some extent similar to those obtained for dielectric photonic crystals. However, in spite of the fact that the crystal has a simple face-centred structure, the existence of complete band gaps with a large width ($\Delta\omega/\omega \sim 10\%$) can nevertheless be observed. This phenomenon can be explained by the very high index contrast existing between the air and the metallic spheres for wavelengths close to the plasma wavelength ($\epsilon \rightarrow 0$). Actually, the structure is almost equivalent to a cubic lattice of air spheres inside a dielectric with a very high permittivity. The widest gap is obtained around the plasma frequency itself, where the wavelength of the plasma reaches an order comparable to the radius of the sphere. When the wavelength of the plasma is lower than the radius of the sphere, several gaps of larger width appear for frequencies below the plasma frequency. In this case, represented in the right-hand side of Fig. 4.5, the existence of transmission bands with a very small curvature, i.e. with a very low dispersion, may also be noted. These transmission bands correspond to group velocities of light that can be estimated to be less than $\sim c / 200$, where c is the speed of light in vacuum.

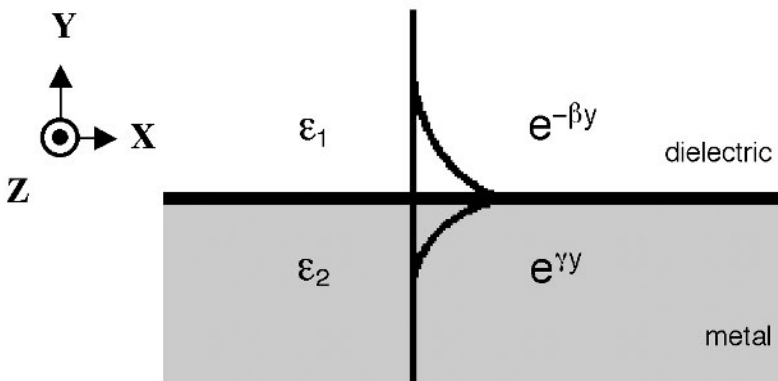


Fig. 4.6. Schematic description of a wave propagating at the interface between a dielectric (ϵ_1) and a metal (ϵ_2). The wave decays exponentially on either side of the interface

4.4 Surface Waves

A property of metals is that they may allow the propagation of surface waves, i.e. electromagnetic waves which stay localised at the interface between the metal and the air or between the metal and any other surrounding dielectric (Fig. 4.6). In the radiofrequency and microwave regions, surface waves are more often referred to as surface currents, due to fact that these electromagnetic waves may actually extend over distances equal to several thousands of wavelengths in the air or in a dielectric. By contrast, in the optical region, surface waves are well localised at the interface. In this context, these waves are also referred to as surface plasmons (or polaritons), since their generation and propagation involve resonant oscillations of the surface charges (Raether 1988).

Nevertheless, in both wavelength regions, the existence of surface waves results from the fact that the real part of the dielectric permittivity of metals is negative. In this section, we shall first recall the general properties of surface waves for metals with a plane interface. We shall then discuss the influence of the periodic corrugation of the surface of the metal in these two wavelength regions. Finally, different possible applications of such periodic structures will be briefly considered near the end of the chapter.

4.4.1 Surface Plasmons at a Metal/Dielectric Plane Interface

Let us here consider a TM wave propagating along the x -direction in the plane interface (Oxz) between two materials with relative permittivity ϵ_1 and ϵ_2 respectively (Fig. 4.6). The first medium of permittivity ϵ_1 is dielectric while the second medium of permittivity ϵ_2 is metallic. The problem to be addressed is therefore to determine the conditions allowing the propagation of surface waves, whose amplitude decreases exponentially on both sides of the interface. In TM polarisation³, the component E_z of the electric field is zero, while the magnetic field has a single non-zero component H_z . Let us denote here by α_{pl} the propagation constant associated with the plasmon wave along the Ox axis. Using Eqs. 1.37 and 1.38 for the propagation in two homogeneous materials, combined with the condition that the amplitude of the surface wave should decrease when $y \rightarrow \pm\infty$, the magnetic field can be as expressed in the form:

³ In this section, we shall adopt the standard conventions used for electromagnetic waveguides. Surface-plasmon modes propagate in the x -direction. The magnetic field of TM modes is therefore normal to Ox and parallel to Oz . This implies that when the plane interface will be replaced with a grating with grooves parallel to Oz (Section 4.4.2), the definition of TM modes will be different from that adopted for the discussion of two-dimensional photonic crystals in Chapter 1 of this book (Section 1.1.5), where TM modes were defined in such a way that the electric field rather than the magnetic field was parallel to the cylinder axis (in this case the groove axis). The same remark applies to TE modes.

$$H_z = A_{pl} \exp(i\alpha_{pl}x - \beta_{pl}y) \quad \text{if } y > 0 \quad (4.18)$$

$$H_z = B_{pl} \exp(i\alpha_{pl}x + \gamma_{pl}y) \quad \text{if } y < 0 \quad (4.19)$$

with:

$$(\alpha_{pl})^2 - (\beta_{pl})^2 = k_0^2 \epsilon_1 \quad \text{and} \quad (\alpha_{pl})^2 - (\gamma_{pl})^2 = k_0^2 \epsilon_2 \quad (4.20)$$

where A_{pl} and B_{pl} are scalar, and where the real parts of β_{pl} and γ_{pl} must be positive in order to ensure that the amplitude of the field given by Eqs. 4.18 and 4.19 will be continuously decreasing as the distance to the interface increases. Finally, one must account for the boundary conditions at $y = 0$. The continuity of the tangential component of the magnetic field at the interface imposes that:

$$A_{pl} = B_{pl} \quad (4.21a)$$

Likewise, the continuity of the tangential component E_x of the electric field at the interface implies from Maxwell's equation (Eq. 1.3) that $(1/\epsilon_i)(\partial H_z / \partial y)$ should be a continuous function of the variable y :

$$\frac{\beta_{pl}}{\epsilon_1} A_{pl} = -\frac{\gamma_{pl}}{\epsilon_2} B_{pl} \quad (4.21b)$$

Eq. 4.21a must be consistent with Eq. 4.21b, which leads to:

$$\frac{\beta_{pl}}{\epsilon_1} = -\frac{\gamma_{pl}}{\epsilon_2} \quad (4.21c)$$

Using Eq. 4.21c with Eq. 4.20 and taking the square roots of α_{pl} , β_{pl} and γ_{pl} respectively, the following expressions can finally be derived:

$$\alpha_{pl} = \sqrt{\frac{\epsilon_1 \epsilon_2}{\epsilon_1 + \epsilon_2}} k_0, \quad \beta_{pl} = \frac{i \epsilon_1}{\sqrt{\epsilon_1 + \epsilon_2}} k_0, \quad \gamma_{pl} = \frac{-i \epsilon_2}{\sqrt{\epsilon_1 + \epsilon_2}} k_0 \quad (4.22)$$

The effective decay of the fields which occurs as $y \rightarrow \pm\infty$ can be observed when the square roots in the relations presented in Eq. 4.22 lie within the upper region of the complex plane. It is immediately apparent from the equations for β_{pl} and γ_{pl} that surface waves cannot exist when ϵ_1 and ϵ_2 are both positive, i.e. when the materials on each side of the interface are standard dielectrics. Indeed, if such were the case, β_{pl} and γ_{pl} would be purely imaginary numbers and the boundary

conditions for $y \rightarrow \pm\infty$ would not be fulfilled. The same remark applies to weakly absorbing dielectrics.

The previous analysis can be reproduced in the case of TE polarisation, save for one decisive change: since both materials are assumed to be non-magnetic ($\mu = \mu_0$), the continuity of the H_x component of the magnetic field at the interface reduces now to a simple condition concerning the continuity of the y -derivative of the electric field $\partial E_z/\partial y$. Accordingly Eqs. 4.21b and 4.21c now lead to $\beta_{pl} = -\gamma_{pl}$, which from Eq. 4.20 imposes in turn that $\epsilon_1 = \epsilon_2$. This result is obviously inconsistent with the very existence of an interface. In other words, the propagation of a TE polarised surface plasmon wave is forbidden in the case of a plane metal/dielectric interface, whereas it will be allowed as soon as the metal/dielectric interface presents corrugations or irregularities.

Let us here consider a plane interface between the air and aluminum with a refractive index equal to $0.82 + i 5.99$ at the wavelength $\lambda = 546$ nm. The propagation constant α_{pl} determined from Eq. 4.22 then turns out to be equal to $(1.013 + i 3.8 \cdot 10^3)k_0$. As has been seen, the imaginary part of α_{pl} is very low while its real part is slightly larger than k_0 . This result actually applies to any metal which, like for instance gold or silver, is highly conductive in the infrared and visible regions. Since $\Re\{\alpha_{pl}\}$ is larger than the amplitude of the wave vector in free space, a surface plasmon wave cannot be excited by an incident plane wave nor by an incident beam, since the projection of their wave vector onto the x -axis would necessarily be smaller than k_0 . From the consideration of dispersion diagram, this amounts to saying that no solution $\omega(k)$ exists within the light cone for a surface plasmon propagating along a perfect metallic plane. At optical frequencies, it may be convenient to use the approximated expression for the permittivity of the metal given by the Drude formula (Eq. 4.12). Then, provided that metallic losses can be neglected and that the metal can be assumed to be surrounded with air ($\epsilon_1 = 1$), the equation for the dispersion of a plasmon wave can be deduced from the first equation in Eq. 4.22:

$$\alpha_{pl} = \sqrt{\frac{\omega_p^2 - \omega^2}{\omega_p^2 - 2\omega^2}} k_0 \quad (4.23)$$

A graphical representation of Eq. 4.23 is displayed in Fig. 4.7. The cutoff frequency for plasmon waves is equal to $\omega_p/\sqrt{2}$: in the vicinity of this frequency, the wave vector of the surface wave reaches a very high amplitude compared to k_0 . As can be seen from the observation of this figure, the entire dispersion curve lies below the light line, which confirms that plasmon waves cannot in principle be coupled to free-space waves. Actually, in the optical region, the residual roughness of dielectric/metal interfaces is always high enough to allow the weak coupling of plasmon waves and free-space-waves. Further, the use of a dielectric prism in direct contact with the surface is a well-known classical arrangement for optimising such a coupling via an evanescent wave (Kretschmann 1971).

4.4.2 Propagation of Surface Plasmons along a Periodically Modulated Metal/Dielectric Interface and Local Enhancement of the Field

The possibility for a plasmon wave to propagate along the plane interface between a metal and a dielectric has been demonstrated in the preceding section. However, it was also shown that such a wave could not in principle be excited using an incident light beam. In the present section, we shall see that the excitation of the surface plasmon by an external light beam becomes possible provided that the interface is periodically modulated. The phenomenon can be intuitively explained in the following terms: a periodically modulated surface, i.e. a diffraction grating of the kind represented in Fig. 4.8, induces a coupling between waves whose respective propagation constants at the surface differ by an integer which is a multiple of the spatial frequency $2\pi/d$, where d is the period of the grating. Although the plasmon dispersion curve lies below the light line in the case, represented in Fig. 4.7, of a perfect plane, the band-folding effects associated with spatial periodicity cause the dispersion curves of certain propagation modes to extend beyond the light line, with the consequence that surface plasmon waves can now be excited. We shall present in the following pages a more mathematical description of this phenomenon, which should allow us to explain the increase in the absorption of light by metals under certain conditions, as well as the strong local enhancement of the electromagnetic field at the surface.

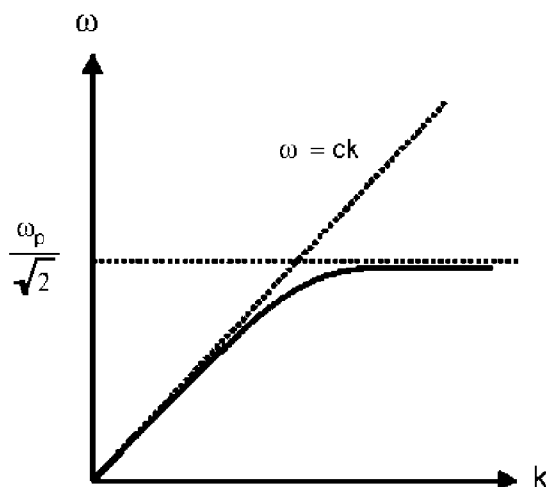


Fig. 4.7. Dispersion of surface plasmons propagating along a metallic plane

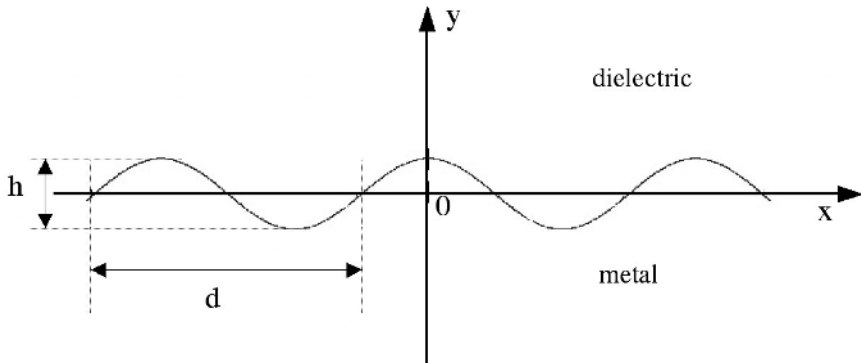


Fig. 4.8. Diffraction grating and conventions used for its description

Let us consider here the metallic diffraction grating represented in Fig. 4.8. The metal has a permittivity ϵ_2 and is assumed to be bounded by a dielectric with a permittivity ϵ_1 . For the sake of simplicity, it will be further assumed here that the surface of the grating presents a sinusoidal modulation. The period of the grating and the groove depth will be referred to as d and h , respectively.

In this respect, the question arises whether a surface wave can propagate along the x -direction. The answer to this question, at least in the case of TM polarisation, is positive: in this specific case, the grating can be derived from the plane interface considered in Section 4.4.1 through a continuous, mechanical deformation. Bloch's theorem allows us to expand the EM field into a series of x -dependent Bloch waves as follows:

$$H_z = \sum_{n=-\infty}^{+\infty} f_n(y) \exp(i\alpha_{pl,n}(h)x) \quad (4.24)$$

$$\alpha_{pl,n}(h) = \alpha_{pl,0}(h) + nK, \quad (4.25)$$

$$\text{where: } K = \frac{2\pi}{d}.$$

Using a Helmholtz equation for the EM field in each medium (see Section 2.1.1), it can be demonstrated that the functions $f_n(y)$ are exponential functions of y on both sides of the inhomogeneous region ($-h/2 < y < h/2$):

$$H_z = \sum_{n=-\infty}^{+\infty} A_{pl,n}(h) \exp(i\alpha_{pl,n}(h)x - \beta_{pl,n}(h)y), \text{ if } y > h/2 \quad (4.26)$$

$$H_z = \sum_{n=-\infty}^{+\infty} B_{pl,n}(h) \exp(i\alpha_{pl,n}(h)x + \gamma_{pl,n}(h)y), \text{ if } y < -h/2 \quad (4.27)$$

where:

$$\left(\beta_{pl,n}\right)^2 = \left(\alpha_{pl,n}\right)^2 - k_0^2 \epsilon_1 \quad \text{and} \quad \left(\gamma_{pl,n}\right)^2 = \left(\alpha_{pl,n}\right)^2 - k_0^2 \epsilon_2 \quad (4.28)$$

The real parts of $\beta_{pl,n}$ and $\gamma_{pl,n}$ in Eq. 4.28 must be positive in order to ensure the decay of the field for each side of the interface.

When the groove depth h of the grating tends towards 0, the equations for the field given in Eqs. 4.26 and 4.27 ought to tend towards the expressions that were given in Eqs. 4.18 and 4.19 in the case of a plane interface. This entails that one of the terms of the series in Eq. 4.26 must correspond to the right-hand part of Eq. 4.18 and that likewise, one of the terms of the series in Eq. 4.27 must correspond to the right-hand part of Eq. 4.19. Since the indices for the terms are arbitrary, we may decide that the non-zero terms for $h = 0$ are the same than those associated with $n = 0$. Hence:

$$\alpha_{pl,0} = \alpha_{pl} \quad (4.29)$$

$$A_{pl,n}(0) = B_{pl,n}(0) = 0 \quad \text{if } n \neq 0 \quad (4.30)$$

$$\frac{A_{pl,0}(0)}{A_{pl}} = \frac{B_{pl,0}(0)}{B_{pl}} \quad (4.31)$$

It is evident that for small values of h , $\alpha_{pl,0}(h)$ remains close to α_{pl} . Further, if the grating has such a period that:

$$-k_0 \sqrt{\epsilon_1} < \operatorname{Re} \left\{ \alpha_{pl} - K \right\} < k_0 \sqrt{\epsilon_1} \quad (4.32)$$

then the dispersion curve of the mode of propagation constant $\alpha_{pl,-l}(h)$ will be contained inside the light cone. This may be the case as well for other modes associated with different constants $\alpha_{pl,n}(h)$. Under such conditions, the imaginary part of $\alpha_{pl,n}(h)$ is small and therefore each corresponding $(\beta_{pl,n})^2$ number in Eq. 4.28 tends towards a negative real number. This obviously entails that the $\beta_{pl,n}$ solution presenting a negative imaginary part must be chosen. In this case, the wave associated with $\alpha_{pl,-l}(h)$ and $\beta_{pl,-l}(h)$ in Eq. 4.26 is very close to a plane wave that would propagate away from the grating surface with an inclination angle θ_{-l} with respect to the y -axis:

$$\sin(\theta_{-l}) = \frac{\operatorname{Re} \left\{ \alpha_{pl,-l}(h) \right\}}{k_0 \sqrt{\epsilon_1}} \quad (4.33)$$

More generally, the waves associated with the different terms in Eq. 4.26 are very close to diffracted waves propagating towards $y = +\infty$ or to evanescent waves, depending on whether the mode with propagation constant $\alpha_{pl,n}(h)$ lies inside or outside the light cone ($-k_0\sqrt{\epsilon_1} < \operatorname{Re}\{\alpha_{pl,n}(h)\} < k_0\sqrt{\epsilon_1}$). Contrary to the case of a plane interface case, the existence of a finite number of leaky waves propagating away from the surface can now be observed, with the result that radiation losses occur in addition to the metallic losses induced by plasmon surface waves, i.e. by a Joule heating effect. Accordingly, a relative increase of the imaginary part of $\alpha_{pl,n}(h)$ is therefore to be expected.

If the imaginary part of $\alpha_{pl,-l}(h)$ were zero for any value of n , the field represented by Eqs. 4.26, 4.31 and 4.32 would propagate exactly along the same directions than the field diffracted by the grating in the case of an incident wave with an incidence angle $-\theta_{-l}$ with respect to the y -axis. A most surprising conclusion can therefore be drawn: the surface plasmon can be considered as being generated from an incident plane wave with a complex propagation constant $\alpha_{pl,-l}(h)$ along the x -axis, notwithstanding the fact this incident wave has a zero-amplitude and is therefore only virtual. The idea that a diffracted wave may exist in the absence of an incident wave may come as a shock, but it should be borne in mind that we are concerned here with homogeneous solutions of Maxwell's equations. The fundamental principles of physics are not at fault here: since the propagation constant has an imaginary part, the amplitude of the surface plasmon decreases during its propagation, for the very reason that the energy carried by an incident wave cannot compensate for the absorption and radiation losses. It would not be correct however to assert that the surface plasmon does not receive any energy: quite on the contrary, the fact that its amplitude tends towards infinity along the direction opposed to the propagation suggests the presence of an energy source at $x = -\infty$. This source cannot obviously be an incident wave. In practice, this energy may be due to a beam of electrons bombarding the surface of the metal with an adequate energy. Such a technique was actually used for the generation of surface plasmons. In any case, the above discussion also emphasizes the main differences between the present equations and the homogeneous equations, used for instance in Section 1.1.5 for the determination of the eigenmodes in a dielectric photonic crystal where the dielectric constants are real numbers and where the field operators are hermitian, thereby resulting in real-valued propagation constants.

The existence of surface plasmons as homogeneous solutions of Maxwell equations has important consequences as regards the diffraction properties of metallic gratings. While surface plasmons may exist in the absence of an incident wave, the presence of an incident wave with a propagation constant approaching $\alpha_{pl,-l}(h)$ may excite inside the metal a large-amplitude wave close to a surface plasmon. This phenomenon is analogous to the oscillations of a damped pendulum, which can be characterised by a complex oscillation frequency: when the real-valued excitation frequency tends to approach the complex-valued free oscillation frequency, forced oscillations with large amplitude are generated. This is all the more true if the imaginary part of the free oscillation frequency is small. In analogy with the forced oscillations of a pendulum, the excitation of surface plasmons can

therefore be described in terms of a classical resonance effect. This observation, first made by A. Hessel *et al* (Hessel 1965), is at the origin of the modern theory of surface plasmons on gratings and has enabled the interpretation of Wood's anomalies, as will be briefly described in the following section.

4.4.3 Wood's Anomalies: Phenomenological Theory

At the beginnings of the twentieth century, the American astronomer R.W. Wood reported the surprising phenomenon that under certain circumstances, waves diffracted by metallic gratings could exhibit extremely abrupt variations of their amplitude while at the same time undergoing only very limited variations of either the incidence angle or the wavelength (Wood 1902). This phenomenon, which came to be known as 'Wood's anomalies' has fascinated researchers in optics for nearly a century. A few years after the discovery of Wood's anomalies, Lord Rayleigh observed that this phenomenon always occurred in the neighbourhood of a transition either from an evanescent wave to a propagating plane wave, i.e. propagating in the y -direction, or conversely, and this observation led him to attribute Wood's anomalies to such a transition. Only half a century later would this simple explanation be recognised to be false. A. Hessel and A. Oliner were the first authors who correctly explained Wood's anomalies in terms of the excitation of surface plasmons (Hessel 1965). Since the real part $\alpha_{pl,0}(h)$ of the propagation constant associated with the surface plasmon is close to k_0 , the phenomenon does indeed occur in the neighbourhood of a transition from an evanescent wave to a propagating plane wave or conversely, but it must not be confused with this transition itself. The excitation of surface plasmons leads to a strong increase in the amplitude of the field in the vicinity of the grating surface: the amplitude of the field may thus be increased by two orders of magnitude. The absorption in the metal is therefore dramatically reinforced while the amplitudes of the diffracted waves undergo abrupt variations. The phenomenological theory of Wood's anomalies has resulted in the mathematical expression of previously intuitive ideas, in particular through the use of polology, i.e. through the study of the properties of functions of complex variables.

We shall present here a brief outline of this theory (Maystre 1976, 1977, 1982; Nevière 1980) only for the case where the dispersion curve of the mode with propagation constant $\alpha_{pl,-l}(h)$ is contained within the light cone. Let us now consider the case of an incident wave of amplitude A' and incidence angle θ , as represented in Fig. 4.9 (*right*). Using the classical analysis of the diffraction by a grating (see Section 2.1.1), we may define as A_n and B_n respectively the amplitudes of the diffracted waves in the dielectric and in the metal. Although normalised amplitudes such as $\tilde{A}_n = A_n/A'$ are generally defined for real values of the incidence angle and of the propagation constant $\alpha = k_0\sqrt{\epsilon_l} \sin\theta$ along the x direction, this analysis can be mathematically extended to the case where α is a complex variable, with the $\tilde{A}_n(\alpha)$ functions remaining defined as functions of real variables. The analytical extension of the functions $\tilde{A}_n(\alpha)$ to the complex plane is

univocal, and the polology consists in determining the poles and the zeros of these functions. In the case under consideration here, one of the poles seems to be obvious. Indeed, when α reaches $\alpha_{pl,-l}(h)$ in the complex plane, the amplitudes A_n and B_n can be non-zero even if the amplitude A' of the incident wave is zero (see Section 4.4.2.). In this case, all normalised amplitudes $\tilde{A}_n(\alpha)$ are infinite. This can be analytically expressed in the following form:

$$\tilde{A}_n = \frac{P_n(\alpha, h)}{\alpha - \alpha_{pl,-l}(h)} \quad (4.34a)$$

where $P_n(\alpha, h) \neq 0$ for $\alpha = \alpha_{pl,-l}(h)$. It might be observed from Eq. 4.25 that the imaginary parts of $\alpha_{pl,0}(h)$ and $\alpha_{pl,-l}(h)$ are identical and from Section 4.4.1 that the modulus of the imaginary part of $\alpha_{pl,0}(0) = c_{pl}$ is close to $3.8 \times 10^{-3} k_0 \sqrt{\epsilon_1}$ for aluminum. Hence, it follows that the amplitudes \tilde{A}_n will undergo a strong variation if an incident plane wave with a propagation constant in the vicinity of $\alpha = k_0 \sqrt{\epsilon_1} \sin \theta_{-l}$ (see Eq. 4.33) strikes the grating. Let us indeed assume here that $\alpha_{pl,-l}(h)$ varies slowly with h . It therefore follows from Eqs. 4.25 and 4.33 that $\alpha_{pl,-l}(h) \approx \alpha_{pl,0}(0) - K = k_0 \sqrt{\epsilon_1} \sin \theta_{-l} + i 3.8 \times 10^{-3} k_0 \sqrt{\epsilon_1}$. Accordingly, under these conditions, a small variation $\delta\theta$ of the incidence angle such that $\delta\alpha = k_0 \sqrt{\epsilon_1} \cos \theta_{-l} \delta\theta = 3.8 \times 10^{-3} k_0 \sqrt{\epsilon_1}$ will be sufficient for causing the denominator of $|\tilde{A}_n(\alpha)|$ to increase by a factor of $\sqrt{2}$. Therefore, since the electromagnetic energy itself is in proportion to the square $|\tilde{A}_n(\alpha)|^2$, it will decrease from a factor of 2. It might be noted that the variation considered here for θ is only of a few tenths of degree. Indeed, a variation ten times larger would lead to a decrease of the electromagnetic energy from a factor of one hundred. This demonstrates the presence here of a resonance phenomenon which appears through the excitation of surface plasmons.

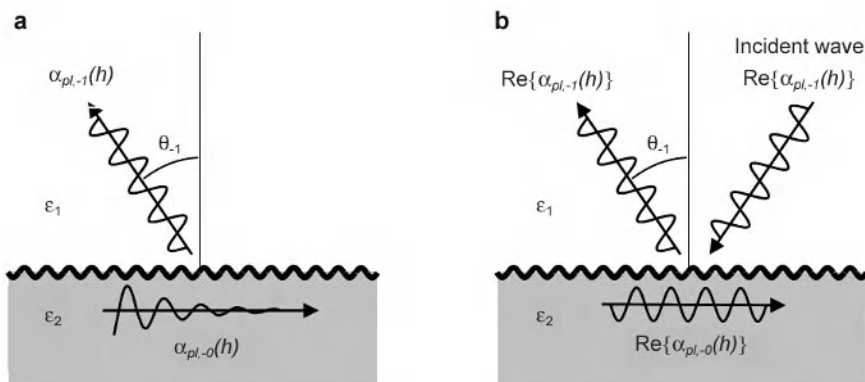


Fig. 4.9. Left. Homogeneous solutions including plasmon waves Right. Resonant excitation of homogeneous solutions by an incident plane wave

A prerequisite for the validity of the previous results is that the numerator in $\tilde{A}_n(\alpha)$ should not present any significant variation in the neighbourhood of $\alpha = \text{Re}\{\alpha_{pl,-l}(h)\}$. However, this approximation is to be rejected for all propagating modes whose dispersion curve is contained inside the light cone, since the conservation of energy must be accounted for. In the case under consideration where only the dispersion curve of the mode with propagation constant $\alpha_{pl,-l}(h)$ is contained inside the light cone, the only wave diffracted by the grating is the reflected wave. Assuming that the metal is a good conductor, it might reasonably be expected that this wave should present an amplitude of the same order than the reflection coefficient of a standard metallic reflector. On the other hand, the law of energy conservation imposes that $|\tilde{A}_{-l}(\alpha)|$ be smaller than unity. This seems to be inconsistent with the variations from two orders of magnitude which have been previously mentioned. This contradiction can be lifted provided that in the neighbourhood of $\alpha = \text{Re}\{\alpha_{pl,-l}(h)\}$, the behaviour of the numerator of $\tilde{A}_{-l}(\alpha)$ is similar to the behaviour of its denominator. In other terms, $P_{-l}(\alpha)$ must possess a zero within the complex plane in the neighbourhood of $\alpha_{pl,-l}(h)$.

As a conclusion, Eq. 4.34a is valid only for evanescent modes whose dispersion curve lies outside the light cone. For $n = -1$, Eq. 4.34a assumes the following form:

$$\tilde{A}_{-l} = Q(\alpha, h) \frac{\alpha - \alpha_z(h)}{\alpha - \alpha_{pl,-l}(h)} \quad (4.34b)$$

If $h = 0$, the surface plasmon cannot be excited. From Eqs. 4.25 and 4.29, it can therefore be deduced that:

$$\alpha_z(0) = \alpha_{pl,-l}(0) = \alpha_{pl} - K \quad (4.35)$$

$$Q(\alpha, 0) = r(\alpha) \quad (4.36)$$

Under these conditions, when the groove depth is cancelled out, both the zero and the pole of $\tilde{A}_{-l}(\alpha)$ tend towards the same value $\alpha_{pl,-l}(0)$, which results in the mutual annihilation of their influences. As a consequence, $\tilde{A}_{-l}(\alpha)$ simply identifies to the reflection coefficient of the plane mirror $r(\alpha)$. The resonance must disappear for evanescent waves as well, which in turn imposes that:

$$P_n(\alpha, 0) = 0 \quad (4.37)$$

As the height h increases, evanescent waves undergo a phenomenon of resonance in the neighbourhood of $\alpha = \text{Re}\{\alpha_{pl,-l}(h)\}$, leading to a local increase of the electromagnetic field in the vicinity of the grating surface. This phenomenon is

obviously accompanied by metallic losses due to Joule heating. As has been previously mentioned, the radiative losses occurring in the reflection order -1 cause the pole to move away from the real axis. The rigorous calculations thus performed demonstrate that as a counterpart the zero generally tends towards the real axis and intersects it for a certain value $h = h_a$, as is represented in Fig. 4.10. If the incidence angle for this specific value of the groove depth is determined in such a way that $\alpha = \alpha_z(h_a)$, then the application of Eq. 4.34b shows that the normalised amplitude of the wave reflected at the grating is strictly zero. Since all other waves are evanescent waves, we reach a most surprising conclusion: it turns out indeed that all the incident energy is absorbed by the grating.

The total absorption of a wave by a grating was first theoretically predicted (Maystre 1976) before being experimentally verified shortly afterwards in the visible region using a holographic grating coated with gold and illuminated with a krypton laser beam working at the 647 nm wavelength (Hutley 1976). The measured reflectivity was found to be as low as 0.3 percent, while the angular peak width was equal to 1.3 degrees. This absorption phenomenon was all the more surprising that the groove depth was no higher than one tenth of the period of the grating. The surface of the grating presented a sinusoidal undulation with a period equal to 555 nm and an amplitude $h = 37$ nm. Thus, a very low degree of undulation at the surface of a mirror may cause a decrease of the experimentally measured reflectivity of the mirror from more than 90 percent to less than 1 percent.

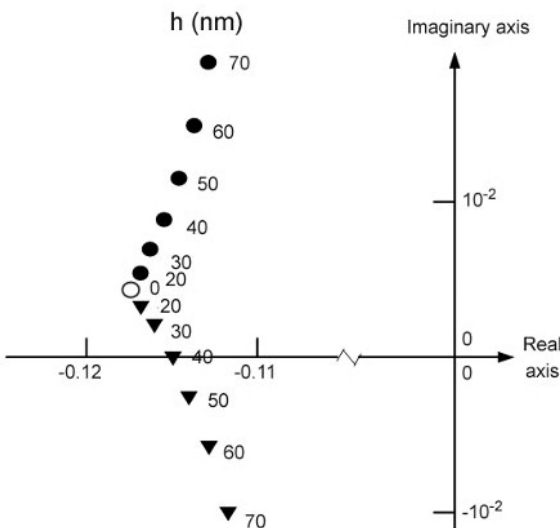


Fig. 4.10. Evolution of the pole (solid circles) and zero (solid triangles) of $\tilde{A}_{-1}(\alpha)$ represented as functions of the modulation height h . The grating here is assumed to be coated with gold and to have a period $d = 555$ nm. The incident wavelength λ is equal to 647 nm (Hutley 1976)

This demonstrates the importance of the resonance phenomena induced by surface plasmons. All these phenomena generally lead to the strong exaltation of evanescent waves, and sometimes to an abrupt decrease of the reflected waves which may even in certain specific cases totally vanish. From a theoretical point of view, this example also illustrates the potential of phenomenological theories based on polology.

4.4.4 Photonic Band Gaps for the Propagation of Surface Plasmons at Periodically Modulated Metal/Dielectric Interfaces

In light of the possibility of creating photonic band gaps in periodic dielectric structures, it might be inquired whether the periodicity of a grating could likewise allow the creation of photonic band gaps for the propagation of surface plasmons. This question is of practical interest for several different reasons: two examples may be considered here.

A first example are the dramatic consequences that the absorption phenomena induced by surface plasmons may cause for diffraction gratings used in spectroscopic studies. For instance, the diffraction gratings mounted at the rear of telescopes are designed for the analysis of the spectral composition of the light emitted by distant celestial objects, often with a very low intensity. If Wood's anomalies cause one or several wavelengths in the spectrum to be occulted, the analysis may be significantly perturbed. In this respect, preventing the propagation of surface plasmons can be an elegant way of answering this problem.

On the other hand, the local enhancement of the field in the vicinity of a grating surface may also be used in a positive manner, for instance for enhancing either the Raman scattering or the light emission of dye molecules deposited over a grating. The creation of photonic band gaps for the propagation of surface plasmons can therefore allow the control of phenomena of this type (Barnes 1996, 1997; Kitson 1996).

A method for creating a surface-plasmon photonic band gap relies on the coupling of two surface plasmons propagating along opposite directions. In order to achieve such a coupling, the spatial frequency of the grating must satisfy the equation:

$$K = 2 \operatorname{Re}\left\{\alpha_{pl}\right\} \quad (4.38)$$

The modulation of the grating results in a folding of the dispersion curves (represented by dashed curves in Fig. 4.11) which originally were located just below the light line (solid curves in Fig. 4.7). The coupling of two plasmons induces a frequency gap whose width increases with the groove depth h . The resulting dispersion curves are the dotted curves represented in Fig. 4.11. However, the frequency gap obtained in this case presents a limited interest since it occurs below the light line, i.e. in a region where the different waves cannot be excited using an incident beam.

A simple geometrical solution exists to this problem: in order that a gap be created inside the light cone, the dispersion curves of Fig. 4.11 have to be shifted by a distance equal to $K/2$. This can be achieved by superimposing a second modulation with a spatial frequency $K/2$, i.e. with a period $2d$, over the original modulation with spatial frequency K , i.e. with period d . Therefore, the grating simultaneously possesses two different modulations with periods $2d$ and d respectively. The first modulation is used for inducing a coupling between the two surface plasmons propagating along opposite directions, while the second modulation is used for positioning a gap within the light cone. As can be seen in Fig. 4.12, this results in the appearance of a gap whose centre lies along the axis of the light cone.

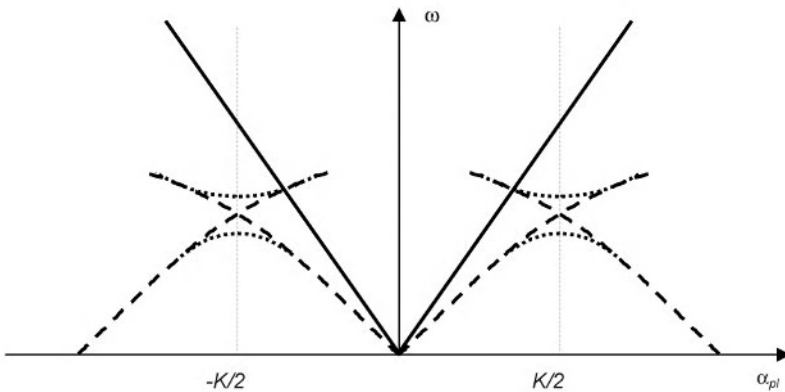


Fig. 4.11. Dispersion curves of two plasmons coupled through the modulation of a grating with a spatial frequency satisfying Eq. 4.38

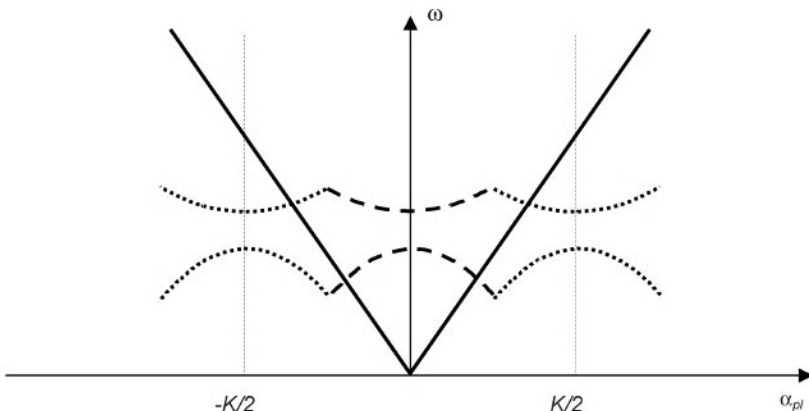


Fig. 4.12. Dispersion curves of a double-modulation grating with a fundamental period $2d$ and a first harmonic period d

It might be pointed out that other solutions for positioning the gap within the light cone exist. For instance, when a metal layer is deposited over a substrate, a solution consists in using a prism placed on the side of the substrate. The light cone associated with the prism thus presents a larger angle of aperture than the light cone associated with vacuum, and therefore partially contains gaps similar to those represented in Fig. 4.11.

Different methods for creating surface-plasmon photonic band gaps have been described here. However, these methods apply to the propagation of surface plasmons along the direction normal to the grooves of a one-dimensional grating, whereas for most applications the problem to be addressed is the creation of a band gap for all directions of propagation along the xOz plane. To this end, a two-dimensional grating must be used in place of a one-dimensional grating. An universal gap was thus actually demonstrated using such a grating fabricated by etching holes inside a metal for creating a hole lattice with an hexagonal symmetry (Kitson 1996).

4.4.5 The Photon Sieve

The resonant phenomena associated with the excitation of surface plasmons may also offer an explanation for the extraordinary light transmission which has been achieved through a thick metallic grid containing holes with a sub-wavelength diameter (Ebbesen 1998). The fact that a metallic grid formed from a perfectly conductive metal behaves like a high-pass filter is a well-known phenomenon, and a rigorous numerical study of this behaviour can be found in (Mc Phedran 1977). The behaviour of the high-pass filter is actually quite intuitive. We may for instance consider here the microwave regime. Basically, a hole drilled inside a thick metal plate is but a truncated waveguide, which possesses a cutoff frequency below which, or equivalently a wavelength above which no propagation is allowed, save in the case of exponentially decreasing modes. The cutoff wavelength is equal to $3.5R$, where R represents the radius of the hole. In the wavelength region extending above the cutoff wavelength, an exponential decrease in the transmission of light can thus be observed.

Yet in the visible region, T.W. Ebbesen was able to demonstrate experimentally the existence of transmission peaks in this long-wavelength region (Ebbesen 1998). This phenomenon can be explained in terms of the excitation of surface plasmons which occurs at the surface of the two-dimensional grating, and more specifically in the region of the geometrical shadow of the incident beam. Surface plasmons do not exist in the microwave region. By contrast, their resonant excitation allows photons to propagate through the holes at certain specific incident wavelengths in the visible region. For this reason, the transmission spectrum exhibits several transmission peaks. A detailed numerical and analytical study of the phenomenon can be found in (Enoch 2002c). The optical properties of surface plasmons may find a practical application for both the miniaturisation of optical circuits and the characterisation of biological structures.

To some extent, an analogy may be drawn between the resonant excitation of surface plasmons and the resonant effects which occur in a microcavity embedded inside a photonic crystal of finite size. When the wavelength of the incident beam coincides with a resonance wavelength of the microcavity, photons may propagate through the whole crystal in spite of the presence of a photonic band gap. The first photons thus accumulate inside the microcavity, with the result that the EM field in the microcavity becomes extremely intense.

4.4.6 Surface Waves in Metals at Radiofrequencies

Plane Metallic Surfaces and Concept of Surface Impedance

Let us here consider an interface between a metal and the air. The permittivity ϵ_1 of the air is equal to 1 and, as has been described in Section 4.1, the permittivity of the metal in the radiofrequency region can be adequately approximated by a purely imaginary number with a large modulus compared to unity. Hence, $\epsilon_2 \approx 1 + i\sigma/\epsilon_0\omega \approx i\sigma/\epsilon_0\omega$. Under these conditions, the formulas given in Eq. 4.22 for α , β and γ can be re-written as follows:

$$\alpha \approx \frac{\omega}{c}, \quad \beta \approx \sqrt{\frac{-1}{\epsilon_2}} \frac{\omega}{c} = \sqrt{\frac{\omega\epsilon_0}{2\sigma}} \frac{\omega(1+i)}{c} \quad \text{and} \quad (4.39)$$

$$\gamma \approx \sqrt{-\epsilon_2} \frac{\omega}{c} \approx \sqrt{\frac{i\sigma}{\omega\epsilon_0}} \frac{\omega}{c} = \frac{1-i}{\delta}$$

where δ represents the skin depth of the metal (see Section 4.1.2). The surface wave thus propagates at approximately the same speed than light in vacuum. Since the attenuation coefficient $\text{Im}\{\beta\}$ is very small, the wave extends largely inside the surrounding medium, in this case in the air. Conversely, since γ is large, the penetration of the surface wave inside the metal is therefore limited and the surface waves are actually in this case surface currents. The existence of these surface currents allows the introduction of the concept of surface impedance in an appropriate manner. The surface impedance is defined as the ratio E/H , where E and H are the electric field and the magnetic field components in the propagation plane respectively.

In the case of a TM polarised wave, the relevant field components are E_x and H_z respectively. Proceeding from the expression for H_z given in Eq. 4.18, an expression for E_x can be derived using Maxwell's equations (Eqs. 1.2 and 1.3). The ratio $-E_x/H_z$ can finally be written in the form:

$$Z_s(\text{TM}) = -\frac{E_x}{H_z} = -\frac{i\beta}{\omega\epsilon_0} \quad (4.40)$$

The presence of a negative sign in front of E_z/H_x ensures that the surface wave will be absorbed and not amplified. Let us here recall that the time dependence of the fields is of the form $\exp(-i\omega t)$. The expression for Z_s in Eq. 4.40 corresponds therefore to an inductance ($-iL$). In other terms, a TM polarised wave will propagate only if the surface impedance is inductive. The equation for the dispersion $\alpha(\omega)$ of the TM wave can thus be easily deduced from the expressions given for α and β in Eq. 4.22 and from the expression given for Z_s in Eq. 4.40:

$$\alpha = \frac{\omega}{c} \sqrt{1 - \frac{Z_s^2(TM)}{\eta^2}} \quad \text{with} \quad \eta = \sqrt{\frac{\mu_0}{\epsilon_0}} = 377 \Omega \quad (4.41)$$

where η is the impedance of vacuum.

In the case of a TE polarised surface wave whose propagation is actually restricted to corrugated metallic surfaces, the relevant field components are E_z and H_x , respectively. Using an expression for the E_z component similar to the expression given for the H_z component in Eq. 4.18 allows the derivation from Maxwell's equations (Eqs. 1.2 and 1.3) of an expression for H_x , and then of an equation for the surface impedance in the following form:

$$Z_s(\text{TE}) = \frac{E_z}{H_x} = \frac{i\omega\mu_0}{\beta} \quad (4.42)$$

Here again, the presence in front of E_z/H_x of a positive sign ensures that the surface wave will be absorbed rather than amplified. Since the time dependence of fields is of the form $\exp(-i\omega t)$, the expression for Z_s now corresponds to a capacitance (i/C). In other terms, a TE polarised wave will propagate only if the surface impedance is capacitive. The equation for the dispersion $\alpha(\omega)$ of such a wave can then be deduced from Eqs. 4.22 and 4.42:

$$\alpha = \frac{\omega}{c} \sqrt{1 - \frac{\eta^2}{Z_s^2(\text{TE})}} \quad (4.43)$$

Periodically Structured Metallic Surfaces

In the last decades, a number of studies have been devoted to the propagation of radiofrequency waves in periodic metallic structures. The reader is referred among others to (Bozzi 2000; Chan 1995; Elahi 1976; Harvey 1959; Kruusing 2001). In the case of metallic surfaces, the terms corrugated surfaces and frequency selective surfaces (FSS) are employed, depending on whether the corrugation depth or the choice of the surface patterns is the determining factor in the behaviour of the structure. In the context of photonic crystals, we shall focus here on the possibility of creating photonic gaps for the propagation of surface waves. More precisely,

we shall consider periodically structured metallic surfaces with patterns much smaller than the wavelengths of interest. Under these conditions, the structure can be adequately described using an effective medium model, while its properties can be analysed in terms of the notion introduced above of surface impedance.

In Fig. 4.13 is represented the cross-section view of the high-impedance surface developed by D. Sievenpiper *et al* (Sievenpiper 1999a, 1999b). The upper surface of the structure consists of metallic patches periodically organised into a square lattice. Each patch is shorted to the metallic ground plane with a via. The whole structure either extends in the air or is embedded inside a dielectric. The enlarged view presented in Fig. 4.13 (*right*) shows that an elementary pattern of the structure can be reduced to a parallel resonant circuit consisting of a capacitor and of a self-inductor. The use of an effective circuit model is justified here insofar as the size of the patterns is small with respect to the wavelength. This structure can therefore be assimilated to a surface with an impedance $Z = -iL\omega / (1 - LC\omega^2)$. Actually, the adequate values to be used in this model are not the capacitance and inductance of the individual elements, but rather the sheet capacitance and sheet inductance, which both depend on the value of each individual element and on their arrangement.

When the frequency is lower than the resonance frequency $\omega_0 = 1/\sqrt{LC}$, the impedance reduces to an inductance, and only TM-polarised surface waves may propagate as was the case for a metallic plane. As ω tends towards ω_0 , the surface impedance $Z = E/H$ dramatically increases, while at the same time the electric field tends to reach its maximum amplitude at the upper surface of the metallic structure. The situation is to some extent reversed with respect to what is generally the case with a classical metallic plane, where the amplitude of the electric field is zero. This property is of prime importance since it entails that an external incident wave might be reflected off the high-impedance surface without any phase shift. For frequencies larger than the resonance frequency, the surface impedance reduces to a capacitance, and only TE-polarised surface waves may propagate in this case.

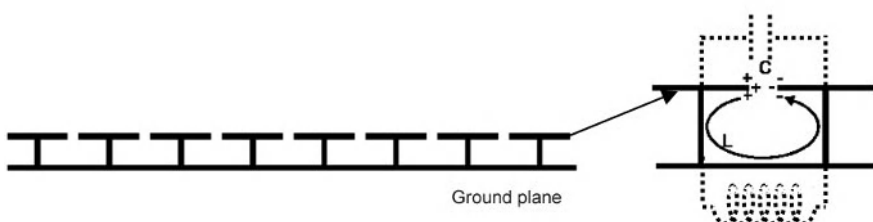


Fig. 4.13. *Left.* Cross-section view of the high-impedance surface developed by D. Sievenpiper *et al* (Sievenpiper 1999a, 1999b). *Right.* Enlarged view of an elementary pattern of the structure

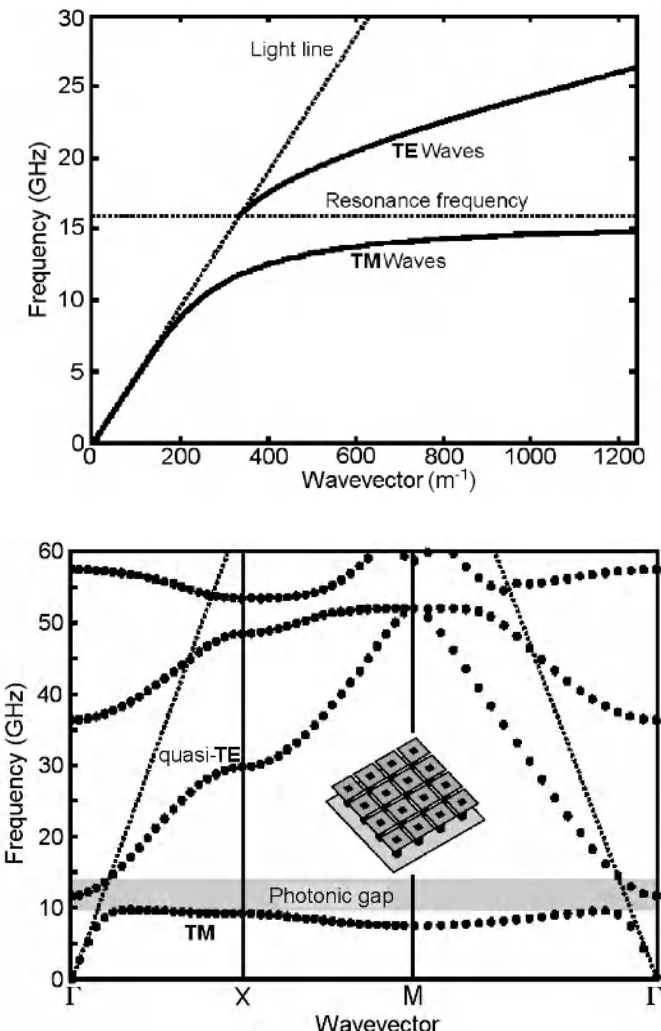


Fig. 4.14. *Top.* Dispersion diagram of a high-impedance surface analytically determined from Eqs. 4.41 and 4.43 (Sievenpiper 1999b). *Bottom.* Band diagram of a similar structure calculated from a finite element model (Quian 1999; Sievenpiper 1999b). The structure represented in the insert consists of a square lattice of metallic patches embedded inside a dielectric and shorted to the metallic ground plane with vias

The dispersion relations of the structure can be determined from Eqs. 4.41 and 4.42 respectively, depending on the respective values for ω and ω_0 . Fig. 4.14 (*top*) represents a dispersion diagram calculated along these lines in the case of a square lattice formed by metallic patches (Sievenpiper 1999b). The period of the lattice is

equal to 2.4 mm, the spacing between the patches to 0.15 mm, the height of the vias to 1.6 mm and their width to 0.36 mm. The surrounding dielectric was made from epoxy used in printed boards, and had a permittivity $\epsilon = 2.2$. Although the dispersion diagram presented in the upper part of Fig. 4.14 does not reveal any band gap, a clear discontinuity occurs at the resonance frequency around 16 GHz, corresponding to the transition from the TM to the TE mode. It can be noted that the two dispersion curves both lie below the light line $\omega = ck$. Accordingly, Eqs. 4.41 and 4.43 only account for modes bound to the surface without radiative losses. An exhaustive analysis of the modes, including leaky modes, necessarily requires the use of more elaborated models, an example of which is being employed in the lower part of Fig. 4.14.

The band diagram of a high-impedance surface represented in the lower part of Fig. 4.14 was calculated from a finite element model (Quian 1999; Sievenpiper 1999b). The structure displayed in the insert is similar to the structure considered in the upper figure. However, it might be pointed out that the numerical calculations now allow predicting the existence of a complete band gap, at a frequency close to the resonance frequency estimated from the analytical model. For the frequency region extending up to 30 GHz below the light line and along the TX and ΓM direction, a relative agreement may also be observed between the analytical and the numerical results. By contrast, the finite element model further accounts for the leaky modes located above the light line, and it also provides a complete description of the band diagram for all directions of propagation and all polarisations of the field. Nevertheless, the essential result to be noted here is the demonstration of the existence of a complete photonic gap. As will be described in the third part of this book, the suppression or even better the control of surface waves are of the highest interest for microwave antennas.

Introduction to Part II. The Many 'Facets' of Photonic Crystals

The first part of this book has been devoted to a survey of the theoretical models used for the description of photonic structures and more generally of periodic structures. To a large extent, we have restricted ourselves to a conception of photonic crystals as the optical analogues of solid-state crystals. However, when considering the optical properties of photonic crystals which can be exploited in optics, it becomes necessary to adopt a much broader perspective. The second part of this book will therefore aim at describing the main properties of photonic crystals which lead to envisioning different forms of control of electromagnetic waves, and beyond the perspective of devising wavelength-scale devices and components. For the sake of simplicity, two different types of optical properties can be distinguished depending on whether photonic crystals are illuminated externally by one or several incident electromagnetic waves, or internally by one or several miniature sources, which can be formed simply by elementary oscillating dipoles. The now classical image of the excited atom immersed in a photonic crystal, which corresponds to the second situation, is precisely the intuition which has led E. Yablonovitch to his first proposal of photonic band gap structures as optical systems for achieving a complete control of the spontaneous emission.

Likewise, the classification of the properties of photonic crystals into two categories, i.e. depending on whether the crystal is seen from outside or from inside, is an oversimplification, which tends to reach certain limits. Actually, the concept of optical confinement is the most suited for analysing all the intermediate cases that may arise, for instance the optical guiding of waves propagating between two photonic crystal mirrors. Chapter 5 will thus proceed from the situation of an external illumination to that of internal illumination, by successively considering different levels of optical confinement. For an electromagnetic wave arriving from a semi-infinite medium and impinging on a photonic crystal, the latter will be seen either as a particular mirror or more generally as a diffracting object (Section 5.1). In the case of a wave confined in a homogeneous medium between two photonic crystal mirrors, different ways of investigating the photonic crystal guiding will be described (Section 5.2.) Planar and linear waveguides realised in two and three-dimensional structures will be considered in this context. Finally, Section 5.3 will address the case of resonators, where the optical confinement is expected to occur along all possible directions, i.e. in all three directions and in two dimensions if the space is arbitrarily limited to two dimensions.

The idea of a ‘control of electromagnetic waves’ suggests the existence of a unifying concept behind the different optical components which have been mentioned above. Indeed, due to their property of acting as ‘optical insulators’, photonic band gap structures offer the opportunity of achieving a more complete optical confinement than was the case with the previous generation of optical devices. For the most part, the latter devices were based on the refractive index confinement which occurs as a plane wave impinges on a plane boundary between two media at an incident angle higher than the critical angle. This form of optical confinement reaches its limits as soon as one moves to micrometric optical devices. For sizes approaching the optical wavelength, an electromagnetic mode can no longer be approximated in a simple way by a unique plane wave. Retaining the notion of incident angle, the waves to be controlled are actually combinations of multiple plane waves impinging on the plane interface at all possible angles of incidence, and it is quite obvious that some of these angles are larger than the critical angle.

In this context, however, no reason opposes the possibility of combining these two types of confinement, for instance a refractive index confinement along one dimension and a photonic band gap confinement in the two other directions. Such a scheme is being currently investigated in the context of developing applications of photonic crystals to integrated optics and optoelectronics. It will be presented in Section 4 of Chapter 5 where the concept of ‘light line’ will be also discussed in more detail. This concept, which has already been mentioned in the first part of this book, is useful in providing an insight into the limitations imposed by the choice of a refractive index confinement, which is often dictated by technological constraints.

The transmission bands of a photonic crystal rather than its photonic band gaps can also be exploited for the propagation of waves extending in the periodically structured medium formed by this crystal, i.e. for the propagation of the Bloch waves which have been introduced in the first part of this book. One of the most interesting features of photonic crystals is the possibility of achieving very small group velocities associated with the flattest bands. This property, as well as other unusual refractive properties like the ultra-refraction and ‘superprism’ effects, will be discussed in Chapter 6. In particular, the realisation of a negative index refraction opens the way to the design of new types of optical lenses based either on photonic crystals or on metamaterials. The correct exploitation of all these effects rests on a large extent on the choice of the interface between the crystal and the external medium, where the usual types of waves (plane, Gaussian, etc) are converted into Bloch waves, while the reverse conversion takes place at the output of the photonic crystal.

The last two chapters of this second part will be devoted to certain issues related to the combination of active media with photonic crystals. Thus, Chapter 7 will address the problem of optical emitters in photonic crystal microcavities. This is one of the major problems in this field, if only because it is at the very origin of the concept of a photonic crystal. In this chapter, simple notions like that of the spontaneous emission factor of emitters will first be introduced as a first approach towards reaching a better understanding of the utility of photonic systems with

highly confined modes, even in the absence of strong singularities in the density of states. We shall then in a second step enter the physics of microsources, which exhibit a very singular density of photonic states. It will be seen in this case that the lifetimes of electromagnetic modes can be dramatically 'reduced' (Purcell effect), and that different quantum electrodynamic effects may also appear. Finally, the performances of standard microcavities with 'shape resonances' (microspheres, microdisks) will be compared to those of photonic crystal microcavities.

Chapter 8 will be devoted to the subject of nonlinear optics in photonic crystals. This field, which remains largely unexplored until now, seems to be very promising in terms of applications. Different nonlinear effects will be successively discussed, depending on the optical waves involved in these effects, namely the fundamental wave, its harmonics or the waves at difference or sum frequencies. Correspondingly, different orders of electrical susceptibility are associated with these effects: the first-order susceptibility ($\chi(1) = \epsilon_r - 1$), the second-order susceptibility $\chi(2)$, etc.

5 Control of Electromagnetic Waves

5.1 The Photonic Crystal Mirror

What happens when a wave propagating in an isotropic, linear and homogeneous medium of index n illuminates a photonic crystal? This question will be first addressed in the case of a semi-infinite crystal, beginning with a general consideration of the problem in Section 5.1, before limiting ourselves to the case of specular reflection in Section 5.2. We finally consider in Section 5.3 the case of a finite crystal, which can be viewed as a semi-transparent mirror.

5.1.1 The Semi-Infinite Photonic Crystal: Mirror or Diffraction Grating?

Let us consider here a semi-infinite photonic crystal with an omnidirectional band gap. The energy flux at frequencies within the band gap cannot penetrate far in the crystal and will therefore be reflected in the general sense of the term. However, since the object illuminated in this case by the wave exhibits a periodic structure, the wave must necessarily satisfy the usual laws on diffraction gratings, which apply to any interface presenting two basic lattice vectors \mathbf{R}_1 and \mathbf{R}_2 :

$$\mathbf{k}_{\text{refl}, \parallel} - \mathbf{k}_{\text{inc}, \parallel} = m_1 \mathbf{G}_1 + m_2 \mathbf{G}_2 \quad (5.1)$$

where $\mathbf{k}_{\text{inc}, \parallel}$ denotes the projection of the incident wave vector onto the plane of the interface and $\mathbf{k}_{\text{refl}, \parallel}$ is the projection of the wave vector associated with a wave diffracted or reflected by the same plane, while \mathbf{G}_1 and \mathbf{G}_2 are the reciprocal wave vectors of the direct lattice and m_1 and m_2 are two integers. This result actually is a direct consequence of the global invariance of the system with respect to translations of the real lattice, and of the application of the Bloch theorem to the total field, which includes the incident field as well as the diffracted or reflected fields:

$$\mathbf{E}(\mathbf{r}, t) = \mathbf{E}_{\text{inc}} + \mathbf{E}_{\text{refl}} \quad (5.2)$$

In order to obtain the usual expression of the grating formula with the angle of incidence, it suffices to take into account the requirement of frequency conservation. The latter states that, for all the elementary waves which compose the incident and diffracted waves (in general, a single incident wave and several diffracted waves exist), the corresponding wave vectors must have the same modulus $n\omega/c$. The allowed diffracted orders are therefore obtained by considering the intersections of the vertical lines drawn through the nodes of the two-dimensional reciprocal lattice with the hemisphere of radius $n\omega/c$, as represented here in Fig. 5.1a. In order that Eq. 5.1 be satisfied, the origin of the reciprocal lattice must be located at the extremity of the projection of \mathbf{k}_{inc} onto the plane of the interface.

The periodicity of the plane of the interface is an implicit assumption in the considerations above. However, it should be emphasised that, from a mathematical point of view, the existence of such a periodicity is the less frequent case, as has already been explained in Chapter 3 when considering quasi-crystal structures, i.e. structures that can be obtained by cutting periodic crystals along planes with complex indices (Miller indices). Nevertheless, such a periodic approximation, even if it may present a very large period compared to the original lattice, still provides a very good compromise for the description of actual electromagnetic phenomena. We shall assume throughout this chapter that we are dealing with such a periodic interface.

It is quite difficult to produce a general rule for the number of allowed diffraction orders, as well as for the dependence of this number on whether the operating frequency lies inside or outside a photonic band gap. Photonic crystal structures have periods of the order of λ and the frequency cutoff of diffracted orders is never very far from the frequencies in the band gaps. We shall here consider two typical configurations, that will be encountered when studying two-dimensional photonic crystals, for an incident wave whose frequency lies within the band gap. First, let us consider the case where a wave arrives from a high-index homogeneous dielectric medium onto a crystal formed by air columns drilled inside the same medium, with a relatively large air filling factor. In such a case, the frequency of the band gap will be relatively high, as can be seen in Fig. 5.1a, and the radius $n\omega/c$ of the hemisphere will therefore be large. Accordingly, even if the interface is formed by a dense surface of the crystal, i.e. if it is associated with the vectors \mathbf{G}_1 and \mathbf{G}_2 as large as possible, diffraction will be allowed at least in one non-specular order (m_1 or $m_2 \neq 0$). In these examples, one of the three dimensions can be ignored for incidences normal to the columns.

Conversely, let us consider now a crystal formed by dielectric rods placed in the air. The hemisphere with radius ω/c is now comparatively small. In addition, if the vectors \mathbf{G}_1 and \mathbf{G}_2 are as large as possible, the construction will yield a single point of intersection, as can be seen in Fig. 5.1.b. In such a case, reflection remains specular for most incidence angles, i.e. for all values accessible for \mathbf{k}_{inc} , while the incident energy is entirely reflected in the specular beam, $m_1 = m_2 = 0$.

Once the allowed diffracted orders have been determined, another problem is the determination of the respective intensities of these orders. This requires the use of more advanced modelling methods of the kind described in Section 2.1 in

Chapter 2, for instance the scattering matrix method, which is a generalisation of the classical models for diffraction gratings.

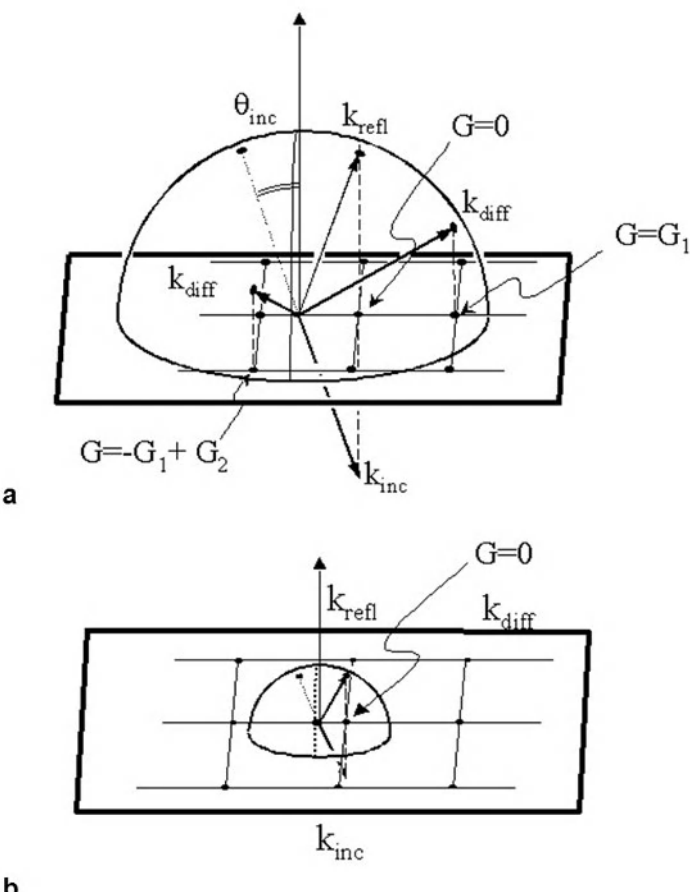


Fig. 5.1. Grating formula in the reciprocal space. The reciprocal lattice of the surface is represented with its origin located at the projection in the horizontal plane of the incident wave vector \mathbf{k}_{inc} . **a.** The allowed orders are therefore to be found at the intersection between the vertical lines drawn through the nodes of the two-dimensional reciprocal lattice, and the hemisphere where the modes of the semi-infinite medium are located at the frequency under consideration. In addition to the specular reflection $\mathbf{G} = \mathbf{0}$ (wave denoted by \mathbf{k}_{refl}), only two particular diffracted waves are represented here in order not to overload the figure: (i) $\mathbf{G} = \mathbf{G}_1$, which is similar to the usual grating formula with the plane of incidence normal to the grooves of the lattice (ii) more general case where $\mathbf{G} = -\mathbf{G}_1 + \mathbf{G}_2$. **b.** For a surrounding medium with a lower index, like the air, or for lattices with a small period, the only remaining intersection is $\mathbf{G} = \mathbf{0}$. In other terms, only specular reflection occurs

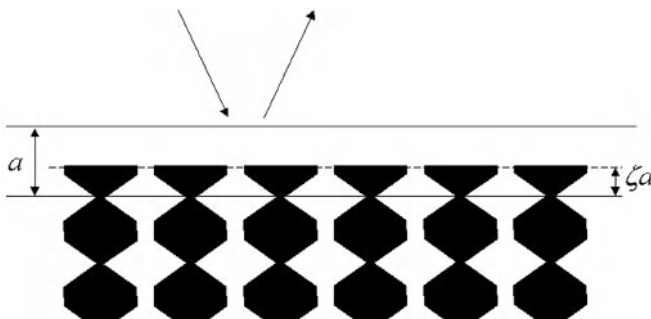


Fig. 5.2. Reflection of a beam on a crystal cut at a fraction ξ inside the last layer of unit cells along a dense plane. The reflection phase is not a linear function of ξ

5.1.2 Specular Reflection at a Semi-Infinite Crystal

From all the diffraction/reflection configurations for a wave incident on a semi-infinite photonic crystal, the simplest configuration is specular reflection, where only one reflected order exists, while all the others are actually of an evanescent rather than of a propagating nature. As we shall see later in Section 13.1.2 of Chapter 13, this is also the more interesting case for shaping the radiation of antennas. The specific interest of this configuration lies in its reflection phase and amplitude, which can be significantly different from those of the metallic ground plane used in the field of microwaves. This can be illustrated by considering the schematic example of the two-dimensional photonic crystal represented in Fig. 5.2, with a cutting plane which can be continuously translated until an extra unit cell is finally added. This assumption amounts to letting the parameter ξ continuously vary from 0 to 1.

It is quite apparent that the periodical pattern in the plane of the interface may evolve in a complex manner, and therefore there is no reason for the reflection phase to be a linear function of the variable ξ . For the same physical reason, in the case where the value for ξ is fixed, there is no simple rule for the dependence of the reflection phase on the angle of incidence θ or on the frequency ω . For instance, one may go from a band gap to a transmission band by tuning the frequency or by changing the direction of propagation. As a consequence, all the conceptions which had been acquired in the context of plane interfaces must be revised. Experiments and calculations conducted on two and three-dimensional crystals used as reflective planes for antennas (Kesler 1996) have demonstrated that, for a given frequency and angle of incidence, the behaviour of these crystals was in all respects comparable to that of a perfectly conducting metallic plane, but one that would have been buried at a distance $d(\theta, \omega)$ beneath the surface. A precise analysis of $d(\theta, \omega)$ as a function of θ and ω allows on the one hand to retrieve the emission diagram of an antenna located in front of the photonic crystal and on

the other hand to observe a narrowing of the emission lobes at specific frequencies. In addition to these beam-shaping effects, photonic crystals used as reflective planes can be expected to exhibit an almost constant phase in a certain frequency range, a quite desirable feature.

However, research on this subject has been thus far limited to studies concerned with specific examples, and there are to the best of our knowledge no simple rule that would allow predicting the behaviour of a given photonic crystal, be it two nor three-dimensional. This is clearly at variance with the one-dimensional case, where the phase evolution is well-known. Thus, for traditional Bragg mirrors, the phase presents a lower slope in the band gap after an abrupt transition at the edges of the gap. Yet, for two and three-dimensional structures, and in the cases where diffraction can be neglected, it seems intuitively sound to consider that, at a certain incidence, only one periodicity of the crystal is really involved in the reflection. The behaviour of the structure can therefore be expected to be similar to that of the one-dimensional stack realised by an adequate averaging along this direction. However, it remains difficult to predict the behaviour of such structures in more complex cases, for instance for directions at the intersection of two reciprocal planes, where two different periods of the crystal may act simultaneously. Among these complex cases, it might be of interest here to mention the ‘anticrossing’ effects observed in studies on the reflective properties of opals at angles very oblique with respect to the (111) growth axis of the opal (van Driel 2002; Vos 2001).

5.1.3 Finite Photonic Crystals as Semi-Transparent Mirrors

We shall end our review of mirrors with the consideration of photonic crystals with a finite thickness. These structures can act as semi-transparent mirrors. Here again we shall assume that the crystals are infinite in the plane of the interface, and correspondingly we shall remain within the assumption of an infinite plane wave. Otherwise, refraction, focalisation or collimation phenomena, that will be addressed later in Chapter 6 of this book, would occur. For a uniform plane wave propagating at a frequency within the photonic band gap, the transmission of N ‘atomic’ planes of the crystal assumes the form $T_0 \exp(-AN)$, where A and T_0 are constant parameters. The transmitted wave may also emerge in several diffracted orders as was the case for reflection. The fact that the crystal presents an omnidirectional band gap ensures that all orders will follow the exponential decreasing behaviour that has been previously described, but with factors A and T_0 depending on the diffraction order.

The physical analysis becomes complex as soon as photonic crystals are considered in a frequency range where transmission bands may coexist with directional band gaps. In terms of wave vectors, each order has a specific constraint associated to it and will therefore undergo a different fate. Thus, while some orders can be associated with gaps and therefore give rise to an exponential decreasing evolution, other orders can be associated with Bloch waves. These waves propagate without undergoing any attenuation, but their relative intensities as well as

the coupling factors between these waves and external plane waves, either incident or transmitted, can take any arbitrary value. Further, for a very thin slab of only a few periods, it is no longer possible to neglect the power transmission occurring from one interface to the other, due to the partial overlap of the tails of waves associated to evanescent orders in the semi-infinite situation.

5.2 Photonic Crystal Waveguides

5.2.1 Index Guiding and Photonic-Bandgap Guiding

The principles of classical guiding, or index guiding, are represented here in Fig. 5.3a. This guiding mechanism is based on the total internal reflection of light at the interface between a high-index medium H and a medium L with a lower index: these two media are referred to as the core and the cladding of the waveguide respectively. More detail on this subject, concerning for instance the number of modes allowed by these waveguides or the mathematical expression of their mode profile, will be provided in Chapter 9 devoted to planar waveguides. By contrast, Fig. 5.3b illustrates the principles of photonic bandgap guiding, where the confinement of light is achieved by exploiting the photonic band gap of a periodic medium. By analogy with index guiding and with optical fibres, the term ‘cladding’ will be used here for describing this medium.

It is known that within a given band gap, even a directional band gap, the reflectivity of a photonic crystal rapidly approaches unity when the number of rows increases, and this is all the more true that the index contrast is high. In other words, even in the case where the cladding is finite, a wave may undergo a large number of successive reflections without any noticeable attenuation. If the classical zigzag ray model representing the propagation of rays between two parallel mirrors is used here for the description of the guiding, this situation turns out to be simply the general case of a classical Fabry-Perot resonator at generic incidence angles. When the multiple interferences of all these rays are in phase, i.e. when each ray is actually a wave with an infinite extension along the axis of the waveguide, a resonance condition is achieved, so that the energy stored in the resonator, i.e. in this case in the waveguide, reaches its maximum. This phase-matching condition, or optical path length condition, establishes a relation between the frequency and the wave vector. This expression can be generically expressed in the form $f(\omega, k) = 0$, but it can also be written in terms of a dispersion relation $\omega = \omega(\mathbf{k})$, possibly with multiple branches.

These elementary considerations have allowed us to retrieve the dispersion relation of the guided mode. However, it should be noted here that k itself has an unequivocal meaning only in the case where the structure presents a complete translational invariance in the direction of the waveguide. In the case of a periodic structure like photonic crystals are, the periodicity along the direction of the

waveguide implies that infinitely many values for k exist, all of which being formally identical save for the spatial frequency of the photonic crystal waveguide.

Returning to the Fabry-Perot model, we shall denote by R_1 and R_2 respectively the reflection coefficients of the two walls of the waveguide, while L_{opt} will denote the optical path between two successive reflections. The lifetime of a photon in the waveguide will be given by the equation $\tau \sim L_{opt}/[c\ln(1/R_1R_2)]$ since a number of $N \sim 1/\ln(1/R_1R_2) \sim 1/(1-R_1R_2)$ reflections are required before the guided wave may undergo any noticeable attenuation. This means that attention should be paid not only to the value for k but also to the frequency, since the finite lifetime τ induces a corresponding broadening $\Delta\omega \sim 1/\tau$ of the resonances associated with the guided modes. Only in the case of an ideal Fabry-Perot with an infinite τ would the Airy function tend towards a set of zero-width Dirac functions. This reveals a similarity between the physics of Fabry-Perot resonators and the physics of a waveguide formed by two photonic crystals. This similarity even turns into an identity for planar multilayer systems, i.e. when k is unambiguous: in this case, one simply deals with a one-dimensional photonic crystal with a defect (see Section 1.4.1 in Chapter 1), or in other terms, with a planar microcavity confined by Bragg mirrors.

Planar microcavities based on semiconductors have been most intensively studied since 1988, first with the primary intent of realising vertical cavity surface emitting lasers (VCSELs) and later for the investigation of such fundamental phenomena as the strong coupling between a confined wave and excitons in semiconductors (see Chapter 7). More recently, interest in these structures has further increased with the development of very high efficiency light-emitting diodes (Delbeke 2002; Rattier 2002).

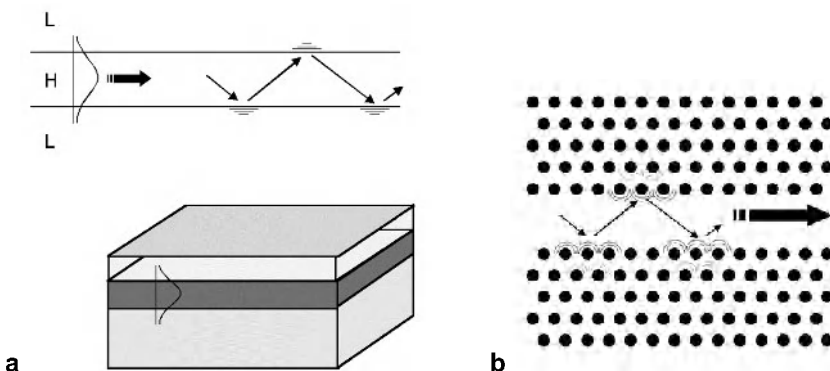


Fig. 5.3. a. Index guiding: the upper part of the figure is a cross-section view representing the field profile and the zigzag ray model with total internal reflections and evanescent waves; the lower part of the figure represents the usual planar guiding **b.** Photonic bandgap guiding: the successive reflections are ‘created’ by the entire set of interferences generated by all atoms of the crystal, both along and normally to the axis

The limitations presented by these planar multilayer systems are exactly the same as those that led to the research on photonic crystals: the band gap is only directional. Going back to the zigzag ray model, this implies that as soon as the incidence angle will be outside a certain limited range, a leakage of light through the walls of the waveguide is bound to occur, with the consequence that confinement will cease to be effective. An optimally designed waveguide therefore requires that a three-dimensional structure with an omnidirectional band gap be used in order to prevent leakage along the two other directions.

5.2.2 Three-Dimensional Photonic Crystal Waveguides

The guiding of light in a three-dimensional photonic crystal raises the same issues as those which have been discussed in Section 5.2.1. However, as illustrated in Fig. 5.4, it becomes necessary here to specify the geometry used for the guiding, for instance whether the light will be confined along one or two dimensions while the propagation along the two or one other dimensions respectively will be left free. These two configurations correspond to a planar and to a channel waveguide respectively. Accordingly, it is legitimate to define a one or two-dimensional wave vector that will be associated with the guided wave in each of these situations. A large variety of methods may be devised for designing a planar or a channel waveguide in a three-dimensional photonic crystal. As an example, let us here consider first the case of a planar waveguide created inside an inverse opal structure. This structure is face-centred cubic (fcc, see Section 12.2.2 in Chapter 12) with a stacking order ABCABC.... Possible geometries for creating a waveguide in such a structure include:

- the introduction of a spacing between two perfect semi-infinite crystals, as represented here in Fig. 5.4a,
- the introduction of a single stacking fault among the crystalline planes of the crystal, for instance ABCABABC,
- the removal of a crystalline plane,
- the removal in a two-dimensional periodic fashion of certain ‘atoms’ inside a crystalline plane of the crystal,
- the periodic modification of a series of atoms (or cells) inside a crystalline plane, with respect to their size, index or shape.

This enumeration is by no means exhaustive. It is of course quite obvious that when the propagation is free along the two in-plane dimensions, i.e. when $\omega = \omega(k_x, k_y)$, the presence of the underlying crystal lattice may result in guided modes exhibiting a series of specific features. The in-plane azimuthal orientation here becomes a crucial parameter, as can be seen in Fig 5.4d for a different type of lattice. At the very least, a significant anisotropy along the different crystallographic directions of the walls of the waveguide can be expected in such a case.

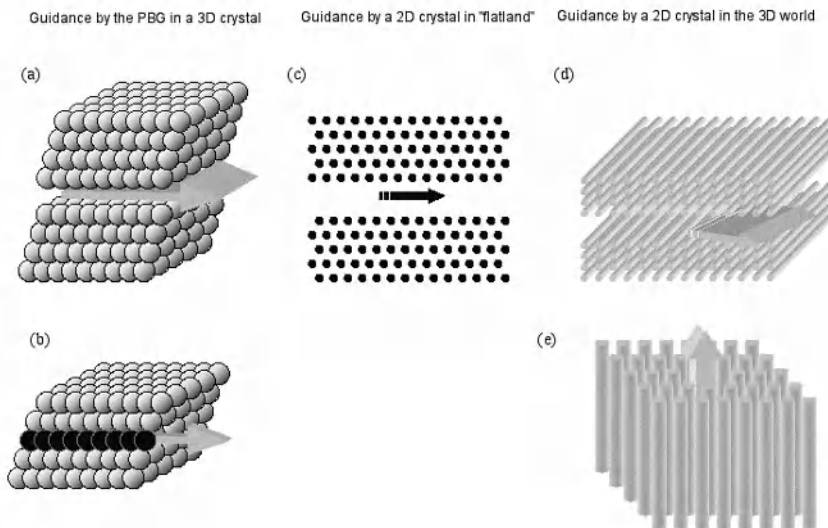


Fig. 5.4. Waveguides in two and three-dimensional photonic crystals. *a.* and *b.* Guiding in a three-dimensional crystal in the cases of a planar and of a linear defect respectively *c.* Linear guiding in a two-dimensional crystal, represented in a purely two-dimensional way, as it would be in ‘Flatland’ (Abbott 1992) *d.* and *e.* Guiding along two or one dimensions respectively in a two-dimensional crystal, with a three-dimensional representation of the system

Similarly, examples of methods for creating a channel waveguide in a three-dimensional crystal include:

- the removal of a row of atoms, as in the case represented in Fig. 5.4b, or of several adjacent such rows,
- the removal of a periodic series of atoms inside a given row,
- the modification of a series of atoms inside a given row, with respect to their size, index or shape.

As in the case of a planar waveguide, this enumeration is not exhaustive. For a further insight into the very large variety of possible combinations, the interested reader is referred among others to (Noda 2002b).

These channel waveguides can be expected to exhibit specific features as regards their dispersion relation. Since the situation now is comparable to the propagation in a one-dimensional periodic medium, the dispersion relation $\omega = \omega(k_x)$ is likely to be strongly affected by the periodicity thus induced on the channel. Contrary to what was the case in a planar waveguide, the appearance of band gaps at wave vectors multiple of (π/period) may now correspond to a region with a true zero-density of states, i.e. to a region where no states are allowed, provided that no

other branch exists at this gap frequency. In the planar case, there is no reason for omnidirectional gaps to be present in the dispersion diagram.

In the specific case of the fundamental band gap associated with the one-dimensional periodicity of such a channel waveguide ($k_z = \pi/\text{period}$), there is no obvious reason why it should lie inside the omnidirectional band gap of the surrounding three-dimensional crystal: thus it may be below, inside or above this band gap. It may even not exist at all if the crystal does not allow any guiding at its nominal frequency. For very large periods, associated with the so-called ‘vicinal’ directions of the three-dimensional crystal, i.e. with small angles with respect to the direction of a dense row, the fundamental band gap tends obviously to extend over very low frequencies, and it is therefore quite probable that certain higher-order guided modes will be within the three-dimensional band gap.

5.2.3 Two-Dimensional Photonic Crystal Waveguides

An arbitrary limitation to a purely two-dimensional world would actually amount to considering that propagation occurs along a single direction within the (x,y) plane in a system assumed to be perfectly invariant and infinite along z . In this case, examples of photonic band gap structures can be found in the form of dielectric columns in the air or of infinite air holes in a dielectric matrix. Taking a three-dimensional view of these two-dimensional structures, it can be seen that the only remaining canonical geometry for the guiding is of a planar type, as in the example represented in Fig. 5.4c, which was created by removing a row of columns. In the case where $k_z = 0$, the guiding can be described by a vector \mathbf{k} with a single component, for instance k_x . The dispersion relation for the guided modes will therefore reduce to $\omega = \omega(k_x)$. In view of the complete invariance of the system along z , including the field, it becomes perfectly legitimate to describe this case as a channel guiding in the xy plane.

The question arises however of the behaviour of such a two-dimensional system when the restriction to $k_z = 0$ is removed and when all other possible directions of propagation are allowed. Such a ‘mixed’ geometry calls for a specific analysis, since the wave may not be guided at all for certain values of k_z at which the cladding does not exhibit a two-dimensional band gap.

According to this more general view, two different types of waveguides may be distinguished, depending on the nature of the defects created in a two-dimensional crystal:

- two-dimensional defects, which have been described earlier in this chapter: such defects are formed by a plane of missing atoms along Oxz between two semi-infinite two-dimensional crystals with the same axis z (Fig. 5.4d). Thus far, this geometry remains of a purely academic interest.
- one-dimensional defects, formed for instance by a missing dielectric column or by a missing air hole in two-dimensional crystals respectively formed by dielectric columns in the air or by air holes inside a dielectric. This case is represented in Fig. 5.4e, and corresponds exactly to the geometry of photonic crystal

fibres, or microstructured fibres, which will be discussed later in Chapter 11. The most studied situation in the literature is the case where guiding is achieved only for large values for k_z with respect to the transverse components k_x and k_y . The physics of such a waveguide are therefore quite different from what has been seen thus far, since there is no longer any necessity for the period of the crystal to be of the order of the half-wavelength. This period can be much larger, which not only leads to a simplification of the fabrication process, but also to relaxing requirements on index contrast, thus allowing silica (SiO_2 , $n \sim 1.46$) and glass to be used.

The physics of a waveguide created by a one-dimensional defect can be summarised as follows. Since the main component of the wave vector lies along an invariant direction of the system, the value of this component may now approach $n\omega/c$, where n is the index of the ‘waveguide’ (with $n = 1$ in the case of a missing column). Therefore, if we limit ourselves to small angles with respect to the Oz direction, the photonic band gap phenomenon comes into play only along the xy coordinates, i.e. with respect to transverse propagation. Patterns with a large period are sufficient due to the fact that the transverse components k_x and k_y remain small. This is comparable to what occurs in a number of optics experiments described in textbooks, where large, visible fringes are associated with extremely small angles with respect to the axis. Let us consider here the case of an air/glass system, where the index contrast is 1 : 1.5, and let us go from $k_z = 0$ to the largest values for k_z . For the case, of practical interest for fibres, of air holes in glass, it is known from Section 1.3.3 in Chapter 1 that the low index contrast prevents the appearance of a two-dimensional omnidirectional band gap for $k_z = 0$. In this case, transmission bands, separated by thin directional band gaps appear instead in the band diagram (see Section 11.1 in Chapter 11). When oblique directions of propagation are allowed, i.e. when $k_z \neq 0$, the introduction of k_z will result in an increase in the frequency of the partial band gaps for a given period a of the lattice. In other terms, a/λ increases. The same effect can be observed for one-dimensional structures, where it is a well-known fact that, for low index contrasts, a blue-shift occurs in the spectral features depending on the $\cos\theta$ factor, where θ is an average angle in the stack. It has been recognised since 1996 and the researches by P. St-John Russell *et al.*, that for certain specific two-dimensional structures two-dimensional omnidirectional band gap can be created for large values of k_z . The interested reader will find more detail on this subject in (Knight 2003; Ortigosa-Blanch 2000; Russell 2003). In this case, a defect formed by a single missing ‘atom’ may allow the guiding of light, with a dispersion relation of the form $\omega = \omega(k_z)$. This dispersion relation can be interpreted in the following terms: for each value of k_z , at least within a certain range, a guided mode corresponding to this frequency exists with a well-defined field pattern in the Oxy plane. The dispersion relation $\omega = \omega(k_z)$ represents in a sense a concatenation of these modes. This shall be discussed in more detail in Chapter 11 devoted specifically to the issue of photonic crystal fibres.

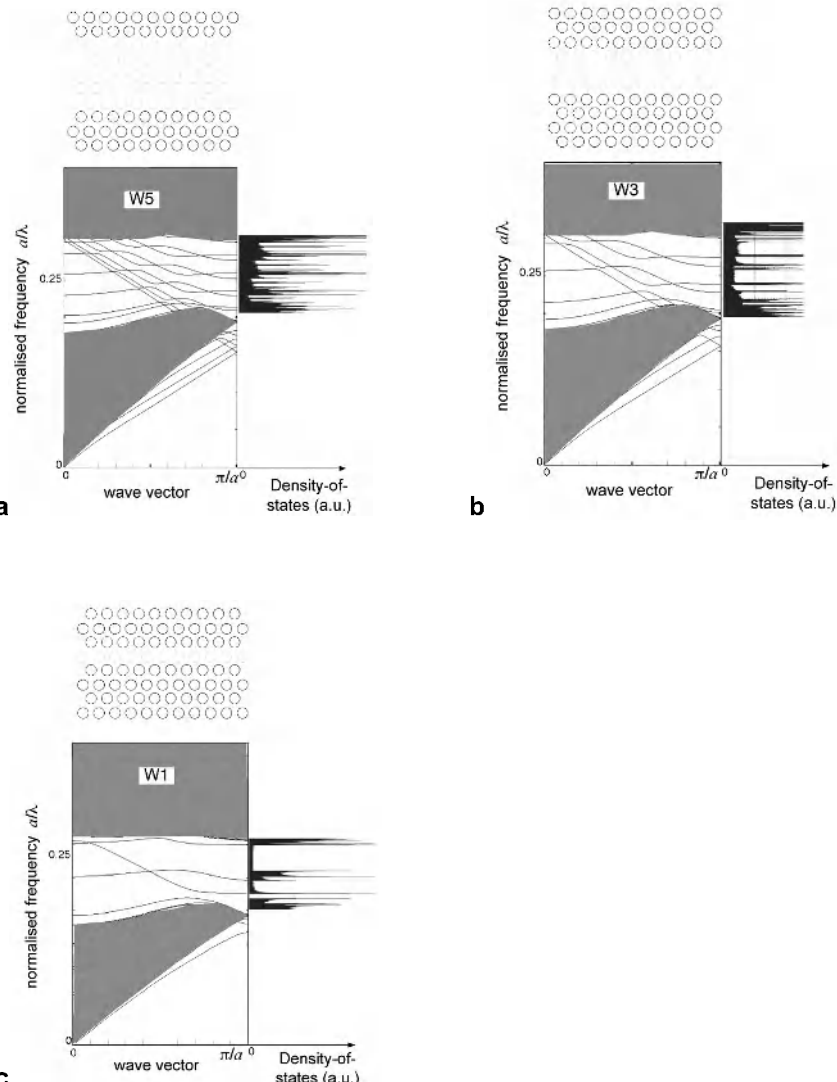


Fig. 5.5. Dispersion diagrams and corresponding density of states, represented on the right of the diagrams, for waveguides with: **a.** five missing rows of holes (W5) **b.** three missing rows of holes (W3) **c.** one missing row of holes (W1). In all three cases, the waveguide is schematically represented above the corresponding diagram. The photonic crystal is formed by air holes in a dielectric matrix ($\epsilon = 11$, $f = 0.37$). The grey areas in the diagrams represent the projections of the transmission bands of the bulk crystal without defects. The diverging singularities in the density of state (peaks in the dispersion diagrams) are bounded due to the discretisation of the calculations over a finite, albeit large number of values for k

5.2.4 Density of States and Multiplicity of Guided Modes

A photonic crystal waveguide can be generically described as a medium 2, in the form either of an homogeneous ordinary medium or of any photonic crystal, surrounded by a medium 1 with a photonic band gap ensuring the confinement of electromagnetic wave. The density of states of a one-dimensional channel is defined as the ratio $dN/d\omega dl$ calculated per unit length of the channel, while in the case of a two-dimensional planar waveguide the density of states is the ratio $dN/d\omega dS$ calculated per unit area of the waveguide. The presence of a waveguide results in the formation of nonzero density of states in the band gap of the confining material, i.e. in the cladding.

Let us first consider the case of a channel waveguide along Ox . Dispersion branches of the form $\omega = \omega_i(k_x)$ associated with the guided modes appear in the band gap. Each of these branches contributes to a number of states which is in proportion to the length of the waveguide. The associated density of states can be formally written in the form:

$$D(\omega) = \int_{BZ} dk_x \delta(\omega - \omega_i(k_x)) \propto (d\omega_j / dk_x)^{-1} \quad (5.3)$$

The number of guided modes at a given frequency and their dispersion (group velocity) determine the total density of states. As is the case for conventional index guiding (see Chapter 9), the dispersion branches cover only a limited frequency range: each mode has one or several cutoff frequencies. The dispersion curve often tends to flatten when reaching a cutoff frequency ($d\omega/dk_x = 0$), while the density of states either diverges or presents singularities ($dk/d\omega \rightarrow \infty$), a phenomenon which corresponds to the van Hove singularities in solid state physics (Ziman 1992).

Only in the case of waveguides presenting relatively large transverse dimensions, formed from an homogeneous material with index n can some simple predictions be made. Within the limits just indicated, the number of modes per unit volume of the waveguide tends asymptotically towards that of a bulk system formed by the homogeneous material filling the whole space. Assuming that the density of states in such a medium is, for either of the two polarisations:

$$D_2(\omega) = \frac{1}{V} \frac{dN}{d\omega} = \frac{1}{V} \frac{dN}{dk} \frac{dk}{d\omega} = \frac{1}{8\pi^3} 4\pi k^2 \frac{n}{c} = \frac{1}{2\pi^2} \frac{n^3 \omega^2}{c^3} \quad (5.4)$$

and that the section of the waveguide is equal to $S = L_y L_z$, where L_y and L_z are large with respect to λ/n , then the linear density of states of the waveguide should be of the order:

$$\frac{dN}{dx d\omega} = S D_2(\omega) = \frac{S}{2\pi^3} \frac{n^3 \omega^2}{c^3} \quad (5.5)$$

Different examples of dispersion diagrams and density of states calculated for three different waveguides realised in a photonic crystal formed by air holes in a dielectric medium are presented here in Fig. 5.5. Each waveguide corresponds to a given number of missing rows of holes along a dense direction of the crystal. In the examples considered in this figure, this number is equal to 5, 3 or 1. The problem is analysed in a purely two-dimensional way. Each diagram is calculated using the supercell method described in Section 1.4.3 in Chapter 1. The grey areas here correspond to the multiple transmission bands of the bulk crystal surrounding the waveguides. When going from the broad waveguide represented in Fig. 5.5a to the narrow waveguide represented in Fig. 5.5c, it can be seen that the density of states evolves from a continuum $D(\omega) \propto \omega$ superimposed onto multiple singularities associated with flat bands, towards a more structured form displaying more prominent gaps and singularities. We shall return hereafter in Section 5.2.5 to the issue of some of these internal gaps.

When the guiding medium itself is structured, we need to restart the basic reasoning from the beginning and to explicitly write that the number of states is equal to the number of values for k allowed by boundary conditions of the Born-von Karman type common in solid state physics (Ziman 1992). This amounts to considering the waveguide as being approximately a very elongated rod with a section $S = L_y L_z$. The density of states per unit volume $D^s(\omega)$ of such a structured medium is obtained by integration over the elements dS_ω of the iso-frequency surfaces S_ω in the k -space. For a frequency interval $d\omega$, the thickness of the shell containing the dN states searched for in the k -space reads as follows: $dk = v_g d\omega$. This generic density of states can be expressed in the form of a summation over the elementary volumes $dS_\omega dk$, and more specifically in the form:

$$D^s(\omega) = \frac{1}{V} \frac{dN}{d\omega} = \frac{1}{8\pi^3} \int_{S_\omega} dS_\omega v_g d\omega \quad (5.6)$$

In the case under consideration here of a channel waveguide with a section S , and remaining within the assumption, to be verified afterwards, that the number of branches is relatively large, the linear density of states is approximately:

$$D_{lin}^s(\omega) = S D^s(\omega) \quad (5.7)$$

The planar form of this equation can be readily obtained by replacing S with the thickness of the waveguide, which will be denoted here by L_y . While the above equations are somewhat trivial, it might be noted here that photonic crystals may exhibit a large variety of different types of volume densities of states $D^s(\omega)$, for instance a very low density of states over a large frequency interval. Such a material, used in the form of relatively thick guiding layers, will allow the propagation of only a relatively small number of modes, down to a single mode.

Let us return now to the examples represented in Fig. 5.5. When the width of a waveguide decreases, the number of allowed states decreases as well, and the mode cutoffs associated with regions where the group velocity is zero result in the appearance of more marked singularities in the density of states. However, the description of these singularities turns out to be more complex in the two-dimensional (planar waveguides) than in the one-dimensional case since they are now going to depend on the finer structure of the Brillouin zone. Here again, it might be emphasised that there is not in general any isotropy between the x and y directions of a planar waveguide.

When the width of a waveguide further decreases, only one or two dispersion branches remain, be it in the channel or in the planar case. These dispersion branches may not extend over the entire band gap of the cladding and therefore they may leave frequency ranges with a true zero-density of states. For extremely thin waveguides, the remaining modes can be compared to shallow defects in semiconductors, as those formed by dopants, since they typically extend only over a very small band near one of the edges of the band gap. For the simplest types of structures, the high-frequency band located just above the band gap is an air band, whereas the low-frequency band below the same gap is a dielectric band (see Chapter 1). The introduction of an ultrathin waveguide proceeds either by adding or by removing dielectric. The corresponding guided mode then presents essentially the same characteristics as the associated band, save for a small frequency shift. In particular, the electromagnetic field of the mode extends mainly in the cladding, where the defect formed by the waveguide ‘anchors’ this mode, much in the same way as shallow dopants or defects do in semiconductors. A strong similarity also exists with the surface modes which have been described in Section 1.4.6 of Chapter 1.

5.2.5 Coexistence of Index Guiding and Photonic Bandgap Guiding

Nature of the Defect Mode

Index guiding and photonic bandgap guiding should not be viewed as exclusive of one another. As has just been recalled in the preceding section, the introduction of a defect in a bulk crystal creates a mode whose characteristics are essentially the same than those of the air band (at high frequency) or of the dielectric band (at low frequency) depending on whether the defect is formed by adding or by removing some material. For instance, creating the ‘air’ defect amounts to separating two semi-infinite photonic crystals in such a way as to form an air layer between these two crystals. This approach is frequently used when dealing with dielectric columns. By contrast, the method generally favoured for forming a waveguide in an array of holes consists in suppressing some of these holes, i.e. in filling them.

In the case of an ‘air’ defect, no index guiding occurs, since the effective phase index of the mode, i.e. the ratio kc/ω , is not high enough compared to that of the

cladding. Indeed, if the cladding has transmission bands, then their effective index are to be higher than unity. For all values for k along the dispersion branch, the confinement of the guided wave involves multiple reflections on the photonic band gap material. A genuine ‘photonic bandgap guiding’ can thus be achieved. The general idea of such a system can be traced back to the pioneering work by Yeh and Yariv (Yeh 1976). However, the use of a high index contrast and of the entire frequency range of the band gap makes for a much powerful approach than the scheme originally proposed by Yariv, since the latter relied on the use of one-dimensional structures with very limited operating ranges.

In the case of a dielectric defect, the situation is quite different. At the lowest values for k along the dispersion branches in the band gap, the physical mechanism still involves multiple reflections at the cladding formed by a photonic crystal material. If this crystal were to be replaced with a cladding formed by an homogeneous material with a low index, then the guided modes would turn into a series of weak resonances. This is quite different from the situation occurring at higher values for k . Indeed, in the latter case, the guiding mechanism would be essentially the same if the photonic crystal were to be replaced with an homogeneous material with an average index of the same order of magnitude. In other terms, the physics of this phenomenon are in most respects the same as those of index guiding.

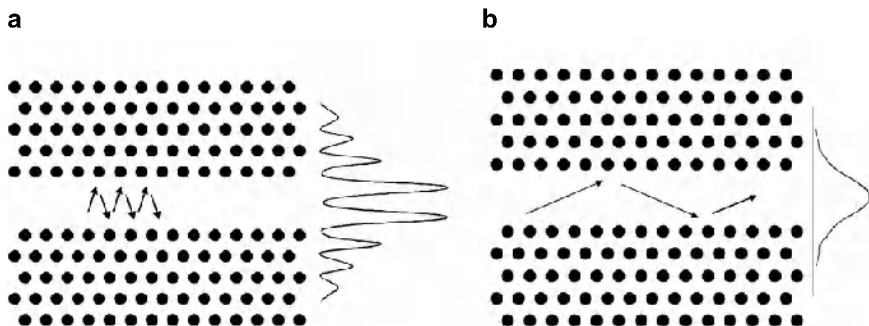


Fig. 5.6. Waveguide created in a triangular array of holes by omitting to drill a few rows of such holes **a**. Propagation (represented by arrows) and schematic intensity profile of a Fabry-Perot type mode close to the normal incidence **b**. Propagation and schematic intensity profile for a mode in the case where index guiding is the main guiding mechanism

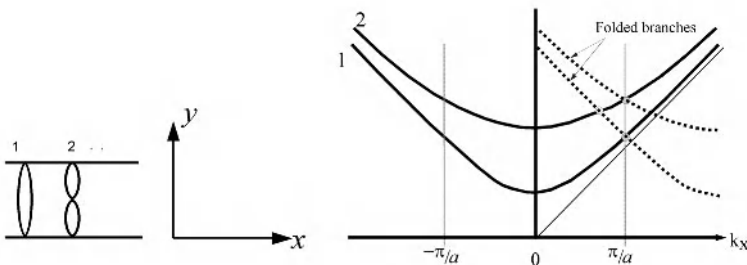


Fig. 5.7. Effects induced by periodicity. *a*, Ideal waveguide with a cladding formed by perfectly conducting metals *b*, Dispersion diagrams (solid lines) and effects induced by periodicity on an ‘empty lattice’ (dotted lines). The duplication at a $2\pi/a$ interval creates the impression of a folding of the dispersion branches

Thus, in the case of dielectric effects, index guiding occurs on a part of the dispersion branch of each mode. Let us consider here again the case, represented in Fig. 5.6, of a dielectric matrix where a triangular lattice of round air holes has been drilled save for a few rows that were omitted for creating a waveguide. At $k_x = 0$, the ‘guided’ mode will be analogous to the mode of a Fabry-Perot resonator formed by two perfect mirrors ($R \sim 1$), as is represented in Fig. 5.6a.

In spite of a certain penetration of the field in the photonic crystal, leakage is formally prevented by the fact that the cladding of the photonic crystal waveguide is assumed to be infinitely thick. This remains true for non-zero, albeit relatively small angles of incidence ($k_x \neq 0$), whereas for larger angles, index guiding will occur. We may assume that one goes to lower branches in order to remain within the band gap of the cladding when k_x and the frequency increase. However, as has been discussed in Section 2.3 of this chapter, index guiding may well subsist even in the absence of an omnidirectional band gap. Finally, for the largest values of k , the field of the fundamental mode does not penetrate far in the cladding, whose effective index is low enough for enforcing index guiding and the exponential decay of the field, as can be seen in Fig. 5.6b. This is all the more true in the case where we have travelled along the dispersion branches down to the fundamental guided mode. This effect will be met again in Chapter 11 when studying microstructured fibres.

Effects of Periodicity on Photonic Bandgap Waveguides

Index guiding is the main guiding mechanism for waveguides formed by photonic crystals where a dielectric defect has been created. However, these waveguides present a marked periodicity which must be accounted for. In order to provide a simple analysis of the effect induced by periodicity, we shall begin with the only type of waveguide which can easily be modelled, that of a perfect waveguide con-

fined by ideal metallic planes. In addition, we shall restrict ourselves here to a two-dimensional analysis and to a scalar approach.

This restriction can be justified by the fact that even in the case of simple slab waveguides, it is not possible to arrive at an analytical expression of the dispersion relation (see Chapter 9). The idealised waveguide represented in Fig. 5.7a presents a width L along y and allows the propagation of modes with a scalar field of the form:

$$E = E_0 \sin(k_y y) \exp(ik_x x) \exp(-i\omega t) \quad (5.8)$$

with $k_y = m\pi/L$, where m is an integer. The latter condition ensures that the boundary conditions calling for a zero field at the walls of the waveguide are satisfied (Fig. 5.7a). Denoting by n the refractive index of the waveguide, the dispersion relations assume the following form:

$$\omega_m = \frac{c}{n} \sqrt{k_x^2 + \left(m \frac{\pi}{L}\right)^2} \quad (5.9)$$

while the corresponding dispersion curves are hyperbolic branches, as can be seen in Fig. 5.7b. Similar hyperbolic branches can be observed around $k_x = 0$ in the diagrams represented in Fig. 5.5. This emphasizes the relevance of this model.

Let us now introduce a fictitious period a , corresponding to what is referred to as the ‘empty lattice’ in crystallography. In this case, everything will occur as if k_x were defined modulo $2\pi/a$, which results in the appearance of a ‘folding’ in the dispersion diagram at the edge of the Brillouin zone $k_x = \pi/a$. Actually, a $2p\pi/a$ shift is indeed required in order to bring all dispersion branches back into the first Brillouin zone $[-\pi/a, \pi/a]$. However, since $\omega(-k_x) = \omega(k_x)$, the impression created is exactly that of a folding at the edge of the zone. In the example considered here of a metallic waveguide, such a periodicity could be introduced in the form of a corrugation with a period a along the metallic walls of the waveguide. The Fourier components of the permittivity would then be non-zero at all multiples of $2\pi/a$, and in particular they would be so at $2\pi/a$ itself.

Such a folding of the dispersion branches may induce dramatic effects on guided waves. This is especially true when two branches tend to cross one another, i.e. when two of the ideally guided modes in Fig. 5.7 interact due to the $2\pi/a$ shift between them. At the edges of the zone, i.e. in this case at $-\pi/a$, 0 or at π/a , photonic gaps similar to those described in Section 1.3.2 of Chapter 1 appear. Fig. 5.5 presents examples of such phenomena, more particularly for the lowest branches at π/a .

The most original effect occurs when a crossing takes place outside the edges of the zone. In this case, two dispersion branches associated with modes of a different nature are necessarily involved. The coupling between modes induced by periodicity allows energy transfers from one mode to the other, provided that the

symmetry rules are satisfied, as will be seen later. According to a microscopic and unfolded view, the polarisation induced by one of the two modes presents a small spatial component at the spatial frequency of the other mode. This simply results from the multiple Fourier components of the dielectric constant which are seen by the two modes. Accordingly, the interaction between the two modes results in a lifting of the degeneracy at the crossing point and in an anticrossing of the dispersion curves. In other terms it leads to the appearance of a band gap between the two modes. This phenomenon can be observed in several of the examples presented in Fig. 5.5. Indeed, when considering the propagation of the fundamental mode at variable frequencies, a significant attenuation can be observed in the spectral region where the anticrossing occurs. This phenomenon has been termed by some authors as a ‘mini-stopband’ in order to distinguish it from the usual stop band (Olivier 2001b). In reality, this phenomenon is not a photonic band gap in the strict sense of the term since the cancellation of the photonic density of states can be actually prevented by the contribution of other modes which, while not being involved at all in the process discussed here, may nonetheless exist with the same frequency. For instance, if a large number of guided modes exist in the spectral region where the anticrossing of two modes occurs, no significant change will arise in the density of states at the corresponding frequencies inside the mini-gap, although a very strong attenuation of the fundamental mode will be measured in practice.

It might be noted here that an interpretation of this phenomenon in terms of a diffraction by a grating can also be attempted. Indeed, the law of diffraction by a grating, expressed in terms of wave vectors, comes down simply to $\Delta k = 2p\pi/a$. Accordingly, and going back to the representation of guided modes as a superposition of two oblique plane waves (represented by zigzag rays in Figs. 5.3 and 5.6), these plane waves can be diffracted by the grating formed by the walls of the waveguide themselves. For the sake of simplicity, we shall assume here that the corrugation of the wall of the waveguide is reasonably ‘flat’, and therefore that plane waves will arrive with the same well-defined incidence at all points of the wall. Likewise, the diffracted plane waves will undergo the same multiple reflection processes at the walls than the original waves from which they have been generated. However, since the diffracted waves propagate with a different angle, these multiple reflection processes will generally lead in this case to destructive interferences, with the consequence that almost no energy will be taken out of the original guided mode. By contrast, in the specific situation where the phase-matching condition is achieved for the multiple reflections of the diffracted waves, another eigenmode (guided mode) of the structure can be excited from the original guided mode. In other terms, the phase-matching that results from the periodicity may lead to a coupling between two different modes. The general ideas of coupled mode theory are relevant in this context, and the reader is referred for instance to the work by H. Kogelnik in (Tamir 1990). As for the one-dimensional photonic band gaps discussed in Section 1.3.2 in Chapter 1, the spectral width allowed around resonance, i.e. in this case the spectral width of the anticrossing, is strongly dependent on the amplitude of the Fourier component of the dielectric constant, which is involved in either of the two coupled modes.

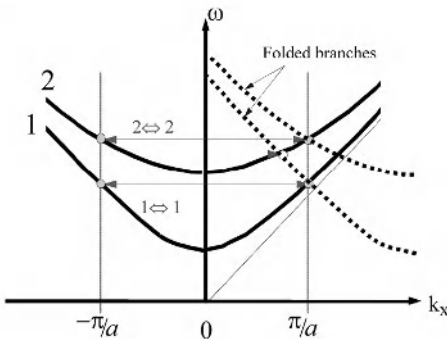
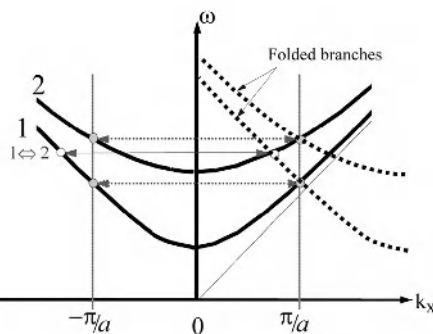
a**b****c**

Fig. 5.8. Effects induced by periodicity (*continued*): **a.** ‘Diagonal’ coupling with a band gap at the edge of the Brillouin zone **b.** Coupling between different modes and gap in the middle of the Brillouin zone, **c.** Schematic representation of a waveguide created in a triangular lattice with 1, 2 and 3 missing rows: the spectral interval between the dispersion branches decreases when the number of missing rows increases. The symmetry alternates: W1 and W3 have a symmetry plane along the axis of the waveguide and only branches with the same parity are coupled, with the $1 \Leftrightarrow 2$ coupling being forbidden in particular. Conversely, W2 requires a glide operation (shift of a half period + symmetry) in order to remain invariant and only branches with opposite parities are coupled

When the periodicity of the two walls of the waveguide is symmetric with respect to the axis of the waveguide, which is the case for all the examples represented in Fig. 5.5, coupling phenomena occur only between modes with the same

parity. Conversely, for modes with opposite parities, the overlap integral between the fields of the modes and the periodic ‘potential’ is zero. This is similar to what occurs in quantum mechanics, where the selection rules are reflective of the cancellation of the matrix elements.

As will be seen in the third part of this book, triangular lattice of holes of the type represented in Fig. 5.8 are generally preferred in guided optics over other structures. In this case, the periodic structures at each side of the waveguide are symmetric with respect to the axis of the latter if an odd number of rows is omitted along dense directions of the crystal. Conversely, for an even number of missing rows, the holes alternate, with a shift of a half period being required in addition to the symmetry operation for retrieving the original structure. In the latter case, only modes with opposite parities will be coupled. It can easily be seen that in the real space, the contributions of modes with the same parity shall be in phase opposition (with respect to the spatial period a) at the two walls of the waveguide. In the reciprocal space, this amounts to introducing a structure factor $\exp(-i\pi) = -1$, hence a mutual cancellation of these contributions, which here are dependent on the optical polarisation $\mathbf{E}\delta\epsilon(\mathbf{r})$. The considerations developed above suggest that at the frequencies where such crossings occur, an original method exists for controlling the interaction between two guided modes through the control of the relative spatial phase of the two walls of the waveguide.

At this point, it might be emphasised that the irregularities of the photonic crystal waveguide resulting from an imperfect fabrication, for instance irregularities in the shape of the holes at the edges of the waveguide, may actually induce parasitic mode coupling effects. These irregularities induce irreproducible, albeit non-zero Fourier components and therefore non-zero couplings in a system where the effects must exactly compensate for one another. The risk therefore exists here that any crossing will result in a coupling and in an energy transfer, although this phenomenon can be expected to remain of a much lower order of magnitude than the structural coupling previously described.

Before concluding these remarks on the subject of irregularities, it seems intuitively sound that, when there are either one too many or one too few entire patterns, significant perturbations will occur in a photonic crystal waveguide. In this respect it might be noted that the insertion or removal of such a pattern brings us closer to resonators, which will be discussed in the following section. From a practical point of view, ‘deterministic’ fabrication processes only induce more or less important irregularities between the patterns. By contrast, photonic crystals obtained by self organisation (see Section 12.2.2 in Chapter 12) may precisely present the kind of defects which have been discussed here, in the form for instance of a missing sphere in an opal. When defining a waveguide in such a system, one needs of course to carefully avoid such ‘native’ defects.

It is quite clear that the mode coupling phenomena which have been discussed here cannot occur in the case where the waveguide is by construction single-mode. We shall later discuss in the third part of this book the conditions needed for achieving such a single-mode regime.

5.3 Resonators

5.3.1 Localised Modes. Origin of Losses

The introduction in an infinite crystal of a point defect, for instance through the modification or the removal of some pattern, leads to the appearance of at least one localised mode within the photonic band gap. Assuming an infinite lossless crystal with an internal excitation of such a localised mode, the energy stored in the mode would never decrease. In reality however, a crystal is necessarily finite, and the electromagnetic field of the localised mode, even if it decreases exponentially with the distance from the defect, will couple at some point with the radiation modes outside the crystal. In practice, two limit situations may arise: first, in the case where a relatively large number of crystal rows or planes exist around the defect, the leakage due to radiation modes is negligible compared to other energy decay mechanisms such as the residual absorption or the imperfections of the structure, whatever the type of the photonic crystal is, for instance whether it is a self-assembled or a deterministic structure. By contrast, the second limit case occurs when the number of planes or of rows is limited, and typically lower than five, along one or several direction(s) of space (see Fig. 5.9, and Section 1.4.2 in Chapter 1). In this case, the main energy decay mechanism is the coupling of the defect mode to the radiation modes of the surrounding medium, which occur through the limited number of planes or rows.

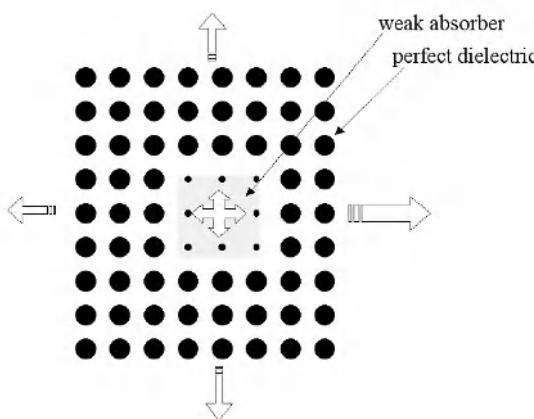


Fig. 5.9. Localised mode in a defect formed by one missing atom and eight smaller ones, with some internal dissipation (*grey absorbing zone*) as well as radiation losses due to the leakage occurring through the photonic crystal (*outgoing arrows*)

It is convenient to quantify each loss channel with a quality factor which is in inverse proportion to the resulting photon flux. For instance, Q_{sys} shall denote here the quality factor associated with the absorption and imperfections of the crystal, while Q_{PBG} shall denote the quality factor associated with the field leakage and the subsequent radiation losses resulting from the finite size of the crystal. Denoting by N the number of layers around the defect, then Q_{PBG} will increase exponentially with N . The overall quality factor Q , which describes the number of periods of the oscillating electric field after which the energy of the localised mode has decreased by $1/e^2$, and the amplitude of the field by $1/e$, is then simply given by the equation:

$$Q = (Q_{\text{sys}}^{-1} + Q_{\text{PBG}}^{-1})^{-1} \quad (5.10)$$

One may further distinguish losses resulting from microscopic, fluctuating and irreproducible imperfections of the crystal and losses associated with some intrinsic geometrical feature of the system under consideration. Losses of the first type are at the origin of Rayleigh scattering phenomena (Born 1965) in strongly textured environments, and more particularly in three-dimensional crystals. Examples of losses of the second type include etching defects, for instance the frequent narrowing from top to bottom of the holes in two-dimensional arrays of holes. In two-dimensional systems where in-plane confinement is generally accompanied by an index confinement along the vertical direction (see Section 5.4 in this chapter and Chapter 9), radiation losses may also occur in the substrate or superstrate layers of the cladding, which add to radiation losses due to the finite size of the crystal (Q_{PBG}). Indeed, as has been discussed earlier in Section 5.1, index guiding is significantly less efficient than photonic bandgap guiding as regards the suppression of radiations along all directions. For instance, in the case of a photonic crystal created by etching a membrane, radiation losses are systematically and almost inevitably associated with all localised modes.

5.3.2 Density of States

Since the modes of a localised defect are discrete, the density of states turns out to be a series of Dirac peaks (see Section 1.4.7 in Chapter 1), whose amplitude in the sense of distributions reflects the possible degeneracies of the modes. These degeneracies are in general associated with certain geometrical invariances. The presence of leakage mechanisms transforms the density of states into a series of Lorentzian peaks with a finite width. If these Lorentzian peaks were to significantly overlap, then the description in terms of localised modes would cease to be adequate.

The number of modes associated with a defect follows the general laws applying to waveguides which have been described in Section 5.2.4 of this chapter. If the defect consists of a volume of some homogeneous material, then, for large

volumes, the number of modes per unit frequency tends asymptotically towards the value associated with this bulk material $V \times D_2(\omega)$. Therefore, for a three-dimensional system, $D(\omega)$ will be in proportion to $n^3 \omega^2$ (see Section 1.4.7).

The different localised modes of a given defect may exhibit very different loss characteristics, and therefore different quality factors. The problem of losses in this context presents much the same issues as for the photonic crystal mirrors which have been discussed in Section 5.1. It is apparent that evanescent waves generated in the vicinity of the defect shall exhibit different characteristics along the different directions of the crystal. In general, evanescent waves propagating along different directions have different spatial decay constants (imaginary part of k). However, all the modes localised in the band gap have an evanescent part in the crystal, which actually is a superposition of such evanescent waves, with coefficients depending in a nontrivial way on the shape and index structure of the defect. As a consequence, the determination of the quality factors will also be nontrivial. In most studies, modes are first classified according to the spatial field pattern and symmetry, as for instance the whispering-gallery modes of microspheres and microdisks. The characteristics of the modes as regards the frequency or the losses are then investigated with respect to some variable parameter, for instance the air filling factor of the surrounding crystal, or the shape of the defect or cavity. The results thus obtained are then used in order to quantitatively verify that the mechanisms that were heuristically inferred are actually present (Vuckovic 2002a).

As an example, in the case where photonic crystal microcavities are used as filters between two access waveguides, the central issue will be the coupling with external waves, and in this example with guided waves. If this coupling is intrinsically weak, then the maximum transmission of the microcavity shall remain low even if the quality factor Q of the excited mode is high. In this case, there simply is not point in increasing the number of rows or planes of crystal isolating the cavity from the waveguides. This is only one aspect of the broader issue of the coupling between a waveguide and a cavity, which still remains an open field for research.

5.3.3 Waveguide formed by Coupled Cavities

While the coupling between a waveguide and a photonic crystal microcavity is of a great importance for a number of applications, the possibility also exists of devising applications that would rely on a coupling between such microcavities. This intuition led N. Stefanou in 1998 (Stefanou 1998), and more pedagogically A. Yariv in 1999 (Yariv 1999), to propose the concept of a coupled resonator optical waveguide (CROW) or chain of coupled resonators. The underlying idea is to create a waveguide by approaching isolated cavities from one another so as to form in the end a periodic chain of such cavities. The principles of this waveguide are schematically represented here in Fig. 5.10.

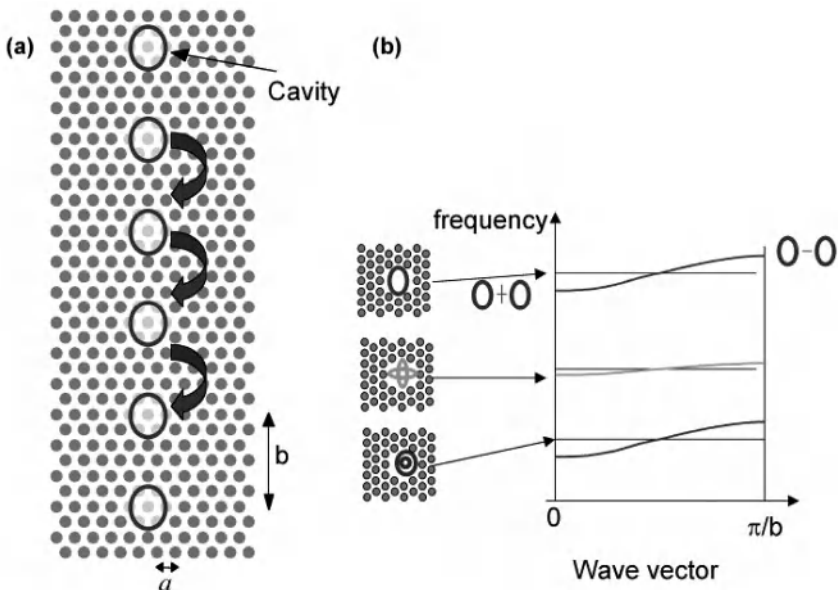


Fig. 5.10. *a.* Example of a coupled cavity waveguide, formed in a triangular lattice of holes by cavities of seven missing holes each. The ovals in the figure represent isolated cavity modes *b.* Formation of narrow bands around each frequency of an isolated cavity mode, for frequencies within the photonic band gap. Note the transition along each branch from a totally symmetric global mode at low frequency ($k_x = 0$) to an anti-symmetric global mode at the edge of the zone ($k_x = \pi/b$)

Readers familiar with solid state physics will immediately recognize here the tight-binding approach, where an electron is strongly bound to an ion although its wave function only marginally overlaps neighbouring ions. For the description of the electromagnetic field and for the dispersion relations, we shall remain here within the formal framework introduced earlier in Section 5.2. The interest of the coupled cavity waveguide is that it leads to dispersion relations which are both simple and quite remarkable for the guided modes. These relations are simple due to the fact that each band is centred in frequency around the eigenmodes of a single cavity. Thus, the equation for the frequencies is:

$$\omega(k_x) = \omega_0 + \Delta\omega \cos(k_x b) \quad (5.11)$$

where ω_0 has about the same value as the frequency of an isolated cavity eigenmode, b is the spatial period of the cavity in the chain and $\Delta\omega$ is a spectral width which depends on the strength of the coupling between the cavities, and therefore on the number of crystal rows separating any two cavities. $\Delta\omega$ also depends on the

value of the quality factor Q_{PBG} introduced in Section 5.3.1, which represents the total intrinsic radiation loss associated with a given cavity.

Slightly increasing the number of rows between the cavities, hence the value for b , causes the spectral width $\Delta\omega$ to decrease and therefore the group velocity to decrease as well. As can be seen in the band diagram represented in Fig. 5.10b, the guided branches become narrow bands, each of which is almost centred on a mode of the isolated cavity.

The main argument in favour of coupled cavity waveguides is their conceptual simplicity. In standard photonic crystal waveguides, there are almost no simple guideline for the resolution of certain inverse problems, for instance the problem of finding shapes and frequencies that would minimise the group velocity of propagating waves.

From a practical point of view, it is quite obvious that the individual cavities of the CROW should not present too high a level of losses, since such losses would result in a dissipation of most of the energy before even reaching the next cavity. In other terms, propagation in such a case would be achieved only at the price of unacceptable attenuation losses.

By way of concluding Sections 5.1, 5.2 and 5.3, it has been seen in these three sections that a confinement of the electromagnetic energy by photonic band gap crystals can always be achieved. However, due to the complexity of the interactions between light and photonic crystals, this confinement may assume a large variety of forms. The fundamental phenomenon, which is without equivalent in perfectly metallic waveguides, is simply the diffraction induced by the periodicity. When considering this effect in the context of guiding, a further degree of complexity arises due to the interplay between diffraction, which leads to certain values for Δk being privileged, and confinement, which imposes that a phase-matching condition be satisfied between the two walls of the waveguide. The guiding mechanism in such waveguides can be partly an index guiding. Systems based on the combination of waveguides and resonators are a very promising branch of research on photonic crystals, provided however that an optimal mode engineering be developed. In the following section, we shall see that for the actual, and more easily realisable two-dimensional structures, another level of complexity arises.

5.4 Hybrid Structures with Index Guiding. The Light Line

The higher degree of maturity of two-dimensional systems, compared to three-dimensional systems, is the main incentive for attempting to achieve a control of light in these two-dimensional systems while at the same time trying to implement a ‘partial’ confinement along the third direction. The latter objective can be achieved by using an index contrast, i.e. by resorting to a phenomenon of total internal reflection. The confinement by a homogeneous medium of lower index along the third direction is necessarily partial, since we are no longer dealing with simple planar interfaces. Accordingly, the very concept of total internal reflection

needs in this case to be abandoned or at least to be significantly revised. An understanding of the specific features displayed by these hybrid structures is therefore necessary since, as will be seen in Chapter 9, they are a strategic issue for the development and implementation of photonic crystal integrated optics.

5.4.1 Light Cone of a Uniform Waveguide

Let us first recall here the concept of ‘light cone’ in the simple case of an optical slab with a finite thickness and an index n_{core} , cladded by media with index n_{clad} . The guided modes of such a slab possess a propagation constant $\beta = k_{\parallel}$, which is necessarily larger than $n_{clad}\omega/c$.

The dispersion curves of these modes lie outside the cone $k_{\parallel} = n_{clad}\omega/c$, referred to as the light cone. In the example represented in Fig. 5.11a, \mathbf{k}_{\parallel} is a two-dimensional vector while the line(s) $k_{\parallel} = n_{clad}\omega/c$ would describe a cone in the space (k_x, k_y, ω) . Any mode in the light cone is said to be a ‘radiation’ mode: such a mode is a wave arriving at a certain incidence angle from one of the claddings, which undergoes multiple reflections at the two interfaces of the core as it travels through it, before propagating at infinity in the other cladding. Contrary to guided modes, these modes form a continuum with a variable density of states, which however exhibits a singularity just at the surface of the light cone. This density of states will turn out to be a crucial parameter when the coupling of localised modes to the continuum will be analysed as a perturbation. According to this view, the proper guiding of the wave in the core is ensured by the fact that no mode with a value for k_{\parallel} high enough exists in the cladding, thus preventing the coupling to the continuum formed by radiation modes. This description is strictly equivalent to the argument that $\sin\theta < 1$, in the account given by Snell’s law of total internal reflection.

5.4.2 Fictitious Periodicity

Proceeding along the same lines as in Section 5.2.5, we shall now introduce a one-dimensional fictitious periodicity in the core of the planar waveguide. It should be borne in mind however that the core of the waveguide actually remains fully invariant. The period and the periodic axis will be denoted by a and x respectively. Any guided mode can then be decomposed into Bloch modes. In other terms, the guided modes can be described in terms of a multiplicity of wave vectors k_{\parallel} defined modulo $2\pi/a$ and associated each with a given dispersion branch. This leads to indefinitely duplicating the initial dispersion diagram by $2\pi/a$ shifts. The result is identical with the ‘folding’ of the dispersion branches that has been observed earlier, with the specificity here that, according to this representation, branches with opposite group velocities tend to meet at $k_{\parallel} = \pm \pi/a$, as can be observed in Fig. 5.11b.

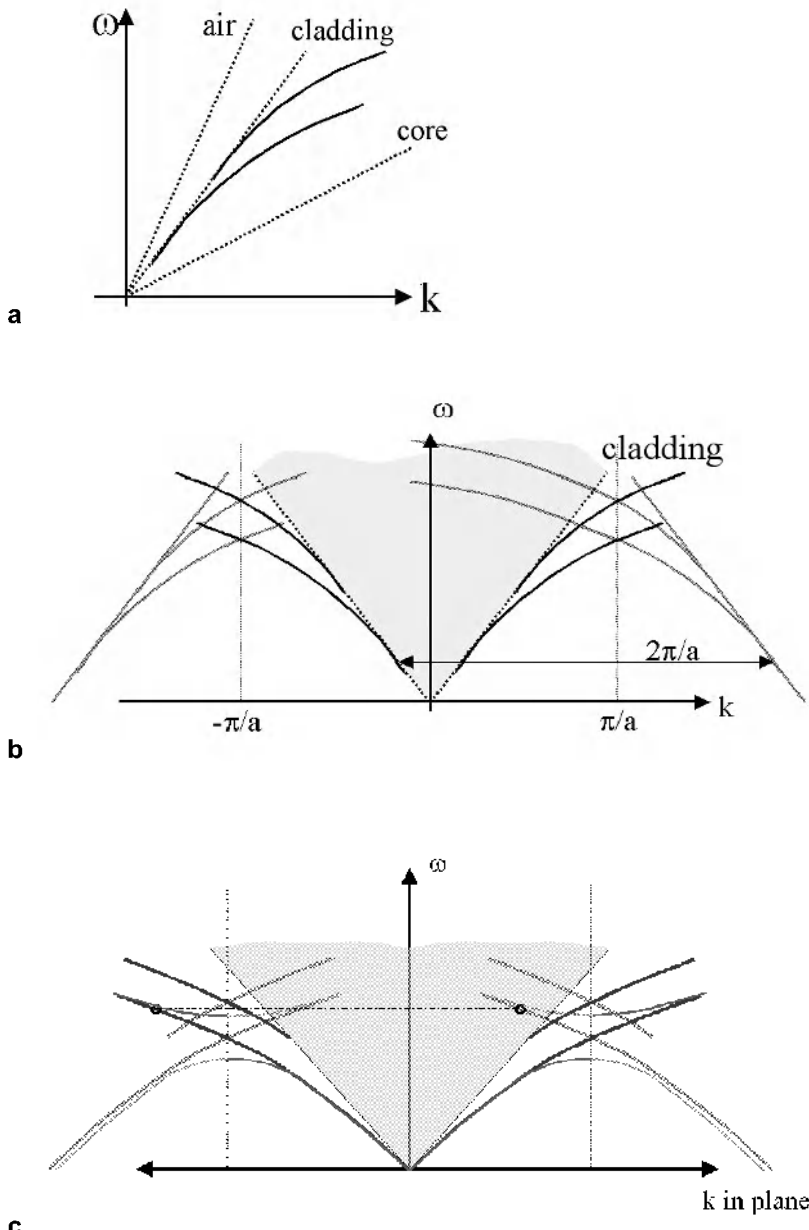


Fig. 5.11. The light line (or light cone). **a.** Case of a uniform slab **b.** Waveguide with a fictitious periodicity, where a folding phenomenon occurs **c.** Waveguide with a true periodicity: band gaps appear but contrary to **b** the modes above the light line present proper non-zero coefficients for the corresponding Fourier components, resulting in the possibility of leakage and radiation loss in the cladding

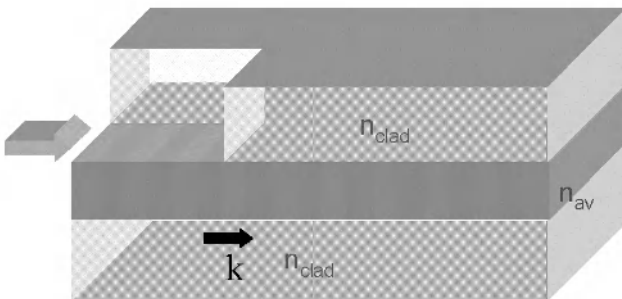


Fig. 5.12. Waveguide with a true one-dimensional periodicity (in this case a variation in the refractive index of the core)

Quite strikingly, this implies that branches that previously were outside the light cone may now partly or completely lie inside it. At this stage, the folding expresses the fact that the periodic part of the Bloch wave can be developed into a Fourier series whose successive orders are the spatial periods multiple of $K = 2\pi/a$. According to the Bloch theorem, the coefficients of these different components are generally non-zero. Yet, since the periodicity in this case is only fictitious, only the fundamental Fourier component associated with the dispersion relation represented in Fig. 5.11a actually exists. The introduction of a fictitious period has therefore led to introducing harmonics of this wave, albeit with rigorously zero coefficients. For this very reason, and despite the branches lying in the light cone, no leakage whatsoever occurs in the continuum of modes.

5.4.3 True One-Dimensional Periodicity

Let us now turn to the consideration of a true periodicity rather than a fictitious periodicity (Figs. 5.11c and 5.12). In this case, the Bloch wave now actually contains several components with non-zero coefficients. Another effect induced by true periodicity is to cause couplings, either between counterpropagating modes at the edges of the Brillouin zone, or inside this zone between modes of a different nature (see Section 5.2.5). In particular, band gaps appear for dispersion branches located near the edge of the Brillouin zone at $k_{\parallel} = \pm \pi/a$.

From the observation of the band diagram represented in Fig. 5.11c, two possible situations may be distinguished. These two situations will be extended to waveguides with a core formed by a two-dimensional photonic crystal, where the

concept of light cone is to be preferred over the concept of light line¹. These two situations correspond respectively to:

- lossless modes, which can be defined as modes lying outside the light cone in the folded band diagram, i.e. in the diagram restricted to $[-\pi/a, \pi/a]$ according to the one-dimensional approach, and without any harmonics inside the light cone, since all these harmonics are outside the Brillouin zone.
- ‘resonant’ modes, also referred to as ‘leaky’ or as ‘lossy’ modes. These modes can be defined as modes lying inside the light cone in the first Brillouin zone. The case may arise where only one component, for instance, the zero-order component identified in a perturbative approach, lies in the light cone while the others lie outside. This will nonetheless suffice to induce a leakage and therefore radiation losses. The strength of the coupling to the continuum modes depends on the value of this non-zero coefficient.

Fig. 5.13 illustrates for a waveguide with a true one-dimensional periodicity the three cases of a pure guided mode (Fig. 5.13a), of a pure ‘radiation’ mode (Fig. 5.13b) and of a ‘resonant’ mode lying above the light line (Fig. 5.13c) respectively. The wave vectors associated with these different modes are also presented in these figures.

As far as ‘resonant’ modes are concerned, the existence of a coupling of these modes to a continuum prevents them from being described as modes in the strict sense of the term. Even in the case of lossless materials, the lifetime τ of a photon in the state considered is finite. The spectrum of the mode can no longer be represented by a Dirac peak as was possible for discrete modes. It now exhibits a Lorentzian profile, whose width at half the maximum is inversely proportional to the lifetime of a photon. Accordingly, the mode may only propagate over a finite distance. In terms of wave vectors, the resonance has a width Δk which is inversely proportional to the propagation length.

The use of the term ‘resonance’ can be justified as follows: if a wave propagates from the cladding with appropriate values for \mathbf{k}_{\parallel} and ω , its energy will be concentrated in the waveguide during a time τ , just as would be the case in a Fabry-Perot resonance. A description in terms of modes can therefore be restored, but only at a high price since the whole universe is now to be considered for all modes, while the ‘resonances’ will be denoted by the relative concentration of energy in the waveguide.

¹ In the case where not only the core but also the cladding are formed from a periodically structured material, the concept of light cone may still be used provided that the modified photon dispersion relation of the cladding be taken into account. This obviously leads to a distortion of the straight cone represented in Fig. 5.11. A first approximation consists however in modelling the cladding as an homogeneous material with an average index.

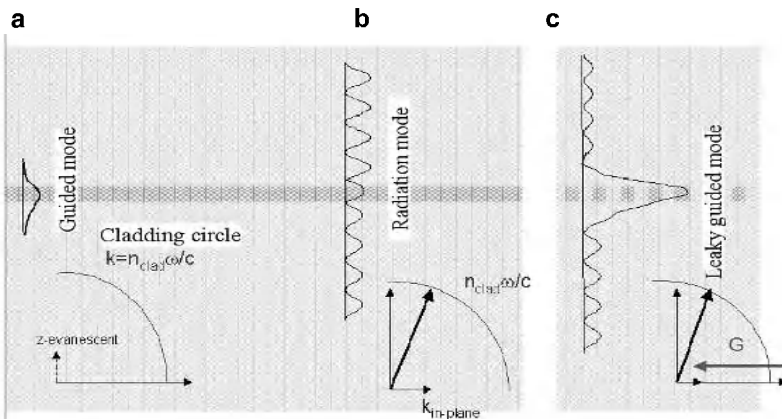


Fig. 5.13. *a*, Uniform waveguide and profile of a guided mode *b*, The same waveguide with the profile of a radiation mode *c*, Corrugated waveguide and profile of a resonant mode. The relevant components of the wave vector in each case are schematically represented below these figures, in particular the in-plane component k_{\parallel} . This component is larger than the radius $n_{\text{clad}}\omega/c$ for the guided mode represented in *a* and smaller than $n_{\text{clad}}\omega/c$ for the pure radiation mode represented in *b*. For the resonant mode represented in *c*, the periodic modulation (G) couples the two types of modes. The resulting hybrid mode presents Fourier components which are related both to the guided and to the radiation cases

An elegant mathematical description of such a resonance consists in using the complex poles ($\mathbf{k}_{\parallel}, \omega$) in the scattering matrix, following an approach similar to the method described in Section 2.1.1 in Chapter 2, but adapted to structures with a finite height (Le Vassor d'Yerville 2002; Whittaker 1999). From an experimental point of view, these resonances are revealed by the presence of singularities in the reflectivity curves when the system is illuminated from the cladding at variable angles and frequencies (Astratov 2000; Patrini 2002). The anomalous reflection by gratings and its modelling are still intensively studied in the field of electromagnetism, and these researches should benefit to the study of photonic crystals as well. This method provides an access in the band structure of quasi two-dimensional systems, at least for the part which lies in the light cone.

5.4.4 Channel Waveguides in Two-Dimensional Photonic Crystals

When a channel waveguide is created by omitting one or several rows of elements in a two-dimensional photonic crystal, the situation is in most respects the same as what has just been described in Section 5.4.3. This case will be addressed in more

detail in Chapter 9. The essential modification is that consideration must now be given to modes confined both laterally by the photonic band gap effect and vertically by an index contrast. Of course, the problem of the confinement of modes propagating at the frequency of the band gap did not occur in the case of a two-dimensional crystal without defects.

In light of the preceding discussion, the guided modes of a channel waveguide created in a two-dimensional photonic crystal can be expected to be either lossless modes or ‘resonant’ lossy modes. This is a crucial issue for the development of applications of these waveguides.

It might be appropriate at this point to provide a few indications on the subject of two-dimensional cavities in the context of a vertical index guiding. In the case of a localised mode, defining a wave vector is not of course possible, and the very concept of light cone is no longer valid. A coupling necessarily occurs between the cavity modes and the radiation modes, which in turn leads to a reduction of their quality factor. Hence, while lossless modes may theoretically exist for waveguides formed from a two-dimensional photonic crystal slab waveguide, the cavity modes created in the same structure will necessarily be leaky. Nevertheless, the possibility exists from an experimental point of view of designing intermediary systems where potentially lossless waveguides and (leaky) cavities would be combined. For instance, let us here consider an elongated waveguide closed at both ends. Actually, such a waveguide is but a very elongated cavity. While light may propagate without undergoing any loss along the waveguide, a leakage is bound to occur due to the reflection of light at the closed ends. Whatever the length of the waveguide is, the situation is locally the same at both ends (at least asymptotically, since the radiation losses occurring at one end should not be seen by the other). Accordingly, when analysing such an elongated cavity, it might be considered that it presents localised losses. This is clearly at variance with the usual analysis of cavities, where losses are generally considered as a whole.

In this section, we have described in formal terms the physical aspects of systems where a double optical confinement is achieved, i.e. where both a photonic bandgap guiding and an index guiding are involved. These aspects will be of particular importance for applications of these systems. In this respect, a most important problem is that of quantitatively determining the losses of ‘resonant modes’. In view of both the complexity of the underlying electromagnetic problems and the relatively recent development of theoretical tools for their resolution, an exhaustive analysis of this subject would be beyond the scope of this book. Nevertheless, this question will be discussed in the third part of this book in relation to certain specific examples which have now become well-known.

6 Refractive Properties

Photonic crystals can be used either as mirrors or as reflective walls in waveguides at wavelengths corresponding to band gaps. The possibility also exists however of using them at wavelengths corresponding to their transmission bands, where these structures exhibit most particular refractive and dispersive properties. As has already been seen, the periodic structuring of a material profoundly modifies its optical properties by generating anisotropy and dispersion effects. In turn, these effects induce dramatic changes in the refractive properties of such material, which shall be specifically considered in the present chapter.

In order to correctly analyse the modifications thus induced on the refractive behaviour of a material, we shall first recall the essential differences between the phase refractive index and the group refractive index. The necessary approximation of the effective refractive index will also be briefly discussed.

6.1 Phase Refractive Index, Group Refractive Index and Energy Propagation

6.1.1 Phase Velocity and Group Velocity

The propagation of a monochromatic wave in a linear, isotropic and homogeneous medium can be described by the wave equation (Eqs. 1.6a and 1.7 in Section 1.1.1 of Chapter 1). The most elementary solutions to this equation are plane monochromatic waves with a sinusoidal field distribution in space and time. The propagation speed of such a wave is referred to as the ‘phase velocity’ since this speed is but the displacement speed of a point in space, associated with a given value of the phase. Assuming the phase to be equal to $\varphi(x, t) = \omega t - k_0 x + \varphi_0$, the phase velocity will be given by the equation:

$$v_\varphi = dx/dt = \omega/k_0 \quad (6.1)$$

Monochromatic waves cannot transmit information as they are perfectly periodic in time and space. Indeed, such waves fill the whole space from $x = -\infty$ to $x = +\infty$ and extend from the beginning to the end of time, i.e. from $t = -\infty$ to

$t = +\infty$. Such waves do not actually exist in reality, and information is actually introduced through a modulation in the amplitude or the phase of the monochromatic wave. As an example, let us consider the field distribution $u(x,t)$ defined at time $t = 0$ as follows:

$$u = \operatorname{Re} \left\{ f(x) \exp(-ik_0x) \right\} \quad (6.2a)$$

where the amplitude $f(x)$ varies slowly with respect to $\exp(-ik_0x)$. We assume that the function $f(x)$ can be expressed in the form of a Fourier integral:

$$f(x) = \int_{-\infty}^{\infty} g(k) \exp(-ikx) dk \quad (6.3a)$$

where:

$$g(k) = \int_{-\infty}^{\infty} f(x) \exp(ikx) dx \quad (6.3b)$$

The slow variation of $f(x)$ with respect to $\exp(-ik_0x)$ implies that $g(k)$ has significantly non-zero values only in the case where $|k| \ll k_0$. Under these conditions, the distribution given in Eq. 6.2a is but the distribution of a wave packet, i.e. a group of waves with a certain distribution, of wave vectors centred at k_0 . This distribution can also be written at time $t = 0$ in the following form:

$$\begin{aligned} u(x,0) &= \operatorname{Re} \left\{ \exp(-ik_0x) \int_{-\infty}^{\infty} g(k) \exp(-ikx) dk \right\} = \\ &= \operatorname{Re} \left\{ \int_{-\infty}^{\infty} g(k) \exp(-i(k_0 + k)x) dk \right\} \end{aligned} \quad (6.2b)$$

A frequency ω is associated to each component k in the distribution of the wave vectors, so that at any time t the distribution of the wave packet can be written as

$$u(x,t) = \operatorname{Re} \left\{ \int_{-\infty}^{\infty} g(k) \exp(i\omega t - i(k_0 + k)x) dk \right\} \quad (6.4)$$

In the same way as for a wave with a constant amplitude, the wave packet could be expected to propagate at the speed $v_p = \omega_0/k_0$, where ω_0 is the central frequency of the spectrum. Such an hypothesis would not however be valid in the case of a dispersive medium, i.e. when ω is a nonlinear function of k . Nevertheless, since the spectrum of the wave packet has a limited width, $\omega(k)$ can be approximated by a two-term polynomial defined as follows:

$$\omega = \omega_0 + \left(\frac{\partial \omega}{\partial k} \right)_{k=k_0} \times k \quad (6.5)$$

By combining these two last equations, we arrive at:

$$u(x, t) \approx \operatorname{Re} \left\{ \exp(i\omega_0 t - ik_0 x) \int_{-\infty}^{+\infty} g(k) \exp \left(-ik \left[x - \left(\frac{\partial \omega}{\partial k} \right)_{k=k_0} \times t \right] \right) dk \right\} \quad (6.6a)$$

This equation can also be written in the following form:

$$u(x, t) \approx \operatorname{Re} \left\{ f \left[x - \left(\frac{\partial \omega}{\partial k} \right)_{k=k_0} \times t \right] \exp(i\omega_0 t - ik_0 x) \right\} \quad (6.6b)$$

As can be seen, the phase velocity of the wave packet is still $v_\varphi = \omega_0/k_0$, but the signal itself, and therefore the light energy, propagates at group velocity defined by:

$$v_g = \left(\frac{\partial \omega}{\partial k} \right)_{k=k_0} \quad (6.7)$$

The same relation between the group and the phase velocity can also be demonstrated in wavelength space. Proceeding from the definition given in Eq. 6.7 with $\omega = k v_\varphi$ and $k = 2\pi/\lambda$, we then arrive at Rayleigh's equation:

$$v_g = v_\varphi - \lambda \frac{\partial v_\varphi}{\partial \lambda} \quad (6.8)$$

In a medium with a reasonably low dispersion, the wave packet travels as a whole, without undergoing any significant 'diffusion' nor spreading. Under these conditions, the group velocity describing the propagation speed of the wave packet also represents the speed at which energy propagates (Born 1965). As can be seen from Eq. 6.8, the group velocity can be either positive or negative, while its modulus can be either larger or smaller than the phase velocity. The idea of a negative group velocity is not an abstraction. This phenomenon is exploited for instance in vacuum tubes known as 'cavotrons' or as backward wave tubes, which are used for the generation of millimeter electromagnetic waves.

Nevertheless, certain situations exist where the group velocity does not correctly describe the propagation of energy. This is the case for instance near strong absorption peaks in media with a strong anomalous dispersion. In such cases, the Poynting vector should be used instead of the group velocity vector. The notion of 'ray velocity' which derives from the Poynting vector is sometimes used when studying the optical properties of anisotropic crystals (Born 1965).

6.1.2 Refractive Indexes and Dispersion Diagrams

The phase and group refractive indexes can be deduced from the phase and group velocities respectively using the following simple equations:

$$n_\varphi = c / v_\varphi \quad (6.9)$$

$$n_g = c / v_g \approx n_\varphi - \lambda \frac{\partial n_\varphi}{\partial \lambda}$$

Since the dispersion diagrams (band structures) yield the relations $\omega(\mathbf{k})$ in the different directions of propagation in the crystal, the phase and group refractive indexes can be quite readily obtained from these diagrams using Eqs. 6.1, 6.7 and 6.9. Fig. 6.1 illustrates graphically the manner in which the phase and group velocities can be deduced from the dispersion diagrams. For a wave packet with frequency ω propagating along a given direction, one or more solutions may exist for \mathbf{k} depending on the shape of the dispersion curves. The phase velocity is defined as the ratio ω/k at the corresponding points of the dispersion diagram (Fig. 6.1, left). The group velocity is deduced from the slope of the curve at the same points (Fig. 6.1, right). Depending on the exact location of the points in the dispersion curve, one may find different values, either positive or negative, for the group velocity.

Actually, the simple construction presented in Fig. 6.1 is valid only for one-dimensional crystals and for a direction of propagation perpendicular to the layers of the crystal. In the more general case of two and three-dimensional crystals, the phase velocity can still be determined from the ratio ω/k for a given direction of the wave vector \mathbf{k} . In this case, however, there is no reason for the group velocity of the wave packet centred at ω_0 and \mathbf{k}_0 to be necessarily collinear with the phase velocity. In such a case, the algebraic formulation given by Eq. 6.7 for the group velocity needs therefore to be replaced with the following vector equation:

$$\mathbf{v}_g = \mathbf{grad}_{\mathbf{k}=\mathbf{k}_0} \omega \quad (6.10)$$

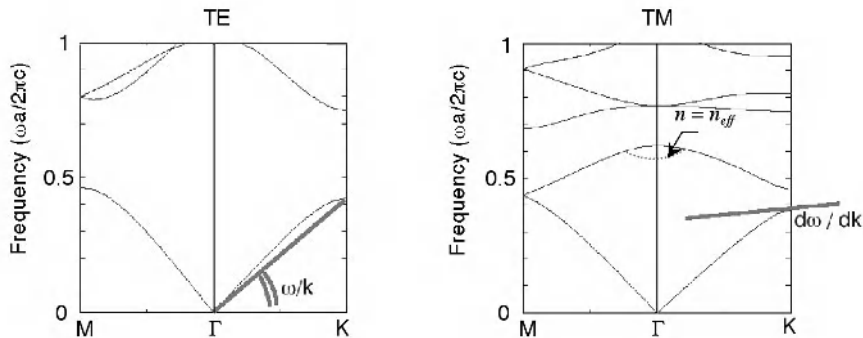


Fig. 6.1. Dispersion curves of a two-dimensional photonic crystal and graphical representations of the phase and group velocities. At the apex of the second photonic transmission band, indicated by the point Γ in the right-hand side of the figure, the isofrequency curve tends towards a circular shape so that a negative refractive effective index can be assigned to the photonic crystal

The group velocity is therefore defined by the normal to the isofrequency surface ($\omega(\mathbf{k}) = \omega_0$) at point (k_x, k_y, k_z) . The expression for the group refractive index is the same as in Eq. 6.9, provided however that the algebraic value for v_g be used here, its sign being positive or negative depending on whether v_g is directed towards the exterior or the interior of the isofrequency contour respectively. It can easily be seen that the anisotropy of the photonic crystal frequently imposes different directions for the group and phase velocities. We shall later comment on this point in Section 6.2.2.

6.1.3 Effective Phase Index and Group Refractive Index

In view of the preceding discussion of the anisotropy of two and three-dimensional photonic crystal, the question may arise whether the notion of effective refractive index should be retained and used for the description of these structures. In the long wavelength region, i.e. at low frequencies, the approximation of the crystal as a homogeneous material does not create any particular difficulty. Mathematicians have indeed developed homogenisation techniques based on limit analysis (see Section 2.4 in Chapter 2). In such a case, the effective refractive index is an asymptotic notion, which becomes rigorous for wavelengths infinitely long with respect to the size of the elementary cell of the crystal (Felbacq 1997). Analytical formulas exist for describing such a situation (Bao 2000).

For wavelengths of an order comparable to the period of the structure, the situation becomes more complex. Nevertheless, numerical simulations of the propagation of the field as well as experiments have revealed that under certain conditions a periodic or a quasi-periodic structure may behave like a bulk homo-

geneous material except for the interfaces of the structure at which scattering effects may always occur. For a two-dimensional (respectively three-dimensional) photonic crystal, these conditions are especially approached when the isofrequency curve or surface tend towards a circle or a sphere respectively. Such a case occurs for instance for frequencies near the Γ point in the conduction band of a hexagonal photonic crystal (Fig. 6.1, right). It therefore seems that we are entitled under these circumstances to define an effective refractive index in spite of the fact that its mathematical justification has not been clearly established. If the group velocity is negative (negative slope in the right-hand part of Fig. 6.1), then the effective refractive index will be negative as well (Gralak 2000). Assigning an effective refractive index to the photonic crystal simplifies the description of the propagation of waves in such a structure.

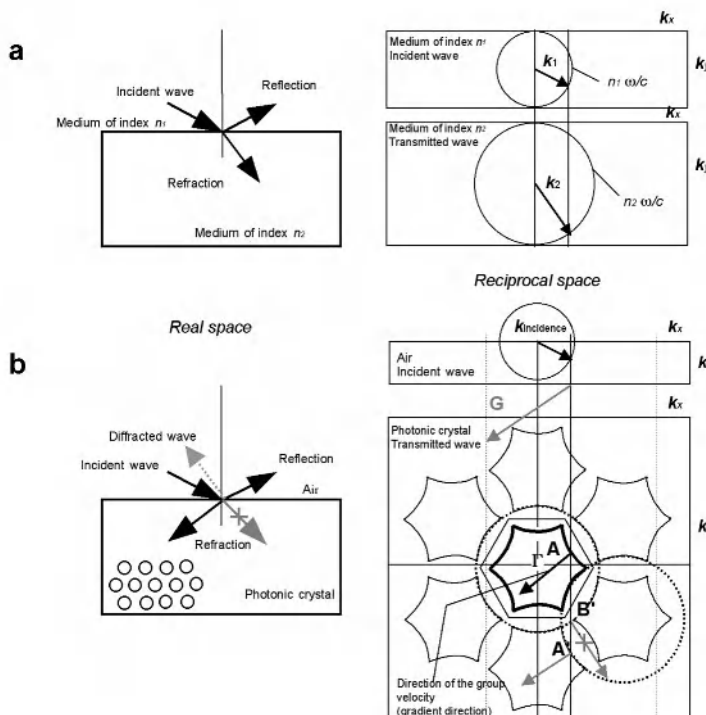


Fig. 6.2. **a.** Refraction at the interface between two homogeneous media **b.** Refraction at the interface between the air and a two-dimensional photonic crystal with an hexagonal symmetry. The left-hand figures show the trajectories of the light rays in the real space, while the right-hand figures represent the construction of the transmitted wave vectors in the reciprocal space. In these latter figures, the isofrequency curves can be seen to be circles (Ewald circles) in case **a** and to assume a more complex shape with an hexagonal symmetry in case **b**. The crossed arrows indicate the trajectories of the ordinary refracted rays that are suppressed due to the presence of a photonic gap, as described in Section 6.2.3

6.2 Refraction of Waves at the Interface between a Periodic Medium and a Homogeneous Medium

6.2.1 Summary of Refraction Laws in Homogeneous Media

As has already been emphasised in Section 6.1, and leaving aside some very specific cases that will not be addressed here, the direction of propagation of a light beam in any medium is defined by the group velocity vector. This direction is indeed the same as the direction of the Poynting vector ($\sim \mathbf{E} \times \mathbf{H}$) or the time averaged energy flux. In a homogeneous isotropic medium, the group velocity vector is collinear with the wave vector. Assuming that the medium is non-dispersive, which amounts to considering a spectral region sufficiently distant from the resonances and to restricting ourselves to a relatively narrow spectral range, the phase and group refractive indexes are also identical. We may therefore adopt here the simple account given by geometrical optics of this phenomenon, where the propagation of the electromagnetic energy is represented by light rays associated to the wave vectors k and propagating in a medium with a unique index n . The transition from a homogeneous medium with index n_1 to a second medium with an index n_2 depends on the incident angle of the ray with respect to the interface. The excitation of the transmitted wave entails that the component of the wave vector parallel to the interface will be conserved during the transition at the interface. In other terms, the projections of the incident and transmitted wave vectors onto the plane of the interface are equal. This condition leads to the formulation of Snell's law $n_1 \sin\theta_1 = n_2 \sin\theta_2$. The refracted ray can also be determined using Ewald spheres, as can be seen in Fig. 6.2 (upper right). For each of the media represented in this figure, the isofrequency curve is a circle with a radius defined by the absolute value of the wave vector in the medium ($n\omega/c$).

6.2.2 Some Well-Known Anisotropic Media: Birefringent Solid State Crystals

The phenomenon of refraction undergoes dramatic modifications as soon as one of the media on either side of the interface is anisotropic. While two and three-dimensional photonic crystals are by construction anisotropic, a number of solid state crystals that are both transparent and anisotropic exist in nature. The optical anisotropy of these crystals manifests itself in the form of a birefringence, which merely expresses the dependence of the refractive index on the direction of propagation and on the polarisation of light. The fundamental principles of the optics of anisotropic crystals were established by A. Fresnel in 1820, long before the development of the electromagnetic theory. The reader will find a more detailed introduction to the optical properties of anisotropic crystals in the reference works (Born 1965; Landau 1969). Generally, the angular dependence of the phase re-

fractive index in such solid state crystals can be described by an index ellipsoid, which allows an analytical formulation for the refraction of light in birefringent crystals. Compared to solid state crystals, photonic crystals present dispersion curves of a much more complex shape, as can be seen in Fig. 6.3. The spatial profiles of the index $n(k_x, k_y, k_z)$ at a given frequency in the reciprocal space, or in other terms, the isofrequency curves or surfaces (Notomi 2000a) are therefore very far from being ellipsoidal.

In the two-dimensional case represented in Fig. 6.3, the isofrequency profiles are obtained by horizontally cutting the dispersion surfaces separately calculated by means of a plane wave model. Fig. 6.2 (lower right) presents an idealised example of an isofrequency curve for the same two-dimensional triangular crystal with an hexagonal symmetry. The value selected for the frequency is slightly higher than the frequency of the fundamental band gap. The group velocity vector is directed here towards the interior of the contour, which corresponds to a negative group refractive index. The isofrequency surfaces of photonic crystals are actually a direct analogue to Fermi surfaces for solid state crystals (Kittel 1971).

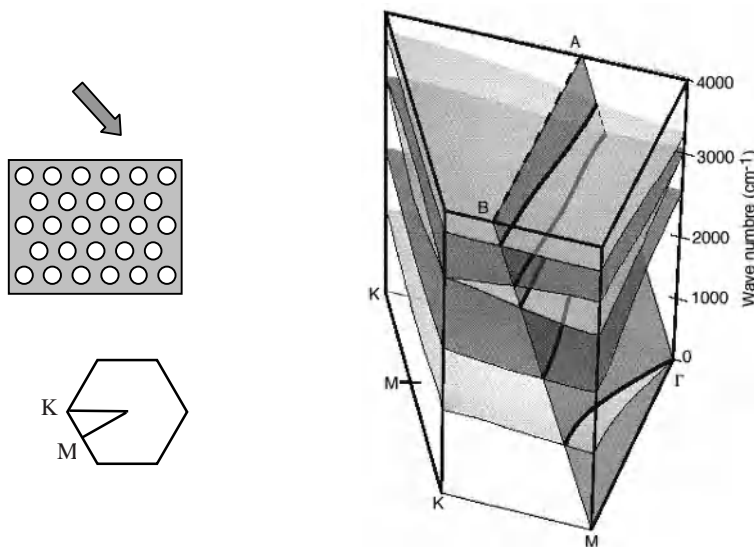


Fig. 6.3. Right. Three-dimensional representation of the band diagram of a two-dimensional photonic crystal with an hexagonal symmetry. The horizontal axes correspond to the Γ K and Γ M directions respectively while the vertical axis corresponds to the frequency ω . Left. Photonic crystal with a finite size illuminated from the air. The interface of the crystal is parallel to the Γ K direction. The transmitted wave vector(s) is (are) obtained from the intersections of the dispersion surfaces with a plane $\omega/k_{\Gamma K} = \text{constant}$

6.2.3 Construction of Transmitted Waves in a Photonic Crystal

In the refraction of a ray at an interface between a homogeneous medium and a photonic crystal, both the phase and the group velocities, or equivalently the phase and group refractive indexes, are involved. The relation between the phase refractive indexes of the two media determines the transition at the interface (conservation of the component of the wave vectors parallel to the interface), while the group velocity determines the subsequent propagation of the beam and of the electromagnetic energy in the crystal.

Fig. 6.2 (*lower right*) shows how the wave(s) transmitted inside a photonic crystal with a triangular symmetry can be constructed for an incident wave arriving from a homogeneous medium. The vertical line which passes through the extremity of the incident wave vector corresponds to the component k_x that will be conserved in this case. Each intersection of this line with the star-shaped isofrequency curve defines the extremity of a Bloch vector of the field transmitted in the crystal, or coupled with it. The periodicity of photonic crystals implies that multiple intersections are possible. We shall only consider here waves whose group velocity vector is directed towards the lower hemisphere, i.e. towards the interior of the photonic crystal. However, there also exists diffracted waves that will be redirected back into the homogeneous medium (see Fig. 5.1).

In the case under consideration here, only one direction of propagation is allowed in the crystal (intersection point *A*). The group velocity vector, normal to the isofrequency curve, is directed towards the interior of the curve, with the consequence that the crystal seems to behave in the same way as a material with a negative refractive index would do.

It might be noted that using the same geometrical parameters but with an infinitely small index contrast, the isofrequency curves tend towards a circular shape, as can be seen in Fig. 6.2. At certain frequencies, the vertical straight line can be seen to intersect two times the isofrequency curves (intersection points *A'* and *B*), which corresponds to the existence of two transmitted waves. The conclusion must therefore be drawn here that the increase in the index contrast and the subsequent appearance of the band gap prevents ‘ordinary’ refraction from occurring (Notomi 2000a).

Let us now consider frequencies in the second transmission band (see the band diagram represented in Fig. 6.1) so that the representative points (ω, k) will now be located in the vicinity of the point Γ of the Brillouin zone. If a high index contrast exists, the shapes of the isofrequency curves will tend towards circles with, however, a smaller radius than was previously the case. The photonic crystal behaves here like a homogeneous medium with an ‘average’ refractive index. This ‘average’ refractive index can be negative provided that the normals to the dispersion curves be directed towards the negative part of the frequency axis (Section 6.1.3 in this chapter).

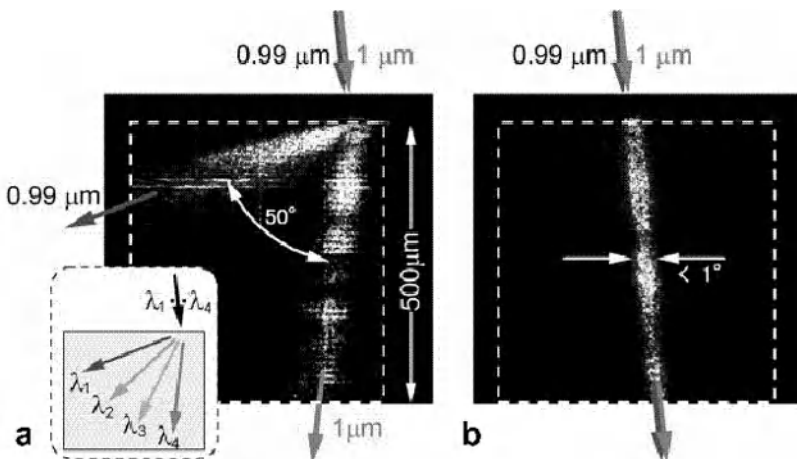


Fig. 6.4. Photographs showing the trajectories followed by light rays: **a.** In a photonic crystal **b.** In a silica layer. Two incident laser beams at two different wavelengths equal to 0.99 and 1.0 μm respectively were used in these experiments (Kosaka 1999). The TM polarised laser beams become visible due to the light scattering which occurs outside the plane of the crystal or of the silica layer. The two-dimensional crystal has a triangular symmetry and its lateral dimensions are $500 \times 500 \mu\text{m}^2$. The edge of the crystal is oriented along the ΓK direction. The incidence angle with respect to facet of the crystal is equal to 15°

6.3 Superprism and Ultra-Refraction Effects

6.3.1 The Superprism Effect

The strong chromatic dispersion of photonic crystals was first demonstrated by SY Lin *et al* (Lin 1996) in experiments where a 20% variation of the effective (isotropic) refractive index was obtained for a relative change in frequency equal to 30%. These first results were followed by a series of theoretical and experimental studies (Gralak 2000; Kosaka 1998, 1999; Notomi 2000a; Wu 2002). In particular, H. Kosaka *et al* reported a spectacular superprism effect with an angular deviation of 50° for a relative variation of the wavelength equal to 1%, which means that an angular dispersion equal to $5^\circ/\text{nm}$ had been achieved, as can be seen in Fig. 6.4. Unlike the first experiments realised by SY Lin *et al*, the experiments conducted by H. Kosaka *et al* relied both on the anisotropy of the crystal and on negative refraction index effects. Actually, the experimental conditions were chosen in such a way as to exploit the isofrequency surfaces in the regions where deformation is the

most intense (the branches of the stars in Fig. 6.2). As a consequence, even a slight variation in the wavelength was sufficient to induce dramatic changes in the direction of the group velocity. The superprisms used in these experiments consisted of photonic crystals with a triangular symmetry and fabricated using the autocloning method. The fabrication of these crystals is described in more detail in Chapter 12, which is devoted to three-dimensional photonic crystals (see Fig. 12.11).

6.3.2 Ultra-Refraction

Ultra-refraction effects are not fundamentally different from superprism effects insofar as they are both related to the dispersion properties of photonic crystals. However, this term more specifically refers to the situation where the photonic crystal can be assigned an effective index less than unity, and more particularly a negative index. In such a case, the crystal behaves like an isotropic dielectric medium, where refraction can be described by Snell's law again. A typical situation is that of a two-dimensional crystal for frequencies within the second transmission band and near the centre Γ of the Brillouin zone. In this case, the shape of the isofrequency curve is very close to a circle, while for a three-dimensional crystal, it would likewise be close to a sphere. It has also been numerically demonstrated that a negative refractive index could be obtained in all directions at frequencies corresponding to the fundamental transmission band near the extremity of the Brillouin zone rather than at its centre (Luo 2002).

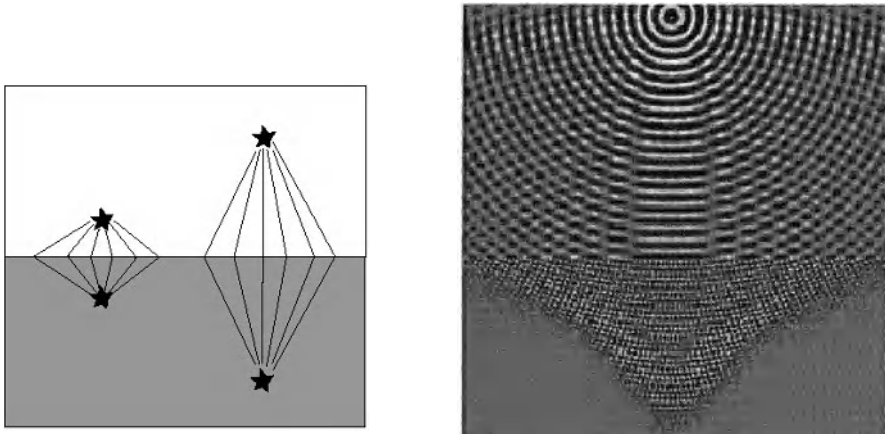


Fig. 6.5. *Left.* Schematic construction of the light rays refracted by a photonic crystal with a negative effective index (in this example, $n_{\text{eff}} = -1$). The surface of the crystal behaves like a mirror-lens. *Right.* Numerical simulation of the distribution of the field in an ultra-refractive photonic crystal illuminated by an external point source (Notomi 2000a)

An analogy can be drawn between the effective index of photonic crystals and the effective mass of charge carriers in semiconductors. In semiconductors, the electronic states associated with negative effective masses are simply the empty states of the valence band. The existence of effective masses with opposite signs simply reflects the difference in the curvature of the electronic band on the two opposite sides of the gap (Kittel 1971).

The phenomenon of ‘negative refraction’ is schematically illustrated in the left-hand part of Fig. 6.5, while the right-hand part of this figure represents the corresponding field distribution in the crystal when illuminated by an external point source (Notomi 2000a).

It can be observed that a material with a negative refractive index can focus light beams in a very specific fashion, and that it actually behaves like a ‘slab lens’ or like a ‘mirror lens’. While a conventional lens possesses a focal plane and produces images in a two-dimensional plane at a short distance from its focal plane, a negative refractive index lens produces three-dimensional images through a spatial inversion process similar to that of a mirror: $(x, y, z) \rightarrow (x, y, -\beta z)$, where $\beta = \ln_{eff}/n_0$. The lens thus realised has no principal axis, but exhibits on the contrary a translational symmetry in the plane of the interface.

6.4 Metamaterials

The approach to negative refraction which has just been described here is essentially based on the periodicity of dielectric structures. However, a different approach exists towards this phenomenon. This approach is based on the concept of a metamaterial, and finds its origin in a series of experiments that were conducted on artificial dielectrics during the 1950s and 1960s. These experiments demonstrated that a composite material may present a very different electromagnetic response from that of the ‘natural’ materials used in its composition. However, most of these results remained confined to the radar science community, without reaching at this time a wider audience.

Thus, the concept of a metamaterial is that of a composite material obtained by combining different types of structures or materials, and allowing the simultaneous control of both the effective permittivity ϵ_{eff} and the effective permeability μ_{eff} in order to answer a requirement needed for a certain application. As regards more particularly negative diffraction, the aim is to obtain a metamaterial, possibly periodic and with a negative refractive index at frequencies much lower than the frequencies of the band gap.

6.4.1 Simultaneous Control of the Dielectric Permittivity and of the Magnetic Permeability

Transparent materials of the most usual types typically present positive values for the dielectric permittivity ϵ and for the magnetic permeability μ . However, certain materials can also be found where either ϵ or μ is negative, although these two conditions are never to be simultaneously met. For instance, a neutral non-collisional plasma presents a negative permittivity at frequencies lower than the plasma oscillation frequency. Likewise, certain metals and semiconductors may exhibit the same type of response under specific conditions and for a limited range of frequencies. As has been described in Section 4.1 of Chapter 4, the condition $\epsilon < 0$ necessarily entails that the material is opaque and reflective.

If magnetic charges, i.e. Dirac's monopoles existed, then a gas formed from such charges would present a magnetic permeability of much the same type as the dielectric permittivity of the plasma mentioned above: $\mu = \mu_0(1 - \omega_m^2/\omega^2)$. However, since magnetic charges do not exist in the nature, only antiferromagnetic systems may exhibit a negative permeability $\mu < 0$ at frequencies near the resonances. However, these materials are also at the same time strongly anisotropic.

V. Veselago was probably the first author who, in 1964, considered the possibility of an artificial material presenting negative values for both ϵ and μ (Veselago 1964, 1968). After theoretically investigating the properties of such materials using Maxwell's equations, he concluded that the refractive index of such a material would be negative and that it would present very unusual optical properties. Thus, the sign of the Doppler effect would be reversed in such a way that the apparent frequency of a source approaching from a detector would actually be lower than the frequency measured for the same source as it propagates away from this detector. Likewise, the Vavilov-Cherenkov effect would also be reversed in such a material. The electromagnetic wave emitted by a charged particle propagating at the speed $v > c/n$ in a medium with a negative refractive index would propagate along a direction opposite to the direction of the movement of this particle. Finally, the optical law of refraction would be modified much in the same way as for photonic crystals with a negative refractive index, or with a 'negative photonic mass' (Fig. 6.5). As has already been described, a layer formed by such a material would act like a lens. For instance, a concave lens made from such a material would focus light instead of diverging it, etc.

For a monochromatic plane wave propagating in a medium characterised by its average permittivity and permeability, the two following equations are valid:

$$\mathbf{k} \times \mathbf{E} = \frac{\omega}{c} \mu \mathbf{H} \quad (6.11)$$

$$\mathbf{k} \times \mathbf{H} = -\frac{\omega}{c} \epsilon \mathbf{E} \quad (6.12)$$

It can be seen from these equations that the vectors \mathbf{E} , \mathbf{H} and \mathbf{k} form a right-handed basis if $\epsilon > 0$ and $\mu > 0$. This basis becomes left-handed in the case where simultaneously $\epsilon < 0$ and $\mu < 0$. For this reason, materials presenting this property are often referred to as ‘left-handed materials’. Since there is a risk that some confusion may arise with chiral materials, where left-handed as well as right-handed helical structures exist, other terms have been suggested for use: negative refractive material, negative index material, backward medium, double negative medium, negative phase velocity medium, etc. All these different terms point to the fact that the direction of the wave vector \mathbf{k} is opposed to the direction of the energy flux, or Poynting vector $\mathbf{S} \sim \mathbf{E} \times \mathbf{H}$.

It might be noted that the values of ϵ and μ can be simultaneously negative only in the presence of dispersion. Indeed, in the absence of dispersion phenomena, the total energy of the electromagnetic field in this medium is :

$$W = \epsilon E^2 + \mu H^2 \quad (6.13)$$

Therefore, this energy would be always negative. In the presence of dispersion, the electromagnetic energy satisfies the following equation (Veselago 1968):

$$W = \frac{\partial(\epsilon\omega)}{\partial\omega} E^2 + \frac{\partial(\mu\omega)}{\partial\omega} H^2 \quad (6.14)$$

For the energy to be positive, the following conditions must be fulfilled:

$$\frac{\partial(\epsilon\omega)}{\partial\omega} > 0 \quad \text{and} \quad \frac{\partial(\mu\omega)}{\partial\omega} > 0 \quad (6.15)$$

Thus, only in a limited frequency range can the desired properties, i.e. $\epsilon < 0$ and $\mu < 0$, actually be produced.

The practical problem of realising such negative refractive index materials was not considered at the time when V. Veselago conducted the first researches on this subject (Veselago 1964). As a consequence, these results remained largely forgotten for more than thirty years, and only with the development of photonic crystals was the interest in this subject revived.

6.4.2 Fabrication of Negative Refractive Index Metamaterials at Centimeter Wavelengths

In the course of his researches on metallic photonic crystals (see Section 4.2.1 in Chapter 4), JB Pendry observed that crystals formed by conducting rods with a small diameter (Fig. 6.6a) presented the same frequency response than non-collisional plasmas (Pendry 1996). Three years later, he suggested an artificial electromagnetic crystal with a negative magnetic permeability (Pendry 1999). This

second structure was formed from LC-type resonators consisting of split metallic rings, as represented in Fig. 6.6b.

In 2000, a research group from the University of California in San Diego (UCSD) fabricated the first artificial material with $\epsilon < 0$ and $\mu < 0$ in the centimetre wavelength range. The material thus realised was a combination of the two structures previously proposed by JB Pendry (Smith 2000c). More precisely, the artificial material thus realised consisted of a two-dimensional lattice of conducting wires interleaved with double split ring resonators. All these structures were fabricated from printed circuit boards, as represented in Fig. 6.7. The presence of a negative refraction effect was confirmed by microwave measurements (Shelby 2001).

The potential applications of negative refractive index materials started being investigated at the same time as these first experimental results. JB Pendry suggested that a layer of such a material could be used as a ‘perfect’ lens (Pendry 2000) in accordance with the principle schematically represented in Fig. 6.5. The underlying idea was that the lens thus realised would preserve and transmit the near-field evanescent waves excited by the optical source. Such a system would therefore present a resolution higher than the resolution imposed by the diffraction limit, i.e. a resolution higher than the wavelength. As a first approximation towards realising such a perfect lens in the visible range, the author suggested using a thin silver layer with $\epsilon < 0$, but $\mu > 0$. The first experimental tests seem to vindicate theoretical predictions (Melville 2004).

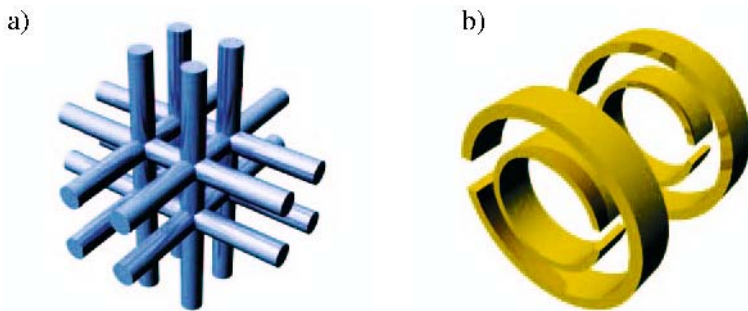


Fig. 6.6. *a.* Three-dimensional structure formed by thin metallic rods exhibiting a low frequency behaviour similar to that of a neutral plasma. *b.* Periodic structure exhibiting a negative magnetic permeability at low frequencies. The elementary pattern consists of LC resonators formed by two concentric split metallic rings

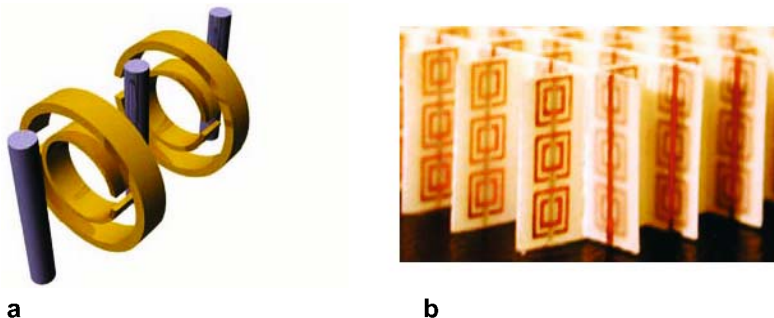


Fig. 6.7. Negative refractive index material fabricated by a research group at the University of San Diego (Smith 2000) **a**. Schematic view showing the combination of two periodic lattices shifted from one other by half a period (conducting wires and double split ring resonators). **b**. View of the actual structure realised from printed boards

All these pioneering works stirred up a certain controversy in the scientific community. For instance, doubts were cast as to whether the principle of causality had not been violated (Valanju 2002) in the experiments realised by RA Shelby *et al* (Shelby 2001). It was also argued that the mere combination of two media, one with $\epsilon < 0$ and the other with $\mu < 0$, would not allow the propagation of plasma modes (Pokrovsky 2002a). Other authors also pointed out to the fragility of the ‘perfect lens’ effect when the losses of the metamaterial had to be taken into account (Garcia 2002a). This controversy originated for a large part from the desire to explain and describe all the characteristics of negative refractive materials with simple arguments, or even better with analytical formulas. A similar situation had already happened a few years earlier with the ‘discovery’ of the ‘superluminal’ propagation of light in photonic crystals (Chiao 1997; D’Aguanno 2001), which had arisen the same type of doubts, in particular concerning the possibility of a violation of the principle of causality. In this case, however, subsequent numerical simulations clearly demonstrated the impossibility of a superluminal propagation or tunnelling of light (Konsek 2003).

All experiments and numerical simulations conducted with the FDTD method have now vindicated the existence of the negative refraction effect (Grbic 2002; Kärkkäinen 2002; Ziolkowski 2001). Additional confirmation of this phenomenon was provided in direct answers to these criticisms (Garcia 2002b; Maslovsky 2002; Pendry 2002a, 2002b; Veselago 2002).

One of the main results achieved by the UCSD research group, namely the focusing of an electromagnetic wave by a slab with a negative refractive index metamaterial, was reproduced in the experiments conducted by A.K. Iyer *et al*, where a two-dimensional lattice of LC resonators formed by lumped elements was used (Iyer 2002). From a theoretical point of view, a clear approach to the issues surrounding the principle of causality in metamaterials was presented in (McDonald 2000). It has also been demonstrated that even ‘non-perfect’ lenses based on

metamaterials could exhibit a higher optical resolution than conventional lenses (Pokrovsky 2002b; Shen 2002). In the microwave region, it has been shown that the limits imposed on the dispersion of the material by the requirement of a positive total energy (see Eqs. 6.14 and 6.15) can be relaxed through the incorporation of lumped amplifiers in the structure (Tretyakov 2001). Interesting potential solutions have also been suggested for realising a transposition of negative refractive index metamaterials to higher frequencies approaching the optical region (Dewar 2001; O'Brien 2002).

7 Confinement of Light in Zero-Dimensional Microcavities

The perspective of achieving a better control of the spontaneous emission in optoelectronic devices has been a major impetus to research on photonic crystals in its early developments. Thus, in his founding paper, E. Yablonovitch mentioned as a major incentive in the search for structures with complete photonic band gaps the possibility of inhibiting the spontaneous emission in the spectral range of the photonic band gap (Yablonovitch 1987). A few years later, he also introduced the concept of a single-mode light emitting diode (Yablonovitch 1991b, 1993). Such a device, which ultimately rests on a defect created in a three-dimensional photonic crystal, would allow achieving a complete control of spontaneous emission.

Spontaneous emission plays a major role in optoelectronic devices, either positively or negatively. We may first consider here the case of light emitting diodes (LED): these devices represent by far the main share of the market for optoelectronic devices (totalling around 4 billions USD in 2002), with high-brightness LEDs accounting for 50% of this market. The emission of a LED is generally ensured by the spontaneous emission of a semiconductor active medium; being able to efficiently extract this light emission from the semiconductor is essential here if the efficiency of LEDs is to be maximised.

In a laser diode, the spontaneous emission into the lasing mode is useful and even essential, since it acts here as a trigger for the amplification by stimulated emission, whereas the spontaneous emission into all other modes unnecessarily dissipates energy (Yokoyama 1995a). In conventional edge-emitting laser diodes, of the kind used for optical communications or compact disk players, the useful fraction β of the spontaneous emission is as low as 10^{-5} . As a consequence, the current injected at the lasing threshold serves for the most part to compensate for the radiative recombination of the electron-hole pairs by spontaneous emission (Coldren 1995). In principle, increasing β would lead to a reduction by several orders of magnitude of the threshold current of laser diodes and to a significant increase of their efficiency.

In addition to the improvement of existing devices, the control of the spontaneous emission would open the way to the development of novel devices, with very original functions (Burstein 1995; Chang 1996; Yokoyama 1995b). A beautiful example is that of the single-photon source capable of deterministically emitting a light pulse containing but a single photon. As will be discussed in more detail in Chapter 10, a promising approach towards the actual realisation of single-photon sources relies on the Purcell effect, i.e. on the enhancement of the spontaneous

emission rate of a single quantum dot in a pillar microcavity. Another important example from a conceptual point of view is the ‘thresholdless laser’, that would be obtained in the limit where $\beta \sim 1$, and where all the spontaneous emission would be funnelled into the lasing mode. Since a series of very attractive properties are expected to occur in this regime, this has largely contributed to stimulating research on semiconductor optical microcavities in the early 1990s (Yamamoto 1991; Yamamoto 1993; Yokoyama 1992).

This brief introduction should have highlighted the diversity and the importance of the potential applications of the control of the spontaneous emission in optoelectronics. In this context, photonic crystal microcavities come into competition with other well-established approaches to three-dimensional optical confinement, for instance those based on micropillars and on microdisks. We shall therefore first discuss in general terms the main effects of optical microcavities on the properties of the optical emission, including the physics of thresholdless lasing (Section 7.1). We shall then present the experimental state of the art on this subject in Section 7.2, with a special emphasis on results obtained for optical cavities containing semiconductor quantum dots. From there, we shall compare the main figures of merit of photonic crystal microcavities and of other optical microcavities, and discuss their respective assets for the control of spontaneous emission. The first realisations of microcavity-based optical sources will be presented and analysed in Chapter 10.

7.1 Microcavity Sources. Principles and Effects

7.1.1 A Classical Effect: the Angular Redistribution of the Spontaneous Emission and the Example of Planar Microcavities

For any cavity defined between mirrors, the electromagnetic modes of interest are shaped by the boundary conditions imposed by the mirrors. When an emitter is placed inside the cavity, all the physical effects which are to be expected actually originate from its coupling to the cavity modes. If the cavity is not totally enclosed by the mirrors, there remain propagation directions along which the electromagnetic modes involved in these effects form a continuum similar to that of the surrounding homogeneous space (dielectric, air, vacuum). Only the modes ‘spreading’ over the mirrors will be truly discretised. In order to be detected outside the cavity, the photons need to either propagate through the ‘leaky modes’ or to be channelled into one of the discrete modes, before being subsequently transmitted through the associated mirrors. In the latter case, it is quite plain that the far-field angular pattern of the emitter will be directly affected by the spatial structure of the underlying cavity modes, and in particular by their lobes and their nodal lines or planes.

The angular redistribution of the spontaneous emission is a classical effect which has been established for solid-state emitters as well as for atoms in microwave or optical cavities. This effect can be illustrated by considering the case of a planar (Fabry-Perot) cavity with an emitter placed in vacuum between two mirrors. These two mirrors are assumed to be parallel, while their respective reflectivities r_1 and r_2 are independent of the frequency and on the incidence angle. From an historical perspective, A. Kastler was among the first physicists who considered this case using an elementary classical formalism where polarisation effects are neglected (Kastler 1962).

All the relevant modes of this ideal system thus defined are Fabry-Perot modes and obey the quantification of the wave vector \mathbf{k} along the z direction normal to the mirrors: $k_z = m\pi/L$, where L is the distance between the mirrors and m is an integer (Fig. 7.1a). Denoting by θ the angle formed by the wave vector \mathbf{k} and the z axis, k_z can also be expressed in the form $k_z = k \cos \theta$, with $k = \omega/c$. The resonant modes are associated with the constructive interferences created by the multiple reflections at the two mirrors. It is under these conditions that the transmission of the cavity described by the Airy function reaches its maximum (Fig. 7.1b). Outside the cavity, the intensity of the field is distributed over circular fringes (Fig. 7.1c), whose finesse, i.e. the ratio of the interval of these fringes to their individual width, is given by the classical formula $F = \pi (r_1 r_2)^{1/2} / (1 - r_1 r_2)$, which depends only on the reflectivities of the mirrors (Born 1965). The number of fringes at a given frequency is finite ($m_c = \text{integer } [L/(\lambda/2)]$) and corresponds to what could be called the order of the cavity. Inside the cavity, the electromagnetic energy is concentrated in resonant modes, with stationary waves forming due to the fact that each plane wave is almost totally reflected for $r_1 \sim 1$ and $r_2 \sim 1$.

The efficiency of the coupling between the emitter and resonant modes can be best understood by using the principle of reciprocity. If the emitter is illuminated by a light source located outside the cavity, the field at the emitter will be either reinforced or reduced compared to the situation where no cavity is present. The coupling will therefore be either enhanced or inhibited respectively. The distribution of the emitted power between the different modes, i.e. between the different fringes which can be observed outside the cavity (Fig. 7.1c) actually depends on the location of the emitter with respect to the ‘local electric field’ of each mode, and especially with respect to their nodes and antinodes. Accordingly, the angular redistribution of the spontaneous emission caused by the presence of the Fabry-Perot cavity will result in two different effects. First, at a given frequency, the directions of propagation associated with Fabry-Perot modes are favoured over all other directions, as is described by the Airy function. Secondly, the distribution of the power among the different modes, i.e. the circular fringes, is far from being necessarily trivial, since it depends on the local value of the field at the emitter. In the case of a symmetric cavity ($r_1 = r_2$) and of an emitter located at its centre, the coupling occurs only for even modes with an antinode in the centre of the cavity. Odd modes will simply not be coupled, although the Airy function is maximal for the corresponding angle and frequency. Overall the effect induced by the cavity is the suppression of the radiation along non-resonant directions and its concentra-

tion along certain other directions (resonant modes) without any losses occurring (Benisty 1998a, 1998b).

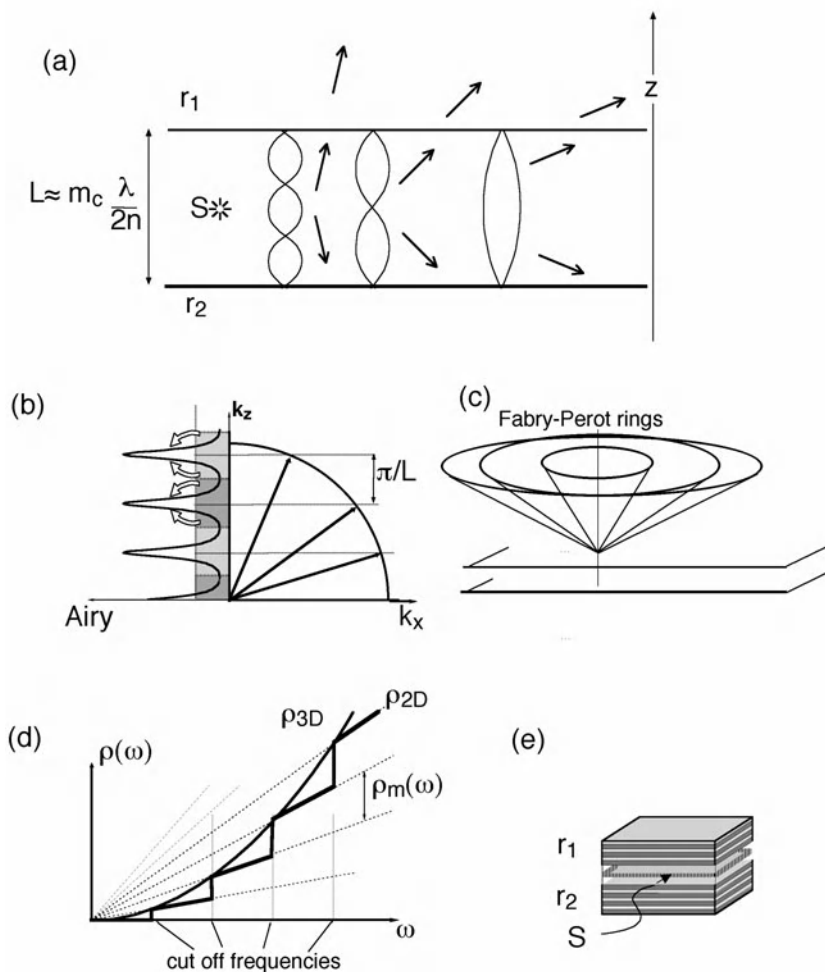


Fig. 7.1. **a.** Fabry-Perot cavity (mirrors with reflectivities r_1 and r_2) with a localised source S . Three modes ($m_c \approx 3$) are represented here in the form either of stationary waves or of rays **b**. Quantification of the projection of the wave vector k_z . The locus of \mathbf{k} describes a circle with radius ω/c , whereas the cavity transmission expressed as a function of k_z evolves like the Airy function **c**. Circular fringes where the emitted radiation energy and the corresponding modes are concentrated **d**. Photonic density of states of the planar microcavity for TE modes **e**. Example of a cavity with Bragg mirrors or with a one-dimensional photonic crystal

Let us now consider the influence of the length L of the cavity. If L is small, then m_c will be small as well, and the emitter will be coupled only to a limited number of resonant modes. In the limit case where m_c is just above unity, all the emitted light can be coupled to a single mode per polarisation. This simply means that the source S , which originally was isotropic, has been turned into a truly directional source, with a directivity depending on the finesse F of the cavity. One may also select, in much the same way as in lasers, the main output mirror by increasing the transmission (t_1 or t_2) of one of the mirrors with respect to the other. From this simple model, it can be seen that the isotropy of the spontaneous emission completely changes as soon as considering the system formed by the emitter and the cavity. It is also quite apparent that, for a cavity with a given length, the direction of emission depends on the frequency, this being due to the fact that, for a given mode, the $\omega \cos\theta$ product is constant. Thus, any increase of the output angle, causing $\cos\theta$ to decrease, will lead to an increase of ω , resulting in a blue shift of the emission.

At this point, one may already perceive the existence of a dynamical effect that will be described in more detail in Section 7.1.2 of this chapter: the change in the strength of the coupling to the resonant modes, in other terms the Purcell effect. Let us note first that the three-dimensional photonic density of states in the cavity (ρ_{2D}) increases stepwise when a new cavity mode appears (Fig 7.1d, $\omega_m = m\pi/cL$). Therefore, the smaller the value for m , the more different the value of the density of states will be from its value in vacuum ($\sim\omega^2$). Let us for instance consider the case of a dipole emitting in vacuum at the frequency ω , released in a cavity with a length L such that the frequency of the first resonance $\omega_1 = \pi c/L$ is slightly larger than ω . Since $\rho_{2D} = 0$, for TE polarised modes (i.e. modes whose \mathbf{E} field is parallel to the plane of the mirrors), the TE spontaneous emission of the dipole will therefore be inhibited (Fig. 7.1d). When L increases, ω_1 falls under ω , and the spontaneous emission rate changes abruptly due to the appearance of modes characterised by ($k_z = \omega_1/c$, $|\mathbf{k}| = \omega/c$), which provide efficient deexcitation channels for the emitter. As is often the case in the literature, the term ‘mode’ will be used here both for the discrete set of modes along the z direction (in this sense, ‘one mode = one fringe’) and for the more genuine photonic modes which form a two-dimensional continuum for each z -quantised value m .

For a more precise study of the spontaneous emission rate, both the exact location and orientation of the emitting dipole need to be accounted for, as is the case either in simplified models (Kastler 1962; Benisty 1998a, 1998b) or in more elaborated ones (Björk 1994; Brorson 1990). These latter models indicate that for a planar cavity confined by ideal mirrors ($r_1 \sim r_2 \sim 1$), the spontaneous emission rate could be enhanced by a factor of 3 compared to its value in vacuum, provided however that the emitter be polarised parallel to the plane of the cavity and that it be located at its very centre. Even in such an ideal case, the enhancement remains limited. Further, the inhibition of the spontaneous emission is never complete in planar cavities, due to the fact that TM modes, i.e. modes whose \mathbf{H} field is parallel to the mirrors, have no cutoff.

Let us now turn to the consideration of more realistic cavities, formed either from Bragg mirrors (Fig. 7.1e) or from lossy metallic mirrors, several additional effects need to be considered. First, a medium with a high index may allow the propagation of perfectly discrete guided modes. ‘Leaky’ modes may also be present due to absorption. Another series of effects originates from the limited angular and spectral acceptance of Bragg and other distributed mirrors. Within these limits, the phase behaviour of these mirrors is analogous to that of ideal mirrors that would be placed at a certain distance from the first interface with the cavity. The fact that the wave penetrates over a certain depth in the distributed mirror (which is the equivalent of the skin effect for metals) amounts to virtually enlarging the cavity, and therefore to increasing the number m_c of resonances allowed at a given frequency. In the example represented in Fig. 7.1d, this means that the total photonic density of states will only exhibit limited relative singularities. To mention but a single numerical example, the total density of states is not modified by more than $+/- 20$ percent for a microcavity formed by GaAs/GaAlAs Bragg mirrors. For microcavities confined by metallic mirrors, the penetration of the field is much lower. It can even be demonstrated, by taking into account the phase difference of the wave at the reflection at the mirror, that the first resonance of the cavity is obtained for an optical thickness smaller than $\lambda/2$. The total density of states for such an ultimate cavity is therefore enhanced by a factor of 5 (Abram 1998). However, cavities of such a type are rarely used in practice, since the absorption of the mirror limits their quality factor and their transmission, resulting in a lower photon extraction efficiency.

In spite of these limitations, the angular redistribution of the spontaneous emission in planar cavities formed from Bragg mirrors has been used for increasing the extraction efficiency of solid state emitters, and more particularly of semiconductor emitters. Since semiconductors have a high refractive index, the critical angle for total internal reflection is small and ranges only from 15° to 30° . A large fraction of the light isotropically emitted in the bulk of a chip cannot be transmitted through the interface between the semiconductor and the air. Sandwiching the emitter in a planar microcavity thus allows concentrating the light that otherwise would be lost in a cone with much lower angular aperture. This analysis will be further developed in Chapter 10 when discussing light emitting diodes.

7.1.2 Spontaneous Emission Dynamics in Microcavities

In this section, we shall consider the general situation where the presence of a cavity results in strong singularities in the photonic mode density. The interaction between light and matter will be analysed here in terms of a strong coupling between the field of the cavity and a single emitter. We shall also reconsider in more detail the weak-coupling situation which had been previously discussed with respect to planar cavities.

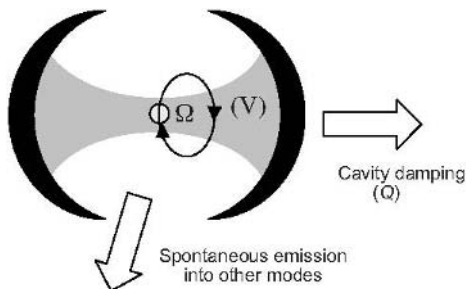


Fig. 7.2. Schematic representation of a single emitter in a cavity

Strong Coupling. Formation of Mixed Exciton-Photon States

Let us consider here a single localised emitter, resonantly coupled to a single lossless cavity mode, as represented in Fig. 7.2. The emitter is assumed to be in an excited state at $t = 0$. In the absence of dissipation, a system of two coupled oscillators, formed by the excited atom on the one hand and of the field of the cavity on the other hand, has thus been created. Each oscillator periodically exchanges its energy with the other, so that the spontaneous emission becomes reversible: thus, a photon emitted by the atom will be reabsorbed, before being re-emitted, and so on. This phenomenon is known in quantum mechanics under the name of Rabi oscillations.

Actually, damping occurs as soon as the coherent interaction is destroyed or when losses are present, leading to an exponential decrease of the Rabi oscillations. These phenomena have been intensively studied in atomic physics from the beginning of the 1980s. In particular, famous experiments have been conducted for atomic transitions in the radiofrequency region, using a confocal cavity with superconductor mirrors presenting ultra-small losses (Haroche 1989).

We shall only provide here a short theoretical survey of the physical quantities involved in this interaction, which will lead us to briefly sketch the quantum theory of fields. This theory will not be used anywhere else in this book (Cohen-Tannoudji 1992; Loudon 1983).

The electric field for a given cavity mode can be written in the form:

$$\hat{E}(\vec{r}, t) = i\epsilon_{\max} \vec{f}(\vec{r}) \hat{a}(t) + h.c. \quad (7.1)$$

where \hat{a} is the photon creation operator, \vec{f} is a complex vector, which is a function of the space variables and represents the local polarisation field (\vec{f} is normalised at one of the anti-nodes of the field and satisfies Maxwell's equations) and *h.c.* stands for the conjugate hermitic operator in the first term of the right-hand side of Eq. 7.1. The prefactor ϵ_{\max} , which is sometimes improperly referred to as the ‘maximum field per photon’, determines the absolute strength of the atom/field

coupling. Since the field energy of vacuum (zero photon) for a mode with a frequency ω is $\hbar\omega/2$, i.e. half the quantum of the harmonic oscillator in the fundamental state, ϵ_{max} can be written in the following form:

$$\epsilon_{max} = \sqrt{\hbar\omega/2 \epsilon_0 n^2 V} \quad (7.2)$$

where:

$$V = \frac{1}{n^2} \iiint_{\vec{r}} n(\vec{r})^2 |\vec{f}(\vec{r})| d^3 \vec{r}$$

The physical quantity V in the equation for ϵ_{max} reduces simply to the usual mode volume in the case where \vec{f} is defined in a medium with a constant refractive index. Nevertheless, as indicated by the second formula, the possibility always exists of defining an effective volume ($V = V_{eff}$) if the refractive index is variable, as is indeed the case in photonic crystals. In this second formula, $n(\vec{r})$ is the spatially dependent refractive index, while n is the value of the refractive index at the field maximum.

Using the formalism of quantum mechanics, the interaction Hamiltonian is given by the following equation:

$$\hat{H}_{int} = -i\epsilon_{max} \vec{d} \cdot \vec{f}(\vec{r}_e) |g\rangle \langle e| \hat{a} + h.c. \quad (7.3)$$

where $|g\rangle$ and $|e\rangle$ denote respectively the fundamental state and the excited state of the emitter. The assumption is made that the emitter can be described by a two-level system, and that it is located at $\vec{r} = \vec{r}_e$. The dipole moment of the optical transition is denoted here by \vec{d} . The Rabi frequency characterizes the speed at which the system goes from one state to another due to its interaction with the optical field. We shall take for granted here that the Rabi frequency is associated with the dimensioned factor of the Hamiltonian:

$$\hbar\Omega = |\epsilon_{max} \vec{d} \cdot \vec{f}(\vec{r}_e)| \quad (7.4)$$

Using this formalism, the energy levels of the global system in the absence of interaction can be written in the form $|g, 0\rangle$ for the fundamental state, and either as $|e, \bar{n}\rangle$ or as $|g, \bar{n}+1\rangle$ for the two degenerate excited states respectively. The second term in each ket stands for the number of photons in the cavity, corresponding to the intensity of the field according to the classical approach. In the case where interactions occur, the degeneracy of the excited levels is lifted, leading to non-degenerate states which are irreducible linear combinations of the uncoupled states $|e, \bar{n}\rangle \pm |g, \bar{n}+1\rangle$ ($\bar{n} = 0, 1, \dots$). The energy difference between non-degenerate

states is but the Rabi splitting: $2\hbar\Omega\sqrt{n+1}$. It is quite apparent that, while the fundamental state $|g,0\rangle$ will not be affected, new states will form as a result of the association between the empty cavity and the excited state $|e\rangle$ of the emitter, i.e. $2^{-1/2}(|e,0\rangle \pm |g,1\rangle)$. The energy difference between these states is generally referred to as the vacuum Rabi splitting $2\hbar\Omega$. Thus, if the system is originally prepared at $t=0$ in the excited state with no photon, it has to be analysed as the linear and symmetrical combination of two states $2^{-1/2}(|e,0\rangle \pm |g,1\rangle)$. The energy difference between these states induces a beating at the frequency 2Ω . From a classical point of view, the excitation goes from the emitter to the cavity and conversely.

Still remaining within this formalism, one may introduce two ‘decoherence’ sources, namely the leakage of one photon out of the cavity and the deexcitation of the atom through other channels than the emission of one photon in the cavity mode. If two spectral widths $\Delta\omega_c$ and $\Delta\omega_e$ are associated to these two processes respectively, it can be demonstrated that the oscillations which characterize the strong coupling regime subsist only for relatively small linewidths. In the first approximation, strong coupling will be observed if $2\Omega > (\Delta\omega_e + \Delta\omega_c)$. In other terms, the Rabi oscillation needs to be faster than the ‘sum’ of the two decoherence processes.

The previous inequality reveals the importance of the physical quantities involved in the Rabi pulsation: the electrical dipole strength associated with the optical transition and the cavity field strength, which itself is intimately related to the volume of the cavity. We shall see later in Section 7.2.4 of this chapter that, even in vacuum (Eq. 7.2), impressive field strengths can be obtained for ultimately small volumes. The quality factor $Q = \omega_c/\Delta\omega_c$ of the cavity exerts here its influence through the spectral width $\Delta\omega_c$ of the mode.

It might be recalled here that the strong coupling between a photon and a quantum excitation of matter has been known since quite a long time in the field of solid state physics. The study of semiconductor-based planar microcavities has been a unique opportunity to revisit this phenomenon.

In a three-dimensional medium, the phonon polariton due to the coupling between optical phonons and photons is the first example of a strong coupling phenomenon in condensed media (Ashcroft 1976). In semiconductors, the main electronic excitations, i.e. the electron-hole pairs, exhibit a continuous spectrum, which does not in general allow for strong coupling phenomena. The major exception is the exciton resulting from a bound state between one electron and one hole. The dispersion relations for excitons are such that only one optical frequency will be associated to a given three-dimensional wave vector. The wave vector is conserved both in the creation of an exciton by photon absorption and in the emission of a photon by exciton recombination. This selection rule, which is directly related to the translational invariance of the crystal, leads to the formation of mixed exciton-photon particles, known as excitonic polaritons. In a true solid state crystal, these mixed particles are extremely ‘fragile’. Thus, at any disruption in the periodicity of the crystal (surfaces and interfaces), these particles are decomposed into their elementary constituents, resulting for instance in the leakage of one photon out of the crystal.

In quantum well structures, the excitons are confined in the layers of the quantum layers. The components of their wave vector are well-defined only for directions parallel to the plane of the quantum well (\mathbf{k}_{\parallel}). Accordingly, the excitons can couple to the continuum of photonic modes with all possible values for k_z . However, the situation changes dramatically when the quantum well is embedded in a planar microcavity where k_z is quantified. Due to the translational invariance within the plane of the quantum well, an exciton with momentum \mathbf{k}_{\parallel} can only couple to a photon with the same momentum \mathbf{k}_{\parallel} . Under these conditions, k_z and \mathbf{k}_{\parallel} are now interrelated and a strong coupling regime can therefore be achieved, resulting in the formation of microcavity ‘polaritons’ (Weisbuch 1992). While the photon leakage occurring through the cavity mirrors irremediably contributes to the damping of the Rabi oscillations, it also provides a convenient way of observing these coupled excitations and of analysing their linear and nonlinear properties, for instance in terms of dispersion or saturation. This experimental scheme has allowed different research groups to reproduce in the field of solid state physics some of the most fundamental phenomena which had previously been demonstrated in atomic physics. From this point of view, it can be easily understood that photonic crystal structures offer the opportunity of investigating these phenomena in unprecedented conditions.

Weak Coupling and the Purcell Effect

As early as 1946, EM Purcell noted in his pioneering work that the spontaneous emission is not an intrinsic property of an emitter, and that it also depends on the coupling between the emitter and its electromagnetic environment (Purcell 1946). At this time, EM Purcell was essentially interested in the enhancement of the spontaneous emission rather than in its inhibition. It has already been suggested in Section 7.1.1 of this chapter that, even in simple planar microcavities, the spontaneous emission rate can be either enhanced or inhibited. E. Yablonovitch was the first author who suggested the possibility of achieving the total inhibition of spontaneous emission in a three-dimensional photonic band gap material (Yablonovitch 1987). A partial inhibition also occurs when an emitter is placed in a cavity without any resonant mode at the emission wavelength. This effect has been observed for atoms suitably polarised and released in a cavity with two metallic mirrors, where no resonance was occurring at the atomic frequencies (Jhe 1987).

The Purcell effect can be described in terms of a ‘weak’ coupling between an emitter and a discrete cavity mode. In other terms, the assumption is made here that, since the quality factor Q of the cavity is relatively low, it loses photons at such a rate that $\Omega < \Delta\omega_c$. Let us first assume that the linewidth of the emitter is much smaller than the linewidth of the cavity mode, i.e. $\Delta\omega_e \ll \Delta\omega_c$. In this case, everything happens as if the emitter were ‘seeing’ a mode continuum with a spectral density $p(\omega)$. The coupling of the emitter to the cavity mode can be described using the standard formalism with Fermi’s golden rule (Cohen-Tannoudji 1973; Ho 1999). The mode density is represented by a Lorentzian function whose width $\Delta\omega_c = \omega/Q$ is dependent on the finite lifetime of the photon in the cavity. By ap-

plying a normalisation law $\int \rho(\omega) d\omega = 1$ to one mode, the peak value for the mode density turns out to be equal to $\rho_{\max}(\omega) = (2/\pi)Q/\omega$. The other parameters involved in the spontaneous emission process can be adequately rewritten using once more Ω for characterising the interaction between light and matter. Accordingly, for an emitter at the frequency ω_e , coupled to a single non-degenerate cavity mode at the frequency ω_c , the spontaneous lifetime is given by the equation:

$$\frac{1}{\tau} = \frac{4\Omega^2 Q}{\omega} \frac{\Delta\omega_c^2}{4(\omega_e - \omega_c)^2 + \Delta\omega_c^2} \quad (7.5)$$

This value is to be compared with the value of the spontaneous emission rate in the case where the emitter is embedded in a homogeneous medium with index n (Ho 1999):

$$\frac{1}{\tau_{bulk}} = \frac{|\vec{d}|^2 \omega_e^3 n}{3\pi\epsilon_0 \hbar c^3} \quad (7.6)$$

where \vec{d} still denotes the electric dipole associated with the optical transition.

The dynamics of spontaneous emission are therefore modified as soon as the emitter is coupled to the cavity mode. The exaltation (or inhibition) factor for the spontaneous emission is defined as the ratio between the emission rates given in Eqs. 7.5 and 7.6 respectively, and can be expressed in the form of a product of three terms:

$$\frac{\tau_{bulk}}{\tau_{cav}} = \frac{3Q(\lambda_c/n)^3}{4\pi^2 V} \cdot \frac{|\vec{d} \cdot \vec{f}(\vec{r}_e)|^2}{|\vec{d}|^2} \cdot \frac{\Delta\omega_c^2}{4(\omega_e - \omega_c)^2 + \Delta\omega_c^2} \quad (7.7)$$

The first term in this equation depends on the intrinsic parameters (Q , V) of the cavity, while the second and third terms are always less than unity and depend on (i) the relative amplitude of the field at the location of the emitter, (ii) the orientation of the dipole with respect to the field of the cavity and (iii) the spectral shift of the emitter with respect to the cavity mode. The first term is usually considered as the factor of merit of the cavity, since it represents the upper bound which can be obtained if the position, orientation and frequency of the emitting dipole are optimal. This factor of merit is the same as the one proposed by EM Purcell:

$$F_p = \left(\frac{\tau_{bulk}}{\tau_{cav}} \right)_{\max} = \frac{3Q(\lambda_c/n)^3}{4\pi^2 V} \quad (7.8)$$

As can be seen, the Purcell factor may assume arbitrarily large values, much larger than unity. If $F_p > 1$, an emitter adequately coupled to the cavity mode shall faster de-excite by spontaneous emission in this mode than in all free-space modes. This exaltation of the spontaneous emission predicted by Purcell in 1946 (Purcell 1946) was demonstrated for the first time in spectacular experiments conducted on Rydberg atoms released in a microwave cavity with $\tau_{vacuum}/\tau_{cav} = 500$ (Haroche 1989).

In practice, for solid state emitters at room temperature, the dephasing mechanisms (other than spontaneous emission) become so efficient that the homogeneous linewidth of the emitter $\Delta\omega_e$ is larger than $\Delta\omega_c$. Assuming that $\Omega < \Delta\omega_c$ is fulfilled, the preceding calculations remain valid provided however that $\rho(\omega)$ be replaced by:

$$\int L(\omega) \rho_{cav}(\omega) d\omega \quad (7.9)$$

where $L(\omega)$ is a Lorentzian function representing the statistical distribution of the energy around the emission frequency. Assuming the cavity mode and the emitter to be in resonance ($\omega_c = \omega_e$), $1/Q$ must be replaced in Eq. 7.8 by:

1. $1/Q_{em} = \Delta\omega_e/\omega$ if a significant homogeneous broadening can be observed, i.e. if $\Delta\omega_e \gg \Delta\omega_c$,
2. $1/2Q$ if $\Delta\omega_e = \Delta\omega_c$,
3. $1/Q + 1/Q_{em}$ (as a good approximation) in the general case.

More specifically, the preceding discussion shows that the Purcell effect is considerably attenuated if the emitter has a linewidth much larger than the linewidth of the cavity mode. For this reason, demonstrating the Purcell effect in condensed matter physics took a longer time than would otherwise have been needed. As will be seen in Chapter 10, the lack of adequate solid state emitters still remains an important limitation for the practical implementation of the Purcell effect.

A few more remarks can be made concerning the dimensionality of the cavity. As has been seen in Section 7.1.1, F_p is smaller than 3 in a planar two-dimensional cavity formed by ideal mirrors. By contrast, F_p can be arbitrarily high in zero-dimensional cavities since in this case there are no physical limits for Q . Above a certain value for F_p , the strong coupling regime will be reached. It now remains to consider the case of one-dimensional cavities, formed for instance by a metallised fibre.

In principle, the photonic density of states of one-dimensional cavities presents singularities for each mode cutoff ($\omega = \omega_i$) and follows a $(\omega - \omega_i)^{-1/2}$ evolution. Likewise, the inverse of the group velocity ($1/v_g = dk/d\omega$) to which the photonic density of states is proportional, follows the same type of evolution. In actual systems however, the lower the group velocity, the higher the losses and therefore the properties of one-dimensional systems are necessarily reflective of their finite

length. A one-dimensional system with a finite length is equivalent to a zero-dimensional system where damping and decoherence phenomena occur.

Single-Mode Emission, Low Threshold Microlaser, 'Thresholdless Laser'

Due to the Purcell effect which has been described above, the spontaneous emission can be selectively enhanced in one or several microcavity modes. Therefore, the spontaneous emission is for the most part dynamically channeled into these modes. When the emitter is coupled to a single resonant mode, the spontaneous emission factor β becomes (Gérard 1998):

$$\beta = \frac{F}{F + \gamma} \quad (7.10)$$

where F/τ_{bulk} is the emission rate in the cavity mode exalted by the Purcell effect, while $\gamma/\tau_{\text{bulk}}$ is the emission rate in the continuum formed by non-resonant modes. In most cases, γ is close to 1, and the value for β tends therefore to approach unity when the Purcell effect is marked. This behaviour can be used both for lasers and for optical devices directly exploiting the spontaneous emission, like for instance light emitting diodes or single-photon sources.

The control of spontaneous emission is of primary importance for lasers. A simple solution for minimising the threshold current of semiconductor lasers is to use a single-mode structure, where only a single mode may benefit from the amplification of the spontaneous emission. The problem then consists in reducing as much as possible the $(1-\beta)$ fraction of the spontaneous emission which is lost in leaky modes, since this parasitic emission consumes needlessly the electron-hole pairs injected in the semiconductor.

Another interesting case from a conceptual interest is the ‘thresholdless’ laser, that would be obtained for $\beta = 1$ (Yokoyama 1992). Contrary to conventional lasers, such a device would ideally convert any electrical signal into an optical signal. The characteristic of this laser would be strictly linear, since any injected electron-hole pair would finally generate a photon, either by spontaneous emission or by stimulated emission. Contrary to standard lasers where the amplification of the fluctuations by stimulated emission causes an excess noise to occur near threshold, no such noise would be added to the pumping noise in a thresholdless laser.

This second property would allow the conversion of an electrical signal with low amplitude noise into an optical with a low amplitude noise. Indeed, electrical currents can be easily generated with an amplitude noise well below shot noise. The only condition is that the non-radiative carrier recombinations should be negligible, since any electron loss would irremediably increase the electrical pump noise.

This type of a laser is said to be ‘thresholdless’ only in the sense that the traditional ‘accidents’ occurring near threshold tend to be suppressed when $\beta \rightarrow 1$. This

is true as regards both the light-current characteristic and the noise properties of the laser. However, it should be stressed that this device is not a zero threshold laser. Indeed, two different regimes can be distinguished depending on the average number of photons \bar{n} in the lasing mode. If this number is less than 1, photons are spontaneously emitted, whereas if the number is more than 1, the stimulated emission becomes predominant. In this sense, a threshold can still be defined for such a device ($\bar{n} = 1$). This threshold can be determined experimentally as well. The emitted beam exhibits a spectral coherence only when the stimulated emission becomes predominant. The linewidth of the laser will decrease in inverse ratio to the number of photons in the cavity above threshold and will be essentially imposed by the quality factor Q of the cavity below threshold. The reduction of the linewidth above threshold is known for standard lasers as the Schawlow-Townes law (Schawlow 1958).

For the purpose of discussing the potential interest of photonic crystals in this context, we shall present here a simple model for the description of the main processes involved in a thresholdless laser (Björk 1991). Let us here consider a single-mode cavity assumed to be containing a total number N_t of two-level atoms. N and N_0 here are the number of atoms in the excited state and fundamental state respectively, while \bar{n} is the number of photons in the mode, β is the coupling factor of the spontaneous emission into the mode, $1/\tau$ is the spontaneous emission rate, which may be enhanced by the Purcell effect and is assumed to remain the same for all atoms, P is the pumping rate, g is the gain coefficient, and $\varphi = 1/\tau_{ph}$ is the photon loss rate. If the homogeneous linewidth of the emitters is larger than the linewidth of the cavity mode, the evolution of the coupled system can then be described by a set of two rate equations (RE) for the atom and photon populations respectively (Björk 1991; Yamamoto 1993; Yokoyama 1989, 1992; Morimura 1997). Following the same approach as in the works mentioned here, we shall adopt a modified set of equations where the stimulated emission rate is explicitly written, as a function of the number of atoms in the ground state N_0 , while the number of emitters is imposed by the relation $N_t = N + N_0$. The latter condition is more specifically adapted to account for the saturation effects occurring in quantum dot systems. The model also provides a good physical insight in the physics of quantum well microlasers with single-mode cavity, in spite of a certain overestimate of the saturation effects in this case. The system of rate equations is therefore:

$$\frac{dN}{dt} = P - \frac{N}{\tau} - g(N - N_0)\bar{n} \quad (7.11)$$

$$\frac{d\bar{n}}{dt} = \beta \frac{N}{\tau} - \varphi \bar{n} + g(N - N_0)\bar{n} \quad (7.12)$$

From Einstein relations, the spontaneous emission rate in the mode needs to be equal to the stimulated emission rate induced by a single photon, and therefore

$g = \beta/\tau$. It therefore readily follows that, in the steady-state regime, the microlaser threshold ($\bar{n} = 1$) will be reached for the following pumping rate:

$$P_{th} = \frac{\varphi}{3\beta} [1 + 2\beta + 2\xi(1 - \beta)] \quad (7.13)$$

where $\xi = N\beta/2\tau\varphi$ actually is only the average number of spontaneous photons in the mode at transparency ($N = N_0 = N_t/2$). Let us note that in the case where $\xi > 1$, the laser threshold is reached below the transparency threshold, i.e. before the inversion of the atomic medium. Lasing thus occurs without any population inversion. While the fact that ξ is larger than unity might seem surprising, it should be noted that, as β tends towards 1, the emission rate of spontaneous photons remains well beyond the usual values for standard lasers.

The population inversion ratio for the atomic system at threshold can be deduced from Eqs. 7.11 and 7.13:

$$\frac{N - N_0}{N_t} = \frac{1}{3} \left[\frac{1}{\xi} - 1 \right] \quad (7.14)$$

This ratio is necessarily less than 100%, and the system can therefore operate in true laser regime only in the case where $\xi > 1/4$.

It might be of interest to analyse the behaviour of microlasers below and above the threshold, by using approximate solutions of Eqs. 7.11 and 7.12 for the two limit cases where $\bar{n} \gg 1$ and $\bar{n} \ll 1$. In the steady-state regime, the resolution of these equations leads to simple analytical expressions for P and N as functions of \bar{n} . The output optical power (P_{out}) and the number of excited atoms (N) can therefore be written respectively as:

– for $\bar{n} \gg 1$:

$$P_{out} = \varphi\bar{n} \approx P, \quad N - N_0 = \frac{\varphi\tau}{\beta} = \frac{2N_t}{\xi} \quad (7.15)$$

– for $\bar{n} \ll 1$:

$$P_{out} = \varphi\bar{n} \approx P \frac{\beta}{1 + 2\xi(1 - \beta) - 2P\beta/\varphi} \approx P \frac{\beta}{1 + 2\xi(1 - \beta)}, \quad N \approx P\tau \quad (7.16)$$

When the pumping rate is increased, the number of excited atoms linearly increases before saturating above the threshold. This is quite a classical phenomenon. However, since the total number N_t of atoms is finite, saturation may occur for a pumping rate lower than originally expected. In order to convince oneself of the existence of such a possibility, it suffices to observe that, if ξ would be smaller than 1/2, the asymptotic limit of N in the second relation (Eq. 7.15) would be

higher than N_t . Since obviously such a situation is forbidden, the total inversion will be reached for a certain value of the pump power above which the output power of the microlaser will no longer increase.

On the other hand, the consideration of Eqs. 7.13 and 7.16 allows us to distinguish two different behaviours depending on the value of $2\xi(1-\beta) = N\beta(1-\beta)/\tau\varphi$ compared to unity. If $2\xi(1-\beta)$ is lower than (or close to) unity, the efficiency below threshold is directly proportional to β . Any increase of β leads to a decrease of the threshold pump power in approximately the same proportion. If $2\xi(1-\beta)$ is larger than unity, it will be the predominant term in the denominator of P_{out} (Eq. 7.16). The β factor has a very limited influence not only on the evolution of \bar{n} , but also on the microlaser threshold and on the power efficiency below threshold. Actually, in order for β to have a stronger influence, its value needs to be very close to unity. It might be noted here that for a value for $2\xi(1-\beta)$ much higher than unity, the pump power at threshold (Eq. 7.13) can be approximated well by $P_{th} = N(1-\beta)/3\tau$. The latter value is 1.5 times lower than the pump power needed for reaching the transparency threshold ($P_{th} = N/2\tau$).

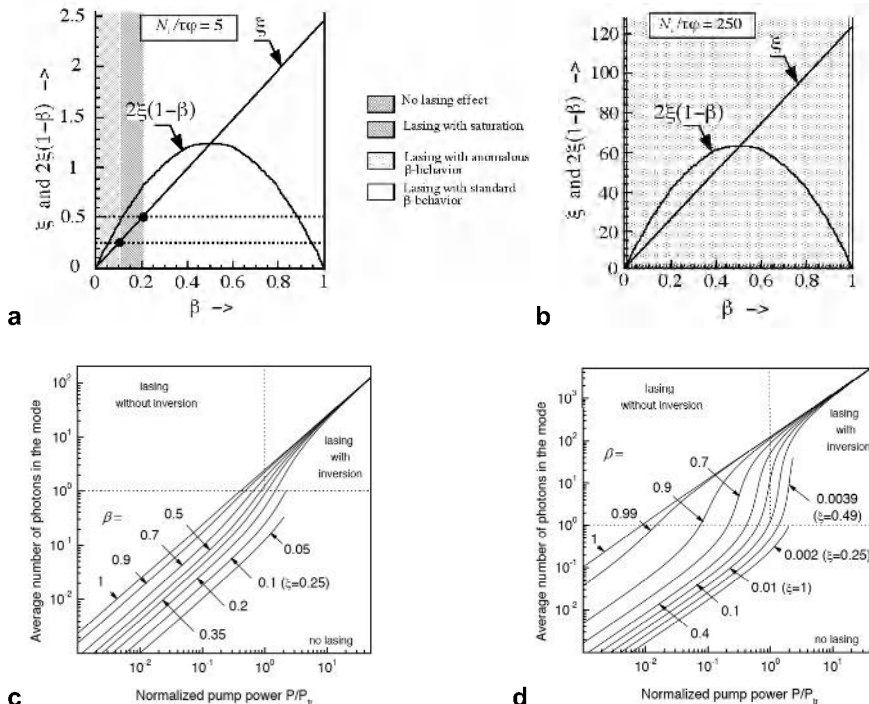


Fig. 7.3. **a.** and **b.** Evolution of ξ and $2\xi(1-\beta)$ versus β for two different values for the parameter $N/\tau\varphi$ (**a.** $N/\tau\varphi = 4.5$ **b.** $N/\tau\varphi = 250$) and microlasers with different behaviours **c.** and **d.** The number of emitted photons as a function of the pump power, in this case the number of electron-hole pairs, for different values for β . The two cases **c** and **d** correspond to the two values for the parameter $N/\tau\varphi$ that was chosen in **a** and **b** respectively

The preceding remarks are not without practical implications. Indeed, for semiconductor lasers, $\log(\beta)$ is usually estimated from the amplitude of the ‘step’ observed in the experimental characteristic $P_{out}(P)$, presented on a logarithmic scale. It is quite clear that if $2\xi(1-\beta) \gg 1$, the value for β estimated from the measured characteristic will be erroneous. The previous discussion is illustrated in Fig. 7.3. The different possible behaviours of the laser are represented in Figs. 7.3a and 7.3b, with $N/\tau\varphi$ used as a parameter. Fig. 7.3c and 7.3d represent the corresponding evolutions of the number of emitted photons as a function of the injected pump power.

Using this simple analytic model, different possible approaches towards the realisation of a low-threshold microlaser can be developed:

- a first approach would be to use a true single-mode cavity ($\beta = 1$) based on a three-dimensional photonic crystal. This approach is conceptually very powerful: indeed, since ξ does no longer play any role in the equations previously described, it completely removes the constraint imposed on the number of emitters. The pump power at threshold is given by $P = \varphi$. Indeed, exciting one atom, or creating one electron-hole pair in a semiconductor over the damping time τ_{ph} of the cavity is sufficient for reaching the threshold condition $\bar{n} = 1$, since all the photons are emitted in this case into a single cavity mode. Assuming an emission wavelength around $1 \mu\text{m}$ and a realistic value for Q around 2000, the threshold would correspond to a pumping rate of 10^{12} electrons-hole pairs per second, equivalent to an injection current of $0.16 \mu\text{A}$.
- an alternative approach consists in removing the condition imposing a single-mode cavity, and in selecting a microcavity with a high β coefficient, for instance by exploiting the Purcell effect. In view of the remarks previously developed, it is essential to adjust the number of emitters, i.e. the size of the active medium for a semiconductor source, in order for ξ to be neither too large nor too small, while at the same time preventing the gain saturation problem to occur ($\xi > 0.5$). Let us for instance consider two different types of microcavities that will be presented in more detail in Section 7.2.1 of this chapter: first a GaAs/AlAs micropillar, with a $1 \mu\text{m}$ diameter and a quality factor Q around 2000, and then a microcavity formed by a two-dimensional photonic crystal with an ultimately small volume ($\sim 0.3 (\lambda/n)^3$) and a quality factor of the same order ($Q = 2000$). Let us insert in each cavity a small fraction of a semiconductor quantum well with a surface of $0.3 \times 0.3 \mu\text{m}^2$. This would correspond to inserting an equivalent number of emitters $N_e \sim 3000$ for a joint density of electronic states equal to $3 \cdot 10^{12} \text{ cm}^{-2}$. The linewidth of this ensemble of emitters, which is of the order of kT , is much larger than the linewidth of the cavity mode (0.6 meV for $\lambda \sim 1 \mu\text{m}$). Assuming the emitter to be in resonance with the cavity mode, the magnitude of the Purcell effect can then be calculated to be of the order of 0.8 for the micropillar and 16 for the photonic crystal microcavity, since the latter presents a much smaller effective volume ($F = F_p \Delta\omega_{cav}/\Delta\omega_{em}$ as has been shown in Section 7.1.2 of this chapter). As-

suming the cavity mode to be non-degenerate in both cases, it turns out that $\beta = F/(F+\gamma) \sim 0.45$, $\tau \sim 0.5$ ns for the micropillar and $\beta \sim 0.93$, $\tau \sim 60$ ps for the photonic crystal cavity respectively, while on the other hand, a quality factor equal to 2000 leads to $\varphi \sim 10^{12} \text{ s}^{-1}$. Finally, the values for the main parameters of the laser are $\xi \sim 1.5$, $2\xi(1-\beta) \sim 1.6$ and $P_{th} \sim 0.3 \mu\text{A}$ in the case of the micropillar, and $\xi \sim 27$, $2\xi(1-\beta) \sim 0.89$ and $P_{th} \sim 0.4 \mu\text{A}$ in the case of the photonic crystal cavity. At first sight, it might be somewhat puzzling that the higher lasing threshold should be obtained for the cavity which actually displays the *largest* value for β . This however can be explained by the much larger value of the term $2\xi(1-\beta)$ in the photonic crystal cavity. It can clearly be seen here that the optimisation of the size of the active medium is an essential step in the design of a microlaser. Actually, reducing the surface of the quantum well down to $60 \times 60 \text{ nm}^2$ in the photonic crystal cavity would lead to $\xi \sim 1$ and $P_{th} \sim 0.17 \mu\text{A}$. The latter value is actually very close to the value $P_{th} = 0.16 \mu\text{A}$ that would be obtained in the ideal case where $\beta = 1$

- finally, a completely different approach consists in reducing as much as possible the amount of the cavity losses φ , at the price of a lower value for β . The experiments which have been conducted on silica microspheres are quite representative of this approach (Sandoghdar 1996). For this purpose, the active material, consisting for instance of rare earth atoms, can be embedded in the sphere itself. Another possibility is to place an external emitter, for instance a semiconductor nanostructure, in the near vicinity of the sphere.

This discussion shows that the optimisation of microlasers could lead to a significant reduction of the threshold current of semiconductor lasers, whose minimum value is currently of the order of $30 \mu\text{A}$ for the best vertical cavity surface emitting lasers (Huffaker 1997). Conversely, any further decrease of the threshold current would open new perspectives in the field of optical sensors, for instance for environmental or biomedical applications. Further, lasers with simultaneously high values for β , φ and $1/\tau$ could potentially operate at very high modulation frequencies. In order to turn these hopes into reality, it will be necessary to reduce the non-radiative recombination processes down to a negligible level. In practice however, this poses a considerable challenge, as does the electrical pumping of such microstructures.

In this respect, the localisation of electron-hole pairs in semiconductor quantum dots seems to be a very attractive method for limiting the diffusion of the charge carriers which takes place towards the defects and the free surfaces, and therefore for reducing the efficiency of the non-radiative recombination processes (Gérard 1996a). For the purpose of discussing the feasibility and potential performances of quantum dot microlasers, let us first consider a microcavity containing an ensemble of quantum dots. At low temperatures, a single quantum dot exhibits a spectrally narrow emission with a typical width of a few μeV in the case of InAs/GaAs quantum dots. Due to their size dispersion, the different quantum dots are more or less in resonance with the cavity mode, and therefore they experience a more or less strong Purcell effect. In turn, the average β factor becomes much smaller than unity when the linewidth of the cavity mode becomes spec-

trally narrower than the inhomogeneously broadened emission linewidth of the ensemble of quantum dots. The situation is quite different at room temperature, this being due to the strong *homogeneous* broadening in this case of the emission lines of individual quantum dots, which may range from 5 to 10 meV for InAs dots. Assuming a typical value for the inhomogeneous broadening of state-of-the-art quantum dot ensembles (15 meV for InAs quantum dots), it can be seen that a large fraction of the quantum dots contributes to the lasing mechanism.

For a photonic crystal cavity with a volume of $0.3 (\lambda/n)^3$ and a quality factor equal to 2000, it can be readily demonstrated that a few hundred quantum dots would be necessary for reaching the lasing effect. Having such a large number of dots in so small a cavity could be quite prohibitive in terms of fabrication, since the surface density of quantum dot layers with a good homogeneity is typically of the order of $100 \mu\text{m}^{-2}$ in the best of cases. The recent improvement of the quality factor Q of photonic crystal microcavities (Akahane 2003) represents a real opportunity from this point of view. Indeed, the number of emitters required for lasing varies in inverse proportion to the Q factor, and a lasing effect can be reasonably expected in view of the standard level of fabrication of quantum dots.

Let us finally consider a system formed by a single quantum dot in a microcavity. In such a system, lasing can be achieved only in the low temperature regime, where the homogeneous linewidth of the quantum dots becomes sufficiently narrow. In the same way as for micromasers or single-atom lasers (Meschede 1985), quantum fluctuations play a key role in the operation of such a device, and sophisticated quantum models, which would be beyond the scope of the present book, need to be used in order to properly describe them. Nevertheless, from our general discussion on microlasers, we may understand the two main approaches which are currently being investigated for the fabrication of a single quantum dot in a microcavity. In the first case, the single quantum dot is coupled to a cavity with a very high quality factor Q and a low loss rate φ . A threshold current as low as 10 pA was thus predicted for such a system (Pelton 1999). According to the second approach, the laser would be operating in the regime of a very strong Purcell effect (see Section 7.1.2 in this chapter) thanks to the use of a semiconductor microcavity, in the form for instance of a microdisk of the kind described in Section 7.2.1 of this chapter (Gérard 2003). In order to reach the lasing threshold, the emission rate into the cavity mode must be higher than the photon loss rate. We therefore have $1/\tau > \varphi$, whence it follows that $\Delta\omega_{\text{cav}} < \Delta\omega_{\text{em}}$. If the linewidth $\Delta\omega_{\text{em}}$ of the emitter itself is smaller than the Rabi frequency Ω , the system formed by the quantum dots and the cavity will experience a strong-coupling regime (Section 7.1.2). Let us therefore assume that this regime has been achieved at a low temperature. By increasing the temperature, the emission line of the quantum dots could be progressively broadened. Therefore, starting from a strong coupling regime, one would then observe a weak coupling regime with $1/\tau > \varphi$, where single-atom lasing could be achieved. Such a laser would operate through the very strong enhancement of the spontaneous emission rate of the quantum dot, and β would therefore be very close to unity. By further increasing the temperature, thereby by reducing the magnitude of the Purcell effect, one would reach a regime where

$1/\tau < \varphi$ and lasing would become impossible. In the intermediate regime, a number of original effects are expected to occur. An example of such an effect, which would be observable under strong injection conditions, is the blinking of the laser emission caused by the fluctuations of the number of charges in the quantum dot.

7.2 Three-Dimensional Optical Confinement in Zero-Dimensional Microcavities

7.2.1. Different Types of Zero-Dimensional Microcavities¹

Considerable efforts have been devoted during the 1990s towards the development of cavities allowing the confinement of light at the wavelength scale and thus the exploration of cavity quantum electrodynamics (CQED) in solid state systems. For this purpose, two basic phenomena can be used, either alone or in combination. The first one is the phenomenon of total internal reflection, used for achieving three-dimensional confinement in microspheres (Braginsky 1989), in microtires (Armani 2003) and in microdisks (Mc Call 1992). The second such phenomenon is the distributed Bragg reflection, implemented in one-dimensional dielectric mirrors and more generally in photonic band gap crystals. Micropillars (Jewell 1989) are based on a combination of guiding along the axis of the pillars and reflection by one-dimensional Bragg mirrors in order to achieve a three-dimensional confinement. By contrast, two-dimensional photonic crystal membranes combine a guiding in the semiconductor slab and a lateral confinement by the photonic crystal. While the highest Q factors are obtained with microspheres and with microtires, microdisks, micropillars and photonic crystal microcavities exhibit the smallest volumes V . Further, these devices can be fabricated using available semiconductor technologies, which bring the perspective of a large-scale integration for applications. In what follows, we shall focus on this second series of microcavities. Different examples of such microcavities are represented in Fig. 7.4. These cavities are not perfect 'photonic boxes' in the strict sense of the term, since they present a continuum of non-resonant or leaky modes in addition to a discrete series of electromagnetic modes confined along all directions of space. Only the use of three-dimensional photonic crystals would allow the total suppression of leaky modes. Chapter 12 in this book will be devoted to these crystals, and more particularly to the advances which have taken place since the pioneering experiments of E. Yablonovitch for their fabrication at optical wavelength scales. This being, remarkable results have already been obtained with each of the microcavities.

¹ A three-dimensional optical confinement results in zero-dimensional microcavities presenting a discrete series of resonant electromagnetic modes, possibly accompanied by a continuum of non-resonant modes. These two terms will be used indifferently in this section.

ties represented in Fig. 7.4, both in terms of high Q factors and of small volume. To a large extent, these results were made achievable thanks to the possibility of easily embedding ‘artificial atoms’, i.e. semiconductor quantum dots, in these cavities, which facilitates their characterisation and their optimisation (Gérard 1996b). Semiconductor quantum dots are generally obtained through a self-organisation process. The latter typically occurs during the growth of a thin epitaxial layer exhibiting a strong lattice mismatch with the substrate. Quantum dots have a typical volume of $10^2 - 10^3 \text{ nm}^3$, and exhibit a high size dispersion. Although the linewidth of an individual quantum dot is relatively narrow ($\Delta E \sim 1 \mu\text{eV}$), the luminescence of a quantum dot layer might cover a very broad spectral range. In other terms, an ensemble of quantum dots forms a broadband source with negligible intrinsic absorption losses. Such an internal source is ideally suited for probing the optical properties of quasi-empty microcavities of the kind represented in Fig. 7.4.

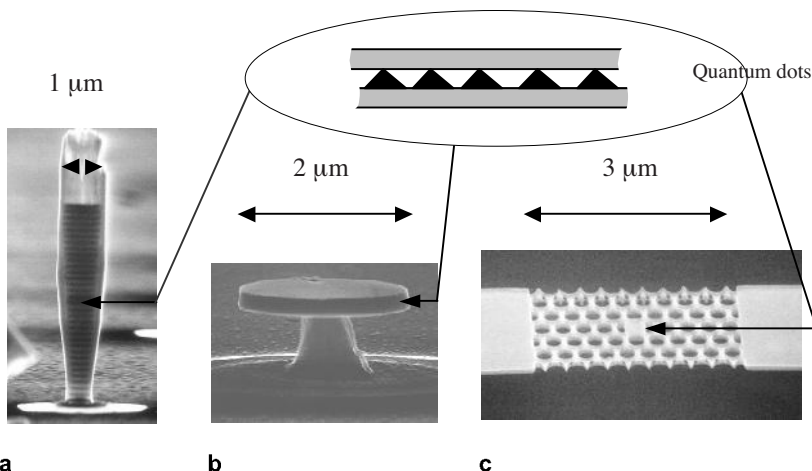


Fig. 7.4. Micrographs of different optical microcavities fabricated at the ‘*Laboratoire de Photonique et de Nanostructures*’ (LPN) in Marcoussis, France **a.** Micropillar **b.** Microdisk **c.** Two-dimensional photonic crystal cavity. Quantum dot layers are incorporated in each cavity. A schematic representation of such a layer is displayed at the top of the figure. The higher factors of merit reported for each of these cavities are: **a.** $Q = 2100$, $V = 5 (\lambda/n)^3$, $F_p = 32$ (Gérard 1998) **b.** $Q = 12000$, $V = 6 (\lambda/n)^3$, $F_p = 150$ (Gayral 1999) **c.** $Q = 2800$, $V_{eff} = 0.43 (\lambda/n)^3$, $F_p = 490$ (Yoshie 2001)

Pillar Microcavities

Micropillars have received much attention since the first realisations of vertical cavity surface emitting lasers. The possibility that they might exhibit interesting features for the enhancement of the spontaneous emission rate and for low-threshold lasing was recognised at the beginnings of the 1990s. In the example represented in Fig. 7.4a, the micropillars were fabricated by the reactive ion etching (RIE) of a GaAs/AlAs λ -cavity. The cavity was resonant at 0.9 μm , while the radius of the cylinders was typically less than 10 μm . Actually, for micropillars with a sufficiently large radius, the mode energies can be quantitatively understood by using a simple model based on the decoupling of the vertical and lateral confinements. The guided photons are vertically confined by the distributed Bragg reflection, but their velocity is modified owing to the lateral confinement. In practice, the resonance condition is the same as for planar microcavity, provided however that the index of the active semiconductor layer be replaced by the effective index of the guided mode (Gérard 1996b). However, for narrow micropillars ($r < 1 \mu\text{m}$), this model turns out not to be adequate. In such cases, FDTD calculations are needed for analysing the modal properties of the cavity (Vuckovic 2002b).

These FDTD calculations show that, through the optimisation of the thickness of the layers, values for Q as high as 10,000 could be achieved, with effective volumes as small as $\sim 5 (\lambda/n)^3$ in the GaAs/AlAs system. This would ultimately lead to Purcell factors larger than 150. Actually, experimental results have revealed that Q decreases for micropillars with a radius smaller than $\sim 3 \mu\text{m}$ (Rivera 1999; Tezuka 1993). This evolution can be readily explained from the significant roughness of the sidewalls of the pillars. The best values for Q reported thus far for micropillars with a 1 μm radius are between 2000 and 3000.

The luminescence spectrum of quantum dots embedded in micropillars is typically composed of a series of narrow peaks associated with resonant modes and a broad pedestal associated with the continuum of non-resonant modes. The influence of the cavity on the luminescence efficiency of the quantum dots can then be directly revealed by time-resolved photoluminescence experiments of the kind described in Section 7.2.2. A shorter luminescence decay time, i.e. a shorter lifetime of the excitons, will be observed for quantum dots whose optical transition coincides with a resonant mode.

Microdisks

Semiconductor microdisks of the kind represented in Fig. 7.4b allow the propagation of whispering gallery modes. These modes are guided towards the periphery of the microdisk by a phenomenon of total internal reflection, thereby leading to a strong confinement of light (Chang 1996). Microdisks are generally fabricated by using two different types of etching: the semiconductor multilayer at the top of the substrate is etched by RIE into a cylindrical post, while the pedestal of the disk is fabricated by the selective wet etching of a sacrificial layer (Baba 1997; Gayral 1999; Michler 2000c; Mohideen 1994; Slusher 1993). Microdisks provide a more

efficient three-dimensional confinement than micropillars, where resonant modes are partially localised both in the periphery of the cylinder and in the Bragg mirrors. For a microdisk with a small radius ($\lambda/n < r < 20 \lambda/n$), the effective surface of the whispering gallery mode with lower quantum radial number is approximately given by $0.86 \lambda^2(r/\lambda)^{3/2}$, where the different lengths are expressed in microns (Gérard 1999). The effective vertical thickness h_{eff} of the gallery mode can be estimated by considering the field distribution of the guided mode of the air-confined semiconductor slab which forms the microdisk. For a 250 nm thick GaAs slab, h_{eff} is equal to 175 nm, i.e. approximately $0.6 \lambda/n$ in the case where the wavelength is of the order of 1 μm . One finally obtains an effective mode volume equal to $\sim 6 (\lambda/n)^3$ in the case of a microdisk with a 1 μm radius. Values for Q as high as 20000, limited by the absorption of the quantum dot array, have been theoretically predicted for such a radius in spite of the absorption of the quantum dots embedded in the plane of the microdisk. Values for Q equal to 12000 (Gayral 1999) and to 17000 (Michler 2000c) were experimentally measured for radii equal to 0.9 μm and 2.25 μm respectively. As is the case for micropillars, the photoluminescence spectrum of microdisks reveals narrow peaks due to resonant modes and a broad pedestal associated with leaky modes. A large number of whispering gallery modes associated with the different radial indexes and with the different polarisations can actually be observed. Microdisks are excellent candidates for the study of the Purcell effect in solid state microcavities, as well for the demonstration of the thresholdless laser or of the strong coupling between light and a quantum dot (see Sections 7.1.3 and 7.2.4 in this chapter).

Photonic Crystal Microcavities

Until now, three-dimensional confinement in photonic crystal microcavities has been achieved essentially by using one-dimensional (Foresi 1997) or two-dimensional (Labilloy 1998; Painter 1999a; Vuckovic 2001) photonic crystal cavities and by resorting to a combination of guiding in a semiconductor slab and of reflection on photonic crystal mirrors integrated in the slab. As an example, Fig. 7.4c represents a two-dimensional photonic crystal microcavity fabricated in a suspended membrane. The photonic crystal presents a triangular symmetry, and its parameters have been chosen in such a way as to obtain resonant modes near 1 μm . The membrane is used here as a planar waveguide, while the photonic crystal ensures the confinement along in-plane directions. The combination in this geometry of a strong vertical confinement with a limited penetration of the field in the surrounding photonic crystal allows the formation of defect modes with an effective volume as small as $0.3 (\lambda/n)^3$. As a counterpart, the quality factor of these photonic crystal cavities is essentially limited by the optical scattering occurring out of the plane of the membrane. Nevertheless, optimised designs based on FDTD calculations have led to a significant reduction of these losses by more than one order of magnitude (Vuckovic 2001; Akahane 2003). Thus, for GaAs systems, state-of-the-art microcavities in a two-dimensional photonic crystal slab display very impressive figures of merit ($V_{\text{eff}} = 0.43 (\lambda/n)^3$, $Q = 2800$) and in particular,

they present the highest Purcell factors from all solid state microcavities ($F_p = 490$) (Yoshie 2001). Still higher figures of merit have been reported for Si systems ($V_{eff} = 0.7 (\lambda/n)^3$, $Q = 45000$) (Akahane 2003), which seem to be very promising for the future development of photonic crystal microcavities.

As a summary, all zero-dimensional semiconductor microcavities which have been described here provide a much stronger confinement than silica microspheres ($V_{eff} = 1000 (\lambda/n)^3$, $Q = 10^9$) (Collot 1993) or microtores ($Q = 10^8$) (Armani 2003), but they also present a much lower quality factor. From an optimistic point of view, it might be considered that the small volumes of these semiconductor cavities could compensate for this lower quality factor. High Purcell factors would thus be within reach for moderate values for Q (10^3 - 10^5). Accordingly, the constraints imposed on the linewidth of the emitter would be less severe, which opens the way to the utilisation of greater variety of emitters for achieving a Purcell effect, including for instance quantum wells or quantum dots operated at room temperature. The same argument also applies to photonic crystal microcavities in comparison to other types of semiconductor microcavities. For applications at room temperature, photonic crystal microcavities with an ultimately small mode volume seem to be preferable to microdisks with a high quality factor, provided that the non-radiative carrier recombination at the air/semiconductor interfaces be low enough.

7.2.2 Control of the Spontaneous Emission in Weak Coupling Regime. Some Experimental Results

As has already been mentioned in Section 7.1.1 of this chapter, planar microcavities formed by distributed Bragg reflectors modify only marginally the spontaneous emission rate of embedded emitters. This is due for the most part to the penetration of the electromagnetic field in the mirrors, which results in an increase of the effective length of the microcavity. For instance, in the case of the GaAs/AlAs system, a cavity with a ‘physical’ length equal to λ/n results in a total effective length close to 4λ . The measurements of the time-resolved photoluminescence of InAs quantum dots embedded in such a microcavity has revealed only limited variations of the radiative lifetime of quantum dots, which is consistent with the theoretical predictions. Indeed, this lifetime turns out to increase or decrease at most by 20% depending on whether the optical transition energy of the quantum dots is higher or lower than the resonance energy of the microcavity at normal incidence respectively (Bayer 2001). Similar results have been reported for rare-earth atoms embedded in $\text{SiO}_2/\text{TiO}_2$ dielectric microcavities (Vredenberg 1993).

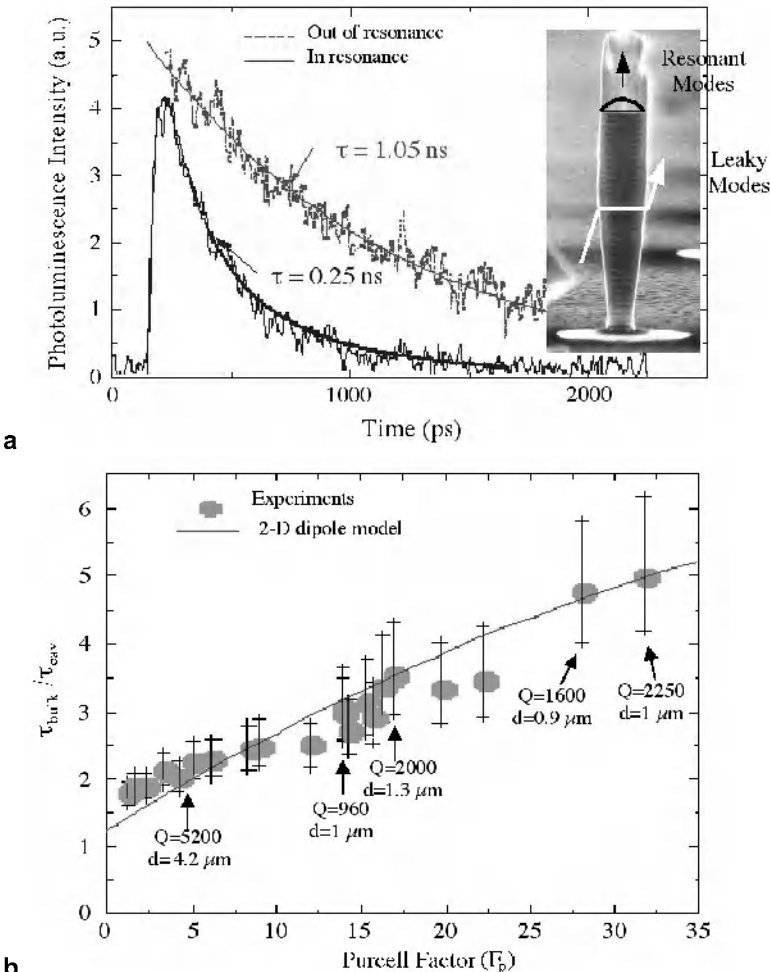


Fig. 7.5. **a.** Time-resolved photoluminescence (PL) signals measured for two groups of quantum dots in a circular micropillar ($d = 1 \mu\text{m}$, $Q = 2250$, $F_p = 32$). The dots in the first group are resonant with the fundamental cavity mode, and exhibit the fastest photoluminescence decay. The dots in the second group are out of resonance and exhibit the slowest photoluminescence decay **b.** Experimental evolution of the relative photoluminescence decay rate $\tau_{\text{bulk}} / \tau_{\text{cav}}$ versus the estimated Purcell factor F_p (ovals). The diameter d of the micropillars and the quality factor Q of the cavity are reported for some of the micropillars. The error bars correspond to a time uncertainty of 70 ps relative to τ_{cav} . The solid curves represented in **a** and **b** were calculated for resonant quantum dots under the assumption that these dots were arbitrarily located in the cavity plane and that their emission frequencies were arbitrarily positioned with respect to the cavity mode frequency. It was further assumed that the emitting dipoles were oriented in the plane and that the relaxation time of the carriers injected in the quantum dots was equal to 35 ps

Let us mention at this point that a strongly enhanced luminescence decay rate ($\times 2$) had previously been observed for quantum wells and for organic dye molecules embedded in planar cavities (Suzuki 1991). Contrary to quantum dot arrays or to the collections of rare earth-atoms used in the experiments reported above, emitters of this type cannot be considered as being independent light emitters: the faster luminescence decay rate is due in this case to such collective effects as superradiance or stimulated emission.

To this date, the approach which has been the most successful towards the observation of a strong enhancement of the spontaneous emission rate (or Purcell effect) for solid state emitters is based on the combination of a zero-dimensional microcavity, in the form for instance of a micropillar or of a microdisk, with semiconductor quantum dots (Gérard 1998). Experiments have been conducted either on ensembles of quantum dots, or on isolated single quantum dots at sufficiently low temperature (5-77K), in order to ensure the monochromatic emission of each of the quantum dots. In the first case, the cavity mode collects the emission from a large number of quantum dots, each with a specific spontaneous emission rate, which depends both on the location of the quantum dot inside the cavity and on its frequency detuning with respect to the cavity mode. At first sight, this might be considered a disadvantage, since the average magnitude of the Purcell effect is much lower than that of a single quantum dot ideally located in the cavity and ideally tuned to the cavity mode. However, this property actually turns out to be an advantage when experimental results are to be quantitatively interpreted. For large ensembles of quantum dots, the average Purcell effect can indeed be modelled from the spatial and spectral statistical distribution of the emitters. By contrast, experiments conducted on single quantum dots should be analysed with much caution, since the exact location of the quantum dot in the cavity is either unknown or very poorly known. The experimental results that will be presented hereafter shall illustrate how complementary these approaches are in practice (Solomon 2001).

In Fig. 7.5a are represented photoluminescence decay curves obtained for a collection of quantum dots in a high- F_p ($F_p = 32$) GaAs/AlAs pillar microcavity. As mentioned in Section 2.1 of this chapter, the photoluminescence spectrum consists of a series of sharp peaks corresponding to the resonant cavity modes, and of a weak background emission associated with the emission of quantum dots in the continuum of the non-resonant pillar modes. A multispectral time-resolved setup, based on a streak camera, is used for simultaneously measuring the decay rates of the different types of quantum dots, whether they be in resonance or out of resonance with the fundamental mode of the micropillar. For quantum dots out of resonance with the fundamental mode, the decay rate is very similar to the radiative lifetime of similar InAs quantum dots in a bulk GaAs matrix. By contrast, the photoluminescence decay time is reduced by a factor of 5 for the dots which are in resonance with the fundamental mode of the cavity. This selective reduction of the lifetime of the quantum dots in resonance with this mode confirms the intrinsic nature of the underlying phenomenon, and is a very clear indicative of the Purcell effect. Similar studies conducted for different types of micropillars (Fig. 7.5b) have shown that this enhancement of the luminescence decay rate is a function of

the Purcell figure of merit F_p defined by Eq. 7.8. More precisely, all these results can be quantitatively interpreted by taking into account the spectral and spatial statistical distributions of the quantum dots with respect to the cavity mode (Gérard 1998, 2003).

Increasing the spectral resolution in the previous experiment also allows studying the dependence of the Purcell effect on the spectral detuning with respect to the mode. As might have been expected from Section 7.1.2, the enhancement factor of the spontaneous emission rate follows a Lorentzian evolution (see Eq. 7.5), which reflects the contribution of the fundamental mode to the spectral density of modes in the pillar microcavity.

Since they present a high Purcell factor, microdisks allow the observation of even greater modifications of the spontaneous emission rate for quantum dots in resonance with a whispering gallery mode. An average enhancement factor of the order of 12 was thus observed for a $1.8\text{ }\mu\text{m}$ diameter microdisk with $Q = 10000$ and $F_p = 160$ (Gayral 2001). Interestingly enough, the radiative lifetime would be about 10 ps for a single quantum dot ideally coupled to the cavity mode. It might also be noted here that the correct modelling of the experiments needs to take into account the finite value of the relaxation time of the electron-hole pairs injected from the GaAs barrier states to the quantum states of the dots (~ 30 ps).

Time-resolved photoluminescence experiments have been extended to the case of single quantum dots by embedding, either in a micropillar or in a microdisk, a very dilute quantum dot array with a surface density no higher than a few 10^9 cm^{-2} (Moreau 2001b; Solomon 2001). Here again, the enhancement effect was selectively observed for the isolated quantum dots that were resonantly coupled to a cavity mode. An even more spectacular demonstration of the Purcell effect, achieved by tuning the energy of the quantum dots with respect to the mode energy, has also been reported (Kiraz 2001). By varying the temperature of the quantum dot sample, the spontaneous emission rate of a single quantum dot was found to be enhanced by a factor as high as 6.

Finally, the Purcell effect can also be demonstrated in a rather simple way by studying the photoluminescence signal as a function of the pump power for a continuous non-resonant excitation of the wave. The emission associated with the fundamental optical transition of a single quantum dot, or of a set of quantum dots with identical band gaps, tends to saturate when the first levels in the conduction and valence bands of the dots are completely occupied. It is quite obvious that the pumping power needed for inducing this saturation effect will be all the larger that the radiative lifetime of the quantum dots is short. Assuming the pumping efficiency to be the same for all the quantum dots, be they in resonance or out of resonance, the presence of a Purcell effect results for the different groups of quantum dots in very different evolutions of the photoluminescence signal with respect to the excitation power. Using this approach, an enhancement factor of the spontaneous emission rate close to 18 has thus been observed for InAs quantum dots in a GaAs microdisk (Gayral 2000). This method has also allowed the first observation of a Purcell effect ($\times 10$) for an array of quantum dots in a two-dimensional photonic crystal microcavity ($Q = 680$, $F_p = 19$) (Happ 2002).

7.2.3 Single-Mode Coupling of the Spontaneous Emission

A major incentive for the studies conducted during the early 1990s on semiconductor micropillars was the theoretical prediction of a 'quasi-single-mode' behaviour of the spontaneous emission ($\beta \rightarrow 1$) within the limit of small pillar diameters and narrow linewidth emitters (Baba 1992). This behaviour can be simply seen as a consequence of the Purcell effect, which selectively enhances the spontaneous emission rate into the resonant micropillar mode and provides a dynamic channelling for the majority of the photons emitted in this mode (Gérard 1998). As has been previously discussed in Section 7.1.3, this behaviour should also lead to very-low threshold lasers, and ideally to thresholdless lasers. In the case where the resonant mode of the cavity is non degenerate, Eq. 7.10 leads to $\beta = F/(F + \gamma)$, where γ/τ_0 is the spontaneous emission rate in the continuum of leaky modes, and F/τ_0 is the spontaneous emission rate in the resonant mode, enhanced by the Purcell effect. In the case of micropillars using GaAs/AlAs Bragg mirrors with a relatively low contrast index, the γ term is found to be close to unity, both theoretically and experimentally, with the consequence that β assumes a high value as soon as the Purcell effect becomes pronounced. Among the most spectacular results which have been reported for micropillars of this type, the results obtained by E. Moreau *et al* (Moreau 2001b) and S. Santori *et al* (Santori 2002) deserve a particular mention, since the number of InAs quantum dot emitters was sufficiently low for spectrally resolving the emission of each individual dot. In these experiments, the polarisation degeneracy of the fundamental mode was lifted thanks to the use of micropillars with non-circular (e.g. elliptical) cross-sections or, in other terms, by resorting to the use of a 'form birefringence' (see Chapter 8). Low-temperature time-resolved photoluminescence measurements performed on the quantum dots yielded $(F + \gamma) \sim 5$ for the dots that were optimally coupled to the resonant mode, while the value for γ was estimated from the emission of non-resonant dots to be near unity. Measurements then led to $\beta \sim 0.8$.

The results described above represent an important advance in comparison to those achieved with more conventional cavities where the fundamental mode displays a degeneracy. This degeneracy might be due either to a polarisation effect, for instance in the case of micropillars with a circular cross-section, or to a propagation effect, as is the case for microdisks, where two counterpropagating whispering gallery modes may coexist. Indeed, the spontaneous emission rate $\beta = F/(2F + \gamma)$ in these standard microlaser structures reaches at most 0.5 in the strong enhancement regime ($F \gg 1$) due to the identical coupling of the emitters with each of the two degenerate cavity modes, which is the usual case for semiconductor emitters. It might also be mentioned that the research of high β values has also led to a more efficient control of the polarisation of quantum dot emitters. For instance, InAs/GaAs quantum dots have an optical dipole parallel to the plane of the layers, which statistically presents the same amplitude along all directions in this plane. Therefore, when such dots are inserted in a bulk layer of GaAs, the emission collected at normal incidence is essentially unpolarised. The same applies to

InAs quantum dots in a micropillar with a circular cross-section, due to the identical coupling to the two degenerate and cross-polarised fundamental modes. For micropillars with an elliptic cross-section, this degeneracy is lifted, and the fundamental modes are linearly polarised either along the long axis and or along the short axis of the ellipse. As a result, a very strong linear polarisation degree ($> 90\%$) has been experimentally observed for the emission of single quantum dots that were in resonance with either of these modes. The polarisation of the quantum dot emission results from the fact that the Purcell effect induces a preferential coupling of these dots to a single linearly-polarised cavity mode. This effect has been used for realising a source of linearly-polarised single photons. For more detail on this subject, the reader is referred to Chapter 10 of this book and to (Moreau 2001).

The partial inhibition of the spontaneous emission into the continuum of the leaky modes of the microcavity is a highly desirable feature for further increasing β beyond 0.8–0.9. For pillar microcavities, a metallic coating of the sidewalls can be used in order to reduce the density of the leaky modes and therefore the spontaneous emission rate by approximately one order of magnitude ($\gamma \sim 0.1$), while at the same time maintaining a strong Purcell effect for the quantum dots which are in resonance with one of the cavity modes ($F \sim 2.2$). It has been suggested that such an experimental arrangement would provide remarkably high values for the β factor ($\beta \sim 80\%$) (Solomon 2001), ($\beta \sim 96\%$) (Bayer 2001). Of course, it would be very interesting if these values could be confirmed by more direct measurements of β . The most usual approach for measuring β consists in studying the input/output characteristic curve in the vicinity of the laser threshold. However, as has been seen in Section 7.1.2, no laser clearly operating in the regime of a strong Purcell effect has yet been demonstrated thus far. As will be discussed in more detail in Chapter 10, the direct measurement of the efficiency of a single photon source can be used as an alternative approach. Experimental results on single photon sources based on quantum dots have confirmed that high values for β can actually be achieved in the regime of a strong Purcell effect.

Finally, it might be noted here that the experimental values for β reported in the literature are much higher for quantum dot sources than for quantum well microlasers such as vertical cavity surface emitting lasers, where $\beta \sim 0.04$ (Kukšenkov 1997) or microdisk lasers, where $\beta \sim 0.2$ (Slusher 1993). The reason can be found in the fact that the homogeneous broadening of the emission line of the quantum wells is too strong for permitting any significant enhancement of the spontaneous emission rate by the cavity, especially under the injection conditions attained above the laser threshold. In such structures, the enhancement of the β factor compared to conventional edge-emitting diodes ($\beta \sim 10^{-5}$) is due for the most part to geometrical factors. For microcavities with a comparable geometry, significantly higher β factors can be obtained by using quantum dots at a low temperature as emitters instead of quantum wells. The narrow band emission of these quantum dots is here the key factor which permits to fully benefit from the Purcell effect for efficiently channelling the emitted photons into the resonant cavity mode.

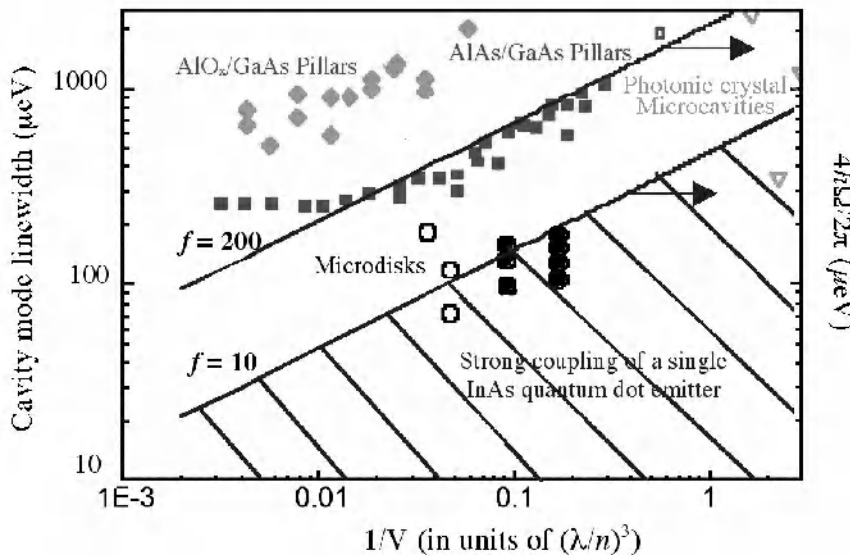


Fig. 7.6. Linewidth of modes confined in zero-dimensional microcavities represented as a function of the inverse of the mode volume. Comparison between the results of experimental measurements for different types of microcavities (*lozenges, squares, circles and triangles*) and the values calculated from $4\pi\Omega$ (*continuous lines*) where Ω is the Rabi frequency. For the sake of calculations, a single quantum dot emitter was assumed to be ideally coupled to the microcavity mode while the values of the oscillator strengths correspond to the optical transitions in InAs dots ($f = 10$) and GaAs dots ($f = 200$) respectively. The experimental data come from works realised at the CNRS/LPN in France (solid symbols), at the University of Santa Barbara (open circles), at the MIT and Caltech (triangles) and at Stanford (open squares). The dashed area corresponds to the situation of a strong coupling between the cavity and the emitter

7.2.4 Towards Strong Coupling Regime for Solid State ‘Artificial Atoms’

Extensive studies have been devoted to the strong coupling of excitons and photons in planar microcavities since the first observation of this phenomenon in 1992 in the case of an active medium consisting of semiconductor quantum wells (Weisbuch 1992). In such a two-dimensional system, both the photonic modes and the excitonic states form continuous bands. However, a coupling between excitons and photons occurs only if the in-plane wave vector is conserved for the optical transition (see Section 7.1.2 in this chapter). This condition ensures the coupling of a given excitonic state to a single photonic mode. It is now clearly established that the properties of this system cannot be properly described save by

taking into account the formation of the mixed exciton-photon states, i.e. the cavity polaritons. However, the analogy with the physics of a single atom in a microcavity remains limited, due to the fact that polaritons states form bands and therefore that the dynamic properties of the system are dominated by such scattering processes as the elastic interactions between polaritons or the inelastic interactions with phonons.

In order to obtain a solid state system that, from a conceptual point of view, would be closer to the model of a ‘single atom in a cavity’, an attractive approach consists in resorting to the most elementary system in cavity quantum electrodynamics (CQED), i.e. to the insertion of a discrete solid-state emitter in a zero-dimensional microcavity. Here again, single quantum dots are the best candidates for such experiments. An experimental demonstration of the strong coupling regime for such artificial atoms would be a decisive breakthrough for the development of solid state CQED. In addition to the possible realisation of single quantum dot lasers (see Section 7.1.3 in this chapter), this would open the way to the possibility of important advances in the field of quantum information processing. A quantum computing scheme has thus been proposed, where quantum dots would be used as the physical support of quantum bits (qubits) in order to create, through their coupling to a photonic mode of the usual type, an effective interaction between distant quantum dots (Imamoglu 1999).

The combination of a semiconductor quantum dot and of a zero-dimensional semiconductor microcavity seems to be a particularly promising approach to the problem of achieving a strong coupling regime. First, the oscillator strength f of the fundamental optical transition of a quantum dot is quite high. Thus, for the InAs/GaAs system, $f = 10$, which corresponds to an electric dipole moment ten times that of actual atoms emitting in the same spectral range. Secondly, semiconductor microcavities display small effective volumes, which leads to the possibility of huge amplitudes for the vacuum field fluctuations in the cavity mode ($\epsilon_{max} \sim 2 \cdot 10^5$ V/m for $V_{eff} = (\lambda/n)^3$ and $\lambda \sim 1 \mu\text{m}$). According to Eq. 7.4, the Rabi energy $\hbar \Omega$ is as high as 100 μeV for a single InAs quantum dot located at the antinode of a confined mode ($| \vec{f} | = 1$) with $V_{eff} = (\lambda/n)^3$ and $| \vec{d} | \sim 10^{-28} \text{ C.m}$. This Rabi energy is found to be typically two orders of magnitude higher than in CQED experiments conducted on single atoms trapped in optical microcavities (Hood 1998).

However, in order that a strong coupling regime be observed, the Rabi oscillation needs to be faster than all the decoherence phenomena which may affect either the exciton or the photon. This constraint can be expressed in terms of frequencies by the approximate condition: $2\Omega > \Delta\omega_e + \Delta\omega_c$, which has already been discussed in Section 7.1.2. The broadening of the emission line of the quantum dots at high temperatures, caused by the interaction between phonons and electrons, prevents the observation of the strong coupling regime for temperatures typically higher than 100K. Conversely, at low temperatures, the emission linewidth of the quantum dots becomes negligible in comparison to the Rabi frequency, and the cavity losses become in practice the most serious decoherence process. In this case, the relevant necessary condition for achieving a strong cou-

pling regime is $\Delta E_{cav} < 4\hbar\Omega$ (Andreani 1999). In order to discuss the prospects of observing such a regime, the linewidth of the mode measured for different types of semiconductor microcavities has been represented in Fig. 6 as a function of the inverse of the mode volume. The results of these measurements are compared to the corresponding values of $4\hbar\Omega$ calculated for a quantum dot located at the antinode of the confined mode.

Let us first consider the case of micropillars. As has been seen, their optical losses are far too important for reaching a strong coupling regime for single InAs quantum dots. In this respect, microdisks and small photonic crystal cavities seem to offer much more promising prospects. It is quite obvious that each of these cavities offer different advantages, i.e. high quality factors for microdisks and ultimately small effective volumes for photonic crystal cavities. In either case, it is not unthinkable that a strong coupling regime could already be achieved for a single InAs quantum dot, provided that the latter be ideally located at the antinode of the mode. However, the cavity losses in this case would still limit the number of Rabi oscillations that could be observed. A further increase of the Q/\sqrt{V} figure of merit (which is in proportion to $\Omega/\Delta\omega_c$) is therefore necessary in order to clearly observe such a strong coupling between a single quantum dot and a microcavity. This is also a condition for any practical exploitation of this phenomenon.

Increasing the oscillator strength of the optical transition could be an alternative approach (Andreani 1999). As an example, a very large oscillator strength can be observed for GaAs quantum dots, formed by monolayer-step fluctuations of the thickness of a GaAs/AlGaAs quantum well. This effect actually results from the delocalization of the exciton wave function over large terraces. Inserting such quantum dots either in a microdisk or in a photonic crystal microcavity seems to be one of the most promising approaches towards the observation of single quantum dots in the strong coupling regime.

8 Frequency Conversion

Thus far, it has been implicitly assumed that photonic crystals interact with electromagnetic waves only through linear processes. This assumption ultimately rested on the fact that the dielectric permittivities of the materials were considered as not being dependent on the intensity of light. However, as will be illustrated in this chapter, the notion of a photonic crystal can actually be extended to the case where it is formed from nonlinear components, which opens the way to the possibility of developing new applications.

This transition to nonlinear optics is necessary for a broader development of photonic crystals, in particular if, as has been prophesized, photonic crystals are ever to play a role comparable to that of semiconductors in the past. Actually, these expectations are based on the mere transposition in the historical course of physics and technology of an analogy between electrons and photons, which in the end only exists between certain formal equations. In this sense, concluding from the formal similarity of these equations to the possibility of achieving with photons results similar to those achieved with electrons is a very bold move, which runs however into certain difficulties.

A first difficulty lies in the fundamental difference between the respective statistics of electrons and photons. It is well known that Fermi-Dirac statistics and the Pauli exclusion principle play a fundamental and crucial role for certain key devices in microelectronics. Other differences, like the vector or scalar character of the electromagnetic field or of a wave function respectively, the role of the mass, which causes electrons to stay still and prevents photons from being ever confined (*'lazy electron, crazy photon'*) should also warn us against overly extending this analogy. However, the most significant difference between electrons and photons in this context is undoubtedly the Coulomb force. From a theoretical point of view, the fact that there is no interaction force between photons first appears as an interesting feature, since it permits to avoid the difficult problem of the self-consistent solution to the coupled Schrödinger-Poisson equations, and to complete calculations of photonic band gap structures. However, when the problem consists instead in designing devices based on photonic band gap materials, this absence of interaction between photons removes the possibility of directly transferring the principles on which electronic devices are based. Indeed, the transistor, this key device of the microelectronic industry, ultimately rests on the very possibility of displacing electron populations thanks to the presence of other electrons. In this regard, the very possibility of realising logic and three-terminal devices ultimately derives from the existence of the Coulomb force.

A prerequisite to the possibility of achieving similar results with photons rather than with electrons would be the ability of influencing an electromagnetic wave by another. Such a property belongs to the field of nonlinear optics, even if it significantly appears for important optical powers. While linear optics comes down to a one-photon problem, the symmetry between electrons and photons is restored in nonlinear optics: the electrons interact through the Coulomb force, with photons acting as the vectors of these interactions, while the photons interact according to a nonlinear processes: in the latter case, the vector of the interaction is the electron in the potential, which gives the material its nonlinear susceptibility.

After having reviewed the significance of nonlinear optics for photonic crystals, it might be pointed out that nonlinear optics is a very broad field, where one needs to distinguish between phenomena of the second order and phenomena of the third and higher orders. The order corresponds here to the amplitude of the field to which the linear effect is proportional (Yariv 1989).

In this chapter, we shall limit ourselves to the consideration of phenomena of order 2, i.e. for the most part to frequency conversion phenomena. It should be borne in mind however that phenomena of higher order also offer a wealth of perspectives, in particular in the field of photonic crystals. The interested reader will find an example of a nonlinear effect in photonic crystals associated with the population saturation in the optical medium in the works conducted by HB Lin *et al* on a photonic crystal optical limiter (Lin 1997).

8.1 The Problem of Phase-Matching

Frequency conversion is a process used in nonlinear optics for the generation of light in spectral regions which are often insufficiently covered by lasers (Armstrong 1962 ; Fejer 1994). Frequency doubling, also referred to as second harmonic generation, is used for instance for producing green light using YAG lasers, while frequency difference and parametrical processes are at the heart of tunable sources, in the mid-infrared as well as in the visible ranges (optical parametrical oscillators). The efficiency of a frequency conversion process is essentially determined by two different parameters: the nonlinear susceptibility $\chi^{(2)}$ of the material considered on the one hand, and the phase difference between the waves propagating at the frequencies ω and 2ω respectively on the other hand. Indeed, the dispersion of the material induces a difference in the wave number $\Delta k = k^{2\omega} - 2k^\omega = 2\omega/c(n^{2\omega} - n^\omega)$, which itself results in a difference in the propagation speed of these two waves. After a length $L_\varphi = \pi/\Delta k$, referred to as the ‘coherence length’, destructive interferences appear between the source wave at the frequency ω and the harmonic wave at 2ω , thereby resulting in a decrease in the efficiency of the nonlinear process. Therefore, in order to achieve an efficient frequency conversion, the value for Δk needs to be low enough in order that the coherence length be as long as possible. However, the ideal situation remains the case where $\Delta k = 0$, a situation referred to as the phase matching condition. This condition can be

achieved in birefringent materials provided however that the various waves propagate with different angles or polarisations.

The two conditions for an efficient frequency conversion process are therefore the existence of a high value for the linear susceptibility $\chi^{(2)}$ on the one hand, and the possibility of a phase matching on the other hand. Thus, although III-V semiconductors and GaAs in particular, present very high nonlinear coefficients, phase matching by birefringence cannot be achieved with these materials due to the fact that they exhibit a cubic symmetry, and therefore are optically isotropic. As a consequence, these materials are in principle not adapted to frequency conversion. This is precisely the reason why optical heterostructures and photonic crystals are of a great interest for artificially achieving phase matching. The possibility of obtaining different dispersion relations by modifying the Bravais lattice or the air filling factor of a photonic crystal is already known. Likewise, since the design of a photonic structure allows for a large number of degrees of freedom, it is quite obvious that a phase matching condition can easily be achieved with different photonic structures specifically designed for this purpose. However, rather than restricting ourselves to the consideration of structures where the dispersion is designed in such a way as to fulfil the phase matching condition, we shall also examine here the case of structures which are periodical only as regards their nonlinear susceptibility. It will be seen that similar properties in terms of frequency conversion can be achieved with these structures as well.

In this chapter we shall describe different approaches which can be followed for achieving such a phase matching in the case of a nonlinear process of the second order. In this case, the material can be completely described by its linear susceptibility $\chi^{(1)}$, which depends on the refractive index¹, and by its nonlinear susceptibility $\chi^{(2)}$, which is the source term of the wave at the frequency 2ω . There exist two different approaches for the realisation of a photonic crystal, in the general sense of the term, depending on the value of the susceptibility selected for the periodicity of this crystal. We shall first discuss the case of ‘classical’ photonic crystals, where the linear susceptibility is periodical, and where the dispersion properties of light can be ‘modelled’ according to the specific requirements of the intended application. We shall then consider the case of materials whose nonlinear susceptibility is periodically structured. These materials are known in the literature as ‘quasi-phased-matched materials’, and their efficiency of frequency conversion is already well established. Finally, this concept will be extended by considering the case of $\chi^{(2)}$ two-dimensional photonic crystals

¹ The linear susceptibility links the electric field E to the polarisation $P = \epsilon_0 \chi E$ of the material, which itself is related to the displacement vector D through the equation $D = \epsilon_0(E + P) = \epsilon_0 \epsilon_r E$. Since the refractive index n is defined by the equation $n^2 = \epsilon_r$, this leads to the equation $\chi = \epsilon_r - 1 = n^2 - 1$.

8.2 $\chi^{(1)}$ Photonic Crystals

8.2.1 One-Dimensional $\chi^{(1)}$ Photonic Crystals

Phase matching can be achieved through the generation of a phenomenon of ‘form birefringence’ in a multilayer structure. This scheme was first successively implemented in 1998, in a GaAs-AlAs oxide (AlO_x) multilayer system (Fiore 1998). The optical isotropy of the GaAs is disrupted by the insertion of AlO_x layers which have a different refractive index than GaAs. The difficulties of finding two materials that would simultaneously present both a high nonlinear susceptibility and a high index contrast explains why this technique is still quite recent.

Form birefringence can be explained in intuitive terms from the symmetry of the multilayer structure. Introducing AlO_x layers in the GaAs (100) removes the symmetry of order 3: the material obtained in the end belongs to the same point group as the KDP crystal, which is known both for its birefringence and for its applications to frequency conversion (Yariv 1989). However, the multilayer structure thus realised still presents the nonlinear characteristics of GaAs, in particular its nonlinear tensor and its value for the coefficient $\chi^{(2)}$, provided however that the AlO_x layers, which are amorphous, and therefore present a zero susceptibility $\chi^{(2)}$, are thin enough. On the other hand, the insertion of the AlO_x layers in the GaAs (111) causes this time the rotation axes of order 4 of the zinc-blende structure to be disrupted. The symmetry group of the resulting material is the 3m point group, to which also belongs lithium niobate, another well-known birefringent nonlinear material (Yariv 1989). In other terms, this method allows retaining the advantages associated with the microscopic structure at the atomic scale of GaAs, namely its high nonlinear susceptibility, while at the same time permitting the use of a refractive index engineering at the macroscopic scale for achieving the desired dispersion and for reproducing the birefringence of a different material.

The modifications thus induced on the symmetry of the original structure by the introduction in a GaAs substrate of thin amorphous layers are schematically summarised in Fig. 8.1.

The phenomenon of form birefringence can also be explained from the distribution, represented here in Fig. 8.2, of the electric field in the multilayers depending on the polarisation of the wave. Thus, in the case of a wave whose magnetic field is contained in the plane of the layers, i.e. of a transverse magnetic (TM) mode of propagation, the boundary condition at the interfaces imposing that ϵE be constant causes the electric field to substantially overlap with the medium of lower index, which results in a corresponding decrease of the effective refractive index of the TM mode. On the contrary, when the wave is polarised in the plane of the layers, i.e. in the case of a transverse electric (TE) mode of propagation, the continuity of the electric field at the interfaces ensures that the effective refractive

index will remain near the effective index of the layers. Multilayer structures are therefore necessarily birefringent. However, only in the case where a high index contrast exists between the layers can a marked birefringence be observed. As an example, the contrast between the refractive indexes of GaAs and AlAs is not high enough for reaching a level of birefringence high enough and for achieving phase matching. It therefore turns out necessary to resort to the use of AlAs oxide, whose refractive index (1.6) is at least two times lower than the refractive index of GaAs, which is higher than 3. This is the reason why, although form birefringence had been suggested as early as 1975 by Van der Ziel (Van der Ziel 1975) as a possible technique for achieving phase matching in semiconductors, this method had to wait more than twenty years before being experimentally implemented. This decisive breakthrough was made possible only with the control of AlAs oxidation at the beginnings of the 1990s and with the generation of the GaAs/AlAs oxide pair of materials which present a very high index contrast.

For wavelengths larger than the period of the periodic multilayer, the dielectric constants are given by the following simple approximations:

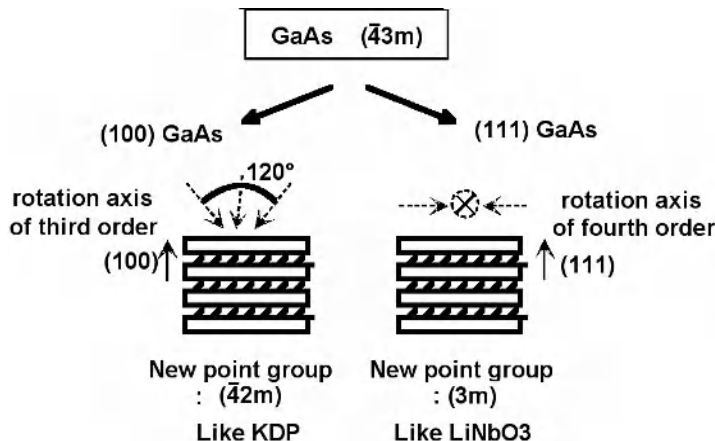


Fig. 8.1. Point groups of multilayer structures containing GaAs. As a bulk material, GaAs is not birefringent. However, the introduction of amorphous layers along the (100) plane of GaAs (left-hand figure) disrupts the symmetry of order 3: the point group of the synthetic material thus created is the same as that of the KDP. If the amorphous layers are inserted along the (111) plane, the symmetries of order 4 disappear this time: the symmetry group of the resulting material is the 3m point group, to which also belongs niobate lithium. The two materials which have thus been copied in terms of symmetry at a macroscopic scale are among the most currently used in nonlinear optics

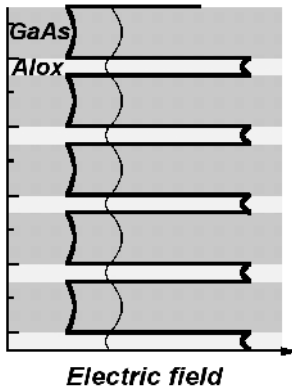


Fig. 8.2 Distribution of the electric field in the multilayers depending on the polarisation of the Bloch wave propagating in the plane of the layers, i.e. normally to this figure. The thick line corresponds to TM polarisation, i.e. to the case where the magnetic field is in the same plane as the layers: a substantial overlap with the AlOx layers arises in this case. The thin line represents the TE polarisation, i.e. the case where the electric field is in the same plane as the layers :

$$\epsilon_{TE} = \alpha_1 \epsilon_1 + \alpha_2 \epsilon_2 \quad (8.1)$$

$$\frac{1}{\epsilon_{TM}} = \frac{\alpha_1}{\epsilon_1} + \frac{\alpha_2}{\epsilon_2} \quad (8.2)$$

where α_1 and α_2 are the filling factors associated with the two materials with indexes equal to ϵ_1 and ϵ_2 respectively. In other terms, if d_1 and d_2 denote the thicknesses of the layers formed by these two materials respectively, then $\alpha_{1,(2)} = d_{1,(2)}/(d_1 + d_2)$. It can be observed that Eqs. 8.1 and 8.2 are the analogue of the equations expressing the equivalent capacitances of an ensemble of two parallel or series capacitors. This simply results from the fact that the equation for the charge equality $C_1 V_1 = C_2 V_2$ between capacitors in series is formally the analogue of the continuity equation in TM polarisation $\epsilon_1 E_1 = \epsilon_2 E_2$. Conversely, the equation for the equivalent voltages at the terminals of two parallel capacitors $V_1 = V_2$ is the analogue of the equality between the fields $E_1 = E_2$ for TE waves at the interface between the two materials. These approximations are extremely useful since they provide in a very simple way orders of magnitude for the form birefringence.

It is of course quite infrequent in the field of photonic crystals to have such simple analytical formulations, and it would therefore be of interest if these formulations could be extended to two-dimensional photonic crystals, where the presence of elongated rods results in the same type of birefringence. However, it turns out that these formulations are valid only within the approximation of a long wavelength. This region corresponds to the part of the dispersion diagrams which lies in the vicinity of the origin, where the relation $\omega(k)$ is approximately linear (see the first part). Actually, the two equations Eqs 8.1 and 8.2 simply yield the squares ($\varepsilon_r = n^2$) of the slopes at the origins of dispersion relations in TE and in TM polarisations respectively. Using these very simple formulations, it can immediately be seen that the birefringence, i.e. the difference between the square roots of ε_{TE} and ε_{TM} , increases with the index contrast $n_2 - n_1$ between the two materials. This of course is far from being surprising for a phenomenon whose physical origin lies in the discontinuity of the field at the interface between the two materials. This discontinuity appears only in TM polarisation, and is all the more marked that the index step is high. Fig. 8.3 presents two examples of phase matching phenomena associated with form birefringence. Diagrams of this type have been called in the literature ‘photon interband transition’ (Winn 1999). This denomination, which probably overly extends the well-known analogy between electrons and photons, is not in our opinion appropriate. Indeed, the principle of phase matching has been known under this name since quite a few decades already: thus, phase-matching schemes can be represented, in a very general way, on dispersion diagrams similar to the one represented in Fig. 8.3, but they have never been referred to as photon interband transitions in the past.

The efficiency of the phase matching achieved by form birefringence was first demonstrated for a process of frequency difference (Fiore 1998), and later in experiments conducted on second harmonic generation and on parametrical fluorescence (De Rossi 2002). Fig. 8.4 displays an example of a structure where the different modes are phase matched by form birefringence, while Fig. 8.5 presents a typical experimental result. The signal obtained during a process of frequency difference follows a sine cardinal evolution and is a function of the wavelength of one of the two pump lasers. This evolution is clearly reflective of the phenomenon of momentum conservation which is involved here (Fiore 1998).

Semiconductors like GaAs can therefore be used as nonlinear materials with a very high efficiency for frequency conversion in the field of integrated optics. These nonlinearities can be further enhanced by exploiting the properties of quantum well structures. This opens the way to the realisation of optical parametrical oscillators capable of being continuously in operation at room temperature, as well as that of two-photon compact sources for quantum cryptography. In principle, such devices become perfectly feasible using semiconductor technology, and the first experimental measurements of parametrical fluorescence in these structures are reported here in Fig. 8.6. However, researches conducted in this direction are presented with severe technological problems, in particular the problem of realising nonlinear waveguides that would exhibit an extremely low amount of losses.

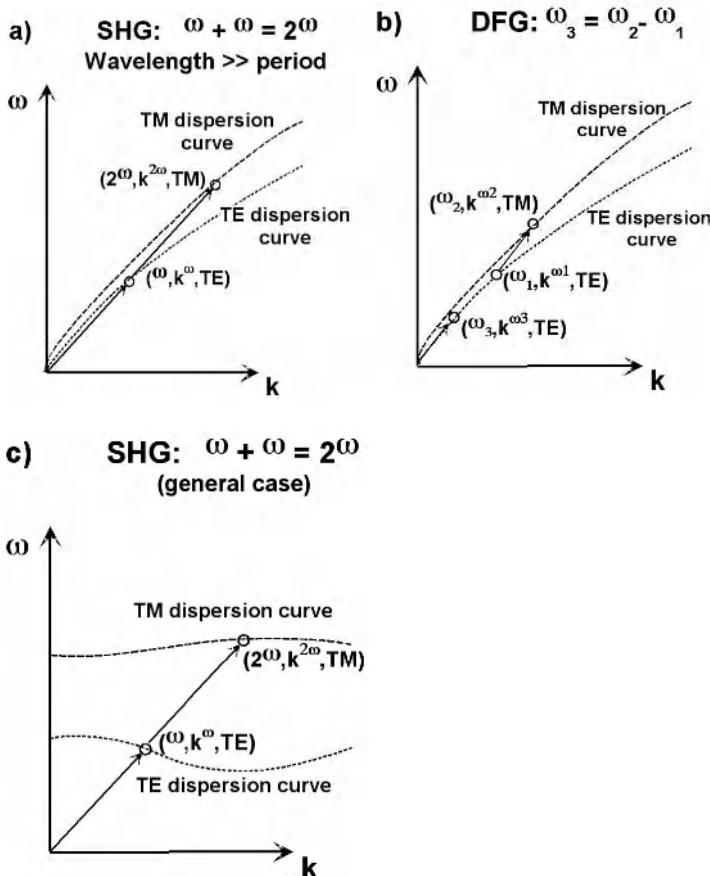


Fig. 8.3. A nonlinear phase matching process allows a coherent transfer of energy between two modes (ω, k) with a conservation of momentum and energy. Such a phase matching phenomenon can always be represented on a dispersion diagram. Two examples of phase matching phenomena relevant to the study of form birefringence are presented here **a**. Second harmonic generation: this process allows a transfer of energy from a wave ($\omega, k^\omega, \text{TE}$) to an harmonic wave ($2\omega, k^{2\omega}, \text{TM}$). The phase matching condition is equivalent here to the fact that the two arrows are identical. This ensures both the conservation of energy (identity of the ordinates of the two arrows) and that of the momentum (identity of the abscissas) **b**. The case of frequency difference is similar **c**. As a general rule, i.e. without any specific restriction to form birefringence, a phase matching phenomenon creates a coupling between two modes which can be represented by a diagram of this type with identical arrows. However, some aspects have not been represented in these diagrams, since the condition of a phase matching, while being of course necessary, is not sufficient. In particular, an efficient conversion process also requires a nonlinear overlap integral between the two modes

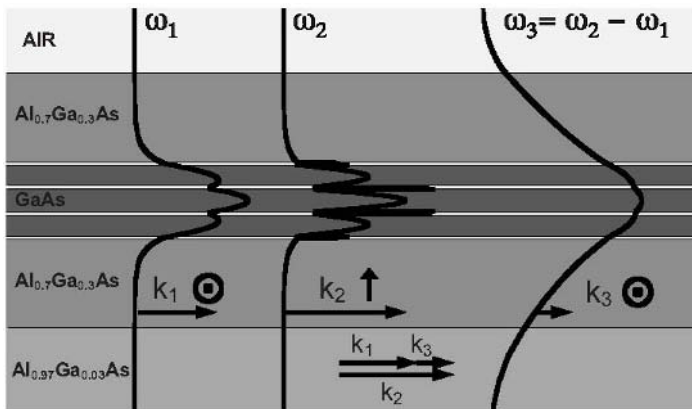


Fig. 8.4. Example of the application of a form-birefringent phase-matched structure to a process of frequency difference. The waveguide used here is realised by molecular beam epitaxy. The guiding structure is clad itself with two AlGaAs confining layers containing 70% of Al, while the waveguide is separated from the GaAs substrate by a thick AlGaAs layers containing 97% of Al. The core of the waveguide itself consists simply of three GaAs layers with a 325 nm thickness and of four AlAs layers (represented by white lines in this figure) with a 40 nm thickness. The fine tuning of the values for the thickness and composition of the different layers allows achieving the dispersion relation needed for phase-matching the nonlinear process. It can be observed here that the mode with frequency ω_2 in TM polarisation substantially overlaps with the oxide layers, this being due to the discontinuity of the field at the interfaces in this polarisation

One-dimensional $\chi^{(1)}$ photonic crystals can also be used for frequency conversion in schemes where the waves propagate normally to the layers. The first case is that where the crystal or the Bragg mirror is used near the edge of the band gap (Dumeige 2001, 2002): in such a case, the crystal exhibits a very high dispersion which can be used for achieving phase matching while at the same time exploiting the resonant amplification of the fields within the layers. Compared to a bulk semiconductor, the enhancement of the efficiency of the frequency conversion process (normalised per unit length of the nonlinear material) results therefore from two distinct effects occurring simultaneously: the high density of states of the electromagnetic field, or in other terms the increase in the amplitude of the field at a resonance in the Bragg structure on the one hand, and phase matching on the other hand. The second case corresponds to that of a microcavity formed by Bragg mirrors (Berger 1997; Simonneau 1997): the phase matching in the cavity is achieved by adjusting the reflection phases of the mirrors in order to compensate for the phase difference arising between the wave at the frequency ω and the wave

at 2ω as they propagate in the cavity. While these two methods are intellectually rich and exciting, their present conversion efficiencies are markedly lower than those obtained in integrated optics, this being essentially due to the limited interaction length. Any significant increase of this length would result in severe technological problems.

Finally, we may mention here another phase-matching phenomenon observed in a microcavity where a quantum well had been embedded. Through the influence exerted by the quantum well on the dispersion of the cavity, phase matching was here achieved in certain configurations for four-wave mixing processes involving two photons at the same frequency ω on the one hand, and two other photons at the frequencies $\omega - \Delta$ and $\omega + \Delta$ respectively on the other hand. These experiments were interpreted using the formalism of cavity polaritons (Savvidis 2001), and the configuration where the phase-matching was optimised was given the name of 'magic angle configuration'. However, the phase-matching phenomenon described by the authors is actually similar to a phenomenon which had previously been reported in another experiment, where the absorption in a quantum well had been used for controlling the index function (Almogy 1994). While there may not be any 'magic' involved in this phenomenon, it nonetheless finds its place among other phase matching phenomena (Baas 2004; Eastham 2003; Whittaker 2001).

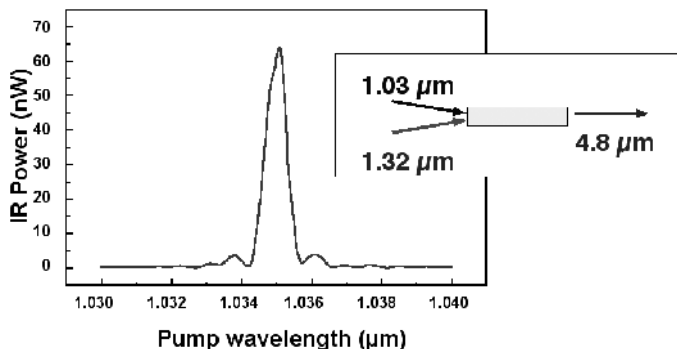


Fig. 8.5. Frequency difference signal represented as a function of the wavelength of one of the Titanium :Sapphire pump lasers. The pumping powers of these two lasers are equal to 0.2 mW and 1.6 mW for pump beams at $1.32\mu\text{m}$ and $1.03\mu\text{m}$ respectively. The fact that the output signal is quite low (a few ten nW) can be explained by the very high optical losses occurring in these samples, which had been realised in 1998. The technological advances which have since then taken place in the realisation of waveguides have led to an enormous reduction of optical losses. Experiments on parametrical fluorescence have also been realised on samples based on the same principles (see Fig. 8.6)

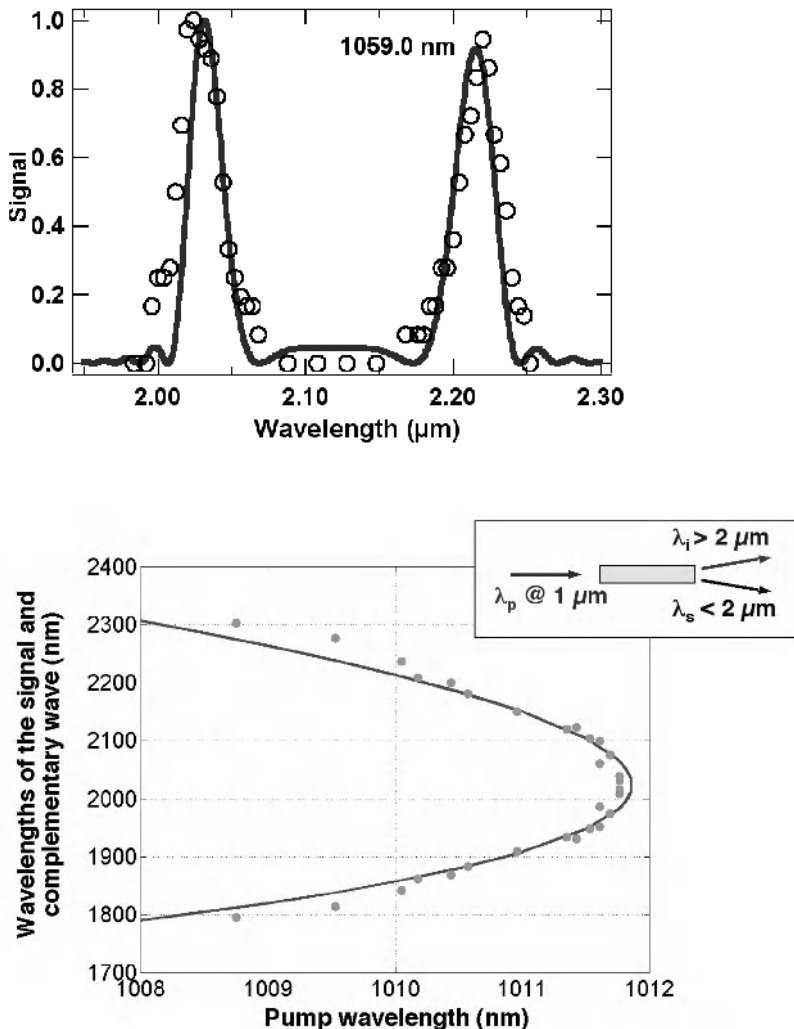


Fig. 8.6. *Top.* Parametrical fluorescence signal for a pumping frequency equal to $1.064 \mu\text{m}$. The points correspond to the actual experimental measurements, whereas the continuous curve only serves as a visual cue. A form-birefringent structure can therefore be used as a source for the generation of twin photons *Bottom.* Dependence of the wavelengths of the twin photons, associated with the signal and with the complementary wave respectively on the pump wavelength. This result shows the very high degree of tunability that could be achieved with an optical parametrical oscillators based on these new materials. The sample used in the upper part of the figure is not the same as the sample used in the lower part

8.2.2 Two-Dimensional $\chi^{(1)}$ Photonic Crystals

As a consequence of the use of the molecular beam epitaxy method for their realisation, GaAs/AlOx heterostructures exist only in the form of thin films of a few microns. However, the reason for researching nonlinear materials with a sufficient thickness lies precisely in the possibility of focusing important energies onto such materials, and therefore of achieving high levels of energy at the new frequencies thus generated. In this respect, two-dimensional photonic crystals represent a possible solution for obtaining materials with both a sufficient thickness and a form birefringence. As for multilayer structures, the latter property results from the very elongated symmetry of these materials. In the general case of two-dimensional photonic crystals, the difference between the dispersion relations of TE and TM modes can be clearly seen from the observation of Figs. 1.9, 1.10, 1.11 and 1.12. This difference, combined with the very structure of two-dimensional photonic crystals formed from holes lattices, can be exploited for materials which generally are not favourable to optical nonlinearities. We shall see that macroporous silicon is one of the two-dimensional photonic crystals in the optical region which exhibits the best characteristics as regards both the depth of the pores which can be attained ($> 100 \mu\text{m}$, see Section 5 in Chapter 9) and the surface over which a lattice formed by such pores may extend ($> 1 \text{ cm}^2$). By construction, a structure realised from macroporous silicon necessarily presents a form birefringence. However, since silicon is centrosymmetric, it does not possess nonlinear coefficients of second order. This can be obviated for instance by filling the pores with a nonlinear material, while an alternative approach would consist in relying instead on the third-order nonlinear processes in the silicon, even though processes of third order are less efficient than processes of second order.

8.3 $\chi^{(2)}$ Photonic Crystals

8.3.1 One-Dimensional $\chi^{(2)}$ Photonic Crystals

A one-dimensional $\chi^{(2)}$ photonic crystal is simply a multilayer structure ($\chi^{(2)} - \chi^{(2)}$) of a very well-known type in nonlinear optics under the name of quasi-phase-matched structures. It might be noted that, contrary to the previous case where light propagated in the plane of the layers, light now propagates along a direction normal to the layers. Further, $\chi^{(1)}$ is now assumed to be constant in the entire structure, so that no phenomenon of photonic band gap may occur. The principle of quasi-phase matching, first suggested by N. Bloembergen *et al* in a pioneering work (Armstrong 1962), consists in reversing the sign of the nonlinear coefficient at the end of a coherence length, i.e. when a phase difference accumulates to π .

between the wave at the frequency ω and the harmonic wave at the frequency 2ω . The sign of the interaction can be reversed for instance by reversing the crystalline orientation, thereby leaving unchanged the construction of the harmonic wave. A detailed explanation of the principles of quasi-phase matching is presented here in Fig. 8.7. An excellent review of the literature on this subject is presented in (Fejer 1992). A large variety of realisations based on quasi-phase matching have been demonstrated, including the 'periodically poled lithium niobate' (PPLN) (Myers 1995), an artificial nonlinear crystal upon which an increasing number of commercial devices are currently being based. Finally, we may mention here interesting results which have been recently emerging on dielectric thin films perforated with two-dimensional photonic crystals, where phase matching can also be achieved as well (Pacradouni 2000).

It might be noted that certain analogies can be drawn between Bragg mirrors on the one hand, and more generally between multilayer structures of the type used in linear optics, where a linear phase-matching function is somehow realised, and quasi-phased matched structures on the other hand. Thus, it has been demonstrated that the transmission spectrum of multilayer structures depends on the Fourier transform $\chi^{(1)}$, and this property has even been used for developing a method for the design of multilayer optical filters on the basis of a Fourier transform principle (Dobrowolski 1978). For instance, in the case of a one-dimensional photonic crystal, the spectral width of the n^{th} band gap is in proportion to the $(n - 1)^{\text{th}}$ Fourier component of the periodical index function (Yeh 1988). This also explains why, in the case of a perfect Bragg reflector where all layers have an optical thickness equal to $\lambda/4$, the spectral width of the band gaps of even order become zero, exactly as Fourier coefficients of odd order do (see also Section 1.3.2 in Chapter 1). In the case where quasi-phase matching is achieved, the evolution of the field is given by an equation of the form (Fejer 1992):

$$\frac{dE^{2\omega}}{dz} \propto (E^\omega)^2 \chi^{(2)}(z) \exp(i(\Delta k)z) \quad (8.3)$$

From the previous equation, the harmonic field turns out therefore to be the Fourier transform of the nonlinear susceptibility function $\chi^{(2)}$:

$$E^{2\omega} \propto \int (E^\omega)^2 \chi^{(2)}(z) \exp[i(\Delta k)z] dz \quad (8.4)$$

Thus considered the principle of quasi-phase matching becomes quite clear: assuming here that the function $\chi^{(2)}$ has a component $\exp(-i\Delta kz)$, the harmonic field is going to constructively increase over a large distance. This is exactly what happens when $\chi^{(2)}$ is constant and when $\Delta k = 0$, which corresponds to the case of the phase matching of a material by birefringence. Likewise, this is also what happens when $\chi^{(2)}$ is periodical with a period $2L_{coh}$, where $L_{coh} = \pi/\Delta k$ is the coherence length. This latter situation corresponds to the case of quasi-phase matching.

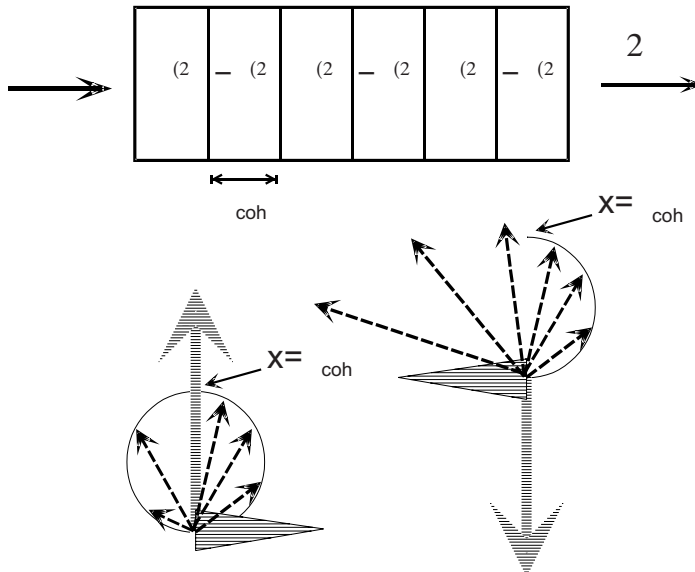


Fig. 8.7. Principles of quasi-phase matching. The quasi-phased matched structure represented at the top of the figure is a $\chi^{(2)}$ photonic crystal. Waves propagate normally to the $\chi^{(2)}$ layers, whose thickness is equal to the coherence length of the nonlinear process. The example considered here is a process of frequency doubling. In the bottom left figure, the broad dashed arrow represents the nonlinear polarisation generating the wave at 2ω . The coordinate system is assumed to be rotating with an angular speed equal to $2k^\omega$ in order for polarisation to remain constant. This nonlinear polarisation generates a field in quadrature, which entails that the field at 2ω thus generated will be given at any time by the direction of the triangle represented in dashed lines at the origin. This triangle is assumed to be fixed in the coordinate system used here. By contrast, since $2k^\omega \neq k^{2\omega}$ the field at 2ω will be rotating in this coordinate system. Different vectors representing the field at 2ω at different times are indicated here in the form of bold dashed lines. This field rotates due to the dispersion relation which causes a dephasing of the nonlinear source (whose phase evolves like two times the phase of the pump wave) and of the nonlinear field (which propagates with its own phase). As a consequence, after a certain propagation length, referred to as the coherence length, the harmonic field moves to left-hand side of the figure. This is to be interpreted as meaning that the nonlinear source starts to destructively interfere with this field. The principles of quasi-phase matching are illustrated in the right-hand part of the figure. After one coherence length, the sign of the nonlinear coefficient is changed by modifying the orientation of the material. This causes the sign of the nonlinear polarisation to stay reversed until time is needed in order for the interaction with the harmonic field to remain constructive

Following this analogy between $\chi^{(1)}$ multilayers (Bragg mirrors) and $\chi^{(2)}$ multilayers (quasi-phase matched materials), a large number of quasi-phase matched structures have been realised. This can be paralleled to the great variety of Bragg multilayer structures. Examples of quasi-phase matched structures include structures with a wide band frequency response, obtained through the use of a variable period ('chirped structures') (Bortz 1994) or structures intended at widening or compressing a pulse in the nonlinear domain (Arbore 1997) much in the same way as in linear optics, multilayer mirrors are used for compensating the intrapulse frequency shift of femtosecond lasers. In the following section, we shall further explore this analogy between $\chi^{(1)}$ periodical structures and $\chi^{(2)}$ periodical structures, by turning this time to the consideration of two-dimensional structures.

8.3.2 Two-Dimensional $\chi^{(2)}$ Photonic Crystals

After discussing successively one and two-dimensional $\chi^{(1)}$ structures and one-dimensional $\chi^{(2)}$ structures, it is quite natural to turn now to the consideration of the periodical structuring of $\chi^{(2)}$ in two dimensions (see Fig. 8.8). This problem was first theoretically addressed in 1998 (Berger 1998), while the first experiments on this topic were conducted by N. Broderick *et al* (Broderick 2000).

Let us here consider the case of a plane wave propagating in a medium formed by $\chi^{(2)}$ cylinders perpendicular to the plane represented in Fig. 8.8. In such a case, the linear susceptibility is constant, with the consequence that no anomalous dispersion or photonic band gap phenomenon occurs. We are therefore presented with a generalisation to the two-dimensional case of the principle of quasi-phase matching. It can be demonstrated that an harmonic wave can develop efficiently in the crystal, provided that the conservation of the momentum of the photons be ensured through the possible contribution of a wave vector \mathbf{G} of the reciprocal lattice:

$$\mathbf{k}^{2\omega} - 2\mathbf{k}^\omega \cdot \mathbf{G} = 0 \quad (8.5)$$

A relatively straightforward argument (Berger 1998) shows that this momentum conservation leads to the formulation of a nonlinear Bragg's law, which expresses the wavelength of the harmonic wave obtained in the crystal by frequency doubling as a function of the walk-off angle θ between the fundamental and the harmonic waves, i.e. the angle formed by the two directions of propagation at ω and 2ω :

$$\lambda^{2\omega} = \frac{2\pi}{G} \sqrt{\left[1 - \frac{n^\omega}{n^{2\omega}}\right]^2 + 4 \frac{n^\omega}{n^{2\omega}} \sin^2 \theta} \quad (8.6)$$

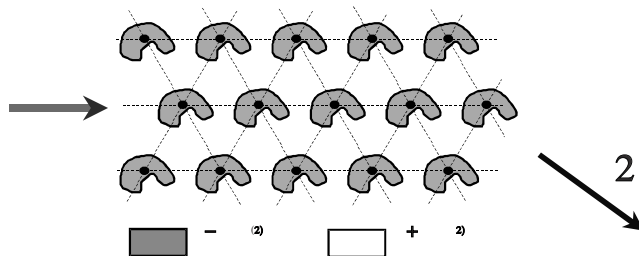


Fig. 8.8. Two-dimensional $\chi^{(2)}$ photonic crystals. The frequency conversion of a wave emerging from a composite material follows a nonlinear Bragg's law

This equation represents a generalisation of Bragg's law describing the refraction of X rays by crystals to the field of nonlinear optics. Actually, the classical form of Bragg's law can be retrieved by imposing that $n^\omega = n^{2\omega}$, which leads to $\lambda^{2\omega} = 2d \sin\theta$, where $d = 2\pi/G$ is the distance between two reticular planes. The frequency conversion process can therefore be likened to the diffraction of an ensemble of nonlinear sources (at 2ω), excited with a certain phase relation by the fundamental wave at the frequency ω , and which collectively emit in accordance with the Huygens-Fresnel principle. This analogy also allows the introduction of various concepts that were first developed in the context of the diffraction of X rays by solid state crystals, like for instance the non-linear Ewald sphere, the rotating crystal method or the nonlinear Laue method (Berger 1998). The first experimental study of two-dimensional $\chi^{(2)}$ crystals was realised in 2000 with lithium niobate (Broderick 2000), thereby vindicating the generalised Bragg's law which has just been described here. A first application for this type of structures is the frequency or wavelength tuning of nonlinear processes. Indeed, for a given frequency ω , the possibility always exists, by some rotation of the $\chi^{(2)}$ crystal, of finding an incidence at which phase matching will be achieved. The versatility of this method, which is not met by one-dimensional quasi-phase-matched materials, compares only to that of the rotating crystal method applied to the X-ray analysis of solid-state crystals, where the rotation of the crystal can always be used for finding a direction allowing the diffraction of X rays. A second possible application is the cascading of different nonlinear processes occurring along different directions of propagation, which has been experimentally demonstrated (Broderick 2000).

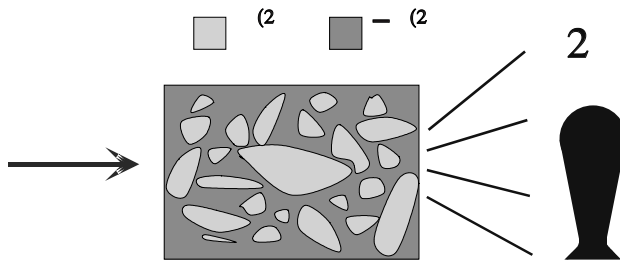


Fig. 8.9. Two-dimensional $\chi^{(2)}$ photonic crystal structure. The shapes of the $\chi^{(2)}$ regions are chosen in such a way as to force the nonlinear emission of the structure under illumination to assume a certain requested shape (nonlinear holography)

A further refinement of the notion of a nonlinear photonic crystal has led to the proposal of nonlinear materials which, rather than being periodically structured in two dimensions, would be structured in such a way as to adapt the harmonic wave to the spatial distribution of the fundamental excitation wave (Berger 1999). This leads to the possibility of developing a genuine nonlinear holography, according to a principle schematically represented here in Fig. 8.9. This concept opens interesting perspectives, but its practical implementation presents a series of difficulties. Thus, assuming a certain spatial distribution of the pump wave, the problem consists in structuring the nonlinear material in such a way as to finally obtain the desired nonlinear emission. In other terms, the problem which needs to be solved within the framework of nonlinear optics is the inverse of the Huygens-Fresnel principle.

Part III

Fabrication, Characterisation and Applications of Photonic Band Gap Structures

Introduction to Part III

The last part of this book will be devoted to a survey of the potential applications of photonic crystals to different fields, as well as to the fabrication and characterisation methods which are the most suited to these crystals. The miniaturisation of existing optical devices and the exploitation of novel properties of the kind presented in the second part of this book are among the main incentives for the development of photonic crystals. This applies not only to semiconductor devices in planar integrated optics, which will be discussed in Chapter 9, but also to microsources (Chapter 10) and optical fibres (Chapter 11). We shall also devote a specific chapter to the subject of three-dimensional photonic crystals (Chapter 12). Since the fabrication of these crystals remains a difficult process, they may appear more ‘futuristic’ than other existing types of photonic crystals, but they are also a possible prefiguration of what could be three-dimensional optoelectronics. Finally, in order for this survey to be as complete as possible, we shall examine in Chapter 13 the potential applications which can currently be expected for photonic crystals in the long wavelength range, i.e. in the field of microwave devices and antennas. In spite of its distinctive features, it is becoming apparent that the microwave region share many common aspects with optics.

9 Planar Integrated Optics

9.1 Objectives, New Devices and Challenges

Planar integrated optics plays a key role in many fundamental optoelectronic devices. These devices can be conveniently classified according to the materials on which they are based. Thus, doped silica/silica systems are used for the fabrication of passive integrated devices with an extremely tight tolerance. As an example of such devices, we may mention here the case of phased arrays or ‘PHASARs’, which are integrated spectrometers intended at multiplexing or demultiplexing signals. Semiconductors, and more specifically III-V semiconductors, are essential to the operation of laser diodes and compact optical amplifiers, used for generating and reinforcing signals, and contain a waveguide for maximising light-matter interaction. Semiconductors also permit the implementation of a large variety of optoelectronic functions and nonlinear optical functions, provided however that the carrier dynamics can be adequately controlled. Dielectric materials with high electro-optical coefficients are more particularly interesting for the realisation of modulators or very fast nonlinear functions (without carrier) used for the generation of signals by the frequency sum or difference of two signals. An example of such a material, which in addition can be polarised, is lithium niobate. Finally, attempts at introducing organic materials are continually made, for the realisation either of low-cost devices or of optical backplanes in board-to-board interconnects. In addition, some of these organic media present a thermal drift of the index $dn/dT < 0$, which is the opposite of the standard case where $dn/dT > 0$. Such a property is of particular interest for the compensation of the thermal drift.

As suggested by this reference to temperature compensation, integrated optics is already a few decades old, enough to find solutions to such problems as the insensitivity to polarisation or parasitic reflections. For all the functions mentioned above, the pioneering devices were indeed developed in the 1960s. Contrary to electronic integration, optical integration has not developed at the fast pace of Moore’s law: no more than two or three functions can currently be cascaded on sixteen channels, and more generally on only two or four channels. The reasons for the limits imposed on integration are far from being trivial. A first limitation is the higher cost of the fabrication of small-scale device. Another limitation lies in the necessity of a coupling of these devices to single-mode fibres with at least a sub-micrometer resolution, without any excessive reflection: the easy mounting of

'optical chips' on 'optical printed circuit boards' still remains a remote prospect. A third limitation is the existence of incompatible technologies, which leads to the hybrid integration of devices: for instance, chips from different technologies (lasers, modulators, etc.) are embedded on another board where an adequate optical circuit has been defined. During the telecom bubble of the late 1990s, the demand for a rapid production of such hybrid devices by an exponentially expanding market diverted research groups from monolithic integration. In any case, realising optical chips as compact and versatile as electronic chips remains at the present time a distant dream.

In this context, the concept of photonic crystal has aroused considerable expectations. After an early naive period, the possibility of implementing integrated optical functions using photonic crystals really started being investigated at the turn of the millennium. A more complex picture of photonic crystals has thus emerged, and we are now in a position to understand how the basic properties of photonic crystals which have been described in the second part of this book can be turned into applications to integrated optics.

As will be seen in this chapter, two-dimensional crystals remain the main focus of attention. The main advantages of two-dimensional photonic crystals, namely their simpler fabrication and easier modelling, lead to the possibility of completely controlling the incorporation of defects or the implementation of certain original dispersion effects. Conversely, it can be said that planar integrated optics provide an elegant method for 'freezing' the third dimension in the two-dimensional problem: starting from a slab with a single-mode behaviour along the third direction, a photonic crystal type structuring is then defined on this slab. To some extent, this amounts to considering the world as being two-dimensional, as in Edwin A. Abbott's 'Flatland' (Abbott 1992).

In such a two-dimensional world, the use of photonic crystals as 'optical insulators' naturally leads to envision the possibility of realising optical circuits bounded by such insulators in order to channel, analyse and combine an increasing number of optical signals in a more compact form than in the solutions which had previously been developed in the field of integrated optics. In particular, the classical guiding method used in integrated optics, i.e. index guiding, leads to severe limitations as regards the curvature of bends, especially for low index contrasts, as is the case with doped silica /silica systems. For this reason, index guiding does not lend itself very well to miniaturisation, since several square centimetres may be necessary for the implementation of a single optical function. Similar considerations apply to devices or functions based on resonant cavities. It is hoped that these limitations could be overcome through the use, either as waveguides or as cavities, of defects in two-dimensional photonic crystals. More specifically, one expects that waves guided in photonic crystal defects could follow bends at the wavelength scale, i.e. at the micron scale for instance. Even if catching up Moore's law remains beyond reach, such a decisive breakthrough would lead to a tremendous acceleration of the evolution towards integration.

Photonic crystals with a strong index contrast also provide the possibility of exploiting the Bloch waves of photonic transmission bands, which are markedly different from usual plane waves propagating in unbounded homogeneous media.

This stake had been clearly perceived by Philip St. J. Russell in his pioneering work on one-dimensional structures in the 1980s. One of the effects expected to occur near a band edge is the superprism or ultra-refraction effect which has been discussed in Chapter 6. It might be recalled here that the wave vector exhibits an enhanced dependence on the frequency ω in the vicinity of a band edge, since $d\omega/dk$ becomes zero in one dimension. This effect is interesting for the demultiplexing of very close signals, with for instance a relative frequency spacing $\Delta\omega/\omega = 0.1\%$. After propagating through a superprism, the different wave vectors could be converted into different propagation angles, with for instance a 10° divergence.

This mux/demux function is necessary for the analysis of an entire series of signals carried by a comb of nearby frequencies (wavelength division multiplexing, WDM). All these signals need to be regenerated, routed, etc. However, in many cases, a single channel, which physically consists of a narrow frequency band, needs to be separated or injected into a fibre. This is the case for instance when a transmission bus line goes by a user: it needs to leave the signal addressed to this user (drop) and to insert the signal received from him (add). This add/drop function is currently one of the most intensively researched. A simple scheme for implementing this function consists in the selective coupling of a guided wave to an optical resonator: the energy is transferred to the resonator only at the frequency of the resonator, and not at any other frequency. After the energy has been transferred, it then needs to be directed onto another element, for instance a detector or another waveguide.

A completely different use of the geometry of two-dimensional photonic crystals will be described when considering the case of microstructured fibres. Contrary to planar integrated optics, which are to be addressed in the present chapter, the propagation of waves in these fibres occur along the invariant direction of the crystal. This is a most important distinction, which can be summarised by saying that the attention focuses in this case on the transverse rather than the longitudinal control of light. Chapter 11 will be more specifically devoted to these fibres, which are also referred to as ‘photonic crystal fibres’. As a consequence of both their relative simplicity, since they are fabricated from a unique material (SiO_2), and their input/outputs, which are as simple as those of usual fibres, these fibres are likely to become the first two-dimensional photonic crystal device to reach the market.

In all these cases, the confinement and the guiding are key functions. We shall therefore begin this chapter with a brief survey of classical optical guiding, based on a refractive index step rather than on periodicity. Different applications in this field will then be described, as well as the choices to be made for actual two-dimensional photonic crystals. Finally, we shall discuss certain problems which have not been satisfactorily answered yet, and which are likely to remain intensively investigated during the next decade. For engineers looking for innovations in the field of integrated optics, it is quite clear that there will be, around the year 2000, a before and an after photonic crystals. Even if applications of photonic crystals were to remain of a limited scope in the near future, their influence on concepts cannot be ignored.

9.2 Fundamentals of Integrated Optics and Introduction of Photonic Crystals

9.2.1 Conventional Waveguides

As a wave propagates away from its source, it generally tends to diverge and to decay. The guiding of light is intended at obviating this effect. The analogue of the potential step which confines for instance water in a canal or electrons in a copper wire is the refractive index step between the core and its cladding with lower index. As will be seen later, such a pure index confinement can be achieved in certain simple configurations. However, since by construction this confinement is not omnidirectional, its implementation is quite delicate in certain critical parts of actual devices. In this respect, photonic crystals bring a more elegant and more general answer to the problem of confinement, even if it is at the price of a greater complexity.

The fundamental phenomenon involved in ordinary index confinement is the total internal reflection of a plane wave propagating from a medium with a high index n_2 towards a plane interface formed by a dielectric with an index $n_1 < n_2$, at an incidence angle beyond the critical angle $\sin \theta_c = (n_1/n_2)$. This leads to the generation, on the side with the lower index, of an evanescent wave, whose amplitude decreases exponentially as the distance to the interface increases.

The two edges of our light channel are therefore two such plane and parallel interfaces, separated by a distance L from one another and clad with two, possibly different, indices n_1 and n_3 , sandwiching the core with higher index n_2 . We now need to account for the wave aspect of the problem, and to search for harmonic solutions at the pulsation ω in the absence of any source. In the planar waveguide geometry, which presents an invariance along two directions, the six components of the electromagnetic field can be separated into two groups of three components respectively, referred to as TE and TM polarisations (see Section 1.1.5 in Chapter 1). Thus, in much the same way as for infinite two-dimensional crystals, the time-harmonic Maxwell's equations reduce to a scalar equation involving one of these two groups of three components. Using the same reference axes as in Fig. 9.1a, where x is the propagation axis and (xz) is the plane of the invariant directions, the TE and TM polarisations are associated with the component groups (H_x, E_z, H_y) and (E_x, H_z, E_y) respectively. The scalar equation may involve either E_z or H_z . From a mathematical point of view, the problem consists in searching for solutions satisfying the two boundary conditions between the field propagating in the core and decreasing evanescent waves in the claddings. Since the system is separable and invariant along the z axis, it turns out that in TE polarisation, the form of E_z is:

$$E_z = A(y) \times \exp(ik_x x) \times \exp(-i\omega t) \quad (9.1)$$

where $A(y)$ satisfies an equation deduced from Eq. 1.6a, which turns out to be completely analogous to the one-dimensional Schrödinger equation if one substitutes $-\omega^2/c^2n^2(y)$ to the potential $V(y)$ and the opposite of the squared propagation constant $-k_x^2$ to the energy eigenvalue E . This analogy is especially valid in TE polarisation, and is less so in TM polarisation. Thus considered, the higher indices can be viewed as potential wells and the claddings as potential barriers. One can therefore draw from the fact that the spectrum of the solutions for k_x^2 is partly discrete with discrete solutions $A_p(y)$ and adequate constants $k_x^{(p)}$, with the sign here being arbitrary. Two solutions $A_1(y)$ and $A_2(y)$ have been schematically represented in Fig. 9.1a in the case of a symmetric waveguide. Note the alternate parities for the field $A_p(y)$ of such a waveguide.

In this symmetric case, the number of allowed discrete solutions is intuitively dependent on the number of oscillations that a wave may complete between the two interfaces, when approaching the critical angle. $A_p(y)$ is actually of the form $\cos(k_y y)$ or $\sin(k_y y)$ in the core, where:

$$k_x^2 + k_y^2 = n_2^2 \omega^2/c^2 \quad (9.2)$$

Let us now reconsider the total internal reflection condition. Actually, this condition means that k_x needs to be large enough in order to prevent the wave from coupling to the radiation modes of the cladding with index n_1 , i.e. to modes whose wave vector is bounded by $n_1\omega/c$.

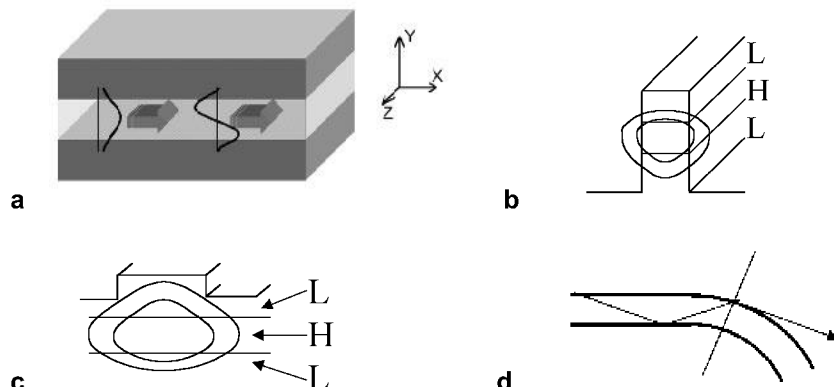


Fig. 9.1. **a.** Planar waveguide and profiles of its first two modes $A_1(y)$ and $A_2(y)$ **b.** Deep-etched ridge waveguide **c.** Shallow-etched ridge waveguide **d.** Bend and role of the critical angle. H and L in figures **b** and **c** are for high-index and low-index, respectively

Since the equation $k_x = k_2 \sin\theta = n_2 (\omega/c) \sin\theta$ also holds, the relation $\theta > \theta_c$ can be rewritten in the form:

$$k_x > n_2 (\omega/c) \sin\theta_c = n_1 \omega/c \quad (9.3)$$

The lowest value allowed for k_x by the total internal reflection condition is therefore $k_x = n_1 \omega/c$. Accordingly, the highest possible value for k_y will be $k_y = (\omega/c) \sqrt{n_2^2 - n_1^2}$, while the number of oscillations has therefore an upper bound $k_y L / \pi$ with this value for k_y . By using simply $(\omega/\pi c) = (2/\lambda)$, and taking into account the fundamental mode which does not complete a full oscillation, the number of allowed modes turns out to be equal to:

$$\text{Number of modes} = 1 + \text{Integer} [(L/(\lambda/2)) \sqrt{n_2^2 - n_1^2}] \quad (9.4)$$

From this equation, it can be seen that in order to achieve a single-mode guiding, i.e. to ‘freeze’ the third degree of freedom of light to a single discrete value, it is necessary that the value for the thickness L should be relatively small. Indeed, while L is small in the case of a high index contrast ($\sqrt{n_2^2 - n_1^2} \sim n_2$ and $L \sim \lambda/2n_2$), it becomes much larger for lower index contrasts, up to ($L \sim \lambda/2 \sqrt{2n\Delta n}$), within the limit of a small index step $\Delta n = n_2 - n_1$, as is the case for instance with doped silica /silica. In practice, the concept universally used in integrated optics is that of the effective refractive index, which depends on the mode p and is defined as follows:

$$n_{\text{eff}}^{(p)} = k_x^{(p)} c / \omega. \quad (9.5)$$

The considerations developed above show that all guided modes satisfy the relation $n_1 < n_{\text{eff}} < n_2$. In the case of a single-mode planar waveguide, everything takes place as though the waveguide were a block of material with index n_{eff} where the beams would however never vertically diverge, i.e. along y .

The asymmetric case has been extensively treated in the literature (Marcuse 1974). We shall contend ourselves here with noting that, in such a case, the conditions for single-mode guiding, and even for the very possibility of such a guiding to exist, do no longer assume a simple form.

Another case which can be algebraically analysed in a one-dimensional fashion is that of fibres whose index profile presents an azimuthal invariance. Proceeding to an adequate transformation of variables, and under the assumption of an $\exp(im\phi)$ azimuthal dependence, ϕ can be eliminated, leaving only the radial variable. In other terms, the ‘azimuthal quantum number’ is set to the value m . For

each value of m , one has then to resolve a one-dimensional equation whose solution $A_n(r)$ is indexed by an integer radial number n . In order to go any further, the use of Hankel or Bessel functions would become necessary.

Let us now return to planar waveguides and let us assume that $\omega = \omega^{(p)}(k_x)$ is the dispersion relation of the p^{th} mode. The guiding condition $k_x > n/\omega/c$ means that the dispersion curve of a lossless guided mode necessarily lies below the ‘light line’ whose equation $k_x = n/\omega/c$ defines the limit of grazing incidence in the cladding (see Chapter 5). An asymmetric waveguide presents but a single genuine light line, which is the ‘lowest’ one in the $\omega = \omega(k_x)$ diagram and is associated with the cladding with higher index. In such a case, the regions of the dispersion diagram extending between the light lines of the two claddings correspond to waves propagating both in the core and in the higher index cladding, but undergoing a total internal reflection at the interface with the lower index cladding.

Let us now consider an additional lateral confinement of the waveguide (Coldren 1995; Tamir 1990). For this purpose, let us define stripes in the planar waveguide, by etching away material, in order to force the optical signals to follow certain specified trajectories. Two limit cases might be considered: first, that of a ‘strong’ guiding created by using a deep-etched ridge, as represented in Fig. 9.1b, and that of a ‘weak’ guiding, where a simple ‘dielectric load’ (Fig. 9.1c) is used for confining laterally a mode of the waveguide. In such a system, we need to restrict ourselves to the case of a straight channel waveguide if a genuine propagation constant is to be defined. Within this assumption, the two previously decoupled polarisations become coupled nonetheless: all six components of the electromagnetic field are rigorously nonzero for the eigenmodes of this waveguide. However, it often remains possible to consider the modes as being quasi-TE or quasi-TM, especially if the in-plane width defined by the lithography is larger than the thickness of the core, which is generally small in order to achieve a single-mode regime for the basic planar waveguide. The thickness of the core is controlled by wafer-scale thin-film deposition techniques. In the case of the deep-etched ridge waveguide represented in Fig. 9.1b, simple considerations apply to the effective index n_{eff} . Due to the additional confinement enforced along the lateral directions, this effective index will be smaller than the effective index of the originally non-etched planar waveguide $n_{\text{eff}}^{\text{planar}}$. In the case of the dielectric load represented in Fig. 9.1c, the confinement is enforced by adding material, and $n_{\text{eff}}^{\text{planar}}$ will obviously be smaller than n_{eff} due to the presence of the load. In the specific case of a quasi-TE mode propagating in such a dielectric-loaded waveguide, it is often accurate enough to describe the horizontal guiding by starting with two different planar effective indices: $n_{\text{eff}}^{\text{stripe}}$, calculated as though the stripe had no lateral boundary, and $n_{\text{eff}}^{\text{planar}}$, calculated in the absence of the load. The lateral guiding can thus be regarded, in the plane of the waveguide, as resulting from the confinement of the wave by the one-dimensional profile $n_{\text{eff}}^{\text{planar}} / n_{\text{eff}}^{\text{stripe}} / n_{\text{eff}}^{\text{planar}}$. However, it is necessary to proceed cautiously at this point: indeed, the main component of the field in the ‘plane’ of the interface is not E_z , but H_z , and we are therefore in a TM-like situation.

Since semiconductors present a high index n , they lend themselves to the realisation of waveguides with index steps $\Delta n \sim 0.1\text{--}0.5$ much higher than those of silica fibres, where $\Delta n \sim 0.01$. As a consequence, the modes tends to be very small, and to have a width well in the sub-micron range, which contrasts with the modes of fibres whose typical width is of the order of $8\text{ }\mu\text{m}$. The coupling between a fibre and a semiconductor waveguide is therefore weak unless a taper structure is used, inside which the mode of the waveguide can extend both laterally and vertically.

These waveguides already allow the realisation of very sophisticated devices, intended more particularly at telecommunication applications. Examples of such applications include beam splitters and couplers, demultiplexers of the ‘PHASAR’ type (Smit 1996), which exhibit a high spectral dispersion, Mach-Zehnder interferometers, etc. It might be interesting here to adopt a monolithic approach and to integrate sources in these devices. Indeed, not only does such an approach allow optical switchboards to remain of a small enough size, but it may also ensure such advanced functions as wavelength transposition at the nodes of WDM networks. A specific issue in photonic crystals and all high-index systems, the dependence on polarisation, can be ignored for integrated laser sources, since these devices have a fixed polarisation and are quasi-TE polarised in most instances.

As has been mentioned earlier in the chapter, the limited curvature of the bends is one of the main factors limiting the compact integration of these functions. It also results in very important losses as soon as the radius falls down below a certain relatively high critical value, typically of the order of a few hundred microns, which is directly determined by the lateral index step $\Delta n_{\text{eff}} = n_{\text{eff}}^{\text{stripe}} - n_{\text{eff}}^{\text{planar}}$. This issue can be best understood by considering a simple ray tracing model, where the problem consists in not exceeding the critical angle when arriving from a straight to a curved section of the waveguide. The angular margin between the equivalent angle in the straight waveguide and the critical angle thus determines the critical radius (Fig. 9.1d). Silica/doped silica systems are the most penalised in this respect, since they require radii at the centimetre scale. At the opposite extreme, deep-ridge silicon waveguides, where Δn can be larger than 2, allow radii of a few microns.

However, the realisation of such abrupt bends in deep-ridge waveguides is at the price of power and coherence losses due to the roughness of the walls of the waveguide. For single-mode deep-ridge waveguides, these losses tend to become unacceptable when the distance of propagation reaches the order of 1 mm. Another negative effect associated with these high contrasts is the important polarisation conversion which takes place at the bends.

9.2.2 Photonic Crystals in Integrated Optics

We shall now turn to the question of the interest of two-dimensional photonic crystals for integrated optics. Owing to their band gaps, these crystals may ensure a new form of lateral guiding, which physically would be better than index guiding. Actually, different advantages are expected from such a guiding: (i) the

miniaturisation of bends drawing on the property of photonic crystals of ‘blocking’ light, thereby preventing its leakage, (ii) the realisation in a single technological step of a number of different functions such as guiding, dispersion (super-prisms), filtering (microcavities) as well as coupling and confinement functions (laser mirrors).

Basic Devices

Fig. 9.2 presents a series of applications envisioned for photonic crystals to the field of integrated optics. The most elementary application would be straight and bent waveguides, as represented in Fig. 9.2a. Other simple functions consist in separating signals depending on their polarisation or their wavelength, as in the case of the polarization beam splitters represented in Fig. 9.2b. All these functions rely on a relatively direct way on the concept of photonic band gap, used for opening or closing in the spectrum broad transmission windows that will not be the same for the different polarisations. It might be recalled here that the aggregated transmission bandwidth of optical fibres can be increased by simultaneously exploiting a few dozen wavelength channels, spaced by 100 GHz (0.8 nm) between 1530 and 1560 nm, and with a 25 to 40 GHz bandwidth each. Telecommunication operators now consider the possibility of using a 50 GHz spacing (0.4 nm), and of extending this technique to neighbouring bands. A single fibre would thus carry 128 channels, each to be routed at a different node in an optical network.

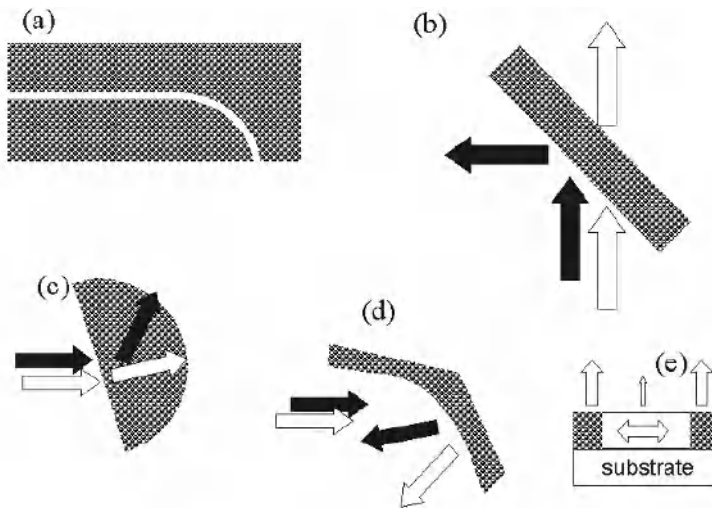


Fig. 9.2. Applications envisioned for photonic crystals **a.** Straight and bent waveguides **b.** Polarisation beam splitters (TE and TM beams are sketched by black and white arrows) **c.** Superprism (beams of different frequencies are sketched by black and white arrows) **d.** Miniature monolithic gratings **e.** Light-emitting diodes with enhanced light extraction

In this context, more sophisticated functions consist in demultiplexing all these channels onto a set of physically distinct waveguides, in much the same way as a dispersive glass prism does with a white light beam. In this respect, the superprism effect represented in Fig. 9.2c (see also Section 6.3 in Chapter 6), and the miniature in-plane echelle-type gratings represented in Fig. 9.2d, are two possible solutions to this problem. Presently, arrays of distributed waveguides, referred to either as arrayed waveguide gratings (AWG) or as phased arrays (PHASAR), are used for the multiplexing and demultiplexing of channels. These systems offer high performances, and equating them would be quite an exciting challenge.

The add/drop function, which consists in filtering a single wavelength out of a multiplicity of signals in order either to extract it or to insert it into a network, can be achieved by inserting two microcavities in a photonic crystal. Of course, these microcavities must resonate at exactly the intended frequency, while being adequately coupled to the waveguide carrying the multiple signals.

Lateral guiding and partially reflective mirrors can also be implemented in laser diodes. These two functions are more particularly interesting for semiconductor lasers based on the coupling of two cavities, known for their frequency tunability (see Section 9.2 in this chapter), and for master oscillator power amplifier (MOPA) systems, adapted to the high power laser diodes used for the pumping of fibre amplifiers.

Light Extraction

The properties of photonic crystals can also be used for the extraction of light, be it the light guided in a channel waveguide, or the more randomly directed spontaneous emission of a light-emitting diode (LED) (Fig. 9.2e). The ultimate goal here is to prevent the active semiconductor region from radiating along unwanted directions, especially in the direction of the substrate and of the lateral sides of the active region. The photonic crystal can act along these directions by suppressing all unwanted photon modes, especially guided modes.

In principle, this effect could benefit light-emitting diodes, which today represent the largest share of the market for optoelectronic components. Indeed, the extraction efficiency of LEDs remains low, from 2 to 20% depending on the technology used for their fabrication. Planar microcavities have already demonstrated their potential for achieving an optical confinement in the vertical direction and the angular redistribution of the spontaneous emission (see Section 7.1.1 in Chapter 7). A state-of-the-art survey of planar microcavities will be presented in Section 10.1 of Chapter 10.

Most planar structures, even those realised in laboratory, still present, regardless their ‘vertical’ extraction performances, a noticeable density of in-plane guided modes. A naive solution would be to use photonic crystals for preventing the propagation of these modes. However, the realisation of a good quality *p-n* junction in the very middle of a ‘holey’ photonic crystal structure remains a delicate issue from a technological point of view. In the short term, the main application which can be expected for photonic crystals in this field would be to use them

in the vicinity of the device for the extraction of the guided light arriving from the active region. Here again, these issues will be discussed at more length in Chapter 10 devoted to microsources.

Choice of the Two-Dimensional Crystal

The consideration of the ideal two-dimensional geometry described in the first part of this book (see Section 1.3.3 in Chapter 1) shows that the type of lattice where band gaps are the most likely to appear are typically lattices consisting of a triangular array of holes. Indeed, these lattices exhibit a Brillouin zone approaching a circle, a property which tends to favour the overlap of the band gaps in the different symmetry directions. The period a is set in such a way that a band gap will appear for at least one polarisation at the wavelengths of interest, such as $1.3 \mu\text{m}$ and still more $1.55 \mu\text{m}$ (Fig. 9.3).

As a first approximation, the matrix index to be used in two-dimensional simulations in order to be able to predict the behaviour of the crystal used for the guiding is the effective index n_{eff} of the fundamental guided mode. The consideration of the ‘gap map’ presented in Fig. 9.3b, which shows a typical value for the effective index $n_{\text{eff}} \sim 3$, indicates that the frequency range should fall within the limits $0.2 < a/\lambda < 0.5$, hence that the period a should be between 300 and 700 nm. The air filling factor f may range from 0.2 to 0.75, while the period to be used will be increasing with f at a fixed value for λ .

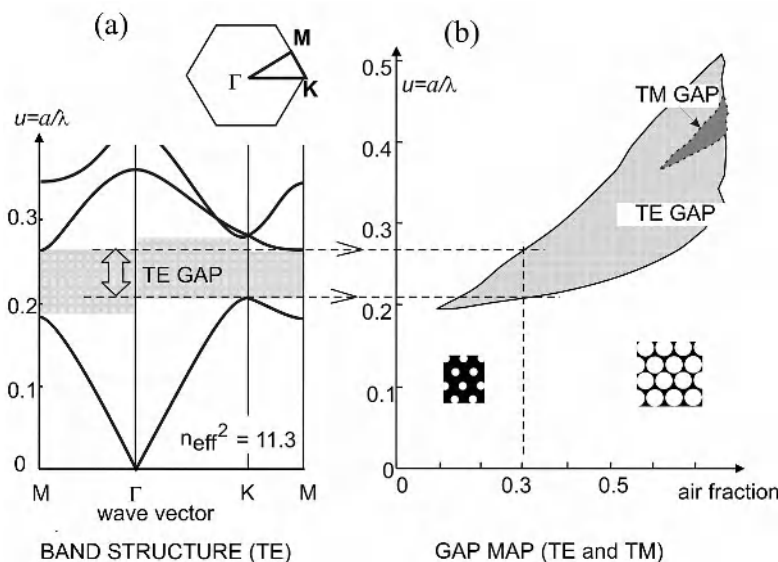


Fig. 9.3. Triangular photonic crystal **a.** Band diagram in TE polarisation for $f = 30\%$ and $\epsilon = 11.3$ **b.** Associated ‘gap map’: the TE and TM band gaps represented as functions of the air filling factor f . The number of plane waves used here is $N = 127$

It might be noted here that unfortunately a ‘direct’ photonic crystal, consisting of dielectric columns in the air, would not be adapted at all to a dielectric guiding in the third dimension. From a practical point of view, this results from the fact that channel waveguides would have to be obtained in this case by omitting rows of columns. While the first calculations for an in-plane two-dimensional propagation had led to seemingly encouraging results (Mekis 1996), the importance of radiation losses in these structures became apparent when properly taking into account the third dimension along the axis of the columns. There would still remain the possibility of introducing a dielectric type defect, in the form for instance of a row of columns with a larger diameter. However, while this solution is not without justification from a theoretical point of view, no experiment has been conclusive thus far: a practical difficulty is that these columns need to be held on a substrate located at a distance large enough from the guided wave. The comparison with the difficulties which have already been met in the ‘standard’ case, where holes were drilled in a planar waveguide, can be useful for understanding the difficulties presented by a photonic crystal formed by such dielectric columns.

Choice of the Planar Waveguide

We need now to turn to the problem of choosing the most appropriate planar waveguide to be etched with the photonic crystal pattern described above. This question is still disputed. Since these two types of waveguides have been investigated along quite distinct lines, a convenient classification consists in distinguishing between waveguides with a high vertical index contrast and waveguides with a low vertical index contrast. The highest index contrast can be found between a semiconductor and the air. In order to realise such a semiconductor membrane, a specific technology needs to be used for holding it by the edges or on posts. We shall also include in this category the case of semiconductor layers on low-index layers ($n < 1.7$) since the physics of these systems are similar. All these systems will be referred to hereafter as ‘membrane waveguides’.

For lower index contrasts, which are typically the case for industrial optoelectronic devices like laser diodes, the waveguide is often buried or sandwiched between two cladding layers with relatively high indices n_1 and n_3 ($n > 2.5$). Of course, intermediary situations may exist, for instance that of silicon clad with silicon nitride ($n = 2.2$). However, the objective of an optoelectronic integration justifies the use of a low index-contrast cladding, as the latter is compatible for instance with electrical injection.

In the next section of this chapter, we shall successively consider buried and membrane waveguides. In this context, we shall make use of the crucial concept of ‘light line’, which has already been introduced in the second part of this book (Chapter 5). However, it seems necessary first to summarise the fabrication techniques used for the definition of the photonic crystal patterns for either of these waveguides.

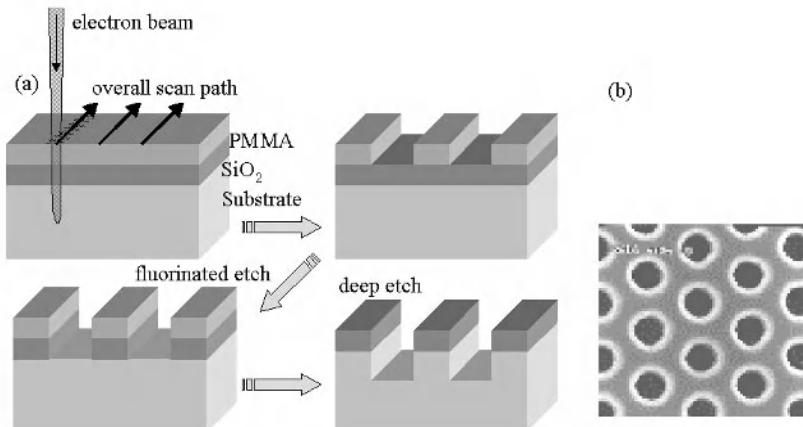


Fig. 9.4. *a.* Electron-beam lithography technique and application to the etching process. The semiconductor/SiO₂/PMMA tri-layer structure is first exposed to the scanning electron beam (the global trajectory of the beam is represented in thick dark lines, while its local trajectory is represented by grey lines. The scanning beam is stopped during each return scan). The exposed PMMA is then dissolved by wet etching, while the unprotected silica is removed by dry etching with a fluorinated plasma. The residual PMMA is finally removed in order to proceed to the dry etching of the semiconductor material (GaAs, InP, Si...) using reactive ions from an adequate plasma *b.* Micrograph of a photonic crystal consisting of a triangular lattice of holes in a GaAs heterostructure. The period of the lattice here is 260 nm. The crystal presented here was fabricated at the University of Glasgow

Mask Writing Technology

The first step in the fabrication process is generally the exposure of the resist coated wafer where the required patterns have to be defined, followed by a development step in order to proceed to the deposition or to the etching. Due to the typical size of the features, of the order of 100 nm, and of the required accuracy (about 10 nm or less), the most adequate method for the definition of photonic crystal patterns in semiconductor substrates is the electron-beam (e-beam) lithography: a focused electron beam, with a typical spot size below 10 nm, scans all the parts of the resist which are to be dissolved (Fig. 9.4a). In the case of a positive resist such as the polymethylmethacrylate (PMMA) resist commonly used for e-beam lithography, the exposed region is subsequently dissolved in an adequate solution. A typical lithography step, as well as the subsequent exposure and etching steps are schematically represented here in Fig. 9.4a.

The possibility of using deep-ultraviolet (DUV) lithography with the projection of a mask at a high resolution has also been recently demonstrated. This method should be preferred for mass production as its throughput is an order of magnitude higher than with serial e-beam lithography. Further, it should undoubtedly benefit from the current advances in the miniaturisation of silicon microelectronics, where

the size of the grids for transistor gates is expected to fall well below 100 nm within the next few years.

Finally, the possibility of using laser holography has also been considered (see Section 12.2.1 in Chapter 12). For the time being, this technique allows only the fabrication of uniform crystals, and it does not seem thus far to be well-suited to the realisation of ‘periodicity defects’ in photonic crystals, that would be essential for the implementation of genuine optoelectronic devices.

9.3 Buried Waveguides

9.3.1 DFB and DBR Laser Diode Structures

We shall begin the detailed study of photonic crystal waveguides, also known as planar photonic crystals, by considering the case of buried waveguides, i.e. waveguides where the indices of the two claddings are close to the index of the core. This approach is also known in the literature as the ‘substrate approach’. The light line is therefore very low, a situation which in principle favours the leakage of light. These systems are quite ubiquitous in semiconductor optoelectronics, since they are the essential photonic structure of edge-emitting laser diodes. Owing to the simultaneous electronic and optical confinement properties of semiconductor multilayer stacks these structures are also known under the name of ‘double heterostructures’, invented in 1963 and for which Z.I. Alferov and H. Kroemer were awarded the Nobel prize in 2000.

From a technological point of view, the main issue here is the depth of the holes. From an historical point of view, laser diode waveguides were first processed into gratings in the 1970s in the wake of the seminal article by Kogelnik and Shank (Kogelnik 1971) with the development of distributed feedback (DFB) laser diodes and distributed Bragg reflector (DBR) laser diodes. Let us briefly consider here these devices. In both DFB and DBR laser diodes, the gratings are etched with a very limited depth, 50 or 100 nm in such a way as to be localised in the upper tail of the guided mode profile. The subsequent regrowth on top of a layer with a relatively small index difference ($\Delta n = 0.15$) tends to further smooth the index modulation. These gratings are intended at enforcing the longitudinal single-mode operation of the laser by favouring feedback only for the guided waves whose half spatial period ($\lambda /2n_{\text{eff}}$) coincides with the pitch of the lattice Λ , exactly as is the case in the Bragg backscattering of X rays by a very large number of equidistant atomic planes. The gratings can be etched either along the entire active region, as is the case for DFB lasers, or in the region immediately surrounding the latter, as in DBR lasers, in a passive section injected with a separated electrode. An additional interest of the injection in a separate section of the DBR laser is that it leads to minimising the absorption and/or to modulating the real and imaginary effective index by shifting or modifying the backreflection peak. For a $1.55 \mu\text{m}$ emission,

the value for the pitch Λ in these InP-based devices is equal to 220 nm for first-order feedback and to 440 nm for second-order feedback: the first-order feedback can be used in this case for outcoupling light. This simply results from the fact that the effective index of InP/GaInAsP/InP waveguides is typically around 3.2. The interaction length is typically larger than 200 μm , which is approximately the length of the active region. This clearly shows the weakness of the interaction between the laser wave and the grating: about 1000 periods are needed in order to obtain any sizeable effect. The directional stopband thus obtained has only a 1-2 nm width.

9.3.2 Photonic Crystals, a Strong Perturbation for Guided Modes

In order to create a photonic crystal, and thus to obtain larger one or two-dimensional band gaps, the interaction has to be reinforced. For this purpose, a first approach consists in increasing the etch depth in order to reach the centre of the core: if the etched region is left unfilled, this allows achieving an index contrast 3 : 1 between the semiconductor and the air. Unfortunately, if the etching is not carried until the lower cladding, the local interruption of the guiding may result in an extremely large leakage: the wave is repelled towards the lower cladding, and only a few periods are necessary before it totally leaks into the substrate (Chen 1996a): this effect will be all the more marked than the index of the wave is high. It should be borne in mind that the band gap will necessarily be above the light line of the cladding, whose index is of the order of 3. Under such conditions, not only is the coupling to the cladding modes allowed, but it will even be maximised if the etching is performed to the centre of core. This corresponds to the top of the ‘loss bell’ represented in Fig. 9.5, where singularities may occur since the dimensions are of the order of the half-wavelength.

Since 1996 and the pioneering article by TF Krauss, it is generally recognised that is necessary for ensuring the guiding that the etching be performed also through the lower cladding, until the entire vertical profile $A(y)$ of the field of each guided mode is intercepted by the holes (Krauss 1996a). In other terms, it is necessary to pass beyond the loss bell of Fig. 9.5d, which schematically represents the losses as a function of the etch depth. From a mathematical point of view, and in the ideal case where no holes are present, the field profile extends at infinity and decreases exponentially in the cladding with the form $\exp(-y/L)$, where L is the decay length of the evanescent wave, as given by the classical formula:

$$L_{\text{decay}} = \lambda / [2\pi\sqrt{n_{\text{eff}}^2 - n_l^2}] \quad (9.6)$$

As an example, in the case of a GaAs core and of a $\text{Ga}_{0.2}\text{Al}_{0.8}\text{As}$ cladding, where $n_{\text{eff}} - n_l \sim 0.3$, the decay length is $L_{\text{decay}} = 50 \text{ nm}$ for $\lambda = 1 \mu\text{m}$ whereas for an InGaAsP core ($n = 3.35$) and InP cladding ($n = 3.17$) where $n_{\text{eff}} - n_l \sim 0.1$, the decay length is equal to $L_{\text{decay}} = 200 \text{ nm}$ at $\lambda = 1.55 \mu\text{m}$.

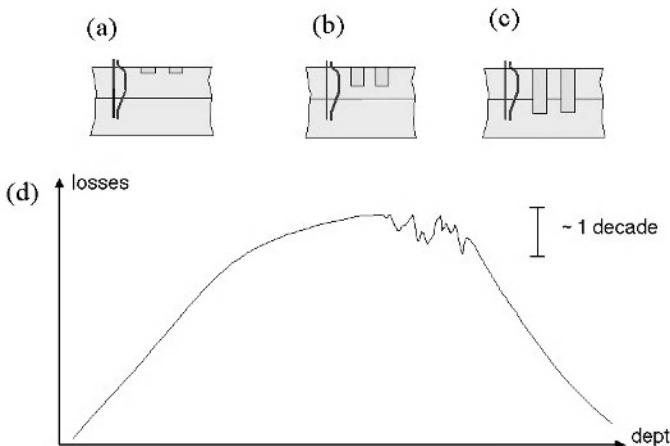


Fig. 9.5. Grating etched at a variable depth into a semiconductor waveguide and schematic representation of the losses as a function of the etch depth. **a** DFB type grating. These gratings are more commonly buried **b**. Grating etched halfway through the core **c**. Grating etched throughout the core **d**. Schematic ‘loss bell’ diagram. For the sake of clarity, the singular features which may occur, especially in the case **b**, have been minimised

In all these cases, the etching depth needs to be significantly larger than the thickness of the core of the waveguide, resulting in a high aspect ratio as well as in a delicate technological process. In this context, there are two main reasons for preferring TE polarisation over TM polarisation. First, the profile of a TE mode is much more confined than that of a TM mode. Secondly, band gaps appear in TE polarisation for much smaller air filling factors.

9.3.3 Choice of the Diameter of the Holes and of the Period of the Crystal

For a given period a of the triangular lattice of holes and for a typical effective index $n_{\text{eff}} = 3.34$, a ratio $\phi/a = 0.35$ between the size of the holes and the period is enough for an omnidirectional TE band gap to appear. This corresponds to an air filling factor no higher than 15%. By contrast, a ratio $\phi/a = 0.75$, corresponding to an air filling factor $f = 60\%$ would be required in order to simultaneously obtain complete TE and TM band gaps.

In the latter case, the holes become so large that they are separated by such a small semiconductor vein that 10 nm fluctuations in the thickness of this vein are likely to have a noticeable influence on the properties of the photonic crystal device. Another reason for adopting a relatively small diameter for the holes pertains to the fact that the profile of the guided field in the etched region will not be significantly different from its profile in the non-etched region, a favourable feature

for optoelectronic integration. Thus, a guided wave, arriving for instance from a crystal free region will propagate into the crystal region without undergoing any significant mismatch nor radiation loss, provided however that its wavelength be in one of the transmission bands of the crystal.

The solution of using small holes, and thus of having small air filling factors f , also leads to the possibility of a relatively independent analysis of the vertical and lateral guiding. In other terms, this entails that an approximation of the form $A(y) \times B(x, z)$ for the guided waves will become more acceptable.

Unfortunately, as far as applications are concerned here, favouring one polarisation over the other would not be an ideal solution. Indeed, with the exception of lasers, polarisation insensitivity is on the contrary a requirement for integrated optical devices receiving their signals from fibres. A possible solution, known as ‘polarisation diversity’ consists in separating the TE and TM polarisations immediately after the input. The TM polarised signal is then converted into a TE polarised signal and injected in a circuit duplicating the TE polarisation. The two signals are finally recombined in the two orthogonal polarisation states at the output.

Thus far, we have paid little attention to the upper cladding of the waveguide. In the most simple designs for planar waveguides, this layer is simply absent, since the waveguide is directly realised by the mere deposition of a layer with index n_2 on a substrate with index $n_1 < n_2$. Thus, two different regimes occur for the evanescent tails of the guided modes, with air being of course the medium where the propagation velocity is the highest. We shall see later, using the ‘light line’ formalism, that important losses may arise in this regime at the bends of integrated photonic circuits. These losses can therefore be significantly reduced by starting from a genuinely buried waveguide (Fig. 9.6a), where the index profile is $n_1/n_2/n_1/\text{air}$ or $n_1/n_2/n_3/\text{air}$, hence with a relatively low index step ($n_2 - n_3 \ll n_2$). As a consequence of the presence of this additional cladding layer, the etch depth, denoted here by h , increases. However, this increase can be minimised by reinforcing the confinement on the side of the substrate, in such a way as to obtain indices satisfying the relation $n_1 < n_3 < n_2$. A truly optimal solution requires an in-depth modelling, either in three dimensions or at least in the yz plane (Bogaerts 2001; Lalanne 2001).

9.3.4 Specific Parameters for InP- and GaAs-Based Systems

In Table 9.1 are presented typical values of the relevant parameters in TE polarisation for photonic crystal buried waveguides, realised either on an GaAs or an InP substrate. These two types of waveguides are adapted to operate at wavelengths around 1 μm and 1.55 μm respectively. In either cases, the air filling factor is assumed to be equal to $f = 30\%$. This assumption allows the limitation of the vertical modification of the profile of the guided modes in the section of the waveguide under consideration.

Table 1. Parameters for photonic crystals etched in buried waveguides grown on GaAs and InP substrates, and displaying TE photonic band gaps around $1\text{ }\mu\text{m}$ and $1.55\text{ }\mu\text{m}$, respectively (the air-filling factor is the same in both cases, and is equal to $f = 30\%$)

Substrate	Lower cladding	Core	Upper cladding	Δn	Period a [nm]	Diameter ϕ [nm]	Height h [nm]
GaAs	$\text{Ga}_{0.2}\text{Al}_{0.8}\text{As}$ $\geq 400\text{ nm}$	GaAs $\sim 250\text{ nm}$	$\text{Ga}_{0.8}\text{Al}_{0.2}\text{As}$ $\sim 300\text{ nm}$	0.2-0.5	220-300	110-160	≥ 750
InP	InP ^a	GaInAsP ^b	InP $\sim 300\text{ nm}$	0.1-0.2	330-550	180-280	≥ 1500

^aundoped buffer layer

^b $\text{Ga}_x\text{In}_{1-x}\text{As}_y\text{P}_{1-y}$ lattice-matched to InP

It can be seen from this table that for the value of the air filling factor $f = 30\%$, corresponding to $\phi \sim 0.6a$, the aspect ratio h/ϕ of the holes is higher than 5 in GaAs ($\phi \sim 160\text{ nm}$) and still higher in InP ($\phi \sim 280\text{ nm}$), where it is more than 7. With this in mind, we shall devote the next section to a discussion of the dry etching methods which permit to achieve such high aspect ratios.

9.3.5 Deep Etching

The most traditional anisotropic dry etching technique is reactive ion etching (RIE). The term anisotropic refers here to the fact that the sidewalls are vertical at the edges of the mask. By comparison, a pure chemical etching results in significantly undercut sidewalls which follow the crystallographic planes. At the opposite extreme, a pure physical etching, such as milling by Ar+ ion bombardment, erodes the material, which results in rounded sidewalls. When correctly adjusted, the RIE technique produces similar patterns in the <110> and <1-10> directions of the <001> plane for a standard III-V substrate. In its standard version, this technique is based on the use of a plasma produced by a simple RF discharge, and different gas inlets containing in particular silicon tetrachloride, methane and hydrogen. The rectification by the plasma produces the bias voltage needed for accelerating the ions towards the sample holder. This method has been instrumental for the first applications of photonic crystals to the field of integrated optics (Smith 2000a, 2000d), by allowing in particular the realisation of holes in GaAs with an aspect ratio $h/\phi = 5$.

However, RIE etching tends to become less efficient for aspect ratios of 4 in InP, this being due to the lower volatility of the In-containing residues. These limits can be overcome using modified methods based on the independent control of the plasma density and its energy, i.e. the bias. In order to enhance the plasma density, energy can be injected either by RF electron cyclotron resonance reactive ion etching (ECR-RIE) or by inductively coupled plasma reactive ion etching (ICP-RIE). The latter method seems very promising, especially for silicon and for InP, but has not yet reached maturity. To this date, silicon etching by ICP-RIE al-

lows surely the realisation of photonic crystal patterns with a large size ($>> 1 \mu\text{m}$). Finally, we may mention here another method which has also been successfully implemented in laboratory, the chemically assisted ion beam etching (CAIBE). In this method, an Ar⁺ ion beam is used for milling the sample while at the same time an active chemical species, like chlorine, is introduced above the sample in order to form volatile compounds, for instance indium compounds. The CAIBE method has been used in particular in the first experimental attempts directed at the realisation of three-dimensional photonic crystals at optical wavelengths (see Chapter 12).

9.4 Membrane Waveguide Photonic Crystals

9.4.1 Free-Standing Membranes

The idea of etching a photonic crystal in a membrane held only by its edges was first introduced around 1994, when researchers in optoelectronics started exploiting processes used in the fabrication of micro-opto-electro-mechanical systems (MOEMS). As far as applications to integrated optics are concerned here, these membranes are defined with a typical thickness ranging from 200 to 400 nm, ideally forming a single-mode planar waveguide. The tremendous advantage of these membranes is that their realisation requires a relatively small etching depth, hardly larger than the thickness mentioned above: this is enough to access the underlying ‘sacrificial’ layer, i.e. a layer that will be subsequently removed by selective dissolution, as represented in Figs. 9.6b and 9.6c. Such a membrane presents an index $n = 3$ or higher, and it naturally behaves like a relatively good ‘trap’ for light. The critical angle varies from 16 to 18° with respect to the normal of the membrane, resulting in a very sharp-angled light cone in the dispersion diagram. The band gaps of a photonic crystal etched in the layer of the membrane overlap only to a limited extent with this cone. If a straight waveguide is introduced in the membrane, it can be reasonably expected that the in-plane guided modes will also lie below the light cone and therefore that these modes will be lossless. Accordingly, all the advantages offered by waveguides (Fig. 9.1) will be retained and, conversely, all the functions that are expected from photonic crystals, like the possibility of radiation-free bends or the coupling with cavities with a very high Q factor, could be tested. More precisely, the only residual losses for modes of straight waveguides are expected to result only from irregularities and fluctuations associated with the fabrication process. Further, the latter losses might even be very low in the case of a photonic crystal device, since the radiation associated with an irregularity can itself be inhibited, resulting only in the generation of an evanescent wave. However, in all cases where the translational invariance is disrupted on purpose (bends, cavities), the limitations are those of the modal engineering and of

the design of the structure itself (Chutinan 2002; Yoshie 2001), and have not been completely identified yet.

Membrane technology has been regularly improving during the last few years, especially for InP-based systems. In order to realise a membrane, it is necessary to dissolve the underlying sacrificial layer. In this respect, the chemistry of wet etching of GaInAsP quaternaries allows a great latitude in this process, and permits in particular to dissociate the design of the heterostructure, for instance as an active structure, from the technological constraints associated with the formation of the membrane. Further, the use of membranes has been extensively explored during the 1990s for the realisation of numerous micromechanical devices and all-semiconductor tunable vertical cavities (Dantec 1999). A further advantage of the InP system is the low rate of the non-radiative recombinations in spite of the vicinity of the interfaces between the air and a semiconductor, leading to much better luminescence efficiencies than in comparable GaAs-based structures. InP systems typically present recombination rates ten to a hundred times lower than GaAs systems. In particular, InP systems have been used for realising the first optically pumped photonic crystal laser operating up to room temperature (Painter 1999a), a decisive achievement which was very instrumental in demonstrating within the scientific community the relevance of the photonic crystal approach. The topic will be discussed in more detail in Chapter 10 on microsources.

As far as alternative materials are concerned, the FESTA group in Tsukuba (Kawai 2001) recently succeeded in fabricating perfect free-standing GaAs membranes. As an aside, it might be mentioned that a two-dimensional band gap was also demonstrated with this system. Another possibility for fabricating membranes is to use the silicon-on-insulator (SoI) technology, which allows the production of perfect crystalline Si membranes on top of a silica layer with a few hundred nanometers by dissolving the underlying silica in hydrofluoric acid etchants. The Cal'tech/Corning group has recently achieved a breakthrough in this direction (Loncar 2002a).

Etching a membrane only requires a relatively low aspect ratio between the depth and the diameter. Since a membrane generally presents a thickness between 200 and 400 nm, this ratio should be no higher than unity. It is also much easier to obtain vertical sidewalls along the entire height than with buried waveguides systems, and the number of degrees of freedom in the design of the geometrical parameters of the lattice increase accordingly. Thus, it was with membrane systems rather than with buried systems that it has been possible to reach high air filling factors, well above 50% and even approaching 70%. In this extreme case, the holes are separated only by extremely small veins, and the TM band gap tends to coincide with the high-frequency TE band gap. The counterpart of this benefit is that the amount of material left in the membrane is drastically reduced. For this reason, the membrane can no longer be described in terms of a two-dimensional model, where the effective index of the waveguide is used as the two-dimensional matrix index, and it becomes necessary to resort to the methods of three-dimensional electromagnetism, with their unavoidable complexity.

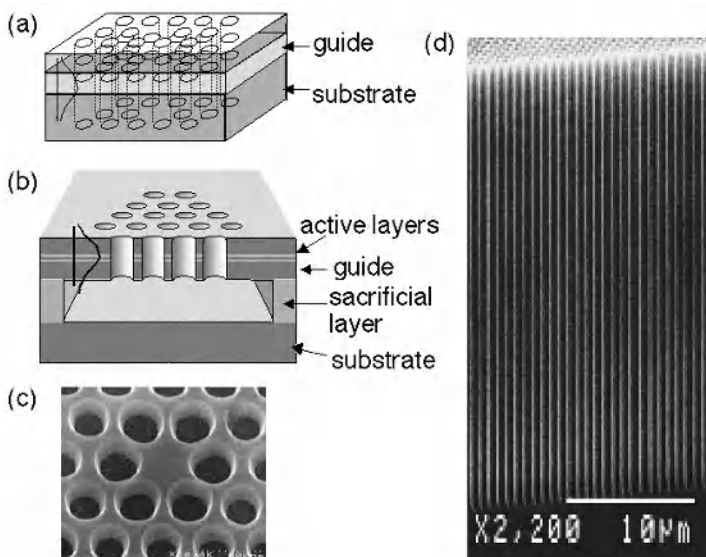


Fig. 9.6. *a.* Photonic crystal etched in a buried waveguide *b.* Membrane photonic crystal, fabricated by dissolving a sacrificial layer, made accessible by the presence of the holes, during a wet etching process *c.* Example of a microcavity formed by a single missing hole in a photonic crystal (Yoshie 2001) *d.* Example of realisation in macroporous silicon (Rowson 1999a). Note the remarkable perfection of the columns over several dozen microns

9.4.2 Reported Membranes

An interesting variant of the free-standing membrane is based on the report of a membrane on a low-index substrate, for instance silica with index $n = 1.48$ to mention a common configuration. Such an arrangement answers a series of mechanical problems inherent to membranes, in particular the risk that they would stick when drying. Further, it also leads to a better thermal management of these devices, even if silica remains a poor thermal conductor. Another technique implemented by the Sandia group in New Mexico in the course of their collaboration with the Massachusetts Institute of Technology (MIT) on Ga(Al)As systems relies on the use of 'AlOx', a non-stoichiometric aluminum oxide obtained by the lateral oxidization of Al-rich GaAlAs layers. The original waveguide used in these experiments consists of a GaAs core deposited onto a thick $\text{Al}_{0.95}\text{Ga}_{0.05}\text{As}$ layer (60–200 nm). The latter is selectively oxidized, typically in a water vapour atmosphere at 450°C, which leads to its conversion into quasi-alumina with index $n \sim 1.6$.

In all the systems mentioned here, the substrate, which may for instance consist of silica, can be perforated in principle, due to the fact that the etching is per-

formed only after the report of the membrane on the substrate. However, other choices can be made. For instance, if a non-perforated substrate is used, the light line decreases following an $1/n$ law, and goes from unity (air) for a free-standing film to typically $2/3$ for a non-perforated substrate. A risk exists here of greatly reducing the photonic band gaps, leaving only very restricted regions for the propagation of possible lossless guided modes. Nevertheless, it is with such a system that the first investigations on straight waveguides have been carried out in 1999 by the group of T. Baba in Yokohama (Baba 1999).

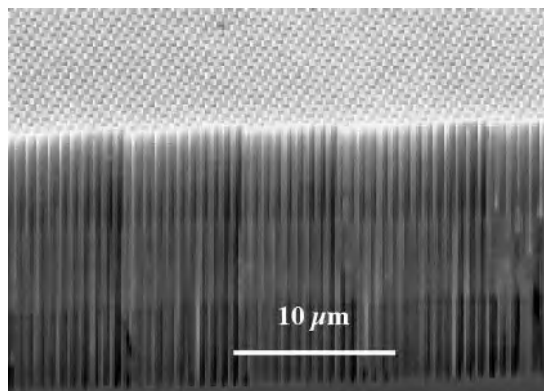
9.5 Macroporous Silicon Photonic Substrates

Macroporous silicon does not fall into any of the categories presented above, and is rather considered as an outsider in integrated optics. This material, obtained from a bulk n -doped Si crystal or wafer, is invariant along the third dimension, and therefore it is undoubtedly the material which most resembles the ideal two-dimensional photonic crystal. As can be seen in Fig. 9.6d, a photoelectrochemical etching carried out in a hydrofluoric acid based electrolyte allows one to obtain pores with an aspect ratio higher than 50 and perfectly aligned along the $\langle 100 \rangle$ direction normal to the usual polished face of the wafer. In the absence of an adequate preparation of the surface, the location of the pores will be determined by the native defects of the electrochemically active interface, resulting in a certain disorder in their distribution. In practice, this defect is avoided by first imprinting etch pits at specified locations using a classical photolithographic process followed by a chemical etching with a potassium hydroxide solution. A large and very uniform lattice of holes extending over more than one centimetre square can be obtained using an holography technique where the photomask is defined from the fringe pattern resulting of the interference of three laser beams (Berger 1997b). More detail on this technique will be presented in Section 12.2.1 of Chapter 12. The choice of the period for the lattice of pores is intimately related to the n -doping level, which therefore needs to be correctly anticipated. Since a free carrier screening process is involved in the selection mechanism of the sizes of the pores, the period varies in inverse ratio to the doping level. An inappropriate doping may for instance result in the spontaneous appearance of unwanted ‘interstitial’ pores. The advantages offered by this system need therefore to be balanced with these factors when designing such a device. Thus, in order to obtain good quality holes, the holes must be thought as being uniformly distributed over the entire device, since a hole without neighbours would be prone to instabilities.

Since the pioneering studies realised by U. Grüning *et al*, where a complete photonic band gap was reported around $5\text{ }\mu\text{m}$ for both TE and TM polarisations (Grüning 1996), important advances have taken place towards the control of photonic crystals formed from macroporous silicon at telecommunication wavelengths (Rowson 1999a). The example represented Fig. 9.6d convincingly demonstrates that these photonic crystals are among the new materials which could be used for achieving the transition from ‘free space’ optics to integrated optics.

More precisely, if these systems are to be realistically used in integrated optics, then light needs to be confined both vertically, i.e. along the axis of the pores, and horizontally, i.e. in the plane of periodicity. For the realisation of cascaded optical functions, such a confinement is much preferable to the use of a simple collimated light beam that would impinge with an intrinsic divergence on the pores. An elegant solution for simultaneously achieving a vertical confinement and a single-mode guiding consists in reducing the diameter of the pores over a certain height Δh . For narrower holes, a guiding effect is achieved due to the fact that the average index of the slab with height Δh is higher than the average index in the surrounding medium. Various authors (Rowson 1999b; Schilling 2001) have demonstrated that the diameter of the pores could be modulated within some appropriate range by simply varying the current during the photo-electrochemical etching process (Fig. 9.7).

a



10 μm

b

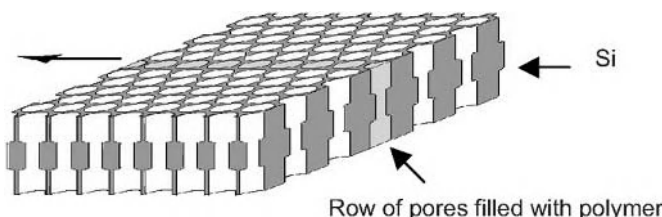


Fig. 9.7. **a.** Micrograph of a planar waveguide defined in a macroporous silicon photonic crystal adapted to telecommunication wavelengths (period 0.65 μm). The vertical confinement is achieved through the modulation of the diameter of the pores along the vertical direction. This diameter is typically 250 nm in the core of the waveguide, whereas it reaches 420 nm in the cladding regions. The total depth of the pores is more than 20 μm **b.** Schematic representation of a macroporous silicon waveguide with confinement of light along both the vertical and the horizontal directions. The horizontal confinement is achieved by filling one or several rows of pores with a transparent polymer

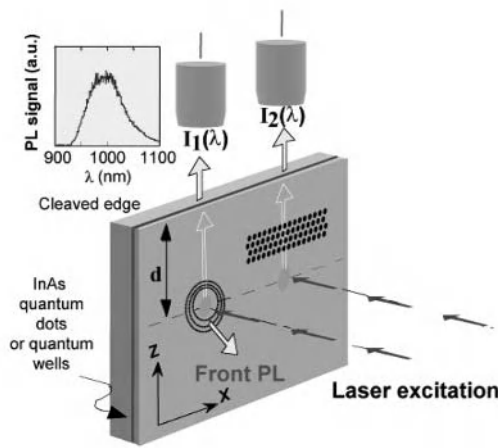
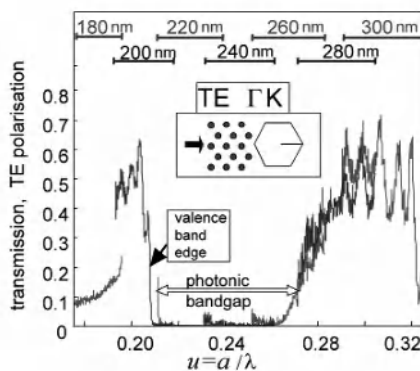
**a****b**

Fig. 9.8. **a.** Principle of the internal light source method used for the characterisation of photonic crystals in integrated optics: a localised laser spot generates electron-hole pairs in a quantum well or in a layer of quantum dots. Radiative recombinations (photoluminescence) occur and the corresponding photons are emitted in the waveguide in the form of circular waves. The reabsorption of these photons is low enough to allow a substantial fraction of the light to reach a cleaved edge located at a distance d ranging from 50 to 100 μm from the source. If light propagates through a photonic crystal structure etched in this waveguide, the transmission of the crystal can be determined by comparing the resulting signal I_2 to the reference signal I_1 . **b.** Example of a measurement realised by combining seven transmission spectra measured for seven photonic crystals with different periods, indicated here above the graph. The spectra are plotted against the normalised frequency $u = a/\lambda$, represented in abscissa

In order to simultaneously achieve a single-mode behaviour, an optimised coupling with fibres, and a relative insensibility to the residual imperfections due to the fabrication process, both the height Δh and the variation of the diameter need of course to be optimised. A possible solution for achieving the in-plane confinement along the horizontal direction consists in the in-filling of selected pores with a polymer material, which leads to an increase of the local average index. Recent experiments have demonstrated that pores with a $0.65 \mu\text{m}$ diameter could be filled over a $10 \mu\text{m}$ height with a polymer exhibiting a good transparency in the 1550 nm window (David 2002). However, in order to fill the desired set of pores, it turned out necessary to resort to a complementary lithographic technology, for instance e-beam lithography, for masking all but the desired region, so that the patterns of the waveguide will be aligned with the axis of the photonic crystal (Birner 2001). In spite of these relative difficulties, macroporous silicon remains a promising material. Indeed, not only is this material of a relatively low cost for the study of photonic crystal waveguides, but it allows the realisation of pores at depths that would be out of reach with any other techniques. It can reasonably be expected that these promises will be fulfilled in the forthcoming years.

9.6 Characterisation Methods for Photonic Crystals in Integrated Optics

9.6.1 Internal Light Source Method

When a photonic crystal reduces to a very small $20 \mu\text{m} \times 2 \mu\text{m}^2$ object, etched in a GaAs or InP substrate with for instance a $4 \times 8 \text{ mm}^2$ area, the question arises of the most appropriate method for determining its transmission. The solution of using an external source raises difficulties as regards the possibility and the reproducibility of the coupling. However, as will be seen hereafter in Section 9.6.2, a few solutions to these problems exist. This being, the idea of generating light inside the structure itself obviates most of these difficulties, and we shall now consider the problem of inducing such an internal source.

In the specific case of III-V semiconductors, this can be answered through the insertion of photoluminescent layers in the core of the waveguide during the epitaxy process. These layers can be reduced to a single quantum well with a thickness of a few nanometers. They may also consist of a series of self-assembled quantum dots, for instance based on InAs, a system which has been known since about 1985 and which exhibits a large inhomogeneous broadening. By pumping with a visible laser focused with the objective of a microscope, as represented in Fig. 9.8a, the recombination of the electron-hole pairs created in the core of the waveguide occurs mostly in the lower energy quantum well or quantum boxes with the lower energy. The optical cladding, formed for instance by $\text{Al}_x\text{Ga}_{1-x}\text{As}$ in

the case of a GaAs substrate and a GaAs core, also plays the role of a confinement barrier for the electrons and the holes. A substantial fraction of the generated photons, which typically is of the order of 40 percent, is coupled to the guided mode, while the remaining photons are coupled to the continuum formed by the non-guided radiating modes.

This localised photoluminescence source can then be used as a ‘lamp’ for illuminating the waveguide and then the device under test. This source can be easily positioned at the desired location, and a signal $I_2(\lambda)$ is collected at a cleaved edge after the propagation of light in the photonic crystal under consideration (Labilloy 1997, 1999). Layers with a good quality present a uniform photoluminescence efficiency, and the intensity of the source is therefore the same at any point. In order to normalise the signal, it suffices to measure the light spectrum $I_1(\lambda)$ after a simple free propagation in the waveguide to the cleaved edge.

However, even in the case where a single quantum well is inserted in the core, reabsorption effects occur within a relatively limited length, of the order of 100 μm . Indeed, no pumping at all takes place anywhere else in the waveguide, and the generated photons, whose energy is about the same as that of the fundamental transition of the quantum well, only undergo a band-to-band absorption caused by this well. It is not necessarily simple to indicate a unique value for the reabsorption due to the very nature of the band gap region, where the absorption coefficient rapidly evolves from a zero value to a bulk value equal to 10^4cm^{-1} , with an excitonic maximum occurring between these two values. After propagating over a distance equal to 100 μm , the spectrum of the guided light reduces to its low energy part, this being due to the fact that reabsorption essentially affects its high energy part. The effective wavelength range for spectral measurements therefore decreases down to $\Delta\lambda = 20\text{ nm}$ for an $\text{In}_x\text{Ga}_{1-x}\text{As}$ quantum well grown on a GaAs waveguide. The relative width is approximately $\Delta\lambda/\lambda \sim 2\%$ for a central wavelength $\lambda \sim 950\text{ nm}$.

In order to characterise the crystal over a broader spectral range, one may take advantage of the fact that, in the first order, the transmission depends only on the normalised frequency a/λ . The technique known as ‘lithographic tuning’ can then be applied, using a series of samples with the same air filling factor f , but with regularly increasing periods a . The transmission data are finally plotted on a single graph as a function of a/λ . It can be easily calculated that the measurements need to be carried over approximately thirty different crystals in order to continuously cover a broad spectral range ($\Delta\lambda/\lambda > 50\%$).

An internal source with a much broader and useful spectral range can be obtained by using InAs quantum dots (or quantum wires) whose characteristics and luminescence have already been addressed in Chapter 7. Quantum dot layers can be produced through a self-organising process during the growth by molecular beam epitaxy (MBE) of materials with a high positive mismatch of the lattice parameter. Quantum dot sources have been widely adopted for GaAs studies (Benisty 1999; Labilloy 1999; Reese 2001) as well as for InP studies (Letartre 2001; Pottier 1999; Seassal 2002). In order to increase the spectral width of the source as much as possible, the conditions are chosen in such a way as to produce

inhomogeneous dots: the distribution of the sizes of these dots will result in different electronic confinement energies, and therefore in a larger spectral width. A spectral width ranging 150 nm from 250 nm around 1050 nm can thus be obtained on GaAs, corresponding to a useful spectral width $\Delta\lambda/\lambda \sim 15\text{-}25\%$. Not only can a spectral dilution of the source be observed, but the reabsorption also decreases by a factor of ten or more, while the modal absorption is of the order of 20 - 30 cm⁻¹ per quantum dot layer. A risk, when going to extreme growth conditions in terms of surface, flux and temperature, is the spatial inhomogeneity of the photoluminescence efficiency. This effect can be obviated by using two or three quantum dot layers.

With a spectral width of $\Delta\lambda/\lambda \sim 10\text{-}15\%$, a couple of structures with different periods are sufficient to cover the photonic band gap and regions extending well beyond it. Fig. 9.8b presents an example where measurements were carried out over seven photonic crystals with different periods so as to cover almost a frequency octave in terms of the normalised frequency $u = a/\lambda$, ranging from 0.175 to 0.325 (Labilloy 1999). In these experiments, the spectral range was further limited to short wavelengths ($\lambda < 1060$ nm) due to the intrinsic properties of the silicon-based CCD device. In the absence of such a limitation, four samples would have been enough. The dispersion of the material is also the cause of the small mismatches which can be observed in this diagram

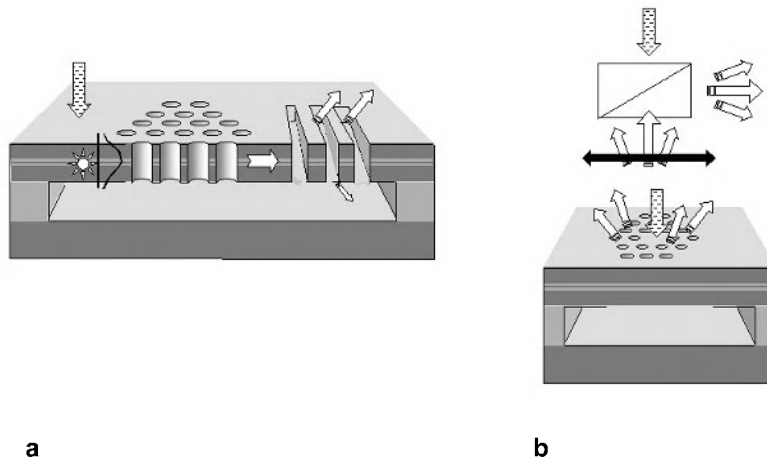


Fig. 9.9. Internal excitation of a membrane **a**. In order to avoid the effects of the non-reproducible optical transmission which may occur at the edges of the membrane, the light is collected by means of an extraction grating placed before the cleaved facet of the sample **b**. The photoluminescence diffracted at the boundaries of a microcavity is directly collected. A dichroic beam splitter is used in the experimental arrangement in order to separate the diffracted signals from the exciting beam with shorter wavelength

This internal light source method can also be used for membrane-type photonic crystals (Park 2001; Pottier 1999; Seassal 2002). However, since the edges of the membrane are not necessarily regular, the optical transition from the membrane to the non-etched region may not be reproducible. It is therefore preferable either to cleave within the thin film to be analysed, which also presents certain difficulties, or to extract light by using an output grating located after the crystal for outcoupling the beam to be measured towards the air (Fig. 9.9a). In addition, the extraction characteristics should be carefully modelled and calibrated using adequate experimental means.

We shall later discuss some of the issues associated with the study of completely closed resonators. In this case, the spectral characteristics of the resonances which are expected to occur (cavity peaks) can be measured from the out-of-plane diffraction. This applies to membrane waveguides as well as to buried waveguides. Light is then collected normally to the plane of the waveguide, either along approximately the same axis as the exciting beam, or merely through the same objective, by using in the latter case an adequate beam splitter (Fig. 9.9b).

9.6.2 End-Fire Method

External sources present obvious advantages as regards the selection of the wavelength, of the intensity or of the injected mode. The coupling of the light emitted by an external source into a photonic crystal structure can be achieved through the edge of the waveguide, either by cleaving the sample or by using a grating coupler similar to the one represented of Fig. 9.9a, but located at the input end of the waveguide.

Let us focus for instance on the injection by a cleaved edge. Different types of geometry can be considered for characterizing the photonic crystal structure:

- the photonic crystal lies isolated in a planar waveguide, as in the example represented in Fig. 9.10a. The situation is similar to that of the internal light source represented in Fig. 9.8 with a spot located just at the edge of the sample. A significant divergence of the injected light occurs in this case. The intensity of the wave decreases with $1/r$, but the residual absorption (an $\exp(-\alpha r)$ factor) can be low due to the fact that the waveguide has no absorbers at all, i.e. that it forms a passive system. In other terms, absorption will not significantly affect the signal until distances of the order of 1 mm, since α will be no higher than 10 cm^{-1} under these conditions.
- light is injected into a single-mode ridge waveguide which channels light to the structure under study. In the example represented in Fig. 9.10b, this structure is a photonic crystal waveguide (Talneau 2001). In order to collect light as efficiently as possible, it should be injected only in the desired polarisation, for instance in TE polarisation.

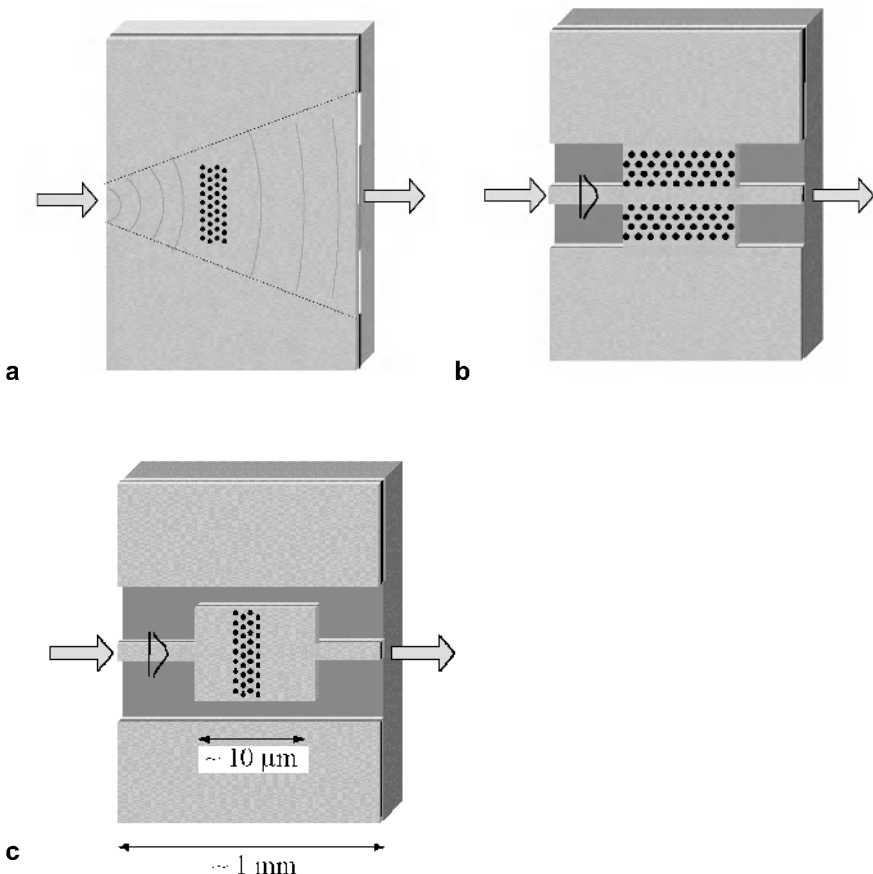


Fig. 9.10. End-fire method **a**. Injection in a simple planar waveguide. The decrease in the transmission caused by the crystal under study is revealed by the shadow appearing on the opposite edge **b**. Injection in a deep-etched ridge waveguide, leading to the photonic crystal waveguide under study **c**. Intermediate geometry where light is injected in a ridge waveguide leading to an enlarged region containing the photonic crystal under study. The divergence of light is less marked than in case **a**, and the detected signal is therefore less attenuated

- the photonic crystal lies in an enlarged region of a straight ridge waveguide, as can be seen in Fig. 9.10c. Such an intermediate situation is also reported in (Chow 2000; Lin 2000, 2001a).

The sources used in these experiments are typically fibre or semi-conductor lasers with an external cavity providing a spectral tunability of the order of $\Delta\lambda/\lambda = 6$ percents. In the long wavelength range (mid-infrared), the only tunable coherent

sources are optical parametric oscillators, which however are difficult to use. In the short wavelength range, towards visible wavelengths, tunable solid state lasers like Ti : sapphire lasers are often the most appropriate. Finally, we may mention here the specific category of amplified spontaneous emission sources. The spectral width of these sources is of the order of kT , i.e. of a few percents in terms of $\Delta\lambda/\lambda$, and they present a lower coherence in order to avoid spurious interferences. One may thus understand that it is often necessary to use a battery of several sources or samples in order to fully investigate a photonic band gap.

The end-fire injection at a cleaved edge requires very accurate alignments as regards the angles and the positions. It also requires a beam with an aperture matched as much as possible to the guided mode, thus with an elliptic shape and a linear polarisation. A beam with a mismatched shape may excite other modes than the fundamental mode. This also justifies the use of long single-mode ridge waveguides for accessing the photonic structure: indeed, since the parasitic modes are of a radiative nature, they will eventually escape from the ridge waveguide towards the substrate, so that they will not be taken into account in the measurements.

9.6.3 Wideband Transmission-Reflection Spectroscopy

The methods presented above are not well-suited to 'bulk' photonic crystals like macroporous silicon. Here again, an external source is needed. However, this source needs to present an appropriate output beam in order to probe samples with a thickness of a few ten micrometers, for instance a collimated beam with a $50 \mu\text{m}$ diameter. In order to gain an accurate insight into the influence of the different length scales involved here, like the size of the holes, the period of the lattice and the three dimensions of the crystal, the use of a source with a very wide band, extending over two or three octaves, is preferable. Contrary to measurements on planar waveguides, there is obviously no risk that cutoff effects due to the guided modes might occur. The different conditions enumerated here can be fulfilled by using a Fourier transform spectrometer coupled to a microscope equipped with a Cassegrain-type reflective objective presenting a slight central obscuration. The size of the spot can thus be reduced to a few ten microns, and there is no need of using any particular spatial filter along the trajectory of the beam. Such an arrangement has been used for measuring the reflection spectra of macroporous silicon photonic crystals in the mid-infrared, ranging from about 1.3 to $20 \mu\text{m}$ (Rowson 1998). The wideband transmission method can also be applied to microstructured fibres in the visible and near-infrared regions. The reader is referred to Chapter 11 for more detail on the latter subject.

9.7 Losses of Photonic Crystal Integrated Optical Devices

9.7.1 Analysis of the Losses

The losses of photonic crystals in integrated optics have several origins. Two of them are the same as in classical waveguides, that is, the absorption and the scattering by sub-wavelength irregularities. In addition to these two mechanisms, the out-of-plane radiation losses that the crystal itself undergoes are a specific and additional loss mechanism. Depending on their value, these losses may restrict the possible applications of photonic crystals. We shall discuss here this issue, with a special emphasis on the relations between theory and experiments.

The theoretical considerations developed in Section 5.4 of Chapter 5 predict that any guided mode below the light line will be lossless. This however supposes that the crystal extends at infinity. In practice, the transition from a standard waveguide (a non etched region) to a perforated region may result in losses, even if the mode coupled to the crystal lies under the light line. This leads to the necessity of formally separating the losses into two distinct contributions, the losses due to the propagation in the photonic crystal itself on the one hand and the losses resulting from the input/output transitions on the other hand. The total losses are a combination of these two distinct losses, and can be viewed to some extent as being a coherent combination. However, in the common case where the incident wave has a frequency in the photonic band gap and where it penetrates over a very limited length in the crystal, this distinction becomes useless.

In the case of buried waveguides, the guided modes most often lie above the light cone, and out-of-plane losses may arise for any wave geometry. A simple approach suggested for determining these losses in a two-dimensional simulation relies on the use of a complex refractive index in the air holes $n = 1 + i\eta$ (Benisty 2000). This amounts to considering that the energy leaking out of the plane of the waveguide is actually dissipated in the air of the holes, i.e. in the regions where there is no guiding (Krauss 1996a). This analogy can be justified by certain theoretical considerations that will be summarised hereafter.

In the spectrum represented in Fig. 9.8b, the high-frequency band edge is less abrupt, not only than the low frequency band edge, but also than the band edge predicted in a two-dimensional lossless simulation where the effective index of the waveguide in the absence of the holes was used as the matrix step. This difference can be explained by the in-plane fractional overlap of the air holes and the photonic modes, which is significantly smaller at the lower band edge than at the upper band edge, as can be seen in the one-dimensional examples that were considered in Section 1.3.2 of Chapter 1 (see for instance Fig. 1.6). This comforts the idea that the losses would be ‘localised’ in the air holes. A further reasoning leads to considering the actual system as a perturbation to another separable and lossless system (Benisty 2000). This leads to considering each hole as a dipole excited by

the guided field and radiating in all directions. This local approach can be adapted to any type of structure, be it regular or not (straight waveguides, bends, cavities with any shape and symmetry, etc) and is therefore distinctly different from the collective modal approach based on infinitely extended modes. However, the dipole strength is directly dependent on the strength of the ‘leaky’ component of the Bloch wave, i.e. the component associated with the wave vector lying above the light line. This reconciles the local and collective approaches. The local radiating dipole approach can also be exploited in the frequent case where the holes are insufficiently deep due to the limitations of etching technology: in this case, the dipole is now associated with the excess material at the bottom of the hole (Lalanne 2001). The respective contributions of each component of the waveguide, i.e. of the cladding and the core respectively, can thus be extracted (Ferrini 2003).

Let us now turn to the losses resulting from the finite etch depth. It can be demonstrated that these losses are, in the first order, proportional to the fractional overlap of the vertical profile of the field with the non-etched region, i.e. to the part of the field which does not overlap with the holes. In practice, the optical intensity decreases very rapidly as the depth increases: for instance, in a GaAs system corresponding to the values presented in Table 9.1, it decreases from a factor $e = 2.718$ every ~ 50 nm, and increasing the etch depth by only 50 nm can therefore be decisive. Let us finally mention that this approach can also be used for determining the influence of the shape of the holes, for instance their conicity (Ferrini 2003). This amounts in this case to modulating the fraction of excess material (compared to an infinite perfect hole) with respect to the etch depth. This semi-analytical approach permits to reach certain simple physical conclusions which can be useful for minimising the losses of any photonic crystal structure, for instance by selecting optimised heterostructures or etching conditions.

9.7.2 Measurement of Propagation Losses in Straight Photonic Crystal Waveguides

In a straight channel waveguide, i.e. in a line defect, defined for instance by a missing row in a triangular crystal, genuine propagation losses occur for modes located above the light cone. Due to the scale difference between the lengths of the waveguide (100 μm or more) and of the coupling region to such a waveguide ($\sim 1 \mu\text{m}$), the coupling and propagation losses can be separated unambiguously.

It is no longer possible, for the measurement of the propagation losses, to resort to the cutback method which had previously been transposed from fibres to long ridge waveguides and where the length of a given waveguide is progressively reduced under constant injection conditions. Indeed, this method would require a length equal to 1 mm or more of photonic crystal waveguide. This is much more than the 10 to 200 μm which can be currently obtained using e-beam lithography, and which also correspond to the typical length of future miniature applications. Alternative techniques, based on the characterisation methods which have been described earlier, include:

- the use of the internal source method for comparing the attenuation undergone by waveguides with different lengths and realised from the same substrate (pseudo-cutback method). The accurate positioning of the spot, which is necessary in order to induce a similar excitation of the waveguide from a modal point of view, can easily be achieved (Smith 2000a).
- the end-fire method can also be used for comparing losses associated with photonic crystal waveguides of different lengths excited under identical conditions (Talneau 2001; Lin 2000a). The excitation conditions can be indeed fixed by long single-mode access ridge waveguides, as represented in Figs. 9.10b and 9.10c. However, the cleaved facets induce a large amount of reflection, which cannot be easily eliminated when using highly coherent laser sources. An interesting alternative consists in considering these facets as mirrors with a known and reproducible reflectivity, and the whole sample as a Fabry-Perot cavity. When scanning a tunable source, the analysis of the fringe contrast provides the cumulated losses arising during the propagation between the facets, including the coupling losses and the genuine propagation losses. The two contributions can then be retrieved by comparing samples with different lengths. More exactly, one retrieves the difference between the propagation losses of the ridge waveguide and of the photonic crystal. The ridge waveguide itself can be calibrated using the same method.
- also using the end-fire method, the scattered light is collected above and along the photonic crystal waveguide and is then analysed, both spectrally and spatially. This restricts the observation to the modes which are lossy in the collection angle. The precise measurement of the total scattered light is obviously hampered by the substrate and by the complex evolution of the rays radiating in it in the case where the latter is not absorptive.

The losses of a waveguide are obviously dependent on its width. In a system with a strong index contrast, a waveguide larger than $\sim \lambda/2n$ becomes multimode, but the fundamental mode extends less and less in the photonic crystal as the width increases, as in a standard ‘refractive’ waveguide. This leads to a significant reduction of the amount of losses, which approximately scale as $1/(\text{width})^2$. The propagation losses can therefore be made acceptably low with a relatively limited width, corresponding for instance to three to five missing rows.

9.7.3 Waveguide Bends in Photonic Crystals and Bend Losses

The bends in a photonic crystal waveguide raise a complicated design issue, due to the fact that they disrupt the very periodicity of the waveguide. Thus, the input mode, which may for instance be the fundamental mode, tends to couple to all output modes. The multimodal nature of a waveguide is obviously a major obstacle to achieving a good bend transmission. Ideally, no higher-order mode should be excited, be it on the transmitted side or on the reflected side. This issue is somehow related to that of furtive electromagnetic obstacles (aircrafts) which must not scatter waves along certain directions.

At this point, we need to comment on the well-known numerical simulation realised by the MIT group and predicting a near-unity transmission in 90° bent photonic crystal waveguides (Mekis 1996). Actually, the two-dimensional photonic crystal considered for this simulation was a crystal formed by dielectric columns, where an air waveguide had been realised by removing one row of rods. Under these conditions, the wavelength in the waveguide remains significantly larger than the period of the crystal. As a consequence, the wave does not undergo any significant diffraction. On the contrary, in an experimental waveguide, the photonic crystal is formed by a lattice of air holes, and the waveguide itself consists of one or several missing rows of holes. Accordingly, the waveguide now exhibits the higher index in the whole system, and since the wavelength λ/n is small, the wave propagating in the waveguide is diffracted.

This diffraction effect, which has been discussed in the second part of this book, gives rise to transmission mini-stopbands for straight multimode waveguides, this being due to the existence of minigaps between the dispersion branches of two guided modes. Actually, the same effect can also be observed for a single missing row (W1), when closely examined. Note that between these mini-stopbands, the quasi-'refractive' behaviour of the modes of the waveguide entails that the diffraction will be frustrated by multiple reflections and by the photonic band gap, preventing energy to build up save in the relevant mode(s).

A number of possible improvements, based on a variety of different configurations, have been suggested. Thus far, good performances are obtained only at the price of a lower bandwidth, with resulting bandwidths of the same order as the WDM 'C' band (30 nm at 1550 nm, i.e. 2 %). The influence exerted by several different factors, like for instance the polarisation of the field, and more generally the physical limits of these devices, remain unclear, which leaves room for improvement in their design. In practice, the measurement of a bent waveguide proceeds essentially by comparing it to a straight waveguide with identical length.

9.7.4 Photonic Crystal Resonators and Quality Factors

Realising a resonator by adding the two in-plane confinements to an integrated optical configuration necessarily results in a certain leakage of light along the third dimension, since the k -spectrum of the confined in-plane field present components whose values decrease down to $k = 0$ within the light cone. The problem is therefore to quantify these losses and to develop strategies adapted to each type of waveguide, i.e. to buried and to membrane waveguides respectively. For membrane waveguides, the resonators can be designed in such a way as to minimise the fraction of the 'leaking' k -components, i.e. those within the light cone (Yoshie 2001). In the case of buried waveguides, no such possibility exists, and the problem is therefore more open. The trivial solution, which consists in increasing the size of the resonators, is of limited interest. Indeed, the behaviour of the modes tends in this case towards that of delocalised plane waves, resulting in a multiplication of the number of these modes. As a consequence, one tends to loose the interesting features of microcavities for light emission (see Chapter 10) or to de-

crease the free spectral range for filtering applications. However, the underlying physics are far from being trivial and interesting modes may exist in relatively large cavities. These modes can be compared to whispering gallery modes, whose volume is much smaller than that of the microdisk where they are confined.

For an isolated resonator consisting of a set of missing or smaller holes drilled in a large uniform photonic crystal, the method described in Fig. 9.9.b allows the direct determination of the quality factors from the spectral width of the observed peaks in the diffracted photoluminescence. This simply results from the fact that the presence of a resonant microcavity mode enhances the field in the cavity. The same applies to the edges of the cavity, which results in a resonance peak in the spectrum (Benisty 1999; Lin 2001a; Park 2001; Pottier 1999; Reese 2001; Yoshie 2001). A spatial filtering can be used for optimising the collected signal by eliminating the photoluminescence directly emitted through the upper surface of the cavity, i.e. without the guiding and diffraction processes, which does not exhibit a structured spectrum.

A drawback of this method, which is restricted to cavities allowing the existence of a large number of modes, i.e. to cavities ranging from three to a hundred missing rows, lies in the fact that only modes whose wavefronts are aligned with the edges of the crystal have a high emission along the vertical direction (Smith 2000d). In the case of an elementary microcavity with a $1\ \mu\text{m}$ side or diameter, realised in a GaAs-based photonic crystal, there typically exists more than five modes in a 100 nm spectral range. Most of these modes present complicated wavefronts, which never give rise to a plane wave in the normal direction, but radiate in different scattering lobes. Indeed, due to the complex relation between the phases of the radiating elements, i.e. the holes around the resonator, the far field becomes locally zero, in much the same way as in dark-field and phase-contrast microscopies. For ultimately small cavities, a classification of the modes with respect to their symmetry can be determined, and a sizeable fraction of power can be captured for usual geometries (see later the remarks concerning the recent results by the group of S. Noda).

Another obstacle is the presence in the cavity of a 'load' which is associated with the absorption of the luminescent system. While this effect can be reduced by resorting to an optical pumping, there is no simple method for determining the transparency point with respect to the pump power. A risk exists here of actually measuring a laser, whose spectral linewidth can be much narrower than that of the 'cold' cavity, i.e. of the cavity in the absence of the load. In spite of the interest of such a property, let us recall that we are primarily interested here in the determination of the quality factor of microcavities.

In a triangular crystal, the hexagonal cavities have sides consisting of dense rows and form a series of canonical cavities. It is convenient to name these cavities according to the number of periods along each side. Thus, a microcavity with a single missing hole will be termed H1, a microcavity with seven missing holes H2, etc. The amplitude maps of the magnetic fields of two modes of an H2 cavity are shown in Fig. 9.11. These two modes are non-degenerate modes. Such modes are much easier to analyse than doubly degenerate modes, which unfortunately are the most common type of modes. The analogy between these resonant modes and

the energy levels of the canonical benzene molecule is useful for understanding the degeneracy of the modes. The mode represented in Fig. 11a is of the ‘radial’ type, with wavefronts which tend to align to the edges of the cavity. A similar mode with a wavefront aligned along the sides, albeit with a different intensity at the apices, can also be observed. The mode represented in Fig. 11b is analogous to the so-called whispering-gallery modes, typical of microdisks, as will be seen in Chapter 10. There are no simple rules for the evolution of the modes when the size of the cavity increases. For H3, H4 and higher order cavities, the term of ‘modology’ might even be coined out.

The smaller the cavity, the lower will be its quality factor. Thus, H1 cavities present the lowest quality factor. This being, there is no simple rule for the evolution of the Q factors either. In one-dimensional Fabry-Perot cavities, the quality factor is given by the equation $Q = mF$, where $m = L/(\lambda/2n)$ is the order of the cavity and F is dependent only on the reflectivity of the mirror. However, it rapidly turned out that the modes of interest in H1 cavities were double degenerate dipole modes. By lifting the degeneracy in such a way that the field had minimal Fourier components within the light cone, the Cal’tech group reached in 2001 the record value of $Q = 2800$, thereby opening the way to ultracompact resonators for telecommunication applications within the WDM framework. It seems likely that the race towards higher Q factors will continue in the near future. Thus, at a conference held in 2002, the Kyoto team directed by S. Noda presented results approaching $Q = 4000$ for a cavity consisting of three aligned holes coupled to a waveguide. This method seems to have a far greater potential (Noda 2002a), as shown by the breakthrough value of $Q \sim 30,000$ recently announced, and the perspective of reaching $Q > 10^5$ in view (Akahane, 2003).

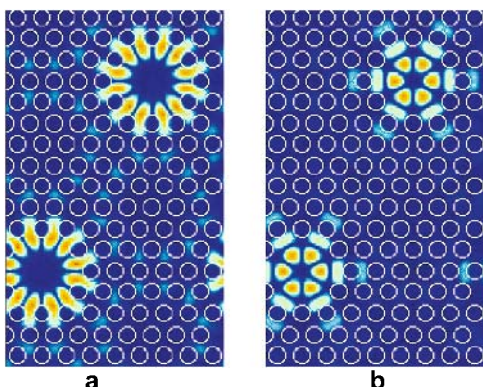


Fig. 9.11. Amplitude maps of the magnetic fields of two TE modes of ‘H2’ microcavities, calculated through a two-dimensional numerical simulation **a**. Mode of the ‘radial’ type. The lobes near the edges of the cavity are elongated. Therefore, since the phase of the mode is the same at the different holes of the periphery, the mode can radiate along the direction normal to the plane **b**. Mode of the ‘whispering-gallery’ type: the phase of the mode alternates at the periphery. The air filling factor is equal to $f = 0.40$, and the dielectric constant to 10.5. Both these two modes lie within the photonic band gap of the crystal at a short distance from the normalised frequency $u = a/\lambda = 0.3$

9.8 Some Noteworthy Devices and Functions

9.8.1 Coupled Resonators and Waveguides

The problem of the coupling of a resonator to the ‘external world’ is currently being investigated by several groups, with the objective of finding systems that would be capable of selectively inserting or extracting a single wavelength from a signal (with a WDM resolution, $Q = \Delta\lambda/\lambda$ should lie between 3000 and 100000). The coupling of a photonic crystal waveguide to a photonic crystal microcavity remains of course a privileged scheme. While some of the early proposals seem to have been unrealistic in terms of fabrication (Fan 1996, 1998), other configurations have already been implemented and have led to interesting results as far as applications are concerned.

Among these configurations, we may mention here the following ones:

- the lateral coupling of an H7 cavity to a W3 waveguide, as represented in Fig. 9.12a (Smith 2001). The infrared signal in the cavity modes locally induced by the photoluminescence of a laser beam focused onto the sample is transferred onto the waveguide, before being channelled in the direction of a cleaved edge. Light is then collected at this edge, in much the same way as in the experiments conducted with internal light sources. The lateral coupling between a cavity and a waveguide is favoured here by the coupling occurring between the modes, as described in Section 5.2.5 of Chapter 5. This phenomenon results in the formation of a mini stopband with a width equal to 10 nm around $\lambda = 1000$ nm. An interesting point to note is that, within the limits of the experimental resolution, the quality factor of the mode was found not to be degraded by the coupling, but remained of the order of $Q = 800$.
- H2 or H3 cavities cascaded with photonic crystal waveguides (Olivier 2002b). The Hn cavities are coupled to waveguides by their apices, which, intuitively, is not an optimal solution. In the example presented in Fig. 9.12b and 9.12c, this drawback was circumvented by using a cavity with a larger size. The inverse solution would be to change the orientation of the waveguide from 30°, which would result in a relatively strong corrugation of the waveguide, with larger and more numerous mini-stopbands than Wn waveguides with a similar physical width.
- a coupled-cavity waveguide, also referred to as a coupled resonator optical waveguide (CROW) (Olivier 2001a; Yariv 1999). An example of such a waveguide is presented here in Fig. 9.12d, while the phenomena of transmission minibands and minigaps associated with it are clearly visible on the spectra presented in Fig. 9.12e. This system is actually a good model for photonic engineering and provides in particular the possibility of controlling the group velocity simply by varying the degree of coupling between the cavities.

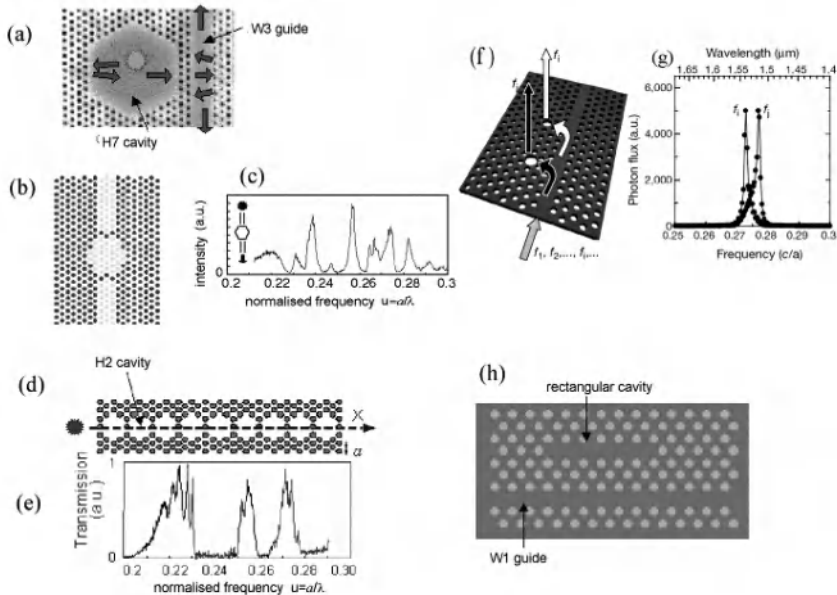


Fig. 9.12. Coupling between a waveguide and a cavity **a**. H7 cavity laterally coupled to a W3 waveguide (Smith 2001) **b**. Cavity adapted to in-line coupling with a W3 waveguide and inserted in such a waveguide (Olivier 2002a) **c**. Transmission spectrum for the cavity represented in **b** **d**. Example of a coupled-cavity waveguide, also referred to as a coupled resonator optical waveguide (CROW) consisting of nine H2 cavities **e**. Transmission spectrum represented as a function of the normalised frequency $u = a/\lambda$, measured using the internal light source method (Olivier 2001a) **f**. Defects consisting of enlarged holes coupled to a W1 waveguide **g**. Transmission spectrum measured along the vertical direction above the defect (Noda 2000) **h**. Rectangular cavity consisting of a few missing holes coupled to a W1 waveguide (Seassal 2002)

- a cavity based on a single modified hole, in this case an enlarged hole (Noda 2000), and coupled to a W1 waveguide (Fig. 9.12f). The selective drop of a wavelength with a quality factor close to 500 has thus been obtained. The difficulty in this arrangement is to reach the critical coupling condition, i.e. the condition where the radiation of the cavity towards the air is equal to the losses in the direction of the waveguide. This seems to require an exceptional degree of accuracy in the fabrication process. It might be noted that, in spite of the result reported here, no convincing result demonstrating a coupling between a H1 cavity and a waveguide has been obtained, which might be due to the dipolar nature of the relevant modes of H1 cavities.
- rectangular cavities, consisting actually of sections of W1 waveguides, which themselves are coupled to another W1 waveguide, as represented here in

Fig. 9.12f (Seassal 2002). Similar arrangements have also been recently reported by the group of Noda. The objective here is the same as in the realisations that have been previously described, i.e. to achieve the critical coupling condition.

As a summary, it can be noted that different coupling schemes between photonic crystal cavities and waveguides are currently being intensely investigated. The studies conducted for the optimisation of these devices have been concerned with the adaptation of the thickness of the barrier between the two elements as well as with the adaptation of the cavity modes themselves, since their complex field profiles often result in a very uneven coupling of the guided modes. Another delicate issue which is currently being investigated is the control of the cavity losses, and their relation to the k components within the light cone.

9.8.2 Other Devices and Optical Functions

Among the new devices and functions which have been realised with photonic crystals in the field of integrated optics, the following ones deserve a special mention in this review:

- transition devices, whose function is to provide the necessary transitions between classical ridge waveguides and photonic crystal waveguides. Taper transitions with a length equal to a few μm have thus been developed (Talneau 2002). The mode matching must be achieved without causing any excessive reflection, especially in the case of a waveguide based with a very confined geometry, like W1 waveguides. We may also mention as belonging to the same broad category the successful attempts at achieving a coupling between a planar membrane waveguide and a single-mode fibre held vertically above the surface of the membrane (Taillaert 2002). The transition was adapted to the size of the transverse mode of the fibre, which typically is of the order of 8 μm , while the coupling ratio was in the 20 % range.
- superprisms based on the exploitation of the specific refractive properties of Bloch modes in photonic crystals, which had been presented in Chapter 6. The first realisations of such devices (Kosaka 1998, 1999) were not actually based on an integrated optical geometry. For more recent waveguide configurations, an angular deviation as large as 10° for a 20 nm spectral shift around 1300 nm was obtained by the groups of TF Krauss at St Andrews (Wu 2002) and of T. Baba in Yokohama (Baba 2002).
- miniature devices based on the “autocloning technique” developed by the group of Kawakami at the University of Tokohu (Sato 2002) (see also section 12.2.2 in chapter 12). Channel waveguides with a very low loss of 0.1 dB/mm have been fabricated using this technique (Ohkubo 2004). The result of propagation loss can be regarded as a “milestone” in view of the practical fabrication of photonic circuits that contain functional components such as chromatic dispersion equalisers and wavelength filters.

This brief review shows that photonic crystals have both the potential and the momentum to become a disruptive technology in the field of integrated optical devices. The degree of accuracy that will be achieved in the fabrication of micro-structures and nanostructures, and more generally the future advances that will be taking place in the field of micro- and nano- technology, will be decisive factors for the evolution of integrated optical devices based on photonic crystals.

10 Microsources

10.1 High-Efficiency Light-Emitting Diodes

10.1.1 Solutions for the Extraction of Light without Confinement

The efficiency or quantum yield of a light-emitting diode (LED) is the product of two factors η_1 and η_2 . The first factor, also referred to as the internal quantum yield, quantifies the efficiency of the conversion of the injected electrons into internal photons, while the second factor represents the efficiency of the extraction of photons from the semiconductor towards air. The internal quantum yield η_1 may easily reach typical values of the order of 90 percent, while η_2 rarely goes beyond a few percents due to the strong refractive index of the semiconductor material itself ($n \approx 3$). This results from the phenomenon of total internal reflection which occurs for all internal angles above the critical angle, i.e. such that $\theta > \theta_c = \sin^{-1}(n)$, and from the fact that the cone of the half-angle θ_c represents therefore but a fraction $\eta_2 \approx 1/4n^2$ of the 4π steradians over which an isotropic emitter radiates. We may here consider an emitter placed in GaAs and with a uniform spontaneous emission, in the form for instance of an electron-hole pair or of GaAs itself (Fig. 10.1.a). In this case, and neglecting Fresnel reflections, only 2% of the spontaneous emission escapes the GaAs/air interface. This figure is doubled if the semiconductor is encapsulated in epoxy, as is common for light-emitting diodes ($n = 1.5$).

Several different solutions have been devised in order to collect a larger number of photons (Delbeke 2002). An example of such a solution is the use of thick transparent layers sandwiching the entire active semiconductor. Such layers allow the extraction of the light emitted sideways that would otherwise be reabsorbed within a few tens of microns (Fig. 10.1.b). This type of LED provides efficiencies in the 5-20% range, and has invaded the signalling market owing to both its simplicity and intermediate cost. Still higher efficiencies can be obtained by relying on purely geometrical considerations for optimising the geometrical shape of the chip in such a way as to allow most rays to escape the device after at most one total internal reflection. By using a truncated inverted pyramid structure, the company AGILENT has thus achieved an external quantum yield $\eta_1\eta_2$ higher than

50%. This configuration, which can be seen in Fig. 10.1c, is now being employed in the GaP-based orange LEDs used for the signalling of battery-powered work (Krames 1999).

Another solution consists in removing the initial substrate of the LED and in reporting the active epilayers onto a metallic mirror. As delicate as this process may be, it tends to becoming increasingly well mastered. The light which has not been directly extracted remains trapped between the metal and the semiconductor/air interface, and the trick consists in redirecting these photons into the extraction cone prior to any possible re-absorption. This can be achieved for instance through the wavelength-scale texturing of the upper interface, as represented in Fig. 10.1d (Windisch 1999). In order to preserve a high brightness, it is of interest to devise textures that will redirect from a few microns the trapped photons. A possibility is to use structures with a strong index contrast which provide an efficient coupling with free-space continuum modes. The properties of such structures have already been described in Chapter 9 when discussing the losses of integrated-optical systems, whereas they are now on the contrary considered with respect to the objective of maximising losses.

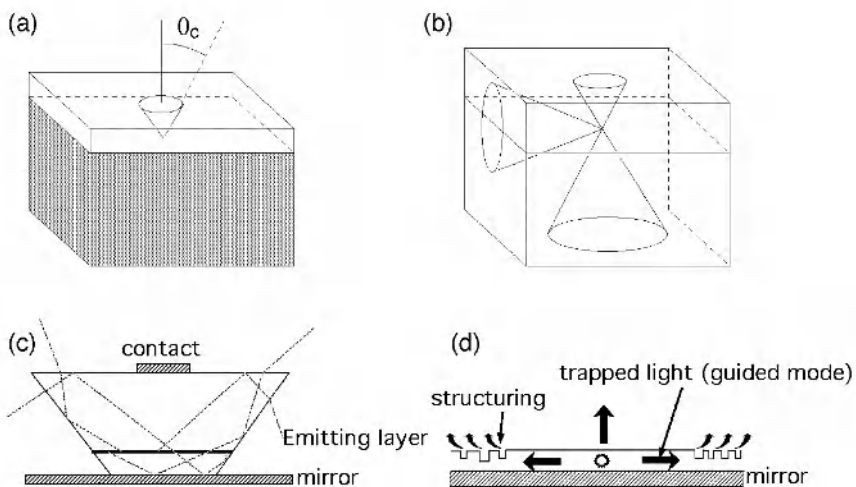


Fig. 10.1. *a*, Single extraction cone in a classical LED structure grown onto an absorbing substrate *b*, Extraction cones at the six faces of a parallelepiped *c*, Cross-section of the truncated inverted pyramid structure suggested by Agilent *d*, Substrate-less structure with extraction of the trapped light using a textured surface

10.1.2. Enhanced Extraction Efficiency through Planar Confinement

As described in Section 7.1, when an emitter is placed inside a planar cavity, its emission is concentrated into annular rings or lobes. This angular re-distribution of spontaneous emission can be exploited in order to increase the extraction efficiency η_2 (Fig. 10.2). The relative spectral emission width ($\Delta\omega/\omega$) of LEDs remains moderate at room temperature and typically assumes values between 2 and 20%. In order to estimate the conditions required for the actual enhancement of the extraction efficiency using planar mirrors placed before the source, the assumption may thus be made of a monochromatic emission. As the consideration of Fig. 7.1 allows us to easily understand, a genuine enhancement of the extraction corresponds to the case of a single resonance of the Airy function in the extraction cone ($\theta < \theta_c$) (Fig. 10.2a).

The above condition amounts to imposing a minimum spacing between the Airy peaks, i.e. a sufficiently small cavity order $m_c = L/(\lambda/2n)$. This condition can be expressed in quantitative terms as follows:

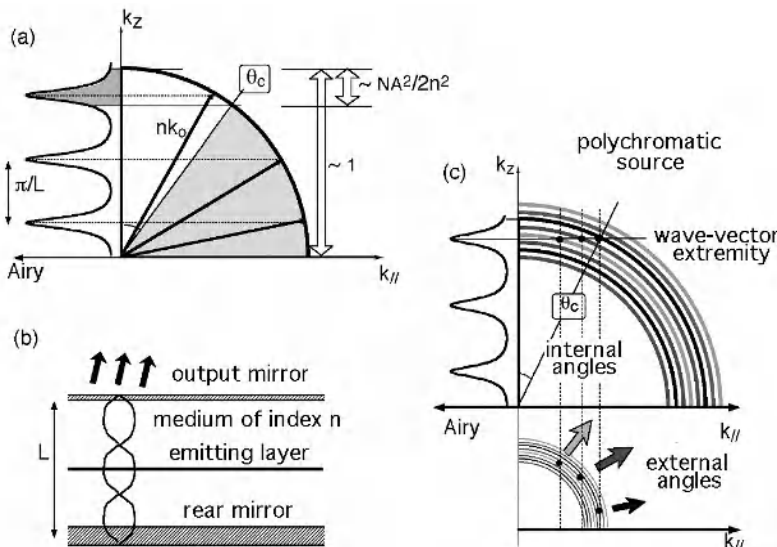


Fig. 10.2. *a*, The Airy function and the locus of wavevector for a monochromatic source represented in a diagram with axes k_{\parallel} and k_z . Note the extraction cone *b*, Elements of a microcavity LED *c*, Spectral narrowing and angular dependence of the emission for a polychromatic source: same diagram as *a*, with the addition of a schematic representation of the wavevectors in air (lower figure). The vertical lines joining the two figures provide for the conservation of k_{\parallel} which underlies Snell-Descartes law of refraction

$$m_c < 2n^2/NA^2 \quad (10.1)$$

where NA is the numerical aperture (see Fig. 10.2.a). The extraction may indeed be generalised to any required aperture by replacing n with n/NA , where $NA = 0.2$ for typical silica fibres, $NA = 0.5$ for plastic optical fibres and $NA = 1.5$ for a semiconductor LED with encapsulating epoxy.

For an emitter that would be identically coupled to all cavity modes, the extraction efficiency simply reduces to:

$$\eta = 1/m_c \quad (10.2)$$

In the case of a monochromatic emitter at a specified wavelength $\lambda = \lambda_{\text{em}}$, designing a ‘good’ microcavity LED (MCLED) amounts to individually optimising all the constitutive elements which are schematised in Fig. 10.2b (Benisty 1998a, 1998b):

- the back mirror should be as reflective as possible, but without resulting in any excessive increase of the cavity order m_c . A metallic mirror with a reflectivity $R = 0.9$ may thus be preferable to a Bragg mirror whose reflectivity reaches $R = 0.99$. Indeed, such a high reflectivity is achieved at the cost of a penetration depth of a few half-wavelengths, and of even higher values for substrates like InP. Further, in the latter case, it is difficult to grow Bragg mirror epilayers with strong index contrast without risking severe problems in terms of stress and dislocation,
- the tuning of the cavity should be realised in such a way as to position the Airy peak (at λ_{em}) in the best possible way in the extraction window. The length L of the cavity must therefore be slightly larger than $m_c(\lambda/2n)$, corresponding to the value for normal-incidence resonance familiar to Fabry-Perot practitioners. By thus proceeding, the emission angular lobe comes to correspond to directions of emission substantially inclined with respect to the normal direction, up to 30-45° in the case of an extraction in the air,
- the emitting layer(s) should be located at the antinode(s) of the cavity mode profile, as is the case for vertical cavity surface emitting lasers (VCSELs),
- the exit mirror, here the upper mirror, should have a reflectivity suitable for the construction of an Airy resonance. The reflectivity does not need to be as high as in the case of VCSELs, where the problem is not to shape the spontaneous emission, but to compensate for the minute gain of sub-μm thick active layers. Since this gain is of a few percents, the reflectivity of the mirrors in VCSELs must be in the 99-100% range. By contrast, a first order approximation for the adequate reflectivity of the upper mirror in the MCLED yields $R \sim 1 - m_c NA^2/n^2 \sim 40\text{-}80\%$ (Benisty 1998a, 1998b). Under these conditions, the cavity reaches an appropriate finesse, and the Airy peak represented in Fig. 10.2a tends to become narrow enough for validating the efficiency value predicted by Eq.

10.2. Since metals tend to present significant transmission losses, they are excluded in favour of one-dimensional photonic crystals (Bragg mirrors) and even in certain specific cases of the mere semiconductor/air interface ($R = 0.3$). The optimisation of the exit mirror illustrates how the control of spontaneous emission leads to revisiting cavity concepts, more particularly in terms of size and finesse.

Having thus reviewed the physics underlying the case of a monochromatic emission, the influence of the spectral width of the emitter may be more easily assessed (the ‘material’s Q ’, as represented in Fig. 10.2.c). The monochromatic approximation presented here remains valid as long as the relative spectral width $\Delta\omega/\omega \approx \Delta\lambda/\lambda$ does not exceed the ratio $\Delta k_z/k_z$ corresponding to the extraction cone (Fig. 10.2a). This ratio can also be equated to the quantity $NA^2/2n^2$ introduced above. For large spectral widths, the use of the planar cavity comes down to an angular redistribution of the emission according to its spectral components, without however resulting in any overall net gain. The spectral narrowing along a given direction may nonetheless present a specific interest. This is the case for the coupling of light with an optical fibre, since spectral filtering limits the excessive effects of spectral dispersion in the further transmission of the signal.

Quantitatively, the overall efficiency reaches $\eta = 23\%$ at $\lambda = 980$ nm for GaAs microcavities enclosed with a metallic mirror at one side and a Bragg mirror with reflectivity $R = 60\%$ at the other (De Neve 1997a, 1997b). This value could be further enhanced to 29 % at $\lambda = 980$ nm by replacing the back mirror with a Bragg mirror with strong index contrast (AlOx/GaAs layers) and the upper mirror with the simple air/GaAs interface respectively (Rattier 2002). The theoretical limit is actually closer to 40%, but the lateral current injection through extremely thin layers (< 50 nm) would become quite difficult in this case. For red LEDs emitting at 650 nm and marketed for coupling with plastic optical fibres (by OSRAM-OS), the utilisation of Bragg mirrors (one-dimensional photonic crystals) remains limited due to the weak index contrast $\Delta n \sim 0.25$ which can be obtained with their constitutive materials.

10.1.3 Increase of the Extraction Efficiency Using Two-Dimensional Photonic Crystals

Two-dimensional photonic crystals are considered as suitable candidates for increasing the emission efficiency of LEDs beyond the limit values reached in planar cavities. Not only is the fabrication of Bragg mirrors with strong index contrast difficult, but planar microcavities do not remove the significant photon leakage which occurs through the guided modes propagating in the active layer plane. Indeed, the different layers of the microcavity tend to form a waveguide, and this horizontal emission, which may represent up to 50% of the total emission, is not detected. A two-dimensional photonic crystal placed at the periphery of the emitting area can be used as a reflector for exploiting this radiation. The reflector allows ‘recycling’ the guided photons by absorbing them and giving them a new

opportunity of being emitted in the mode of the planar microcavity (Benisty 1998a, 1998b). However, this phenomenon has a practical interest only provided that the internal quantum yield η_1 is very high and that the emission in leaky modes, i.e. in continuum modes which are neither guided nor resonant, is negligible (Rattier 2002). For GaN blue-green-white LEDs, the extraction is higher at the beginning ($n = 2.5$) and a sizeable effect can be more easily achieved.

A different approach relies on the use of the photonic crystal as a second order grating in order to diffract the guided light towards air in its first order (Boriditsky 1999, Delbeke 2002). This configuration is more deterministic than the random texturing of the surface of a thin film, represented in Fig. 10.1d (Windisch 1999). One of the problems which arise here is that of the relative sizes of the emitting and extracting areas. In order to avoid any increase in the apparent size of the source, different solutions have been experimentally investigated where only the guiding regions at the periphery of the emitting area are structured with two-dimensional photonic crystals (Delbeke 2002, Rattier 2002). In this context, it may be worth mentioning the intrinsic difficulty of calibrating photoluminescence measurements in configurations where the active medium is textured. This difficulty arises from the fact that such textures may significantly affect the actual efficiency of the pumping efficiency of the active medium. More detail on this subject can be found in the articles published in the special issue of the *IEEE J. Selected Topics in Quantum Electronics*, vol. 8, 2002.

More radically, an extraction of 100% has been predicted for a membrane-based two-dimensional photonic crystal where the frequency of the emitter lies either in a complete bandgap or in an allowed band of higher order (Fan 1997). In the first case, in-plane propagation is forbidden, while in the second case the emission is strongly coupled to free-space modes. The membrane configuration is akin to that of the so-called ‘band edge lasers’ which will be examined shortly hereafter (Section 10.3.). Actually, an in-depth analysis reveals that as far as the extraction of luminescence is concerned an identical 100% performance can be obtained using other types of diffraction gratings (Rigneault 2000). Further, the implementation of membrane-type structures and deeply etched crystals is made difficult by the possibility of important non-radiative recombination phenomena at etched interfaces. Electrical pumping also presents a number of problems. Similar problems arise for the ‘band edge’ lasers and microlasers which are described in Sections 10.3 and 10.4 respectively. In the mid-term, it would be out of the question to compromise the electrical and thermal performances of such mass-produced devices as light-emitting diodes. This means that the control of the spontaneous emission should comply with existing technological constraints. This condition leads to favouring techniques restricted to the extraction of the guided modes while further allowing the possibility of including the transfer over a mirror. The use of the omnidirectional extraction properties of Archimedean lattices, described in Chap. 3, is one of the directions which are being currently investigated (Rattier 2003).

10.2 Ridge-Type Waveguide Lasers Confined by Photonics Crystals

The most classical geometry for semiconductor lasers is that of the waveguide edge-emitting laser, which presents a typical output mirror reflectivity of ~ 30 percent for a cleaved facet in the absence of optical processing. As has been previously discussed in Chap. 9 devoted to integrated optics, both the ridge waveguide and the end mirrors can be based on photonic crystals. For ridge waveguides, a practical interest of air-hole photonic crystals is that electrical continuity can be more easily achieved with these crystals than with deep-ridge waveguides. As far as end mirrors are concerned, the use of a one-dimensional or two-dimensional photonic crystal defined through the etching of a waveguide may ensure a high reflection coefficient for guided modes ($R > 0.97$). The reduction of optical losses at these mirrors leads to very short cavity lasers. As an example, we may mention here the fabrication of an ultra-short cavity GaAs/GaAlAs laser ($12 \mu\text{m}$) using one-dimensional air/GaAs deep etched mirrors obtained by the ECR-RIE etching method (Rennon 2001). In principle, these short cavity lasers have a very small active volume and a threshold current far beyond the submilliampere threshold. However, the possibility of achieving such threshold currents still depends on the resolution of other technological problems.

Another interest of photonic crystal mirrors/guides lies in the possibility of revisiting earlier single-mode laser configurations, like the so-called C³ laser, or *Cleaved Coupled Cavity* laser (Agrawal 1993, Tsang 1983). The development of these lasers had been abandoned in the 1970s and 1980s as a result of technical difficulties. The compound cavities of these lasers were indeed created from the mechanical assembling of two separated cavities through the mere juxtaposition of two chips. As may easily be imagined, the phase of the coupling remained quite imprecise. By contrast, a well-designed photonic crystal mirror should offer a well-defined phase for the coupling, as has been demonstrated by T. Happ *et al* (Happ 2001). Fig. 10.3.b presents an example of a laser formed from two coupled linear cavities, both of which were entirely carved inside a two-dimensional photonic crystal. The number of technological stages remains limited compared to the complexity of the overall device.

A rather extreme case of a system based on coupling is that of a laser using a waveguide formed by coupled hexagonal cavities, such the CROW (Coupled Resonator Optical Waveguide) proposed by A. Yariv *et al* (Yariv 1999). Such a device, represented here in Figs. 10.3c and 10.3d, has been fabricated at the University of Würzburg and a single-mode emission has been achieved (Happ 2003).

Going back to more ‘canonical’ photonic crystal waveguides, the periodic corrugation of the guide edges can be used for optical feedback. This interesting possibility must be dissociated from the concept of a photonic band gap. In the usual case of DFB (Distributed Feedback) lasers (Casey 1978), the period Λ of the grating above the active layer is a multiple of $\lambda/2n_{\text{eff}}$, whence $\Lambda/\lambda = (1, 2, 3, \dots)/2n_{\text{eff}}$. For DFB lasers emitting at $1.55 \mu\text{m}$, this series turns out to be equal to 0.15, 0.30, 0.45, etc. In the case of the optical feedback imposed by a

triangular photonic crystal waveguide oriented along the Γ K direction (see Figs. 9.10b, 9.12a, 9.12b, 9.12f, 9.12h in Chap. 9), the reader may readily verify that only the odd terms 0.15, 0.45 etc. are effective, while the corresponding wavelengths remain outside the two-dimensional photonic band gap (see Fig. 9.3). In the example presented in Fig. 10.3b, the photonic crystal waveguide is oriented along the Γ M direction, with the consequence that the modulation period of the end mirrors is as small as possible with respect to the wavefront of the guided wave: such dense mirrors permit to escape the phenomenon of modal mixing caused by diffraction (Happ 2001). Since the modulation period along the waveguide in the Γ M direction is $\sqrt{3}$ times larger than along the Γ K direction, feedback should occur at wavelengths in the two-dimensional photonic band gap. However, no feedback was observed in these experiments (Happ 2001), as a result probably of inadequate values for other parameters, for instance the spectral gain curve. Further investigations are thus required in order to study with a greater precision the existence of feedback effects in photonic crystal lasers.

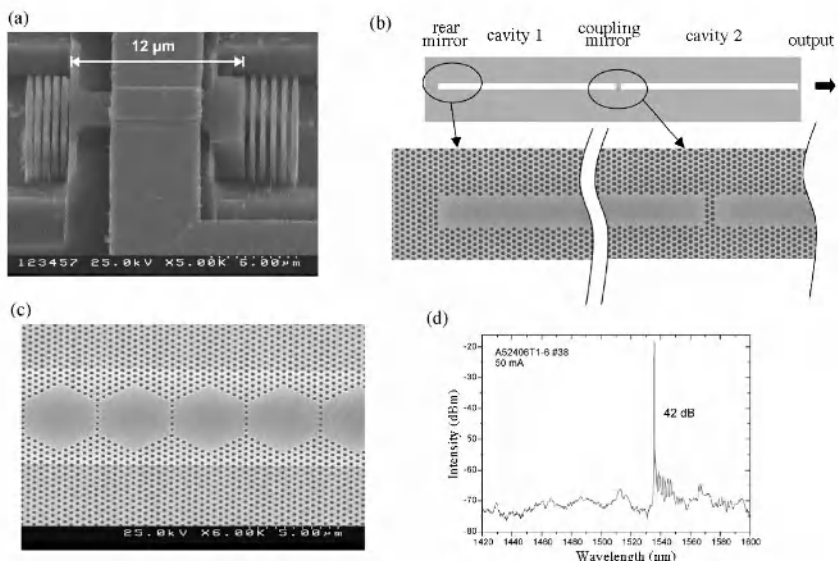


Fig. 10.3. *a.* Short laser based on one-dimensional photonic crystal mirrors (Rennon 2001) *b.* Ridge photonic crystal laser with two coupled cavities; principle and side view (SEM micrographs) (Happ 2001) *c.* Laser consisting of a set of hexagonal cavities coupled together *d.* Corresponding single-mode emission spectrum with a high rejection of secondary modes (Happ 2003)

Although the superiority of lasers based on photonic crystal waveguides over classical ridge lasers still remains to be demonstrated, the use of photonic crystals opens unprecedented perspectives for the association of lasers with miniature guided-optical devices (filters, bends, optical ‘plates’, etc. See Chap. 9) as well as for the monolithic integration of distinct lasers over a single chip in a single technological stage. In addition to the high added value of large-scale integrated systems, these prospects for emitters also bring about a certain physical simplification stemming from the fact that photonic crystals ensure that the resulting device will operate in single polarisation mode. For lasers, this opens the possibility of abstracting in first and even in second approximation from the behaviour of the optical chain in the other polarisation, a possibility which sharply contrasts with the requirements imposed on a classical receiving system, more particularly at the extremity of the fibre.

10.3 Photonic Crystal Band Edge Lasers

In the preceding examples of semiconductor microsources, the photonic crystal was located at the periphery of the active region, thereby acting either as a reflector or as a diffraction coupler. In the two following sections, we shall consider examples of semiconductor microsources where the photonic crystal, or some defect of reduced dimensions that it may present, is located within the core of the emitting region.

It is now a well-established fact that the dispersion curve of materials can be dramatically altered through their periodic structuring. More specifically, group velocities close to zero can be obtained near the edges of the photonic band gap as well as at the Γ symmetry point of the Brillouin zone (see Section 6.1.2). Propagation modes presenting an almost flat dispersion curve over almost the entire Brillouin zone may also exist. It should be borne in mind however that these latter modes result from a degeneracy effect (see Section 1.3.3). As a rule, lower group velocities correspond to longer time constants in the interaction between an optical medium and the propagating light. Accordingly, all processes involved in this interaction can be dramatically reinforced if certain conditions are met. This applies to the case of the nonlinear frequency conversion process (Sakoda 1996), as well as to the case of stimulated emission (Dowling 1994; Sakoda 1999a). It has been demonstrated that for an inverted medium, the stimulated gain is in inverse proportion of the group velocity and that lasing can be produced in a photonic crystal without requiring the use of cavity mirrors.

The enhancement of the stimulated emission in photonic crystals was first predicted through the modelling of the propagation of wave packets in the time domain (Dowling 1994). The description has been supplemented by other methods, as developed for instance in (Quang 1997), addressing in particular the fluorescence of a photonic crystal near the edge of the bandgap. A detailed formulation of the stimulated gain in two and three-dimensional crystals has been suggested by K. Sakoda *et al* (Sakoda 1999a, 1999b, 2001). As a first approximation, the lasing

mechanism appears to be the same as for DFB lasers which are currently used in optical telecommunication systems (Agrawal 1993). To some extent, lasers based on ‘bulk’ photonic crystals may be viewed as the two- and three-dimensional extensions of DFB lasers. In all cases, and provided that no defect has been created inside the periodic structure, the lasing occurs at the edges of the band gap, i.e. in frequency domains where the distributed feedback of the propagating waves is marked, but where the propagation of the waves themselves is not forbidden. A DFB laser thus tends to simultaneously lase at two distinct frequencies at the two opposite edges of the band gap. In order to operate in single mode, a defect must be created inside the periodic structure, thereby creating a phase jump in the distributed Bragg grating. An example of such a method can be found in (Utaka 1986). In spite of these similarities, a significant difference remains between DFB lasers and ‘bulk’ photonic crystal lasers. Indeed, the one-dimensional grating of conventional DFB lasers is seldom etched to the point where the active layer is reached. As a consequence, the periodic modulation along the laser is essentially a modulation of the refractive index. By contrast, in the case of photonic crystal band-edge lasers, the active layer is structured. Although the index modulation remains predominant due to the high index contrast between air holes and the semiconductor, the modulation of the laser gain is no longer negligible. Thus, a comparison can be drawn to some extent between band-edge photonic crystal lasers and the so-called gain coupled DFB lasers (Kogelnik 1972).

Laser emission in band-edge microsources based on the use of two-dimensional bulk, i.e. defectless, photonic crystals has been experimentally demonstrated by several groups (Inoue 1999; Kopp 1998; Monat 2002; Notomi 2001; Ryu 2002a). An underlying objective is the idea of realising micro-lasers with large emitting areas without resorting to the use of cavity mirrors. In such a case, there would obviously be no need neither for an alignment of the cavities nor for tuning, and to some extent the realisation of such a laser would come down to cutting up a given two-dimensional photonic crystal at the desired size. Indeed, laser light can in such a case be extracted from the whole surface of the crystal provided however that diffraction effects occur in photonic bands of a sufficiently high order. It may be argued that such an extraction technique is identical to that used in more conventional high-power semiconductor lasers, which are equipped with a one-dimensional diffraction grating of second order. Actually, while a second-order grating behaviour may indeed be found in certain two-dimensional photonic crystal band-edge lasers, new situations may also occur where for instance the distributed feedback effect would involve several directions in the photonic crystal (Fig. 10.4) (Notomi 2001). Interestingly enough, it may be noted here that the first ‘bulk’ photonic crystal lasers were made of polymer layers pre-structured in the form of a two-dimensional grating. To some extent, this reproduces in two dimensions the first experiments on DFB lasers, where doped gelatin layers were used more than thirty years ago (Kogelnik 1971).

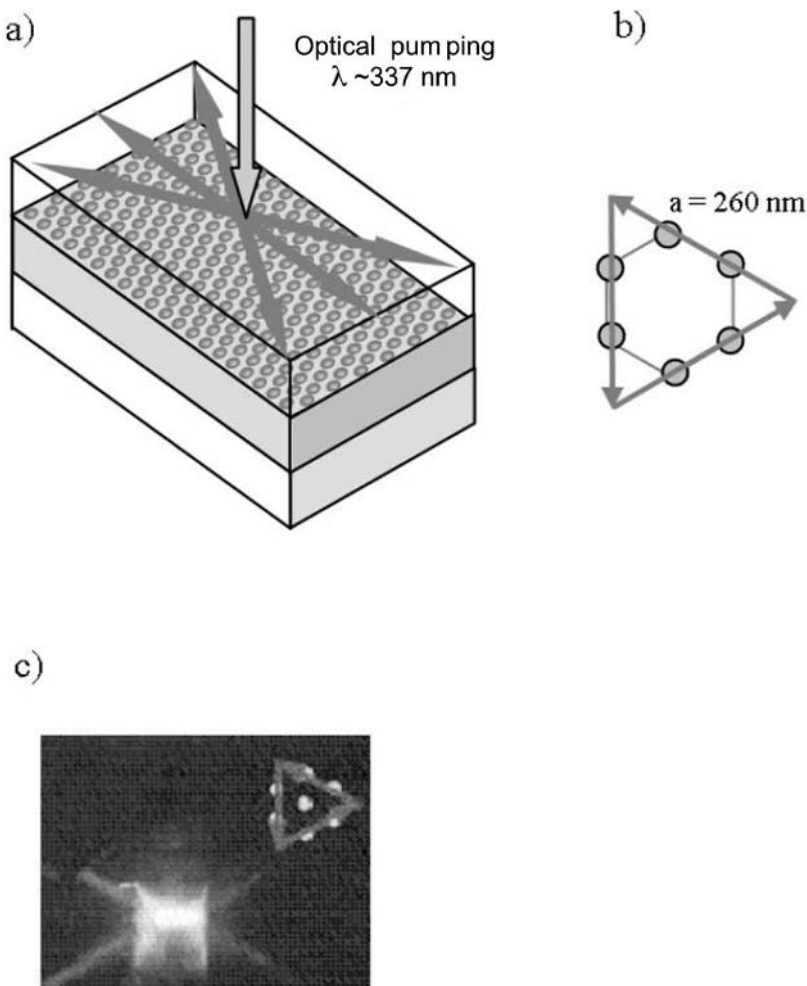


Fig. 10.4. *a.* Schematics of an optically pumped photonic crystal band-edge laser with examples of optical feedback directions *b.* Optical feedback simultaneously involving three directions of a triangular photonic crystal *c.* Photograph showing the trajectories of the rays inside the organic photonic crystal laser used as a reference (Notomi 2001). The operating conditions are as represented in *b*. The photograph is taken from the upper surface of the laser (scattered light) using a CCD camera

Experiments using etched semiconductor membranes have recently been carried out, and have led to very encouraging performances: a lasing effect has thus been obtained for InGaAsP membranes over a $\sim 50 \mu\text{m}^2$ emitting area for optical pump powers as low as 35 μW (Ryu 2002a). The operating temperature was 80 K. In another experiment, a $\lambda = 1.5 \mu\text{m}$ emission was obtained even at room temperature from an InAsP quantum well membrane pumped over a $3 \times 3 \mu\text{m}^2$ emitting area. The optical pumping threshold in this experiment was 1.1 mW (Monat 2002). However, the deep etching of the active layers may result in a strong reinforcement of the non-radiative carrier recombinations at the air/semiconductor interfaces. This phenomenon may account for the use of a low operating temperature in one case, as well as the higher lasing threshold in the other case.

10.4 Microcavity Lasers

As has been seen in Section 7.1.3, the increase of the coupling factor of the spontaneous emission β to a given cavity mode and the simultaneous reduction of the active layer volume may potentially provide microcavity lasers with very original and interesting properties. While the best performances to date in terms of threshold current have been reported for vertical cavity surface emitting lasers (VCSELs) or for microdisk lasers, rapid advances in the performances of two-dimensional photonic crystal microlasers can be observed since 2000. The only exception in this field concerns electrical pumping, which has only been reported in few experiments (Park 2004).

After briefly reviewing the best results obtained thus far for these different microlasers, we shall identify their respective limitations using the didactic model already presented in Section 7.1.3.

The most recent technological advance in the development of VCSELs and their optimisation has been the introduction of an oxide ring located just above the active layer containing the quantum wells or dots in order both to localise the carrier injection and to laterally confine the optical mode (Fig. 10.5a).

A record threshold current of 36 μA , which is the lowest ever achieved for all semiconductor lasers, was thus reported in the continuous wave (CW) regime for the (In)GaAs/GaAlAs system at 300K (Bond 1998; Huffaker 1997). To this date, this system remains by far the most advanced as regards both its material quality and the very structure of the device. The active layer generally consists of a single or several quantum wells emitting at around $\lambda = 0.98 \mu\text{m}$. The reduction of the actual lateral size of this device, which is generally accompanied with a significant increase of the β factor, is limited here by the diffraction of the oxide ring. An optimal diameter indeed exists for the latter, beyond which strong diffraction effects may take place. This optimal diameter can be typically achieved for a lateral size equal to $2 \mu\text{m}$ by placing the oxide layer at a field node of the laser mode so as to minimise the amount of optical losses. The value for β is about 0.04 in the best case (Kuksenkov 1997).

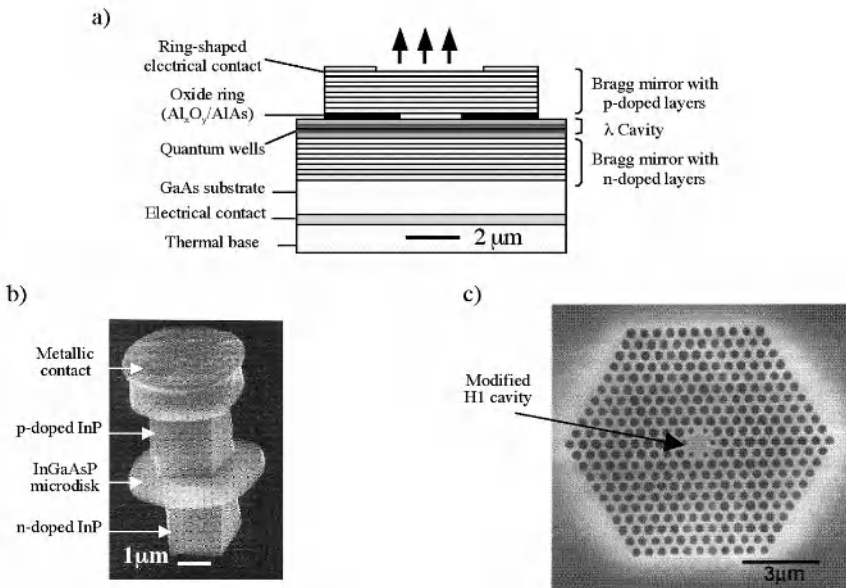


Fig. 10.5. *a*. Schematic view of a vertical cavity surface emitting laser fabricated upon a GaAs substrate *b*. Micrograph of a microdisk laser (Fujita 2000) *c*. Micrograph of a photonic crystal microcavity laser (Park 2001)

The recent advances in the fabrication of microdisk lasers and the reduction of their lateral dimensions have allowed a better carrier injection in these lasers with a significant improvement of their threshold current in the CW regime (Fig. 10.5b). The lowest threshold currents reported thus far are around $40 \mu\text{A}$ (Fujita 2000). Microdisk lasers are fabricated in the InGaAsP/InP system, which exhibits moderate non-radiative carrier recombinations at the air/semiconductor interfaces. The best threshold performance was obtained for a disk with a diameter of $2.7 \mu\text{m}$ and a β factor equal to 0.1 (Fujita 2001).

Minimising non-radiative carrier recombination at the air/semiconductor interfaces is crucial for photonic crystal microcavity lasers. The approach generally used for circumventing this difficulty consists in using either the InGaAsP/InP system (Painter 1999b) or an active medium with quantum dots (Yoshie 2002). In the latter case, the carrier diffusion at the interfaces can be dramatically reduced. Several groups have reported an optically pumped laser emission for InGaAsP quantum wells in microcavities with very small effective volume ($V < (\lambda/n)^3$) (Loncar 2002b; Painter 1999b; Park 2001; Ryu 2002b). These microcavities were realised on suspended membranes (Fig. 10.5c). In the first experiments performed using a microcavity with a small Q -factor ($Q = 250$), the emission of the laser was maintained up to the temperature of 143 K for a threshold pump power of 7 mW , a value that would correspond to a very high current density of several kA.cm^{-2} in

the case of an electrically pumped laser. At such a current density, it is well-known that the non-radiative Auger recombinations become prohibitive in the InGaAsP system. Fortunately, better quality factors resulting from an optimised geometry of the defect in the microcavity have led to a significant reduction of the threshold pump power down to 220 μW for a microcavity with a Q factor equal to ~ 2000 (Loncar 2002b; Park 2001). However, the best results in terms of threshold pump power have been obtained for InAs quantum dots embedded in GaAs structures, where the emission of the laser occurred at 300 K with a threshold of $\sim 120 \mu\text{W}$. The two-dimensional photonic crystal was of square symmetry. In order to compensate for the small gain amplitude associated with quantum dots, it was necessary to use multiple quantum dot layers and to couple several microcavities of the C1 type. For all these results, it should be noted that due to the poor thermal dissipation of photonic crystal membrane lasers they can only be operated in pulsed regime. This geometry also results in difficulties in implementing the electrical pumping of membrane structures, and the possibility of a CW electrically pumped photonic crystal microcavity laser still remains to be demonstrated.

It is thus apparent that microcavity lasers have dramatically progressed during the last five recent years, although their performances are still far from the ultimate performances that were expected to border on those of a ‘thresholdless’ laser (where $I_{\text{th}} \sim 0.1 \mu\text{A}$ for $Q \sim 2000$ as discussed in Section 7.1.3). For each type of microlaser, their physical limitation can actually be identified by estimating the ξ and β parameters involved in the rate equation model in Section 7.1.3.

In the case of InGaAsP quantum well structures, either with a microdisk or with a photonic crystal microcavity, the value for ξ lies between a few tens and a few hundreds. The laser threshold can be relatively well estimated assuming that non-radiative recombinations can be neglected. In principle, a lower threshold could be achieved by decreasing the value for ξ through diminution of the ‘number of emitters’, i.e. by reducing either the number of quantum wells or their active areas.

From this point of view, the GaAs VCSEL presented in (Huffaker 1997) is already quite optimised, since the active medium consists of a single InGaAs quantum well. In view of the relatively low value for β (~ 0.04) which had been measured for very similar structures (Kuksenkov 1997), one obtains here $\xi \sim 2$ (with $N_T/S \sim 4 \cdot 10^{12} \text{ cm}^{-2}$, $S \sim 5 \mu\text{m}^2$, $\phi \sim 10^{12} \text{ s}^{-1}$, $\tau \sim 10^{-9} \text{ s}$), and from Eq. 7. 13 the threshold current I_{th} can be predicted to be about 2 μA . However, the performances of the laser are actually limited, in the first place by the heating effects induced on active layers by the electrical injection in this special configuration. The gain curve broadens, thereby leading to a carrier loss through non-radiative recombinations as well as to electrical leakages. Eventual improvements of the device are therefore to be expected essentially from the optimisation of the electrical injection (Huffaker 1997).

Let us finally consider the case of the quantum dot photonic crystal microcavity laser described in (Yoshie 2002). This laser consists of several C1 microcavities, formed by gaps inside a crystal presenting a square symmetry. Each individual microcavity has a Q factor of ~ 1300 and contains about 1000 InAs/GaAs quantum dots. These different microcavities are strongly coupled to one another. The

lasing is achieved for a set of two or four coupled cavities, albeit not for a single cavity. It might first be noted that only a limited fraction f of the quantum dots is coupled to the lasing mode. This fraction is close to the ratio between the homogeneous linewidth and the inhomogeneous linewidth. Further, the laser threshold cannot be reached save if a strong Purcell effect exists. In the absence of a Purcell effect, the following values would hold $\xi \approx \beta/16 \ll 1/4$ for a single cavity and $\tau \sim 1\text{ ns}$, $\phi \sim 2 \cdot 10^{12} \text{ s}^{-1}$, $f \sim 1/4$. Under the realistic assumption that $f \sim 1/4$, the minimum amplitude of the Purcell effect required for reaching the laser threshold with a set of two coupled cavities can be estimated as follows: $F = 3$, $\tau = 0.3 \text{ ns}$, $\beta = 0.75$. In the absence of non-radiative carrier recombination, the laser threshold calculated from Eq. 7.13 would be equal to $\sim 0.5 \mu\text{W}$ for an optical pumping with a 100 percent efficiency.

In practice, several effects associated with the geometry of the device may actually contribute to the increase of the laser threshold:

- the pump beam is only partially absorbed inside the photonic membrane,
- the optically pumped area is much larger than the cross-section of the cavity,
- some quantum dots are pumped while not being coupled to the resonant cavity mode. The latter effect increases the laser threshold from a factor higher than two.

However, these effects are insufficient to explain the overall increase of the laser threshold, which reaches $120 \mu\text{W}$ in place of the $10 - 20 \mu\text{W}$ which was theoretically predicted. This demonstrates the predominant role of non-radiative carrier recombinations at the air/semiconductor interfaces. Unlike for the InGaAsP/InP system, the passivation at the air/semiconductor interfaces is critical for the development of microdisk and photonic crystal microcavity lasers in the GaAs/GaAlAs system, even if InAs/GaAs quantum dots were to be used.

Within the microlaser family, and in spite of a relatively low β factor, VCSELs thus appear to offer the best compromise in terms of threshold performances, of practical utilisation (due to their directive emission) and of ease of fabrication. Besides, a better thermal dissipation, as well as the implementation of electrical pumping, are imperative for allowing the CW operation of photonic crystal microcavity lasers. These objectives cannot be easily addressed with the use of membrane microcavities. As a consequence, it might reasonably be thought that future studies are going to privilege photonic crystal microcavities on semiconductor substrates, be it at the cost of an increase of the effective volume of the cavity mode and of the subsequent reduction of the Purcell effect. From a more fundamental point of view, photonic crystal microcavities on membranes are certainly among the more adequate systems for demonstrating the Purcell effect at room temperature, either in quantum wells or in quantum dots, as well as for investigating laser emission in the regime of a strong enhancement of the spontaneous emission ($F \gg 1$, $\beta \rightarrow 1$). In this respect, the few results which have been summarised here should probably be considered as the preliminary phase in a long series of results to appear in this field.

10.5 Potential Interest for Single Photon Sources

A single photon source is an optoelectronic device capable of generating on demand a light pulse containing but a single photon. The development of single photon sources, and more generally the generation of non-classical states of light by solid-state devices are key issues for the practical implementation of the concepts of quantum information science (Bouwmeester 2000).

In the midterm, the most promising field of application for single photon sources is likely to be quantum cryptography. Single photon sources should allow us to implement the intrinsically secure transmission protocols which had been proposed in the early eighties and which rely on the polarisation state of single photons for the encoding of information (Bennett 1992). Indeed, the fundamental principles of quantum mechanics ensure that a complete knowledge of the polarisation state of a photon cannot be achieved from measurements save from a polarisation basis known beforehand. By contrast, in conventional optical communications, each light pulse contains many photons, thus potentially allowing an eavesdropper to proceed to several measurements and retrieve precise information concerning the common polarisation state of these photons.

These quantum cryptography protocols have already been validated for conventional telecommunication systems based on optical fibres using strongly attenuated laser sources delivering on an average less than 0.1 photon per pulse. It is quite obvious that a coherent source is but a very rough approximation of the properties of a real single photon source: the probability for a given light pulse not to contain any photon is quite high, and a non-zero probability further exists that it might contain two photons or more. Two main problems thus arise (Brassard 2000):

1. multi-photon pulses can be used by a potential eavesdropper for extracting information. This imposes to work in a regime of strong attenuation so as to limit the amount of information that could be accessed by such an eavesdropper.
2. the range for secure communication is in practice limited by the losses of the channel and by the dark counts of the detectors. Indeed, the errors induced on quantum keys by dark counts can be corrected only as long as the bit error rate typically remains smaller than 10%. Obviously, this problem becomes all the more acute for light pulses of weak intensity.

Using attenuated lasers, the maximum secure transmission length is the result of a compromise between these two problems. For realistic quantum cryptography systems on optical fibres, the replacement of attenuated lasers with perfect single photon sources would typically allow one to increase the maximum secure length from a factor of 2. Alternately, at constant channel length the bit rate per pulse could be increased from two orders of magnitude (Brassard 2000).

Single photon pulses are quantum states of light. As such, they cannot be generated by ‘classical’ sources such as a black body or a laser. The most efficient strategy for the production on demand of single photons relies on the pumping of a

single quantum system. For solid state systems, the triggered generation of single photons has been reported using a variety of isolated emitters: a molecule (Lounis 2000), a centre coloured inside the diamond (Kurtsiefer 2000), a semiconductor nanocrystal (Michler 2000a), or a semiconductor self-assembled quantum dot (Michler 2000b; Moreau2001a). Thus far, quantum dots are the most likely to be adopted for a practical application in quantum cryptography, as they combine two major specific advantages. Indeed, not only can they be pumped relatively easily using electrical injection (Yuan 2002), but optical microcavities can further be used in order to adjust their emission properties and collect more efficiently their emission (see Section 7.2). A single-mode single photon source has been realised by placing a single InAs quantum dot inside a GaAs/AlAs pillar microcavity (Moreau 2001b; Santori 2002). When the quantum dot is in spectral resonance with the cavity mode, it undergoes a strong Purcell effect (see Section 7.1.2), and its spontaneous emission is very preferentially funnelled into this mode. As a result of the directional emission of the pillar microcavity, single photons can be very efficiently collected. A photon collection with an efficiency higher than 40% has thus been independently measured in two different laboratories (Moreau 2002; Pelton 2002). Further, the use of anisotropic cross-sections allows lifting the polarisation-degeneracy of the fundamental micropillar mode (see Section 7.2.3) and controlling the linear polarisation of single photons (Moreau 2001b). In practice, this property is extremely interesting, since the necessity always exists of preparing single photons in a given polarisation state prior to any encoding of information. When non-polarised single photon sources are used, half of the photons get lost at this stage of the preparation.

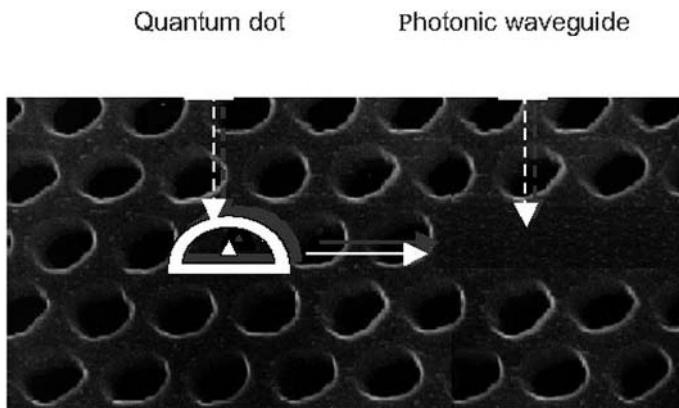


Fig. 10.6. Schematic view of an integrated single-photon source consisting of a single quantum dot in a two-dimensional photonic crystal

Finally, a ‘plug-and-play’ single photon source for quantum cryptography ought to combine three main properties: an emission in the telecom spectral window, a high efficiency in single mode (space and polarisation) and an electrical pumping. Thus far, these three properties have been separately demonstrated. Their combination in a single device is not beyond reach, and is most likely to be achieved in a near future using InAs quantum dots embedded in GaAs/AlAs micropillars.

In this context, the potential interest of photonic crystal microcavities results from two significant limitations of single photon sources based on a single quantum dot embedded in a micropillar. These two limitations are of an intrinsic and of an extrinsic nature respectively:

1. the generation of single photon pulses relies on the strong Coulomb interaction between the electrons and the holes trapped inside the quantum dot (Gérard 1999). It rests upon a very simple principle: several electron-hole pairs are first injected into the quantum dot using a non-resonant pulsed optical or electrical excitation. The quantum dot relaxes towards its ground state through a radiative cascade; each emitted photon has a specific energy, which depends on the number p of electron-hole pairs remaining in the dot at this stage of the sequential recombination process. Therefore, a spectral filtering of the ‘exciton’ emission line of the quantum dot ($p = 1$) allows preparing for each excitation cycle a triggered light pulse containing the last photon emitted by the quantum dot. A requirement for implementing this protocol is quite obviously that the exciton and multi-exciton ($p > 1$) lines of the quantum dot be spectrally separated at the scale of their linewidth. In practice, the electron-phonon interaction tends to broaden these lines with the consequence that this approach applies only to temperatures lower than 100 K for InAs quantum dots. By contrast, nanocrystals, as well as certain molecules, are able to generate single photons at room temperature. The coupling of such an emitter to the resonant mode of a microcavity based on two-dimensional photonic crystal is a very appealing approach. First the ‘open’ nature of such cavities allows the selection of an adequate emitter, thus permitting to ensure spectral resonance, as well as the optimisation of its position at the antinode of the resonant mode. Further, in spite of the broad linewidth of these emitters at room temperature, the very small modal volume of the cavities should entail a strong Purcell effect and therefore a good coupling of the photons emitted in cavity mode, resulting in the possibility of expecting an efficient photon collection.
2. Experimentally, the efficiency of single photon sources based on micropillars is systematically lower than the spontaneous emission coupling coefficient β in the resonant cavity mode, which can be estimated from the magnitude of the Purcell effect using Eq. 7.10 (see Section 7.1.3.). This effect directly results from the additional extrinsic optical losses which are mostly due to scattering by the rough cylindrical sidewalls of the micropillar. This effect is particularly marked for small-diameter micropillars ($d < 2\mu\text{m}$ typically for GaAs/AlAs) and for micropillars with highly-reflective Bragg mirrors. Since in the latter case the intrinsic losses, which are related to the finite reflectivity of the mirrors, are

low, the properties of the cavities tend to being extremely sensitive to the existence of additional extrinsic losses. The optimisation of micropillars for high-efficiency sources must therefore result from a compromise between the search for a strong Purcell effect, favoured by a decrease of intrinsic losses, and the necessity of minimising the effects of extrinsic losses. When all these effects are taken into account, it can be demonstrated that the external efficiency of such single photon sources is typically limited to 70% with a state-of-the-art processing of GaAs/AlAs micropillars (Barnes 2002). In this respect, the use of photonic crystal microcavities might very well represent a decisive breakthrough and contribute to pushing back this limitation. Let us consider for instance the case of the single photon source schematically represented in Fig. 10. 6, which combines an hexagonal cavity H1 containing a single InAs quantum dot on resonance and a photonic waveguide. Let us assume that the quality factor Q_{iso} of the isolated cavity is of the order of 3000, as has been experimentally observed for H1 cavities (Yoshie 2001), and let us further adjust the efficiency of the coupling to the waveguide in such a way that the quality factor Q of the coupled cavity be of the order of 300. In this case, the following values can be derived from Eqs. 7.8 and 7.10 respectively: $F_p \sim 50$ and $\beta \sim 98\%$. Further, the coupling of the cavity to the waveguide is, by construction, the main loss mechanism for the cavity. The efficiency of such a source, which can be estimated from the product $\beta (1 - Q/Q_{iso})$, would thus be of the order of 90%.

11 Photonic Crystal Fibres

11.1 Another Implementation of Periodic Structures

As has been exposed in the present book to this point, photonic crystals in the near-infrared and visible regions were primarily conceived with the aim in mind of permitting the complete control of electromagnetic waves in semiconductor materials. Yet, in spite of the numerous advances which have occurred in the fields of guided optics and microsources, the fact must be admitted that the initial expectations placed by researchers on this direction have not totally materialised thus far. At the same time, different and previously unforeseen types of applications involving other materials have appeared in the ‘tree’ of photonic crystals. In the field of photonic crystals, the most striking illustration of the unexpected fruitfulness of such generic concepts as that of photonic crystal is most probably the photonic crystal fibre and more generally the microstructured optical fibre (MOF). For an insight into the state-of-the-art performances achieved with microstructured optical fibres, the reader is referred to (Ortigosa-Blanch 2000; Russel 2003), where further references are also presented.

In conventional optical fibres, which have been the basis of the terrestrial telecommunication industry since the first demonstration of fibres with a high transmission capacity in the spectral window extending around 1550 nm, the light is guided owing to the phenomenon of total internal reflection. The guiding itself occurs inside a silica core with an optical index higher than the optical index of the layers which form the cladding and are also themselves made of silica. The index step is achieved through the use of a different doping for the core and the cladding respectively. In this respect, microstructured optical fibres present a completely different structure: as can be seen in Figs. 11.1 and 11.2, these fibres appear in the form of silica matrices drilled with a number of parallel holes periodically organised into a two-dimensional array. While the periodic arrangement of the air holes would justify the use of the term photonic crystal fibre, this name is more specifically reserved to those fibres where the propagation inside a defect with a low index defect is ensured by a true photonic band-gap effect, as is represented in Fig. 11.2a. For this reason, photonic crystal fibres are also referred to as hollow-core microstructured optical fibres.

Actually, most of the results which have been presented to this day concern solid-core microstructured optical fibres, examples of which can be seen in Figs. 11.2b and c. The study and the fabrication of these fibres is indeed much simpler than it is the case for hollow-core microstructured optical fibres. It might

be pointed out here that the propagation in solid-core microstructured optical fibres occurs due to a specific form of modified total internal reflection where photonic band-gap reflection is not necessarily involved. In the present chapter, after providing a brief description of the fabrication process used for the realisation of photonic crystal fibres we shall proceed to describe the main properties and applications of these fibres. Hollow-core photonic crystal fibres will then be addressed at the end of the chapter.

11.2 Fabrication of Photonic Crystal Fibres

Photonic crystal fibres are obtained by carefully stacking silica tubes in order to design a ‘preform’ with the desired geometry: to this end, hollow-core as well as solid-core tubes can be indifferently used. Similarly, certain individual tubes can be omitted in the periodic array in order to provide some specific optical functionality. The tubes are assembled at the macroscopic scale since their diameter lies in the millimetre range, which ensures the easy manipulation of the individual elements. By heating the assembly at a high temperature, for instance around 1800°C, the silica softens to the point where it can be drawn using a similar technique to the one employed for the fabrication of classical fibres. This process is schematically represented here in Fig. 11.1. A miniaturised version of the initial array of silica tubes is thus obtained after the drawing process. The most fascinating feature of this technique, which rests on an extremely simple concept, is the perfection of the miniaturised version thus realised. As can be observed in the micrographs presented in Fig. 11.2, the final structure exhibits a lateral period which lies in the micrometer range, i.e. three orders of magnitude below the period of the preform. The structure exhibits in this case a quasi perfect regularity, without any apparent deformation. Nevertheless, the possibility still exists in practice that noticeable deformations may arise.

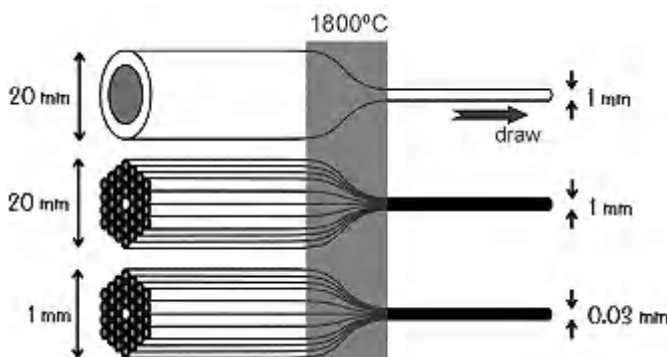


Fig. 11.1. Schematic principle of the fabrication of photonic crystal fibres or ‘holey’ fibres

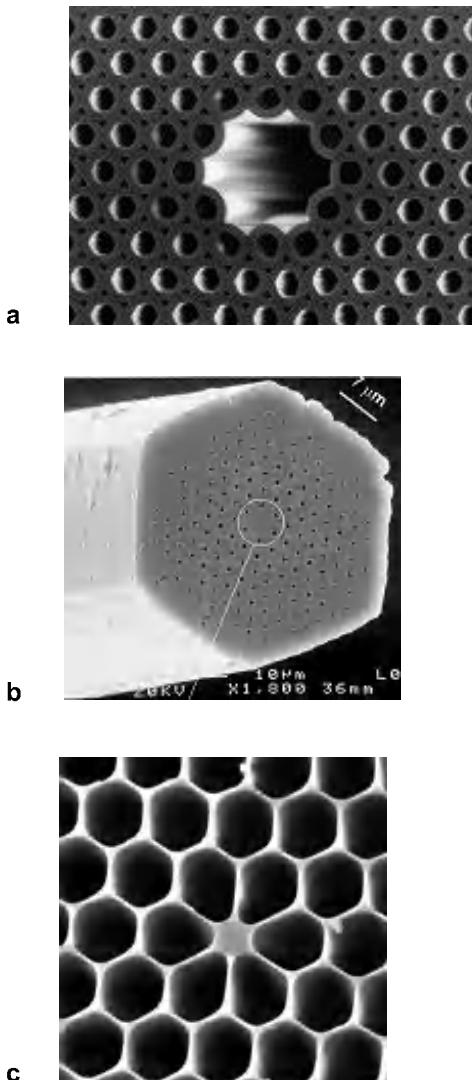


Fig. 11.2. Examples of microstructured optical fibres (MOF), displaying the variety of structures which can be obtained using the fabrication process described in Fig. 11.1. The perfection of the structure at the sub-micrometer scale can be noticed. Contrary to the solid-core microstructured optical fibres represented in *b* and *c*, the fibre represented in *a* has a hollow core. In this case, the confinement of light is achieved through a photonic band-gap reflection at the periodic structure which surrounds the central core

The standard fabrication process represented here in Fig. 11.1 concerns for the most part silica glass microstructured optical fibres. For non-silica glasses, like tellurite or chalcogenure glasses, other fabrication processes are being used like for instance extrusion (Kiang 2002) where the realisation of the perform proceeds by injecting molten glass inside a grid with the desired inclusion structure (Kumar 2002). Extruded jacketing tubes can also be realised using the same technique. Like in the standard stack-and-draw process represented in Fig. 11.1, the pattern formed by the holes may undergo modifications during the drawing of the fibre.

The large number of degrees of freedom provided for the design of the structure, as regards such parameters as the number of tubes, their diameter, their profile, the material from which they are made, the use of either hollow or solid-core tubes or the periodic arrangement of the different tubes, result in a great variety of possible realisations. Photonic crystal fibres thus open to the possibility of a proper engineering system of the refractive index.

11.3 Solid-Core Microstructured Optical Fibres

11.3.1 Confinement Losses and Second Mode Transition

As a model of a microstructured optical fibre (MOF), we shall consider here an infinite matrix pierced with a finite number of parallel holes forming the cladding region: as a consequence of the finite dimensions of the confining region, all electromagnetic modes of such a structure are leaky modes (Kuhlmeijer 2002; White 2002; Snyder 1983). Each leaky mode is associated with a complex effective index n_{eff} which itself is linked to the propagation constant along the fibre axis β through the equation $n_{eff} = \beta/k_0$, where k_0 is the wave number of light ($k_0 = 2\pi/\lambda$). In the limit case of long wavelengths, the MOF can be viewed as a cylindrical waveguide with a silica core of index n_s surrounded by a cladding with lower index $n_c = [f n_a^2 + (1-f) n_s^2]^{1/2}$, where f is the air filling factor and n_a is the air index.

The confinement losses L of the guided modes, expressed in decibels per meter, can be determined from the imaginary part of n_{eff} using the following equation:

$$\mathcal{L} = \frac{40\pi}{\ln(10)\lambda} \operatorname{Im}(n_{eff}) 10^6 \quad (11.1)$$

where λ is expressed in micrometers. It might be emphasised here that confinement losses may occur even in the case where the material absorption is completely neglected. The most common type of MOF consists of a subset of a triangular lattice formed by air holes where the central hole is missing. Several different parameters are used for the description of the fibre: the period Λ of the lattice subset, the diameter d of the holes and the number N_r of hole rings. These

parameters are schematically represented in Fig. 11.3. For a structure with a λ/Λ ratio low enough, the confinement losses \mathcal{L} decrease almost exponentially with N_r , and decrease also with the d/Λ ratio.

One of the earliest known and perhaps most surprising properties of MOFs is the possibility for these fibres of being endlessly single-mode (Birks 1997). This behaviour cannot be achieved with classical fibres, due to the fact that at short wavelengths a multimode regime is irreparably reached. This phenomenon can be explained in qualitative terms as follows: in the short-wavelength region, the effective index n_c of the cladding of the MOF increases since the electromagnetic field tends to penetrate ever deeply in the silica between neighbouring holes, resulting in a decrease of the air filling factor of the cladding. The index contrast between the silica core and the cladding thus becomes lower as the wavelength decreases. Accordingly, all guided modes present a larger extension in the cladding, while the higher-order modes tend to be eliminated due to the amount of losses.

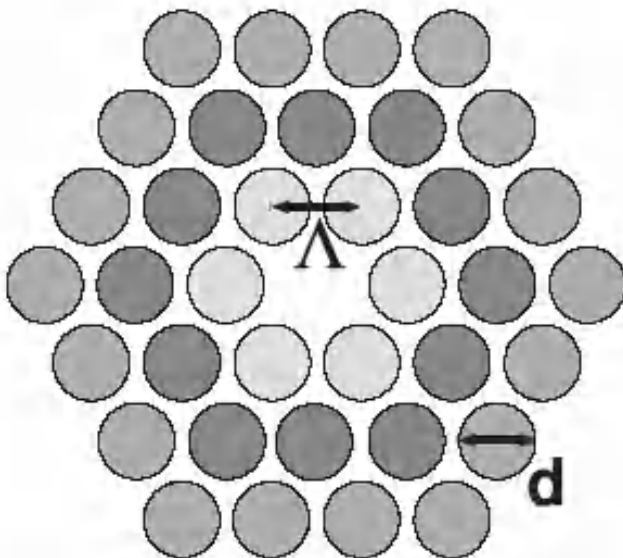


Fig. 11.3. Cross-section of an idealised solid-core MOF with three rings of holes (the holes are coloured with a different shade of grey for each individual ring). $N_r = 3$. Λ is the period of the triangular lattice C_{6v} , and d is the diameter of the holes. The solid core is formed by a single missing hole at the centre of the structure

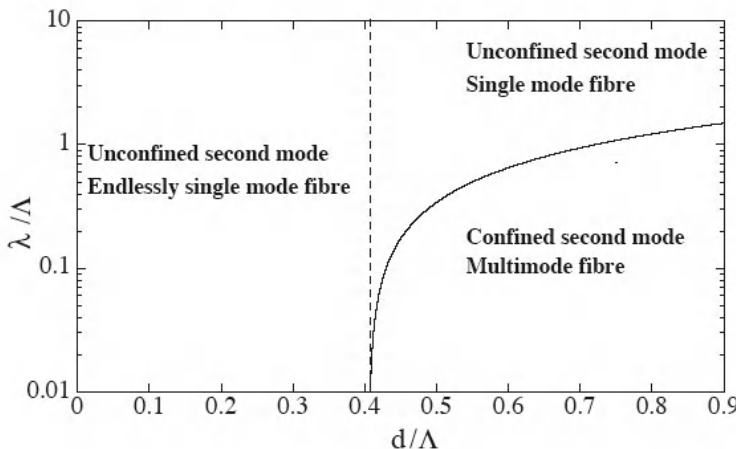


Fig. 11.4. Transition diagram of the second mode for a solid-core MOF. This diagram was obtained for a MOF based on a subset of a triangular lattice of circular holes inside a silica matrix. The solid line corresponds to the loci of the transition of the second mode. In the upper region of the $(d/\Lambda, \lambda/\Delta)$ plane, the fundamental mode is the only mode confined inside the core of the MOF (single mode regime), whereas in the lower region of the plane, the second mode is confined as well (multimode regime). The vertical dashed line represents the approximate limit of the endlessly single-mode regime

In fact, a MOF where the confinement of light is due exclusively to a finite number of rings of holes actually presents an infinite number of modes, all of which are leaky modes. Following the qualitative explanation which has been outlined above, the relative losses of the modes have to be compared in order to determine if the MOF is single-mode. If the modes present such relative losses that after a given propagation length all the modes save one have leaked away, the MOF can then be considered as being single-mode for this specific propagation length. However, such a definition of a single-mode MOF is not fully satisfactory on several counts: not only does this definition depend on the actual propagation length, but it also depends on the period of the lattice and on the number of hole rings. In the limit case of an infinite number of rings, no MOF can possibly be single-mode if such a definition is admitted.

A possible solution for achieving a more precise characterisation of single-mode MOFs is to study the second mode¹ of such a fibre as a function of the parameters associated with it. This second mode actually undergoes a transition inside the core of the MOF from an unconfined state to a confined state. Thus, this transition can be identified with a cutoff which is observable on the loss curves for

¹ The second mode is defined as the mode whose real part approaches the most the real part of the one of the fundamental mode.

all the values of N_r under study. The higher the value for N_r , the steeper the transition is. The transition curve for the second mode is represented here in Fig. 11.4, where the normalised hole diameter d/Λ and the normalised wavelength λ/Λ were taken as reference parameters. As can be seen from the consideration of this figure, the $(d/\Lambda, \lambda/\Lambda)$ plane divides into two regions: the second mode is confined below the transition curve, whereas it is not confined and extends spatially above this curve. It might be noted that the curve intersects with the abscissa axis at $d/\Lambda = 0.406$, and that below this limit value for d/Λ , the second mode never becomes confined. As a consequence, the fundamental mode is the only mode which remains potentially confined at any wavelength: the MOF is therefore endlessly single-mode.

11.3.2 Chromatic Dispersion Properties

The chromatic dispersion, or equivalently the group velocity dispersion, plays a fundamental role in conventional fibre optics (Okoshi 1982), be it in the linear or in the nonlinear optical regimes (Agrawal 2001), and this remains true when microstructured optical fibres are considered (Ranka 2000; Dudley 2002; Ferrando 2003). For a given propagation mode, the chromatic dispersion D_c is linked to the spectral evolution of the effective index n_{eff} by the following equation:

$$D_c = -\frac{\lambda}{c} \frac{d^2 n_{\text{eff}}}{d\lambda^2} \quad (11.2)$$

where n_{eff} depends on the indexes of the core and of the cladding, as well as on the distribution of the field over the two regions of the fibre (Pagnoux 2003).

It was stressed quite early in the development of MOFs that these new waveguides could exhibit specific and interesting dispersion properties, and therefore that they might be considered for the management of chromatic dispersion in optical systems (Mogilevstev 1998; Ferrando 2000; Knight 2000). The control of the chromatic dispersion in MOFs is indeed much more powerful than in conventional optical fibres due to the higher index contrast and to the greater number of available geometrical parameters, for instance the diameters of the holes, the period of the lattice and more generally the location of the holes in the array.

The systematic study of the chromatic dispersion in MOFs (Ferrando 2000b) really began when a vector description of higher-order modes in terms of periodic boundary conditions was developed (Ferrando 2000a).

Nevertheless, the finite cross-section of MOF must be accounted for in order to be able to accurately describe the chromatic dispersion and thus correctly determine the propagation losses (Kuhlmey 2003). Recently, some authors have suggested MOFs specially designed in such a way that the diameters of the inclusions increase with the distance from the axis of the fibre until a maximum diameter is reached (Renversez 2003). An ultraflattened chromatic dispersion, associated with a low amount of propagation losses, was predicted for such fibres. In principle, in

the case where such a structure with only three different hole diameters were used, only seven rings of low-index inclusions would be needed for reaching a 0.2 dB/km loss level at $\lambda = 1.55 \mu\text{m}$ with a dispersion exhibiting a variation amplitude below $3.0 \cdot 10^{-2} \text{ ps nm}^{-1} \text{ km}^{-1}$ in the [1.5 - 1.6 μm] wavelength range. This value for N_r compares favourably with the eighteen rings which are required in the case of an usual MOF consisting of identical inclusions. A dispersion lower than $1.2 \text{ ps nm}^{-1} \text{ km}^{-1}$ was experimentally achieved between the 1000 and 1600 nm wavelengths using a fibre consisting of eleven rings of holes with diameter $d = 0.58 \mu\text{m}$ and $\Lambda = 2.59 \mu\text{m}$ (Reeves 2002).

11.3.3 Main Applications of Solid-Core Microstructured Optical Fibres

As a result of their technological maturity, a variety of applications can be envisioned for solid-core microstructured optical fibres. A number of startups are already selling such fibres, and at least one worldwide company is producing them for its own internal research use. Further, the number of academic laboratories where MOFs are being realised is increasing, be it in Europe or in Asia.

At least five main types of applications can be distinguished:

1. chromatic dispersion management (Knight 2000; Reeves 2002; Renversez 2003),
2. rare-earth doped lasers (Wadsworth 2000; Furusawa 2001),
3. optical amplifiers (Knight 1998a; Limpert 2003; Hougaard 2003),
4. supercontinuum generation (Dudley 02; Husakou 2001),
5. highly-birefringent fibres (Ortigosa-Blanch 2000).

Devices of a more ‘exotic’ type, including sensors (MacPherson 2001), have also been proposed (Eggleton 2001).

1. The management of the chromatic dispersion of MOFs can be achieved in a variety of different ways. It has been previously mentioned in Section 11.3.2 that an ultraflattened dispersion could be obtained over a wide spectral range. The dispersion of MOFs can also be cancelled at wavelengths under 1300 nm, even in the case where a high material dispersion exists. As an example, a MOF with a silica core with a diameter equal to $0.5 \mu\text{m}$ surrounded by holes fifty times this size was found to exhibit a zero dispersion at $\lambda = 560 \text{ nm}$, in spite of a material dispersion equal to $-360 \text{ ps nm}^{-1} \text{ km}^{-1}$ (Knight 2000).

2 and 3. Single-mode MOFs can be designed with a silica core of a much larger diameter than is possible with conventional fibres, where a single-mode behaviour generally imposes the use of a core with a small diameter unless a great precision can be achieved in the management of the index contrast between the core and the cladding. By contrast, the core of a single-mode MOF can be more than fifty times larger than the working wavelength (Knight 1998b). Large-core MOFs, represented for instance in Fig. 11.2b, present an immediate interest as regards the

transmission of high optical power transmission as well as the realisation of rare-earth doped lasers and optical amplifiers.

4. Single-mode MOFs can also be designed in such a way as to present modes with a very small size, as is the case with the fibre represented in Fig. 11.2c. This property tends to ensure a high degree of optical nonlinearity (Ranka 2000). An ultra-high nonlinearity combined with an appropriate group velocity dispersion was used for generating under femtosecond pulse pumping a supercontinuum extending inside MOFs from the infrared to the visible ranges (Dudley 02; Husakou 2001).

5. Although a low birefringence in MOFs can be achieved as well, the very manufacturing process of these fibres lends itself much more to the realisation of highly birefringent fibres. Indeed, a twofold rotational symmetry can be easily induced by resorting to air holes with different sizes and symmetrically placed along the periphery of the pure silica core. Such a fibre was reported in (Ortigosa-Blanch 2000) where small holes with a diameter $d = 0.4 \mu\text{m}$ were introduced among larger holes of diameter $d = 1.16 \mu\text{m}$ inside a periodic array with a period $\Lambda \approx 2 \mu\text{m}$. A birefringence (index difference) as high as 410^{-3} was measured, resulting in a beat length equal to $0.56 \text{ mm at } \lambda = 1.55 \mu\text{m}$.

11.4 True Photonic Crystal Fibres

11.4.1 Photonic Bandgap Cladding

The use in fibre technology of photonic band-gap claddings can be traced back to the 1970s, at the time when the theory of Bragg fibres with concentric layers was first advanced (Yeh 1978). Today however, photonic band-gap fibres or true photonic crystal fibres are more generally described in the form of two-dimensional periodic arrays of holes inside a silica matrix, where the propagation of light occurs due to a low-index (air) defect created at the centre of the array, as has been represented in Fig. 11.2a.

Actually, the physics underlying such periodic arrays of holes are different from the two-dimensional photonic band gaps created in semiconductors which have been described in Chapter 9, insofar as the light propagates in this case along the invariance axis, i.e. perpendicularly to the cross-section of the fibre. Indeed, in spite of the relatively low index contrast between silica and the air, the periodic structuring of the fibre dramatically modifies the modal behaviour of the fibre waveguide. Since the wave vector component k_z of the modes guided along the propagation axis is significantly higher than the two other components k_x and k_y along the transverse directions, a photonic band gap can no longer be defined as a frequency domain where the propagation of light is forbidden for any direction within the (x, y) plane, but needs instead to be defined as a frequency domain

where no (k_x, k_y) state is allowed for a given value of k_z (see Chapter 5). If a defect is created at the centre of the periodic structure, a propagation mode will be allowed for an appropriate value of the k_z component, and the light propagating will be confined inside the core of the fibre.

As an illustration, Fig. 11.5 represents a mapping of the photonic band gaps calculated for a silica fibre where the photonic crystal consisted of a triangular lattice of holes with an air filling factor equal to 0.45 (Birks 1995). The presentation adopted in this figure differs somewhat from those previously used throughout the present book, insofar as the forbidden frequencies are represented here as functions of the k_z wave vector component. Actually, two different types of frequency domains where the propagation of light is forbidden need to be distinguished: the first domain extends from the lower frequencies and its upper boundary corresponds approximately to the straight line defined by the equation $\omega/c = k_z/n_{\text{eff}}$ where n_{eff} is the effective index of the composite material (silica + air holes: $n_{\text{eff}} = \sqrt{\epsilon_m}$ with $\epsilon_m = 0.55 \epsilon_{\text{silica}} + 0.45 \epsilon_{\text{air}}$). This domain, which appears in Fig 11.5 in the form of a grey triangle, corresponds to the classical guiding in fibres by total internal reflection, which entails that as long as $k_z/n_{\text{eff}} \geq \omega/c (= k_{\text{free space}})$, the propagating wave will remain confined inside the fibre for the simple reason that no refraction angle exists that would allow the transmission to occur from the holey silica into the air.

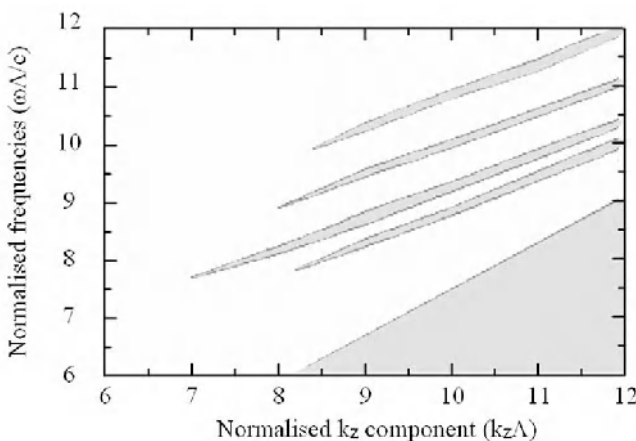


Fig. 11.5. Mapping of the photonic band gaps (represented in grey) calculated for a photonic crystal fibre with a triangular lattice of circular holes inside a silica matrix (Birks 1995). The normalised frequency ($\omega\Lambda/c$) is represented as a function of the normalised wave vector component along the invariance axis ($k_z\Lambda$), where Λ is the period of the lattice. Only the four narrow bands at high frequencies correspond to proper photonic band gaps of the crystal, while the triangular frequency band at low frequencies corresponds in fact to refractive modes inside the fibre

A second type of frequency domains where propagation is forbidden can be discerned in Fig. 11.5 in the form of the four narrower grey bands. These four frequency domains, which are located at high frequencies, correspond to the proper guiding imposed by the photonic crystal and associated with the Bragg reflections. These band gaps can be obtained for all polarisations of the electromagnetic field. It might be emphasized here that, contrary to planar optics involving semiconductors, photonic band gaps can be achieved in the visible and near-infrared ranges without requiring the need of a (sub)-micrometric period of holes. This arises simply from the fact that the guided light propagates along the invariance axis rather than within the periodicity plane, thereby resulting in lower values for k_x and k_y . In principle, breaking the periodicity of the crystal by creating a central hole with a different size, as is represented in Fig. 11.2a should allow the propagation of one or several guided modes with a frequency in narrow bands similar to those represented in Fig. 11.5 (Knight 1996). Such guided modes were first achieved in practice by using a graphite-type hexagonal lattice of holes (Knight 1998a). More detail on such lattices can be found in Section 1.3.3 of Chapter 1. These results were generalised the following year to triangular lattices of holes with different profiles (Cregan 1999).

11.4.2 Losses of Photonic Crystal Fibres with Finite Cladding

Let us here consider a hollow-core MOF with a finite photonic crystal cladding. The genuine dispersion curve of the air-guided mode in such a fibre can be calculated as represented in Fig. 11.6 for a lattice with parameters similar to those presented in Fig. 11.5. Actually, the dispersion curve of the fundamental air-guided mode of the finite photonic crystal fibre does not lie totally within a given band gap, in the present case in the fourth one, but crosses its boundaries at certain frequencies. This phenomenon can be readily explained by the simple fact that the modal dispersion curve was calculated for finite structures with either three or four hole rings, whereas the band gap had been calculated for the case of an infinite lattice of holes. Nevertheless, at most frequencies, the dispersion curve remains above the light line, which demonstrates that the real part of the effective index of the mode is actually smaller than one. Indeed, the distribution of the field which can be calculated using one of the elaborate methods described in Sections 2.2 and 2.3 in Chapter 2 vindicates the conclusion that defect modes are proper air-guided modes propagating inside the hollow core of the MOF.

As is also the case for solid-core MOFs, the losses of the confined fundamental mode of hollow-core MOFs have been found to decrease almost exponentially with the number of rings of air holes for wavelengths located in the band gap. The wavelength associated with the lower loss level increases slightly with the number N_r of hole rings surrounding the core, while the slope of the loss curve increases with N_r around the optimal wavelength. If the working wavelength is far from this optimum, the losses then reach a considerable level, with the consequence that the hollow-core MOF simply becomes unusable. This behaviour is consistent with the relative narrowness of the photonic band gaps which can be observed in Fig. 11.5.

Contrary to solid-core MOFs, photonic crystal fibres allow an efficient guiding of light only over limited spectral ranges. For a detailed theoretical analysis of the loss characteristics of hollow-core as well as solid-core MOFs, the reader is referred to the works by Kuhlmeijer (Kuhlmeijer 2002a, Kuhlmeijer 2002b, Kuhlmeijer 2003).

From an experimental point of view, it might be mentioned here that the measured losses of hollow-core MOFs have been regularly decreasing each year since 1999 (Cregan 1999; Broeng 1999), and that they now reach the order of 13 dB/km (Smith 2003). It is not clearly established yet where the loss limit lies. In such a case, the phenomenon of Rayleigh scattering is no longer caused by the material, in the form for instance of silica, from which the solid core is made, but by the gas which fills the hollow core. Accordingly, a dramatic decrease of the Rayleigh scattering might be experienced provided that vacuum could be achieved inside the core. It might be recalled here that the Rayleigh scattering which occurs inside silica prevents losses inside present-day fibres of going below the value of 0.2 dB/km.

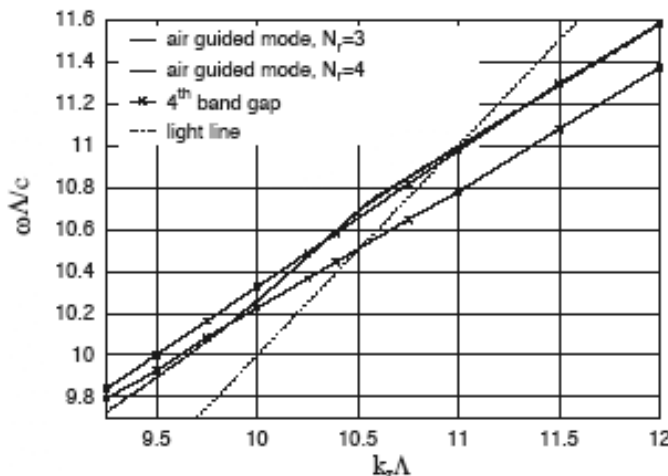


Fig. 11.6. Dashed curves. Dispersion curves of the fundamental air-guided modes for two photonic crystal fibres with a core of the same diameter ($\phi = 13.1 \mu\text{m}$, and $n_{\text{core}} = 1.0$), but with different numbers of cladding layers ($N_r = 3$ and $N_r = 4$ respectively). The cladding consists in either case of a periodic lattice of holes drilled inside silica ($n_{\text{matrix}} = 1.39$), with a period $\Lambda = 5.7816 \mu\text{m}$ and a hole diameter $d = 4.026 \mu\text{m}$. Solid curves with the crosses. Boundaries of the fourth band gap for the infinite lattice of holes ($n_{\text{hole}} = 1.0$, $n_{\text{matrix}} = 1.39$). Thin dashed curve. Light line $\omega = ck_0$

11.4.3 Main Applications of Photonic Crystal Fibres

It is most likely that the development of hollow-core photonic crystal fibres (PCFs) will lead to a large variety of applications. Indeed, the use of these fibres would permit to release the constraints imposed on the properties of waveguides by the material forming the core of the fibre. Another application of photonic crystal fibres would be the reinforcement of the interaction between light and a gas filling the core of the fibre.

Hollow-core photonic crystal fibres might be used for the transfer of high optical powers, as is already the case for solid-core microstructured optical fibres with cores of a large diameter. Further, hollow-core PCFs should exhibit a lower optical nonlinearity, a lower damage threshold, and a lower Fresnel coefficient at their extremities than solid-core MOFs, provided however that the residual absorption in the hollow core is small enough. Let us here recall that the air is more absorbing than silica at telecommunication wavelengths. An example of a hollow-core PCF used at high optical levels with a reduced nonlinearity was recently presented by DG Ouzounov *et al* (Ouzounov 2003), where megawatt optical solitons were generated inside the core of a fibre filled with xenon gas.

Applications of hollow-core PCFs may also be developed along the opposite direction, involving nonlinear processes in active molecular gases: indeed, both the confinement of light and the length of interaction can be dramatically increased when compared to conventional gas systems. A stimulated Raman scattering was thus achieved inside a hollow-core MOF filled with hydrogen and with a length of one meter, leading to Stokes and anti-Stokes energy thresholds almost two orders of magnitude lower than those previously obtained with optical systems (Benabid 2002a).

Beyond the well-identified applications of hollow-core photonic crystal fibres which have been mentioned here, more ‘exotic’ applications of these fibres, not necessarily relying on the concept of a photonic crystal, can be envisioned. Examples of such applications include:

- the realisation of gas lasers from holey fibres,
- the realisation of gas sensors from coiled-up holey fibres, allowing simultaneously the gas flow and the injection of a light beam. Here again, the use of hollow-core PCFs would result in a considerable increase of the effective length of interaction between light and the gas. Such a device would be similar to the high quality factor Fabry-Perot cavities currently in use for this type of detection, with the additional advantage however of providing a robust and relatively easy optical alignment,
- the realisation of optical fibres specifically designed for the guiding of UV light, which undergoes a strong absorption inside solid silica.

By way of conclusion, we shall mention here an application which might seem futuristic, but is quite seducing nonetheless. The possibility of using light for trapping objects of small dimensions, ranging from atoms to microspheres, has been recognised for already quite a long time: not only is this trapping mechanism

involved in the cooling of atoms using laser beams, but it is also part of the concept of the optical tweezers which are currently used in biology for instance. Similarly, one may imagine along such lines the possibility of a hollow-core photonic crystal fibre that could be used both for the guiding of light and for the transfer of either atoms or small nanoparticles. Such a fibre would present the same advantages for the transfer of matter than for the transfer of light, i.e. the possibility of controlling at will the direction, the orientation and the curvature of the matter or light beam. The realisation of such highly localised and easily movable ‘matter sprinklers’ would be an unexpected and quite interesting application of photonic crystals to a bottom-up approach to the fabrication of nanostructures. This idea is actually supported by recent experiments where hollow-core photonic crystal fibres have been used for ensuring the propagation of small spheres with a size of a few micrometers using lasers with relatively low power (Benabid 2002b).

12 Three-Dimensional Structures in Optics

Three-dimensional photonic crystals were at the origin of the very notion of photonic crystal, and they still represent the ‘holy Grail’ at which all experimental realisations are directed. The reason lies in the fact that only photonic crystals presenting a three-dimensional periodicity are capable of providing an omnidirectional band gap with the complete suppression of the radiative states in the corresponding frequency range. In turn, controlling the density of radiative states would then allow achieving an absolute control of the radiative properties of the light emitters incorporated inside crystals, and different consequences are expected to follow from the realisation of this objective. These consequences include the complete inhibition of the spontaneous emission, the localisation of light over defects acting as zero-dimensional microcavities, the three-dimensional guiding of light or the realisation of the band edge lasers based on strictly periodic bulk photonic crystals as has been described in Section 10.3.

The realisation of the three-dimensional photonic crystals at optical wavelengths represents a tremendous challenge. Thus far, none of the technologies which have been developed for the fabrication of three-dimensional photonic crystals can be considered to be either predominant or completely established, due of course to the difficulty inherent to the structuring of matter at sub- μm scales. The technological mastery which has been achieved in the fabrication of three-dimensional photonic crystals in the microwave region is still a remote prospect in the optical region. The first three-dimensional structures had indeed been realised as early as the early nineties in the field of microwaves, leading to the considerable development of the studies devoted to photonic crystals which has been taking place ever since (Yablonovich 1991a).

This chapter begins with a review of the three-dimensional structures which have been suggested thus far for application to the optical region. While some of these structures have already been fabricated using presently available technological means, other structures presented in the course of this chapter seem to be realisable, but have not been demonstrated yet. For this reason, the specific aspects associated with the fabrication of three-dimensional crystals will be addressed only in the second part of this chapter. Finally, this chapter concludes with a description of different experiments intended at exploiting the properties of three-dimensional crystals, both in the infrared range (metallic structures) and in the visible range (opals).

12.1 Geometrical Configurations proposed for Three-Dimensional Structures

The choice of a specific geometry for a three-dimensional structure is always more or less in direct relation with the fabrication techniques which are available to an experimentalist. Nevertheless, two general classes of structures may be distinguished, depending on whether an omnidirectional photonic band gap is desired or whether partially forbidden bands are considered to be enough, provided however that the three-dimensional periodicity of the photonic crystal is preserved. As has been seen in the first part of this book, band gaps of lowest order are often the largest and the most robust ones. In contrast, high-order gaps are much more sensitive to the disorder of the crystal, and this fact is of particular significance when searching for an omnidirectional band gap. The irregularities in the structure which result from the fabrication process can never be entirely neglected when working at the very boundaries of technological possibilities, as is the case in the optical region.

12.1.1 Structures with Omnidirectional Photonic Band Gaps

It would be reasonable to assume that a lattice with a Brillouin zone as close as possible to a sphere would be the most likely to possess an omnidirectional band gap of low order. However, numerical tests conducted on structures presenting a fcc lattice geometry have revealed that the shape of the Brillouin zone is not the only factor determining the presence of omnidirectional photonic band gaps, and that the symmetry of the structure also exerts a decisive influence in this respect. The first structure exhibiting such an omnidirectional photonic band gap was correctly predicted by Ho, Chan and Soukoulis in 1990 (Ho 1990), and consisted of dielectric spheres placed according to a diamond crystalline lattice. For such a structure, complete band gaps may exist both for high-index dielectric spheres in the air and for air spheres in a dielectric medium. This requires of course that both the size of the spheres and the dielectric constants be adequately chosen. A more detailed explanation for the necessity of breaking the symmetry of the fcc lattice (with a single ‘atom’ per unit cell) in order to open a complete band gap can be found in (Ho 1990) and in (Yablonovitch 1994).

However, the diamond lattice structure consisting of spherical ‘atoms’ is quite difficult to realise at the sub- μm scale, and these difficulties led E. Yablonovitch to propose the now famous ‘yablonovite’, which was briefly introduced in the preface to this book (Fig. 12.1). In this structure, the fcc geometry with two atoms per unit cell is reproduced by drilling three series of holes inside a block of dielectric material. The directions of the hole axes reproduce the $\langle 110 \rangle$, $\langle 101 \rangle$ and $\langle 011 \rangle$ directions of the diamond lattice, while the surface of the crystal corresponds to the $\langle 111 \rangle$ crystal plane. The symmetry of such a structure is indeed similar to that of the diamond lattice, and its omnidirectional photonic band gap,

located between the second and third permitted bands, presents a relatively low sensitivity to the irregularities resulting from the fabrication.

In the wake of the first demonstration of ‘yablonovites’ in the microwave region (Yablonovitch 1991a), several more or less successful efforts were directed at the realisation of ‘yablonovites’ in the optical wavelength region.

A different type of structure exhibiting the same symmetry than the diamond lattice is the so-called ‘woodpile’ or ‘layer-by-layer’ structure, both of these terms referring to the fabrication scheme itself. Such structures have been advanced and actually implemented for the realisation of three-dimensional crystals exhibiting complete band gaps in the optical region. The details of the fabrication of these structures will be exposed later in the course of this chapter.

It might be mentioned here that the same layer-by-layer method has also been applied for the realisation of simple cubic structures. Provided that the index contrast is high enough, such a structure exhibits a complete band gap for a high air fill factor. This band gap is relatively narrow, albeit of low order (Lin 2001b; Zavieh 1999).

The continuous advances occurring in the field of micro and nano-fabrication allow us to anticipate the realisation in a few years of periodic three-dimensional structures with a very high degree of precision. A few structures with higher-order omnidirectional band gaps have already been suggested for fabrication, and some of them have been actually realised. However, the presence of omnidirectional band gaps in these structures has not been formally vindicated thus far by measurements.

It has thus been predicted that under certain conditions, fcc structures may present an omnidirectional gap between the eighth and the ninth permitted bands. This leads to believe that artificial opals could provide complete higher-order gaps, provided however that their regularity can be perfectly mastered.

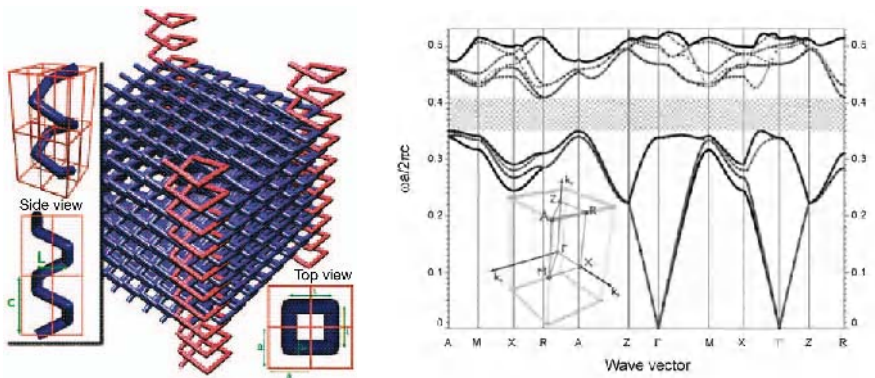


Fig. 12.1. *Left.* Schematic view of a chiral structure. *Right.* Calculated band diagram (Toader 2001)

S. John *et al* have for their part suggested chiral structures consisting of square spirals placed according to a simple tetragonal lattice, as is represented here in Fig. 12.1 (Toader 2001). A complete forbidden band with a 15 percent relative width was predicted for an index contrast equivalent to the index contrast between a semiconductor and the air.

Among the other structures in this ‘exotic’ family, the ‘woven’ photonic crystal suggested by Y.-C. Tsai *et al* may also be mentioned here (Tsai 1999). This crystal actually is a special form of the woodpile (or layer-by-layer) structure with the difference however that the dielectric fibres forming the different layers are interwoven rather than being contained within their respective planes. In much the same way as for the original woodpile structure, two successive layers are shifted from a quarter of the horizontal period in the horizontal plane. This method requires that fibres with two different dielectric constants be used in order to cancel the C4 symmetry which prevents complete band gaps from being opened up.

Metallic photonic crystals represent a special case among the variety of three-dimensional photonic crystals. Due to the strong interaction, described in Chapter 4, which exists between electromagnetic waves and metallic lattices, the existence of complete band gaps is only to a very limited extent determined by the symmetry of the lattice; In certain cases, this interaction may even be strong enough to compensate for the lack of symmetry of the crystal. We have already seen that resorting to metallic crystals is a solution to be privileged in the field of microwaves. More specifically, metallic crystals realised from connected elements present a complete photonic band gap which extends from the zero-frequency (see Section 4.2 in Chapter 4), and the periodicity as well as the size of the constitutive elements of metallic crystals can be significantly smaller than the wavelength at the gap edge. While these small dimensions with respect to the wavelength are an advantage in the microwave region, they may however represent a drawback in the optical region due to the present limits of modern nano-fabrication techniques. The interest of metals in this context rather lies in the fact that metals exhibit a relatively high dispersion of their dielectric constant in the visible wavelength range, a property which in principle could be exploited for realising new optical EM structures.

As has been described in Section 4.1, the dielectric constant of metals can be approximated using the Drude dielectric function of the type $\epsilon_0[1 - \omega_p^2/\omega^2]$, and for some metals the plasmon frequency ω_p lies at the boundary between the UV and visible regions. The excitation of plasmons entails relatively high optical losses. While the amount of these losses might be too high for realising optical microcavities with a high Q-factor, it may on the other hand be low enough to allow the realisation of efficient passband optical filters.

Before proceeding in Section 12.1.2 to the description of incomplete band gap three-dimensional structures, the existence of omni-directional optical reflectors not requiring the use of three-dimensional photonic crystals should be mentioned. Thus, dielectric multilayer stacks (one-dimensional Bragg mirrors) can be realised with a high index contrast so that the light arriving from a low-index medium, for instance the air, will be reflected by the structures at any incidence angle and for

any polarisation of the field (Winn 1998; Chigrin 1999). The stacks do not actually present a complete band gap. However, the incident wave is not coupled to the propagation modes of the crystal, but only to a multilayer mode whose propagation direction is contained within the light cone determined by the critical angle. Due to the existence of this critical angle, a partial band gap (for directions contained within the light cone) is found to be enough for reflecting all incident rays.

Finally, as far as omnidirectional band gaps are concerned here, this review would be incomplete if it did not mention the fact that studies similar to those presented here on three-dimensional photonic crystals have been conducted on acoustic three-dimensional crystals. Of course, certain strong analogies exist between these two types of waves, as well as between their propagation modes (Sigalas 1992). Fundamental complete band gaps for fcc lattices have thus for instance been predicted in the case of elastic waves (Suzuki 1998). The specificity of acoustic crystals lies in the physical existence of longitudinal acoustic waves.

12.1.2 Incomplete Band Gap Three-Dimensional Structures

It might sometimes be interesting to employ three-dimensional periodic structures in situations where omnidirectional gaps are not necessary. This is the case for instance of bulk band edge three-dimensional lasers (Enoch 2002a; Sakoda 1999b). A different example is the photonic crystal used for achieving phase matching in a frequency doubler (see Chapter 8). Such situations tend for a large part to reduce the constraints imposed upon the geometry of the structures to be realised. Accordingly, this opens in practice the possibility of using three-dimensional structures obtained by self-organisation, since none of these structures present omnidirectional band gaps of low order.

The idea of realising nanoscopic structures by self-organisation is quite seducing. At the risk of oversimplifying, the underlying idea is that it suffices for realising the structure to simply put all the necessary constitutive elements inside a test-tube and to shake it well. This apparent simplicity of this method, combined with its intrinsic parallelism, explains the intense research activity surrounding self-organised structures.

In the case of photonic crystals, researches have been for the most part concerned with artificial opals obtained through the sedimentation of sub- μm monodisperse spheres of latex or silica. The lattices thus obtained exhibit the spatial configuration corresponding to the minimal potential energy, i.e. they present a fcc type geometry. As has been mentioned already, fcc lattices may only present complete photonic band gaps of high-order and provided that a high index contrast exists. These high-order bands are extremely sensitive to the irregularities resulting from the fabrication process, and even low dispersions of the size of the spheres, down to 2 percent (Li 2000) or of the air filling factor may cause this gap to vanish.

A different example, albeit a very specific one, of a self-organised three-dimensional structure is the structure obtained by an autocloning process. This methods consists in proceeding from a pre-structured substrate upon which alter-

nated layers of different dielectric materials are successively deposited by RF sputtering, as is schematically described in Fig. 12.2. The deposition of each layer is balanced with its simultaneous etching by the sputtered ions. In actual autocloning conditions, the topology of each deposited layer reproduces the shape of the underlying substrate. As a consequence, the vertical periodicity of the three-dimensional crystal is determined by the alternation of the dielectric layers while its horizontal periodicity is determined by the initial structuring of the substrate. However, the resulting three-dimensional structures do not present the diamond lattice symmetry and therefore they cannot possess complete gaps of low order. The possibility of achieving complete gaps through the combination of autocloning and a subsequent plasma etch of vertical holes, as represented here in Fig. 12.2, has been theoretically investigated (Notomi 2000b), but an experimental demonstration of this method remains however to be performed.

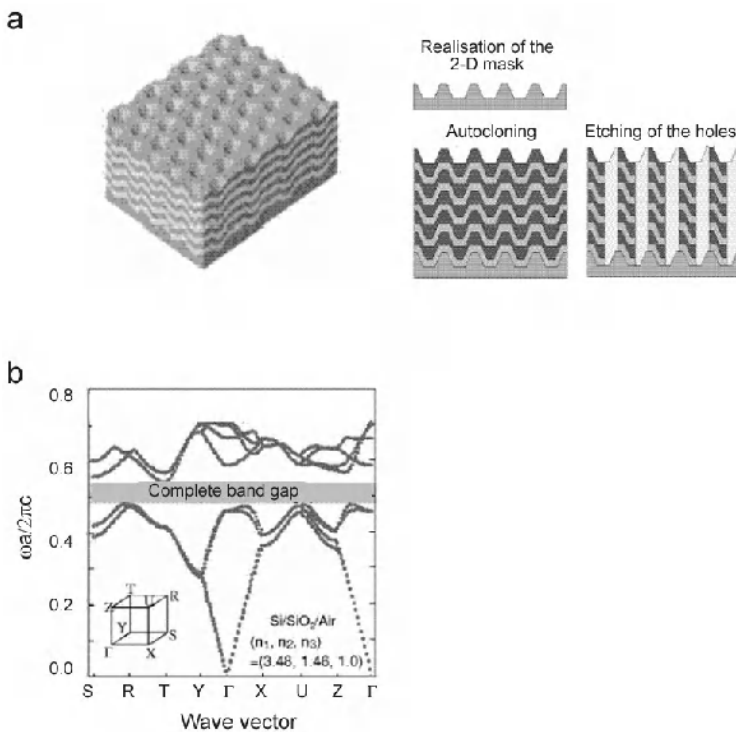


Fig. 12.2. *a.* Left. Schematic view of the hexagonal crystal with alternate dielectric layers, fabricated using the autocloning technique. Middle and right. Method proposed for the fabrication of an autocloned structure with a complete photonic band gap: the autocloning process is followed by the plasma etching of vertical holes (Notomi 2000b) *b.* Band diagram calculated for a structure with a complete band gap: each vertical period is formed by a Si/SiO₂ bilayer while the air holes are organised according to a triangular lattice

As a summary, it may be noted that the structures which can be obtained by self-organisation methods do not present much diversity, and that the insertion of intentional defects in these structures is almost impossible. The major advantage of self-organisation techniques is however to be found in the fact that they allow the realisation of three-dimensional photonic crystals of relatively large size. Nevertheless, in order to extend to the realisation of very regular structures, this method needs to achieve a higher degree of maturity.

12.2 Examples of Fabrication Processes and Realisations of Three-Dimensional Photonic Crystals in the Optical Region

12.2.1 Complete Band Gap Structures

Yablonovites

A considerable technological effort has been devoted worldwide to the realisation of yablonovites adapted to the near-infrared and visible ranges. Indeed, it was correctly assumed that yablonovites could be easily realised using existing micro-fabrication methods, and most of all that their very design could facilitate the realisation of three-dimensional structures.

The first attempts were performed by etching bulk GaAs using the chemically assisted ion beam etching (CAIBE) method, as this technique allows the etching of materials at arbitrary angles with respect to the surface of the sample. However, these attempts did not succeed insofar as they did not permit the realisation of yablonovites with a depth larger than three vertical periods (Cheng 1996b). In this case, the etching depth was limited by the resistance to etching of the mask itself which defines the geometry of the whole structure. As has been previously described, the realisation of a yablonovite requires that three series of holes be etched at different angles through the same mask. In this respect, the maximal three period depth allowed by this method is not sufficient for the development of applications, and no significant advances are to be expected from this technology in the near future.

An alternative approach for the fabrication of yablonovites relies on the use of a polymer periodic mould structured like a yablonovite. This mould is then filled with a high-index material before being finally eliminated: a high-index yablonovite structure can thus be obtained. Sub- μm moulds with a thickness of several periods were fabricated by X-ray lithography using a variant of the LIGA process (Ehrfeld 1998), which had originally been developed for the fabrication of structures, either periodic or not, with a depth of several hundred microns. In practice, a layer of polymer resist with a thickness of the order of 10 μm is exposed to a collimated soft X-ray beam along the three crystalline directions $\langle 110 \rangle$, $\langle 101 \rangle$ and

<011>. Each of these directions forms an angle of $35^{\circ}26$ with respect to the normal to the surface of the sample (crystal plane <111>). The exposure is achieved through a mask opaque to X-rays where a triangular grid of holes has been defined beforehand. Only the regions of the resist which are exposed to the X-rays become soluble in an appropriate solvent. After the dissolution of these regions, the mould can be filled, either with a high-index dielectric material or with a metal. Fig. 12.3 presents an example of such a yablonovite realised by X-ray lithography (Cuisin 2002): the structure considered here had a $1.2\text{ }\mu\text{m}$ period. Six periods in the vertical direction are visible on the SEM image of the cleaved sample, represented in the upper left of the figure. The polymer yablonovite was then filled with copper using an electro-deposition technique, as can be seen from the lower micrographs in Fig. 12.3.

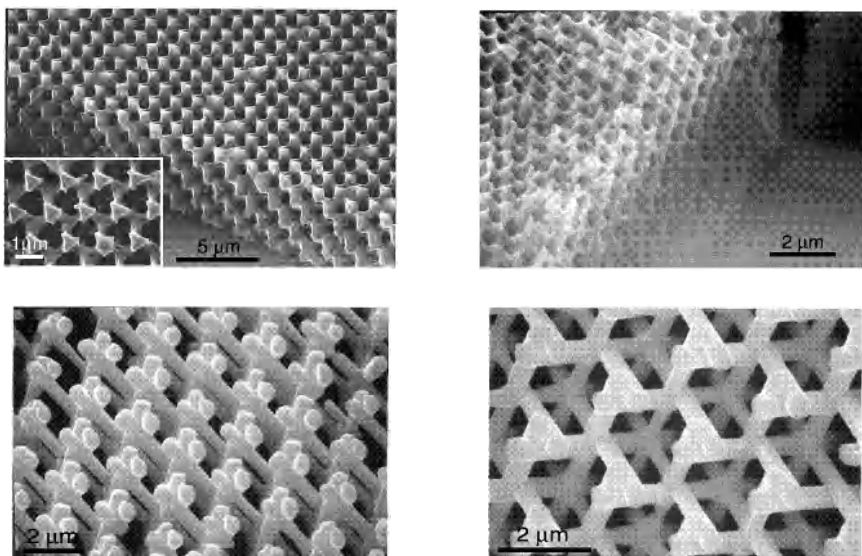


Fig. 12.3. Scanning electron microscope (SEM) images of yablonovites fabricated by X-ray lithography (Cuisin 2002). *Top (left and right)*. Views of a yablonovite mould formed from a polymethyl-methacrylate (PMMA) resist, a polymer sensitive to X-rays. The insert in the left-hand figure represents the upper surface of the yablonovite mould: the imperfect contact between the mask and the PMMA resist has resulted here in the formation of a slightly distorted hexagonal lattice. *Bottom (left and right)*. Micrographs of the copper Yablonovite obtained by dissolving the mould after filling it with PMMA by copper electrodeposition

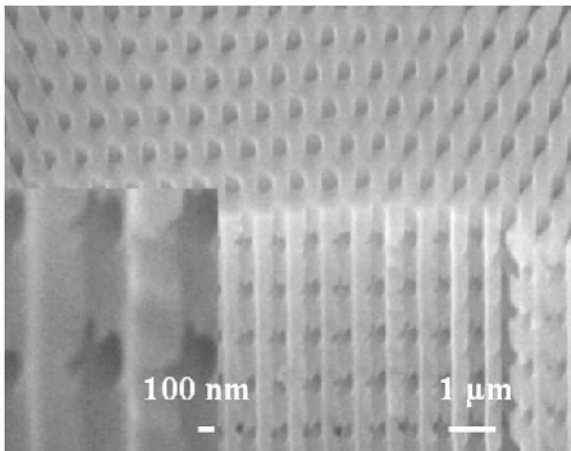


Fig. 12.4. Micrograph of a yablonovite directly fabricated from silicon by combining a photo-electrochemical etching (macroporous silicon etching) with a focused ion beam (FIB) etching (Chelnokov 2000). The left side of the image displays an enlarged view of the holes which emerge laterally from the silicon substrate

Five period thick yablonovite structures were also directly fabricated from bulk silicon by combining a photo-electrochemical etching (macroporous silicon etching) with a focused ion beam (FIB) etching (Chelnokov 2000). In the example displayed here in Fig. 12.4, the first series of holes, i.e. the vertical ones, forms inside the silicon a lattice of macropores of the same type as the lattice presented in Section 9.5. The two other series of holes of the yablonovite are obtained by an oblique FIB drilling at the angle of 51° , instead of 60° , with respect to the normal of the sample: the yablonovite structure thus obtained is therefore slightly distorted. Nevertheless, a complete photonic band gap was reported around the $3\ \mu\text{m}$ wavelength under these conditions (Chelnokov 2000). It should be pointed out that the FIB drilling is performed sequentially, i.e. that only one hole is drilled at a time. As a consequence, this technology is not well-suited to the realisation of large crystals, nor for the realisation of a large number of crystals.

Woodpile Structures

Modern microfabrication technologies are for the most part based on thin-film processes. The so-called ‘woodpile’ structures, whose geometry has been described in Section 12.1.1, are obtained using a standard thin-film processing. More precisely, the semiconductor layers are deposited one by one and dry-etched so as to form a periodic lattice of horizontal rods. The rods of two successive layers are

perpendicular with respect to one another, thereby forming a square grid, as can be seen in Fig. 12.5. Two successive grids are shifted with respect to one another along the diagonal of the square motif by half the diagonal. A set of two grids, i.e. four adjacent layers, constitutes a period of a crystal where the intersections of the rods reproduce the distribution of atoms inside the diamond lattice. It is apparent that the fabrication of a woodpile structure is a quite complicated task, which requires the use of a sub- μm precision processing. No less than seventeen technological steps are required in order to obtain a single crystal period using the standard techniques of silicon microelectronics: an example of a structure realised with this method can be seen in Fig. 12.5 (right) (Fleming 1999; Lin 1999a). In spite of this complexity, structures adapted to the $1.5 \mu\text{m}$ wavelength range and with a three period thickness have been realised in silicon and in III-V materials (GaAs and InP) (Noda 1999) as well as in chalcogenide glass (Feigel 2000). Since the layers of the crystal are structured one after another, the insertion of waveguides or of microcavities is a relatively straightforward process. Three-dimensional microcavities (Lin 1999b), as well as linear waveguides with a 90 degree bend (Noda 2002b) have been experimentally demonstrated. All measurements of the optical properties of structures without defects have been found to be in a very good agreement with theoretical predictions. Numerous perspectives seem to exist for woodpile structures as continuous advances are occurring in the field of planar micro-fabrication processes, resulting in increasingly sophisticated realisations.

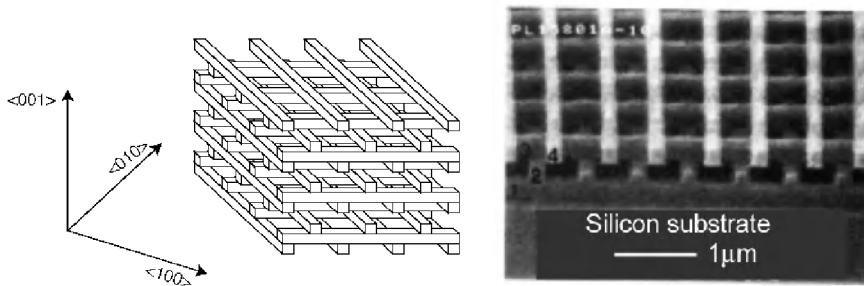


Fig. 12.5. *Left.* Schematic view of a ‘wood-pile’ structure. *Right.* Scanning electron microscope image of a ‘wood-pile’ structure fabricated using the techniques of silicon microelectronics (Fleming 1999). The structure considered here consists of four layers, which together constitute the period of a photonic crystal reproducing the diamond lattice. The photonic band gap is located at around $1.5 \mu\text{m}$

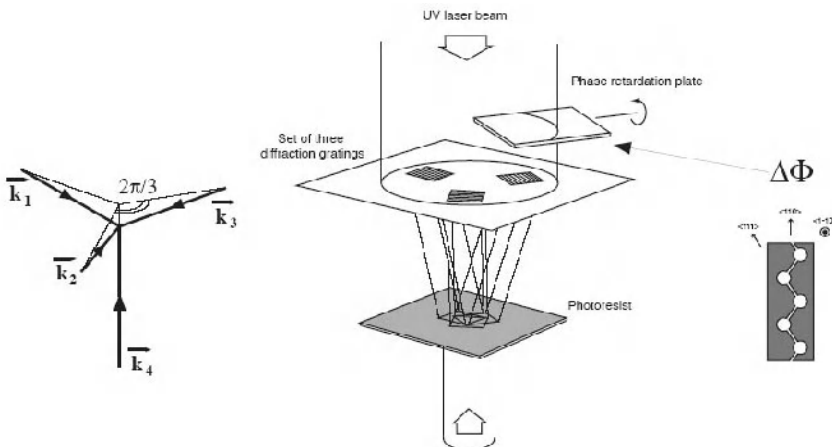


Fig. 12.6. Middle. Experimental arrangement of four laser beams used for the realisation of a fcc lattice by interferential construction inside a UV photoresist (Chelnokov 1999). *Left.* Schematic representation of the wave vectors associated with the different beams. *Right.* Translation of the interferential patterns using a phase retardation plate

Other Fabrication Methods

Several other methods have been suggested for the direct fabrication of ‘diamond’ lattices. Among these different methods, which may seem more or less unusual, multiple-beam interference laser holography and two-photon absorption lithography are of a particular interest.

Laser Holography. Periodic three-dimensional structures can be obtained by ‘freezing’ into a photosensitive resist layer with a large thickness the interference patterns of at least four laser beams operating at the same wavelength, typically in the UV range (Campbell 2000; Shoji 2000). Depending on the precise nature of the resist, the patterns are then developed by dissolving either the weakly or the strongly irradiated regions. The angles, polarisations and respective phases of the laser beams are defined in such a way as to obtain the desired spatial symmetry in the final interference lattice (Chelnokov 1999; Mei 1995). The arrangement displayed in Fig. 12.6 represents an experimental configuration which has been found to be well-suited to the fabrication of the fcc lattice (Chelnokov 1999). In addition, the use of a phase retardation plate across the path of one of the beams allows varying the position of the interference patterns inside the resist layer and thus constructing the diamond structure with two atoms per unit cell. Unfortunately,

the contrast of the photoresists available to this day is not sufficiently high and their absorption in the UV range is still too low for actually permitting a convincing demonstration of three-dimensional photonic band gaps using the laser holography technique. Besides, no optical characterisation has been reported for the first three-dimensional structures fabricated using this technique. Further, while in principle this method should have lend itself to the fabrication of diamond type lattices, the first structures obtained with it did not exhibit this symmetry. It is plain that a significant improvement of UV photoresists is required if the laser holography technique is to reach a higher degree of maturity. Once this condition is reached however, laser holography should allow the realisation of very large, albeit strictly periodic (i.e. without intentional defects) three-dimensional crystals.

Two-Photon Absorption Photolithography. This method represents another example of the use of a laser light for the realisation of three-dimensional photonic crystals. Rapid photo-prototyping is already a well-developed technology which consists, using a strongly focused laser beam, in writing point by point and layer by layer the desired patterns into a thick layer of photo-polymerising resist. Taking into account the laser wavelength (in the blue) typically used for the laser and the limited numerical aperture of the focusing optics, the minimal size for the patterns must be equal to at least 1 μm . For the fabrication of photonic crystals, this resolution has been significantly improved by using a two-photon absorption process. In this case, the wavelength at which the writing laser operates is long enough in order to prevent any direct absorption by the resist, but it must also be chosen in such a way that the second harmonic of the emission of the laser will be located inside the absorption band of the resist, which typically is in the blue or in the near-UV: under these conditions, the illumination of the resist by the laser results in its local polymerisation. Since the efficiency of the two-photon process is proportional to the square of the local photon flux, the intensity of the laser must be increased without however causing an excessive heating of the resist. An infrared Ti : Saphire laser in mode-locking regime is used for this purpose. Mode-locked sub-picosecond optical pulses are generated at the $\lambda \sim 800$ nm wavelength, while the two-photon absorption occurs at half this wavelength ($\lambda \sim 400$ nm). The laser pulses present a high optical peak power, but a low average power, which is perfectly suited to laser writing. The two-photon absorption process and then the polymerisation of the resist only occur in the close vicinity of the focal point of the writing beam, where the photon flux is maximal. The patterns are created by moving the focal point along the three axes. The non-polymerised resist is then removed using an appropriate solvent.

Periodic as well as aperiodic three-dimensional structures with pattern sizes of less than 1 μm have thus been realised from polymer. Optical transmission spectra measured on the periodic structures represented in Fig. 12.7 have revealed the presence of forbidden photonic bands at wavelengths close to 4 μm (Sun 1999). In spite of the sequential writing mode used in this case, which results in an actual decrease of the resolution, this technique seems promising for telecommunication wavelengths in the 1.3-1.5 μm ranges (Deubel 2004). In principle, polymer struc-

tures of this type could be used as moulds for the deposition of a material with a high index contrast.

12.2.2 Incomplete Band Gap Structures

It might be recalled that the present section will be mainly devoted to the consideration of three-dimensional photonic crystals obtained by self-organisation. In spite of the different advantages presented by self-organisation, its lack of flexibility explains the fact that only three-dimensional photonic crystals with partial band gaps have thus far been obtained with this method.

Artificial Opals

Much in the same way as atoms organise into solid-state crystals, uniform latex or silica spheres released in a colloidal solution organise into fcc lattices. An ordered sedimentation can be achieved with the use of a gravitational field, for instance in a centrifuge, by very slowly causing the solvent of the colloidal solution to evaporate or by filtering through microporous substrates the solution where the spheres are contained. The orientation of the ‘crystallised’ lattice of spheres can be forced by prestructuring the substrate where the sedimentation takes place. The structures composed of self-organised spheres thus obtained are referred to as artificial opals, since their microscopic structure, which can be seen in Fig. 12.8, reproduces the structure of natural opals.

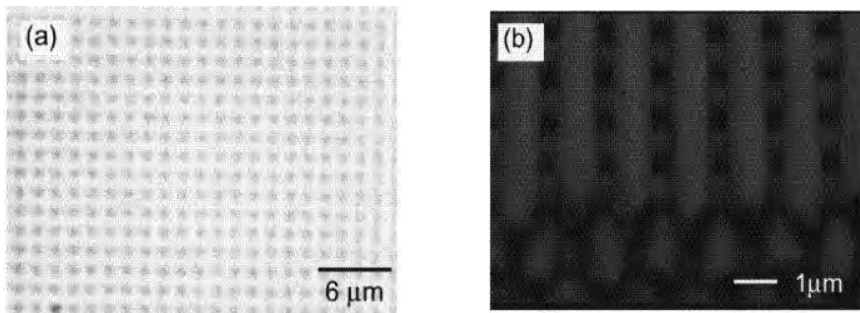


Fig. 12.7. *a.* Top view of a diamond-like structure fabricated by two-photon absorption photo-lithography (Sun 1999). The horizontal period of the lattice is $1.4\ \mu\text{m}$. *b.* Cross-section view of the same structure, obtained by scanning electron microscopy

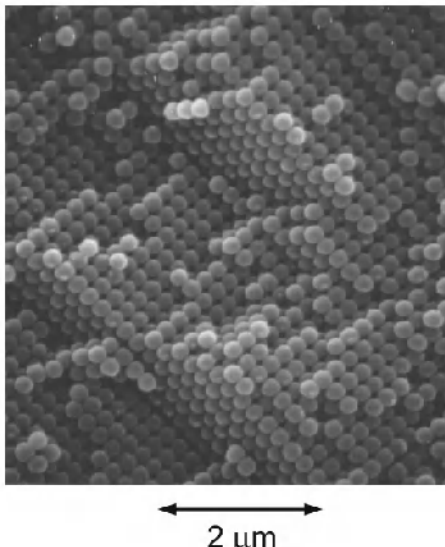


Fig. 12.8. Micrograph of a direct opal (Romanov 1997). The cleaved facet of the structure reveals the presence both of ensembles of spheres with a square symmetry, associated with the $\langle 100 \rangle$ planes, and of ensembles of spheres with an hexagonal symmetry, associated with the $\langle 111 \rangle$ planes

Although the spheres actually tend to ‘crystallise’ inside the lattice presenting the minimal potential energy, i.e. inside the fcc lattice, the energy of the fcc lattice is unfortunately very close to the energy of the hexagonal close packed (hcp) lattice (Wood 1997). As a consequence, artificial opals generally present a significant concentration of stacking defects, which often result in perturbations affecting the optical characteristics of photonic crystals based on artificial opals. However, the uniformity of the structures thus realised has been constantly improving, due to the use either of pre-structured substrates (Braun 2001) or of a high-pressure gaseous flux during sedimentation (Xia 1999).

Recent researches seem to open new perspectives for self-organised structures through the use of spheres of different types or different sizes (Jiang 2001). The use of non-spherical particles for the realisation of self-organised structures may also be considered (Snoeks 2001).

The optical index of the silica or latex spheres from which artificial opals are formed is close to 1.5. In order to increase the index contrast, the voids between the spheres can be filled in with a higher index material. The initial opal matrix is then eliminated, either by chemical dissolution or by thermal processing (calcination). The resulting structure is referred to as an inverse opal: an example of such a structure is presented here in Fig. 12.9. Like direct opals, the symmetry of inverse opals remains that of a fcc lattice, and they do not as a consequence present complete band gaps. It has been theoretically demonstrated that in the case of in-

verse opals with a strong index contrast (i.e. > 2.8) a complete band gap may exist between the eighth and the ninth permitted bands. Unfortunately, the existence of such a high-order forbidden band can be ruined by the presence of even the slightest local variations in the parameters of the crystal.

To this day, inverse opals have been fabricated from such various materials as selenium (Braun 2001), vanadium oxide (Golubev 2001), silicon (Blanco 2000), titanium oxide (Holland 1998), indium phosphide (Romanov 1997), cadmium selenide (Vlasov 1999), II-VI semiconductors (Braun 1999) or tin sulfide SnS_2 (Romanov 2001). It remains however to be demonstrated that these structures are really capable of providing complete band gaps.

Since the possibility exists of inserting different types of materials into the voids between the spheres, artificial opals can be used as a testbed for the development of eventual controllable optical photonic crystals. It has thus been suggested to achieve the control of the photonic band gaps either by varying the temperature or by applying an external electrical field (Bush 1999; Yoshino 1999). Artificial silicon-based opals impregnated with liquid crystals have been fabricated for this purpose. Another approach would consist in using the ‘metal-semiconductor’ phase transition which occurs in vanadium oxide at temperatures close to room temperature (Golubev 2001).

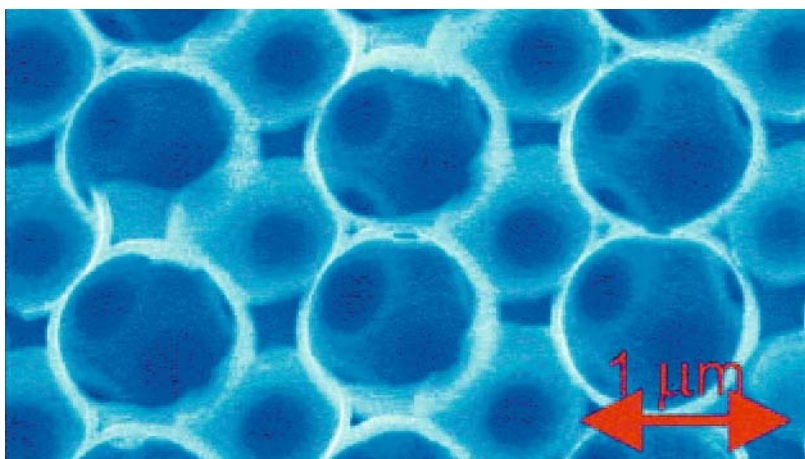


Fig. 12.9. Scanning electron microscope image of the cleaved $<110>$ facet of an inverse opal formed from silicon (website: <http://www.icmm.csic.es/cefe/>). The direct opal used as mould was filled through the chemical vapour deposition (CVD) of silicon. The image shows a lattice of air spheres surrounded by thin silicon shells, a structure which actually is inherited from the fcc lattice of the direct opal. Adjacent spheres are connected to one another by small circular windows resulting from a sintering process

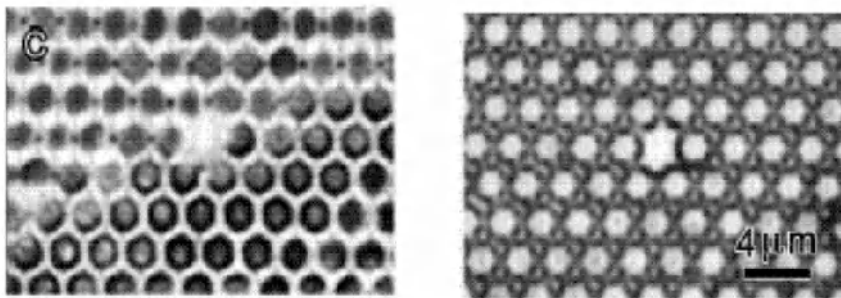


Fig. 12.10. Triangular lattice with a $2 \mu\text{m}$ period, formed by air bubbles inside a polystyrene layer (Srinivasarao 2001). *Left.* Structure observed in reflection. *Right.* Structure observed in transmission. In both cases a krypton laser (568 nm) was used as the illumination source. The defects of the lattice are also clearly visible

It has been previously emphasised that self-organisation processes were not adapted to the incorporation of defects during the sedimentation of the spheres. Some authors have suggested to overcome this difficulty by using two-photon absorption lithography (Lee 2002), a method presented earlier in Section 12.2.1. Three-dimensional optical waveguides were thus created inside an inverse opal by injecting a photosensitive polymer inside the opal before polymerising it locally using a strongly focused IR laser beam. A minimal waveguide width of $1.5 \mu\text{m}$ was achieved, the boundaries of the waveguides being defined with a precision of the order of 100 nm.

As a summary, the use of colloidal crystals as three-dimensional photonic crystals is reaching a higher degree of maturity, while the structures obtained with this method are being constantly improved as regards both their size and their uniformity. The wavelengths of the band gaps extend over both the visible and IR regions. The index contrast can be further enhanced through the fabrication of inverse opals, a technique which is becoming increasingly reliable. Artificial opals allow rapid advances in the experimental investigation of different aspects associated with three-dimensional photonic crystals in the optical region. However, the problem of stacking defects needs to be addressed before this technology can be definitively considered as presenting the same degree of maturity than traditional lithography techniques.

Let us finally mention the growing number of other more ‘exotic’ methods developed for the fabrication of three-dimensional structures by self-organisation. An example of such a method is the insertion of uniform air bubbles inside a polystyrene layer for realising the original structure represented here in Fig. 12.10 (Srinivasarao 2001). The existence of photonic band gaps in the infrared region was demonstrated for this structure. Another example, which has potential applications in the field of microwaves, is the realisation of periodic three-dimensional lattices using magnetic particles (Saado 2001). Finally, three-dimensional ‘crys-

tals' have been obtained in dusty plasmas, i.e. in plasmas containing charged solid particles of microscopic size (Thomas 1994).

Autocloning

Suggested in 1997 by Japanese researchers (Kawakami 1997), autocloning structures can be classified among either self-organised structures or layer-by-layer structures. This technique rests on a balance between three processes occurring simultaneously: the sputtering deposition of dielectric layers, their physical etching by ions accelerated perpendicularly to the surface, and the redeposition of neutral particles torn from the deposited layer by the accelerated ions. The subtle balance thus achieved between these three processes results in the repetition of the topology of a pre-structured growth substrate from one deposited layer to the other (Kawakami 1999). However, due to the restricted possibilities offered in the choice of the relief and materials, and more particularly to the impossibility of inserting air layers inside the structure, complete band gaps could not be achieved with this method. As has been described earlier (Fig. 12.2), another technological step, i.e. an additional plasma etching, would actually be necessary in order to obtain a complete band gap (Notomi 2000b).

In spite of these shortcomings, autocloning was one of the first techniques which demonstrated the possibility of realising actual devices based on three-dimensional crystal photonic crystals even in the absence of a complete band gap. Examples of such devices are the extremely efficient polarisers and phase retardation plates which have been fabricated using this technique (Sato 2002): their structure can be seen in Fig. 12.11b. Ultra-refractivity and superprism effects have also been demonstrated using the same technology.

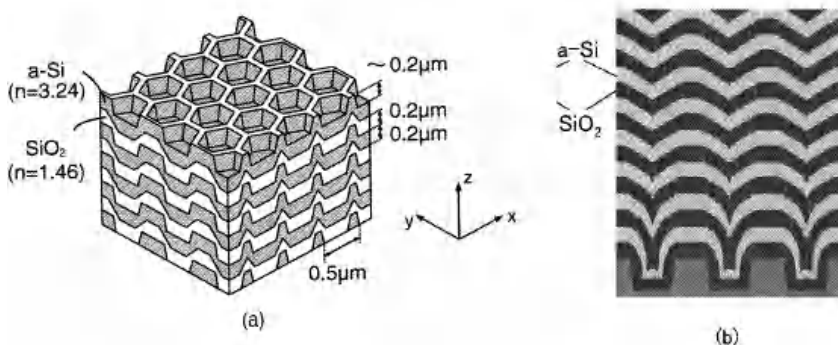


Fig. 12.11. Photonic crystal fabricated by auto-cloning and used either as a polariser or as a phase retardation plate device (Sato 2002). **a.** Schematic three-dimensional view. **b.** Cross-section view of the actual crystal, obtained by scanning electron microscopy

12.3 Metallic Three-Dimensional Photonic Crystals in the Optical Region

As far as applications are considered, one of the most convincing realisations of metallic three-dimensional photonic crystals in the optical region was presented by researchers from the Sandia laboratories: an example of the structure thus obtained is represented here in Fig. 12.12 (Fleming 2002). Metallic woodpile structures with a $4.2\text{ }\mu\text{m}$ period were fabricated using a method similar to that used for the realisation of dielectric layer-by-layer structures. Reflection and transmission measurements performed on the structure revealed a complete photonic band gap extending from the $8\text{ }\mu\text{m}$ to the $20\text{ }\mu\text{m}$ wavelength, which was found to be in agreement with theoretical predictions. A 30 dB attenuation per elementary cell (each individual cell consisting of four planar layers) was achieved. The structures thus obtained could stand temperatures up to 1500°C , and one of the applications envisioned for these structures was the modification of the emission spectra produced by incandescent light sources. An example of such an application would be the enhancement of the emission efficiency in the visible part of the spectrum by suppressing the emission in the mid-IR wavelength range. Another potential application would be the use of these structures for improving the efficiency of thermo-electric converters.

One of the main features of the woodpile structures previously described is their small metal filling factor (28%). A small volume fraction of metal tends to reduce the optical losses of the crystal (Leung 1998), and a $\sim 60\%$ light transmission has been observed in the permitted bands of the structures thus fabricated (Fig. 12.12).

Artificial opals containing metal particles represent another technological approach towards the realisation of three-dimensional metallic photonic crystals in the optical region. Opal crystals composed of metallic spheres disconnected from one another have thus been suggested by A. Moroz (Moroz 1999). Theoretical studies followed by experiments conducted in the microwave region (Zhang 2000) have vindicated the possibility of achieving ‘robust’ band gaps in the visible and infrared regions using periodic structures of dielectric spheres coated with metal. In fact, actual opal structures containing metals are based on dielectric opals which have their voids filled either with silver by chemical deposition (Zhou 2000) or with liquid metals by impregnation under pressure (Zakhidov 2001). The use of silver here in spite of its tendency to oxidise in the air, is motivated by the fact that it has a reflectivity higher than 98% in the visible range and that the corresponding plasmon wavelength is located in the near UV range. Forbidden bands have thus been actually obtained for opals filled with a very low fraction of silver (Zhou 2000). However, the interpretation of the results was complicated in this case by the fact that silver had been deposited in a polycrystalline phase.

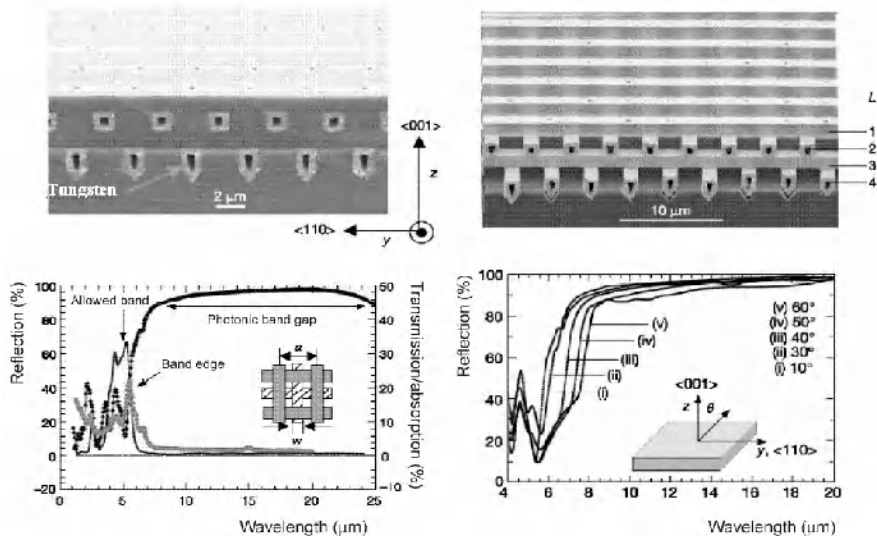


Fig. 12.12. Woodpile metallic photonic crystal formed from tungsten rods with a $4.2\text{ }\mu\text{m}$ period (Fleming 2002). *Top*. Micrographs of the fabricated structure. *Bottom (left)* Reflection and transmission (absorption) spectra measured between the ~ 1 and the $25\text{ }\mu\text{m}$ wavelengths (*right*) Reflection spectra measured at different incidence angles

As a summary, metallic photonic crystals can operate efficiently at wavelengths ranging from the mid-infrared to the microwave region. In the visible range, the existence of intrinsic metallic losses imposes the utilisation of metals with very low metal filling factors (10–20%), like for instance silver. For this very reason, it would be difficult to realise microcavities containing metals with a high quality factor in the visible range.

12.4 Three-Dimensional Photonic Crystals and Light Emitters

In spite of the technological difficulties, three-dimensional photonic crystals have now become a reality in the visible and near-infrared spectral regions. At least one of the proposed technologies, the woodpile or layer-by-layer structures, allows the realisation of photonic crystals with complete band gaps at the optical telecommunication wavelengths. It is plain however that research devoted to the development of micro-structuring and micro-assembling technologies must be pursued before the concept of three-dimensional photonic crystal can be successfully translated

into applications and before the total control of light emission can be really achieved.

It has been demonstrated that the variations of the local density of the radiative states induced by a photonic crystal would result in significant changes affecting the radiative lifetime of an emitter placed inside the crystal, especially in the case where the band gap of the crystal is complete (see Section 7.1.2). In this respect, the pioneered experiments conducted on artificial opals had not been successful, but a spatial redistribution of the spontaneous emission had already been observed (Megens 1999; Petrov 1998). At this time, the low index contrast and the absence of any reference value for the radiative lifetime of the dye used as an internal emitter in the opal were offered as an explanation for these results. More recently however, convincing experimental results demonstrating a reduction of the radiative lifetime by a factor of 5 have been reported in 2002 (Koenderink 2002a, 200b).

Modifications of the thermal emission spectrum (black body radiation) were also demonstrated in the presence of three-dimensional crystals, either metallic (Fleming 2002) or dielectric (Lin 2000b). However, in view of the continuous advances occurring in the field of micro- and nano-fabrication, the results obtained in the mid-infrared and far-infrared ranges should sooner or later find their way to the near-infrared and visible ranges. Thus, the objective of realising the original scheme of a single light emitter in a three-dimensional photonic crystal microcavity seems now to be within reach.

13 Microwave and Terahertz Antennas and Circuits

As has been mentioned already, the idea of achieving a control of the dielectric permittivity in the microwave region through the use of one, two or three-dimensional periodical ensembles of metallic elements is far from being a novelty. Already during the 1960s, the propagation of waves in two-dimensional periodical structures or in three-dimensional stacks of spheres had started being investigated using at this time the concept of an artificial dielectric (Harvey 1959). However, the new found interest for periodical structures in the field of microwaves has largely extended beyond these limits. First, it is quite apparent that microwave devices, which often can be more easily realised than their optical equivalents, have permitted the validation and the simpler demonstration of a series of new effects related to photonic crystals (Danglot 1998; Gadot 1997; Lourtioz 1999 ; Özbay 1996 ; Pendry 1996 ; Shelby 2001 ; Sievenpiper 1996, 1998, 1999a ; Smith 2000b ; Yablonovitch 1991a, 1991b). In the microwave region itself, the detailed study of three-dimensional structures, the analysis of periodicity defects, the combination of photonic crystals with active devices, the increase in frequencies well beyond the gigahertz, and more generally the development of modelisation and characterisation methods, were still in their infancy at the time of artificial dielectrics. Finally, from a practical point of view, the combination of photonic crystals with microwave circuits and antennas has led to envisioning the possibility of important potential applications, even if it is too early, in view of the great variety of currently existing microwave techniques, to assess their actual potentialities. In what follows, we shall first present in Section 13.1 the different possibilities of applications of photonic crystals to antennas. We shall then discuss in Section 13.2 the specific advantages offered by metallic photonic crystals, which can be made controllable or reconfigurable by the introduction of electronic components. The first experiments using metamaterials, described in Section 6.4 of Chapter 6, will also be mentioned in this context. We shall then consider in Section 13.3 the potential applications of ultra-compact photonic crystals for microwave circuits. The extension in frequency up to the terahertz (THz) will be illustrated in Section 13.4. Finally, in Section 13.5, we shall take one step further towards optics by presenting how certain concepts originally developed in the field of microwaves can be applied to optics, and how certain experiments based on the use of THz photonic crystals may announce the realisation of similar experiments at shorter wavelengths.

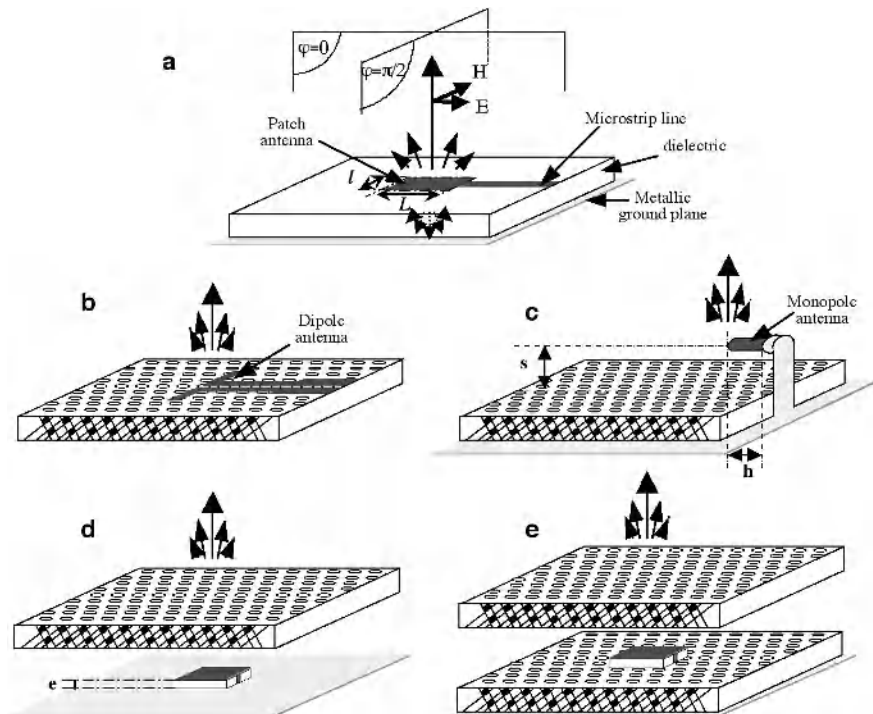


Fig. 13.1. Schematic representations of antennas and of their association with photonic crystals. *a*. Simple patch antenna and definition of the E and H planes *b*. Dipole antenna on a photonic crystal substrate in a coplanar geometry *c*. Monopole antenna with a photonic crystal mirror *d*. Patch antenna with a photonic crystal radome, parallel in this case to the antenna *e*. Patch antenna with photonic crystal substrate and radome. In all these cases save for *b*, the use of a ground plane, represented in grey, is made necessary. In cases *d* and *e*, the patch antenna is supplied by a coaxial cable whereas in case *a* it is supplied by a microstrip line

13.1 Photonic Crystal Antennas

A great variety of antennas exist, designed for different fields of applications and for equally different performances. Among the basic forms used for antennas, one may distinguish monopole antennas, dipole antennas and patch antennas, which are often arranged in arrays. An antenna can be supplied in different ways, either simply with a coaxial cable, or more commonly by coplanar lines or microstrip

lines, which are the two main types of connections in microwave circuits. Thus, in Fig. 13.1a is represented the classical scheme of a patch antenna supplied by a microstrip line on a dielectric substrate, with the ground plane mounted on the rear side. The interest in the potential use of photonic crystals in this context stemmed from the observation that an important part of the radiation emitted by antennas could be lost in dielectric substrates with a permittivity higher than that of the air. This led to the idea that the radiation of the antenna could be totally inhibited under the plane of the antenna by simply replacing the substrate with a photonic band gap material, as represented in Fig. 13.1b (Brown 1993, 1994). In addition, it was also believed that this would allow suppressing the unwanted couplings occurring between antennas arrayed on the same substrate, and induced by surface waves. Later, other forms of applications of photonic structures to antennas have emerged. Photonic crystals have thus been used as antenna reflectors, as in Fig. 13.1c (Kesler 1996), as radomes, also referred to as superstrates, as in Fig. 13.1d (Thevenot 1999), or even simultaneously as substrates and supertstrates, as shown in Fig. 13.1e (Akalin 2001). In what follows, we shall successively review these different forms of applications of photonic crystals.

13.1.1 Photonic-Crystal Antenna Substrates

Two different types of photonic-crystal antenna substrates have been successively developed. While the first such substrates were realised from entirely dielectric structures, high impedance surfaces were later developed from metallocodielectric photonic structures (see Chapter 4 for more detail). We shall therefore successively present these two types of antenna substrates following this order.

Dielectric Photonic-Crystal Substrates

The first experiments intended at using photonic crystals as antennas substrates were conducted by ER Brown *et al* (Brown 1993). The configuration used in these experiments is schematically represented here in Fig. 13.1b for a dipole antenna and a three-dimensional photonic crystal of the yablonovite type. Contrary to conventional substrates, of the kind represented in Fig. 13.1a, it is quite obvious that the electromagnetic field radiated by the antenna cannot propagate in the photonic crystal if the emission frequency is in the omnidirectional band gap. It might be noted here that the radiation of an antenna is typically measured in two principal planes perpendicular to one another, as can be seen in Fig. 13.1a. These two planes, referred to as planes *E* and *H*, are respectively parallel to the electric and magnetic field radiated at infinity by the antenna. In addition to its frequency, different characteristics are relevant for a radiating antenna, in particular its efficiency, its directivity and the preferential polarisation of its emission. In the first experiments carried out by ER Brown *et al*, a promising reduction of the energy loss occurring within the substrate itself was achieved. However, surface modes (see Section 1.4.6 in Chapter 1) remained another source of losses for the antenna,

since the presence of these modes results in parasitic lobes in the radiation diagram measured at a great distance. In principle, for any orientation of the surface of a three-dimensional crystal, a certain termination, i.e. a position of the interface between the air and the crystal inside the elementary mesh, exists for which no surface mode may propagate (Joannopoulos 1995b). In addition, a complete optimisation requires that the phase be zero at the interface, which is exactly the opposite situation to that of a metallic surface, in such a way as to create an antinode of the field on the antenna. Thus, in a second study in 1994, ER Brown *et al* (Brown 1994) succeeded in demonstrating that the radiation of a dipole antenna placed on a yablonovite substrate, as represented in Fig.13.1b, could be optimised for certain terminations of the yablonovite, provided however that the dipole be correctly positioned and oriented on the terminating surface. A similar study was conducted some time after for a photonic crystal of the ‘woodpile’ type (Cheng 1995). Unfortunately, it becomes apparent when operating at frequencies equal to a few gigahertz that devices based on three-dimensional photonic crystals have significant drawbacks in terms of compactness, since four periods of photonic crystal typically correspond to a ~ 50 cm thickness. For this reason, in the frequency ranges that are currently used in most applications, be they civil or military-oriented, research has shifted to structures allowing the realisation of more compact devices.

Substrates realised from High Impedance Surfaces

The high impedance surfaces which have been described in Section 4.4.6 of Chapter 4 have turned out to be the photonic structures which are the better suited to antenna substrates, in terms both of compactness and of possibility of exploiting the properties of photonic band gaps (Sievenpiper 1999a, 1999b). Fig. 13.2 (left) displays a schematic representation of a patch antenna inserted in a square lattice of metallic blocks which form the high impedance surface. As can be seen in the cross-section view, each metallic block is connected to the ground plane by a metallic stud for the realisation of the inductive element of the high impedance surface (see Section 4.4.6 in Chapter 4). The arrangement represented in Fig. 13.2 is exactly the same as in the experiments reported by Y. Qian *et al* in 1999 (Qian 1999).

In this arrangement, the patch antenna is supplied by a microstrip line with a characteristic impedance equal to 50Ω . The emission frequency of the antenna is the same as the resonance frequency of the cavity, which is located between the metallic plate and the ground plane, and whose lateral dimensions are identical to those of the metallic plate itself. For a $TM_{m,n,0}$ mode, where the indices m , n and 0 correspond to the propagation axes Ox , Oz and Oy respectively (see Fig. 13.2), the transverse magnetic field extends for the most part in the plane of the substrate, and the cavity is bounded by vertical magnetic walls and horizontal electric walls, with the latter being formed by metallic planes. The resonance frequency of the cavity is given in the first approximation by the equation:

$$f_{m,n} = \frac{c}{2\sqrt{\epsilon_r}} \sqrt{\left(\frac{m}{a}\right)^2 + \left(\frac{n}{b}\right)^2} \quad (13.1)$$

where ϵ_r is the dielectric permittivity of the substrate, while a are b the lengths of the two sides of the metallic plate.

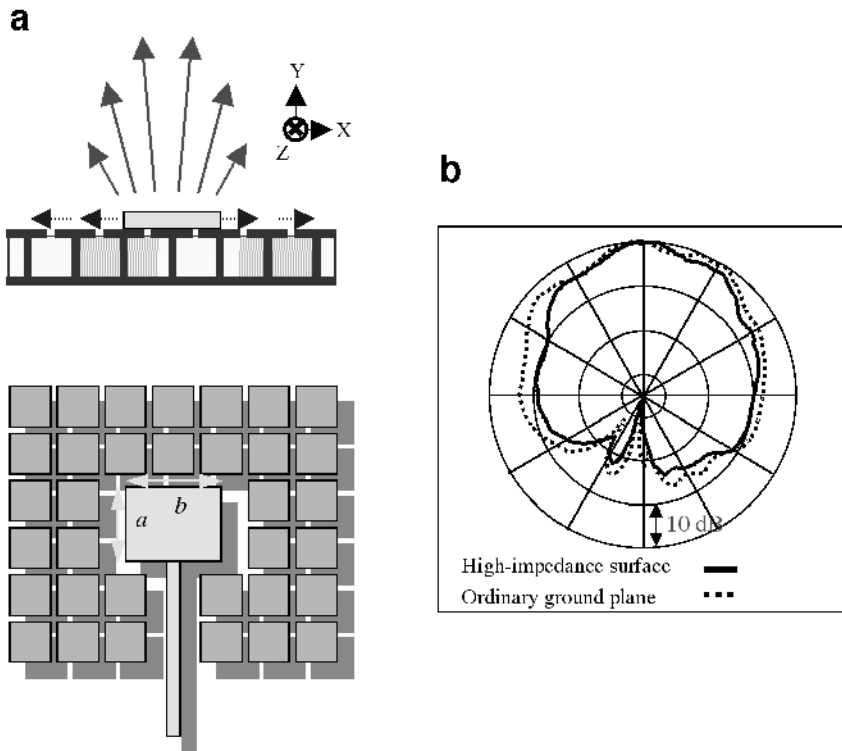


Fig. 13.2. *a.* Cross-section view (top) and top view (bottom) of a patch antenna on a high impedance surface. The principal emission of the antenna, represented by vertical arrows, is increased, while the surface waves, represented by horizontal arrows, are suppressed *b.* Radiation diagrams measured in the cases where the antenna is placed on a conventional substrate and on a substrate with a high impedance surface. The measurements are carried out in the plane E (see Fig. 13.1a). The amplitude is normalised for the two diagrams, thus revealing the decrease of the radiation in the horizontal direction (Qian 1999)

In order for the antenna to operate, the dimensions of the surface grid needs to be selected in such a way as to have the emission frequency of the antenna fall within the photonic band gap. Actually, assuming the emission of the antenna to be generated according to a TM mode, no coupling to a TE surface mode may occur. As a consequence, the actual band gap will extend well beyond the band gap in TM polarisation (see Section 4.6 in Chapter 4 and Fig. 4.14, *bottom*), which provides an additional degree of tolerance. The period of the lattice is typically several times smaller than the length of the patch antenna. Near the frequency of the band gap, the surface impedance reaches such a high level that no surface wave may propagate any longer. Accordingly, the radiation of the antenna will be enhanced in terms both of efficiency and of directivity, this being due to the fact that the diffraction effects induced by the edges of the substrate are in principle suppressed. Fig. 13.2 (*right*) presents a comparison between the radiation of an antenna placed on a conventional substrate and that of an antenna placed on a substrate with a high impedance surface (Sievenpiper 1995b). It can be observed that, in the presence of the photonic structure, the radiation of the antenna in the horizontal direction and its radiation on the rear side are significantly reduced.

In the experiment realised by Y. Qian *et al* (Qian 1999), the dimensions of the patch antenna were $3.05 \times 4.27 \text{ mm}^2$, while the permittivity of the dielectric material, consisting of Duroid with a 0.64 mm thickness, was equal to $\epsilon_r = 10.2$. The emission frequency of the antenna placed on a 'conventional' metallic plane was experimentally measured to be equal to $\sim 14 \text{ GHz}$, a value close to the value which can be calculated using the simplified formula given in Eq.13.1. In the configuration where a substrate with a high impedance surface was used, the surface grid had a 2.43 mm period, while the square metallic blocks had a 2.23 mm side and were separated from one another by a 0.2 mm distance. Under these conditions, the complete photonic band gap has been theoretically estimated as ranging from 8.6 to 12.66 GHz, whereas the actual band gap in TM polarisation extended to 27.36 GHz. As can be seen in the right-hand part of Fig. 13.2, the radiation of the antenna placed on the high-impedance surface is significantly reduced in the horizontal direction and on the rear side. The increase in the effective power on the front side was found to be equal to $\sim 1.6 \text{ dB}$, corresponding to an effective percentage of 45%. This clearly shows that a more advanced optimisation of the device requires the complete modelisation of the system formed by the antenna and the high impedance substrate in order to better match them to one another.

13.1.2 Photonic-Crystal Antenna Mirrors

As for antenna substrates, the first studies on the application of photonic crystal mirrors to antennas were carried out by considering volume structures realised from two or three-dimensional crystals, as represented in Fig. 13.1c (Kesler 1996 ; Sigalas 1996, 1997). Some of the issues associated with these photonic crystal mirrors have been discussed already in Sections 5.1.1, 5.1.2 and 5.1.3. One of the most interesting cases in this respect is that where specular reflection is the only possible diffraction order of the photonic grating (see Section 5.1.2 in Chapter 5).

The phase conditions on reflection of the photonic crystal are markedly different from those of a standard metallic plane. Thus, the reflected waves may combine with the waves which are directly emitted by the antenna, resulting in both a greater intensity and a higher directivity of the far-field radiation. More precisely, the conformation of the radiation of the antenna results from the strong angular dependence of the reflection coefficient. The crystal may thus for instance exhibit a band gap for some angles of incidence, while not for others.

Within a photonic band gap, the phase of the reflection coefficient of a photonic crystal follows as a first approximation a linear evolution as a function of the frequency f . This is illustrated in Fig. 13.3a in the case of a two-dimensional crystal formed by dielectric rods extending in the air. While this linear evolution can actually be verified whatever the incidence angle θ is, (Kesler 1996), the slope of this evolution changes with θ , and the reflection coefficient can therefore be written in the form:

$$\Gamma_{PC}(\theta, f) = \exp[i(A(\theta) - B(\theta)f)] \quad (13.2)$$

where A and B are functions of θ . Eq. 13.2 is valid only if the crystal is perfectly reflective, with a reflectivity equal to unity within the band gap. Actually, the frequency and angular dependences can be reintroduced in Eq. 13.2 by considering that, for each incidence angle, reflection occurs on a virtual metallic plane located inside the crystal, and at a distance $d(\theta)$ from the surface of the crystal (Fig. 13.3b). Assuming the metal to be a perfect reflector whose phase on reflection follows a law of the form $\Phi(\theta)$, the reflection coefficient considered at the surface of the crystal can thus be expressed as follows:

$$\Gamma_M(\theta) = \exp[i(\Phi(\theta) - 2kd(\theta)\cos\theta)] = \exp\left[i\left(\Phi(\theta) - \frac{4\pi f}{c}d(\theta)\cos\theta\right)\right] \quad (13.3)$$

Eq. 13.2 can be retrieved from this equation, provided that the following assumption be made:

$$\Phi(\theta) = A(\theta) \quad \text{and} \quad d(\theta) = \frac{cB(\theta)}{4\pi\cos\theta} \quad (13.4)$$

For the calculation of the radiation diagram of a dipolar antenna placed in the vicinity of the surface of the crystal, the assumption can then be made that, along a given direction, the field is the superposition of the field that would be emitted by the dipole in the absence of the crystal, and of the field due to its virtual image generated by the equivalent reflective plane. The field is calculated of course in the half-plane which extends around the crystal. As an example, let us here consider a dipole with a small height h , where an uniform current propagates and whose axis is parallel to the dielectric rods of the two-dimensional crystal. In the

absence of the crystal, the field lines would assume the form of circles in the plane H perpendicular to the axis of the dipole. Denoting by s the distance between the dipole and the surface of the crystal, the image generated in the equivalent reflective plane will be located at a distance $s + d(\theta)$ from the other side of this surface. The total field radiated in the direction θ follows in this case the following proportionality law:

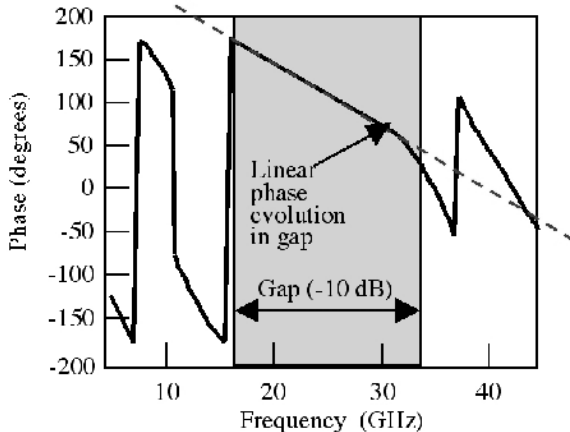
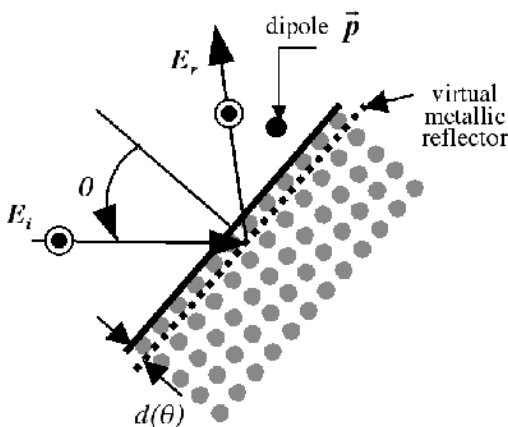
a**b**

Fig. 13.3. **a.** Frequency dependence of the phase of the reflection coefficient of a photonic crystal formed by a square lattice of dielectric rods ($\epsilon = 4.2$) with a 2 mm radius. The period of the lattice is equal to 9 mm (Kesler 1996). The incidence angle is assumed to be zero **b.** Metallic reflector equivalent to the photonic crystal, for an incidence angle θ

$$E_{tot}(\theta) = E_i(\theta) + E_r(\theta) \propto \exp\left[i(\Phi(\theta) - 2k(s + d(\theta))\cos\theta)\right] \quad (13.5)$$

where $\Phi(\theta)$ is as previously defined in Eq. 13.4. The application of Eq. 13.5 supposes that $\Phi(\theta)$ and $d(\theta)$ have been calculated beforehand for each value of θ . The radiation diagrams obtained with this simplified calculation method have turned out to be consistent with experimental values measured for two-dimensional crystals formed from dielectric rods (Carbonell 1998; Kesler 1996). The most favourable conditions for achieving a narrow emission beam and a good efficiency of the dipole have generally been obtained for a distance $s = \lambda/4$ between the dipole and the crystal. In comparison to the 'classical' case where the radiating dipole is at a distance $\lambda/4$ from a metallic plane, the efficiency of the dipole has thus been increased by a factor ranging from 1 to 2 dB. It should be pointed out however that the simplified calculation method which has been presented here does not allow the determination of the detailed structures which appear in the emission lobes experimentally measured, and which can be simulated using more sophisticated methods, in particular the FDTD method (Carbonell 1998). Further, this method does not allow the prediction of the finer modifications appearing in the radiation diagrams when the dipole is moved parallel to the surface of the crystal.

Clearly, high impedance metallic structures can also be used for the realisation not only of antenna substrates, described in the previous section, but also of antenna mirrors which may thus benefit from the compacity of these structures as well. The phase changes on reflection are in this case quite different from those that would be obtained with a perfect metallic mirror. For the sake of simplicity, let us assume here that we are in the case of normal incidence. The impedance at the surface is defined in this case by the equation

$$Z_s = \frac{E_{tot}}{H_{tot}} = \frac{E_i + E_r}{H_i + H_r} \quad (13.6)$$

where E_{tot} and H_{tot} are the electric and magnetic fields at the surface respectively, while (E_i, H_i) and (E_r, H_r) correspond to the incident and reflected waves respectively. For the incident wave and the reflected wave which propagate in the air, the impedance is given by the equation:

$$\left| \frac{E_i}{H_i} \right| = \left| \frac{E_r}{H_r} \right| = \eta \approx 377\Omega \quad (13.7)$$

while on the other hand the phase change on reflection is defined by the equation

$$\Delta\Phi = \text{Im}\left\{\ln\left(\frac{E_r}{E_i}\right)\right\} \quad (13.8)$$

By combining Eqs. 13.6 and 13.7 with appropriate signs, and by reintroducing the result in Eq. 13.8, one reaches the following equation:

$$\Delta\Phi = \text{Im} \left\{ \ln \left(\frac{Z_s - \eta}{Z_s + \eta} \right) \right\} \quad (13.9)$$

When the value for Z_s is very small, we are led back to the case of a perfect metal where $\Delta\Phi = \pm \pi$. Conversely, for high impedance structures, Z_s assumes large values in the vicinity of the resonance and $\Delta\Phi = 0$. This means that the radiating element, in the form either of a dipole or a patch antenna, can be placed at a very small distance from the high impedance surface. In such a case, the efficiency of the antenna can be expected to be higher than that obtained when the radiating element is located at a distance $\lambda/4$ from a metallic reflective plane. Since in this case the tangential magnetic field tends towards zero at the surface, high impedance surfaces are also referred to under the name of 'perfect magnetic conductors'.

13.1.3 Photonic-Crystal Antenna Radomes or Superstrates

The configuration formed by an antenna equipped with a photonic radome (also referred to as a superstrate) is schematically represented here in Fig. 13.1d. Radomes are generally used for controlling the emission of an antenna and/or for protecting it from any external detection. The radome may cover, either partially or totally, with an inclination which can be variable with respect to the plane of the antenna. In the example represented in Fig. 13.1d, the photonic radome totally covers the antenna and is used in emission mode. We shall discuss in Section 2 of this chapter the possibility of alternately operating in emission mode or in 'discretion' mode through the use of 'controllable' photonic crystals. The radome, which is often tilted with respect to the plane of the antenna, ensures in such a case the angular filtering, both in emission and in reception, along certain off-axis directions of propagation. In the example represented in Fig. 13.1d, the photonic radome is parallel to the plane of the antenna, resulting in an enhanced filtering in the principal direction of emission due to a cavity effect. The photonic radome and the metallic ground plane form indeed an asymmetric cavity inside which the emitting antenna is located. Depending on the distance between the radome and the ground plane, and therefore on the position of the cavity frequency with respect to the emission frequency of the antenna, the emission can be either reinforced or attenuated. In the case of a reinforcement of the emission, the spatial filtering is also reinforced as well, and the radiated electromagnetic field can thus be concentrated in a relatively narrow emission lobe.

The group of B. Jecko and A. Reineix from the University of Limoges has investigated in a detailed manner the configuration formed by an antenna and a photonic radome. This configuration is represented here in Fig. 13.1d (Thevenot 1999). The best results in terms of antenna gain, of directivity of the emission and

of overall cost of the system have been obtained for a one-dimensional photonic crystal limited to only three periods (Fig 13.4). The basis of the antenna is formed by a rectangular metallic plate placed on a dielectric substrate ($\epsilon = 2$), which itself lies on a ground plane. The photonic radome consisted for its part of three dielectric plates ($\epsilon = 9.6$) separated with air. The radome and the antenna were arranged in such a way as to form a $\lambda/2$ cavity, where λ is the Bragg wavelength of the one-dimensional crystal. Under these experimental conditions, the resonance was found to be of the order of 20 GHz. At this frequency, the power emitted by the antenna is concentrated for the most part in a narrow emission lobe, whose width corresponds to an effective width of the emitting area equal to ~ 120 mm, i.e. more than 25 times the width of the patch antenna. The antenna gain has thus been increased by ~ 24 dB due to the presence of the radome. This value is close to the value of 27 dB given by the formula:

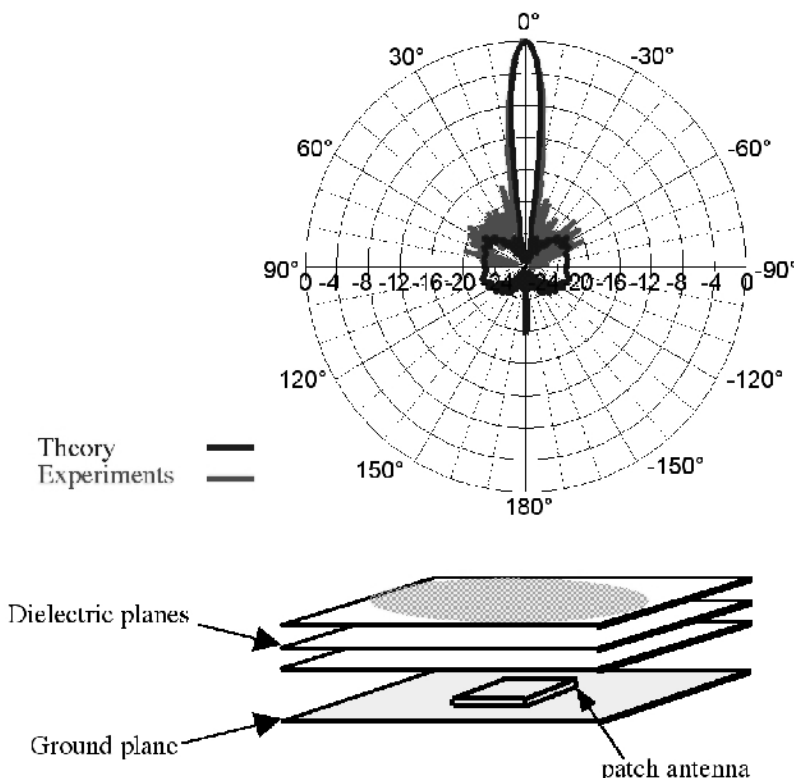


Fig. 13.4. *a.* Patch antenna equipped with a one-dimensional photonic crystal radome (Thevenot 1999) *b.* Radiation diagram of the antenna in the plane E . The values obtained from experimental measurements and from numerical simulations using the FDTD method are represented by black and dark grey lines respectively

$$G = 10 \log [4\pi S/\lambda^2] \quad (13.10)$$

where S is the effective emitting area. Accordingly, the amplitudes of the secondary lobes were found to be 20 dB lower than the amplitude of the principal lobe of the antenna. The radiation diagram measured in the plane E parallel to the electric field is represented here in Fig. 13.4, which shows that these results are consistent with numerical simulations realised using the FDTD method.

A diagram almost identical to the latter, revealing the same agreement between experimental measurements and theoretical values, was obtained in the plane H (Thevenot 1999). At the same time, a theoretical study addressing the case of a dipolar antenna placed between a radome and a one-dimensional photonic substrate (Fig. 13.1e) demonstrated the same effects, namely the enhancement of the antenna gain and that of the directivity of the antenna (Akalin 2001). Actually, the angular refinement of the emission can be interpreted as an effect induced by a planar cavity (see Section 10.1.2 in Chapter 10), even if the cavity involved here is of a rather special type. Both the effective emitting area and the numerical aperture are dependent on the quality factor of the cavity (see Fig. 10.2).

13.2 Controllable Structures and Metamaterials

13.2.1 Principles and Characteristics of Electrically Controllable Photonic Crystals

The use of metallic structures in the microwave region facilitates the insertion of electrically active elements in photonic crystals. This property is at the origin of the very concept of an active or 'controllable' photonic crystal, which was first suggested by two French research groups working at the University of Orsay and at the University of Lille respectively (Lourtioz 1999). In practice, electrically controllable two-dimensional photonic crystals have been fabricated by periodically inserting p-i-n diodes along metallic wires or metallic strips arranged in arrays. Depending on the voltage which is applied to them, the diodes can be either in an on-state or in an off-state. When the diodes are in the on-state, the properties of the crystal are the same as those of a lattice of continuous metallic wires, which have been described in Section 4.2.4 of Chapter 4. When the diodes are in the off-state, the properties of the crystal are the same as those of a lattice consisting of discontinuous wires with dielectric inserts (see also Section 4.2.4). The propagation of electromagnetic waves is less restricted in such lattices (Economou 1993): thus, starting from the zero frequency, a valence (transmission) band appears instead of the plasmon-type band gap. As will be seen in Section 13.2.2 of this chapter, one may also envision the possibility of an arrangement where only a few wires would be equipped with diodes. In this case, instead of modifying the be-

haviour of the photonic crystal as a whole, one locally modifies its properties though the creation of 'active' defects.

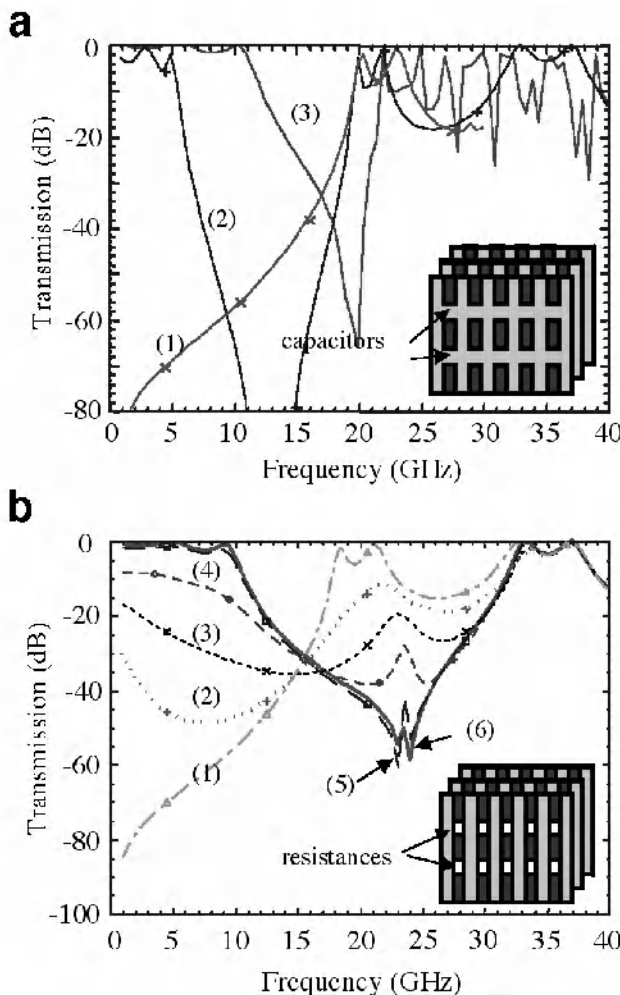


Fig. 13.5. Transmission spectra calculated for photonic crystals with metallic strips, where capacitances (*a*) or resistances (*b*) are periodically inserted along the strips. Three-layer crystals, formed by three printed circuits, are represented in the inserts. The printed circuit boards are separated from one another by 6 mm. For each circuit, the distance between two neighbouring metallic strips is equal to 4 mm, as is the distance between two neighbouring capacitance (or resistances) along a strip. The incident wave is TM polarised. In *a*, the curves (1), (2) and (3) correspond to capacitance values equal to 0, 0.3 and 30 fF respectively, while in *b*, the curves (1) to (6) correspond to resistance values equal to 0, 50, 150, 500, 5000 and 15000 Ω respectively

A p-i-n diode can actually be schematically represented by an equivalent circuit containing a capacitor and a resistance connected in parallel. The behaviour of the photonic crystal is dependent on the respective values of the capacitance or of the resistance. In Fig. 13.5 are represented the transmission spectra calculated in two extreme cases for a two-dimensional p-i-n diode photonic crystal, realised with the standard technology for printed circuits. The crystal presents a square symmetry, and it is further assumed in both cases that the incident wave is TM polarised, i.e. that the field E is parallel to the wires. The calculations are performed using an FDTD model, where each individual diode is simulated by an RC-type localised circuit. Fig. 13.5a corresponds to the situation where the capacitor plays the predominant role in the circuit equivalent to the diode, i.e. in the case where $R = \infty$. As might have been expected, under these conditions the first plasmon-type band gap is replaced by a valence band whose edge progressively shifts towards high frequencies as the capacitance value increases. The transmission spectrum is not otherwise modified. A completely different behaviour can be observed when the resistance plays the predominant role in the circuit equivalent to the diode ($C \sim 0$, Fig. 13.5b). In this case, not only the first band, but also the bands of higher order as well are strongly modified. The lower the resistance, the more important become the modifications of the spectrum. All the results achieved with the FDTD modelisation represented in Fig. 13.5 have been experimentally vindicated (de Lustrac 1999; Brillat 2002). Thus, by changing the polarisation voltage which is applied to the diodes, and therefore the value of the resistance equivalent to each diode, the photonic crystal can be tuned continuously from an on-state corresponding to a high transmission to an off-state corresponding to a strong reflection.

13.2.2 Electrically Controllable Photonic Crystal Antennas

Electrically controllable photonic crystals can be implemented in microwave antennas, in the form either of active radomes or of spatial filters, and different studies have been conducted along these lines (Collardey 2002; de Lustrac 2001; Poilasne 2000). Fig. 13.6a presents results which have been obtained with an active radome in a configuration similar to that described in Fig. 13.4 (de Lustrac 2001). The antenna used here is a patch antenna, while the radome, which is placed parallel to the antenna, is formed by three printed circuit boards where p-i-n diodes have been soldered with a regular spacing along parallel metallic strips. The distance between two nearby strips (4 mm) and the distance between the printed circuit boards (9 mm) were selected in such a way as to obtain an emission frequency of the antenna in the low frequency region of the first transmission band of the two-dimensional photonic crystal, as can be observed in the curve (1) in Fig. 13.5b. The radome is at a small distance from the antenna, which allows reducing the amount of leaky waves on either side of the structure while at the same time optimising the impedance matching between the photonic crystal and the antenna.

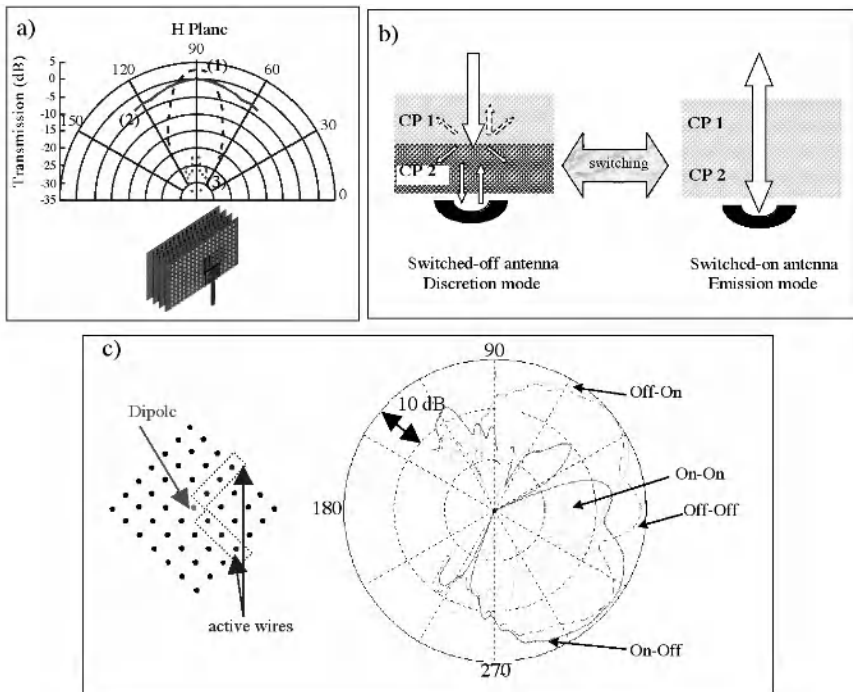


Fig. 13.6. **a.** Patch antenna with an active photonic crystal radome (de Lustrac 2001). The radome was fabricated using the standard technology for the realisation of printed circuits (*insert*). The radiation diagram of the antenna as measured in the absence of the radome reveals a large emission lobe (2). This lobe becomes narrow when the radome is in the transmission state (1). A 30 dB attenuation is obtained when the radome is in the reflection state (3) **b.** Principle of a composite photonic crystal radome (PC1 + PC2) used for the reduction of the radar equivalent surface of the antenna (Collardey 2002). When the two crystals are in the transmission state, the radiation of the antenna is transmitted, and the antenna can receive external signals. When the active crystal PC2 is switched to the reflection state, the transmission decreases, and the diffraction and refraction effects induced by the interface between the two crystals PC1/PC2 contribute to the reduction of the radar equivalent surface of the antenna **c.** Schematic representation of a dipole antenna placed in the centre of a photonic crystal consisting of metallic wires where two rows of wires contain active elements (Poilasne 2000) (*left*). Radiation diagrams measured for the different states of the two series of active elements (*right*). The on-state (resp. off-state) is conductive (resp. non conductive)

As can be seen in Fig. 13.6a, the use of an active radome allows the complete control of radiation diagram of the antenna. When the diodes are in the on-state, the radome transmits the radiation and beam-shaping effects similar to those described in Section 13.1.2, can be exploited for increasing the directivity of the antenna, and therefore the antenna gain compared to the situation where the radome would not be present. When the diodes are in the off-state, the radome reflects the radiation of the antenna, and the transmitted level decreases by nearly 30 dB.

Fig. 13.6b presents a different configuration where the active radome is formed by an ensemble of two photonic crystals (referred to in this figure as PC1 and PC2) with the same mesh, albeit with significantly different periods. The photonic crystal located at the smaller distance from the antenna (PC2) is an electrically controllable crystal (Collardey 2002). The problem addressed here is to prevent the antenna from being detected when not in emission mode. Using the appropriate terminology, the problem is therefore to reduce the 'radar equivalent surface' (RES) of the antenna.

Two different situations may thus arise. When the antenna is in emission mode, the conditions are selected as to ensure that the two crystals will be in the transmission state, and no significant transmission or diffraction loss will be induced by the interface. Conversely, when the PC2 crystal is in the reflection state, not only does the transmission of the antenna strongly decrease, but the refraction and/or diffraction effects occurring at the interface between PC1 and PC2 contribute to the reduction of the reflection of the external waves, thus resulting in a significant attenuation of the radar equivalent surface along certain directions of observation.

Fig. 13.6c shows the application of an active photonic crystal to the spatial filtering and to the switching of antenna arrays (Poislane 2000). Contrary to the two previous schemes, here a dipolar antenna is inserted in a photonic crystal formed by metallic wires. The frequency of the emitting dipole is (2 GHz) in the first band gap of the crystal with square symmetry. Only a few wires located in two rows perpendicular to one another contain active elements. Actually, these two rows of wires form two waveguides which are independent from one another within the crystal. Three different situations may arise then. When all elements are in the on-state, everything happens as though the metallic wires were continuous, and the radiation emitted by the antenna towards the outside decreases down to a very low level. When the active elements of only one series are in the on-state, the radiation of the antenna will be transmitted through only a single waveguide. The simultaneous commutation of the two series therefore allows switching the antenna array from one direction to the other. Finally, when all the elements are in the off-state, the radiation of the antenna is transmitted through the two waveguides, and the emission lobe may in this case become very large. These results suggest the possibility of developing low-cost antennas where the directions of emission would be controlled by photonic crystal structures.

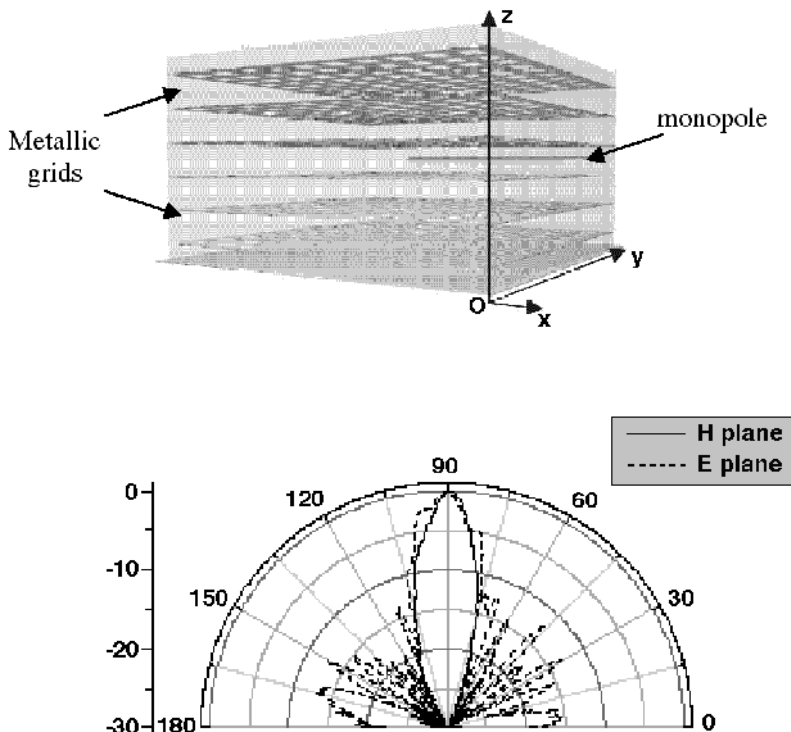


Fig. 13.7. *Top.* Monopole antenna placed in a metamaterial with index much smaller than unity, formed by a stack of perforated metallic grids (Enoch 2002) *Bottom.* Radiation diagrams of the antenna measured in the *H* plane (*continuous lines*) and in the *E* plane (*dashed lines*)

13.2.3 Antennas and Metamaterials

Most of the applications of photonic crystals to antennas which have been described above are based essentially on the exploitation of the amplitude response of the photonic crystal (on- and off-states). However, another possibility consists in exploiting the ultrarefractivity effects which have been discussed in Chapter 6, with respect more particularly to the search for adequate metamaterials (Section 6.4 in Chapter 6). The idea of using a "perfect" lens associated with a negative refractive index represents a possible solution for achieving the control of the far-field radiation of the antenna. The antenna in this case is located outside the

metamaterial. Another possibility consists in inserting the emitting element inside the metamaterial itself. Indeed, if the effective refractive index of the metamaterial is very small with respect to unity, the emitted radiation shall emerge from the metamaterial following a cone with a very narrow aperture. In other terms, the emitted beam will present a high directivity, which generally is a much wanted feature for applications. This effect has been reported in the works by S. Enoch *et al* (Enoch 2002a, 2002b). In these experiments, the metamaterial was formed by a stack of perforated metallic grids assembled in a foam with a refractive index close to unity (Fig. 13.7, *top*). Such a structure exhibits at low frequencies the same behaviour as a charge plasma whose effective index, described by Drude's formula which has been given in Section 4.1.1, can be much smaller than unity. The radiation diagram measured for a monopole antenna located at the centre of this stack reveals the existence of a very narrow lobe corresponding to an angular aperture equal to 8.9° and 12.5° in the *H* plane and in the *E* plane respectively (Fig. 13.7, *bottom*). The directivity thus obtained is of an order of magnitude comparable to the values which have been measured in the best conditions possible with photonic crystal antennas, where one may take advantage of a spatial filtering due to a resonant defect mode (Thevenot 1999; Temelkuran 2000).

13.3 Microwave Circuits and Ultra-Compact Photonic Crystals

13.3.1 Ultra-Compact Photonic Crystals

In the field of microwaves as well as in integrated optics (see Chapter 9), the realisation of circuits imposes the use of extremely compact structures. It has been seen earlier, in Section 13.1.1 of this chapter, that high impedance surfaces could be used for the realisation of antenna substrates with a limited thickness while at the same time allowing one to exploit the concept of a photonic band gap. It has also been seen that the electromagnetic behaviour of these structures could be analysed in terms of localised components, inductances and capacitances, with a band gap at the frequency ω defined by the equation $LC\omega^2 = 1$ (see Section 4.4.6 in Chapter 4). In the examples which have been presented in Figs. 4.13 and 13.2 of high impedance surfaces, the capacitances resulted from the existence of gaps between the metallic patches while the inductances were associated with the metallic 'rods' which connect, inside the substrate, the patches to the ground plane. Despite the limited thickness of these structures, their design remained nonetheless essentially three-dimensional. In this respect, the specificity of ultra-compact photonic crystals lies in the fact that they are intended at being used in circuits based on microstrip or coplanar lines. In such circuits, the two types of elements, i.e. the capacitors and the inductances, coexist on the same metallic plane.

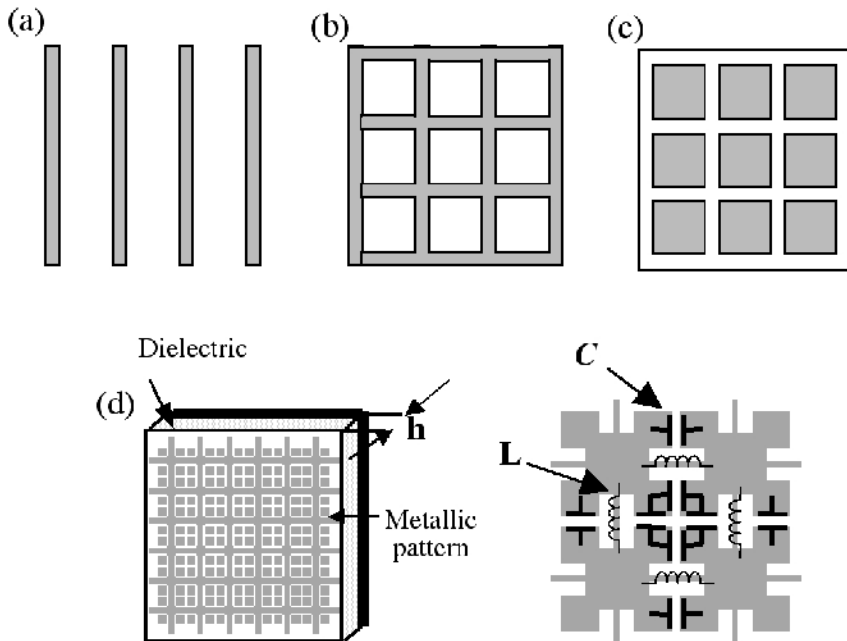


Fig. 13.8. Schematic illustration of the progression from metallic grids to ultra-compact photonic crystals for microwave circuits **a**. One-dimensional inductive grid **b**. Two-dimensional inductive grid **c**. Two-dimensional capacitive grid **d**. *Left*. Ultra-compact photonic crystal realised by the structuring of the ground plane following a 'Jerulaisem cross' periodic pattern *Right*. Circuit equivalent to the elementary cell of the ultra-compact photonic crystal

Fig. 13.8, which represents different types of periodical metallic patterns, shows the increasing level of complexity arising with such structures. One-dimensional lattices of metallic wires or metallic strips represented in Fig. 13.8a have long been used as polarisation-selective filters owing to the inductive couplings arising between the wires. An ensemble of two lattices crossed in the form of a grid, as illustrated in Fig. 13.8b, may act as high-pass filter for the two polarisations. Conversely, the dual system consisting of periodic metallic contacts separated from one another and represented in Fig. 13.8c, involves capacitive couplings and behaves like a low-pass filter. Finally, the 'Jerulaisem cross' pattern, represented in Fig. 13.8d, and which was first suggested by the group of T. Itoh at the University of California (Los Angeles) (Cocciali 1999; Yang 1999a) simultaneously combines inductive effects and capacitive effects: a proper electromagnetic band gap can thus be achieved around the frequency ω defined by $LC\omega^2 = 1$. The equivalent circuit corresponding to an elementary cell is represented in the

right-hand part of Fig. 13.8d by means of capacitors and inductances: the capacitors are associated with the 'gaps' between the metallic blocks, while the inductances are associated with the wires connecting the central regions of these metallic blocks.

In order to realise an ultra-compact photonic crystal, it is therefore sufficient to structure the metallic ground plane of a microwave circuit, without having to modify the dielectric region which forms the core of the guiding lines. This is a decisive advantage, in terms of cost and of simplicity of the design, compared to conventional dielectric photonic crystals. Actually, the resulting geometry is analogous to that of surface selective surfaces (Chan 1995), with the difference however that one considers here a guided wave instead of an external incident wave. An electromagnetic wave propagating along the lines of the circuit will be sensitive to the filtering induced by the structuring of the ground plane. As for planar integrated optics (see Chapter 9), the two-dimensional periodicity of the patterns allows this filtering to be effective in all the directions in the plane. Effects associated with the refractive indexes (or with the propagation speeds of the waves) can also be exploited in the vicinity of the band gaps. In particular, a strong increase of the group index may result, for a given wavelength, in the possibility of reducing the size of the circuit, which is quite a significant advantage for applications at low frequencies.

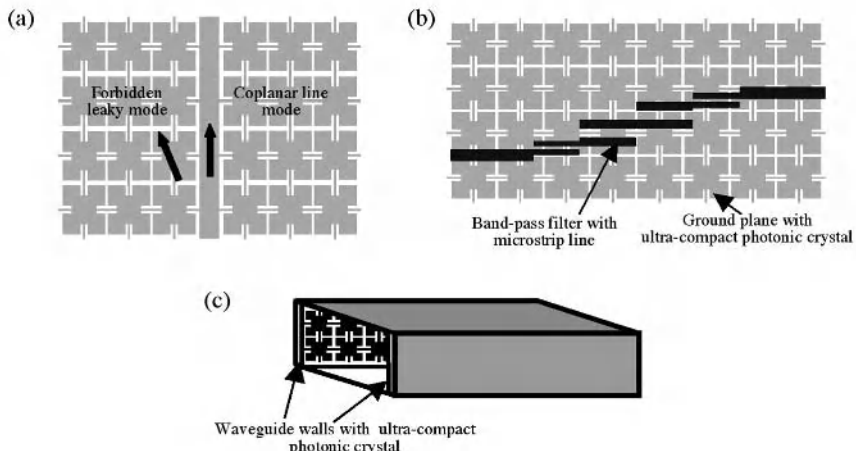


Fig. 13.9. *a.* Top view of a coplanar line where the ground planes on either side of the central conductor exhibit an ultra-compact photonic crystal structure. This configuration prevents the propagation of parasitic waves between the front-mounted ground lines and the rear-mounted ground plane *b.* Top view of microstrip line band-pass filter. The fundamental band is imposed by the coupled cavities defined on the front side. The 2ω component is suppressed due to the ultra-compact photonic crystal realised in the rear ground plane *c.* Schematic representation of a hollow waveguide with ultracompat photonic crystal

13.3.2 Microwave Filters and Waveguides realised from Ultra-Compact Photonic Crystals

Different applications of ultra-compact photonic crystals have been suggested. A few examples of such applications, which are illustrated in Fig. 13.9, will be presented in this section. The first example shown in this figure (Fig. 13.9a) is that of coplanar circuits (Yang 1999a). As its name indicates, the metallic connections in such a circuit generally lie in the same plane, a coplanar line being formed by a central conductor surrounded by two ground lines. Such a configuration allows the optimisation of the performances in terms of frequency of the circuits, while at the same time reducing dielectric 'gaps', and more specifically the thickness of the substrate. However, when this thickness becomes too small, a second metallic ground plane is mounted on the rear side in order to rigidify the substrate. The risk appears here that parasitic waves may be guided between the rear-mounted ground plane and the front-mounted ground lines, whereas guiding should exclusively occur under the central conductor. In this respect, the creation of an ultra-compact photonic crystal through the structuring of the ground lines on the front side can be viewed as an elegant solution to the problem of preventing the propagation of parasitic waves, irrespective of their direction of propagation.

In the second example of an application of ultra-compact photonic crystals represented in Fig. 13.9b, an ultra-compact photonic crystal is used as a band-pass filter in a microstrip line circuit (Yang 1999a). In such a circuit, the guiding will occur in the region of the dielectric extending between the front-mounted metallic strip and the rear-mounted ground plane. Band-pass filters are generally realised by using coupled-cavity structures, represented in Fig. 13.9b by dark bands. The rigidity of the filter depends on the quality factor of each cavity, while the spectral width varies with the number of cavities. One of the main drawbacks associated with these structures results from the fact that the filter also allows the propagation of waves at all the harmonic frequencies of the fundamental frequency. As an example, the component at the 2ω frequency can be suppressed through the use of a ground plane structured in such a way as to prevent the propagation of this component. In other terms, one takes advantage here of the double structuring of the metallic lines of the circuit, which results in the definition of coupled cavities on the front side and of an ultracompact photonic crystal on the rear side. The optimisation of the performances of the filter at simultaneously ω and 2ω depends of course on the position of the strips on the front side with respect to the ultra-compact photonic crystal patterns on the rear side.

The third example represented in Fig. 13.9 is that of a hollow waveguide with an ultra-compact photonic crystal structuring of its sidewalls (Yang 1999b). These hollow waveguides are related to the microstructured hollow fibres which have been described in Section 11.3 of Chapter 11. The fact that the wave is guided in the air permits the injection of high powers. In general, microwave waveguides are bounded by metallic sidewalls which impose a zero field. Conversely, the replacement of metal with a photonic crystal behaving as a 'perfect magnetic conductor' results in reflective walls without any phase change at the reflection (see Section 13.1.2 in this chapter). In such a case, the guided wave exhibits an almost

constant amplitude at all points of the waveguide and fills the entire volume, resulting in an increase by a factor ~ 2 of the power transmission capabilities of the waveguide.

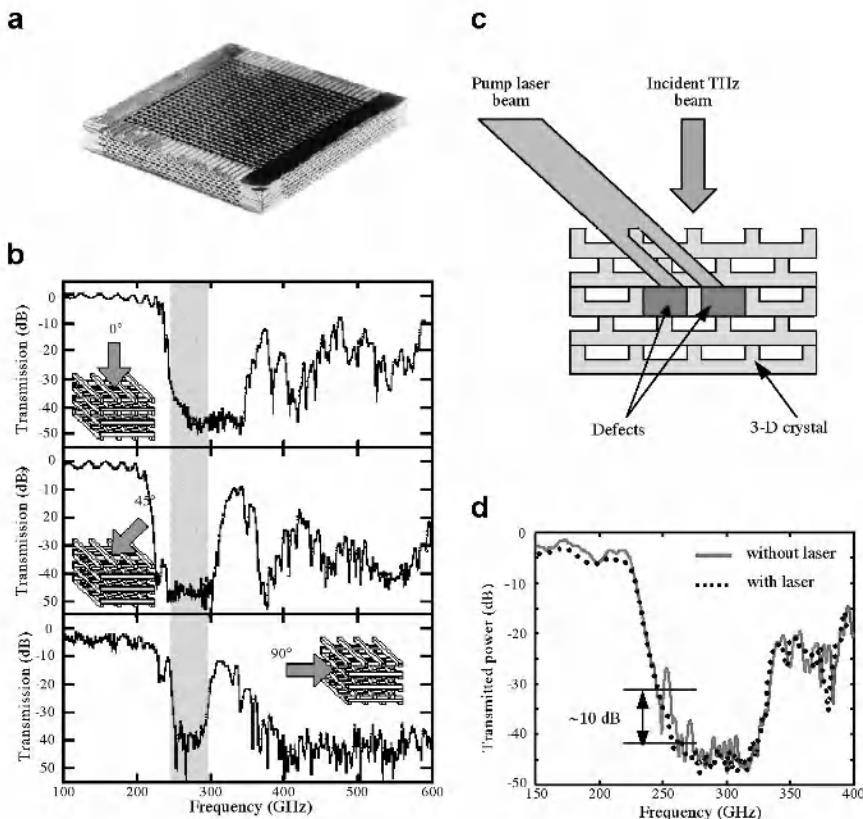


Fig. 13.10. **a.** THz photonic crystal of the 'woodpile' type realised through the mechanical etching of a silicon substrate (Chelnokov 1997). **b.** Transmission spectra measured for three different directions of the incident wave, revealing the existence of a complete photonic band gap. **c.** Principle of a THz controllable filter based on a three-dimensional photonic crystal where defects were introduced (Chelnokov 1998) **d.** Transmission spectra measured along the $<100>$ direction in the absence of illumination (continuous lines) and under illumination (dots)

13.4 From Microwaves to Terahertz Waves

Terahertz (THz) waves, also referred to as submillimeter waves or as far infrared, occupy an intermediate position between microwaves and the near-infrared in the frequency spectrum. These waves have typically wavelengths ranging from a few ten microns to the millimeter, hence frequencies ranging from approximately ~200 GHz to a few terahertz. For this reason, the techniques associated with these waves are generally hybrid techniques between microwave and optical techniques. Thus, the THz emission sources include such diverse systems as gas lasers, for instance lasers optically pumped by means of a carbonic gas laser (Lourtioz 1981), semiconductor lasers, like for instance quantum cascade lasers (Köhler 2002), systems for the frequency doubling or tripling of microwave emitters (Siegel 1999) as well as emitters similar to those used for microwaves, like for instance *impatt* or *Gunn* diodes (Eisele 1998), but with an optimisation of their frequency response. It might also be mentioned that a specific technique of THz spectroscopy exists. This technique is based on the exploitation of the free-space radiation of antennas connected to semiconductor switches which themselves are triggered by an infrared laser operating in a regime of (sub)picosecond pulses (Garet 1997). This technique is commonly used for the characterisation of photonic structures adapted to the THz region.

The field of applications for THz waves is less extended than that of microwaves, this being due to the fact that the absorption of these waves in the atmosphere reduces the distance of propagation in free space at most frequencies of interest. This however can be turned into an advantage when information is transmitted over short distances (indoor telecommunications) or in highly diluted media (satellite communications), since in this case the absorption occurring over longer distances leads to the possibility of discretising the information transmission. At a different level, THz spectroscopy provides specific information concerning vibration/rotation spectra of molecules, with possible applications to the environment, to chemistry or to astronomy. Finally, THz spectroscopy is well suited to the measurement of charge densities in relatively dense plasmas. These different applications justify the interest in THz waves and consequently in photonic crystals in this region. From an historical point of view, another reason for this interest lies in the fact that the THz region, as a field of investigation for photonic structures, can be more easily accessed than optics, while at the same time offering the perspective of a rapid transfer of the results achieved in the THz range to the infrared and visible ranges.

In particular, it might be recalled here that the three-dimensional photonic crystal structures of the 'woodpile' type which have been described in Section 12.2.1 of Chapter 12, had been first developed in the THz field from semiconductor materials (Özbay 1994a, 1994b). Fig. 13.10a represents an example of such a three-dimensional structure realised from a silicon substrate (Chelnokov 1997). The fabrication method used for the realisation of this structure is significantly different from that used for the first realisations, where each lattice in the three-dimensional stack was realised by chemical etching. In the case under considera-

tion, grooves are etched on each side of a silicon substrate by means of a programmable silicon dicing saw of the kind used in the electronic industry. In principle, mechanical etching can be applied to any type of substrate, and any value can be selected for the angle between the grooves mechanically etched on either side of the substrate. The grooves have a $360\text{ }\mu\text{m}$ width and they are spaced from one another by $135\text{ }\mu\text{m}$, while the remaining silicon 'rods' have a $135\text{ }\mu\text{m}^2$ cross section. The rods of two adjacent lattices in the stack are directed along two directions perpendicular to one another, as in the case of the initial 'woodpile' structure which had been described in Section 12.2.1. Transmission measurements carried out for a stack of eight layers, corresponding to 4 periods of a three-dimensional crystal at variable incidence angles have indeed revealed the existence of a complete band gap, which extends from 240 to 290 GHz (Fig. 13.10, *bottom left*).

The possibility of realising a THz modulation filter controllable by infrared beam has been demonstrated through the insertion of defects in the photonic crystal represented in Fig. 13.10, in the form of small silicon blocks (Chelnokov 1998). The structure where these defects are introduced has been previously described in Chapter 1 (Fig. 1.17).

The principle of this modulation filter is schematically represented in Fig. 13.10d. Each small silicon block actually forms a cavity whose quality factor depends on the absorption induced by the infrared laser beam. The absorption itself at the THz frequencies is due to the photocreation of electrons and holes in the silicon, and the variation in transmission of the crystal is measured by injecting a THz beam from above the crystal. The actual behaviour of the modulator is illustrated in Fig. 13.10d, which represents the transmission spectrum of the crystal along the $\langle 100 \rangle$ direction under two different conditions of illumination. In the absence of illumination by a laser beam, the spectrum exhibits a resonance peak with a width equal to ~ 4 GHz within the band gap (at 253 GHz). The fact that the resonance is not much pronounced has already been discussed in Section 1.4.1 in Chapter 1. In the presence of the laser beam operating with a ~ 300 mW illumination power, this resonance peak totally disappears. This corresponds approximately to a 10 dB amplitude modulation of the THz filter. Beyond this application to filtering, the experiment reported in Fig. 13.10 also opens the way to the possibility of realising submillimeter sources optically pumped by infrared laser.

13.5 From Microwaves to Optics

It is not unusual that the development of microwave devices and systems may announce that of future optical devices and systems. Likewise, the study of microwave devices often leads to the development of new analysis and modelisation methods, which may later find their way into optics. In this respect, more than in any other else, the thematic of photonic crystals can be seen as a link between the fields of microwaves and optics. In this section, we shall present two examples of possible transfers from one field to the other.

13.5.1 Impedance Matching of Photonic Waveguides

The problem of impedance matching is a most classical problem for electronic circuits. Each transmission line can be associated to a characteristic impedance Z_C which depends on the inductance and on the capacitance per unit length of the transmission line. In the most usual case, $Z_C = 50 \Omega$. This impedance can also be defined as the ratio between the amplitudes of the electric field and magnetic field of the wave propagating along the line (see Eqs. 4.40 and 4.42). When the line ends with a charge impedance Z_L , the impedance matching or in other terms the optimisation of the electromagnetic power contained in the charge, can be indifferently determined either from the reflection coefficient at the end of the line Γ_L or from the standing wave ratio (SWR), which are respectively defined as follows:

$$\Gamma_L = \frac{Z_L - Z_C}{Z_L + Z_C} \quad \text{and} \quad SWR = \frac{1 + |\Gamma_L|}{1 - |\Gamma_L|} \quad (13.11)$$

An optical waveguide is of course analogous to a microwave transmission line. This leads to the possibility of defining a characteristic impedance for optical waveguides: the charge at the extremity of the waveguide will thus be associated with some perturbation of the waveguide, such as a bend, a widening of the waveguide or the presence of a cavity. However, the difference between a photonic crystal waveguide and a standard waveguide precisely lies in the periodicity of the former, and therefore in its non-uniformity. The study conducted by S. Boscolo *et al* (Boscolo 2002) has nonetheless demonstrated that the notion of characteristic impedance Z_B , which may be referred to as the 'Bloch impedance', can also be introduced in this context. This however requires that the ratio E/H be considered along the transverse direction with respect to the propagation of the wave. Thus, for a TM wave propagating in a channel waveguide created in a two-dimensional photonic crystal formed by dielectric rods (Fig. 13.11), the field E extends along the Oz axis, and the 'Bloch impedance' can be written as follows:

$$Z_B = \frac{\int \eta_B(x, 0) \operatorname{Re}\{P_y(x, 0)\} dx}{\int \operatorname{Re}\{P_y(x, 0)\} dx} \quad (13.12)$$

where:

$$\eta_B(x, y) = \frac{E_z(x, y)}{H_x(x, y)}$$

and where $P_y(x, 0)$ represents the longitudinal component of the Poynting vector in the $y = 0$ plane.

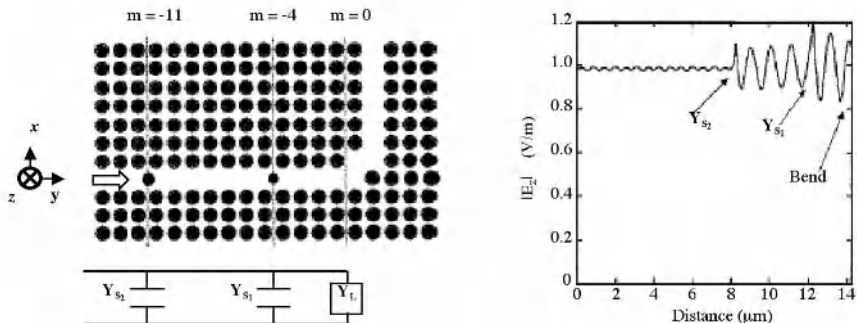


Fig. 13.11. *Left.* Bend in a two-dimensional photonic-crystal waveguide with a square symmetry and equivalent scheme of an impedance-matched transmission line. *Right.* Modulus of the electric field along the main waveguide. The introduction of the two defects allows the impedance matching of the waveguide, resulting in a lower standing wave ratio before Y_{S_2}

Likewise, in the case where a perturbation, in the form for instance of a bend as in Fig. 13.11, is induced at the extremity of the waveguide, a charge impedance Z_L can also be defined, with the consequence that the impedances calculated at different distances from the perturbation (rows formed by rods with rank $m < 0$ in Fig. 13.11) can be expressed as a function of Z_B and Z_L as in the case of a conventional transmission line (Boscolo 2002). Under these conditions, all the impedance matching techniques developed in the field of RF waves can be applied to photonic crystal waveguides. One of these techniques consists in placing localised impedances (stubs), parallel to the transmission line, at two different points before the perturbation. In principle, only two impedances with adequately selected values are sufficient for reducing the standing wave ratio in the transmission line, and thereby for optimising the energy transmission at the end of the line.

This phenomenon can be observed in the example represented in Fig. 13.11. The two localised impedances are obtained by placing two dielectric rods with different radii along the axis of the waveguide in the rows $m = -4$ and $m = -11$ respectively (Fig. 13.11, *left*). In this case, it can be observed that the oscillations of the field beyond the second central rod ($m \leq -11$) tend to disappear (Fig. 13.11, *right*): the standing wave ratio thus tends towards unity. This impedance matching technique turns out to be relatively robust in terms of wavelength, since it permits to keep the reflection losses no higher than 20 dB over a relative spectral range $\Delta\lambda/\lambda \sim 1\%$. This method for the impedance matching of photonic waveguides can thus be extended to other types of perturbations and other types of photonic crystal structures.

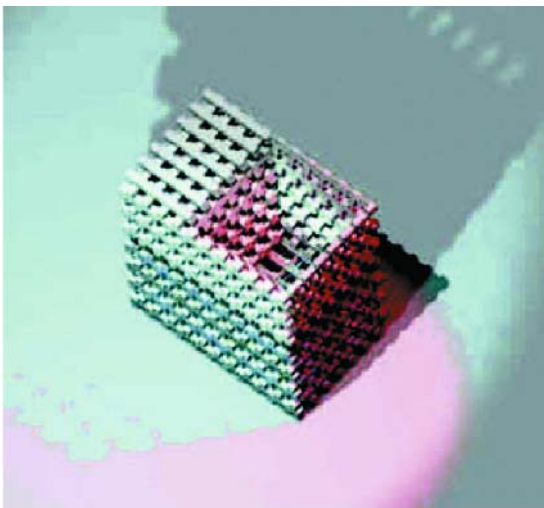


Fig. 13.12. Schematic representation of a THz pixel of the passive imaging system developed within the STARTIGER framework for the 250 and 300 GHz frequencies (STARTIGER 2003). The detecting/mixing element is embedded in a three-dimensional photonic crystal realised by mechanical machining. The aperture on the upper side, with a form similar to that of microwave receiving horns, allows the illumination of the pixel

13.5.2 Photonic Crystal THz Imaging System

Imaging is one of the most important fields of applications for optical systems. Each frequency range provides specific information concerning the scene which is to be 'imaged'. Of course, the visible range is for us the most familiar region. Terahertz detection, like infrared detection, provides information concerning the temperature of objects present in a scene, with the specificity however that the THz radiation emitted by these objects can be transmitted through smoke and clouds, as well as through such materials as glass, plastics, cloth and even sufficiently thin walls. THz imaging systems are less cumbersome than microwave imaging systems, to which they can be substituted in certain cases for observations from small platforms, in particular satellite boarded platforms. While some commercial systems already exist, three-dimensional silicon photonic crystals, of the type presented in Section 4, open the way to the realisation at a low cost of three-dimensional architectures, where not only the detection elements (pixels) and the photonic substrate would be integrated, but also the receiving horns and the connection lines themselves, as can be seen in the example represented in Fig. 13.12 (Gonzalo 2002; STARTIGER 2003). In such an architecture, the existence of the photonic band gap allows isolating the active elements from the pixels as well as from the substrate, thereby preventing diaphony problems from arising. The se-

tion of the termination of the crystal at the location of the emitter also provides the possibility of matching impedances, and thus of optimising the level of the detected signal. In view of the development of fabrication techniques of three-dimensional photonic crystals (see Section 13.4 in this chapter), it seems likely that this experiment on a THz imaging system will be extended to shorter wavelengths.

Conclusion and Perspectives

More than ten years after the first demonstration of photonic band gaps, photonic crystals still remain fascinating in view not only of their analogy with solid state crystals but most of all of the unique opportunity of bringing together knowledge and experience from different fields of research, ranging from solid state physics to optics, microwaves and microelectronics. The large variety of works presented in this book shows the complexity and breadth of this topic, which has now found its way into the curriculum taught to students preparing a master's degree in optics or in electronics.

Beyond these remarks of a general character, it has been seen in this book that photonic crystals have paved the way to the development of a new generation of optical devices with ultimate dimensions and properties, i.e. optical devices at the wavelength scale. Among these devices, microstructured silica fibres are likely to become the first photonic-crystal-based product to reach the marketplace. In the field of semiconductors, going from concept to actual applications took more time than had been expected. Indeed, not only did numerous technological difficulties present themselves, but existing devices in optical communications had already at this time achieved a high level of sophistication. Fortunately enough, most of these difficulties are currently in the process of being solved thanks to the advances which have been taking place in the fields of microtechnology and nanotechnology. One of the major breakthroughs which are expected to occur during the next decade is the fabrication of two and three-dimensional photonic crystals in which ultra-small waveguides and microcavities could be incorporated on demand. More generally, it should be borne in mind that the elementary patterns of photonic crystals in the near-infrared region, i.e. at telecommunication wavelengths, are typically in the range of one hundred of nanometers, with aspect ratios ranging from one to ten. For this reason, the accuracy required for the fabrication of efficient devices can be estimated to be of the order of ten nanometers, and even less. This is about the same accuracy scale as is needed for silicon microelectronics.

Photonic crystals are also at the very origin of the parallel which is now being increasingly drawn between nanoelectronics and nanophotonics. In addition to the miniaturisation of optical devices and systems that they allow, one of the guiding ideas in the practical development of photonic crystals is the possibility of fabricating, in a limited number of technological steps, the main constitutive elements of future large-scale-integration photonic circuits. In simple terms, this would provide a practical 'toolkit' for the design of circuits in optics and optoelectronics combining the most advanced lithography and etching processes. Different meth-

ods are now being proposed for the computer-assisted design of the first elementary photonic circuits. Hybrid circuits where photonic circuits would be associated on the same chip to electronic circuits are also being proposed. One of the decisive advantages of using optical rather than electrical signals would be the perspective of a much weaker interaction between the signals themselves.

Due to the easier control of the two-dimensional topology of planar integrated optics, considerable advances on two-dimensional photonic crystal devices have been taking place during the last decade. In particular, thanks to the numerous modelling and characterisation studies which have been carried out on three-dimensional photonic waveguides, the scientific community has gained a clearer understanding of the limitations of the two main alternatives, i.e. highly-confined and weakly-confining photonic crystal waveguides, corresponding to membrane waveguides and to buried photonic crystal waveguides respectively. Several approaches have been developed for reaching an acceptable level of loss, which remains the most critical issue as far as applications to actual systems are concerned, especially as regards the implementation of such optical functions as the filtering, the guiding or the emission of light. Systems based on photonic crystals will soon be mature enough to compete with the most performing demultiplexer systems in optical telecommunications, such as waveguide arrays or the so-called ‘phasars’. The encouraging results obtained on light bends, on mode matching systems and on ‘add-drop’ filters where photonic crystal waveguides are combined to microcavities, demonstrate that photonic crystals hold even more promises for a great variety of miniature active devices. It suffices here to mention that we are only at the beginnings of the first microsources and nonlinear optical devices based on the use of photonic crystals.

Mentioning the practical applications of photonic crystals without recognizing the important theoretical perspectives opened by the modelling studies conducted on this subject would be an unforgivable omission. This book, not only in its first part, but also in its second part devoted to the optical properties of photonic crystals and to the design of miniature photonic devices, should have allowed the reader to gain an insight into the extraordinary breadth of the problems posed by photonic crystals in terms of electromagnetic modelling. Difficult problems need to be solved for each specific situation, for instance, in the case where a three-dimensional analysis is necessary, and even more so when the crystal is formed from composite elements such as metamaterials or when it is combined with active elements such as emitters or nonlinear materials. It can be safely predicted that the dynamic process started by theoretical studies on photonic crystals will continue to generate new ideas for electromagnetic modelling.

Finally, one of the original dreams of pioneers of research on photonic crystal, i.e. achieving the complete control of light with a single emitter in three-dimensional photonic crystal microcavities, now seem to be within reach. The perspective of developing practical implementation schemes for quantum cryptography is now a further incentive towards achieving this goal. The relevance of photonic crystal microcavities in this context is no longer disputed, even if they are not the only available option. While photonic crystals are no longer in their infancy, it is to be hoped that the continuous advances arising in micro- and

nanotechnology, combined with the intellectual appeal of the questions to which photonic structures give rise, will allow them to definitively reach maturity during the next decade.

Appendix. Scattering Matrix Method: Determination of the Field for a Finite Two- Dimensional Crystal formed by Dielectric Rods

This appendix will be devoted to a more detailed exposition than was possible in Section 3 of Chapter 2 of the scattering matrix method, also referred to as the multipole method or as the modal method. We shall more specifically consider the problem of the determination of the field in two-dimensional photonic crystals formed by an array of dielectric rods in the air.

A.1 Incident Field

In the coordinate system represented in Fig. A.1, the incident field illuminating the array of rods can be written as follows:

$$E_z^i = \exp\left(ik_0 n_{ext} (x \sin \Theta^{inc} - y \cos \Theta^{inc})\right) \quad (\text{A.1a})$$

A.2 Field inside the Rods

Inside an arbitrary dielectric rod with a permittivity $\epsilon_{r,int}$, the total field satisfies the following equation:

$$\nabla^2 E_z + k_0^2 \epsilon_{r,int} E_z = 0 \quad (\text{A.2})$$

We shall use a system of local polar coordinates (r_j, θ_j) with an origin located at the centre of the j^{th} rod. For a fixed value of r_j , the field is a periodic function of θ_j with a period 2π , and it can therefore be written in the form of a Fourier series:

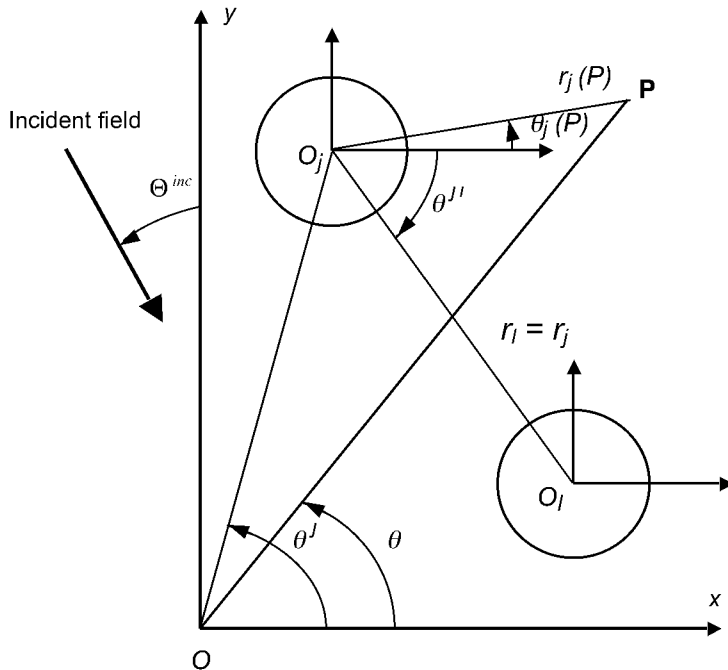


Fig. A.1. Representation of the coordinate system

$$E_z(r_j, \theta_j) = \sum_{m=-\infty, +\infty} E_{z,m}(r_j) \exp(im\theta_j) \quad (\text{A.3})$$

We shall use the expression in polar coordinates of the scalar Laplacian:

$$\nabla^2 V = \frac{\partial^2 V}{\partial r_j^2} + \frac{1}{r_j} \frac{\partial V}{\partial r_j} + \frac{1}{r_j^2} \frac{\partial^2 V}{\partial \theta_j^2} \quad (\text{A.4})$$

Let us now introduce the expression of the field given by Eq. A.3 in Eq. A.4. A straightforward calculation demonstrates that the Fourier coefficients satisfy the following equation:

$$\forall m \quad \frac{d^2 E_{z,m}}{dr_j^2} + \frac{1}{r_j} \frac{\partial E_{z,m}}{\partial r_j} + \left(k_0^2 \varepsilon_{r,int} - \frac{m^2}{r_j^2} \right) E_{z,m} = 0 \quad (\text{A.5})$$

Assuming that $r'_j = k_0 n_{int} r_j$, and after proceeding to some simplifications, this equation becomes:

$$\forall m, \quad \frac{d^2 E_{z,m}}{dr_j'^2} + \frac{1}{r'_j} \frac{\partial E_{z,m}}{\partial r'_j} + \left(1 - \frac{m^2}{r_j'^2} \right) E_{z,m} = 0 \quad (\text{A.6})$$

We are therefore led back to Bessel's equation. The general solution of this equation is given by:

$$E_{z,m} = c'_{j,m} J_m(r'_j) + d'_{j,m} Y_m(r'_j) = c'_{j,m} J_m(k_0 n_{int} r_j) + d'_{j,m} Y_m(k_0 n_{int} r_j) \quad (\text{A.7})$$

where J_m and Y_m are Bessel functions of the m^{th} order of the first and second kinds respectively (Abramovitz 1970).

The right-hand side of Eq. A.7 can also be written in the following form:

$$E_{z,m} = (c'_{j,m} + i d'_{j,m}) J_m(k_0 n_{int} r_j) - i d'_{j,m} (J_m(k_0 n_{int} r_j) + i Y_m(k_0 n_{int} r_j)) \quad (\text{A.8})$$

Let us here remind ourselves that the definition of the Hankel function of m^{th} order of the first kind is:

$$H_m^{(1)}(u) = J_m(u) + i Y_m(u) \quad (\text{A.9})$$

It thus turns out that Eq. A.8 can be re-written in the form:

$$E_{z,m} = c_{j,m} J_m(k_0 n_{int} r_j) + d_{j,m} H_m^{(1)}(k_0 n_{int} r_j) \quad (\text{A.10})$$

where the coefficients $c_{j,m}$ and $d_{j,m}$ can be easily deduced from $c'_{j,m}$ and $d'_{j,m}$.

It shall be later demonstrated that this new expression of the field is the most adequate for a physical interpretation of the two terms appearing in its right-hand side. Introducing this expression for $E_{z,m}$ in Eq. A.3, we arrive at an expression of the total field in the rod in terms of a Fourier-Bessel expansion:

$$E_z(r_j, \theta_j) = \sum_{m=-\infty, +\infty} [c_{j,m} J_m(k_0 n_{int} r_j) + d_{j,m} H_m^{(1)}(k_0 n_{int} r_j)] \exp(im\theta_j) \quad (\text{A.11})$$

It can be noted that in the specific case of the field inside the rods, all coefficients $d_{j,n}$ become zero; Indeed, the Hankel function $H_m^{(1)}(s)$ presents a singularity at $s = 0$. Since the field cannot be singular, the corresponding terms have to be removed from the expression of the field, and therefore, for $r_j < R$:

$$E_z(r_j, \theta_j) = \sum_{m=-\infty, +\infty} c_{j,m} J_m(k_0 n_{int} r_j) \exp(im\theta_j) \quad (\text{A.12})$$

The determination of the field inside the rods thus reduces to the calculation of the coefficients $c_{j,m}$ of the Fourier-Bessel expansion given in the right-hand side of Eq. A.12.

A.3 Field in the Vicinity of a Rod

The calculations which have led to the expression of the field inside the rods can be reproduced almost identically for the regions outside the rods.

Thus, the field outside the rods can be shown to satisfy the following Helmholtz equation:

$$\nabla^2 E_z + k_0^2 \epsilon_{r,ext} E_z = 0 \quad (\text{A.13})$$

Let us now consider the circular region surrounding the j^{th} rod and extending to the nearest point of the immediately neighbouring rod. This region is represented by the light grey area in Fig 2.10 in Chapter 2. In this region the value of the refractive index is constant and equal to n_{ext} . Using the same coordinate system and the same mathematical development than in the preceding section, it can be demonstrated that the field in this region assumes the form of a Fourier-Bessel series similar to the series given in Eq. A.11:

$$E_z(r_j, \theta_j) = \sum_{m=-\infty, +\infty} a_{j,m} J_m(k_0 n_{ext} r_j) \exp(im\theta_j) + \sum_{m=-\infty, +\infty} b_{j,m} H_m^{(1)}(k_0 n_{ext} r_j) \exp(im\theta_j) \quad (\text{A.14})$$

In this case however, it is no longer possible to demonstrate that the coefficients $b_{j,m}$ are zero. Indeed, no physical argument prevents here the field from being singular at the origin, since this origin does not belong to the ring itself.

Nevertheless, the two terms appearing in the right-hand side of Eq. A.14 can be given a physical interpretation from the properties of Bessel functions. The field in the ring can indeed be decomposed into three different components:

- the incident plane wave, i.e. the source, given by Eq. A1,
- the field scattered by the j^{th} rod. From the radiation condition at infinity, this field must propagate away from this rod,
- the fields scattered by the all other rods in the direction of the j^{th} rod. These fields behaves with respect to this rod as an incident field. Accordingly, the total incident field at the j^{th} rod is formed by these fields and by the incident plane wave, i.e. the source term.

In order to identify each physical component in Eq. A.14, it might be first noted that the total incident field at the j^{th} rod is necessarily generated by sources located outside this rod. This field must therefore satisfy a Helmholtz equation *inside* this rod without presenting any singularity. This property allows us to conclude that the total incident field is contained in the first sum of Eq. A.14, and therefore that the second sum represents the field scattered by the j^{th} rod. The only remaining question is whether this second sum represents the totality or only a part of the field scattered by the j^{th} rod. In the first case, the first sum would represent the total incident field on this rod, whereas in the second case it would also contain a part of the field scattered by the j^{th} rod complementary to the second sum. This question can be answered by observing that from causality the field scattered by the j^{th} rod must propagate away from this rod. It can be demonstrated that the only Fourier-Bessel functions satisfying this condition are the Hankel functions of the first kind. For instance, apart from a multiplying factor, the Hankel function of zeroth order of the first kind is but the Green's function solution for the Helmholtz equation in an homogeneous space with permittivity $\epsilon_{r,\text{ext}}$, under the assumption of a radiation condition at infinity:

$$\nabla^2 \left[-\frac{i}{4} H_0^{(1)}(k_0 n_{\text{ext}} r_j) \right] + k_0^2 \epsilon_{r,\text{ext}} \left[-\frac{i}{4} H_0^{(1)}(k_0 n_{\text{ext}} r_j) \right] = \delta(x)\delta(y) \quad (\text{A.15})$$

From a physical point of view, the Green's function thus defined represents the field that would be generated by an infinitely thin linear source located along the z axis, i.e. parallel to the rods, the space being assumed to be homogeneous and with a permittivity $\epsilon_{r,\text{ext}}$. In order to verify that Hankel functions of the first kind satisfy the radiation condition at infinity for any order, it suffices to consider their asymptotic expression at infinity (Abramovitz 1970):

$$H_m^{(1)}(k_0 n_{\text{ext}} r_j) \cong \sqrt{\frac{2}{\pi k_0 n_{\text{ext}} r_j}} \exp \left[i \left(k_0 n_{\text{ext}} r_j - m \frac{\pi}{2} - \frac{\pi}{4} \right) \right] \quad (\text{A.16})$$

The second sum in Eq. A.14 represents a field scattered by the j^{th} rod. On the contrary, an arbitrary term of the first sum cannot represent a scattered field since, from Eq. A.9, $J_m(s)$ can be written in the form:

$$J_m(s) = H_m^{(1)}(s) + \bar{H}_m^{(1)}(s) \quad (\text{A.17})$$

where $\bar{H}_m^{(1)}(s)$ denotes the complex conjugate of $H_m^{(1)}(s)$. It is quite apparent from Eq. A.16 that $\bar{H}_m^{(1)}(s)$ does not satisfy the radiation condition. This definitely demonstrates that the first sum in Eq. A.14 represents the total incident field striking the j^{th} rod and the second sum the field scattered by the j^{th} rod.

Let us now proceed to the determination of the contribution of the incident source field to the first sum. This field is given by Eq. A.1a, and at any arbitrary point P of space (Fig. A.1), it can be written in the form:

$$E^i(P) = \exp(i\mathbf{k} \cdot \mathbf{OP}) \quad (\text{A.1b})$$

where $(k_0 n_{\text{ext}} \sin \Theta^{\text{inc}}, -k_0 n_{\text{ext}} \cos \Theta^{\text{inc}})$ are the coordinates of the incident wave vector \mathbf{k} . Writing vector \mathbf{OP} as the sum of vectors \mathbf{OO}_j and $\mathbf{O}_j P$, we arrive at the following equation:

$$\begin{aligned} E^i(P) &= \exp\left(i\mathbf{k} \cdot (\mathbf{OO}_j + \mathbf{O}_j \mathbf{P})\right) \\ &= \exp\left[i k_0 n_{\text{ext}} r^j \sin(\Theta^{\text{inc}} - \theta^j)\right] \exp\left[i k_0 n_{\text{ext}} r_j(P) \sin(\Theta^{\text{inc}} - \theta_j(P))\right] \end{aligned} \quad (\text{A.18})$$

where r^j, θ^j denote the polar coordinates of the origin O_j of the local coordinate system in the general xy system represented in Fig. A.1. Let us now use the following formula, given in (Abramovitz 1970):

$$\exp(i\xi \sin(u)) = \sum_{m=-\infty}^{m=\infty} J_m(\xi) \exp(imu) \quad (\text{A.19})$$

The application of Eq. A. 19 leads to the following expression for $E^i(P)$:

$$\begin{aligned} E^i(P) &= \exp\left[i k_0 n_{\text{ext}} r^j \sin(\Theta^{\text{inc}} - \theta^j)\right] \times \\ &\quad \sum_{m=-\infty, +\infty} \exp(im\Theta^{\text{inc}}) J_m(k_0 n_{\text{ext}} r_j(P)) \exp(-im\theta_j(P)) \end{aligned} \quad (\text{A.20a})$$

Since $J_{-m}(s) = (-1)^m J_m(s)$, m can be replaced by $-m$ in Eq. A.20a. This shall simplify the comparison with the terms in Eq. A.14:

$$E^j(P) = \exp\left[i k_0 n_{ext} r_j \sin(\Theta^{inc} - \theta^j)\right] \times \sum_{m=-\infty, +\infty} (-1)^m \exp(-im\Theta^{inc}) J_m(k_0 n_{ext} r_j) \exp(im\theta_j(P)) \quad (\text{A.20b})$$

Eqs. A.20a and A.20b give the development of the incident source field into Fourier-Bessel series in the coordinate system associated with the j^{th} rod. Going back to Eq. A.14, it is now possible to distinguish the coefficients of the Fourier-Bessel series associated with the source field from the coefficients associated with the field scattered by the other rods. These two sets of coefficients will be denoted by $a_{j,m}^{\text{source}}$ and $a_{j,m}^{\text{rods}}$ respectively, and their sum is equal to $a_{j,m}$. From Eq. A.20b, $a_{j,m}^{\text{source}}$ can be identified with the following expression:

$$a_{j,m}^{\text{source}} = (-1)^m \exp\left(i k_0 n_{ext} r_j \sin(\Theta^{inc} - \theta^j) - im\Theta^{inc}\right) \quad (\text{A.21})$$

The three components of the field in the ring surrounding the j^{th} rod can therefore be expressed respectively as follows:

- the source term is:

$$E_{z,j}^{\text{source}}(r_j, \theta_j) = \sum_{m=-\infty, +\infty} a_{j,m}^{\text{source}} J_m(k_0 n_{ext} r_j) \exp(im\theta_j) \quad (\text{A.22})$$

- the field scattered by the other rods in the direction of the j^{th} rod is:

$$E_{z,j}^{\text{rods}}(r_j, \theta_j) = \sum_{m=-\infty, +\infty} a_{j,m}^{\text{rods}} J_m(k_0 n_{ext} r_j) \exp(im\theta_j) \quad (\text{A.23})$$

- the field scattered by the j^{th} rod is:

$$E_{z,j}^d(r_j, \theta_j) = \sum_{m=-\infty, +\infty} b_{j,m} H_m^{(1)}(k_0 n_{ext} r_j) \exp(im\theta_j) \quad (\text{A.24})$$

It has been demonstrated that the total field in the ring can be expressed in terms of three series of coefficients: $a_{j,m}^{\text{source}}$, $a_{j,m}^{\text{rods}}$ and $b_{j,m}$, from which only the

first is known. Before proceeding to the calculation of these components, an observation should be made on Eq. A.24. The expression given by this equation for the field scattered by the j^{th} rod in the circular region surrounding it (see Figure 2.10 in Section 3 of Chapter 2) extends actually to the whole space surrounding this rod. While this result can be rigorously demonstrated from the properties of Fourier-Bessel functions (Maystre 2002), we shall content ourselves with admitting that the field scattered by the j^{th} rod is generated by sources, i.e. by dipoles, located in this rod. Let us note by contrast that Eq. A.23 cannot be extended to the whole space, since the field generated by the dipolar sources located in the other rods ($\neq j$) may present singularities inside these rods.

The validity of Eq. A.24 in the whole space outside the j^{th} rod is a decisive property. It entails that the field represented by the coefficients $b_{j,m}$ actually is the field scattered by the j^{th} rod in the direction of the other rods, which itself is also a part of the field represented by the coefficients $a_{l,m}^{\text{rods}}$, $l \neq j$. Hence, if we now consider the balance of the total incident field at the l^{th} rod, i.e. if we add the incident source field to the fields scattered by all other rods in the direction of the l^{th} rod, we should now be in the position of expressing the coefficients $a_{l,m}$, $m \in [-\infty, +\infty]$ in terms of the coefficients $a_{l,m}^{\text{source}}$, $m \in [-\infty, +\infty]$ and $b_{j,m}$, $(m \in [-\infty, +\infty], j \neq l)$. For this purpose, it is first necessary to resolve a mathematical problem: indeed, the incident field at the l^{th} rod is expressed in a local coordinate system associated with this rod, whereas the fields scattered by the other rods are expressed in the local coordinate system associated with these rods.

The representation of all fields in the unique coordinate system associated with the l^{th} rod can be achieved by using Graf's formula (Abramovitz 1970). This formula expresses in a mathematical form a physically very intuitive result: the field scattered by the j^{th} rod along the direction of the l^{th} rod satisfies in the vicinity of this rod a Helmholtz equation without exhibiting any singularity. This field can therefore be expressed in the form of a Fourier-Bessel series containing only Bessel functions of the first kind. Using the notations presented in Fig. A.1, this formula can be written, in the case where $r_l(P) \leq r_l^j = O_l O_j$, in the following form:

$$\begin{aligned} & H_m^{(1)}(k_0 n_{\text{ext}} r_j(P)) \exp(im\theta_j(P)) \\ &= \sum_{q=-\infty}^{+\infty} \exp(i(m-q)\theta_l^j) H_{q-m}^{(1)}(k_0 n_{\text{ext}} r_l^j) J_q(k_0 n_{\text{ext}} r_l(P)) \exp(iq\theta_l(P)) \end{aligned} \quad (\text{A.25})$$

Eqs. A.24 and A.25 allow expressing the field scattered by the j^{th} rod in the direction of the l^{th} rod in the coordinate system with origin O_l . Therefore, in the case where $r_l(P) \leq r_l^j - R$:

$$E_{z,j}^d(P) = \sum_{m=-\infty}^{+\infty} b_{j,m} \sum_{q=-\infty}^{+\infty} \exp(i(m-q)\theta_l^j) H_{q-m}^{(1)}(k_0 n_{ext} r_l^j) J_q(k_0 n_{ext} r_l(P)) \exp(iq\theta_l(P)) \quad (\text{A.26a})$$

or, by reversing the indices m and q :

$$E_{z,j}^d(P) = \sum_{q=-\infty}^{+\infty} b_{j,q} \sum_{m=-\infty}^{+\infty} \exp(i(q-m)\theta_l^j) H_{m-q}^{(1)}(k_0 n_{ext} r_l^j) J_m(k_0 n_{ext} r_l(P)) \exp(im\theta_l(P)) \quad (\text{A.26b})$$

The field $E_{z,l}^{rods}$ in the ring surrounding the l^{th} rod, which is obtained by replacing the index j by the index l in Eq. A.23, can be identified to the sum of the fields scattered by the $N - 1$ other rods $\sum_{j \neq l} E_{z,j}^d$. The sum of these fields can be deduced from equations similar to Eq. A.26b. This identification leads to the following equation:

$$a_{l,m}^{rods} = \sum_{j \neq l} \sum_{q=-\infty, +\infty} b_{j,q} \exp(i(q-m)\theta_l^j) H_{m-q}^{(1)}(k_0 n_{ext} r_l^j) \quad (\text{A.27})$$

Adding the coefficient $a_{l,m}^{source}$ of the source field given by Eq. A.22 to the coefficients $a_{j,m}^{rods}$, $a_{l,m}$ can be expressed in terms of the coefficients $b_{j,q}$ of the fields scattered by the other rods:

$$a_{l,m} = (-1)^m \exp(ik_0 n_{ext} r_l \sin(\Theta^{inc} - \theta_l) - im\Theta^{inc}) + \sum_{j \neq l} \sum_{q=-\infty, +\infty} b_{j,q} \exp(i(q-m)\theta_l^j) H_{m-q}^{(1)}(k_0 n_{ext} r_l^j) \quad (\text{A.28})$$

References

- Abbott EA (1992) Flatland, a Romance of Many Dimensions. Dover Publications, New York
- Abramovitz M, Stegun I (1970) Handbook of Mathematical Functions. Dover Publications, New York
- Abram I, Robert I, Kuszelewicz K (1998) Spontaneous emission control in semiconductor microcavities with metallic or Bragg mirrors. IEEE J Quant Elect 34 : 71
- Agrawal GP (2001) Nonlinear Fiber Optics. Academic Press, 3rd edition
- Agrawal GP, Dutta N (1993) Semiconductor Lasers. Van Nostrand Reinhold, New York
- Akalin T, Danglot J, Vanbesien O, Lippens D (2001) A highly directive dipole antenna embedded in a Fabry-Perot type cavity. IEEE Microwave and Wireless Components Lett 12 : 48-50
- Akahane Y, Asano T, Song BS, Noda S (2003) High-Q nanophotonic in a two-dimensional photonic crystal. Nature 425 : 944-947
- Albert JP, Jouanin C, Cassagne D, Bertho D (2000) Generalized Wannier function method for photonic crystals. Phys Rev B 61 : 4381
- Almogy G, Yariv A (1994) Second harmonic generation in absorptive media. Optics Lett 19 : 1828
- Anderson PW (1985) The question of classical localization. A theory of white paint? Phil Mag B 52 : 505-509
- Andreani LC, Panzarini G, Gérard JM (1999) Strong-coupling regime for quantum boxes in pillar microcavities: theory. Phys Rev B 60 : 13276
- Angot A (1982) Compléments de Mathématiques (in French). Masson, 6th edition, Paris New York
- Arbore MA, Galvanauskas A, Harter D, Chou MH, Fejer MM (1997) Engineerable compression of ultrashort pulses by use of second-harmonic generation in chirped-period-poled lithium niobate. Optics Lett 22 : 1341
- Armstrong JA, Bloembergen N, Ducuing J, Pershan PS (1962) Interactions between light waves in a non linear dielectric. Phys Rev 127 : 1918
- Armani DK, Kippenberg TJ, Spillane SM, Vahala KJ (2003) Ultra-high Q toroid microcavity on a chip. Nature 421 : 925-928
- Ashcroft NW, Mermin ND (1976) Solid State Physics. Saunders College Publishing
- Astratov VN, Bogomolov VN, Kapyanskii AA, Prokofiev AV, Samoilovich LA, Samoilovich SM, Vlasov YuA (1995) Optical spectroscopy of opal matrices with CdS embedded in its pores: quantum confinement and photonic band gap effects. Nuovo Cimento D17 : 1349
- Astratov VN, Stevenson RM, Culshaw IS, Whittaker DM, Skolnick MS, Krauss T.F, De La Rue RM (2000) Heavy photon dispersions in photonic crystal waveguides. Appl Phys Lett 77 : 178-180

- Baas A, Karr JPh, Romanelli M, Bramati A, Giacobino E (2004) Optical bistability in semiconductor Microcavities in the nondegenerate parametric oscillation regime: analogy with the optical parametric oscillator. *Phys Rev B* 70 : 161307 -
- Baba T, Hamano T, Koyama F (1991) Spontaneous emission factor of a microcavity DBR surface emitting laser. *IEEE J Quant Electron* 27 : 1347-
- Baba T, Hamano T, Koyama F, Iga K (1992) Spontaneous emission-factor of a microcavity DBR surface emitting laser (II), effect of electron confinement. *IEEE J Quant Electron.* 28 : 1310-
- Baba T, Fujita M, Sakai A, Kihara M, Watanabe R (1997) Lasing characteristics of In-GaAsP-InP strained quantum well microdisk injection lasers with diameter of 2-10 μm . *IEEE Photon Technol Lett* 9 : 878-
- Baba T, Fukaya N, Yonekura J (1999) Observation of light propagation in photonic crystal optical waveguides with bend. *Electron Lett* 35 : 654-655
- Baba T, Matsumoto T. (2002) Resolution of photonic crystal superprism. *Appl Phys Lett* 81 : 2325-2327
- Baliarda CP, Romeu I, Cardama A (2000) The Koch monopole: a small fractal antenna. *IEEE Trans Antennas Propag* 48 : 1773-1781
- Bao KD, McPhedran RC, Nicorovici NA, Poulton CG, Botten LC (2000) The electromagnetic modes and homogenization for a cubic lattice of spheres. *Physica B* 279 : 162-163
- Barnes WL, Preist TW, Kitson SC, Sambles JR (1996) Physical origin of photonic energy gaps in the propagation of surface plasmons on gratings. *Phys Rev B* 54 : 6227-6244
- Barnes WL, Kitson SC, Preist TW, Sambles JR (1997) Photonic surfaces for surface plasmon-polaritons. *J Opt Soc. Am* 14 : 1654-1661
- Barnes WL, Björk G, Gérard JM, Jonsson P, Wasey J, Worthing P, Zwiller V (2002) Solid-state single photon sources : light collection strategies. *Eur Phys J D* 18 : 197-
- Bayer M, Reinecke TL, Weidner L, Larionov A, Mc Donald A, Forchel A (2001) Inhibition and Enhancement of the Spontaneous Emission of Quantum Dots in Structured Microresonators. *Phys Rev Lett* 86 : 3168-
- Benabid F, Knight JC, Antopoulos G, Russell P St.J (2002a) Stimulated Raman scattering in hydrogen-filled hollow-core photonic crystal fiber. *Nature* 298 : 399–402
- Benabid F, Knight JC, Russell P St.J (2002b) Particle levitation and guidance in hollow-core photonic crystal fiber. *Opt.Express* 10 : 1195–1203
- Bennett CH, Brassard G, Ekert AK (1992) Quantum cryptography. *Sci Am* 267 : 50-
- Benisty H, De Neve H, Weisbuch C (1998a) Impact of planar microcavity effects on light extraction: I. basic concepts and analytical trends. *IEEE J Quant Electron* 34 : 1612-1631
- Bénisty H, De Neve H, Weisbuch C (1998b) Impact of planar microcavity effects on light extraction : II. Selected exact simulation and role of photon recycling. *IEEE J Quant Electron.* 34 : 1632-1643
- Benisty H, Weisbuch C, Labilloy D, Rattier M, Smith CJM, Krauss TF, De La Rue RM, Houdré R, Oesterle U, Cassagne D (1999) Optical and confinement properties of two-dimensional photonic crystals. *J Lightwave Technol* 17 : 2063-2077
- Benisty H, Labilloy D, Weisbuch C, Smith CJM, Krauss TF, Béraud A, Cassagne D, Jouannin C (2000) Radiation losses of waveguide-based two-dimensional photonic crystals : positive role of the substrate. *Appl Phys Lett* 76 : 532-534

- Benisty H, Lalanne P, Olivier S, Rattier M, Weisbuch C, Krauss TF, Smith CJM, Jouanin C, Cassagne D (2002) Finite-depth and intrinsic losses in vertically etched two-dimensional photonic crystals. *Optical and Quantum Electronics* 34 : 205-215
- Bérenger JP (1994) A perfectly matched layer for the absorption of electromagnetic waves. *J Computational Physics* 14 : 185-200
- Berger V (1997b) Second harmonic generation in monolithic cavities. *J Opt Soc Am B* 14 : 1351-
- Berger V (1998) Nonlinear photonic crystals. *Phys Rev Lett* 81 : 4136-
- Berger V (1999) Photonic crystals for nonlinear optical frequency conversion in : Benisty H *et al.* (eds) *Confined Photon Systems : fundamentals and applications*. Springer, Heidelberg
- Berger V, Gauthier-Lafaye O, Costard E (1997a) Fabrication of a 2D photonic bandgap by a holographic method. *Electron Lett.* 33 : 425-426
- Birks TA, Roberts PJ, Russell PStJ, Atkin DM, Shepherd T.J (1995) Full 2-D photonic bandgaps in silica/airstructures. *Electron Lett* 31 : 1941-1942
- Birks T.A, Knight JC, Russel PStJ (1997) Endlessly single-mode photonic crystal fiber. *Opt Lett* 22 : 961-963
- Birner A, Wehrspohn RB, Gösele UM, Busch K (2001) Silicon-based photonic crystals. *Adv Mater* 13 : 377-388
- Björk G (1994) On the spontaneous lifetime change in an ideal planar microcavity- Transition from a mode continuum to quantized modes. *IEEE J Quant Electron* 30 : 2314-
- Björk G, Yamamoto Y (1991) Analysis of semiconductor microcavity lasers using rate equations. *IEEE J Quant Electron* 27 : 2386-2396
- Blanco A, Chomski E, Grabczak S, Ibiskate M, John S, Leonard SW, Lopez C, Meseguer F, Miguez H, Mondia JP, Ozin GA, Toader O, van Driel HM (2000) Large-scale synthesis of a silicon photonic crystal with a complete three-dimensional bandgap near 1.5 micrometers. *Nature* 405 : 437-440
- Bloch F (1928) Über die Quantenmechanik der Electronen in Kristallgittern. *Z. Physik* 52 : 555-600
- Bogaerts W, Bienstman P, Taillaert D, Baets R, De Zutter D (2001) Out-of-plane scattering in photonic crystal slabs. *IEEE Phot Technol Lett* 13 (6) : 565-567
- Bohren CF, Huffman DR (1984) *Absorption and scattering of light by small particles*. Wiley, New York, Chap. 9
- Bond A, Dapkus PD, O'Brien J (1998) Aperture placement effects in oxide confined vertical cavity surface emitting lasers. *IEEE Photon Technol Lett* 10 : 1362-
- Born M, Wolf E (1965) *Principles of Optics*. Pergamon Press
- Boroditsky M, Krauss T.F, Cocciali R, Vrijen R, Bhat R, Yablonovitch E (1999) Light extraction from optically pumped light-emitting diode by thin-slab photonic crystal. *Appl Phys Lett* 75 : 1036-1038
- Bortz ML, Fujimura M, Fejer MM (1994) Increase acceptance bandwidth for quasi-phase matched second harmonic generation in LiNbO₃ waveguides. *Electron Lett* 30 : 34-
- Boscolo S, Conti C, Midrio M, Someda CG (2002) Numerical analysis of propagation and impedance matching in 2-D photonic crystal waveguides with finite length. *J Light-wave Technol* 20 : 304-310
- Bossavit A (1989) Simplicial finite elements for scattering patterns in electromagnetism. *Comput Method Appl Mech Eng* 76 : 299-316

- Bouwmeester A, Ekert A, Zeilinger A (2000) The physics of quantum information. Springer, Berlin
- Bozzi M, Perregini L (2000) Frequency selective surfaces in the gigahertz and terahertz region : analysis and experimental results. SPIE Proceedings (The-International-Society-for-Optical-Engineering) 4111 : 141-151
- Braginsky VB, Gorodetsky ML, Ilchenko VS (1989) Quality factor and non-linear properties of optical whispering gallery modes. Phys Lett A 137 : 393-
- Brassard G, Lütkenhaus N, Mor T, Sanders BC (2000) Limitations on practical quantum cryptography. Phys Rev Lett 85 : 1330-
- Braun PV, Wiltzius P (1999) Electrochemically grown photonic crystals. Nature 402 : 603-604
- Braun PV, Zehner RW, White CA, Weldon MK, Kloc C, Patel SS, Wiltzius P (2001) Epitaxial growth of high dielectric contrast three-dimensional photonic crystals. Adv Mater 13 : 721-724
- Bridges T.J, Pollack MA (1970) Variable metal mesh coupler for far infrared lasers. Appl Opt 9 : 2511-2516
- Brillat T, De Lustrac A, Gadot F, Akman soy E (2002) The use of controllable photonic bandgap (CPBG) materials: an antenna application. Optical and Quantum Electronics 34 : 265-277
- Broderick NGR, Ross GW, Offerhaus HL, Richardson DJ, Hanna DC (2000) Hexagonally Poled Lithium Niobate : A two-dimensional nonlinear photonic crystal. Phys Rev Lett 84 : 4345-
- Broeng J, Sondergaard T, Barkou SE, Barbeito PM, Bjarklev A (1999) Waveguidance by the photonic bandgap effect in optical fibres. Journal of Optics A 1 : 477-482
- Borson SD, Yokoyama H, Ippen EP (1990) Spontaneous emission rate alteration in optical waveguide structures. IEEE J Quant Electron 26 : 1492-
- Brown ER, Parker CD, Yablonovitch E (1993) Radiation properties of a planar antenna on a photonic-crystal substrate. J Opt Soc Am B 10 : 404-407
- Brown ER, Parker CD, McMahon CD (1994) Effect of surface composition on the radiation pattern from a photonic planar dipole antenna. Appl Phys Lett 64 : 3345-3347
- Burstein E, Weisbuch C (1995) Confined electrons and photons : New physics and applications. Plenum, New-York
- Bush K, John S (1999) Liquid crystal photonic band gap materials : the tunable electromagnetic vacuum. Phys Rev Lett 83 : 967-970
- Campbell M, Scharp D, Harrison M, Denning R, Tuberfield A (2000) Fabrication of photonic crystals for the visible spectrum by holographic lithography. Nature 404 : 53-56
- Carbonell O (1998) Electromagnetic analysis of active and passive devices for space applications. Ph.D. thesis, Lille University
- Casey HC, Panish MB (1978) Heterostructure Lasers. Academic Press
- Cassagne D, Jouanin C, Bertho D (1996) Hexagonal photonic band gaps. Phys Rev B 53 : 7134-
- Cassagne D (1997) Matériaux à Bandes Interdites Photoniques. PhD thesis (in French) Montpellier University
- Chan CH (1995) Analysis of frequency selective surfaces in : Wu TK Frequency selective surface and grid array (pp. 27-85). Wiley Inter-Science, New York
- Chan YS, Chan CT, Liu ZY (1998) Photonic band gaps in two dimensional photonic quasi-crystals. Phys Rev Lett 80 : 956-

- Chang RK, Campillo AJ (1996) Optical processes in microcavities. World Scientific, Singapore
- Chelnokov A, Rowson S, Lourtioz JM, Duvillaret L, Coutaz JL (1997) Terahertz characterization of mechanically machined 3D photonic crystal. Electron Lett 33 : 1981-1983
- Chelnokov A, Rowson S, Lourtioz JM, Duvillaret L, Coutaz JL (1998) Light controllable defect modes in a three-dimensional photonic crystals. Electron Lett 34 : 1966-1967
- Chelnokov A, Rowson S, Lourtioz JM, Berger V, Courtois JY (1999) An Optical Drill for the Fabrication of Photonic Crystals. J Opt A : Pure and Applied Optics 1 : L3-L6
- Chelnokov A, Wang K, Rowson S, Garoche P, Lourtioz JM (2000) Near-infrared Yablonovite-like photonic crystals by focused-ion-beam etching of macroporous silicon. Appl Phys Lett 77 : 2943-2945
- Chen JC, Haus HA, Fan S, Villeneuve PR, Joannopoulos JD (1996) Optical filters from photonic band gap air bridges. IEEE J Lightwave Technol 14 : 2575-
- Cheng C, Scherer A, Arbet-Engels V, Yablonovitch E (1996) Lithographic band gap tuning in photonic band gap crystals. J Vac Sci Technol B 14 : 4110-4114
- Cheng SD, Biswas R, Ozbay E, McCalmont S, Tuttle G, Ho KM (1995) Optimized antennas on photonic band gap crystals. Appl Phys Lett 67 : 3399-3401
- Cheng SSM, Li LM, Chan CT, Zhang ZQ (1999) Defect and transmission properties of two-dimensional quasiperiodic photonic band-gap systems. Phys Rev B 59 : 4091-
- Chew WC, Gürel L, Wang YM, Otto G, Wagner RL, Liu QH (1992) A generalized recursive algorithm for wave-scattering solutions in two dimensions. IEEE Trans Microwave Theory and Techniques 40 : 716-723
- Chiao RY, Steinberg AM (1997) Tunnelling times and superluminality. Prog Optics 37 : 345-405
- Chigrin D, Lavrinenko A, Yarotsky D, Gaponenko S (1999) Observation of total omnidirectional reflection from a one-dimensional dielectric lattice. Applied Physics A: Materials Science & Processing, 68 : 25-28
- Chow E, Lin SY, Johnson SG, Villeneuve PR, Joannopoulos JD, Wendt JR, Vawter GA, Zubrzycki W, Hou H, Alleman A (2000) Three-dimensional control of light in a two-dimensional crystal slab. Nature 407 : 983-986
- Chul-Sick Kee, Jae-Eun Kim, Hae Yong Park, Ikmo Park, Lim H (2000) Two-dimensional tunable magnetic photonic crystals. Phys Rev B 61 : 15 523-5
- Chutinan A, Okano M, Noda S (2002) Wider bandwidth with high transmission through waveguide bends in two-dimensional photonic crystal slabs. Appl Phys Lett 80 : 1698-1700
- Cocciali R, Yang Fei-Ran, Itoh T (1999) Aperture-coupled patch antenna on UC-PBG substrate. IEEE Trans Microwave Theory and Tech 47 : 2123-2130
- Cohen-Tannoudji C, Diu B, Laloe F (1973) Mécanique quantique (in French). vol.1, Hermann, Paris
- Cohen-Tannoudji C, Dupont-Roc J, Grymborg G (1992) An introduction to quantum electrodynamics and Photons and atoms. Wiley, New York
- Coldren LA, Corzine SW (1995) Diode lasers and photonic integrated circuits. Wiley, New York
- Collardey S (2002) Applications des matériaux à bande interdite photonique à la réduction de la S.E.R. d'un réseau d'antennes. PhD thesis (in French), Rennes University
- Collot L, Lefèvre-Seguin V, Brune M, Raymond JM, Haroche S (1993) Very-high Q whispering – gallery mode resonances observed on fused silica microspheres. Europhys Lett. 23 : 327-

- Cregan RF, Mangan BJ, Knight JC, Birks TA, Russel PStJ, Roberts PJ, Allan DC (1999) Single-mode photonic bandgap guidance of light in air. *Science* 285 : 1537-39
- Cuisin C, Chelnokov A, Decanini D, Peyrade D, Chen Y, Lourtioz JM (2002) Sub-micrometer dielectric and metallic structures fabricated from resist templates. *Optical and Quantum Electronics* 34 : 13-26
- D'Aguanno G, Centini M, Scalora M, Sibilia C, Bloemer MJ, Bowden CM, Haus JW, Bertolotti M (2001) Group velocity, energy velocity and superluminal propagation in finite photonic band gap structures. *Phys Rev E* 63 : 36610-
- Danglot J, Carbonell J, Fernandez M, Vanbésien O, Lippens D (1998) Modal analysis of guiding structures patterned in a metallic photonic crystal. *Appl Phys Lett* 73 : 2714-
- Dantec NL, Benyattou T, Guillot G, Spisser A, Seassal C, Leclercq JL, Viktorovitch P, Rondi D, Blondeau R (1999) Tunable microcavity based on InP-Air Bragg mirrors. *IEEE J Sel Top in Quant Electron* 5 : 111-114
- Dautray R, Lions JL (1984) Analyse mathématique et calcul numérique pour les sciences et techniques (in French). Masson, Paris
- David S (2003) Étude de composants à cristaux photoniques dans la filière silicium pour les longueurs d'onde des télécommunications optiques (in French). Ph.D. Thesis, Orsay University
- David S, Chelnokov A, Lourtioz JM (2000) Wide angularly isotropic photonic bandgaps from 2D photonic crystals with archimedean-like tiling. *Opt Lett.* 25 : 1001-
- David S, Chelnokov A, Lourtioz JM (2001) Isotropic photonic structures : Archimedean-like tilings and quasi-crystal. *IEEE J Quant Electron* 37 : 1427-
- David S, Chelnokov A, Lourtioz JM (2002) Lateral Confinement in Macroporous Silicon Crystals. *J Opt A : Pure and Applied Optics* 4 : 468-473
- Defos du Rau M (1997) PhD Thesis (in French), University of Bordeaux
- Delbeke D, Bockstaele R, Bienstman P, Baets R, Benisty H (2002) High-Efficiency Semiconductor resonant-Cavity Light-Emitting Diodes: A Review. *IEEE J Selected Topics in Quant Electron* 8 : 189-206 ; see other articles in the same issue of this journal.
- De Neve H, Blondelle J, Vandaele P, Demeester P, Baets R, Borghs G (1997a) Recycling of guided mode light emission in planar microcavity light emitting diodes. *Appl Phys Lett* 70 : 799-
- De Neve H (1997b) Study and realisation of microcavity based LEDs. PhD Thesis, University of Gent
- De Rossi A, Berger V, Calligaro M, Leo G, Ortiz V, Marcadet X (2001) Parametric fluorescence in oxidized aluminum gallium arsenide waveguides. *Appl Phys Lett* 79 : 3758-
- Deubel M, von Freymann G, Wegener M, Pereira S, Busch K, Soukoulis CM (2004) Direct Laser Writing of Three-Dimensional Photonic Crystal Templates for the Telecommunication Regime. *Nature Mater.* 3 : 444-447
- Dewar G (2001) Candidates for $\mu < 0$, $\epsilon < 0$ nanostructures. *Intern J Modern Physics B* 15 : 3258-3265
- Dobrowolski JA, Lowe D (1978) Optical thin film synthesis program based on the use of Fourier transform. *Appl Optics* 17 : 3039-
- Dobson DC (1999) An efficient method for band structure calculations in 2D photonic crystals. *J Comput Phys* 149 : 363-376
- Dowling JP, Scalora M, Bloemer MJ, Bowden CM (1994) The photonic band edge laser: a new approach to gain enhancement. *J Appl Phys* 75 : 1896-1899

- Dudley JM, Provino L, Grossard N, Maillotte H, Windeler R, Eggleton B, Coen S (2002) Supercontinuum generation in airsilica microstructured fibers with nanosecond and femtosecond pulse pumping. *J Opt Soc Am B* 19 : 765–771
- Dulea M, Severin M, Riklund R (1990) Transmission of light through deterministic aperiodic nonFibonacci multilayers. *Phys Rev B* 42 : 3680-
- Dumeige Y, Vidakovic P, Sauvage S, Sagnes I, Levenson JA, Sibilia C, Centini M, D'Aguanno G, Scalora M (2001) Enhancement of Second Harmonic Generation in a 1D Semiconductor Photonic Band Gap. *Appl Phys Lett* 78 : 3021-
- Dumeige Y, Sagnes I, Monnier P, Vidakovic P, Abram I, Meriadec C, Levenson A (2002) Phase matched frequency doubling at photonic band edges : efficiency scaling as the fifth power of the length. *Phys Rev Lett* 89 : 043901-
- Eastham PR, Whittaker DM (2003) Steady states of a $\chi^{(3)}$ parametric oscillator with coupled polarizations. *Phys Rev B* 68 : 075324-
- Ebbesen TW, Lezec HJ, Ghaemi HF, Thio T, Wolff PA (1998) Extraordinary Optical Transmission through Sub-Wavelength Hole Arrays. *Nature* 391: 667-669
- Economou EN, Sigalas MM (1993) Classical wave propagation in periodic structures : Cermet versus network topology. *Phys Rev B* 48 : 13434-13438
- Eggleton BJ, Kerbage C, Westbrook PS, Windeler RS, Hale A (2001) Microstructured optical fiber devices. *Opt Express* 9 : 698–713
- Ehrfeld W, Schmidt A (1998) Recent developments in deep X-ray lithography. *J Vac Sci Technol B* 16 : 3526-3534
- Eisele H, Haddad GI (1998) Two terminal millimeter wave sources. *IEEE Trans Microwave Theory and Tech* 46 : 739-746
- Elachi C (1976) Waves in active and passive periodic structures at microwave frequencies. *Proc IEEE* 64 : 1666-
- Elsherbeni AZ, Kishk AA (1992) Modeling of cylindrical objects by circular dielectric and conducting cylinders. *IEEE Trans on Antennas and Propagation* 40 : 96-99
- Enoch S, Gralak B, Tayeb G (2002a) Enhanced emission with angular confinement from photonic crystals. *Appl Phys Lett* 81 : 1588-1591
- Enoch S, Tayeb G, Sabouroux P, Guérin N, Vincent P (2002b) A metamaterial for directive emission. *Phys Rev Lett* 89 : 213902-1/4
- Enoch S, Popov E, Nevière M, Reinisch R (2002c) Enhanced light transmission by hole arrays. *J Opt A: Pure Appl Opt* 4 : S83-S87
- Fan S, Villeneuve PR, Joannopoulos JD, Haus HA (1996) Channel drop tunneling through localized states. *Phys Rev Lett* 80 : 960-963
- Fan S, Villeneuve PR, Joannopoulos JD (1997) High extraction efficiency of spontaneous emission from slabs of photonic crystal. *Phys Rev Lett* 78 : 3294-
- Fan S, Villeneuve PR, Joannopoulos JD, Haus HA (1998) Channel drop filters in photonic crystals. *Optics express* 3 : 4-11
- Feigel A, Kotler Z, Sfez B, Arsh A, Klebanov M, Lyubin V (2000) Chalcogenide glass-based three-dimensional photonic crystals. *Appl Phys Lett* 77 : 3221-3224
- Fejer MM (1994) Nonlinear optical frequency conversion. *Phys Today*, May 1994, p 25
- Fejer MM, Magel GA, Jundt DH, Byer RL (1992) Quasi-Phase-Matched Second Harmonic Generation : Tuning and Tolerances. *IEEE J Quant Electron* 28 : 2631-
- Felbacq D (1994) Étude théorique et numérique de la diffraction de la lumière par des ensembles de tiges parallèles (in French). PhD Thesis (in French), University of St Jerome (Marseille)

- Felbacq D, Bouchitté G (1997) Homogenization of a set of parallel fibers. *Waves in Random Media* 7 : 245-256
- Felbacq D, Tayeb G, Maystre D (1994) Scattering by a random set of parallel cylinders. *J Opt Soc Am A* 11 : 2526-2538
- Felbacq D, Maystre D, Tayeb G (1995) Localization of light by a set of parallel cylinders. *Journal Modern Optics* 42 : 473-482
- Felbacq D, Guizal B, Zolla F (1998) Limit analysis of the diffraction of a plane wave by a stratified periodic medium. *J Math Phys* 39 (9) : 4604-4607
- Ferrando A, Silvestre E, Miret JJ, Andrés P, Andrés MV (2000a) Vector description of higher-order modes in photonic crystal fibers. *J Opt Soc Am A* 17 : 1333-1340
- Ferrando A, Silvestre E, Miret JJ, Andrés P (2000b) Nearly zero ultraflattened dispersion in photonic crystal fibers. *Opt Lett* 25 : 790-792
- Ferrando A, Zácarés M, Fernandez de Cordoba P, Binosi D, Monsoriu JA (2003) Spatial soliton formation in photonic crystal fibers. *Optics Express* 11 : 452-459
- Ferrini R, Houtré R, Bénisty H, Qiu M, Moosburger J (2003) Radiation losses in planar photonic crystals : two-dimensional representation of hole depth and shape by an imaginary dielectric constant. *J Opt Soc Am B* 20 : 469-478
- Figotin A, Vitebsky I (2001) Non reciprocal magnetic photonic crystals. *Phys Rev E* 63 : 066609-1/17
- Fiore A, Berger V, Rosenthaler E, Bravetti P, Nagle J (1998) Phase matching using an isotropic nonlinear material. *Nature* 391 : 463-
- Fleming JG, Lin SY (1999) Three-dimensional photonic crystal with a stop-band from 1.35 to 1.95 μm . *Opt Lett* 24 : 49-51
- Fleming JG, Lin SY, El-Kady I, Biswas R, Ho KM (2002) All-metallic three-dimensional photonic crystals with a large infrared bandgap. *Nature* 417 : 52-55
- Foresi JS, Villeneuve PR, Ferrera J, Thoen E.R, Steinmeyer G, Fan S, Joannopoulos JD, Kimmerling EC, Smith HI, Ippen EP (1997) Photonic bandgap microcavities in optical waveguides. *Nature* 390 : 143-145
- Fujita M, Ushigome R, Baba T (2000) Continuous wave lasing in GaInAsP microdisk injection laser with threshold current of 40 μA . *Electron Lett* 36 : 790-
- Fujita M, Ushigome R, Baba T (2001) Large spontaneous emission factor of 0.1 in a microdisk injection laser. *IEEE Photon Technol Lett* 13 : 403-
- Furusawa K, Malinowski AN, Price JH, Monro TM, Sahu JK, Nilsson J, Richardson DJ (2001) Cladding pumped ytterbium doped fiber laser with holey inner and outer cladding. *Optics Express* 9 : 714-720
- Gadot F (1998) Modélisation et caractérisation expérimentale des matériaux à bandes interdites photoniques (BIP) en micro-ondes (in French). PhD Thesis, University of Orsay
- Gadot F, Chelnokov A, De Lustrac A, Crozat P, Lourtioz JM, Cassagne D, Jouanin C (1997) Experimental demonstration of complete photonic bandgap in graphite structure. *Appl Phys Lett* 71 : 1780-1782
- Garcia N, Nieto-Vesperinas M (2002a) Is there an experimental verification of a negative index of refraction yet? *Opt Lett* 27 : 885-887
- Garcia N, Nieto-Vesperinas M (2002b) Left-handed materials do not make a perfect lens. *Phys Rev Lett* 88 : 207403-1/3, see also answer from: Pendry 2003
- Garet F (1997) Génération optoélectronique d'impulsions électromagnétiques ultracourtes : application à la spectroscopie THz. PhD Thesis (in French), University of Annecy

- Gayral B, Gérard JM (2000) Strong Purcell effect for InAs quantum boxes in high-Q wet-etched microdisks. *Physica E7* : 641-
- Gayral B, Gérard JM, Lemaître A, Dupuis C, Manin L, Pelouard, JL (1999) High-Q wet-etched GaAs microdisks containing InAs quantum boxes. *Appl Phys Lett 75* : 1908-
- Gayral B, Gérard JM, Sermage B, Lemaître A, Dupuis C (2001) Time-resolved probing of the Purcell effect for InAs quantum boxes in GaAs microdisks. *Appl Phys Lett 78* : 2828-
- Gérard JM (2003) Solid-state cavity quantum electrodynamics with self-assembled quantum dots in P. Michler (ed.) *Single Quantum Dots: Physics and Applications, Topics of Applied Physics*, Springer, Heidelberg
- Gérard JM, Gayral B (1999) Strong Purcell effect for InAs quantum boxes in three-dimensional solid-state microcavities. *J Lighwave Technol 17* : 2089-
- Gérard JM, Izraël A, Marzin JY, Padjen R, Ladan FR (1993) Photonic bandgap of two-dimensional dielectric crystals. *Solid State Electr 37* : 1341-
- Gérard JM, Cabrol O, Sermage B (1996a) InAs quantum boxes : highly efficient radiative traps for light emitting devices on Si. *Appl Phys Lett 68* : 3123-3125
- Gérard JM, Barrier JM, Marzin JY, Kuszelewicz R, Manin L, Costard E, Thierry-Mieg V, Rivera T (1996b) Quantum boxes as active probes for photonic microstructures : the pillar microcavity. *Appl Phys Lett 69* : 449-
- Gérard JM, Sermage S, Gayral B, Costard E, Thierry-Mieg V (1998) Enhanced spontaneous emission for InAs quantum boxes in a monolithic optical microcavity. *Phys Rev Lett 81* : 1110-
- Golubev VG, Davydov VY, Kartenko NF, Kurdyukov DA, Medvedev AV, Pevtsov AB, Scherbakov AV, Shadrin EB (2001) Phase transition-governed opal-VO₂ photonic crystal. *Appl Phys Lett 79* : 2127-2129
- Gonzalo R, Martinez B, Mann CM, Pellemans H, Bolivar PH, De Maagt P (2002) A low-cost fabrication technique for symmetrical and asymmetrical layer-by-layer photonic crystals at submillimeter-wave frequencies. *IEEE Trans. Microwave Theory and Tech 50* : 2384-2392
- Gralak B, Enoch S, Tayeb G (2000) Anomalous refractive properties of photonic crystals. *J Opt Soc Am A 17* : 1012-1020
- Granet G, Guizal B (1996) Efficient implementation of the coupled waves method for metallic gratings in TM polarization. *J Opt Soc Am A 13* : 1019-1023
- Grbic A, Eleftheriades GV (2002) Experimental verification of backward-wave radiation from a negative refractive index metamaterial. *J Appl Phys 92* : 5930-5935
- Greffet JJ (1991) Waves in random media 3 : S65-S73
- Grüning U, Lehmann V, Ottow S, Busch K (1996) Macroporous silicon with a complete 2D PBG centered at 5 μm. *Appl Phys Lett 68* : 747-749
- Guenneau S, Zolla F (2000) Homogenization of three-dimensional finite photonic crystals. *Proceedings PIERS 27* : 91-127
- Guenneau S, Nicolet A, Zolla F, Geuzaine C, Meys B (2001) A finite element formulation for spectral problems in optical fibers. *COMPEL 1* : 120-131
- Guida G, Maystre D, Tayeb G, Vincent P (1998) Homogeneization of two-dimensional metallic photonic crystals. *Journ Opt Soc Am JOSA A 15* : 2308-2315
- Happ T, Markard A, Kamp M, Forchel A, Srinivasan A (2001) Single-mode operation of coupled-cavity lasers based on two-dimensional photonic crystals. *Appl Phys lett 79* : 4091-4093

- Happ TD, Tartakovskii I, Kulakovskii VD, Reithmaier JP, Kamp M, Forchel A (2002) Enhanced light emission of InGaAs quantum dots in a two-dimensional photonic crystal defect microcavity. *Phys Rev B* 66 : R041303-
- Happ T, Kamp M, Forchel A, Gentner JL, Goldstein L (2003) Two-dimensional photonic crystal coupled-defect laser diode. *Appl Phys Lett* 82 : 4-6
- Harvey A (1959) Wave propagation in periodic structures: Electric Filters and crystal lattices. *IRE Trans* 8 : 30-
- Harvey A (1963) *Microwave Engineering*. Academic Press, New-York
- Haroche S, Kleppner D (1989) Cavity quantum electrodynamics. *Physics Today* 42 : 24-
- Hessel A, Oliner AA (1965) A new theory of Wood's anomalies on optical gratings. *Appl. Optics* : 332-354
- Hippert F, Gratias D (1994) Lectures on Quasicrystals. Les Éditions de Physique (Hippert F, Gratias D eds), Les Ulis
- Ho K, Chan C, Soukoulis C (1990) Existence of a Photonic Gap in Periodic Dielectric Structures. *Phys Rev Lett* 65 : 3152-3155
- Ho K, Chan C, Soukoulis C, Biswas R, Sigalas M (1994) Photonic bandgaps in three dimensions : new layer by layer periodic structures. *Solid State Communications* 89 : 413-416
- Ho ST, Wang, L, Park S (1999) Spontaneous emission control and microcavity light emitters conversion in : Benisty H *et al.* (eds) *Confined Photon Systems : Fundamentals and Applications* (pp. 243-297). Springer, Heidelberg
- Holland BT, Blanford CE, Stein A (1998) Synthesis of macroporous minerals with highly ordered three-dimensional arrays of spheroidal voids. *Science* 281 : 538-540
- Hood CJ, Chgapman MS, Lynn TW, Kimble HJ (1998) Real-time cavity-QED with single atoms. *Phys Rev Lett* 80 : 4157-
- Hougaard KG, Broeng J, Bjarklev A (2003) Low pump power photonic crystal fibre amplifiers. *Electron Lett* 39 : 599-600
- Huffaker DL, Deppe DG (1997) Improved performance of oxide-confined vertical-cavity surface emitting lasers using a tunnel injection active region. *Appl Phys Lett* 71 : 1449-1451
- Husakou AV, Herrmann J (2001) Supercontinuum generation of higherorder solitons by fission in photonic crystal fibers. *Phys Rev Lett* 87 : 203901-
- Hutley MC, Maystre D (1976) The total absorption of light by a diffraction grating Optics Commun 19 : 431-436
- Imamoglu A, Awschalom D, Burkard G, DiVincenzo DV, Loss D, Sherwin M, Small A (1999) Quantum Information Processing Using Quantum Dot Spins and Cavity QED. *Phys Rev Lett* 83 : 4204-
- Inoue M, Fujii T (1997) A theoretical analysis of magneto-optical Faraday effect of YIG films with random multilayer structures. *J Appl Phys* 81 : 5659-5661
- Inoue M, Arai K, Fujii T (1998) Magneto-optical properties of one-dimensional photonic crystals composed of magnetic and dielectric layers. *J Appl Phys* 83 : 6768-6770
- Inoue K, Sasada M, Kawamata J, Sakoda K, Haus JW (1999) A two-dimensional photonic crystal laser. *Jpn J Appl Phys* 38 : L157-L159
- Iyer AK, Eleftheriades GV (2002) Negative Refractive Index Metamaterials Supporting 2-D Waves. IEEE International Microwave Symposium Digest : 1067-1070, Seattle WA (June 2-7)

- Jewell JL, Mc Call SL, Scherer A, Houh HH, Whitaker NA, Gossard AC, English JH (1989) Transverse modes, waveguide dispersion, and 30ps recovery in submicron GaAs/AlAs microresonators. *Appl Phys Lett* 55 : 22-
- Jhe W, Anderson A, Hinds EA, Meschede D, Moi L, Haroche S (1987) Suppression of spontaneous decay at optical frequencies: Test of vacuum-field anisotropy in confined space. *Phys Rev Lett* 58 : 666-
- Jiang P, Ostoic GN, Narat R, Mittleman DM, Colvin VL (2001) The fabrication and band-gap engineering of photonic multilayers. *Adv Mater* 13 : 389-393
- Joannopoulos JD (1995a) The magical world of photonic crystals in : Soukoulis C (ed) Photonic band gap materials
- Joannopoulos JD, Meade RD, Winn JN (1995b) Photonic Crystals. Princeton University
- John S (1984) Electromagnetic absorption in a disordered medium near a photon mobility edge. *Phys Rev Lett* 53 : 2169-2173
- Kärkkäinen MK (2002) Illustration of wave propagation in DNG materials in : Digest of the XXVII URSI/IEEE Convention on Radio Science, Espoo, Finland (Oct. 17-18, 2002) : pp. 31-33, http://www.hut.fi/Units/Radio/URSI02/ursi_karkkainen_b.pdf
- Kastler A (1962) Atomes dans un interféromètre de Fabry-Pérot. *Applied Optics* 1 : 17-
- Kawakami S (1997) Fabrication of submicrometre 3D periodic structures composed of Si/SiO₂. *Electron Lett* 33 : 1260-1261
- Kawakami S, Kawashima T, Sato T (1999) Mechanism of shape formation of three-dimensional periodic nanostructures by bias sputtering. *Appl Phys Lett* 74 : 463-465
- Kawai N, Inoue K, Carlsson N, Ikeda N, Sugimoto Y, Asakawa K (2001) Confined Band Gap in Air-Bridge Type of Two-Dimensional AlGaAs Photonic Crystal. *Phys Rev Lett* 11 : 2289-2292
- Kesler MP, Maloney JG, Shirley BL, Smith GS (1996) Antenna design with the use of photonic band-gap material as all-dielectric planar reflectors. *Microwave Opt Technol Lett* 11 : 169-174
- Kiang KM, Frampton K, Monro TM, Moore R, Tucknott J, Newak DW, Richardson DJ, Rutt HN (2002) Extruded single-mode non-silica glass holey optical fibres. *Electron Lett* 38 : 546-547
- Kim M, Dainty JC, Friberg AT, Sant AJ (1990) Experimental study of enhanced backscattering from one- and two- dimensional random rough surfaces. *J Opt Soc Am A* 7 : 569-577
- Kiraz A, Michler P, Becher C, Gayral B, Imamoglu A, Zhang L, Hu E. (2001) Cavity-quantum electrodynamics using a single InAs quantum dot in a microdisk structure. *Appl Phys Lett* 78 : 3932-
- Kittel Ch (1958) Introduction à la Physique de l'Etat Solide (in French). Dunod, Paris
- Kittel Ch (1971) Introduction to Solid State Physics. John Wiley & Sons
- Kitson SC, Barnes WL, Sambles JR (1996) Full Photonic Band Gap for surface modes in the visible. *Phys Rev Lett* 77 : 2670-2673
- Knight JC (2003) Photonic crystal fibres. *Nature* 424 : 847-851
- Knight JC, Birks TA, Russell PStJ, Atkin DM (1996) All-silica single-mode fiber with photonic crystal cladding. *Opt Lett* 21 : 1547-1549
- Knight JC, Broeng J, Birks TA, Russell PStJ (1998a) Photonic bandgap guidance in optical fibers. *Science* 282 : 1476-1478
- Knight JC, Birks TA, Russell PStJ, de Sandro JP (1998b) Large mode area photonic crystal fibre. *Electron Lett* 34 : 1347-1348

- Knight JC, Arriaga J, Birks TA, Ortigosa-Blanch A, Wadsworth WJ, Russell PStJ (2000) Anomalous dispersion in photonic crystal fibers. *IEEE Photon Technol Lett* 12 : 807-809
- Koenderink AF, Bechger L, Schriemer HP, Lagendijk A, Vos W (2002a) Broadband five-fold reduction of vacuum fluctuations probed by dye photonic crystals. *Phys Rev Lett* 88 : 143903
- Koenderink AF, Johnson PM, Galisteo Lopez JF, Vos WL (2002b) Three-dimensional photonic crystals as a cage for light. *Comptes Rendus de l'Académie des Sciences* 3 : 67-77
- Kogelnik H, Shank CV (1971) Stimulated Emission in a Periodic Structure. *Appl Phys Lett* 18 : 152-154
- Kogelnik H, Shank CV (1972) Coupled-wave theory of distributed feedback lasers. *J Appl Phys* 43 : 2327-2335
- Köhler R, Tredicucci A, Beltram F, Beere H, Linfield E, Davies AG, Ritchie DA, Iotti RC, Rossi F (2002) Terahertz semiconductor heterostructure lasers. *Nature* 417 : 156-159
- Kohn W, Rostoker N (1954) Solution of the Schrödinger Equation in Periodic Lattices with an Application to Metallic Lithium. *Phys Rev* 94 : 1111-1120 (KKR method, see also : Korringa 1947)
- Kong JA (2000) Electromagnetic Wave Theory. EMW Publishing
- Konsek SL, Pearsall TP (2003) Dynamics of electron tunneling in semiconductor nanostructures. *Phys Rev B* 67 : 45306
- Kopp VI, Fan B, Vithana HKM, Genack AZ (1998) Low threshold lasing at the edge of a photonic stop band in cholestérol liquid crystals. *Opt Lett* 23 : 1707-1709
- Korringa J (1947) On the Calculation of the Energy of a Bloch Wave in a Metal, *Physica (Utrecht)* 13 : 392- (KKR method, see also : Kohn 1954)
- Kosaka H, Kawashima T, Tomita A, Notomi M, Tamamura T, Sato T, Kawakami S (1998) Superprism phenomena in photonic crystals. *Phys Rev B* 58 : 10096-10099
- Kosaka H, Kawashima T, Tomita A, Notomi M, Tamamura T, Sato T, Kawakami S (1999) Photonic crystals for micro lightwave circuits using wavelength-dependent angular beam steering. *Appl Phys Lett* 74 : 1370-1372
- Krauss TF, De La Rue RM (1996b) Exploring the two-dimension photonic bandgap in semiconductors in Soukoulis CM (Ed) *Photonic Band Gap Materials* (pp. 427-436). Kluwer Academic Publishers, Dordrecht
- Krauss TF, De La Rue RM, Brand S (1996a) Two-dimensional photonic-bandgap structures operating at near-infrared wavelengths. *Nature* 383 : 699-702
- Krames MR, Ochiai-Holcomb M, Höfler GE, Carter-Coman C, Chen EI, Tan. IH, Grillot P, Gardner NF, Chui HC, Huang SA, Stockman JW, Kish FA, Craford MG, Tan TS, Kocot C P, Hueschen M, Posselt J, Loh B, Sasser G, Collins D (1999) High-power truncated-inverted-pyramid $(\text{Al}_x\text{Ga}_{1-x})_{0.5}\text{In}_{0.5}\text{P}/\text{GaP}$ light-emitting diodes exhibiting >50% external quantum efficiency. *Appl Phys Lett* 75 : 2365-2367
- Kretschman E (1971) The determination of the optical constants of metals by excitation of surface plasmons. *Z Phys* 241 : 313-324
- Kruusing A, Mellikov E (2001) Photoconductive patterns in semiconductors for electromagnetic field control : A review. *Proceedings-of-the-SPIE (The-International-Society-for-Optical-Engineering)* 4415 : 22-32
- Kuhlmeij B, White TP, Renverze G, Maystre D, Botten LC, Martijn de Sterke C, McPhe- dran RC (2002a) Multipole method for microstructured optical fibers II : Implementation and results. *J Opt Soc Am B* 10 : 2331-2340

- Kuhlmeijer B, de Sterke M, McPhedran RC, Robinson P, Renversez G, Maystre D (2002b) Microstructured Optical fibers : where's the edge. Optics Express 10 : 1285-1290
- Kuhlmeijer B, Renversez G, Maystre D (2003) Chromatic dispersion and losses of microstructured optical fibers. Applied Optics 42 : 634-639
- Kuksenkov DK, Temkin H, Lear KL, Lou HQ (1997) Spontaneous emission factor in oxide-confined vertical cavity surface emitting lasers. Appl Phys Lett 70 : 13-
- Kumar Ravi Kanth VV, George AK, Reeves WH, Knight JC, Russell PStJ, Omenetto FG, Taylor AJ (2002) Extruded soft glass photonic crystal fiber for ultrabroad supercontinuum generation. Optics Express 10 : 1520-1524
- Kurtsiefer C, Mayer S, Zarda S, Weinfurter H (2000) Stable solid-state source of single photons. Phys Rev Lett 89 : 290-
- Labilloy D, Benisty H, Weisbuch C, Krauss TF, Houdré R, Oesterle U (1997) Use of guided spontaneous emission of a semiconductor to probe the optical properties of two-dimensional photonic crystals. Appl Phys Lett 71 : 738-740
- Labilloy D, Benisty H, Weisbuch C, Krauss TF, Smith CJM, Houdré R, Oesterle U (1998) High-finesse disk microcavity based on circular Bragg reflector. Appl Phys Lett 73 : 1314-
- Labilloy D, Benisty H, Weisbuch C, Smith CJM, Krauss TF, Houdré R, Oesterle U (1999) Finely resolved transmission spectra and band structure of two-dimensional photonic crystals using InAs quantum dots emission. Phys Rev B 59 : 1649-1652
- Lalanne P, Morris GM (1996) Highly improved convergence of the coupled wave method for TM polarization. J Opt Soc Am A 13 : 779-784
- Lalanne P, Benisty H (2001) Ultimate limits of two-dimensional photonic crystals etched through waveguides : an electromagnetic analysis. J Appl Phys 89 : 1512-1514
- Landau L, Lifchitz E (1969) Électrodynamique des milieux continus (Physique Théorique Tome VIII, in French). Ed. MIR, Moscou
- Landolt-Börnstein (1982) Numerical Data and Functional Relationship in Science and Technology in: O. Madelung (dir) New Series group III, vol. 17, Springer Verlag, Berlin
- Lawandy NM, Johnston SA, Martorell J (1988) Birefringence and polarization dependence absorption in sheared colloidal crystals. Opt Commun 65 : 425-429
- Lee W, Pruzinsky S, Braun PV (2002) Multi-photon polymerisation of waveguide structures within three-dimensional photonic crystals. Adv Mater 14 : 271-274
- Letartre X, Seassal C, Grillet C (2001) Group velocity and propagation losses measurement in a single-line photonic-crystal waveguide on InP membranes. Appl Phys Lett. 79 : 2312-
- Leung WY, Tuttle G, Sigalas MM, Biswas R, Ho KM, Soukoulis CM (1998) Optimising the Q value in three-dimensional metallic photonic band gap crystals. J Appl Phys 84 : 4091-4095
- Le Vassor d'Yerville M (2002) Modélisation de cristaux photoniques bidimensionnels de hauteur finie (in French). Ph.D. Thesis, University of Montpellier II
- Li L (1996) Use of Fourier series in the analysis of discontinuous periodic structures. J Opt Soc Am A 13 : 1870-1876
- Li ZY, Zhang XD, Zhang ZQ (2000) Disordered photonic crystals understood by a perturbation formalism. Phys Rev B 61: 15738-15748
- Limpert J, Schreiber T, Nolte S, Zellmer H, Tunnermann T, Iliew R, Lederer F, Broeng J, Vienne G, Petersson A, Jakobsen C (2003) Highpower air-clad large-mode-area photonic crystal fiber laser. Optics Express 11 : 818-823

- Lin HB, Tonucci RJ, Campillo AJ (1998) Two-dimensional photonic bandgap optical limiter in the visible. *Opt Lett* 23 : 94-96
- Lin SY, Fleming JG (1999a) A three-dimensional optical photonic crystal. *J Lightwave Technol* 17 : 1944-1947
- Lin SY, Hietala VM, Wang L, Jones ED (1996) Highly dispersive photonic band-gap prism. *Opt Lett* 21 : 1771-1773
- Lin SY, Fleming JG, Sigalas MM, Biswas R, Ho KM (1999b) Photonic band-gap microcavities in three dimensions. *Phys Rev B* 59 : R15579-R15582
- Lin SY, Chow E., Johnson SG, Joannopoulos JD (2000a) Demonstration of highly efficient waveguiding in a photonic crystal slab at the $1.5\text{-}\mu\text{m}$ wavelength. *Optics Lett* 25 : 1297-1299
- Lin SY, Fleming JG, Chow E, Bur J, Choi KK, Goldberg A (2000b) Enhancement and suppression of thermal emission by a three-dimensional photonic crystal. *Phys Rev B* 62 : R2243-2246
- Lin SY, Chow E, Johnson SG, Joannopoulos JD (2001a) Direct measurement of the quality factor in a two-dimensional photonic-crystal microcavity. *Opt Lett* 26 : 1903-1905
- Lin SY, Fleming JG, Lin R, Sigalas MM, Biswas R, Ho KM (2001b) Complete three-dimensional photonic bandgap in a simple cubic structure. *J Opt Soc Am B* 18 : 32-35
- Loncar M, Nedeljkovic D, Pearsall TP, Vuckovic J, Scherer A, Kuchinsky S, Allan, DC (2002a) Experimental and theoretical confirmation of Bloch-mode light propagation in planar photonic crystal waveguides. *Appl Phys Lett* 80 : 1689-1691
- Loncar M, Yoshie T, Scherer A, Gogna P, Qiu Y (2002b) Low-threshold photonic crystal laser. *Appl Phys Lett* 81 : 2680-
- Loudon R (1983) The Quantum Theory of Light. Oxford University Press, Oxford
- Lounis B, Moerner WE (2000) Single photons on demand from a single molecule at room temperature. *Nature* 407 : 491-
- Lourtioz JM (1981) Lasers submillimétriques continus pompés optiquement par laser CO₂. PhD Thesis (in French), University of Orsay
- Lourtioz JM, Berger V (1998) Les matériaux à bandes interdites photoniques (in French). *Images de la Physique* (ed. CNRS) : 37-43
- Lourtioz JM, de Lustrac A, Gadot F, Rowson S, Chelnokov A, Brillat T, Ammouche A, Danglot J, Vanbésien O, Lippens D (1999) Toward controllable photonic crystals for centimeter and millimeter wave devices. *J Lightwave Technol* 17 : 2025-2031
- Luo C, Johnson SG, Jouannopoulos JD, Pendry JB (2002) All-angle negative refraction without negative index. *Phys Rev B* 65 : R201104-
- de Lustrac A, Gadot F, Cabaret S, Lourtioz JM, Brillat T, Priou A, Akmansoy E (1999) Experimental demonstration of electrically controllable photonic crystals at centimeter wavelengths. *Appl Phys Lett* 75 : 1625-1627
- de Lustrac A, Gadot F, Akmansoy E, Brillat T (2001) High-directivity planar antenna using controllable photonic bandgap material at microwave frequencies. *Appl Phys Lett* 78 : 4196-4198
- Marconi G, Franklin S (1919) Reflector For Use In Wireless Telegraphy And Telephony, US patent
- Marcuse D (1974) Theory of Electric Optical Waveguides. New York: Academic
- Maradudin AA, Michel T, McGurn AR, Mendez ER (1990) Enhanced backscattering of light from a random grating. *Ann Phys* 203 : 255-307

- Maslovsky SI (2002) Negative refraction and causality in : Digest of the XXVII URSI/IEEE Convention on Radio Science (Oct. 17-18, 2002) Espoo, Finland, pp. 110-111 (http://www.hut.fi/Units/Radio/URSI02/ursi_maslovski.pdf).
- Maxwell Garnett JC (1904) Colours in metal glasses and metal films, Phil Trans Roy Soc A 203 : 385-
- Maxwell Garnett JC (1906) Colours in metal glasses, in metallic films, and in metallic solutions II, Phil Trans Roy Soc A 205 : 237-
- Maystre D (1982) General study of grating anomalies from electromagnetic surface modes in Boardman AD (ed) Electromagnetic surface modes (Chapter 17, pp 661-724), John Wiley & Sons, Chichester
- Maystre D (1993) Diffraction Gratings. SPIE Milestones series, vol MS83
- Maystre D (1994a) Electromagnetic study of photonic band gaps. Pure Appl Opt 3 : 975-993
- Maystre D, Petit R (1976) Brewster incidence for metallic gratings. Optics Commun 17 : 196-200
- Maystre D, Nevière M (1977) Sur une méthode d'étude théorique quantitative des anomalies de Wood des réseaux de diffraction, application aux anomalies de plasmons (in French). Nouv Rev Optique 8 : 165-174
- Maystre D, Dainty JC (1991) Modern Analysis of Scattering Phenomena. Hilger, New-York
- Maystre D, Saillard M (1994b) Localization of light by randomly rough surfaces: concept of localiton. J Opt Soc Am A 11 : 680-690
- Maystre D, Saillard M, Tayeb G (2002) Special methods of wave diffraction, Academic Press, New York
- McCall SL, Platzman PM, Dalichaouch R, Smith D, Schultz S (1991) Microwave propagation in two-dimensional dielectric lattices. Phys Rev 67 : 2017-
- Mc Call SL, Levi AFJ, Slusher RE, Pearton SJ, Logan RA (1992) Whispering-gallery mode microdisk lasers. Appl Phys Lett 60 : 289-
- McDonald KT (2000) Negative Group Velocity. ArXiv, 0008013., <http://arxiv.org/abs/physics/0008013>
- Mc Phedran RC, Maystre D (1977) On the theory and solar application of inductive grids. Appl Phys 14 : 1-20
- McPherson WN, Gander MJ, McBride R, Jones JDC, Blanchard PM, Burnett JG, Greenaway AH, Mangan B, Birks TA, Knight JC, Russell PStJ (2001) Remotely addressed optical fibre curvature sensor using multicore photonic crystal fibre. Optics Commun 193 : 97-104
- Meade RD, Rappe AM, Brommer KD, Joannopoulos JD, Alerhand OL (1993) Accurate theoretical analysis of photonic bandgap materials. Phys Rev B 48 : 8434-8437
- Megens M, Schriemer HP, Lagendijk A, Vos WL (1999) Fluorescence lifetimes and linewidths of dye in photonic crystals. Phys Rev A 59 : 4727-4731
- Mei D, Cheng B, Hu W, Li Zh, Zhang D (1995) Three-dimensional ordered patterns by light interference. Optics Lett 20 : 429-431
- Mekis A, Chen JC, Kurland I, Villeneuve PR, Joannopoulos JD (1996) High transmission through sharp bends in photonic crystals waveguides. Phys Rev Lett 77 : 3787-3790
- Melville DOS, Blaikie RJ, Wolf CR (2004) Submicron imaging with a planar silver lens. Appl Phys Lett 84 : 4403-4405
- Meschede D, Walther H, Müller G (1985) One-atom maser. Phys Rev Lett 54 : 551-554

- Michler P, Imamoglu A, Mason M, Carson M, Strouse G, Buratto S (2000a) Quantum correlations among photons from a single quantum dot at room temperature. *Nature* 406 : 968-
- Michler P, Kiraz A, Becher C, Schoenfeld W, Petroff PM, Zhang L, Hu E, Imamoglu A (2000b) A quantum dot single photon turnstile. *Science* 290 : 2282-
- Michler P, Kiraz A, Zhang L, Becher C, Hu E, Imamoglu A (2000c) Laser emission from quantum dots in microdisk structures. *Appl Phys Lett* 77 : 184-
- Mie G (1908) Beiträge zur Optik trüber Medien, speziell kolloidaler Metallösungen. *Ann. d. Phys.* 25 (4) : 377-
- Mogilevstev D, Birks TA, Russell PS (1998) Group-velocity dispersion in photonic crystal fibers. *Opt Lett* 23 : 1662–1664
- Moharam MG, Gaylord TK (1986) Rigorous coupled wave analysis of metallic diffraction gratings. *J Opt Soc Am A* 3 (11) : 1780-1787
- Mohideen U, Hobson WS, Pearton SJ, Ren F, Slusher RE (1994) GaAs/AlGaAs microdisk lasers. *Appl Phys Lett* 64 : 1911-
- Monge D (2000) Description des propriétés optiques des cristaux photoniques à l'aide d'une méthode basée sur les fonctions localisées. Ph.D. Thesis (in French), University of Montpellier
- Monat C, Seassal C, Letartre X, Regreny P, Rojo-Romeo P, Viktorovitch P, Le Vassor d'Yerville M, Cassagne D, Albert JP, Jalaquier E, Pocas S, Aspar B (2002) InP-based two-dimensional photonic crystal on silicon : in-plane Bloch mode laser. *Appl Phys Lett* 81 : 5102-5104
- Moroz A (1994) Inward and outward integral equations and the KKR method for photons. *Journal of Physics: Condensed Matter* 6 (1) : 171-182
- Moroz A (1995) Density-of-states calculations and multiple-scattering theory for photons. *Phys Rev B* 51 : 2068-2081
- Moroz A (1999) Three-dimensional complete photonic band gap structures in the visible. *Phys Rev Lett* 83 : 5274-5277
- Moreau E, Robert I, Manin L, Thierry-Mieg V, Gérard JM, Abram I (2001a) Quantum cascade of photons in semiconductor quantum dots. *Phys Rev Lett* 87 : 183601-
- Moreau E, Robert I, Gérard JM, Abram I, Manin L, Thierry-Mieg V (2001b) Single-mode solid-state single photon source based on isolated quantum dots in pillar microcavities. *Appl Phys Lett* 79 : 2865-
- Moreau E, Robert I, Manin L, Thierry-Mieg V, Gérard JM, Abram I (2002) A single mode single photon source based on isolated quantum dots in a micropillar. *Physica E* 13 : 418-
- Morimura S, Ujihara K (1997) Rate equation analysis of a microcavity laser with a finite number of molecules in the mode volume. *Jap Journ Appl Phys* 36 (part 1) : 4307-
- Myers LE, Miller GD, Eckhardt RC, Fejer MM, Byer RL, Bosenberg WR (1995) Quasi-Phase-Matched 1.064 μm -pumped optical parametric oscillator in bulk periodically poled LiNbO₃. *Opt Lett* 20 : 52-
- Nevière M (1980) The homogeneous problem in Petit R (ed) *Electromagnetic Theory of Gratings* (Chapter 5, pp 123-157), Springer Verlag, Berlin
- Nicorovici NA, Mc Phedran RC, Botten LC (1995) Photonic band gaps for arrays of perfectly conducting cylinders. *Phys Rev E* 52 : 1135-1145
- Nishizawa, H, Nakayama T (1997) Magneto-optic anisotropy effect on photonic band structure. *J Phys Soc Jpn* 66 : 613-617

- Noda S, Yamamoto N, Kobayashi H, Okano M, Tomoda K (1999) Optical properties of three-dimensional photonic crystals based on III-V semiconductors at infrared to near-infrared wavelengths. *Appl Phys Lett* 75 : 905-907
- Noda S, Chutinan A, Imada M (2000) Trapping and emission of photons by a single defect in a photonic bandgap structure. *Nature* 407 : 608-610
- Noda S, Imada M, Okano M, Ogawa S, Mochizuki M, Chutinan A (2002) Semiconductor three-dimensional and two-dimensional photonic crystals and devices. *IEEE J Quant Electron* 38 : 726-735
- Notomi M (2000a) Theory of light propagation in strongly modulated photonic crystals: refractionlike behavior in the vicinity of the photonic band gap. *Phys Rev B* 62 : 10696-10705
- Notomi M, Tamamura T, Kawashima T, Kawakami S (2000b) Drilled alternating-layer three-dimensional photonic crystals having a full photonic band gap. *Appl Phys Lett* 77 : 4256-4258
- Notomi M, Suzuki H, Tamamura T (2001) Directional lasing oscillation of two-dimensional » organic photonic crystal lasers at several photonic bandgaps. *Appl Phys Lett* 78 : 1325-1327
- O'Brien S, Pendry JB (2002) Magnetic activity at infrared frequencies in structured metallic photonic crystals. *J Phys Condens Matter* 14 : 6383-6394
- O'Donnell KA, Mendez ER (1987) Experimental study of scattering from characterized random surfaces. *J Opt Soc Am A* 4 : 1194-1205
- Ohkubo H, Ohtera Y, Miura K, Akutsu N, Hikage M, Kawakami S (2004) Reduction of propagation loss to 0.1 dB/mm : Flat core channel waveguides consisting of periodic structures. *IEEE Photon Technol Lett* 16 : 1068-1070
- Okoshi T (1982) Optical Fibers. Academic Press, New York
- Olivier S (2002b) Nouvelles structures miniatures dans des cristaux photoniques bidimensionnels planaires pour les fonctions de l'optique intégrée (in French). Ph. D. Thesis, University of Paris VI
- Olivier S, Smith C, Rattier M, Benisty H, Weisbuch C, Krauss T, Houdré R, Oesterlé U (2001a) Miniband transmission in a photonic crystal coupled-resonator optical waveguide. *Optics Letters* 26 : 1019-1021
- Olivier S, Rattier M, Benisty H, Smith CJM, De La Rue RM, Krauss TF, Oesterlé U, Houdré R, Weisbuch C (2001b) Mini stopbands of a one dimensional system: the channel waveguide in a two-dimensional photonic crystal. *Phys Rev B* 63 : 113311-
- Olivier S, Smith C, Benisty H, Weisbuch C, Krauss TF, Houdré R, Oesterlé U (2002a) Cascaded photonic crystal guides and cavities: spectral studies and their impact on integrated optics design. *IEEE J Quant Electron* 38 : 816-824
- Ortigosa-Blanch A, Knight JC, Wadsworth WJ, Arriaga J, Mangan BJ, Birks TA, Russel PstJ (2000) Highly birefringent photonic crystal fibres. *Opt Lett* 25 : 1325-1327 - and references therein.
- Özbay E, Michel E, Tuttle G, Biswas R, Ho KM, Bostak J, Bloom DM (1994a) Double-etch geometry for millimeter-wave photonic bandgap crystals. *Appl Phys Lett* 65 : 1617-1619
- Özbay E, Michel E, Tuttle G, Biswas R, Ho KM, Bostak J, Bloom DM (1994b) Terahertz spectroscopy of three-dimensional photonic bandgap crystals. *Opt Lett* 19 : 1155-1157
- Özbay E, Temelkuran B, Sigalas M, Tuttle G, Soukoulis CM, Ho KM (1996) Defect structures in metallic photonic crystals. *Appl Phys Lett* 69 : 3797-

- Ouzounov DG, Ahmad FR, Müller D, Venkataraman N, Gallagher MT, Thomas MG, Silcox J, Koch KW, Gaeta AL (2003) Generation of megawatt optical solitons in hollow-core photonic band-gap fibers. *Science* 301 : 702-1704
- Pacradouni V, Mandeville WJ, Cowan AR, Padon P, Young JJ, Johnson SR (2000) Photonic band structure of dielectric membranes periodically textured in two dimensions. *Phys Rev B* 62 : 4204
- Pagnoux D, Peyrilloux A, Roy P, Fevrier S, Labonte L, Hilaire S (2003) Microstructured air-silica fibres : recent developments in modelling, manufacturing and experiments. *Ann Télécommun* 58 : 1238-1274
- Painter OJ, Husain A, Scherer A, O'Brien JD, Kim I, Dapkus D (1999a) Room-temperature photonic crystal defect laser at near-infrared wavelengths in InGaAsP. *J Lightwave Technol* 17 : 2082-2088
- Painter O, Lee RK, Scherer A, Yariv A, O'Brien JD, Dapkus PD, Kim I (1999b) Two-dimensional photonic band-gap defect mode laser. *Science* 284 : 1819-1821
- Park HG, Hwang JK, Huh J, Ryu HY, Lee YH, Kim JS (2001) Nondegenerate monopole-mode two-dimensional photonic band gap laser. *Appl Phys Lett* 79 : 3032-3034
- Park HG, Kim SH, Kwon SH, Ju YG, Yang JK, Baek JH, Kim SB, Lee YH, (2004) Electrically Driven Single-Cell Photonic Crystal Laser. *Science* 305 : 1444-1447
- Patrini M, Galli M, Marabelli F, Agio M, Andreani LC, Peyrade D, Chen Y (2002) Photonic Bands in patterned Silicon-on-insulao waveguides. *IEEE J Quant Electron* 38 : 885-890
- Pelton M, Yamamoto Y (1999) Ultralow threshold laser using a single quantum dot and a microsphere cavity. *Phys Rev A* 59 : 2418-2421
- Pelton M, Santori C, Vuckovic J, Zhang B, Solomon G, Plant J, Yamamoto Y (2002) Efficient Source of Single Photons : A Single Quantum Dot in a Micropost Microcavity. *Phys Rev Lett* 89 : 233602
- Pendry JB (1994) Photonic band structures. *Journ Mod Phys* 41 : 209-229
- Pendry JB (1996b) Calculating photonic band structures. *J Phys Condens Matter* 8 : 1085-1108
- Pendry JB (2000) Negative refraction makes a perfect lens. *Phys Rev Lett* 85 : 3966-3969
- Pendry JB (2003b) Comment on : Left-Handed Materials Do Not Make a Perfect Lens (see Garcia 2002b), *Phys Rev Lett* 91 : 099701-
- Pendry JB, Smith DR (2003a) Comment on : Wave Refraction in Negative-Index Media Always Positive and Very Inhomogeneous (see : Valanju 2002). *Phys Rev Lett* 90 : 029703-
- Pendry JB, Holden AJ, Stewart WJ, Youngs I (1996a) Extremely low frequency plasmons in metallic mesostructures. *Phys Rev Lett* 76 : 4773-4776
- Pendry JB, Holden AJ, Robbins DJ, Stewart WJ (1998) Low frequency plasmons in thin-wire structures. *J Phys Condens Matter* 10 : 4785-4809
- Pendry JB, Holden AJ, Robbins DJ, Stewart WJ (1999) Magnetism from conductors and enhanced nonlinear phenomena. *IEEE Trans Microw Theory* 47 : 2075-2084
- Petit R (1980) Electromagnetic Theory of Gratings. Springer Verlag, Heidelberg
- Petrov EP, Bogomolov VN, Kalosha II, Gaponenko SV (1998) Spontaneous emission of organic molecules embedded in a photonic crystal. *Phys Rev Lett* 81 : 77-80
- Poilasne G, Poulingen P, Mahdjoubi K (2000) Study of beam splitting using periodic metallic photonic band-gap materials. *Microwave Opt Tech Lett* 25 : 36-
- Pokrovsky AL, Efros AL (2002a) Electrodynamics of metallic photonic crystals and problem of left-handed materials. *Phys Rev Lett* 89 : 093901-

- Pokrovsky AL, Efros AL (2002b) Diffraction in left-handed materials and theory of Veselago lens. Cond Mat 0202078 (<http://xxx.lanl.gov/abs/cond-mat/0202078>)
- Popov E, Nevière M (2001b) Maxwell equations in Fourier space: fast-converging formulation for diffraction by arbitrary shaped, periodic, anisotropic media. J Opt Soc Am A 18 : 2886-2894
- Popov E, Bozhkov B, Nevière M (2001a) Almost perfect blazing by photonic crystal rod grating. Applied Optics : 2417-2422
- Pottier P, Seassal C, Letartre X, Leclercq JL, Viktorovitch P, Cassagne D, Jouannin C (1999) Triangular and Hexagonal High Q-Factor 2D Photonic Bandgap Cavities on III-V Suspended Membranes. J Lightwave Technol 17 : 2058-2062
- Powell JL, Craseman B (1965) Quantum Mechanics. Addison-Wesley, Reading
- Purcell EM (1946) Spontaneous Emission Probabilities at Radiofrequencies. Phys Rev 69 : 681
- Qian Y, Cocciali R, Sievenpiper D, Radisic V, Yablonovitch E, Itoh T (1999) A microstrip patch antenna using novel photonic band-gap structures. Microwave Journal : 67-76
- Quang T, John S (1997) Resonance fluorescence near a photonic band edge : Dressed-state Monte Carlo wave-function approach. Phys Rev A 56 : 4273-4277
- Raether H (1988) Surface Plasmons on Smooth and Rough Surfaces and on Gratings. Springer Verlag, New York
- Ranka JK, Windeler RS (2000) Nonlinear interactions in air-silica microstructures optical fibers. Optics and Photonics News : 20-25
- Rattier M, Benisty H, Stanley R, Carlin JF, Houdré R, Oesterle U, Smith CJM, Weisbuch C, Krauss TF (2002) Towards Ultra-High Efficiency Aluminum Oxide Microcavity Light-Emitting Diodes : Guided Mode Extraction by Photonic Crystals. IEEE J Sel Topics in Quant Electron 8 : 238-247
- Rattier M, Benisty H, Schwoob E, Weisbuch C, Krauss TF, Smith CJM, Houdré R, Oesterle U (2003) Omnidirectional and compact guided light extraction from Archimedean photonic lattices. Appl Phys Lett 83 : 1283-1285
- Lord Rayleigh, JW Strutt (1892) On the influence of obstacles arranged in rectangular order upon the properties of a medium. Philos Mag 34 : 481-502
- Reese C, Becher C, Imamoglu A, Hu E, Gerardot BD, Petroff PM (2001) Photonic crystal microcavities with self-assembled InAs quantum dots as active emitters. Appl Phys Lett 78 : 2279-2281
- Reeves WH, Knight JC, Russell PSJ (2002) Demonstration of ultra-flattened dispersion in photonic crystal fibers. Optics Express 10 : 609-613
- Reineix A, Jecko B (1996) A new photonic bandgap equivalent model using Finite Difference Time Domain. Ann Télécommun 51 : 656-662
- Rennon S, Klopf F, Reithmaier JP, Forchel A (2001) 12-micron-long edge-emitting quantum-dot microlaser. Electron Lett 37 : 690-691
- Renversez G, Kuhlmeijer B, McPhedran RC (2003) Dispersion management with microstructured optical fibers: Ultra-flattened chromatic dispersion with low losses. Optics Letters 28 : 989-991
- Rigneault H, Lemarchand F, Sentenac A (2000) Dipole radiation into grating structures. J Opt Soc Am A 17 : 1048-1058
- Rivera T, Debray JP, Legrand B, Gérard JM, Manin-Ferlazzo L, Oudar JL (1999) Optical losses in plasma-etched AlGaAs microresonators using reflection spectroscopy. Appl Phys Lett 74 : 911-

- Romanov SG, Johnson NP, Fokin AV, Butko VY, Yates HM, Pemble ME, Sotomayor Torres CM (1997) Enhancement of the photonic gap of opal-based three-dimensional gratings. *Appl Phys Lett* 70 : 2091-
- Romanov SG, Maka T, Sotomayor Torres CM, Muller M, Zentel R (2001) Emission in a SnS₂ inverted opaline photonic crystal. *Appl Phys Lett* 79 : 731-733
- Rowson S, Chelnokov A, Lourtioz JM, Carcenac F (1998) Reflection and transmission characterisation of a hexagonal photonic crystal in the mid infrared. *J Appl Phys* 83 : 5061-
- Rowson S, Chelnokov A, Lourtioz JM (1999a) Two-dimensional photonic crystals in macroporous silicon photonic crystals : from mid-infrared to telecommunication wavelengths (1.3-1.55 μ m). *J Lightwave Technol* 17 : 1989-1995
- Rowson S, Chelnokov A, Lourtioz JM (1999b) Macroporous silicon : photonic crystal substrates at 1.55 μ m. 25 th European Conference On Optical Communication ECOC'99, Nice, Sept 99
- Russell PSJ (2003) Photonic crystal fibers. *Science* 299 : 358-362
- Ryu HY, Kwon SH, Lee YJ, Lee YH, Kim JS (2002a) Very-low-threshold photonic band-edge lasers from free-standing triangular photonic crystal slabs. *Appl Phys Lett* 80 : 3476-3478
- Ryu H, Kim S, Park H, Hwang J, Lee Y, Kim J (2002b) Square lattice photonic bandgap single-cell laser operating in the lowest order whispering gallery mode. *Appl Phys Lett* 80 : 3883-
- Saadø Y, Golosovsky M, Davidov D, Frenkel A (2001) Fabrication of artificial crystals with tunable lattice constant via self-assembly of floating magnetic particles. *Synthetic Metals* 116 : 427-432
- Sakoda K (1999a) Enhanced light amplification due to group-velocity anomaly peculiar to two- and three- dimensional photonic crystals. *Optics Express* 4 : 167-176
- Sakoda K (2001) Optical Properties of Photonic Crystals. Springer Verlag, Heidelberg New York
- Sakoda K, Ohtaka K (1996) Sum-frequency generation in a two-dimensional photonic lattice. *Phys Rev B* 54 : 5742-5749
- Sakoda K, Ohtaka K, Ueta T. (1999b) Low-threshold laser oscillation due to group-velocity anomaly peculiar to two- and three-dimensional photonic crystals. *Optics Express* 4 : 481-489
- Sandoghdar V, Treussart F, Hare J, Lefèvre-Seguin V, Raimond JM, Haroche S (1996) Very low threshold whispering-gallery-mode microsphere laser. *Phys Rev A* : R1777-
- Santori C, Fattal D, Vuckovic J, Solomon G, Yamamoto Y (2002) Indistinguishable photons from a single-photon device. *Nature* 419 : 594-
- Sato T, Miura K, Ishino N, Ohtera Y, Tamamura T, Kawakami S (2002) Photonic crystals for the visible range fabricated by autocloning technique and their application. *Optical and Quantum Electronics* 34 : 63-70
- Savvidis PG, Ciuti C, Baumberg JJ, Whittaker DM, Skolnick MS, Roberts JS (2001) Off-branch polaritons and multiple scattering in semiconductor microcavities. *Phys Rev B* 64 : 075311-
- Schawlow AL, Townes CH (1958). Infrared and optical masers. *Phys Rev* 112 : 1940-1949
- Schwartz L (1961) Méthodes mathématiques pour les Sciences Physiques (in French). Hermann, Paris

- Schilling J, Müller F, Matthias S, Wehrsporn RB, Gösele U, Busch K (2001) Three-dimensional photonic crystals based on macroporous silicon with modulated pore diameter. *Appl Phys Lett* 78 : 1180-1182
- Seassal C, Désières Y, Letartre X, Grillet C, Rojo-Romeo P, Viktorovitch P, Benyattou T (2002) Optical Coupling Between a Two-Dimensional Photonic Crystal-Based Microcavity and Single-Line Defect Waveguide on InP Membranes. *IEEE J Quant Electron* 38 : 811-815
- Senechal M (1995) Quasicrystals and Geometry. Cambridge Univ. Press, Cambridge
- Shelby RA, Smith DR, Schultz S (2001) Experimental verification of a negative index of refraction. *Science* 292 : 77-
- Shen JT, Platzman PM (2002) Near field imaging with negative dielectric constant lenses. *Appl Phys Lett* 80 : 3286-3288
- Shoji S, Kawata S (2000) Photofabrication of three-dimensional photonic crystals by multibeam laser interference into a photopolymerizable resin. *Appl Phys Lett* 76 : 2668-2671
- Siegel PH, Smith RP, Martin S, Gaidis M (1999) 2.5 THz GaAs monolithic membrane diode mixer. *IEEE Trans Microwave Theory and Tech* 47 : 596-604
- Sievenpiper D (1999b) High impedance electromagnetic surfaces. Ph. D. Thesis, Univ. California, Los Angeles
- Sievenpiper D, Sickmiller M, Yablonovitch E (1996) 3D wire mesh photonic crystals. *Phys Rev Lett* 76 : 2480-2483
- Sievenpiper D, Yablonovitch E, Winn J, Fan S, Villeneuve P, Joannopoulos D (1998) 3D metallo-dielectric photonic crystals with strong capacitive coupling between metallic islands. *Phys Rev Lett* 80 : 2829-2832
- Sievenpiper D, Zhang L, Broas R, Alexopoulos N, Yablonovitch E (1999a) High-impedance electromagnetic surfaces. *IEEE Transactions on Microwave Theory and Techniques* 47 : 2059-2074
- Sigalas MM, Economou EN (1992) Elastic and acoustic wave band structures. *J Sound Vibration* 158 : 377-
- Sigalas MM, Biswas R, Ho KM (1996) Theoretical study of dipole antennas on photonic band-gap materials. *Microwave and Opt Technol Lett* 13 : 205-209
- Sigalas MM, Soukoulis CM, Biswas R, Ho KM (1997a) Effect of the magnetic permeability on photonic bandgaps. *Phys Rev B* 56 : 959-962
- Sigalas MM, Biswas R, Li Q, Crouch D, Leung W, Woodbury RJ, Lough B, Nielsen S, Mc Calmont S, Tuttle G, Ho KM (1997b) Dipole antennas on photonic band-gap crystals – experiment and simulation. *Microwave Opt Technol Lett* 15 : 153-158
- Silberstein E, Lalanne P, Hugonin JP, Cao Qing (2001) Use of grating theories in integrated optics. *J Opt Soc Am A* : 2865-2875
- Silvester P, Pelosi G (1994) Finite elements for wave electromagnetics, IEEE Press, New York
- Simonneau C, Debray JP, Harmand JC, Vidakovic P, Lovering DJ, Levenson JA (1997) Second-harmonic generation in a doubly resonant semiconductor microcavity. *Optics Letters* 22 : 1775-
- Slusher RE, Levi AFJ, Mohideen U, Mc Call SL, Pearson SJ, Logan RA (1993) Threshold characteristics of semiconductor microdisk lasers. *Appl Phys Lett* 63 : 1310-
- Solomon GS, Pelton M, Yamamoto Y (2001) Single-mode spontaneous emission from a single quantum dot in a three-dimensional microcavity. *Phys Rev Lett* 86 : 3903-3906

- Smit MK, van Dam C (1996) PHASAR-Based WDM Devices, Principles, Design and Applications. IEEE J Sel Topics in Quant Electronics 2 : 236-250
- Smith CJM, Benisty H, Olivier S, Rattier M, Weisbuch C, Krauss TF, De La Rue RM, Houdré R, Oesterle U (2000a) Low-loss channel waveguides with two-dimensional photonic crystal boundaries. Appl Phys Lett 77 : 2813-2815
- Smith CJM, Krauss T.F, Benisty H, Rattier M, Weisbuch C, Oesterle U, Houdré R (2000b) Directionnally dependent confinement in photonic-crystal microcavities. J Opt Soc Am B 17 : 2043-2051
- Smith CJM, De La Rue RM, Rattier M, Olivier S, Benisty H, Weisbuch C, Krauss TF, Houdré R, Oesterle U (2001) Coupled guide and cavity in a two-dimensional photonic crystal. Appl Phys Lett 78 : 1487-1489
- Smith CM, Venkataraman N, Gallagher MT, Müller D, West JA, Borrelli NF, Allan DC, Koch KW (2003) Low-loss hollow-core silica/ air photonic bandgap fibre. Nature 424 : 657-659
- Smith DR, Padilla WJ, Vier DC, Nemat-Nasser S, Schultz S (2000b) Composite medium with simultaneously negative permeability and permittivity. Phys Rev Lett 84 : 4184-4187
- Smith DR, Kroll N (2000c) Negative Refractive Index in Left-Handed Materials. Phys Rev Lett 85 : 2 2933-2936
- Snoeks E, Blaaderen A, van Dillen T, van Kats CM, Velikov K, Brongersma L, Polman A, Colloidal assemblies modified by ion radiation. Nucl Instr Methods Phys Res, Sect B Beam interact Mater Atoms : 178 : 62-68
- Snyder AW, Love JD (1983) Optical Waveguide Theory. Chapman & Hall,
- Soto-Crespo JM, Nieto-Vesperinas M (1989) Electromagnetic scattering from very rough random surfaces and deep reflection gratings. J Opt Soc Am A 6 : 367-384
- Srinivasarao M, Collings D, Philips A, Patel S (2001) Three-dimensionally ordered array of air bubbles in a polymer film. Science 292 : 79-83
- STARTIGER (Space Technology Advancements by Resourceful Targeted & Innovative Groups of Expert and Researchers) (2003) THz Imaging and Technology. <http://www.startiger.org/tech.htm>,
- Stefanou N, Modinos A (1998) Impurity bands in photonic insulator. Phys Rev B 57 : 12127-12133
- Sun HB, Matsuo S, Misawa H (1999) Three-dimensional photonic crystal structures achieved with two-photon-absorption, photopolymerisation of resin. Appl Phys Lett 74 : 786-788
- Suzuki M, Yokoyama H, Brorson SD, Ippen EP (1991) Observation of spontaneous lifetime change of dye-containing Langmuir-Blodgett films in optical microcavities. Appl Phys Lett 58 : 998-
- Suzuki T, Yu P (1998) Complex elastic wave band structures in three-dimensional periodic elastic media. Mech Phys Solids 46 : 115-138
- Taflove A (1995) Computational Electrodynamics: the Finite-Difference Time-Domain method. Artech House, Boston
- Taillaert D, Bogaerts W, Bienstman P, Krauss TF, Daele PV, Moerman I, Vertsuyft S, Meesel KD, Baets R (2002) An Out-of-Plane Grating Coupler for Efficient Butt-Coupling Between Planar Waveguides and Single-Mode Fibers. IEEE J. Quant Electron 38 : 949-955

- Talneau A, Gouezigou LL, Bouadma N (2001) Quantitative measurements of low propagation losses at $1.55 \mu\text{m}$ on planar photonic crystal waveguides. *Optics Lett* 26 : 1259-1261
- Talneau A, Lalanne P, Agio M, Soukoulis CM (2002) Low-reflection photonic-crystal taper for efficient coupling between guide sections of arbitrary widths. *Opt Lett* 27 : 1522-1524
- Tamir T (ed) (1990) Guided Wave Optoelectronics. Springer Verlag, Heidelberg
- Temelkuran B, Bayindir M, Özbay E, Biswas R, Sigalas MM, Tuttle G, Ho KM (2000) Photonic crystal-based resonant antenna with a very high directivity. *J Appl Phys* 87 : 603-605
- Tezuka T, Nunoue SY, Yoshida H, Noda T (1993) Spontaneous emission enhancement in pillar-type microcavities. *Jpn J Appl Phys* 32 : L54-L57
- Thevenot M, Cheype C, Reineix A, Jecko B (1999) Directive photonic bandgap antennas. *IEEE Trans Microwave Theory and Tech* 47 : 2115-
- Thomas H, Morfill G, Demmel V, Goree J (1994) Plasma crystal: coulomb crystallisation in a dusty plasma. *Phys Rev Lett* 73 : 652-655
- Toader O, John S (2001) Proposed Square spiral microfabrication architecture for large three-dimensional photonic band gap crystals. *Science* 292 : 1133-1135
- Tretyakov SA (2001) Meta-materials with wideband negative permittivity and permeability., *Microwave and Optical Technology Lett* 31 : 163-165
- Tsai YC, Pendry JB, Shung KWK (1999) Absolute three-dimensional photonic band gap in the infrared regime in woven structures. *Phys Rev B* 59 : R10401-R10404
- Tsang T, Olsson NA, Linke RA, Logan RA (1983) High-speed direct single-frequency modulation with large tuning note and frequency emission in cleaved-coupled-cavity microseiconductor lasers. *Appl Phys Lett* 42 : 650-
- Ulrich R (1967) Far infrared properties of metallic mesh and its complementary structure. *Infrared Phys* 7 : 37-55
- Ulrich R, Renk F, Genzel L (1963) Tunable submillimeter interferometers of the Fabry-Perot type. *IEEE Trans Microwave Theory and Techniques MTT-11* : 363-371
- Utaka K, Akiba S, Sakai K, Matsushima Y (1986) $\lambda/4$ -shifted InGaAsP/InP DFB lasers. *IEEE J Quant Electron QE-22* : 1042-1051
- Valanju PM, Walser RM, Valanju AP (2002) Wave Refraction in Negative-Index Media: Always positive and Very Inhomogeneous. *Phys Rev Lett* 88 : 187401
- Van Der Ziel JV (1975) Phase matched harmonic generation in a laminar structure with wave propagation in the plane of the layers. *Appl Phys Lett* 26 : 60-62
- Van Driel HM, Vos WH (2002) Multiple Bragg wave coupling in photonic-band-gap crystals. *Phys Rev B* 62 : 9872-9875
- Veselago VG (1964) Uspekhi Physicheskikh Nauk (in Russian) 92 : 517-526
- Veselago VG (1968) The electrodynamics of substances with simultaneously negative values of ϵ and μ . *Soviet Physics Uspekhi* 10 : 509-514
- Veselago VG (2002) About the wording of Fermat's principle for light propagation in media with negative refraction index (<http://physics.ucsd.edu/~drs/publications/veselago-preprint-2002.pdf>).
- Vlassis M, McPhedran RC, Nicorovici NA (1996) Radiation modes of multiple core fibres. *Opt Commun* 129 : 256-272
- Vlasov YA, Yao N, Norris DJ (1999) Synthesis of photonic crystals for optical wavelengths from semiconductor quantum dots. *Adv Mater* 11 : 165-169

- Vos WL, Driel HMV, Megens M, Koenderink AF, Imhof A (2001) Experimental probes of the optical properties of photonic crystals in Soukoulis CM (dir) Photonic Crystals and Light Localization in the 21st Century (pp. 191-218), Kluwer Academic Publishers, Dordrecht
- Vredenberg AM, Hunt NEJ, Schubert EF, Jacobson DC, Poate PM, Zydzik GJ (1993) Controlled atomic spontaneous emission from Er³⁺in a transparent Si/SiO₂ microcavity. Phys Rev Lett 71 : 517-
- Vuckovic J, Lonkar M, Mabuchi H, Scherer A (2001) Design of photonic crystal microcavities for cavity QED. Phys Rev E 65 : 016608-
- Vuckovic J, Loncar M, Mabuchi H, Scherer A (2002a) Optimization of the Q factor in photonic crystal microcavities. IEEE J Quant Electron 38 : 850-856
- Vuckovic J, Pelton M, Scherer A, Yamamoto Y (2002b) Optimization of three-dimensional micropost microcavities for cavity quantum electrodynamics. Phys Rev A 66 : R023808-
- Wadsworth WJ, Knight JC, Reeves WH, Russel PStJ (2000) Yb³⁺- doped photonic crystal fibre laser. Electron Lett 36 : 1452-1454
- Wannier GH (1937) The structure of electronic excitation levels in insulating crystals. Phys Rev 52 : 191-
- White T.P, Kuhlmeijer B, McPhedran RC, Maystre D, Renversez G, Martijn de Sterke C, Botten LC (2002) Multipole method for microstructured optical fibers I: formulation. J Opt Soc Am B 10 : 2322-2330
- Whittaker DM (2001) Classical treatment of parametric processes in a strong-coupling planar microcavity. Phys Rev B 63 : 193305-
- Whittaker DM, Culshaw IS (1999) Scattering-matrix treatment of patterned multilayer photonic structures. Phys Rev B 60 : 2610-2618
- Wiersma D, Bartolini P, Lagendijk A, Righini R (1997) Localization of light in a disordered medium. Nature 390 : 671-673
- Windisch R, Heremans P, Knobloch A, Kiesel P, Döhler GH, Dutta, B, Borghs G (1999) Light-emitting diodes with 31% external quantum efficiency by outcoupling of lateral waveguide modes. Appl Phys Lett 74 : 2256-2258
- Winn JN, Fink Y, Fan S, Joannopoulos J (1998) Omnidirectional reflection from a one-dimensional photonic crystal. Optics Letters 23 : 1573-1575
- Winn JN, Fan S, Joannopoulos JD, Ippen EP (1999) Interband transitions in photonic crystals. Phys Rev B 59 : 1551-1554
- Wood RG (1902) Optical resonances from granular films and fogs of the alkali metals. Phil Mag 6 : 396-
- Woodcock LV (1997) Entropy difference between the face-centred cubic and hexagonal close-packed crystal structures. Nature 385 : 141-143
- Wu L, Mazilu M, Karle T, Krauss TF (2002) Superprism phenomena in planar photonic crystal. J Lightwave Technol 38 : 915-918
- Xia Y, Gates B, Park SH (1999) Fabrication of three-dimensional photonic crystals for use in the spectral region from ultraviolet to near-infrared. J Lightwave Technol 17 : 1956-1962
- Yablonovitch E (1987) Inhibited spontaneous emission in solid state physics and electronics. Phys Rev Lett 58 : 2059-
- Yablonovitch E (1993) Photonic band-gap structures. J Opt Soc Am B 10 : 283-
- Yablonovitch E (1994) Photonic crystals. Journ. of Mod Phys 41 : 173-194

- Yablonovitch E, Gmitter T.J, Leung KM (1991a) Photonic band structures : the face-centered-cubic case employing non-spherical atoms. *Phys Rev Lett* 67 : 2295-
- Yablonovitch E, Gmitter T.J, Meade RD, Rappe AM, Brommer KD, Joannopoulos J (1991b) Donor and acceptor modes in photonic band structures. *Phys Rev Lett* 67 : 3380-
- Yamamoto Y (1991) Coherence, Amplification and Quantum Effects in Semiconductor Lasers. John Wiley & Sons, New-York
- Yamamoto Y, Slusher RE (1993) Optical processes in microcavities. *Physics Today* 46(6) : 66
- Yang FR, Ma KP, Qian Y, Itoh T (1999a) A uniplanar compact photonic-bandgap (UC-PBG) structure and its applications for microwave circuits. *IEEE Trans Microwave Theory and Tech* 47 : 1509-1514
- Yang FR, Ma KP, Qian Y, Itoh T (1999b) A novel TEM waveguide using uniplanar compact photonic bandgap (UC-PBG) structure. *IEEE Trans Microwave Theory and Tech* 47 : 2092-2098
- Yariv A (1989) Quantum Electronics. John Wiley & Sons, New York
- Yariv A, Xu Y, Lee RK, Scherer A (1999) Coupled-resonator optical waveguide: a proposal and analysis. *Optics Letters* 24 : 711-713
- Yee KS (1966) Numerical solution of initial boundary-value problems involving Maxwell equations in isotropic media. *IEEE Trans Antennas and Propagation* 14 : 302-307
- Yeh P (1988) Optical Waves in Layered Media. John Wiley & Sons, New York
- Yeh P, Yariv A (1976) Bragg Reflection Waveguides. *Opt Commun* 19 : 427-
- Yeh P, Yariv A, Marom E (1978) Theory of Bragg fiber. *J Opt Soc Am* 68(9) : 1196-1201
- Yokoyama H (1992) Physics and device applications of optical microcavities. *Science* 256 : 66-
- Yokoyama H (1995a) Spontaneous Emission and Laser Oscillation in Microcavities. CRC Press, Boca Raton
- Yokoyama H, Brorson SR (1989) Rate equation analysis of microcavity lasers. *J Appl Phys* 66 : 4801-
- Yokoyama H, Nambu Y, Kawakami T (1995b) Controlling spontaneous emission and microcavities in : Burstein E, Weisbuch (dir.) Confined electrons and photons : New physics and applications. Plenum, New-York
- Yoshie T, Vuckovic J, Scherer A, Chen H, Deppe D (2001) High-quality two-dimensional photonic crystal slab cavities. *Appl Phys Lett* 79 : 4289-
- Yoshie T, Shchekin O, Chen H, Deppe D, Scherer A (2002) Quantum dot photonic crystal lasers. *Electron Lett* 38 : 967-
- Yoshino, K, Shimoda Y, Kawagishi Y, Nakayama K, Ozaki M (1999) Temperature tuning of the stop band in transmission spectra of liquid-crystal infiltrated synthetic opal as tunable photonic crystal. *Appl Phys Lett* 75 : 932-934
- Youssif HA, Köhler S (1988) Scattering by two penetrable cylinders at oblique incidence. I. The analytical solution. *J Opt Soc Am A* 5 : 1085-1096
- Yuan Z, Kardynal B, Stevenson R, Shields A, Lobo C, Cooper K, Beattie N, Ritchie D, Pepper M (2002) Electrically driven single photon source. *Science* 295 : 102-
- Zakhidov AA, Baughman RH, Khayrullin II, Udom IA, Kozlov M, Eradat N, Vardeny VZ, Sigalas M, Biswas R (2001) Three-dimensionally periodic conductive nanostructures: network versus cermet topologies for metallic PBG. *Synthetic Metals* 116 : 419-426
- Zavieh L, Mayer ThS (1999) Demonstration of a three-dimensional simple-cubic infrared photonic crystal. *Appl Phys Lett* 75 : 2533-2535

- Zhang WY, Lei XY, Wang ZI, Zheng DG, Tam WY, Chan CT, Sheng P (2000) Robust Photonic Band Gap from Tunable Scatterers. *Phys Rev Lett* 84 : 2853-2856
- Zhang X, Zhang ZQ, Chan CT. (2001) Absolute photonic band gaps in 12-fold symmetric photonic crystals. *Phys Rev B* 63 : (R)081105-
- Zhou J, Zhou Y, Ng SL, Zhang HX, Que WX, Lam YL, Chan YC, Kam CH (2000) Three-dimensional photonic band gap structure of a polymer-metal composite. *Appl Phys Lett* 76 : 3337-3339
- Zijlstra ES, Janssen T (2000) Non-spiky density of states of an icosahedral quasicrystal. *Europhys Lett* 52 : 578-583
- Ziman JM (1972) Principles of the Theory of Solids. Cambridge University Press, Cambridge
- Ziolkowski RW, Heyman E (2001) Wave propagation in media having negative permittivity and permeability. *Phys Rev E* 64 : 056625-
- Zolla F, Felbacq D, Guizal B (1998) A remarkable diffractive property of photonic quasicrystals. *Optics Commun* 148 : 6-10
- Zoorob ME, Charleton MD, Parker GJ, Baumberg JJ, Netti MC (2000) Complete and absolute photonic bandgaps in highly symmetric photonic quasicrystals embedded in low refractive index materials. *Mater Sci Eng B* 74 : 168-174